Transactions of the ASME

Journal of Applied Mechanics (ISSN 0021-8936) is edited and published quarterly at the offices of The American Society of Mechanical Engineers, United Engineering Center, 345 E. 47th St., New York, N. Y. 10017. ASME-TWX No. 710-581-5267, New York. Second Class postage paid at New York, N. Y., and at additional mailing offices.

CHANGES OF ADDRESS must be received at Society headquarters seven weeks before they are to be effective. Please send old label and new address.

PRICES: To members, $30.00, annually; to nonmembers, $60.00. Single copies $20.00 each. Add $5.00 for postage to countries outside the United States and Canada.

INDEXED by the Engineering Index, Inc.

Journal of Applied Mechanics

Published Quarterly by The American Society of Mechanical Engineers

VOLUME 48 • NUMBER 3 • SEPTEMBER 1981

(Contents continued on Page 688)

CONTENTS (CONTINUED)

DESIGN DATA AND METHODS

BRIEF NOTES

DISCUSSIONS

BOOK REVIEWS

(Contents continued on inside Back Cover)

ERRATA

J. Strigberger[1]
Graduate Student.

A. Plotkin
Professor.
Mem. ASME

Department of Aerospace Engineering,
University of Maryland,
College Park, Md. 20742

A Numerical Study of Nonaxisymmetric Stokesian Flow in a Circular Tube

A numerical study of the nonaxisymmetric Stokesian flow of a Newtonian fluid in a rigid circular tube of fixed radius has been performed. The analysis presented here is an integral part of the problem of modeling the flow of blood near the ostia of the intercostal arteries of rabbits in order to study a possible factor in the initiation of atherosclerosis. The method of lines is used to reduce the mathematical problem to one of solving a system of first-order ordinary differential equations along lines parallel to the tube axis. Solutions are obtained analytically using matrix eigenvalue techniques for the first two Fourier components of the flow and the accuracy of the numerical method is verified by suitable comparison with the results of independent computations.

Introduction

From a fluid-dynamic point of view, the blood vessels of the human circulatory system comprise a complex network of flexible round tubes through which there is a three-dimensional, pulsatile, and usually laminar flow of a non-Newtonian fluid (Mueller [1]). A basic problem in hemodynamics is therefore the study of laminar flows in round tubes.

The present work is concerned with the analysis of a simple mathematical model of this problem; it examines the steady, zero-Reynolds number and nonaxisymmetric flow of a Newtonian fluid inside a rigid circular tube of constant radius. The Newtonian fluid approximation for blood is considered reasonable in all but the smallest of blood vessels (Lighthill [2]). In these, the particulate nature of blood asserts itself, thereby complicating the rheology. Although the steady flow approximation ignores effects due uniquely to pulsatility, such as wave patterns, temporal instabilities, and the dynamic effects of flexible walls, it does give a measure of the steady component of the real flow. The circular geometry model is simple yet more realistic than the more common two-dimensional channel analogies. Although the Reynolds number of blood flow in humans can go as high as 10,000 in the aorta, the Stokesian flow approximation is a logical first one for the modeling of the "slower" flows in and near the smaller blood vessels, especially since the low Reynolds number there may invalidate the use of boundary-layer methods.

Two examples of specific applications of the foregoing problem are Lew and Fung's low-Reynolds number entry length problem [3] and Sobey's mathematical model of the flow near the ostia of the intercostal arteries of rabbits [4].

Lew and Fung analyzed axisymmetric flows in the entry regions of small blood vessels for Reynolds numbers too low for boundary-layer analysis to be valid [3, 5]. They derived an analytical solution to the problem of finding the velocity distribution inside a circular cylinder of fixed radius due to an arbitrary axisymmetric velocity distribution at the entrance. The present work thus represents a generalization of Lew and Fung's zero-Reynolds number problem to nonaxisymmetric flows.

Sobey was interested in examining the fluid-dynamic shear stresses near the ostia of the intercostal arteries of rabbits. The fluid-dynamic forces on arterial walls affect the structure and function of these surfaces and it has been assumed that they are a factor in the initiation of atherosclerosis, a disease characterized by the accumulation of plaques of fat on the arterial walls (Fry [6]). These plaques show a predilection for forming near geometric irregularities such as branches, where large shear gradients undoubtedly exist. In vivo measurements near vessel walls have poor resolution (Nerem, et al. [7]), thereby necessitating the use of physical and mathematical models. Since the intercostal arteries are much smaller and sustain a much lower flow rate than the aorta, from which they branch out, Sobey chose to model the situation as that of a steady laminar flat plate boundary-layer flow past the opening of a small tube at right angles to the plate sucking in a small portion of the outer flow. He further simplified the problem by invoking the Stokesian flow approximation inside the side tube and in the boundary-layer flow very near the mouth of the tube, thereby decoupling the problems of determining the solutions near and far from the hole and also linearizing the former. He first solved the two-dimensional analogy by a combi-

[1] Current address: Department of Aeronautics and Astronautics, Stanford University, Stanford, Calif. 94305.

Contributed by the Applied Mechanics Division for presentation at the Winter Annual Meeting, Washington, D. C., November 15–20, 1981, of THE AMERICAN SOCIETY OF MECHANICAL ENGINEERS.

Discussion on this paper should be addressed to the Editorial Department, ASME, United Engineering Center, 345 East 47th Street, New York, N. Y. 10017, and will be accepted until December 1, 1981. Readers who need more time to prepare a discussion should request an extension from the Editorial Department. Manuscript received by ASME Applied Mechanics Division, June, 1980; final revision, February, 1981. Paper No. 81-WA/APM-16.

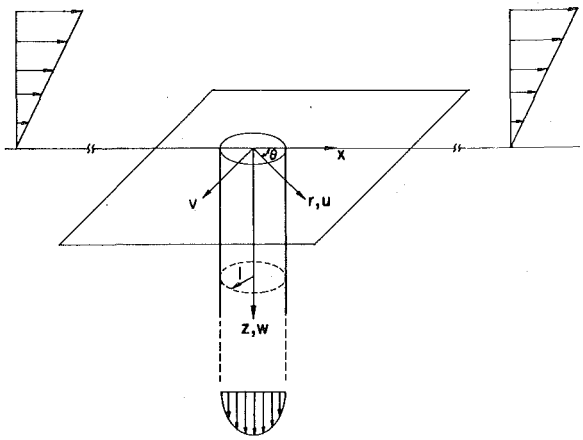

Fig. 1 Flow configuration and coordinate system

nation of analytical and numerical methods, and, for the three-dimensional problem, he found one analytical solution valid far away from the hole and another one, requiring knowledge of the velocity distribution on the hole itself, valid in the vicinity of the hole. However, determining the velocities on the hole requires a solution for the flow inside the tube and a matching of the stresses on the hole. It is thereby seen how the nonaxisymmetric version of Lew and Fung's zero-Reynolds number pipe entry flow problem is a part of Sobey's intercostal mouth model. The analysis of Stokesian flow in a rigid circular tube of fixed radius, in this context, is the subject of what follows.

The Boundary-Value Problem

The problem at hand is that of determining the velocity and pressure distributions of the Stokesian flow in the region consisting of a circular tube of constant radius at right angles to a semi-infinite space with a uniform linear shear flow on the boundary of the latter far away from the mouth of the tube and a prescribed flow rate down the tube. This situation is depicted graphically in Fig. 1.

The foregoing is a linear boundary-value problem governed by the equation of continuity, Stokes' equations of motion and the boundary conditions shown in Fig. 1; in cylindrical coordinates the nondimensional equations are

$$\frac{\partial u}{\partial r}+\frac{u}{r}+\frac{1}{r}\frac{\partial v}{\partial \theta}+\frac{\partial w}{\partial z}=0 \tag{1}$$

$$\frac{\partial^2 u}{\partial r^2}+\frac{1}{r}\frac{\partial u}{\partial r}+\frac{1}{r^2}\frac{\partial^2 u}{\partial \theta^2}+\frac{\partial^2 u}{\partial z^2}-\frac{2}{r^2}\frac{\partial v}{\partial \theta}-\frac{u}{r^2}-\frac{\partial p}{\partial r}=0 \tag{2}$$

$$\frac{\partial^2 v}{\partial r^2}+\frac{1}{r}\frac{\partial v}{\partial r}+\frac{1}{r^2}\frac{\partial^2 v}{\partial \theta^2}+\frac{\partial^2 r}{\partial z^2}+\frac{2}{r^2}\frac{\partial u}{\partial \theta}-\frac{v}{r^2}-\frac{1}{r}\frac{\partial p}{\partial \theta}=0 \tag{3}$$

$$\frac{\partial^2 w}{\partial r^2}+\frac{1}{r}\frac{\partial w}{\partial r}+\frac{\partial^2 w}{\partial z^2}+\frac{1}{r}\frac{\partial^2 w}{\partial \theta^2}-\frac{\partial p}{\partial z}=0 \tag{4}$$

$$u(1,\theta,z)=v(1,\theta,z)=w(1,\theta,z)=0 \quad z\geq 0 \tag{5}$$

$$u(r,\theta,z)=v(r,\theta,z)=0, \quad z\to\infty \tag{6}$$

$$w(r,\theta,z)=W_m(1-r^2), \quad z\to\infty \tag{7}$$

$$u(r,\theta,0)=U(r,\theta), \quad v(r,\theta,0)=V(r,\theta), \quad w(r,\theta,0)=W(r,\theta) \tag{8}$$

where lengths have been scaled by R, the tube radius, velocities by a reference value W_r, and pressure by $\mu W_r/R$, where μ is the viscosity coefficient.

To avoid the large computational "volumes" required for a fully discrete three-dimensional numerical solution, the θ-dependence is separated out of the problem by expressing the dependent variables as Fourier series in $\cos\theta$ or $\sin\theta$, as suggested by Pedley and Moore [8, 9]; limiting ourselves to flow symmetric about the plane $y = 0$, as for Sobey's problem, $\mathbf{v}$ and p are written as

$$\begin{aligned}
u(r,\theta,z)&=\sum_{j=0}^{\infty}u_j(r,z)\cos j\theta\\
v(r,\theta,z)&=\sum_{j=0}^{\infty}v_j(r,z)\sin j\theta\\
w(r,\theta,z)&=\sum_{j=0}^{\infty}w_j(r,z)\cos j\theta\\
p(r,\theta,z)&=\sum_{j=0}^{\infty}p_j(r,z)\cos j\theta
\end{aligned} \tag{9a}$$

$$\begin{aligned}
U(r,\theta)&=\sum_{j=0}^{\infty}U_j(r)\cos j\theta\\
V(r,\theta)&=\sum_{j=0}^{\infty}V_j(r)\sin j\theta\\
W(r,\theta)&=\sum_{j=0}^{\infty}W_j(r)\cos j\theta
\end{aligned} \tag{9b}$$

Substituting these expressions into equations (1)–(8) and collecting coefficients of $\cos j\theta$ and $\sin j\theta$ yields

$$\frac{\partial u_j}{\partial r}+\frac{u_j}{r}+\frac{jv_j}{r}+\frac{\partial w_j}{\partial z}=0 \tag{10}$$

$$\frac{\partial^2 u_j}{\partial r^2}+\frac{1}{r}\frac{\partial u_j}{\partial r}-\frac{j^2u_j}{r^2}+\frac{\partial^2 u_j}{\partial z^2}-\frac{u_j}{r^2}-\frac{2jv_j}{r^2}-\frac{\partial p_j}{\partial r}=0 \tag{11}$$

$$\frac{\partial^2 v_j}{\partial r^2}+\frac{1}{r}\frac{\partial v_j}{\partial r}-\frac{j^2v_j}{r^2}+\frac{\partial^2 v_j}{\partial z^2}-\frac{v_j}{r^2}-\frac{2ju}{r^2}+\frac{jp_j}{r}=0 \tag{12}$$

$$\frac{\partial^2 w_j}{\partial r^2}+\frac{1}{r}\frac{\partial w_j}{\partial r}-\frac{j^2w_j}{r^2}+\frac{\partial^2 w_j}{\partial z^2}-\frac{\partial p_j}{\partial z}=0 \tag{13}$$

$$u_j(1,z)=v_j(1,z)=w_j(1,z)=0 \quad z\geq 0 \tag{14}$$

$$u_j(r,z)=v_j(r,z)=0 \quad z\to\infty \tag{15}$$

for $j = 0, 1, 2, \ldots$.

$$\begin{aligned}
w_0(r,z)&=W_m(1-r^2) \quad z\to\infty\\
w_j(r,z)&=0 \quad z\to\infty \quad j\neq 0
\end{aligned} \tag{16}$$

$$u_j(r,0)=U_j(r), \quad v_j(r,0)=V_j(r), \quad w_j(r,0)=W_j(r) \tag{17}$$

Solutions will be considered for the cases $j = 0$ and $j = 1$. These will henceforth be denoted as the $j0$ and $j1$ problems, respectively. It should be noted that the $j0$ component of the flow is its axisymmetric part and is entirely due to the nonzero volume-flux through the tube (found by integrating the axisymmetric velocity component w across the tube). On the other hand, the $j1$ component is purely a result of the shear flow along the plate far from the hole.

The aforementioned solution will be complete if the initial velocity profiles satisfy

$$U_j(r)=V_j(r)=W_j(r)=0 \quad j>1$$

If this is not the case, the solutions for $j > 1$ can be calculated in a straightforward manner with the technique discussed below for the solution of the $j1$ problem.

Consider the solution of the $j0$ and $j1$ problems in the tube only, what Sobey has called the lower basement. The boundary condition at $z = 0$ (equation (8)) involves the specification of nearly arbitrary but "reasonable" velocity distributions there for $r \leq 1$. The $j0$ and $j1$ lower basement boundary-value problems are therefore given by

$$\frac{\partial u_0}{\partial r}+\frac{u_0}{r}+\frac{\partial w_0}{\partial z}=0 \tag{18}$$

$$\frac{\partial^2 u_0}{\partial r^2}+\frac{1}{r}\frac{\partial u_0}{\partial r}-\frac{u_0}{r^2}+\frac{\partial^2 u_0}{\partial z^2}-\frac{\partial p_0}{\partial r}=0 \tag{19}$$

$$\frac{\partial^2 w_0}{\partial r^2}+\frac{1}{r}\frac{\partial w_0}{\partial r}+\frac{\partial^2 w_0}{\partial z^2}-\frac{\partial p_0}{\partial z}=0 \tag{20}$$

$$u_0(r,0)=U_0(r), \quad w_0(r,0)=W_0(r) \tag{21}$$

$$u_0(1, z) = w_0(1, z) = 0 \tag{22}$$

$$u_0(r, z) = 0, \quad w_0(r, z) = W_m(1 - r^2) \quad z \to \infty \tag{23}$$

and

$$\frac{\partial u_1}{\partial r} + \frac{u_1 + v_1}{r} + \frac{\partial w_1}{\partial z} = 0 \tag{24}$$

$$\frac{\partial^2 u_1}{\partial r^2} + \frac{1}{r}\frac{\partial u_1}{\partial r} - \frac{2}{r^2}(u_1 + v_1) + \frac{\partial^2 u_1}{\partial z^2} - \frac{\partial p_1}{\partial r} = 0 \tag{25}$$

$$\frac{\partial^2 v_1}{\partial r^2} + \frac{1}{r}\frac{\partial v_1}{\partial r} - \frac{2}{r^2}(u_1 + v_1) + \frac{\partial^2 v_1}{\partial z^2} + \frac{p_1}{r} = 0 \tag{26}$$

$$\frac{\partial^2 w_1}{\partial r^2} + \frac{1}{r}\frac{\partial w_1}{\partial r} - \frac{w_1}{r^2} + \frac{\partial^2 w_1}{\partial z^2} - \frac{\partial p_1}{\partial z} = 0 \tag{27}$$

$$u_1(r, 0) = U_1(r), \quad v_1(r, 0) = V_1(r), \quad w_1(r, 0) = W_1(r) \tag{28}$$

$$u_1(1, z) = v_1(1, z) = w_1(1, z) = 0 \tag{29}$$

$$u_1(r, z) = v_1(r, z) = w_1(r, z) = 0 \quad z \to \infty \tag{30}$$

with the direction of the z-axis having been reversed for convenience.

It is noted that far downstream in the tube, for $z \to \infty$, the foregoing equations yield the following conditions on the pressure:

$$\frac{dp_0}{dz} = -4W_m, \quad p_1 = 0 \tag{31}$$

Some of the aforementioned differential equations take on special forms on the axis of the tube, i.e, at $r = 0$. One method of evaluating these equations on the axis is that of expanding them in Taylor series for small r and constant z and then collecting coefficients of like powers of r as suggested by Pedley [8]. The details of these expansions and the resulting equations for $j = 0$ and $j = 1$ may be found in Strigberger [10].

As mentioned in the Introduction, Lew and Fung solved the $j0$ problem analytically. A specific aim of the present work is therefore the solution of the $j1$ problem.

The Method of Lines

The method of lines consists of approximating a set of partial differential equations by a system of ordinary differential equations. This is achieved by keeping one coordinate continuous and approximating the derivatives in all other directions by finite differences. The approximate solutions to the partial differential equations are thus obtained along lines parallel to the axis of the continuous coordinate.

For the partial differential equations of the lower basement problem, if the derivatives in the r-direction are replaced by finite differences, there results a system of ordinary differential equations which are first order, linear, and homogeneous and have constant coefficients. The solution to such a system can be found analytically using matrix eigenvalue methods (Boyce and dePrima [11]). However, it may not be possible to exactly satisfy all of the velocity boundary conditions at $z = 0$ and $z = \infty$. Fortunately, the amount by which the calculated boundary conditions deviate from the exact ones is very small if the finite-difference representations themselves are reasonably accurate for the solution which the given boundary conditions imply.

Before the method of lines was applied to the $j1$ component of the lower basement, it was tested on a $j0$ problem for which an analytical solution was known, Lew and Fung's case. This is an exacting test due to the difficulty in modeling the $z = 0$ conditions, $U_0 = 0$, $W_0 = 1$, on a finite number of lines. The results obtained were reasonably accurate and since the $j1$ solution will be compared to the results of a finite-difference solution, we proceed directly to the $j1$ case.

The first step in applying the method is to divide the domain into M axial strips of width Δr, thereby producing $M + 1$ lines at $r_i = i\Delta r$, $i = 0, 1, 2, \ldots, M - 1, M$. Next, all r-derivatives in equations (24)–(27) are replaced by finite differences of second-order accuracy with constant Δr. (Note that the subscript $j = 1$ is dropped from the dependent variables.) The variables

$$\dot{u}_i = \frac{du_i}{dz}, \quad \dot{v}_i = \frac{dv_i}{dz} \tag{32}$$

are introduced. The following conditions at $r = 0$ are to be satisfied:

$$v(0, z) = -u(0, z)$$

$$w(0, z) = p(0, z) = 0$$

$$\frac{\partial^2 u}{\partial r^2} + \frac{\partial^2 u}{\partial z^2} - \frac{\partial^2 v}{\partial r^2} - \frac{\partial p}{\partial r} = 0 \tag{33}$$

The resulting ordinary differential equations are ($i = 1, 2, \ldots, M - 1$):

r-Momentum:

$$\frac{d\dot{u}_i}{dz} + u_{i-1}\left(\frac{1}{(\Delta r)^2} - \frac{0.5}{r_i \Delta r}\right) + u_i\left(-\frac{2}{(\Delta r)^2} - \frac{2}{(r_i)^2}\right) + u_{i+1}\left(\frac{1}{(\Delta r)^2} + \frac{0.5}{r_i \Delta r}\right) + v_i\left(-\frac{2}{r_i{}^2}\right) + p_{i-1}\left(\frac{0.5}{\Delta r}\right) + p_{i+1}\left(-\frac{0.5}{\Delta r}\right) = 0 \tag{34}$$

$$\frac{d\dot{u}_0}{dz} + \dot{u}_0\left(\frac{4}{(\Delta r)^2}\right) + u_1\left(-\frac{5}{(\Delta r)^2}\right) + u_2\left(\frac{4}{(\Delta r)^2}\right) + u_3\left(-\frac{1}{(\Delta r)^2}\right) + v_1\left(\frac{5}{(\Delta r)^2}\right) + v_2\left(-\frac{4}{(\Delta r)^2}\right) + v_3\left(\frac{1}{(\Delta r)^2}\right) + p_1\left(-\frac{2}{\Delta r}\right) + p_2\left(\frac{0.5}{\Delta r}\right) = 0 \quad \text{at} \quad r = 0 \tag{35}$$

θ-Momentum:

$$\frac{d\dot{v}_i}{dz} + u_i\left(-\frac{2}{r_i{}^2}\right) + v_{i-1}\left(\frac{1}{(\Delta r)^2} - \frac{0.5}{r_i \Delta r}\right) + v_i\left(-\frac{2}{(\Delta r)^2} - \frac{2}{r_i{}^2}\right) + v_{i+1}\left(\frac{1}{(\Delta r)^2} + \frac{0.5}{r_i \Delta r}\right) + p_i\left(\frac{1}{r_i}\right) = 0 \tag{36}$$

z-Momentum:

$$\frac{dp_i}{dz} + \dot{u}_{i-1}\left(\frac{-0.5}{\Delta r}\right) + \dot{u}_i\left(\frac{1}{r_i}\right) + \dot{u}_{i+1}\left(\frac{0.5}{\Delta r}\right) + \dot{v}_i\left(\frac{1}{r_i}\right) + w_{i-1}\left(-\frac{1}{(\Delta r)^2} + \frac{0.5}{r_i \Delta r}\right) + w_i\left(\frac{2}{(\Delta r)^2} + \frac{1}{r_i{}^2}\right) + w_{i+1}\left(-\frac{1}{(\Delta r)^2} - \frac{0.5}{r_i \Delta r}\right) = 0 \tag{37}$$

Continuity:

$$\frac{dw_i}{dz} + u_{i-1}\left(-\frac{0.5}{\Delta r}\right) + u_i\left(\frac{1}{r_i}\right) + u_{i+1}\left(\frac{0.5}{\Delta r}\right) + v_i\left(\frac{1}{r_i}\right) = 0 \tag{38}$$

$$\frac{du_i}{dz} - \dot{u}_i = 0; \quad \frac{dv_i}{dz} - \dot{v}_i = 0 \tag{39}$$

In addition, it is necessary to account for $p(1, z) = p_M(z)$. Any one of the momentum equations can be applied at $r = 1$ to this effect; using the r or θ-momentum equations puts $p_M(z)$ in terms of the other variables at $r = 1$, while employing the z-momentum equation yields an additional ordinary differential equation,

$$\frac{dp_M}{dz} + w_{M-3}\left(\frac{1}{(\Delta r)^2}\right) + w_{M-2}\left(-\frac{4}{(\Delta r)^2} - \frac{0.5}{\Delta r}\right) + w_{M-1}\left(\frac{5}{(\Delta r)^2} + \frac{2}{\Delta r}\right) = 0 \tag{40}$$

The previous system can be expressed in matrix form as

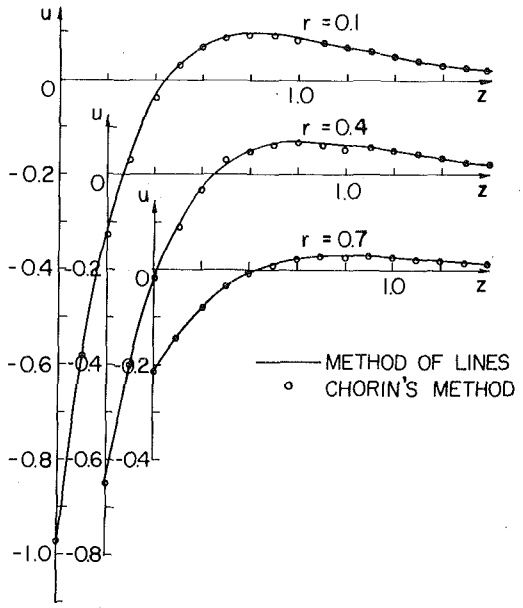

Fig. 2 Comparison between present method of lines results and those obtained using Chorin's [13] method

$$\frac{d\{\phi\}}{dz} + [A]\{\phi\} = 0 \tag{41}$$

where

$$\{\phi(z)\} = \{\dot{u}_0, \dot{u}_1, \dot{u}_2, \ldots, \dot{u}_{M-1};\quad \dot{v}_1, \dot{v}_2, \ldots, \dot{v}_{M-1};$$
$$u_0, u_1, u_2, \ldots, u_{M-1};\quad v_1, v_2, \ldots, v_{M-1};$$
$$w_1, w_2, \ldots, w_{M-1};\quad p_1, p_2, \ldots, p_{M-1}, p_M\}, \tag{42}$$

$[A]$ is the system matrix; p_M is excluded if the z-momentum equation is not employed at $r = 1$. The total number of ordinary differential equations in the system is thus $N = 2 + 6(M - 1) = 6M - 4$ or $N = 2 + 6(M - 1) + 1 = 6M - 3$, depending upon whether or not the z-momentum equation is applied at $r = 1$.

When all the eigenvalues of $[A]$ are distinct, the general solution of equation (41) is given by

$$\phi_i(z) = \sum_{j=1}^{N} r_{ij} c_j e^{-\lambda_j z} \tag{43}$$

where the λ_j are the eigenvalues, the r_{ij} are the components of the "modal" matrix $[R]$, whose columns are the eigenvectors of $[A]$, and the c_j's are determined from the boundary conditions. c_j is set equal to zero whenever the real part of λ_j is zero or negative to insure that all of the variables will vanish asymptotically far downstream.

Before considering the determination of the rest of the c_j's, it should be noted that an interesting feature of the method of lines is that the general solution of the differential equations is found independently of any consideration of the boundary conditions. This means that once the eigensolution of $[A]$ is found, it can be used over and over again with any set of reasonable velocity boundary conditions. This property, along with the fact that the size of $[A]$ is roughly only the square root of that of the type of matrix dealt with in two-dimensional finite-difference schemes makes the method of lines very fast computationally.

The nontrivial c_j's are determined from the specification of $u_0, u_1, \ldots, u_{M-1}, v_1, v_2, \ldots, v_{M-1}, w_1, w_2, \ldots, w_{M-1}$ or their derivatives at $z = 0$. There are therefore $N_e = 1 + 3(M - 1) = 3M - 2$ linear algebraic equations in the c_j's. If the number of eigenvalues with positive real parts is less than N_e, it is possible to satisfy all of the velocity conditions at $z = 0$ only in a least squares or other approximate sense.

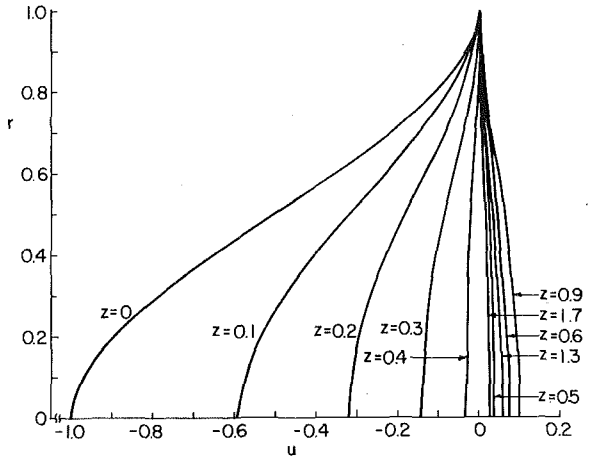

Fig. 3 *u* velocity profiles for *j*1 problem versus distance *z* down the tube

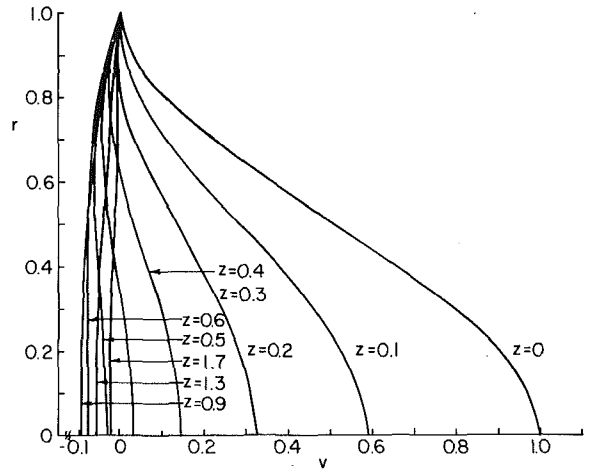

Fig. 4 *v* velocity profiles for *j*1 problem versus distance *z* down the tube

Results

The previous method for the $j1$ problem was applied to an example with the following entrance plane velocity (equation (28)):

$$U_1(r) = -1 + 3r^2 - 2r^3 = -V_1(r)$$
$$W_1(r) = 0$$

This velocity is in the x-direction and satisfies the continuity equation at both $r = 0$ and $r = 1$.

The computational processes were split into two parts. The first part consisted of generating the system matrix $[A]$ and calculating its eigenvalues and eigenvectors. The latter was done by the Eispac subroutine package using its option for real general matrices [12]. This eigensolution was then used to calculate the nontrivial c_j's of equation (41) and to evaluate the velocities on the "lines" at any desired value of z. All computations were carried out on an IBM 370/158 computer.

M was set equal to $10(\Delta r = 0.1)$. All three of the boundary conditions for $p(1, z)$ discussed earlier were tried; the resulting velocities in all three cases differed by no more than 0.005, so only one of these results is presented here, that for the scheme using the θ-momentum equation at $r = 1$. The eigensolution yielded a number of eigenvalues with positive real parts one less than the number of boundary conditions, so that it was necessary to resort to an approximate satisfaction of the boundary conditions using least squares at $z = 0$. The maximum error which resulted at $z = 0$ was only 0.0013.

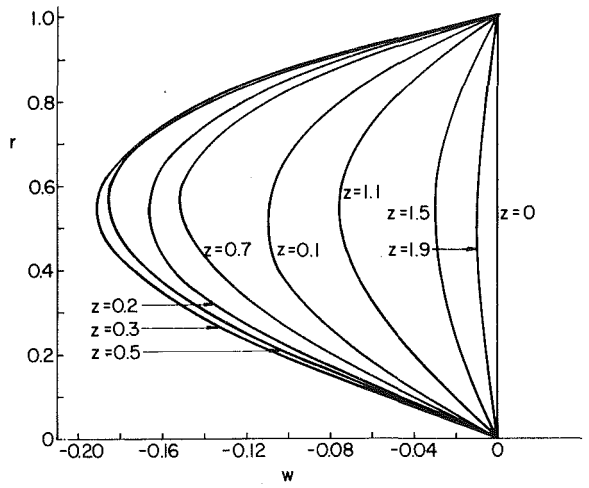

Fig. 5 w velocity profiles for j1 problem versus distance z down the tube

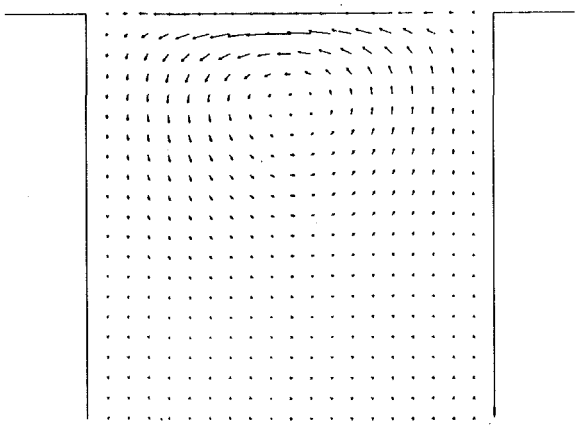

Fig. 6 Velocity vectors in plane $y = 0$ for j1 solution; x and z are positive to the right and downward, respectively

As a test of the method of lines solution, the foregoing example was also solved using a finite-difference approach, Chorin's [13] time-dependent method with artificial transient compressibility. Some results of both methods are presented in Fig. 2 and the agreement is seen to be excellent. The C.P.U. time required for the method of lines solution was approximately 37 sec for the eigensolution and 11 sec for the velocity calculation.

Velocity profiles for the three components u, v, and w are shown in Figs. 3–5 as they develop with increasing distance z down the tube. It is noted that the perturbations caused by the flow at $z = 0$ die out in a distance of the order of the tube radius, as was the case for the $j0$ example of Lew and Fung.

The solution for u and w is also used in Fig. 6 where the velocity vectors in the plane $y = 0$ are presented, thereby showing the vertical eddy structure of the flow. It should be noted that this picture is valid in any radial plane except $\theta = \pi/2$ and $\theta = 3\pi/2$ since

$$u(r, \theta, z) = u_1(r, z) \cos \theta$$

$$w(r, \theta, z) = w_1(r, z) \cos \theta$$

for $j = 1$.

Conclusions

The Stokesian approximation for the steady incompressible low-Reynolds number flow of a Newtonian fluid in a rigid circular tube of fixed radius has greatly simplified the analysis of this problem. The deletion of the inertial terms and resultant linearization of the problem has led to the separation of the θ-dependence by Fourier analysis, thereby transforming the original three-dimensional problem into a set of independent two-dimensional ones. Given the rectangular domain of these problems, the absence of z-dependent coefficients of the unknowns and their derivatives in the governing differential equations and the homogeneity of the velocity boundary conditions at the wall, it has proven feasible to solve these problems in a semi-discrete fashion by the method of lines. Each set of partial differential equations has been approximated by a system of linear first-order homogeneous ordinary differential equations with constant coefficients which could be solved by matrix eigenvalue methods. Although it has become apparent that it is not always possible to satisfy the boundary conditions at the top and bottom exactly, any such error was found to be small for reasonable cases.

The method of lines was tested on Lew and Fung's problem of axisymmetric Stokesian flow in a semi-infinite tube. This was a difficult test because the nearly flat entry profile implied large curvatures and curvature gradients in the velocity distributions near the wall near the entrance. This would cause difficulties for any numerical method using low-order approximations and a small number of grid points, lines, finite elements, etc.

Although the range of M used was limited, slight improvements resulted from small increases in M. Unfortunately, the real-general-matrix option of the Eispac subroutine used to find the eigensolution broke down when trying the axisymmetric problem with $M = 15$. The matrix, $[A]$, although quite sparse, has a slightly complicated band structure, so that what is really needed for its eigensolution when M is large is a fairly general sparse matrix eigensolver.

A solution of an example of a nonaxisymmetric flow component by the method of lines was compared with the solution of the same problem by Chorin's time-dependent method of artificial compressibility. The two solutions compared very well.

For the present problem, the method of lines has three attractive features not found in iterative two-dimensional finite-difference methods. First, it does not require the decision of where to truncate the tube. Second, the eigensolution of the matrix $[A]$ can be found more rapidly than the steady-state solution of the two-dimensional finite-difference equations, owing to the fact that the order of $[A]$ is approximately only the square root of the size of the matrix representing the two-dimensional scheme. Third, for a fixed finite-difference scheme and number of lines but for any set of velocities at the ends, the eigensolution needs to be found but once; the velocities corresponding to any particular set of end conditions can be found from this eigensolution in about half a minute (on an IBM 370/158), typically, if the order of $[A]$ is less than 60.

Acknowledgment

This work was started while the first author (J.S.) was visiting the Department of Applied Mathematics and Theoretical Physics of the University of Cambridge. The authors wish to thank Drs. T. J. Pedley and D. Moore for their many helpful suggestions. The computing was carried out at the Computer Centers of the University of Cambridge and McGill University and their role is hereby acknowledged.

References

1 Mueller, T. J., "Application of Numerical Methods to Physiological Flows," *Numerical Methods in Fluid Dynamics*, eds., Wirz, H. J., and Smolderen, J. J., McGraw-Hill, New York, 1978.

2 Lighthill, M. J., *Mathematical Biofluid-Dynamics*, Society for Industrial and Applied Mathematics, 1975.

3 Lew, H. S., and Fung, Y. C., "On the Low Reynolds Number Entry Flow Into a Circular Cylindrical Tube," *Journal of Biomechanics*, Vol. 2, 1969, pp. 105–119.

4 Sobey, I. J., "Biofluid-Dynamics of Bifurcations," PhD Thesis, University of Cambridge, 1976.

5 Lew, H. S., and Fung, Y. C., "Entry Flow Into Blood Vessels at Arbitrary Reynolds Number," *Journal of Biomechanics*, Vol. 3, 1970, pp. 23–38.

6 Fry, D. L., "Hemodynamic Forces in Atherogenesis," *Cerebrovascular Diseases*, ed., Steinberg, P., Raven Press, 1976.

7 Nerem, R. M., et al., "Hot-Film Anemometer Velocity Measurements of Arterial Blood Flow in Horses," *Circulation Research*, Vol. 34, 1974, pp. 193–203.

8 Pedley, T. J., University of Cambridge: private communication.

9 Moore, D., University of Cambridge: private communication.

10 Strigberger, J., "A Numerical Study of Nonaxisymmetric Stokesian Flow in a Circular Tube," MS Thesis, Department of Aerospace Engineering, University of Maryland, 1979.

11 Boyce, W. E., and dePrima, R. C., *Elementary Differential Equations and Boundary-Value Problems*, Wiley, 1969.

12 EISPAC Manual, NATS Project, Argonne National Laboratory, July 1975.

13 Chorin, J. A., "A Numerical Method for Solving Incompressible Viscous Flow Problems," *Journal of Computational Physics*, Vol. 2, 1967, pp. 12–26.

Jonathan A. Laitone

On June 21, 1981; the author of this paper was killed in a tragic ice avalanche on Mount Rainier, Washington, U.S.A. At the time of his death, he was 27 and had just finished his first year of teaching at the University of Michigan. Jonathan was a remarkable man of many talents and exceptional warmth. We grieve this loss to his family, the loss to the mechanics community, and that the promising beginning of a scientific career was abruptly brought to an end.

C. S. Hsu, Technical Editor

J. A. Laitone

Department of Mechanical Engineering and Applied Mechanics, The University of Michigan, Ann Arbor, Mich. 48109

A Numerical Solution for Gas-Particle Flows at High Reynolds Numbers

Predicting the fluid mechanical characteristics of a gas-solid two-phase flow is critical for the successful design and operation of coal gasification systems, coal fired turbines, rocket nozzles, and other energy conversion systems. This work presents a general grid-free numerical solution which extends a numerical solution of the Navier-Stokes equations developed by Chorin to a solution suitable for unsteady or steady dilute gas-solid particle flows. The method is applicable to open or closed domains of arbitrary geometry. The capability of the method is illustrated by analyzing the flow of gas and particles about a cylinder. Good agreement is found between the numerical method and experiment.

1 Introduction

Aircraft turbines, catalytic cracking units, pulverized coal energy conversion systems, geothermal and MHD power are all fluid mechanical systems that suffer solid particle erosion. The financial loss associated with this type of erosion has led to many investigations of particular detailed problems [1–4].

In most industrial two-phase systems where erosion occurs, the distribution of erosive wear around the surface of the body must be determined. This requires a solution giving the particle velocity and position history; with this information an erosion model may be applied to determine the erosion distribution about the body. Generally, the collective motion of the particles is a desired solution as well as the gas motion; thus the two-phases are treated as separate mechanically interacting mediums.

The vast majority of problems involve two-dimensional subsonic flow. In this case the governing equations for the particle and gas phase are similar in appearance to the well-known Navier-Stokes equations of fluid mechanics. Although several calculational schemes have been developed for a general one-dimensional flow [5–7], much less research has been conducted for two-dimensional flow. The only general two-dimensional model is the "tank-and-tube" cellular approach developed by Crowe [8]. In this method the flow field is subdivided into a series of "tanks" connected to adjacent tanks by "tubes." Finite-difference equations are derived and solved with the appropriate boundary conditions using Gauss-Seidel successive substitution. This technique has been successfully applied to isothermal flow fields in cyclone separators [9] and electrostatic precipitators [10].

However, because of the high Reynolds number found in most industrial flows, the influence of viscosity is confined to narrow regions close to the surface of bodies. These small regions, which are initially invisible to a finite difference grid, grow larger—particularly if under the influence of an adverse pressure gradient. Qualitatively, the effects of these small regions of boundary-layer backflow are quite pronounced; the flow can become separated from the body by a region of reversed or recirculating flow. Finite-difference schemes produce unreliable results in this situation since the computer cannot store enough grid points falling within the boundary layer to predict boundary-layer growth and subsequent separation satisfactorily. Furthermore, it is often observed that in a boundary-layer large truncation errors lead to the formation of an artificial numerical viscosity [11].

A numerical scheme developed by Chorin [12] for gas flow only circumvents these difficulties. The scheme is grid free in that the vorticity within the fluid is partitioned into vortex "blobs" which are moved according to two components. One component is a random displacement of the vortex blob position; in this way the effect of viscous diffusion is modeled. The other component is a deterministic displacement found by moving the blobs according to their mutual interaction effects. This interaction is determined in a way similar to that in which the motion of point vortices interacting in an inviscid fluid is determined, according to the governing equations of classical hydrodynamics.

In this work Chorin's vortex technique is extended to a two-phase mixture. Apart from the capacity of the vortex method to simulate the physics of viscous fluids and the process of vorticity injection, the scheme overcomes a major difficulty in modeling the particle phase boundary conditions. Particles striking a surface boundary can either

Contributed by the Applied Mechanics Division for presentation at the Winter Annual Meeting, Washington, D. C., November 15–20, 1981, of THE AMERICAN SOCIETY OF MECHANICAL ENGINEERS.

Discussion on this paper should be addressed to the Editorial Department, ASME, United Engineering Center, 345 East 47th Street, New York, N. Y. 10017, and will be accepted until December 1, 1981. Readers who need more time to prepare a discussion should request an extension from the Editorial Department. Manuscript received by ASME Applied Mechanics Division, May, 1980; final revision, February, 1981. Paper No. 81-WA/APM-10.

adhere to the surface, leading to particle attrition, or form a bed that slides along the surface, or rebound from the wall. In the vortex method the particles are coagulated into packets which are then followed throughout the flow field. This Lagrangian description of particle trajectories allows precise mathematical consistency with the appropriate physical boundary condition; in an Eulerian formulation the appropriate conditions at a physical boundary are extremely complicated.

In this work the particles are assumed to adhere to the surface upon first impact. This is consistent with typical industrial processes where the particles act as an erosive material, cutting and embedding into the surface. It should be mentioned that this work can be easily extended to include rebound phenomena; it is only necessary to specify rebound angles and velocity coefficients of restitution for an averaged collection of particles.

The unsteady equations of motion are solved outside the body with the "no-slip" boundary conditions for the gas and particle phase.

For the gas and particles

$$\mathbf{u} \text{ (at the boundary)} = \begin{cases} \text{velocity of the boundary,} \\ 0 \text{ if boundary at rest.} \end{cases} \tag{1}$$

In the final section of this work the scheme is applied to a two-phase flow around a cylinder. This problem has been investigated by Glauert [13], Tilly [14], and Pettit [15] under the simplifying assumption of inviscid gas flow. Since many investigations have used potential theory to determine the gas flow, this work will compare the inviscid approximation and the viscous solution given by the vortex method. We can then assess the magnitude of error introduced in the particle phase solution as a result of the inviscid approximation.

It is hoped that this work will serve as another contribution to the study of two-phase, gas-solid flow about a cylinder, and more saliently, introduce a technique useful in solving two-phase flow problems.

The Two-Phase Model

The constitutive equations are well known [16] for flows in which the fluid phase is an incompressible Newtonian fluid and the particle phase is a dilute suspension (i.e., the particle volume fraction is order 10^{-3} or less) made up of uniform solid particles.

The dimensionless equations of continuity and motion, written in terms of vorticity transport, are as follows:

Gas Vorticity Transport

$$\nabla \cdot \mathbf{u} = 0, \tag{2}$$

$$\frac{D\xi}{Dt} = \frac{1}{\mathrm{Re}} \nabla^2 \xi, \tag{3}$$

Particle Equation of Motion

$$\frac{\partial \alpha}{\partial t} + \nabla(\alpha \mathbf{u}_p) = 0, \tag{4}$$

$$\frac{D\mathbf{u}_p}{Dt} = \frac{g(\mathbf{u} - \mathbf{u}_p)}{\lambda} \tag{5}$$

where ξ is a scalar representing the fluid phase vorticity, $\xi = \text{curl } \mathbf{u}$; α is the particle volume fraction, and λ and g are defined as follows:

$$\lambda = \frac{2}{9} \frac{\rho_p}{\rho} \left(\frac{\sigma}{L}\right)^2 \left(\frac{UL}{\nu}\right), \quad g(\mathrm{Re}_p) = \frac{|\mathbf{u} - \mathbf{u}_p| d}{\nu} \frac{C_D}{24}. \tag{6}$$

By fitting experimental data [17] for the drag coefficients of spherical particles, the following formulas are obtained:

$$C_D = 24(1 + 0.15\, \mathrm{Re}_p^{0.687})/\mathrm{Re}_p \quad 0 \leqq \mathrm{Re}_p \leqq 200,$$

$$C_D = 21.9416\, \mathrm{Re}_p^{-0.718} + 0.324 \quad 200 < \mathrm{Re}_p \leqq 2500,$$

$$C_D = 0.4 \qquad \mathrm{Re}_p > 2500.$$

These will be used in the following numerical solution. The drag coefficients of irregularly shaped particles may also be obtained by using the diameter, d, of an equivalent sphere as suggested by Bagnold [18], where d equals 75 percent of the mean sieve diameter.

Physically, λ (referred to as the momentum equilibration number) is the nondimensional distance required for a particle to reduce its initial slip velocity by e^{-1}. Equations (3) and (5) indicate for gas-solids experiments on different scales to be dynamically similar we require λ to be constant and the Reynolds number to be constant between experiments.

Other forces that act on the particles such as the lift force, Brownian motion force, pressure force, Magnus force, Basset force, and virtual mass effects may be neglected [19].

Principal Method of Solution

Equations (2)–(5) are solved by integrating forward in time. At the time step m we assume the vorticity is known for the gas flow field and the particle flow field. We want to determine the gas vorticity and particle distribution at the time step $(m + 1)$. This is done as follows. First, consider a flow field without boundaries present; the vorticity is partitioned into a sum of blobs

$$\xi = \sum_{j=1}^{N} \xi_j, \tag{7}$$

$$\xi_j \in \mathcal{C}_0^\infty (R^2), \tag{8}$$

where the gas vortex blobs, ξ_j each have small support, i.e., the function vanishes uniformly outside a small but finite region (or blob) around a point $\mathbf{r}_j$, in the two-dimensional domain R^2.

Now in the case of the fluid the vortex field is advanced using Chorin's [12] scheme, as described in the following section.

In the case of the particles we must first discuss the characterization of the particle continuum as a set of discrete noninteracting packets and then describe the technique by which these packets are advanced to the $m + 1$ time step.

Partitioning the particles into packets of small support is in physical agreement with the spatial averaging found in an Eulerian description. Also, we are only interested in mean values of the dependent variables, since these are the only ones sampled experimentally. Furthermore the gas-flow solution is statistical in nature, so we cannot know the exact path of any specific particle. We can only determine the mean

Nomenclature

L = characteristic length of system
R = cylinder radius
d = particle diameter
$\mathbf{u}$ = gas velocity, $\mathbf{u} = (u, v)$
$\mathbf{u}_p$ = particle velocity, $\mathbf{u}_p = (u_p, v_p)$
$\alpha(q)$ = single layer source potential function
α = particle volume fraction, $\alpha = \bar{\rho}_p/\rho_p$
ϕ = potential function
Δ = Laplacian operator, $\Delta = \nabla^2$
μ = gas viscosity
ν = gas kinematic viscosity
ξ = vorticity
$\bar{\xi}$ = vorticity strength
ρ = gas density
ρ_p = particle material density
$\bar{\rho}_p$ = particle phase density (mass particles/unit volume mixture)
σ = particle radius

Parametric Groups

Re = flow Raynolds number, UL/ν or $2UR/\nu$
Re_p = particle Reynolds number, $|\mathbf{u} - \mathbf{u}_p| \cdot d/\nu$
λ = momentum equilibration number, $\tau U/L$ or $\tau U/R$, $\tau = \frac{2}{9} \frac{\rho_p \sigma^2}{\mu}$

Subscripts

D = flow due to potential source distribution
0 = conditions at the wall
p = particle phase
ξ = flow due to vortex field
∞ = free-stream conditions

motion of a collection of particles. Thus the information carried by the packets determines the mean motion of the particles contained within the packet.

Now we write the particle momentum equation (5) in discretized form yielding

$$\frac{D\mathbf{u}_{pi}}{Dt} = \frac{g(\mathbf{u} - \mathbf{u}_{pi})}{\lambda} \tag{9}$$

We propose to solve this equation by following the motion of particle packets.

The motion of the particle packets is then described by

$$\frac{dx_p(i_p)}{dt} = u_p(i_p) \quad i_p = 1, \ldots, N_p, \tag{10}$$

$$\frac{dy_p(i_p)}{dt} = v_p(i_p) \quad i_p = 1, \ldots, N_p, \tag{11}$$

where N_p is arbitrary and $u_p(i_p)$, $v_p(i_p)$ are found by using a scheme presented in the section entitled "Numerical Details."

Chorin's Vortex Scheme

This section presents an outline of Chorin's [12] vortex method as it pertains to the problem under investigation. Since the flow is incompressible and two-dimensional, there exists a stream function Ψ; physically Ψ is a measure of the two-dimensional fluid flow rate and is related to the velocity as follows:

$$u = -\frac{\partial \Psi}{\partial y}, \quad v = \frac{\partial \Psi}{\partial x}. \tag{12}$$

We first consider the flow of an inviscid fluid (i.e., Re = ∞). Equation (3) becomes

$$\frac{D\xi}{Dt} = 0, \quad \Delta\Psi = -\xi \tag{13}$$

with the vorticity partitioned into blobs as described in (7), Ψ_j then has the form

$$\Psi = \sum_{j=1}^{N} \Psi_j \quad \text{with} \quad \Delta\Psi_j = -\xi_j.$$

When the distance between some arbitrary point and the jth vortex blob is large (i.e., $|\mathbf{r} - \mathbf{r}_j|$ large), ψ_j will have a form

$$\Psi_j \cong \frac{\bar{\xi}_j}{2\pi} \log |\mathbf{r} - \mathbf{r}_j|, \quad \bar{\xi}_j = \iint \xi_j dx dy.$$

The foregoing equation is the expression for a point vortex stream function. In the neighborhood of a point vortex the fluid's tangential velocity varies inversely with the radius. However, the velocity field created by the vortex blobs is made bounded as opposed to the infinite velocity at the center of a point vortex. This is done by constructing a basic blob of the form

$$\Psi^0(r) = \begin{cases} \dfrac{1}{2\pi} \log r & r \geqq \sigma_1 \\ \dfrac{1}{2\pi} \dfrac{r}{\sigma_1} & r < \sigma_1 \end{cases}, \tag{14}$$

where $r = |r|$ and σ_1 is a cutoff length which will be discussed shortly. Since the blobs are small it is assumed that their total vorticity $\bar{\xi}_j$ is small and hence their interaction effect with neighboring blobs is small.

Now the stream function is written as

$$\Psi = \sum_{j=1}^{N} \bar{\xi}_j \Psi^0(\mathbf{r} - \mathbf{r}_j), \quad \xi = \sum_{j=1}^{N} \bar{\xi}_j \xi_j^0, \tag{15}$$

where each basic blob satisfies

$$\xi_j^0 = -\Delta\Psi^0(\mathbf{r} - \mathbf{r}_j).$$

The motion of the vortex blobs is then described by

$$\frac{dx_i}{dt} = -\sum_{j \neq i} \bar{\xi}_j \frac{\partial \Psi^0}{\partial y}(\mathbf{r} - \mathbf{r}_j) \quad i = 1, \ldots, N,$$

$$\frac{dy_i}{dt} = \sum_{j \neq i} \bar{\xi}_j \frac{\partial \Psi^0}{\partial x}(\mathbf{r} - \mathbf{r}_j) \quad i = 1, \ldots, N$$

the components of the radius vector $\mathbf{r}$ are (x_i, y_i).

These equations can be approximated by

$$x_i^{n+1} = x_i^n + ku^{n,1/2}, \tag{16}$$

$$y_i^{n+1} = y_i^n + kv^{n,1/2}, \tag{17}$$

where k is the time step.

Now consider the case when Re $\neq \infty$. The diffusion equation for the fluid is

$$\frac{\partial \xi}{\partial t} = \frac{1}{\text{Re}} \Delta\xi$$

with initial data $\xi(0) = \xi(x, y, t = 0)$. A solution to this equation using a random walk is obtained as follows. Assume for the moment that ξ is a known function in space and time, then distribute over the x, y-plane points of masses ξ_i with locations $\mathbf{r}_i = (x_i, y_i)$, $i = 1, \ldots, N$, N large. This is done so that the mass density approximates the initial condition $\xi(0)$. Then the points are moved by the following equations:

$$\begin{aligned} x_i^{n+1} &= x_i^n + \eta_1, \\ y_i^{n+1} &= y_i^n + \eta_2, \end{aligned} \tag{18}$$

where η_1 and η_2 are Gaussianly distributed random variables with zero mean and variance $2k/\text{Re}$, k being the time step.

The vorticity density generated by their mutual interaction and random walk is given by

$$\begin{aligned} x_i^{n+1} &= x_i^n + ku^{n,1/2} + \eta_1, \\ y_i^{n+1} &= y_i^n + kv^{n,1/2} + \eta_2, \end{aligned} \tag{19}$$

which approximates the solution to (3), (12), and (13).

This analysis has neglected the effect of boundaries. We must satisfy the no-slip condition and create a potential flow that will exactly cancel the normal component of flow. The normal component is developed in the next section. To satisfy the no-slip condition (tangential component) the vorticity necessary to create a velocity exactly cancelling the flow velocity in the tangential direction must be determined. Integrating the vorticity in the boundary layer will yield the desired result. The total vorticity in a boundary layer of thickness δ and length h is

$$\begin{aligned} \bar{\xi} &= \int_{-h/2}^{h/2} \int_0^{\delta} (\nabla \times u) dy dx \\ &= \int_{-h/2}^{h/2} \int_0^{\delta} \left(-\frac{\partial u}{\partial y}\right) dy dx \cong -U(0, \delta)h, \end{aligned} \tag{20}$$

where the integral has been approximated using the midpoint rule, and $U(0, \delta)$ is the free-stream speed. This total vorticity is assigned to the blob which has a constant velocity field inside a cutoff length σ_1 that exactly annihilates the tangential velocity and gives the approximate value of σ_1 as $\sigma_1 = h/2\pi$ from (12), (14), and (20).

Numerical Details

We must find a potential flow $\mathbf{u}_D$, such that $\mathbf{u}_D \cdot \mathbf{n} = -\mathbf{u}_\xi \cdot \mathbf{n}$ for each point on the boundary of an obstacle. In this way $\mathbf{u}_D + \mathbf{u}_\xi$ will satisfy the normal boundary condition. We require a solution to

$$\Delta\psi = 0 \tag{21}$$

subject to the boundary condition

$$\mathbf{u} \cdot \mathbf{n} = -\mathbf{u}_\xi \cdot \mathbf{n} \quad \text{on} \quad \partial D. \tag{22}$$

Laplace's equation can be satisfied by a flow of the form

$$\mathbf{u} = \nabla\phi, \tag{23}$$

where ϕ is given by

$$\phi(\mathbf{r}) = \frac{1}{2\pi} \int_{\partial D} \alpha(q) \log R(q) dq \tag{24}$$

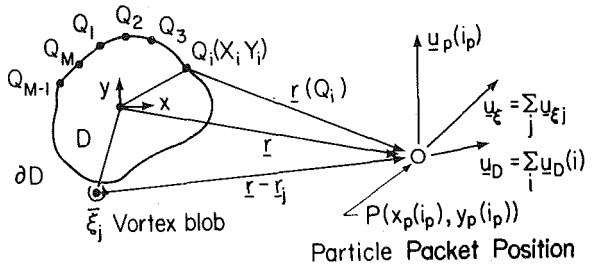

Fig. 1 Vector and notational relationship between domain, vortex blobs, and particle packets

here, $q = (x_q, y_q)$ is a point on the boundary and

$$R(q) = [(x - x_q)^2 + (y - y_q)^2]^{1/2}. \tag{25}$$

This construction results from linear superpositioning of logarithmic potential functions (i.e., sources). It is readily shown [20] that if ∂D has continuous curvature and $\alpha(q')$ is bounded and integrable, $\phi(\mathbf{r})$ is continuous for all finite points $\mathbf{r}$ including passage through ∂D. If $\alpha(q')$ is continuous on ∂D which itself has continuous curvature, then if ξ denotes the exterior to the domain D

$$\left[\frac{\partial \phi_\xi}{\partial n} - \frac{\partial \phi_D}{\partial n}\right]_q = -\alpha(q), \tag{26}$$

$$\left[\frac{\partial \phi_\xi}{\partial n} + \frac{\partial \phi_D}{\partial n}\right]_q = \frac{1}{\pi}\int_{\partial D} \alpha(q')\left[\frac{\partial}{\partial n}(\log R(q'))\right]dq'. \tag{27}$$

This follows from the Green's function solution to the corresponding Dirichlet problem.

Now adding equation (26) and (27) we can solve for the single layer source function $\alpha(q)$ in the integral equation

$$\alpha(q) - \frac{1}{\pi}\int_{\partial D} \alpha(q')\frac{\partial}{\partial n}[\log R(q')]dq' = -2\mathbf{u}_\xi \cdot \mathbf{n}. \tag{28}$$

For a full discussion of the applications of the theory of integral equations to Dirichlet's problem see Muskhelishvili [21].

We approximate (28) by a system of linear equations. A source of strength $\alpha(q) = 1$ at Q_i induces at Q_j, $i \neq j$, a velocity field with components

$$U_1(ij) = -\frac{1}{2\pi}\frac{(X_j - X_i)}{R_{ij}^2}, \tag{29}$$

$$U_2(ij) = -\frac{1}{2\pi}\frac{(Y_j - Y_i)}{R_{ij}^2}, \tag{30}$$

$$R_{ij}^2 = (X_j - X_i)^2 + (Y_j - Y_i)^2. \tag{31}$$

Now $\alpha(q)$ is approximated by the M component vector $\boldsymbol{\alpha} = (\alpha(Q_1), \ldots, \alpha(Q_M))$, which must in turn satisfy the matrix equation, $\mathbf{A}\,\boldsymbol{\alpha} = \mathbf{b}$, where $\mathbf{b}$ has components that are the values of $-\mathbf{u}_\xi \cdot \mathbf{n}$ computed at the points Q_i. The components of the matrix $\mathbf{A}$ are given by

$$a_{ij} = U_1(ij)n_1 + U_2(ij)n_2\ (i \neq j), \quad a_{ii} = \frac{1}{2h}\ i = 1, \ldots, N. \tag{32}$$

The velocity due to the distribution of sources is found by summing up the contribution of each component:

$$u_D(\mathbf{r}) = \sum_{i=1}^{M} \mathbf{u}_D(i), \tag{33}$$

where

$$\mathbf{u}_D(i) = \begin{cases} \dfrac{1}{2\pi}\alpha(Q_i)\dfrac{\mathbf{r}(Q_i)}{r^2(Q_i)} & \text{if} \quad r(Q_i) \geq \tfrac{1}{2}h, \\ \dfrac{1}{2h}\alpha(Q_i)\mathbf{n}(Q_i) & \text{if} \quad r(Q_i) < \tfrac{1}{2}h, \end{cases} \tag{34}$$

where $r(Q_i) = |\mathbf{r}(Q_i)|$, and $\mathbf{n}$ is a unit normal vector (see Fig. 1 for notation).

Summing equation (33) with (34) we obtain the velocity at some arbitrary point $P(x_p(i_p), y_p(i_p))$ where a particle packet may be located. Writing

$$u(i_p) = \frac{1}{2\pi}\sum_i {}_1\alpha(Q_i)\frac{(x_p(i_p) - X_i)}{r^2(Q_i)} + \frac{1}{2\pi}\sum_i {}_2\alpha(Q_i)X_i + u_\xi(i_p) + U, \tag{35}$$

$$v(i_p) = \frac{1}{2\pi}\sum_i {}_1\alpha(Q_i)\frac{(y_p(i_p) - Y_i)}{r^2(Q_i)} + \frac{1}{2\pi}\sum_i {}_2\alpha(Q_i)Y_i + v_\xi(i_p) + V, \tag{36}$$

where

$$r^2(Q_i) = [(x_p(i_p) - X_i)^2 + (y_p(i_p) - X_i)^2],$$

Σ_1 is for $r(Q_i) \geq \frac{1}{2}h$
Σ_2 is for $r(Q_i) < \frac{1}{2}h$
i indicates points on ∂D
U is the gas free-stream velocity in x-direction ($U = 1$)
V is the gas free-stream velocity in y-direction ($V = 0$).

We now have at hand the means to find $u_p(i_p)$ and $v_p(i_p)$ and hence advance the particle packets. First, we rewrite (9) in terms of the i_p particle packet velocity components

$$\frac{Du_p(i_p)}{Dt} = \frac{g}{\lambda}(u(i_p) - u_p(i_p)), \tag{37}$$

$$\frac{Dv_p(i_p)}{Dt} = \frac{g}{\lambda}(v(i_p) - v_p(i_p)) \tag{38}$$

where $u(i_p)$ and $v(i_p)$ are given by (35) and (36). Equations (37) and (38) are integrated using a Runge-Kutta fifth-order integration scheme with variable step size to preserve accuracy near boundaries. We assume over a time step k that $g = g(\mathrm{Re}_p)$ (i.e., the drag coefficient) is constant. A test case of $\lambda = 1.0$ and $\mathrm{Re} = 100{,}000$ showed this to be true even when approaching a boundary in a normal direction.

Once the packet velocity is known the position after the time step is found by approximating (10) and (11) with

$$x_p(i_p)^{m+1} = x_p(i_p)^m + ku_p(i_p)^{m,1/2}, \tag{39}$$

$$y_p(i_p)^{m+1} = y_p(i_p)^m + kv_p(i_p)^{m,1/2}, \tag{40}$$

or more accurately by integrating (10) and (11) directly using the Runge-Kutta scheme. In the computer program[1] equations (37), (38), (10), and (11) are integrated simultaneously yielding the approximate solution to (5).

Boundaries are handled by keeping track of gas and particle vortex blobs; once a blob crosses the boundary it is destroyed. In this way the boundary conditions (1) are satisfied.

The particle continuity equation (4) is satisfied by analyzing the rate at which mass accumulates on the boundary or any other arbitrary boundary. If M is the rate at which mass accumulates, the rate of accumulation can be found by tracing the paths (i.e., following the streamline) of all the particle trajectories from the points (X, Y) where the initial conditions are assumed, to the point (X_0, Y_0) where the path crosses the boundary of the object (∂D). We have, following after Glauert [13],

$$\frac{\dot{M}}{U\rho_{p\infty}} = \frac{\dot{M}}{U\rho_p\alpha_\infty} = \frac{dY}{ds} = \frac{dY}{dY_0}\cdot\frac{dY_0}{ds}, \tag{41}$$

where s is the nondimensional distance around the contour from some fixed origin.

Chorin [12] has conjectured that the mean error in the gas flow is $O(k) + O(\mathrm{Re}^{-1/2})$, where the first term is the error in the deterministic technique used to solve Euler's equations. The second term arises in the random walk solution of the diffusion equation. The standard

[1] The computer program is available from the author.

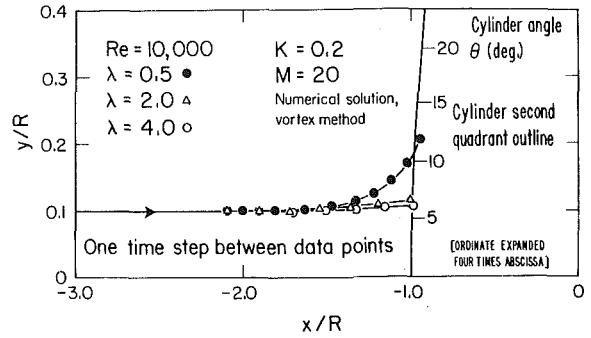

Fig. 2 Particle packet paths (i.e., averaged particle paths) for several values of the momentum equilibration number; the flow is from left to right into the front of the cylinder; the vortex method solution is applied to an incompressible viscous fluid, and dilute particle suspension

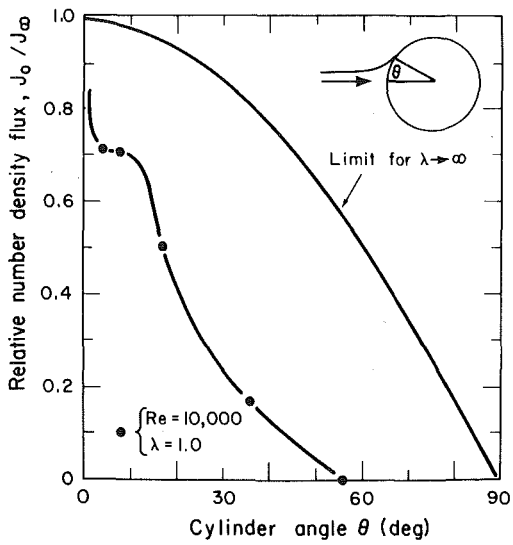

Fig. 3 Relative number density flux as a function of impact location on the cylinder, using the vortex method

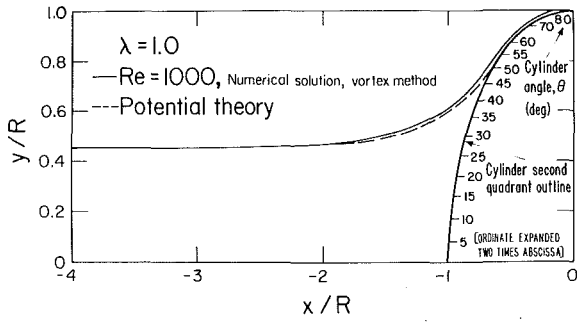

Fig. 4 Particle paths for the vortex method and inviscid flow; in the former case the particles are deflected around the cylinder; the vortex method demonstrates the effect of the displacement thickness on the particle's path since it solves the two-dimensional incompressible Navier-Stokes equations

deviation of η_1 and η_2 is $(2k/\mathrm{Re})^{1/2}$. After m steps the random motion of the vortex blobs will displace the location of the vortex by an amount of order $(m2k/\mathrm{Re})^{1/2} \sim O(\mathrm{Re}^{-1/2})$.

The error in the particle packet may now be estimated. Far from a boundary the flow may be considered inviscid; here, the particle packet is advanced by integrating between each time step taken in advancing the gas vortex blobs. In this way the errors introduced can always be made negligible compared to the error of $O(k) + O(\mathrm{Re}^{-1/2})$ of the gas vortex blobs.

Now, close to a boundary the randomly positioned gas vortex blobs give a randomness to the gas flow field, and convergence on the solution can only be expected by averaging over a large area. Furthermore, with each time step we expect roughly half of the newly created gas vortices to jump randomly over the boundary to be destroyed. Thus we expect the boundary layer to be noisy with convergence occurring over long time averages.

Fortunately, for values of λ, the momentum equilibration number of order unity, the particle's vortex motion depends upon its entire history. In this way the particle packets move through the gas blobs with a motion determined largely by their previous history. In essence, the particle packets sample a space-time average of the gas vortex blobs. A more detailed error analysis considered by the author [19] indicates that for all values of λ, the error in the particle velocity is always less than or equal to the error in the gas velocity.

Application to Flow About a Circular Cylinder

The origin is taken at the center of a fixed cylinder with a nondimensional radius of 1. The negative x-axis is parallel to the undisturbed stream. The flow is from left to right; at time $t = 0$ the flow is started with constant nondimensional velocity of magnitude 1 in the x-direction. Thus the velocity at position $(-\infty, 0)$ is (1, 0). The boundary of the domain, ∂D, is the circumference of the cylinder.

The circumference is divided into $M = 20$ pieces of length $h = 2\pi/M$. The time step is $k = 0.2$. The value of k is chosen so that a decrease in k does not affect the flow. The time step must also be small enough so that the particle equations can be integrated without an excessive number of derivative evaluations. Furthermore, since information concerning the particle packet's position and velocity is only computed at the beginning and end of each time step, the particle path between steps must be small enough to be approximated by a straight line. This allows the impact angle and impact speed (computed vectorially) to be computed accurately. The value of $k = 0.2$ proved accurate for the range of Reynolds numbers of interest.

Once k is chosen, M must be selected large enough so that any increase in M does not change the solution. M must be increased for decreasing values of k because decreases in k give the gas vortices a higher probability of crossing the boundary of the cylinder and being eliminated. We require a minimum number of gas vortices present beyond the boundary; thus more gas vortices need be created on the boundary as some vanish.

The average drag coefficient (averaged over 120 time steps) was calculated using a scheme outlined by Chorin [12]. The gas vorticity near the boundary is sampled and from this the skin friction and pressure drag contribution to the total drag are evaluated. At Re = 100 the average drag is $C_D = 2.02$, the experimental value is 1.9 (Schlichting [22, p. 16]); at Re = 1000, $C_D = 1.04$, the experimental value is 1.00; at Re = 10,000, $C_D = 0.87$, the experimental value is 1.05. Chorin [12] conjectures that the discrete number of vortices roughly representing a smooth boundary-layer trips prematurely the drag crisis, much like a rough wall does. The conjecture is apparently confirmed because at Re = 100,000, $C_D = 0.29$, the experimental value is 0.28 beyond the drag crisis.

Fig. 2 shows the computed data points for Re = 10,000 and λ = 0.5, 2, and 4. Using the vortex method, the cylinder has been expanded in the y-direction to clearly show the particle deflection. The particles, due to the difference in their inertia, are driven away from the gas streamlines and impact with the cylinder. The higher values of λ, corresponding to bigger or heavier particles yield particle paths affected less by the gas flow acceleration away from the stagnation point. These larger particles follow nearly straight line trajectories. It is important to note that the particle trajectory represents the collective average motion of the many particles within a small neighborhood of the particle packet.

Using a distribution of particles the relative number density flux at the cylinder surface is found using (41). This information (see Fig. 3) is useful in determining the distribution of erosion about the cylinder.

Other investigations have ignored boundary-layer and separation

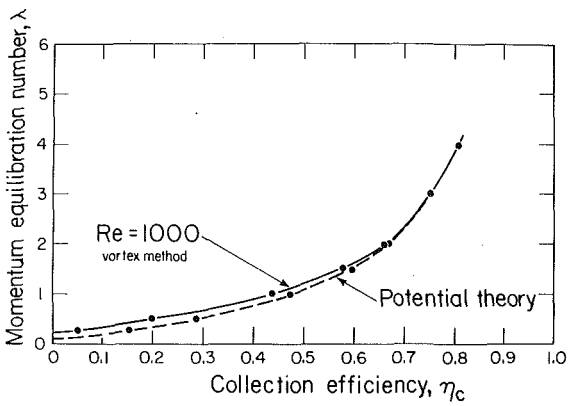

Fig. 5 Collection efficiency for various values of the momentum equilibrium number; the vortex method yields a viscous solution which alters the paths of particles predicted by inviscid potential theory

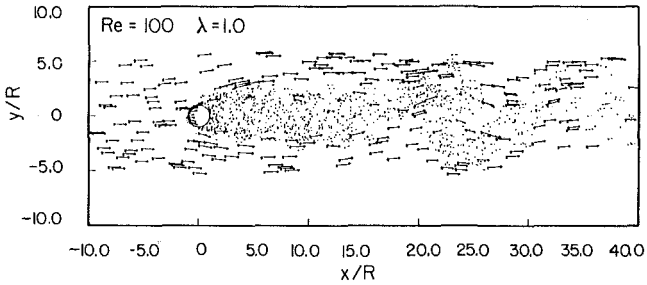

Fig. 6 Particle vectors in the wake region; dimensionless time = 48, Re = 100, and λ = 1.0; the small dots identify vortex blobs shed from the cylinder

effects, assuming inviscid gas flow given from potential theory [13, 14]. One can argue that because the particle residence time in the thin boundary layer is negligibly small that the trajectories will not be substantially affected by its presence. This is because the work done on a particle by the boundary layer depends on the distance traversed which is very small, i.e., $\delta \sim O(\mathrm{Re}^{-1/2})$. However, this overlooks the obvious fact that the boundary layer creates a displacement thickness altering the apparent size of the object and consequently the inviscid flow (see Fig. 4). Even more significant is the separation that may occur. This drastically alters the flow profile and particle trajectories.

In Fig. 5 the collection efficiency of a cylinder is given for various values of the momentum equilibration number for the viscous vortex method and inviscid case. The collection efficiency, a number quoted frequently in the industrial literature, is the ratio of the number of particles impacting with object to the number which would impact if they followed straight line trajectories without deflection by the gas. Clearly the effect of viscosity is to reduce the collection efficiency for a given value of λ. This is directly a result of the increased "apparent" size of the object due to the formation of a displacement thickness. As indicated in Fig. 5 the discrepancy between the viscous (Navier-Stokes) and inviscid (potential flow) case is negligible for larger particles where $\lambda > 2.0$.

We now turn attention toward the back shoulder of the cylinder and the wake region. Shortly after the start of fluid motion the external pressure field causes fluid transversing the rear shoulder to reverse its direction. The reverse motion moves forward and the boundary-layer thickens. This motion gives rise to a vortex which increases in size, until it separates from the cylinder and moves downstream. At a distance from the cylinder a regular pattern of vortices moving alternately clockwise and counterclockwise is apparent. This is known as a Karman vortex street. When viewed in a frame traveling with the vortex street system, the streamlines between the vortices have a sinusoidal appearance.

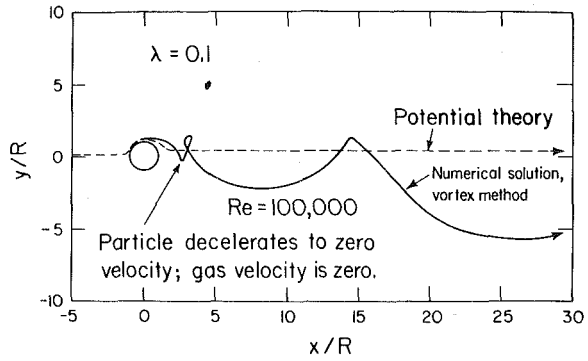

Fig. 7 Particle path for small particle following fluid motion in the wake region

This same effect is visible in the particle paths in the wake region, as calculated numerically (see Fig. 6) for Re = 100 using the vortex method. The small dots and streamlines show the vortex blobs swept downstream from the cylinder. The large circles and vectors indicate the particle's position and velocity. The vortex method predicts separation occurring asymmetrically, and produces the sinusoidal streamlines. It requires about 20 sec of CDC 7600 computer time to follow ten particle packets to the cylinder and about 17 min to follow the evolution from $t = 0$ to $t = 50$. In Fig. 7 the path of a particle completely entrained in the fluid flow is indicated. Here $\lambda = 0.1$ and the motion is identical to fluid elements. This type of submicron size particle is used in laser-doppler anemometry techniques to determine the fluid velocity.

It is difficult to compare the numerical results with experiments since to date two-phase, gas-solid experiments have measured only secondary effects such as erosion of surfaces. With the recent advances in laser-doppler techniques for gas-solid flow it is hoped in future work to measure particle and gas velocity components at any point in the flow domain.

Some experimental work suitable for comparison has been conducted on the velocity dependence of erosion. These experiments indicate that erosion varies with high exponent (typically 2–4) values of the gas free-stream velocity. Previous quantitative erosion models do not predict these high exponent values. It was shown by Laitone [23] that the high exponent values is partly an aerodynamic effect and is not entirely due to particle-surface material interaction mechanisms.

Variations of the numerically determined impact speed q on the cylinder as a function of free-stream speed U shows $q \propto U^m$ where m varies from 1.15 to 1.23. This applies to shallow impacts high on the cylinder's front shoulder, where $\alpha \leq 20°$.

Finnie [2] developed a theoretical erosion model which gives excellent agreement with shallow angle impact experiments. The model gives a relationship between the impact speed of a particle (which must be deduced by solving the fluid mechanical system) and the resulting volume of surface material removed, or erosion, of a ductile metal. The model assumes the particles act as cutting tools with the cutting depth a function of the surface material hardness. The erosion, Er, is predicted to vary with impact speed squared, i.e., $Er \propto q^2$. The vortex method predicts $q \propto U^{1.23}$. Combining this aerodynamic effect with the surface interaction effect predicted by Finnie, we arrive at $Er \propto q^2$, thus $Er \propto (U^{1.23})^2$ and it follows that $Er \propto q^{2.46}$.

In erosion experiments the impact speed is not measured, however the gas velocity, U, and hence particle velocity, U, is measured far from the body. Grant and Tabakoff [4] have conducted experiments with flat plates at shallow angles to attack ($\alpha = 20°$) entrained in a gas-solid flow. They find $Er \propto U^{2.8}$. The agreement between that predicted by the vortex method and experiment is quite good, however more importantly it points out the importance in solving the fluid mechanical system first, before applying an erosion model. Researchers have proposed explanations for exponent values about 2.0 based on particle fragmentation [24] and based on indentation

hardness theory [3]. This analysis shows the exponent values above 2.0 may be due to aerodynamics alone. The vortex method presented in this study can provide researchers with a numerical solution technique suitable for a wide class of two-phase, gas-solid flows about various types of bodies.

Concluding Remarks

It has been the aim of this work to present a general solution technique applicable to a wide variety of commonly encountered geometries in dilute gas-solid flow problems, and to apply the solution technique to a specific geometry and thereby indicate the type of information obtainable which may prove useful to scientists and engineers working with specific industrial systems.

The application to the cylinder demonstrates the discrepancy between the viscous and inviscid solution. At Reynolds numbers of 1000 and lower the inviscid approximation provides an accurate solution only for values of the momentum equilibration number greater than 2.0. By applying an erosion model to the results predicted by the vortex method a good agreement was gained with the erosion found in experiments of particles impacting surfaces at shallow angles of attack.

One of the problems that must be faced in the course of developing this technique to a wider class of flows is the inclusion of a two-way momentum coupling effect. This would extend the capability of the method to include nondilute liquid-solid flows.

Acknowledgment

I am especially indebted to Prof. Maurice Holt for his guidance and encouragement given freely throughout the course of this research. I would like to thank Prof. Alexandre Chorin and Dr. Aleksei Shestakov for their helpful discussions. This work was supported by the Division of Materials Sciences, Office of Basic Energy Sciences, U.S. Department of Energy under Contract No. W-7405-ENG-48.

References

1 Sheldon, G. L., "Similarities and Differences in the Erosion Behavior of Materials," ASME Annual Meeting, Los Angeles, July 31, 1969, ASME Paper No. 69-WA/Met-7.

2 Finnie, I., "Some Observations on the Erosion of Ductile Metals," *Wear*, Vol. 19, 1972, pp. 81–90.

3 Sheldon, G. L., and Kanhere, A., "An Investigation of Impingement Erosion Using Single Particles," *Wear*, Vol. 21, 1972, pp. 195–209.

4 Grant, G., and Tabakoff, W., "Erosion Prediction in Turbomachinery Results From Environmental Solid Particles," *Journal of Aircraft*, Vol. 12, No. 5, 1975, pp. 471–478.

5 Crowe, C. T., et al., "Dynamics of Two-Phase Flow in Rocket Nozzles," United Technical Report, 2102-FR, Sept. 1965.

6 Kliegel, J. R., "One-Dimensional Flow of a Gas-Particle System," IAS Paper No. 60–65, 1960.

7 Wallis, G. B., *One-Dimensional Two-Phase Flow*, McGraw-Hill, New York, 1969.

8 Crowe, C. T., Sharma, M. P., and Stock, D. E., "The Particle-Source-in-Cell (PSI-CELL) Model for Gas-Droplet Flows," ASME Paper No. 75-WA/HT-25.

9 Crowe, C. T., and Pratt, D. T., "Analysis of the Flow Field in Cyclone Separators," Symposium on Application of Computers to Fluid Dynamic Analysis and Design, Paper 2B(4), Polytechnic Institute of Brooklyn, 1973.

10 Stock, D. E., and Crowe, C. T., "Analysis of the Flow Field in Electrostatic Precipitators," Spring Meeting of the Midwestern Section Combustion Institute, 1973.

11 Dorodnicyn, A. A., "Review of Methods for Solving Navier-Stokes Equations," *Proceedings of IIIrd International Conference on Numerical Methods in Fluid Mechanics*, Lecture Notes in Physics, Springer-Verlag, 1973, pp. 1–11.

12 Chorin, A. J., "Numerical Study of Slightly Viscous Flow," *Journal of Fluid Mechanics*, Vol. 57, 1973, pp. 785–796.

13 Glauert, M., "A Method of Constructing the Paths of Raindrops of Different Diameters Moving in the Neighbourhood of (1) A Circular Cylinder, (2) An Aerofoil, Placed in a Uniform Stream of Air; and a Determination of the Rate of Deposit of the Drops on the Surface and the Percentage of Drops Caught," *Aeronautical Research Committee, Reports and Memoranda*, No. 2025, 1940.

14 Tilly, G. D., "Erosion Caused by Airborne Particles," *Wear*, Vol. 14, 1969, pp. 63–79.

15 Pettit, F. S., and Barkalow, R. H., "Design of Materials for Use Under Erosion/Corrosion Conditions at High Temperatures in Coal Gasification and Coal Combustion Systems," Pratt and Whitney Aircraft, East Hartford, Conn., 75-200-7107-6, May 1977.

16 Drew, D. A., "Two-Phase Flows: Constitutive Equations for Lift and Brownian Motion and Some Basic Flows," *Archive for Rational Mechanics*, Vol. 62, No. 2, 1976, pp. 149–163.

17 Boothroyd, R. G., *Flowing Gas-Solids Suspensions*, Chapman and Hall, London, 1971.

18 Bagnold, R. A., *The Physics of Wind Blown Sands and Desert Dunes*, Methuen, London, 1960.

19 Laitone, J. A., "Separation Effects in Gas Particle Flows at High Reynolds Numbers," PhD Dissertation, University of California, Berkeley, Calif., 1979.

20 Sneddon, I. N., *Elements of Partial Differential Equations*, McGraw-Hill, New York, 1957.

21 Muskhelishvili, N. I., *Singular Integral Equations*, Noordhoff, Groningen, 1953.

22 Schlichting, H., *Boundary Layer Theory*, McGraw-Hill, New York, 1960.

23 Laitone, J. A., "Aerodynamic Effects in the Erosion Process," *Wear*, Vol. 56, 1979, pp. 239–246.

24 Tilly, G. D., and Sage, W., "The Interaction of Particle and Material Behavior in Erosion Processes," *Wear*, Vol. 16, 1970, pp. 447–465.

Y. Matsuzaki
Principal Research Engineer,
National Aerospace Laboratory,
Jindaiji, Chofu,
Tokyo, Japan
Mem. ASME

Reexamination of Stability of a Two-Dimensional Finite Panel Exposed to an Incompressible Flow

Stability of a flat or buckled panel exposed to an incompressible flow has been reanalyzed as the analyses on this problem by other investigators have errors in the fluid forces used. The deflection of the panel in an oscillatory motion is assumed in such a way that there occurs no change in the fluid volume in a control surface enclosing the panel. The nonlinear equation of motion of the panel on a continuous elastic spring is solved by using the Galerkin method and the generalized fluid forces which are derived in the author's previous paper. The stability of the flat and buckled configuration in static equilibrium is examined against small disturbances. Existence of the limit cycle oscillation is studied by applying the harmonic balance method. Numerical results are compared with those of the analysis on a two-dimensional finite elastic channel conveying an almost incompressible flow.

1 Introduction

Stability of plates of finite length in a subsonic flow has been examined by many investigators. A controversial point of the problem is possibility of postdivergence flutter oscillation of the plates with the leading and trailing edges supported or clamped. Some debate on this topic was held between Dowell, and Weaver and Unny [1]. Dowell [2] examined the stability of a flat or buckled plate by using a nonlinear plate and linearized potential flow theories, and his numerical result showed occurrence of divergence at a certain critical speed, but no flutter above the divergence boundary. Recently Holmes [3] investigated the behavior of a panel from the view point of differentiable dynamics, taking into account structural nonlinearity and damping. He confirmed Dowell's result.

On the other hand, by using a linear plate theory, Dugundji, Dowell, and Perkin [4] predicted postdivergence flutter of a traveling-wave type and found it experimentally for a two-dimensional panel of 2642 mm length and 610 mm width resting on a continuous elastic foundation. Ishii [5] also observed two different types of postdivergence flutter of a two-dimensional plate of 300 mm length and 70 mm width, that is, small amplitude oscillation with a high frequency and large amplitude oscillation with a low frequency. His interesting finding is that a positive static pressure gradient along the flow direction has a destabilizing effect toward flutter. On the contrary, Gislason [6] reported that no flutter oscillation of the plate with a chord-to-span ratio of 2 was observed when the dynamic pressure was increased up to about twice the divergence speed.

The debate just mentioned remains, still, to be resolved. As is well known, there is the same question about postdivergence flutter oscillation of fluid-conveying tubes supported or clamped at both ends. As for a two-dimensional elastic channel conveying a flow, Matsuzaki and Fung [7, 8] show that no postdivergence flutter of the channel walls can occur if structural nonlinearity and viscous damping are considered and a linearized potential flow theory is used.

Recently, Matsuzaki and Ueda [9] have reexamined the fluid pressure acting on a two-dimensional finite plate at small Mach numbers, and presented simplified expressions for the generalized fluid forces. According to their analysis, as the Mach number tends to zero, the virtual mass induced by an oscillating fluid becomes infinitely large for a natural mode symmetric with respect to the midchord point. That is, for instance, no motion of the plate in the first natural mode is possible for $M = 0$. They also pointed out that for the incompressible and almost incompressible flow cases Ishii [5] and Weaver and Unny [10] have errors in the velocity potentials and generalized forces which are used in the stability analyses of the plate.

Kornecki [11] examined the possibility of flutter of a two-dimensional flat panel constrained to zero displacement at both the edges in the incompressible flow. When $M = 0$, the disturbed velocity potential corresponding to the aerodynamic forces which are defined by equation (A1) of reference [11] agrees with that given by equations (40) and (41) of reference [9]. Therefore, the discussion made in reference [9] can be applied to the generalized incompressible aerodynamic forces which are used by Korneki [11]. As for the flat panel, since unsteady generalized forces cannot be evaluated for the first natural mode, his flutter analysis is invalid.

Contributed by the Applied Mechanics Division for publication in the JOURNAL OF APPLIED MECHANICS.

Discussion on this paper should be addressed to the Editorial Department, ASME, United Engineering Center, 345 East 47th Street, New York, N. Y. 10017, and will be accepted until December 1, 1981. Readers who need more time to prepare a discussion should request an extension from the Editorial Department. Manuscript received by ASME Applied Mechanics Division, August, 1980; final revision, January, 1981.

Therefore, we shall reexamine the stability of the plate, especially taking into account such a symmetric oscillatory mode as given by equation (39) of reference [9], which does not produce a large virtual mass. This means that the behaviors of small disturbances and periodic oscillations are analyzed by considering dynamic coupling between such a particular symmetric mode and an antisymmetric natural mode.

2 Problem Formulation

A two-dimensional plate resting on a continuous elastic spring is simply supported by semi-infinitely long, and flat rigid walls at its ends, as shown in Fig. 1. The equation of equilibrium of the plate undergoing cylindrical bending and the boundary conditions are given, respectively, by

$$\frac{Eh^3}{12(1-\nu^2)}\frac{\partial^4 w}{\partial X^4} - \frac{Eh}{2(1-\nu^2)L}\left[\int_0^L \left(\frac{\partial w}{\partial X}\right)^2 dX\right]\frac{\partial^2 w}{\partial X^2} - p + k^* w + c\frac{\partial w}{\partial t} + \rho_s h\frac{\partial^2 w}{\partial t^2} = 0 \quad (1)$$

$$w = \partial^2 w/\partial X^2 = 0 \quad (2)$$

where $w, h, E, \nu, \rho_s, c, k^*$, and p are, respectively, the deflection of the plate, the plate thickness, Young's modulus, Poisson's ratio, the density of the plate, the viscous damping coefficient, the spring constant, and the fluid dynamic pressure (positive for downward). The flow is assumed to be inviscid and low subsonic. The space below the plate is empty. We will use the pressure expressions obtained by Matsuzaki and Ueda [9] for $M \ll 1$ and $O(k) \lesssim 1$. Although they have been derived under the assumption of a harmonic oscillation, we assume like in references [8, 10] that the expressions are applicable to a slightly divergent or convergent oscillation.

Let the deflection of the plate satisfying equation (2) be

$$w = \sum_{m=1}^{2} w_m \sin\frac{m\pi X}{L} + w_3\left(\sin\frac{\pi X}{L} - 3\sin\frac{3\pi X}{L}\right) \quad (3)$$

As shown in reference [9], the last term of equation (3) represents a symmetric mode which requires no change in the volume of fluid contained by an arbitrary control surface enclosing the elastic plate. Applying to equation (1) the method of weighted residuals in which the weighting functions are taken to be the same as the assumed modes, we obtain

$$\mu\{(1+\beta Q_{11}^{(2)})d^2W_1/dt^2 + (1+\beta Q_{s1}^{(2)})d^2W_3/dt^2\} + \zeta(dW_1/dt + dW_3/dt) + (K_1 - Q_{11}^{(0)}Q)W_1 + (k_1 - Q_{s1}^{(0)}Q)W_3 + \gamma\{(W_1+W_3)^2 + 4W_2^2 + 81W_3^2\}(W_1+W_3) + \sqrt{\mu\beta Q}\,Q_{21}^{(1)}dW_2/dt = 0 \quad (4a)$$

$$\mu(1+\beta Q_{22}^{(2)})d^2W_2/dt^2 + \zeta dW_2/dt + [k_2 - Q_{22}^{(0)}Q + 4\gamma\{(W_1+W_3)^2 + 4W_2^2 + 81W_3^2\}]W_2 + \sqrt{\mu\beta Q}(-Q_{21}^{(1)}dW_1/dt + Q_{s2}^{(1)}dW_3/dt) = 0 \quad (4b)$$

$$\mu\{(1+\beta Q_{1s}^{(2)})d^2W_1/dt^2 + (10+\beta Q_{ss}^{(2)})d^2W_3/dt^2\} + \zeta(dW_1/dt + 10dW_3/dt) + (k_1 - Q_{1s}^{(0)}Q)W_1 + (k_1 + 9k_3 - Q_{ss}^{(0)})W_3 + \gamma\{(W_1+W_3)^2 + 4W_2^2 + 81W_3^2\}(W_1+82W_3) - \sqrt{\mu\beta Q}\,Q_{s2}^{(1)}dW_2/dt = 0 \quad (4c)$$

where

$$Q_{s1}^{(q)} = Q_{1s}^{(q)} = Q_{11}^{(q)} - 3Q_{31}^{(q)}, \quad Q_{ss}^{(q)} = Q_{11}^{(q)} - 6Q_{31}^{(q)} + 9Q_{33}^{(q)} \quad \text{for} \quad q = 0, 2,$$

$$Q_{s2}^{(1)} = -Q_{2s}^{(1)} = Q_{12}^{(1)} - 3Q_{32}^{(1)}, \quad (5)$$

$$W_m = w_m/h, \quad Q = \rho U^2/E, \quad k_m = K^* + \frac{(m\pi)^4}{12(1-\nu^2)}\left(\frac{h}{L}\right)^3, \quad \gamma = \frac{\pi^4}{4(1-\nu^2)}\left(\frac{h}{L}\right)^3$$

$$\beta = \rho L/(\rho_s h), \quad \mu = \rho_s h L/E, \quad \zeta = cL/E, \quad K^* = k^* L/E \quad (6)$$

The generalized forces Q_{mn} are cited from reference [9]:

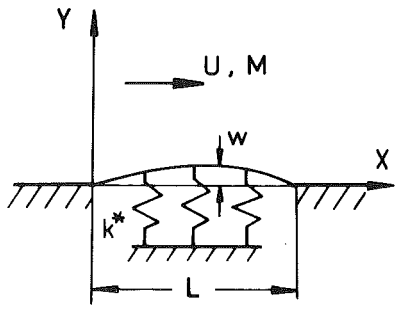

Fig. 1 The panel geometry and a coordinate system

$$Q_{mn} = -Q_{mn}^{(0)} + Q_{mn}^{(2)}\left(\frac{L}{U}\right)^2\frac{d^2}{dt^2} \quad \text{for} \quad m+n = \text{even} \quad (7a)$$

$$Q_{mn} = Q_{mn}^{(1)}\frac{L}{U}\frac{d}{dt} \quad \text{for} \quad m+n = \text{odd} \quad (7b)$$

where

$$Q_{nn}^{(0)} = 2n[\text{Si}(n\pi) - \{1-(-1)^n\}/(n\pi)]$$

$$Q_{mn}^{(0)} = 4mn\{\text{Ci}(m\pi) - \text{Ci}(n\pi) + \ln(n/m)\}/\{\pi(m^2-n^2)\} \quad \text{for } m \neq n$$

$$Q_{mn}^{(1)} = [8\{m\,\text{Si}(n\pi) + n\,\text{Si}(m\pi)\}]/\{\pi^2(n^2-m^2)\}$$

$$Q_{mn}^{(2)} = (1/m\pi)^2[Q_{mn}^{(0)} - (4m/n\pi)\{\text{Ci}(n\pi) - \gamma^* - \ln(n\pi)\}] - (2c^*/mn\pi^3) \times \{1-(-1)^m\}\{1-(-1)^n\} \quad (8)$$

$$c^* = i\pi/2 + \gamma^* + \ln(kM/2), \quad k = U/(\omega L) \quad (9)$$

k, γ^*, Ci, and Si are, respectively, the reduced frequency, Euler's constant, and the cosine and sine integral functions. It is noted that $Q_{mm}^{(0)}$ for $m = 1$ to 3 and $Q_{22}^{(2)}$ are real and positive and $Q_{mm}^{(2)}$ for $m = 1$ and 3 are complex. Numerical values of Q_{mn} for small Mach numbers are given in Tables 1–3 of reference [9].

3 Stability Analysis

We shall now analyze the stability of the static equilibrium configuration by considering small disturbances about it. If the disturbances decrease with time, then we define the static configuration is stable. Let (W_{10}, W_{20}, W_{30}) denote the deflection in static equilibrium.

Two-Mode Approximation ($W_3 = 0$). The stability of the flat or buckled configuration will first be analyzed by employing a conventional two-mode approximation, that is, by putting $W_3 = 0$ in equation (3), like in references [3, 10, and 11]. Omission of the time derivatives from equations (4a) and (4b) yields stationary expressions

$$\{Q_{11}^{(0)}(Q_1 - Q) + \gamma(W_{10}^2 + 4W_{20}^2)\}W_{10} = 0 \quad (10a)$$

$$\{Q_{22}^{(0)}(Q_2 - Q) + 4\gamma(W_{10}^2 + 4W_{20}^2)\}W_{20} = 0 \quad (10b)$$

where

$$Q_m = k_m/Q_{mm}^{(0)} \quad (11)$$

From equations (10), we obtain four different types of the deflections:

(1) *Flat Configuration:*

$$W_{10} = W_{20} = 0 \quad \text{for} \quad Q \geq 0 \quad (12a)$$

(2) *First-Mode Deflection:*

$$W_{10} = \pm\{Q_{11}^{(0)}(Q - Q_1)/\gamma\}^{1/2}, \quad W_{20} = 0 \quad \text{for} \quad Q \geq Q_1 \quad (12b)$$

(3) *Second-Mode Deflection:*

$$W_{10} = 0, \quad W_{20} = \pm \{Q_{22}^{(0)}(Q - Q_2)/\gamma\}^{1/2}/4 \quad \text{for} \quad Q \geq Q_2 \tag{12c}$$

(4) *Mixed-Mode Deflection* ($W_{10} \neq 0$, $W_{20} \neq 0$): When $Q = Q_M$ where

$$Q_M = (4k_1 - k_2)/(4Q_{11}^{(0)} - Q_{22}^{(0)}), \tag{13}$$

equations (10a) and (10b) coincide with each other and become

$$Q_{11}^{(0)}(Q_1 - Q_M) + \gamma(W_{10}^2 + 4W_{20}^2) = 0 \tag{14}$$

and there are an infinite number of static configurations of the mixed mode. It is necessary for the mixed mode to exist that $Q_M - Q_1$ is positive. Then, we obtain $Q_M < Q_1 < Q_2$ from equation (13).

Let $\alpha_m(t)$ for $m = 1$ and 2 be infinitesimal disturbances about the static equilibrium configuration W_{m0}. Then, the disturbed motion is written as

$$W_m(t) = W_{m0} + \alpha_m(t) \quad \text{for} \quad m = 1 \text{ and } 2 \tag{15}$$

Substituting equations (15) into equations (4a) and (4b) and neglecting the higher-order terms of α_1 and α_2, we obtain

$$a_1 d^2\alpha_1/dt^2 + \zeta d\alpha_1/dt + I_1\alpha_2 + \sqrt{\mu\beta Q}\, Q_{21}^{(1)} d\alpha_2/dt = 0 \tag{16a}$$

$$-\sqrt{\mu\beta Q}\, Q_{21}^{(1)} d\alpha_1/dt + a_2 d^2\alpha_2/dt^2 + \zeta d\alpha_2/dt + I_2^*\alpha_2 = 0 \tag{16b}$$

where

$$a_m = \mu(1 + \beta Q_{mm}^{(2)}) \quad \text{for} \quad m = 1, 2 \tag{17}$$

$$I_1 = Q_{11}^{(0)}(Q_1 - Q) + \gamma(3W_{10}^2 + 4W_{20}^2) \tag{18a}$$

$$I_2^* = Q_{22}^{(0)}(Q_2 - Q) + 4\gamma(W_{10}^2 + 12W_{20}^2) \tag{18b}$$

Letting

$$\alpha_m = \bar{\alpha}_m \exp(\epsilon t) \quad \text{for} \quad m = 1, 2 \tag{19}$$

and substituting equations (19) into equations (16), we have a characteristic equation for nontrivial solutions

$$C_4\epsilon^4 + C_3\epsilon^3 + C_2\epsilon^2 + C_1\epsilon + C_0 = 0 \tag{20}$$

where

$$C_4 = a_1a_2, \quad C_3 = \zeta(a_1 + a_2), \quad C_2 = \zeta^2 + a_1I_2^* + a_2I_1 + \mu\beta Q(Q_{12}^{(1)})^2,$$

$$C_1 = \zeta(I_1 + I_2^*), \quad C_0 = I_1I_2^* - 64\gamma^2W_{10}^2W_{20}^2 \tag{21}$$

The real parts of c^* and a_1 become infinitely large as M tends to zero. If the real part of a_1 is sufficiently larger than a_2, then equation (20) may be written as

$$a_1(a_2\epsilon^2 + \zeta\epsilon + I_2^*)\epsilon^2 + C_1\epsilon + C_0 = 0 \tag{22}$$

The first and second modes become less and less coupled to each other with decreasing M, since the smaller the Mach number is, the larger the real part of a_1 is.

Incompressible Flow. Let us here assume $M = 0$. Then, it follows from equation (22) that

$$\epsilon^2 = 0 \tag{23a}$$

$$a_2\epsilon^2 + \zeta\epsilon + I_2^* = 0 \tag{23b}$$

Equations (23a) and (23b) are related to the first mode W_1 and second mode W_2, respectively. Since the disturbance of the first mode remains to be constant, only that of the second mode need to be examined.

From equation (23b), we obtain

$$\epsilon = (-\zeta \pm \sqrt{D})/(2a_2) \tag{24}$$

where

$$D = \zeta^2 - 4a_2I_2^* \tag{25}$$

It is obvious that, if $I_2^* > 0$, i.e., if $D < \zeta^2$, then the static equilibrium is stable. However, if $I_2^* < 0$, that is, if $\sqrt{D} > \zeta$; then the disturbance of the second mode grows in a divergent manner.

We shall examine the stability of the deflections in static equilibrium described by equations (12) and (14).

(1) *Flat Configuration.* Substituting equations (12a) into equation (18b) yields

$$I_2^* = Q_{22}^{(0)}(Q_2 - Q) \tag{26a}$$

Therefore, the flat configuration is always stable for $Q < Q_2$ and unstable for $Q > Q_2$ regardless of the value of Q_1.

(2) *First-Mode Deflection* ($Q \geq Q_1$). Similarly, using equations (12b) we have

$$I_2^* = (4Q_{11}^{(0)} - Q_{22}^{(0)})(Q - Q_M) \tag{26b}$$

When $Q_1 > Q_M$, the first-mode deflection is always stable. If $Q_1 < Q_M$, the deflection is unstable for $Q_1 < Q < Q_M$ and stable for $Q > Q_M$.

(3) *Second-Mode Deflection* ($Q \geq Q_2$). This configuration is always stable since

$$I_2^* = 2Q_{22}^{(0)}(Q - Q_2) > 0 \quad \text{for} \quad Q > Q_2 \tag{26c}$$

(4) *Mixed-Mode Deflection* ($Q = Q_M$). Substituting $Q = Q_M$ and equation (14) into equation (18b), we have

$$I_2^* = 32\gamma W_{20}^2 > 0 \tag{26d}$$

Hence, the mixed-mode deflection in static equilibrium is stable.

We have seen that dynamic coupling between the first and second modes becomes weak as M decreases, and that a complete decoupling between the modes occurs when $M = 0$. For $M = 0$, no motion of the plate in the first mode can occur, since the virtual mass for the first mode becomes infinite. The instability is of divergence type.

2 Three-Mode Approximation ($W_3 \neq 0$). For the incompressible flow, the three-mode approximation is now taken in order to examine instability which is caused by dynamic coupling between the second and last modes in equation (3). The last mode W_3 is consists of the first and third natural modes. Being different from the first or third natural mode itself, this symmetric mode with respect to the midchord point induces much smaller virtual mass for $M \ll 1$, and may oscillate more rapidly. Since the flow is incompressible, no motion of the first or third natural mode is possible [9]. The time derivatives of W_1 in equations (4) must be deleted. Small disturbances can be considered only in terms of the second and last modes. Therefore, the disturbed motion is given as

$$W_1 = W_{10}$$

$$W_2 = W_{20} + \bar{\alpha}_2 \exp(\epsilon t) \tag{27}$$

$$W_3 = W_{30} + \bar{\alpha}_3 \exp(\epsilon t)$$

When W_{10} vanishes, equation (4a) is discarded. Otherwise, we must use all of equations (4).

(1) $W_{10} = 0$. Two types of static configurations are derived from the stationary expressions for equations (4b) and (4c).

(1a) *Flat Configuration*

$$W_{10} = W_{20} = W_{30} = 0 \quad \text{for} \quad Q > 0 \tag{28a}$$

(1b) *Second-Mode Configuration*

$$W_{20} = \pm\{Q_{22}^{(0)}(Q - Q_2)/\gamma\}^{1/2}/4$$

$$W_{10} = W_{30} = 0 \quad \text{for} \quad Q > Q_2 \tag{28b}$$

Substituting equations (27) into equations (4b) and (4c) and neglecting the higher-order terms of $\bar{\alpha}_2$ and $\bar{\alpha}_3$, we obtain a fourth-order characteristic equation defined by equation (20). The coefficients of the equation are

$$C_4 = a_2a_3 > 0, \; C_3 = \zeta(a_2 + a_3) > 0,$$

$$C_2 = \zeta^2 + a_2I_3 + a_3I_2 + C_{22},$$

$$C_1 = \zeta(I_2 + I_3), \quad C_0 = I_2I_3 \tag{29}$$

$$I_2 = Q_{22}^{(0)}(Q_2 - Q) + 4\gamma\{(W_{10} + W_{30})^2 + 12W_{20}^2 + 81W_{30}^2\} \tag{30a}$$

$$I_3 = \{Q_{ss}^{(0)}(Q_3^* - Q) + 328\gamma W_{20}^2\}/10 \tag{30b}$$

$$a_3 = \mu(1 + \beta Q_{ss}^{(2)}/10), \quad C_{22} = \mu\beta Q(Q_{s2}^{(1)})^2/10 > 0 \tag{31}$$

$$Q_3^* = (k_1 + 9k_3)/Q_{ss}^{(0)} \tag{32}$$

Since all the coefficients are real, the stability of the disturbances can be examined by using the Routh-Hurwitz criterion. If and only if

$$C_n > 0 \quad (n = 0, \ldots, 4) \tag{33}$$

and

$$R > 0 \tag{34a}$$

where

$$R \equiv C_1C_2C_3 - C_0C_3^2 - C_1^2C_4 = \zeta^2\{(a_2 + a_3)(I_2 + I_3)(\zeta^2 + C_{22}) + (a_2I_3 - a_3I_2)^2\} \tag{34b}$$

then the disturbances will decrease with increasing time and the static configuration is stable.

(1*a*) Since $Q_{22}^{(0)}$ and $Q_{ss}^{(0)}$ are both positive, the flat configuration is stable for a range of $0 < Q < Q_s$, which is defined as the smaller of Q_2 and Q_3^*, but becomes statically unstable at $Q = Q_s$ because of $C_0 = 0$. For $Q > Q_s$ the configuration is always unstable because at least C_0 or C_1 is negative.

(1*b*) Next, we examine the second-mode configuration. Substitution of equations (28*b*) into equations (32) yields

$$I_2 = 2Q_{22}^{(0)}(Q - Q_2)$$

$$I_3 = (20.5Q_{22}^{(0)} - Q_{ss}^{(0)})(Q - Q_A) \tag{35}$$

where

$$Q_A = \{20.5k_2 - (k_1 + 9k_3)\}/(20.5Q_{22}^{(0)} - Q_{ss}^{(0)}) \tag{36}$$

It is clear that I_2 is always positive for $Q > Q_2$. Since $20.5Q_{22}^{(0)} - Q_{ss}^{(0)}$ is positive, if Q_A is greater than Q_2, then the second mode is unstable for $Q_2 < Q < Q_A$. Otherwise, this configuration is always stable.

(2) $W_{10} \neq 0$. Let us omit the time derivatives in equations (4*a*) and (4*c*). From the resulting equations, it is clear that W_{10} and W_{30} are always coupled, that is, W_{30} cannot vanish whenever $W_{10} \neq 0$.

(2*a*) *Symmetric Coupled-Mode Configuration* ($W_{10} \neq 0$, $W_{30} \neq 0$, $W_{20} = 0$). This configuration is numerically evaluated by using the stationary expressions of (4*a*) and (4*c*). We will here examine the number of the configurations and the range of Q in which the configurations exist.

From the stationary equations, we obtain the following quadratic characteristic equation with respect to J for nontrivial solutions of W_{10} and W_{30}

$$9(\gamma J)^2 + A_1\gamma J + A_0 = 0 \tag{37}$$

where

$$J = (W_{10} + W_{30})^2 + 4W_{20}^2 + 81W_{30}^2 \tag{38}$$

$$A_0 = (Q - Q_{B+})(Q - Q_{B-}) \tag{39a}$$

$$A_1 = (9Q_{11}^{(0)} + Q_{33}^{(0)})(Q - Q_C) \tag{39b}$$

$$Q_{B\pm} = [Q_1 + Q_3 \pm \{(Q_1 - Q_3)^2 + 4Q_1Q_3(Q_{31}^{(0)})^2\}^{1/2}]/[2\{1 - (Q_{31}^{(0)})^2/Q_{11}^{(0)}Q_{33}^{(0)}\}] \tag{40}$$

$$Q_C = (9k_1 + k_3)/(9Q_{11}^{(0)} + Q_{33}^{(0)}) \tag{41}$$

J must be real and positive. Since the discriminant of equation (37) is always positive, that is,

$$D \equiv A_1^2 - 36A_0 = \{9k_1 - k_3 - (9Q_{11}^{(0)} - Q_{33}^{(0)})Q\}^2 + (6Q_{31}^{(0)})^2 > 0 \tag{42}$$

J is assured to be real. Therefore, it follows from the requirement of positiveness that there are two static configurations for $Q > Q_{B+}$ or $Q < Q_{B-}$, and $Q > Q_C$ because of $A_0 > 0$ and $A_1 < 0$, one for $Q_{B-} < Q < Q_{B+}$ because of $A_0 < 0$, and none for the remaining range of Q.

Next, we analyze the stability of the configurations. Subtract equation (4*a*) from equation (4*c*). Substituting equations (27) into the resulting equation and equation (4*b*), and neglecting the higher-order terms of α_2 and α_3, we may again derive a fourth-order characteristic equation, the coefficients of which are given by equations (29). The necessary modifications in equations (30) and (31) are

$$a_3 = \mu(1 + \beta Q_{s3}^{(2)}/3), \quad C_{22} = \mu\beta QQ_{23}^{(1)}Q_{s2}^{(1)}/3,$$

$$Q_{s3}^{(p)} = 3Q_{33}^{(p)} - Q_{31}^{(p)} \quad \text{for} \quad p = 0, 2,$$

$$I_3 = -Q_{s3}^{(0)}(Q - Q_4)/3 + \gamma\{(W_{10} + 2W_{30})^2 + 242W_{30}^2\}/9 \tag{43}$$

$$Q_4 = 3k_3/Q_{s3}^{(0)} \tag{44}$$

As in the preceding section, the dynamic behavior of small disturbances about the configurations can be examined by applying the Routh-Hurwitz criterion to equations (29).

(2*b*) *Mixed-Mode Configuration* ($W_{10} \neq 0$, $W_{20} \neq 0$, $W_{30} \neq 0$). Like the mixed-mode configuration of the two-mode approximation, this configuration exists at a discrete value of the dynamic pressure. The stability of the configuration in static equilibrium can be examined in a similar manner.

4 Harmonic Balance Method

Let us study the possibility of a limit cycle oscillation about the flat or buckled configuration with the viscous damping included, i.e., $\zeta \neq 0$. We shall assume the limit cycle oscillation in a form of

$$W_1 = A_{10} \tag{45a}$$

$$W_2 = A_{20} + A_{21}\sin\omega t \tag{45b}$$

$$W_3 = A_{30} + A_{31}\sin(\omega t + \theta) \tag{45c}$$

Like in the preceding section, equation (4*a*) is discarded when $A_{10} = 0$.

(1) $A_{10} = 0$. Substituting equations (45*b*) and (45*c*) into equations (4*b*) and (4*c*), and balancing the terms of the constants and first harmonics, respectively, yields the following six equations:

Constant terms:

$$[Q_m + \gamma\beta_m\sum_{r=2}^{3}\beta_r(A_{r0}^2 + A_{r1}^2/2)]A_{m0} + \gamma\beta_m[\beta_mA_{m0}A_{m1} + \beta_jA_{j0}A_{j1}\cos\theta]A_{m1} = 0 \tag{46a}$$

$\sin\omega t$ or $\sin(\omega t + \theta)$:

$$[(17 - 9m)a_m\omega^2 + Q_m + \gamma\beta_m\sum_{r=2}^{3}\beta_r(A_{r0}^2 + A_{r1}^2/2) + \gamma\beta_m^2(2A_{m0}^2 + A_{m1}^2/4)]A_{m1} + [\omega\sqrt{\mu\beta Q}Q_{2s}^{(1)}\sin\theta + \beta_2\beta_3\gamma(2A_{20}A_{30}\cos\theta + A_{21}A_{31}\cos 2\theta/4)]A_{j1} = 0 \tag{46b}$$

$\cos\omega t$ or $\cos(\omega t + \theta)$:

$$(-1)^m(17 - 9m)\zeta\omega A_{m1} + [\omega\sqrt{\mu\beta Q}Q_{s2}^{(1)}\cos\theta + \beta_2\beta_3\gamma(2A_{20}A_{30}\sin\theta + A_{21}A_{31}\sin 2\theta/4)]A_{j1} = 0 \tag{46c}$$

where $m = 2$ and 3, and $j = 5 - m$,

$$Q_2 = Q_{22}^{(0)}(Q_2 - Q), \quad Q_3 = Q_{ss}^{(0)}(Q_3^* - Q), \quad \beta_2 = 4, \quad \beta_3 = 82 \tag{47}$$

For nontrivial solutions of A_{21} and A_{31}, we obtain, from equations (45*c*),

$$10(\zeta\omega)^2 + \{\omega\sqrt{\mu\beta Q}Q_{s2}^{(1)}\cos\theta + \beta_2\beta_3\gamma(2A_{20}A_{30}\sin\theta + A_{21}A_{31}\sin 2\theta/4)\}^2 = 0 \tag{48}$$

It follows from equation (48) that

$$\omega = 0 \tag{49}$$

because of $\zeta \neq 0$. That is, there is no limit cycle oscillation about the flat ($A_{10} = A_{20} = A_{30} = 0$) or second-mode ($A_{10} = A_{30} = 0$, $A_{20} \neq 0$) configuration.

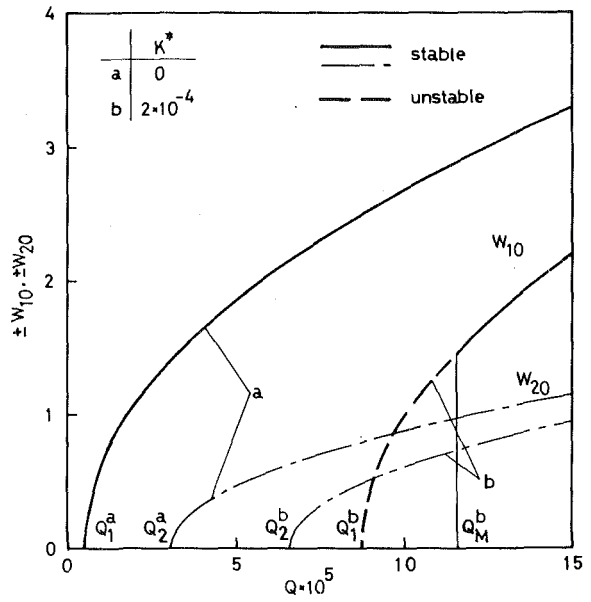

Fig. 2 Static equilibrium deflections of the first and second modes and their stability; W_{10}: —— (stable), — — (unstable); W_{20}: — - — (stable)

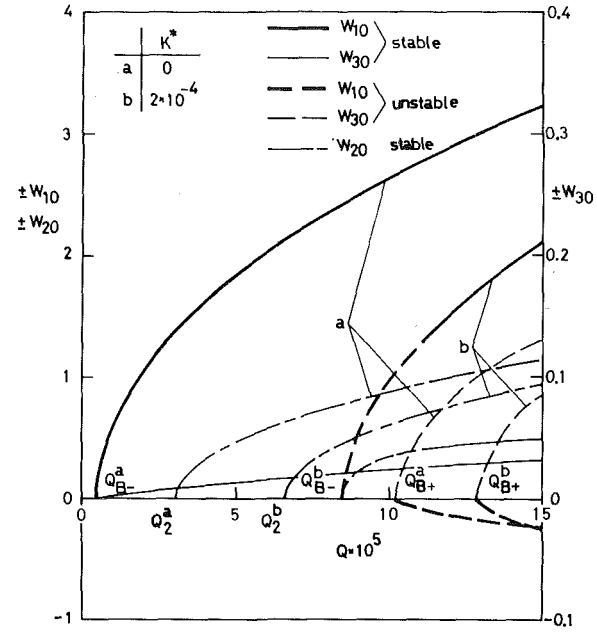

Fig. 3 Static equilibrium deflections of the symmetric coupled mode ($W_{10} \neq 0$, $W_{30} \neq 0$) and second mode ($W_{20} \neq 0$), and their stability, W_{10}: ——(stable), — —(unstable); W_{30}: — (stable), — — (unstable); W_{20}: — - — (stable)

(2) $A_{10} \neq 0$. In the same way as for the case of $A_{10} = 0$, using equations (4*a*)–(4*c*), we obtain seven equations governing A_{m0} (m = 1, 2, 3), A_{m1} (m = 2, 3), ω, and θ. In this case, the equation corresponding to (48) becomes

$$10(\zeta\omega)^2 + [\omega\sqrt{\mu\beta Q}Q_{32}^{(1)} \cos\theta + \beta_2\beta_3\gamma \{2A_{20}(A_{10}/\beta_3 + A_{30}) \sin\theta + A_{21}A_{31} \sin 2\theta/4\}]^2 = 0 \quad (50)$$

Consequently, we have again equation (49) for $A_{10} \neq 0$.

Therefore, we conclude that no limit cycle oscillation is predicted about flat and buckled configurations, even though two modes being capable of oscillatory motions are taken into account in the analysis.

5 Numerical Results and Discussions

Numerical calculations were carried out for a latex rubber panel exposed to airflow. The parameters used are the same as in references [7, 8]: $L/h = 100$, $\beta = 0.143$, $\mu = 0.952 \times 10^{-9}$sec^2, $\nu = 0.5$, $K^* = 0, 2 \times 10^{-4}$, $\zeta = 0.01\zeta_c$ where $\zeta_c = 2\sqrt{\mu k_1}$.

(*1*) *Two-Mode Analysis.* In Fig. 2, the static deflections of the first or second buckling mode of the panel are represented by solid and broken curves or thin chain-dotted curves, respectively, for (*a*) $K^* = 0$ and (*b*) $K^* = 2 \times 10^{-4}$. The critical boundary pressures associated with the Case (*a*) or (*b*) are indicated by a suffix *a* or *b*, respectively. As is shown analytically, the second-mode deflection is always stable against small disturbances, while the first-mode deflection may become statically unstable. This occurs for Case (*b*) since Q_M^b becomes greater than Q_1^b. The broken curve represents the unstable deflection.

(*2*) *Three-Mode Analysis.* Fig. 3 illustrates the static deflections of the symmetric coupled-mode ($W_{10} \neq 0$, $W_{30} \neq 0$, $W_{20} = 0$) and the second mode against the dynamic pressure Q. W_{10} or W_{30} is, respectively, shown by thick or thin solid and broken curves, W_{20} chain-dotted ones. Since the symmetric and second modes are not coupled, the deflections of the second mode are exactly the same as in Fig. 2. Since the numerical result shows that $Q_{B-} < Q_C < Q_{B+}$, there are two configurations of the coupled mode for $Q > Q_{B+}$, but none for $Q < Q_{B-}$. The coupled-mode deflection which starts to exist at $Q = Q_{B-}$ is considered to correspond to the first-mode configuration given in Fig. 2, as the amplitude of W_{30} is quite small compared with that of W_{10}. Like the first-mode configuration, this static deflection is always stable for $K^* = 0$. For $K^* = 2 \times 10^{-4}$, it is unstable below $Q = 1.11 \times 10^{-4}$ which corresponds to $Q_M^b = 1.16 \times 10^{-4}$, and gains its stability above it. As for the second coupled-mode configuration, the ratio of the amplitude of W_{30} to that of W_{10} is negative and of order of unity. It is unstable for both $K^* = 0$ and 2×10^{-4}. According to the numerical result, Q_A is negative for the Cases (*a*) and (*b*). Hence, the second-mode deflection is always stable. Additionally, since Q_2 is smaller than Q_3^*, the flat configuration remains to be stable up to $Q = Q_2$ like in the two-mode approximation.

The effect of dynamic modal-coupling on the stability is taken into account in the three-mode approximation analysis, but not in the two-mode analysis. The static configurations in equilibrium and their stability which are predicted by the two and three-mode analyses are similar.

Let us compare the present results with those of the analysis on a two-dimensional channel conveying a compressible, but almost incompressible flow which are given in reference [8]. First, we shall summarize the results of reference [8]: The flat configuration of the channel walls in static equilibrium is stable up to $Q = Q_s$, that is, the smaller of Q_1 and Q_2, but unstable above $Q = Q_s$. When $Q_1 < Q_2$, the static first-mode configuration is always stable, whereas the second mode is always unstable. If $Q_2 < Q_1$, then the second mode is stable for $Q_2 < Q < Q_M$ but becomes unstable above $Q = Q_M$. The first-mode configuration which is unstable for $Q_1 < Q < Q_M$ obtains its stability above $Q > Q_M$. No occurrence of the limit cycle oscillation of the walls is predicted.

The main difference between both results is the number of the stable static equilibrium configurations. At any dynamic pressure there is always only a single one for the channel walls. On the other hand, there may be two for the panel, as is seen in Figs. 2 and 3 of this paper. The addition of one more stable configuration of the panel might be caused by the limitation on modal oscillation due to the assumption of incompressible flow. If the compressibility is accounted for, then, for instance, the stable flat configuration in the range between Q_1 or Q_{B-}, and Q_2 for $K^* = 0$ might become unstable since the disturbance in the first mode would be able to increase with time there.

According to the linear stability analysis of reference [4], a finite flat panel is unstable for a narrow band range of the flow speed. Above this range, however, the flat configuration regains its stability. It was concluded that flutter oscillation occurs with further increase in the speed. In order to compare with this analysis, we will go back to (1*a*) *Flat Configuration* of Section 2.

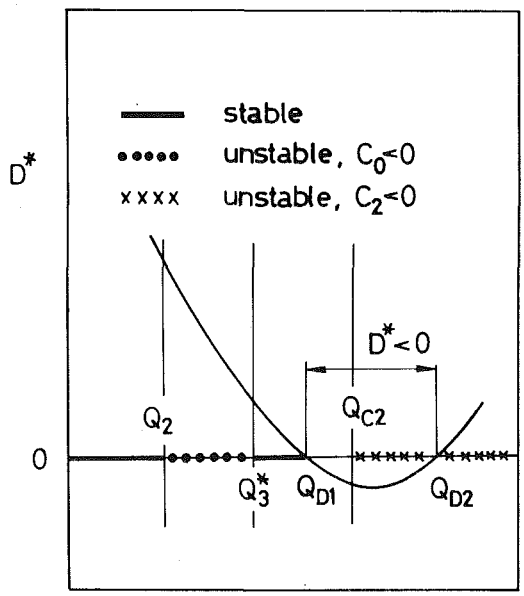

Fig. 4 The curve of D^* and the stable and unstable ranges of the small disturbances about the flat static configuration. ——: stable, - · -: $C_0 < 0$, — × —: $C_2 < 0$

In equations (29) and (30), let us put $W_{10} = W_{20} = W_{30} = 0$ as well as $\zeta = 0$ like in reference [4] so that we have, instead of equation (20), a biquadratic characteristic equation

$$C_4\epsilon^4 + C_2\epsilon^2 + C_0 = 0 \tag{51}$$

Since C_4, C_2, and C_0 are real, if a set of $a \pm ib$ (a, b: real) is a pair of complex conjugate roots, so is $-a \pm ib$. In this case the small disturbances described by equation (19) will increase oscillatorily. For stability ϵ^2 must be real and negative. Because of $C_4 > 0$, the condition for stability is

$$C_2 > 0, \quad C_0 > 0, \quad D^* > 0 \tag{52}$$

where

$$\begin{aligned} D^*[Q] &= C_2^2 - 4C_0C_4 \\ &= (a_2I_3 - a_3I_2)^2 + 2C_{22}(a_2I_3 + a_3I_2) + C_{22}^2 \end{aligned} \tag{53}$$

Let Q_{C2} be the dynamic pressure at which C_2 vanishes

$$Q_{C2} = \{(1 + \beta Q_{22}^{(2)})Q_{ss}^{(0)}Q_3^* + (1 + \beta Q_{ss}^{(2)}/10)Q_{22}^{(0)}Q_2\}/C_{de} \tag{54}$$

where

$$C_{de} = (1 + \beta Q_{22}^{(2)})Q_{ss}^{(0)} + (1 + \beta Q_{ss}^{(2)}/10)Q_{22}^{(0)} - \beta(Q_{s2}^{(1)})^2/10 \tag{55}$$

Q_{C2} is a monotonic function with respect to β. When

$$\beta > \beta_c \equiv 10Q_{22}^{(0)}(Q_3^* - Q_2)/[\{(Q_{s2}^{(1)})^2 - Q_{ss}^{(2)}Q_{22}^{(0)}\}Q_3^* + Q_{ss}^{(2)}Q_{22}^{(0)}Q_2], \tag{56}$$

Q_{C2} is greater than Q_3^*. In this case, putting

$$Q_{C2} = Q_3^* + \alpha \quad (\alpha > 0)$$

we obtain

$$D^*[Q_{C2}] = -4a_2a_3Q_{22}^{(0)}Q_{ss}^{(0)}\alpha(Q_3^* - Q_2 + \alpha) < 0$$

because of $Q_3^* > Q_2$. In addition, it is obvious from equations (53) that $D^* > 0$ for $0 < Q < Q_3^*$. Let us illustrate the curve of D^* and the stable and unstable regions in Fig. 4 where Q_{D1} and Q_{D2} satisfy $D^* = 0$.

The stability characteristics of this plate is the same as predicted in reference [4]. That is, the flat configuration is stable for both $0 < Q < Q_2$ and $Q_3^* < Q < Q_{D1}$ and unstable because of divergence for $Q_2 < Q < Q_3^*$. The small disturbances will increase in an oscillatory manner for $Q_{D1} < Q < Q_{D2}$. In reference [12], the similar linearized analysis is detailed for a cylindrical tube conveying a flow. As is analytically shown in Section 2 of the present paper where the viscous damping is taken into account, i.e., $\zeta \neq 0$, once the flat configuration starts to be unstable, its stability is never regained at the higher dynamic pressure. And no limit cycle oscillation is predicted about the flat configuration. Above the divergence boundary, there always exists at least one stable buckled configuration. Therefore, the oscillatory growth of the small disturbances about the flat configuration does not necessarily lead to occurrence of flutter oscillation. In this regard, it is recommended to reexamine the stability analyses on the simply supported tube conveying fluid, for instance, reference [13], in which the occurrence of flutter oscillation is predicted. Needless to say, the effect of the damping must be included.

In order to take into account dynamic instability due to coupling between the symmetric and antisymmetric modes, the third term is included in equation (3). In a higher-mode approximation, the deflection might be assumed like equation (3) to be

$$\begin{aligned} w = w_1 \sin\frac{\pi X}{L} + \sum_{m=1}^{N} w_{2m} \sin\frac{2m\pi X}{L} \\ + \sum_{m=1}^{N} w_{2m+1}\left\{(2m+1)\sin\frac{(2m+1)\pi X}{L} - \sin\frac{\pi X}{L}\right\} \end{aligned}$$

$$\text{for } N = 1, 2, 3, \ldots \tag{57}$$

A simpler modal assumption is, however, given by the ordinary Fourier sine series

$$w = \sum_{m=1}^{2N+1} w_m \sin\frac{m\pi X}{L} \quad \text{for} \quad N = 1, 2, 3, \ldots \tag{58}$$

When the stability is examined, it is necessary that the disturbed motion represented by

$$W_m = W_{m0} + \alpha_m \quad \text{for} \quad m = 1, 2, \ldots, 2N+1 \tag{59}$$

satisfies

$$\sum_{m=0}^{N} \alpha_{2m+1}/(2m+1) = 0 \tag{60}$$

Otherwise, the condition of no change in the fluid volume is violated.

Anyway, the present simplest analysis is considered to clarify the characteristic features of the stability. It is pointed out that the incompressible flow assumption imposes an artificial condition, and that there may exist the excess stable static configuration. Therefore, it is most important to employ a compressible flow theory in a further investigation.

6 Concluding Remarks

The stability of a two-dimensional panel of finite length exposed to an incompressible flow has been reexamined by using the generalized aerodynamic forces which are presented in the author's previous paper. In analyzing the dynamic behavior of the panel the deflection is assumed in such a way that during the oscillation of the panel there occurs no change in the fluid volume in an arbitrary control surface enclosing the plate. For the numerical example used, the flat configuration in static equilibrium is stable below $Q = Q_2$ regardless of the values of Q_1 and Q_{B-} for the two and three-mode approximations, respectively. Therefore, there are pressure ranges in which the panel possesses two stable static configurations. No limit cycle oscillation is predicted about the flat or buckled static configuration. A comparison with the stability analysis on a two-dimensional channel conveying an almost incompressible flow suggests that the assumption of incompressibility of the flow may induce an excess stable static configuration. Therefore, it is recommended to use a compressible flow theory in a future investigation. In addition, it is important to take into account the damping which always exists in reality.

Acknowledgment

The author would like to express his sincere thanks to Dr. T. Ueda of the National Aerospace Laboratory for his valuable comments.

References

1 Weaver, D. S., Unny, T. E., and Dowell, E. H., "The Hydroelastic Stability of a Flat Plate," ASME JOURNAL OF APPLIED MECHANICS, Vol. 38, 1971, p. 565.

2 Dowell, E. H., "Nonlinear Oscillations of a Fluttering Plate, II," *AIAA Journal*, Vol. 5, No. 10, 1967, pp. 1856–1862.

3 Holmes, P. J., "Bifurcations to Divergence and Flutter in Flow-Induced Oscillations: A Finite Dimensional Analysis," *Journal of Sound and Vibration*, Vol. 53, No. 4, 1977, pp. 471–503.

4 Dugundji, J., Dowell, E., and Perkin, B., "Subsonic Flutter of Panels and Continous Elastic Foundations," *AIAA Journal*, Vol. 1, No. 5, 1963, pp. 1146–1154.

5 Ishii, T., "Aeroelastic Instabilities of Simply Supported Panels in Subsonic Flow," AIAA Paper No. 65-772, 1965.

6 Gislason, T., Jr., "Experimental Investigation of Panel Divergence at Subsonic Speeds," *AIAA Journal*, Vol. 9, No. 11, 1971, pp. 2252–2258.

7 Matsuzaki, Y., and Fung, Y. C., "Stability Analysis of Straight and Buckled Two-Dimensional Channels Conveying an Incompressible Flow," ASME JOURNAL OF APPLIED MECHANICS, Vol. 44, 1977, pp. 548–552.

8 Matsuzaki, Y., and Fung, Y. C., "Nonlinear Stability Analysis of a Two-Dimensional Model of an Elastic Tube Conveying a Compressible Flow," ASME JOURNAL OF APPLIED MECHANICS, Vol. 46, 1979, pp. 31–36.

9 Matsuzaki, Y., and Ueda, T., "Reexamination of Unsteady Fluid Dynamic Forces on a Two-Dimensional Finite Plate at Small Mach Numbers," ASME JOURNAL OF APPLIED MECHANICS, Vol. 47, 1980, pp. 720–724.

10 Weaver, D. S., and Unny, T. E., "The Hydroelastic Stability of a Flat Plate," ASME JOURNAL OF APPLIED MECHANICS, Vol. 37, 1970, pp. 823–827.

11 Kornecki, A., "Static and Dynamic Instability of Panels and Cylindrical Shells in Subsonic Potential Flow," *Journal of Sound and Vibration*, Vol. 32, No. 2, 1974, pp. 251–263.

12 Matsuzaki, Y., and Fung, Y. C., "Unsteady Fluid Dynamic Forces on a Simply Supported Circular Cylinder of Finite Length Conveying a Flow, With Applications to Stability Analysis," *Journal of Sound and Vibration*, Vol. 54, No. 3, 1977, pp. 317–330.

13 Paidoussis, M. P., and Issid, N. T., "Dynamic Stability of Pipes Conveying Fluid," *Journal of Sound and Vibration*, Vol. 33, No. 3, 1974, pp. 267–294.

D. C. Drucker
Dean,
College of Engineering,
University of Illinois,
Urbana, Ill. 61801
Fellow ASME

L. Palgen
Aspirant du Fonds National Belge de la Recherche Scientifique,
Department of Theoretical and Applied Mechanics,
University of Illinois,
Urbana, Ill. 61801

On Stress-Strain Relations Suitable for Cyclic and Other Loading

The analysis and design of pressure vessels and other structures subjected to cyclic loading and occasional large overloads requires stress-strain relations sufficiently simple to be usable with computer programs and yet adequate to describe the essential aspects of the response of the material. One such form with two quite different options is proposed for the time-independent domain which avoids the difficulties of earlier approaches. It has the kinematic hardening attributes needed for reversal of loading, allows for cyclic hardening or softening, gives zero mean stress as the asymptotic response to cyclic straining between fixed limits of strain, and reduces to a J_2 stress-hardening form for radial or proportional loading so that it can model both cyclic and other loading to a good first approximation.

Introduction

Many important machines and structures such as pressure vessels, turbines, and railroad wheels are subjected to cycles of load, or to cycles of temperature, or both, that produce significant inelastic response. Their design also must encompass the probabilities of occasional large excursions of load or temperature that may precede, interrupt, or follow this exposure to low cycle fatigue.

Considerable attention has been devoted to the experimental determination of the behavior of material subjected to cycles of uniaxial stressing or straining, or subjected to cycles of shear. Cyclic hardening, cyclic softening, and the usual approach to cyclic stability have been demonstrated by the extensive investigations of Dolan, Morrow, their colleagues and students, and many others throughout the world [1, 2]. However, little is known about the response of materials to more complex cycles beyond the preliminary study made by Lamba [3, 4].

Many models have been proposed to fit one or more aspects of the response that has been observed in experiments. Time-independent behavior is of sufficient interest and complexity to have attracted major attention, but with the full recognition that time effects often are significant and may well govern design. Some models aim at a detailed and accurate representation of observed behavior over a wide range of loading paths. Consequently, they are rather elaborate and difficult to incorporate in computer programs for complex structures. Others are addressed to an important but limited aspect of the behavior of the material and are not to be used outside of that range of applicability.

Contributed by the Applied Mechanics Division for presentation at the Winter Annual Meeting, Washington, D. C., November 15–20, 1981, of THE AMERICAN SOCIETY OF MECHANICAL ENGINEERS.

Discussion on this paper should be addressed to the Editorial Department, ASME, United Engineering Center, 345 East 47th Street, New York, N. Y. 10017, and will be accepted until December 1, 1981. Readers who need more time to prepare a discussion should request an extension from the Editorial Department. Manuscript received by ASME Applied Mechanics Division, July, 1980; final revision, January, 1981. Paper No. 81-WA/APM-6.

The purpose of this paper is to propose a model for consideration that is simple enough to be used effectively in computer programs and yet matches the essential features of the time-independent inelastic behavior of materials reasonably well for cyclic loading and for occasional overloading separately and in combination. In the sections that follow, an outline will be given of the features of material behavior perceived as most essential and relevant. A simple model with two options will be proposed for cyclically stable material. One option matches the rounding of cyclic stress-strain curves, the other without the rounding matches the behavior on reloading following almost purely elastic unloading. The difficulties or limitations of earlier models will be exhibited along with possible physical or mathematical explanations for them. Cyclic hardening or softening then will be introduced into the simple model for each of the two options and the ability to match experimental information will be demonstrated. Finally, more elaborate forms of such a model, that include time-dependent behavior and other ignored aspects of the real world, will be touched upon briefly. Their development seems premature in the absence of an accepted, broadly useful, elementary form for the time-independent idealization.

Material Behavior Perceived as Most Essential and Relevant

The complexity of all the details of the inelastic behavior of material is infinitely great even when all time effects are ignored. Obviously, therefore, the selection of just a few key aspects as the most essential and relevant for the purpose is a debatable matter of judgment and definition of essential. The choice is strongly dependent upon the perception of purpose and relevance. Our purpose here is to write a simple usable form that will include as a minimum both large excursions of loading well out into the plastic range and the cyclic loading that gives plastic hysteresis loops and can result in low cycle fatigue. Our short list of the most essential and relevant aspects of material behavior prior to significant material damage is:

1 Load excursions well out into the plastic range overwhelm or

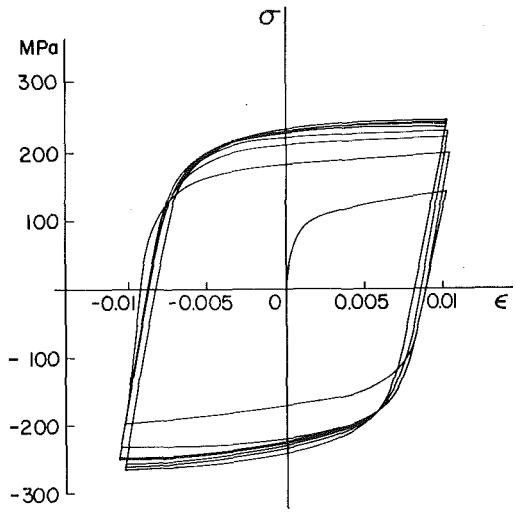

Fig. 1 Data on 304 stainless steel [18]

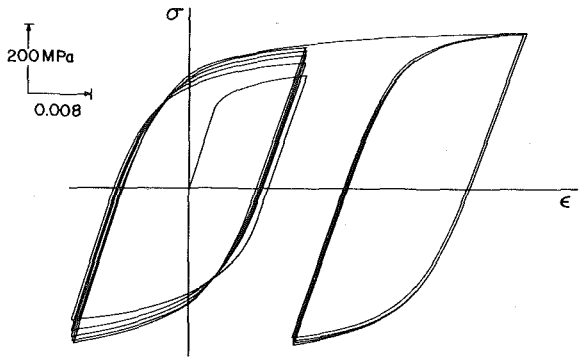

Fig. 2 Data on 2024-T4 aluminum

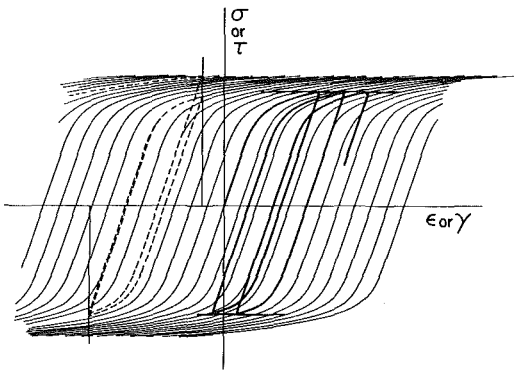

Fig. 3 Unsymmetric cycles of strain and of stress for cyclically stable material

wipe out many of the effects of the history of plastic deformation prior to such large overloads. It is relevant but not essential that, for such excursions, a Mises or J_2 stress-hardening form is usually a satisfactory approximation for those metals and alloys that are fairly isotropic in their initial state.

2 Under symmetric cycles of stress or strain, metals and alloys in a soft or annealed state to start will harden cyclically and tend to a stable limit cycle, Figs. 1, 2; those in a very hard or cold-worked condition to start will soften to the stable cycle; and those already in the stable condition neither harden nor soften but simply go through the stable cycle so evocative of kinematic hardening [5].

3 Unsymmetric cycles of stress in the plastic range will cause progressive "creep" or "ratcheting" in the "direction" of the mean stress, right-hand side of Fig. 3.

4 Unsymmetric cycles of strain in the plastic range will cause progressive relaxation to zero of the mean stress in the cycle, left-hand side of Fig. 3.

A model will be presented here with two options, each of which satisfies our four requirements 1–4. The first option gives full rounding of the stress-strain curve on each load reversal following appreciable plastic deformation, a condition often encountered in practice. The second option gives a sharp transition when going from purely elastic to elastic-plastic response, which is the correct picture for reloading following almost purely elastic unloading. Neither of these model options is as appropriate for both types of loading as are the models of Mroz [6] and the other assemblages of many simple models in parallel that correspond to a large set of closely nested yield or loading surfaces [7]. However, the broader match by such assemblages is at the sacrifice of simplicity and some important elements of reality.

A Simple Model for Cyclically Stable Material

The expression for the increment or rate of plastic strain $\dot{\epsilon}^p_{ij}$ of a time-independent material with a smooth yield surface $f = 0$ is

$$\dot{\epsilon}^p_{ij} = G \frac{\partial f}{\partial \sigma_{ij}} \frac{\partial f}{\partial \sigma_{mn}} \dot{\sigma}_{mn} \tag{1}$$

where G is a scalar multiplier, σ_{ij} is the current stress, $\dot{\sigma}_{mn}$ its increment or rate, and repeated subscripts denote summation.

Cyclic creep or ratcheting and stress relaxation can occur whether the material hardens, softens, or is stable. Therefore, it is reasonable to postpone the examination of hardening or softening and consider a cyclically stable material first.

A combination of the Mises stress-hardening form and the kinematic hardening proposed by Prager [5] and modified by Shield and Ziegler [8, 9] includes the key aspects 1 and 2 of cyclically stable material behavior. The simplest permissible and yet appropriate choices appear to be

$$G = A J_2^N \tag{2}$$

and

$$f = \tfrac{1}{2}(s_{ij} - s^c_{ij})\,(s_{ij} - s^c_{ij}) - k^2 = 0 \tag{3}$$

where A, N, and k are constants, $J_2 = \frac{1}{2} s_{ij} s_{ij}$, s_{ij} is the stress deviator $\sigma_{ij} - \frac{1}{3}\sigma_{qq}\delta_{ij}$, s^c_{ij} is the center of the spherical yield domain in stress deviator space, and k is the yield stress in simple shear when the yield domain is centered at the origin, $s^c_{ij} = 0$. The center moves in the direction of $s_{ij} - s^c_{ij}$ at a rate equal to the projection of $\dot{s}_{mn}$ on that direction in accordance with a Ziegler type of rule that satisfies the consistency condition of the stress point s_{ij} remaining on the current yield surface, or $\dot{f} = 0$

$$\dot{s}^c_{ij} = (s_{ij} - s^c_{ij})\,(s_{mn} - s^c_{mn})\,\dot{s}_{mn}/2k^2 \tag{4}$$

and

$$\dot{\epsilon}^p_{ij} = A J_2^N\,(s_{ij} - s^c_{ij})\,(s_{mn} - s^c_{mn})\,\dot{s}_{mn} \tag{5}$$

for this simplest of the analytic models of an initially isotropic and symmetric cyclically stable elastic-plastic material.

Simple tension or simple shear or any radial (proportional) loading is represented by

$$\sigma_{ij} = R\,\sigma^0_{ij}, \quad s_{ij} = R\,s^0_{ij}, \quad \dot{s}_{ij} = \dot{R}\,s^0_{ij} \tag{6}$$

where the fixed state of stress σ^0_{ij} or stress deviator s^0_{ij} is on the (initial) yield surface for $s^c_{ij} = 0 = \sigma^c_{ij}$. The response of the material is purely elastic up to $R = 1$ and then is elastic-plastic in accord with equations (4) and (5) as R increases. When plastic deformation takes place in this forward direction or in the reverse direction as R decreases and becomes negative

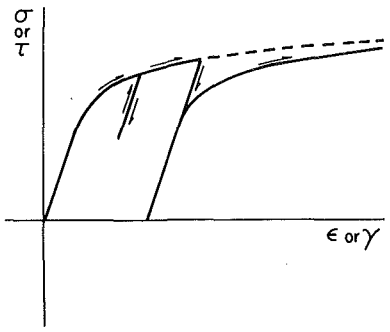

Fig. 4 A poor representation by the rounding option when plastic deformation occurs on unloading to zero stress and on subsequent reloading

$$\dot{s}^e_{ij} = \dot{s}_{ij}; \quad s_{ij} - s^e_{ij} = \pm s^0_{ij}; \quad \sigma_{ij} - \sigma^e_{ij} = \pm\sigma^0_{ij} \tag{7}$$

The stress-strain relation (5) can be written in terms of $\dot{s}^e_{ij}$ from (4) and then with $\dot{s}_{ij}$ from (7)

$$\dot{\epsilon}^p_{ij} = 2k^2 A J_2^N \dot{s}^e_{ij} = 2k^2 A J_2^N \dot{s}_{ij} = 2A k^{2N+2} |R|^{2N} \dot{s}_{ij}$$
$$= 2A k^{2N+2} |R|^{2N} \dot{R} s^0_{ij} \tag{8}$$

For monotonically increasing R, direct integration of (8) gives the total plastic strain

$$\epsilon^p_{ij} = \frac{2A k^{2N+2}}{2N+1} (R^{2N+1} - 1) s^0_{ij} \tag{9}$$

but the incremental form (8) will normally be more useful here.

When the radial loading path is simple tension $\sigma = R\sigma_0$, where $\sigma_0 = \sqrt{3}k$ is the initial tensile (or compressive) yield stress, the plastic tensile strain

$$\dot{\epsilon}^p = 2A (\tfrac{1}{3}\sigma_0^2)^{N+1} (|\sigma|/\sigma_0)^{2N} (\tfrac{2}{3}) \dot{\sigma} \tag{10}$$

When the path is simple shear $\tau = R\tau_0$, where $\tau_0 = k$ is the initial yield stress in shear and $\dot{\epsilon}^p_{12} = \frac{1}{2}\dot{\gamma}^p$

$$\tfrac{1}{2}\dot{\gamma}^p = 2A (\tau_0^2)^{N+1} (|\tau|/\tau_0)^{2N} \dot{\tau} \tag{11}$$

The introduction of a stress-dependent plastic modulus inversely proportional to J_2^N gives the correct qualitative picture of cyclic creep and stress relaxation in simple tension or simple shear. This is shown in Fig. 3, where the elastic-plastic stress-strain curves are identical except for a translation along the strain axis.

The rounding option, illustrated in Fig. 3, uses a yield surface of small diameter. Unfortunately, on reloading following appreciable unloading or reverse loading with small plastic deformation, the stress-strain curve exhibits full rounding well before reaching the stress level from which unloading began, Fig. 4. This is the price paid to obtain proper rounding of the hysteresis loops. There is also a somewhat more subtle problems with this option. When reverse plastic deformation occurs on unloading (before reaching zero stress) the reciprocal of the plastic tangent modulus starts off with a positive value but then decreases to zero as the stress goes to zero before it begins to increase again. This clearly is an incorrect representation. However, it occurs only in the region of small stress for a reasonable choice of k and, although not aesthetic, can be ignored because the plots obtained will differ only very little from purely elastic response. The apparent elastic range is extended. For all practical purposes, no significant plastic deformation is computed until the sign of the stress reverses and the magnitude of the reversed stress is a significant fraction of the initial yield stress.

Corresponding errors of representation appear for loading paths and cycles that do not include the origin, paths for which the J_2 form itself is a less satisfactory approximation.

The sharp corner option or representation, appropriate for a sequence of unloading and reloading, is obtained by introducing a large diameter yield surface, so that only the flat portion of the elastic-plastic stress-strain curves of Fig. 3 is used. This rules out reverse plastic deformation on unloading.

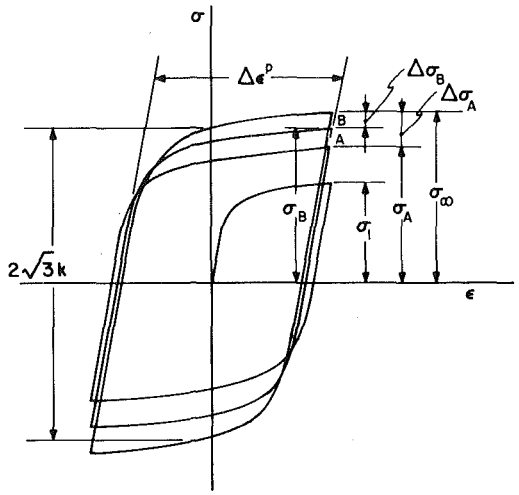

Fig. 5 Elastic range for the sharp corner option and measurements for the determination of α and W_0

The choice of a small or large diameter yield surface will be governed by the aspects of behavior most important for the application at hand.

The parameters of the model are found from the upper or lower half of a stable hysteresis loop of the material. $2N$ comes from the slope of a plot of $\log \dot{\epsilon}^p/\dot{\sigma}$ or $\log \dot{\gamma}^p/\dot{\tau}$, the logarithm of the reciprocal of the plastic tangent modulus, versus $\log \sigma$ or $\log \tau$, in the range of plastic strains that is of greatest interest to the user of the model. Elastic strain increments must, of course, be taken into account in reducing the data; $\dot{\epsilon}^e = \dot{\sigma}/E$, $\dot{\gamma}^e = \dot{\tau}/\mu$, etc., add to the plastic strain increments or rates to give total increments or rates, $\dot{\epsilon} = \dot{\epsilon}^e + \dot{\epsilon}^p$, etc.

In the rounding option k should be taken as large as possible consistent with the desired rounding of the loop, in order to suppress or minimize plastic deformation on unloading and to reduce improper rounding on direct reloading. Except for these two and closely related loading cases, the model will be insensitive to the particular choice of k, as can be seen from Fig. 3.

In the sharp corner approach, however, the size of the yield surface has a dominant effect because it determines the stress level of the plastic response. The elastic range $2\sqrt{3}k$ in tension-compression is comparable to the total height of the hysteresis loop and is taken as the vertical distance at zero total strain, Fig. 5. Because of their flatness, the computed stress-strain curves (Fig. 7) will be affected little by large variations of N.

Finally, A should be chosen to match the value of stress at some intermediate value of strain within the range of plastic strains of greatest interest.

A wide variety of more complex stress-strain relations are available for time-independent behavior [10–14] that can model one or more aspects of material behavior more closely than the simple three constant form proposed here. Before considering the next step of modifying the present form to include cyclic hardening or softening, it is worth examining those time-independent models that have been proposed and used for cyclic loading.

Scope and Limitations of Some Earlier Models

One or another aspect of reversed or of cyclic loading has attracted attention in the past and led to suggestions of mathematical models. A set of bars in parallel can model a simple tension curve as accurately as desired. If each bar is elastic-perfectly plastic with the same properties in tension and compression, the assemblage is immediately cyclically stable for an unsymmetric cycle of stress or strain [7], Fig. 6. The assemblage does not "creep" or relax as it should in accord with the requirements 3 and 4 listed under essential material behavior.

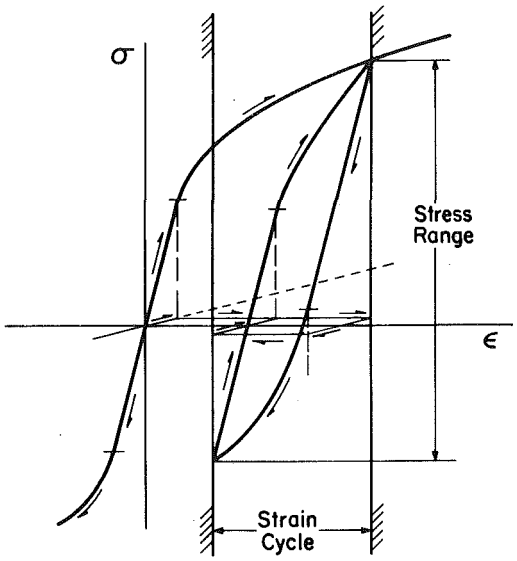

Fig. 6 An immediate and inappropriate unsymmetric stable cycle

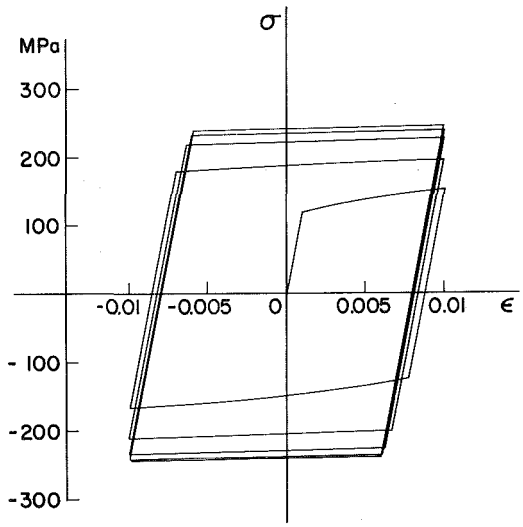

Fig. 7 Model simulation by the sharp corner option computed with data of Fig. 1

The more general assemblages of elastic-perfectly plastic homogeneous elements or states in parallel with their nested yield surfaces have the same ability to model stress-strain behavior accurately for generally outward loading paths and to exhibit a significant realistic Bauschinger effect for a single reversal of loading. However, they too suffer from the defect of not creeping as they should in the direction of the mean stress in an unsymmetric plastic cycle of stress and not settling down to zero mean stress in an unsymmetric plastic cycle of strain.

Permitting one or more elements of the assemblage to harden, as each strains plastically, produces a model of a cyclically hardening material but does not overcome the basic difficulty of an inappropriate response to unsymmetric plastic cycles of stress or of strain. The models of Caulk and Naghdi [13] and of Popov [12] have this basic drawback. So also to a far lesser extent does the model of Mroz [6] with two or more nested yield or loading surfaces. However, each model was devised for its own special set of requirements for matching particular aspects of real world behavior. None began with all the requirements 1–4 that have been chosen here as essential.

Differences in principle of the degree of thermodynamic reversibility between assemblages of states in parallel or series and dislocation structure were pointed out still earlier by Drucker [7] for both conventionally cyclically stable models with nested loading surfaces and cyclically hardening models with intertwined loading surfaces. Useful and physically appealing as such assemblages may be for a variety of problems, whether they are in the forms just described or in the form of parallel layers for beams, plates, and shells [15], they cannot represent unsymmetric cyclic behavior properly.

Alternative approaches have been proposed to give proper rounding of reversed loading curves as well as proper cyclic response [11]. They, as well as several of the earlier suggestions, seem more elaborate than can be handled economically on computers today for boundary-value problems with pointwise varying multiaxial states of stress in which large load excursions are superposed occasionally on low-cycle fatigue loading. Some of the complexity appears to be caused by the manner in which the consistency condition is employed.

It is necessary for the stress point to remain on the yield surface(s) and for the center of each surface to move appropriately as plastic deformation continues. However, when this is built into the model automatically through a specification in stress space as in equation (4), the choice of a reasonable stress-strain relation is quite free. The reverse approach, which relates the motion of the stress point and the center of the yield surface through an incremental stress-strain relation that is chosen in advance, can lead to a consistency relation that may not be satisfied conveniently. This more difficult approach so common today for nonlinear plastic hardening has not given good results except for the model of Arutyunyan and Vakulenko [14]. It may have developed as a consequence of generalizing Prager's illustrative example of linear kinematic hardening, in which the motion of the yield surface in stress space is proportional to plastic strain. Any linking of the location of the yield surface in stress space to the current components of plastic strain causes a severe difficulty. This class of models can match observed Bauschinger effects for a single reversal of loading extremely well, as demonstrated in a paper with Edelman [10]. However, such models are not appropriate for cyclic loading because unsymmetric strain cycles give unsymmetric stress cycles.

The temptation to think of the special form $f(\sigma_{ij}, \epsilon^p_{pq})$ as a good first approximation to reality must be resisted here. Writing

$$f = 0 = \frac{\partial f}{\partial \sigma_{ij}} \dot{\sigma}_{ij} + \frac{\partial f}{\partial \epsilon^p_{mn}} \dot{\epsilon}^p_{mn},$$

and replacing

$$\frac{\partial f}{\partial \sigma_{ij}} \dot{\sigma}_{ij} \text{ by } -\frac{\partial f}{\partial \epsilon^p_{mn}} \dot{\epsilon}^p_{mn}$$

generally leads to undesirable and misleading constraint.

Modification of the Proposed Simple Model to Include Hardening or Softening

The term hardening or softening in the cyclic context could refer to the increase or decrease in the diameter of the yield surface or to the increase or decrease in the plastic tangent modulus at a given stress or to both. The first definition is appropriate for the generalization of the sharp corner approach and the second definition for the rounding representation. Pure kinematic hardening with a translating yield surface as given by equation (3) and a purely stress-dependent plastic modulus as given by equation (5) is neither hardening nor softening in either sense although the stress-strain relation (5) gives rise to the usual work-hardening picture for each radial loading as exhibited by form (10) for simple tension and form (11) for simple shear.

The sharp corner form with cyclic hardening or softening is obtained by replacing k^2 in (3) by F, a positive scalar function of the path of straining, thereby permitting the diameter of the yield surface to change. Increase in F gives cyclic hardening, decrease gives cyclic softening. However, the more general expression

$$f = \tfrac{1}{2} (s_{ij} - s^c_{ij}) (s_{ij} - s^c_{ij}) - F = 0 \tag{12}$$

does not require any alteration in the form of expression (5) of the stress-strain relation

$$\dot{\epsilon}^p_{ij} = A\, J_2^N\, (s_{ij} - s^c_{ij})\, (s_{mn} - s^c_{mn})\, \dot{s}_{mn}$$

and any of the specialized forms such as (10) for simple tension. The somewhat strange result is that for a hardening material purely in the sense of σ_0 increasing, the plastic modulus $\dot{\sigma}/\dot{\epsilon}^p$ at a given value of stress σ *decreases*. The motion of the center of the yield surface $\dot{s}^c_{ij}$ is affected significantly by the increase or decrease in F. Equation (4) is replaced by a more general form that reduces to (4) when F is constant.

$$\dot{f} = 0 = (s_{ij} - s^c_{ij})\, (\dot{s}_{ij} - \dot{s}^c_{ij}) - \dot{F} \tag{13}$$

or

$$\dot{s}^c_{ij}\, (s_{ij} - s^c_{ij}) = (s_{mn} - s^c_{mn})\, \dot{s}_{mn} - \dot{F} \tag{14}$$

With the Prager-Ziegler type of assumption that $\dot{s}^c_{ij}$ is in the direction of $s_{ij} - s^c_{ij}$

$$\dot{s}^c_{ij} = [(s_{mn} - s^c_{mn})\, \dot{s}_{mn} - \dot{F}]\, (s_{ij} - s^c_{ij})/2F \tag{15}$$

Any one of a variety of choices for the functional dependence of F might be selected on a trial basis. F as a function of plastic work,

$$W^p = \int_t \sigma_{ij}\, \dot{\epsilon}^p_{ij}\, dt = \int_t s_{ij}\, \dot{\epsilon}^p_{ij}\, dt,$$

or of cumulative plastic strain measured by

$$\int_t \sqrt{\dot{\epsilon}^p_{ij}\, \dot{\epsilon}^p_{ij}}\, dt,$$

is not unreasonable. The choice of F as a function of

$$W^{pc} = \int_t (s_{ij} - s^c_{ij})\, \dot{\epsilon}^p_{ij}\, dt \tag{16}$$

will be made here instead because it also is not unreasonable and it does result in a convenient form for $\dot{s}^c_{ij}$. When plastic deformation takes place, (16) may be rewritten using (5) and (12) as

$$W^{pc} = \int_t (2F)\, A\, J_2^N\, (s_{mn} - s^c_{mn})\, \dot{s}_{mn}\, dt \tag{17}$$

It is of some interest to note that $\int_t \sqrt{\dot{\epsilon}^p_{ij}\, \dot{\epsilon}^p_{ij}}\, dt$ is given by the same form (17) except for $\sqrt{2F}$ instead of $2F$ and so is proportional to W^{pc} for cyclically stable material. Substitution of

$$\dot{F} = (dF/dW^{pc})\, \dot{W}^{pc} \tag{18}$$

in (15) gives

$$\dot{s}^c_{ij} = [1 - 2F(dF/dW^{pc})\, A\, J_2^N] \times [(s_{mn} - s^c_{mn})\, \dot{s}_{mn}]\, (s_{ij} - s^c_{ij})/2F \tag{19}$$

One of many reasonably simple choices for F that permits an adjustable asymptotic approach to the cyclically stable value $F = k^2$ is

$$F = k^2\, [1 \mp \alpha \exp\, (-W^{pc}/W_0)]^2 \tag{20}$$

where the upper sign applies for hardening from $F = k^2(1 - \alpha)^2$ to $F = k^2$, with α restricted to lie between zero and one. The lower sign applies for softening from $F = k^2(1 + \alpha)^2$ to k^2 for any positive α. The other disposable constant W_0 in (20) permits adjustment of the rate of hardening or softening. W_0 is the value of W^{pc} at which $F = k^2(1 \mp \alpha/e)^2$. Also, from (20)

$$\frac{dF}{dW^{pc}} = \pm\, 2k^2\, \frac{\alpha}{W_0} \exp\, (-W^{pc}/W_0)\, [1 \mp \alpha \exp\, (-W^{pc}/W_0)] = \pm\, \frac{2F(\alpha/W_0) \exp\, (-W^{pc}/W_0)}{1 \mp \alpha \exp\, (-W^{pc}/W_0)} \tag{21}$$

In the rounding representation, expansion or shrinking of the yield surface does not affect the hysteresis loops appreciably. Cyclic hardening or softening must be provided by the alternate definition, i.e., an increase or decrease in the plastic tangent modulus at each stress point. Perhaps the simplest approach is to maintain a constant (small) diameter yield surface and to give a hardening form by rewriting (5) as

$$\dot{\epsilon}^p_{ij} = B \left(\frac{J_2}{\bar{\sigma}^2}\right)^N (s_{ij} - s^c_{ij})\, (s_{mn} - s^c_{mn})\, \dot{s}_{mn} \tag{22}$$

Cyclic hardening is given by an increase in the normalizing stress $\bar{\sigma}$, cyclic softening by a decrease. Following the same steps which lead to the functional dependence of F in the previous form, one can write, similarly to equation (20),

$$\bar{\sigma} = \sigma^*\, [1 \mp \alpha \exp\, (-W^{pc}/W_0)] \tag{23}$$

where σ^* is a constant stress and the sign before α is chosen in the same way as for equation (20). The stable form of (22) is identical to (5) if one lets

$$A = \frac{B}{(\sigma^*)^{2N}} \tag{24}$$

Because the size of the yield surface remains constant, the motion of its center is still described by (4). However, the specialized forms for radial loading, (8)–(11), must be modified. For example, (10) becomes

$$\dot{\epsilon}^p = \frac{2B\sigma_0^2}{3^{N+1}} \left(\frac{|\sigma|}{\bar{\sigma}}\right)^{2N} (2/3)\, \dot{\sigma} \tag{25}$$

No matter what form of incremental stress-strain relation is chosen, the solution to a boundary-value problem requires keeping track, at each point of the body, of the state of stress, the location of the current yield surface in stress space or equivalent information, and the increment or rate of strain accompanying the increment or rate of stress. The iterative process to be followed for each increment of load and displacement or temperature change applied to the body, and the direct updating of s^c_{ij} to give the state and response of the material at each point, can be done sequentially within the accuracy of representation of the model. Equation (19) for the motion of the center of the yield surface in the sharp corner option and equation (22) for plastic strain rates in the rounding option are more complicated than the corresponding equations (4) and (5) for the cyclically stable material, but their use and the calculation of $\dot{W}^{pc}$ are straightforward given $\dot{s}_{ij}$ and current values of W^{pc}, F or $\bar{\sigma}$, s_{ij}, and s^c_{ij}.

The parameters of the model for both forms are conveniently chosen from a fully reversed, strain-controlled test in tension-compression, as explained below, or analogously for shear. Material constants A or $B/(\sigma^*)^{2N}$, k, N are determined in the manner already described for the stable loop.However, in the sharp corner form, and for a cyclically hardening material, the log-log plot of the reciprocal of the plastic tangent modulus versus stress, which provides N, is now a plot for the initial loading curve, where N has the most influence on model predictions, Fig. 7. Similarly, in the rounding form, k is taken as large as possible, consistent with the stress level of the initial loading curve.

Quite independently of the values chosen for A or $B/(\sigma^*)^{2N}$, k, N, the initial response and the approach to the stable cyclic response determine the remaining constants α and W_0/k. Let σ_1 and σ_∞ be the stresses at the end of the initial curve and at the tip of the stable loop, Fig. 5. Equations (20) for the sharp corner option or (23) for the rounding option suggest that a first approximation to α is

$$\sigma_1/\sigma_\infty = 1 \mp \alpha \tag{26}$$

The choice of W_0/k for the rounding option requires picking two points A and B at the end of any two curves in the course of hardening or softening and measuring the stress differences $\Delta\sigma_A$ and $\Delta\sigma_B$ from the tip of the stable loop, Fig. 5. In view of the exponential rate of approach to the stable cycle described by (23), an approximate value of W_0/k is given by

$$\frac{\Delta\sigma_B}{\Delta\sigma_A} = \exp\left[-\frac{\sqrt{3}\, k\, (2n)\, \Delta\epsilon^p}{W_0}\right] \tag{27}$$

where n is the number of cycles between A and B and $\Delta\epsilon^p$ is the average plastic strain range of a cycle and is measured as indicated in Fig. 5. For the sharp corner option, one must in addition use the stresses σ_A and σ_B, Fig. 5, to get W_0/k from

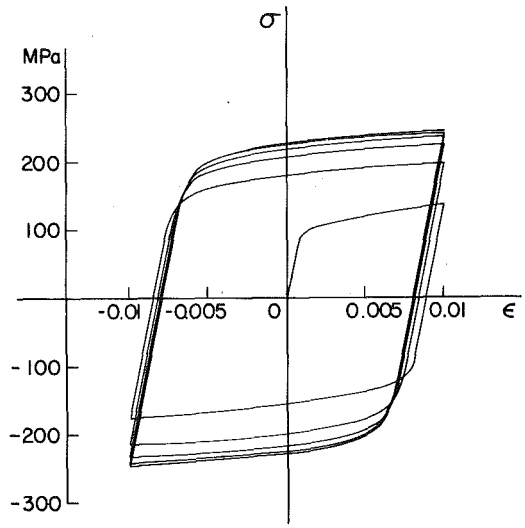

Fig. 8 Model simulation by the rounding option computed with data of Fig. 1

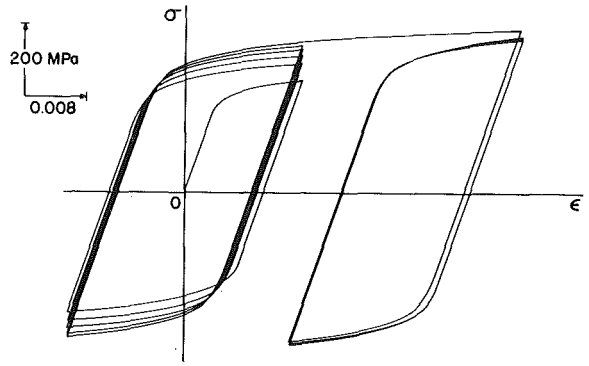

Fig. 9 Model simulation by the rounding option computed with data of Fig. 2

$$\frac{\sigma_A}{\sigma_B}\frac{\Delta\sigma_B}{\Delta\sigma_A} = \exp\left[-\frac{\sqrt{3}\,k\,(2n)\,\Delta\epsilon^p}{W_0}\right] \tag{28}$$

More elaborate methods can determine α and W_0 more accurately. However, they probably are not worth developing because a close match of a single set of data does not guarantee a correct response to a different, e.g., nonradial, loading path.

Of course, a model with 3 constants available for radial loading and stable cyclic response and two more for cyclic hardening or softening cannot aim at a precise description of material behavior for a variety of paths of loading. Far more elaborate forms than the J_2 or Mises form are known to be required for radial loading alone. Quite complicated functions of the history of loading, not constants, are needed to obtain just a moderately good representation in detail of the strain history for more general loading paths.

However, just as the very crude approximation of perfect plasticity and the resulting plastic limit theorems and the shakedown theorems have a meaningful place in analysis and design [16, 17], so also should a simple but essentially valid approximation to both cyclic behavior and response to occasional overloads provide a useful basis for life prediction and safe design. It is too early to tell how well the particular proposed simple form will do, but some comparisons with the experimental results of others will prove encouraging. Surely, much more detailed matching of cyclic stress-strain behavior is not essential for low cycle fatigue prediction. Some scalar measure such as W^{pc}, or perhaps W^p or $\int_t \sqrt{\dot\epsilon^p_{ij}\,\dot\epsilon^p_{ij}}\,dt$ based on the proposed simple model should provide a first approximation of value.

It is obvious that any representation that matches the stable cyclic stress range of a material, and is flexible enough to permit a choice of the initial response and the rate of approach to the stable cycle, will match the data from which it is taken reasonably well.

Fig. 7 demonstrates this for the sharp corner form and the test of Fig. 1 on 304 stainless [18] with the choice of $A\,k^{2N+3} = 0.3$, $k = 140$ MPa(20 Ksi), $N = 1$, $\alpha = 0.5$, $W_0/k = 0.05$, $E = 120$ GPa(17×10^3 Ksi).

The rounding form, Fig. 8, shows better agreement with these data, where the improper representation of Fig. 4 cannot appear. Fig. 9 demonstrates how closely the same form matches the cyclic hardening of 2024-T4 aluminum in a symmetric strain cycle followed by a large excursion which in turn is followed by an unsymmetric strain cycle. Corresponding data, Fig. 2, were provided by Morrow and Kurath. Parameters in Figs. 8 and 9 were, respectively, $(B/(\sigma^*)^{2N})\,k^{2N+3} = 9 \times 10^3$, $k = 50$ MPa(7.3 Ksi), $N = 6$, $\alpha = 0.5$, $W_0/k = 0.07$, $E = 120$ GPa(17×10^3 Ksi), $(B/(\sigma^*)^{2N})\,k^{2N+3} = 7 \times 10^{-5}$, $k = 140$ MPa(20 Ksi), $N = 5$, $\alpha = 0.3$, $W_0/k = 0.2$, $E = 70$ GPa(10^4 Ksi).

No claim can be made that either choice of constants in the foregoing examples is adequate to describe the stress-strain behavior of the material for more general paths of loading. Nevertheless, in distinction to all other simple models that have been proposed, and many of the complex, the character of the response to unsymmetric plastic cycles of stress or strain is correct in principle as is the general behavior for combinations of large excursions of stress with a dominant pattern of cyclic loading.

Concluding Remarks on Rounding, Time Effects, and Other Aspects of Reality

It is possible to break the connection between the desirable rounding of the stress-strain curves for reversed plastic loading and the undesirable rounding for reloading following an almost elastic reversal, Fig. 4, by keeping track of the unloading-reloading paths and introducing the physically correct transition from elastic to elastic-plastic response. Whether this added degree of reality is worth the complexity for general paths of loading is doubtful. The inclusion of time and temperature effects certainly is of far greater practical importance for many materials, such as the stainless steels, under operating or emergency conditions in pressure vessels and piping or other engineering structures and devices. Although much is known about time-dependent creep and relaxation at a variety of temperatures [19], very little experimental information exists on the time effects occurring in conjunction with cyclic loading interspersed with large excursions of load, along with temperature variation. Bodner [20] and Onat [21] have suggested forms on the basis of the limited available experimental information. When time and temperature effects are primary, entirely different models of material behavior are required from that proposed here. However, when elastic-plastic response dominates but time and temperature effects are significant, a modified form of the proposed simple model should be appropriate, one which adds a linear or nonlinear viscous response and employs a temperature modified stress [22] along with a time at temperature modified stress for plastic response.

This assumes the simple model proposed is an adequate model or can be made adequate with minor revision, an assumption that requires further experimental exploration and study. The generalization from isotropic to anisotropic cyclic hardening or softening suggested by the data of Lamba [3] poses no difficulty in principle within the mathematical theory of plasticity. However, the functional form for the yield surface $f = 0$ will be far more complicated and could hardly be classed as a minor revision.

In concluding it is worth returning to the two somewhat related classes of models that have long been popular because they can exhibit a proper Bauschinger effect for a reversal of loading. One includes the current individual components of plastic strain explicitly and separately in the yield function f. The other assembles well-defined time-independent simple elements in parallel to produce a model that has great physical appeal because it can actually be constructed and its mechanical behavior is easily visualized. Unfortunately, neither of these classes of models is basically appropriate for cyclic loading.

Neither exhibits a proper response for repeated unsymmetric plastic cycles of stress or of strain.

References

1 Dolan, T. J., "Nonlinear Response Under Cyclic Loading Conditions," *Proceedings of the Ninth Midwestern Mechanics Conference*, Madison, Wis., 1965, pp. 3–21.

2 Morrow, J., and Sinclair, G. M., "Cycle-Dependent Stress Relaxation," Symposium on Basic Mechanisms of Fatigue, ASTM STP 237, American Society for Testing and Materials, 1958, pp. 83–109.

3 Lamba, H. S., and Sidebottom, O. M., "Cyclic Plasticity for Nonproportional Paths: Part 1—Cyclic Hardening, Erasure of Memory, and Subsequent Strain Hardening Experiments," ASME *Journal of Engineering Materials and Technology*, Vol. 100, 1978, pp. 96–103.

4 Lamba, H. S., and Sidebottom, O. M., "Cyclic Plasticity for Nonproportional Paths: Part 2—Comparison With Predictions of Three Incremental Plasticity Models," ASME *Journal of Engineering Materials and Technology*, Vol. 100, 1978, pp. 104–111.

5 Prager, W., "The Theory of Plasticity—A Survey of Recent Achievements," *Proceedings of the Institution of Mechanical Engineers*, London, Vol. 169, 1955, pp. 41–57.

6 Mroz, Z., "On the Description of Anisotropic Workhardening," *Journal of the Mechanics and Physics of Solids*, Vol. 15, 1967, pp. 163–175.

7 Drucker, D. C., "On the Continuum as an Assemblage of Homogeneous Elements or States," *Proceedings of the IUTAM Symposia 1966*, Springer-Verlag, Wien-New York, 1968, pp. 77–93.

8 Shield, R. T., and Ziegler, H., "On Prager's Hardening Rule," *Zeitschrift für angewandte Mathematik und Physik*, Vol. 9a, 1958, pp. 260–276.

9 Ziegler, H., "A Modification of Prager's Hardening Rule," *Quarterly of Applied Mathematics*, Vol. 17, 1959, pp. 55–65.

10 Edelman, F., and Drucker, D. C., "Some Extensions of Elementary Plasticity Theory," *Journal of The Franklin Institute*, Vol. 251, 1951, pp. 581–605.

11 Eisenberg, M. A., "A Generalization of Plastic Flow Theory With Application to Cyclic Hardening and Softening Phenomena," ASME *Journal of Engineering Materials and Technology*, Vol. 98, 1976, pp. 221–228.

12 Dafalias, Y. T., and Popov, E. P., "Plastic Internal Variables Formalism of Cyclic Plasticity," ASME JOURNAL OF APPLIED MECHANICS, Vol. 43, 1976, pp. 645–651.

13 Caulk, D. A., and Naghdi, P. M., "On the Hardening Response in Small Deformation of Metals," ASME JOURNAL OF APPLIED MECHANICS, Vol. 45, 1978, pp. 755–764.

14 Arutyunyan, R. A., and Vakulenko, A. A., "On Repeated Loading of an Elastoplastic Medium," *Izv. Akad. Nauk SSSR, Mekh.*, No. 4, 1965, pp. 53–61.

15 Zienkiewicz, O. C., Nayak, G. C., and Owen, D. R. J., "Composite and Overlay Models in Numerical Analysis of Elasto-Plastic Continua," *Foundations of Plasticity*, ed., Sawczuk, A., Noordhoff, 1972, pp. 107–123.

16 Massonnet, Ch. E., and Save, M. A., *Plastic Analysis and Design—Volume One—Beams and Frames*, Blaisdell Publishing Company, 1965.

17 Save, M. A., and Massonnet, Ch. E., *Plastic Analysis and Design of Plates, Shells and Disks*, North-Holland Publishing Company, 1972.

18 Pugh, C. E., et al., "Currently Recommended Constitutive Equations for Inelastic Design Analysis of FFTF Components," ORNL-TM-3602, 1972.

19 Leckie, F. A., "A Review of Bounding Techniques in Shakedown and Ratcheting at Elevated Temperature," Welding Research Council Bulletin, No. 195, 1974, pp. 1–32.

20 Bodner, S. R., Partom, I., and Partom, Y., "Uniaxial Cyclic Loading of Elastic-Viscoplastic Materials," ASME JOURNAL OF APPLIED MECHANICS, Vol. 46, 1979, pp. 805–810.

21 Onat, E. T., "Representation of Inelastic Behavior," Department of Engineering and Applied Science, Yale University, ORNL-SUB-3863-3, 1976.

22 Drucker, D. C., "On Time-Independent Plasticity and Metals Under Combined Stress at Elevated Temperature," *Recent Progress in Applied Mechanics*, The Folke Odqvist Volume, eds., Broberg, B., Hult, J., Niordson, F., Almqvist & Wiksell, Stockholm, Wiley, New York, London, Sydney, 1967,

Y. S. Lee
L. C. Smith

Nuclear Energy Systems,
Westinghouse Electric Corp.,
P.O. Box 355,
Pittsburgh, Pa. 15230

An Analysis of Power Law Viscous Materials Under a Plane-Strain Condition Using Complex Stream and Stress Functions

The equilibrium and compatibility equations for nonlinear viscous materials described by the power law are solved by introducing the complex stream and stress function. The stresses, strain rates, and velocities derived from the summation form of the stream function and the product form of the stress function are identical to the results obtained from the axially symmetric field equation. The stream function solution is used in the deformation analysis of a viscous hollow cylindrical inclusion buried in an infinitely large viscous medium assuming an equal biaxial boundary stress. The stream function approach is used in determining the stress-concentration factor for a cavity in a viscous material subject to the identical boundary biaxial stress. The results agree with the results of Nadai. The effect of the strain-rate-hardening exponent, the geometry of the inclusion, and the material constants on the hoop stress-concentration factor in the interface between the inclusion and the matrix are discussed.

Introduction

When a hollow cylinder buried in a matrix is subjected to various loading conditions a fracture may be observed due to the stress concentration of the interface. The stress concentration causes a void growth [1, 2] and eventually a ductile fracture. This kind of phenomenon needs to be addressed in order to adequately perform the general deformation analysis, to predict the fracture or to establish the fracture criteria.

Presented herein is the deformation analysis for a hollow cylindrical inclusion of a rate-dependent material buried in another rate-sensitive material subjected to equal biaxial tension or compression boundary stresses. The constitution equation of the material is assumed to be expressed by the power law in the steady creep stage. The direction of the applied boundary stress is perpendicular to the inclusion axis. The strain rate perpendicular to the plane is neglected, thus the plane-strain condition is valid.

The analysis consists of three parts:

1 The analysis associated with the complex conjugate stream function.

2 The analysis using the complex conjugate stress function approach.

3 The analysis of the axially symmetric problem with a uniform external pressure.

Reducing the results to the solution of the problem of a single hole in a rate-sensitive material the hoop stress-concentration factor in the cavity is compared with the results of Nadai [3]. The comparison shows the validity of the complex conjugate stream and stress function approach associated with nonlinear viscous creep materials.

From the results of the analysis

1 The effect of the rate-sensitive exponent on the stress distribution at the interface is discussed.

2 The effect of the radius ratio of the hollow cylinder, a_2/a_1, on the stress concentration at the interface is addressed.

3 The validity of the complex conjugate stream or stress function approach associated with nonlinear viscous materials is proved by comparison of the results herein and the results of Nadai [3].

Analysis

The Stream Function Approach. Nadai [3] considered that the shearing stress is assumed to be expressed in terms of the shear rate in the octahedral plane during the steady stage of creep (strain-rate-hardening material) even though the stress components of the

Contributed by the Applied Mechanics Division for presentation at the Winter Annual Meeting, Washington, D. C., November 15–20, 1981, of THE AMERICAN SOCIETY OF MECHANICAL ENGINEERS.

Discussion on this paper should be addressed to the Editorial Department, ASME, United Engineering Center, 345 East 47th Street, New York, N. Y. 10017, and will be accepted until December 1, 1981. Readers who need more time to prepare a discussion should request an extension from the Editorial Department. Manuscript received by ASME Applied Mechanics Division, April, 1980; final revision, December, 1980. Paper No. 81-WA/APM-1.

rate-dependent material may, in general, be expressed in terms of the rate of the deformation tensor. Nadia [3] then established the relation between plastic stress and strain rates. The plastic strain-rate components are given by a scalar multiplier ($\dot{\lambda}$) times the deviatoric stress components as in the Levy-Mises law without assuming rate-independence and without a yield condition. Hence, the applicability of the analysis is limited to small strains and the steady creep stage. The analysis is not valid in the early portion of creep. A detailed explanation of the constitutive equation for a steady creep material is given by Nadai [3].

The governing equation (in the absence of work hardening) for plastic flow under a plane strain condition in accordance with the Levy-Mises equations is derived for materials with stress-strain rate behavior of the type

$$\tilde{\sigma} = \sigma_0 \dot{\tilde{\epsilon}}^m \tag{1}$$

where $\tilde{\sigma}$, $\tilde{\epsilon}$, and σ_0 in equation (1) are the effective stress, strain rates, and flow function, respectively.

The constitutive equation given by $\dot{\lambda}(\sigma_{ij} + \sigma_p \delta_{ij}) = \dot{\epsilon}_{ij}$ where σ_p is hydrostatic pressure, the strain rate given by $\dot{\epsilon}_{ij} = \frac{1}{2}(u_{i,j} + u_{j,i})$ and the incompressibility condition under a plane-strain condition are substituted into the two equilibrium equations. Using the stream function definition, $u = \partial\phi/\partial y$ and $v = -\partial\phi/\partial x$, the equilibrium equations are expressed in terms of the hydrostatic pressure gradient and the higher derivatives of the stream function with respect to x and y. Eliminating the hydrostatic pressure gradient from the two equilibrium equations gives [4],

$$\frac{\partial^2}{\partial x \partial y}\left(\frac{2}{\dot{\lambda}}\frac{\partial^2\phi}{\partial x \partial y}\right) + \left(\frac{\partial^2}{\partial y^2} - \frac{\partial^2}{\partial x^2}\right)\left\{\frac{1}{2\dot{\lambda}}\left(\frac{\partial^2\phi}{\partial y^2} - \frac{\partial^2\phi}{\partial x^2}\right)\right\} = 0 \tag{2}$$

On transformation of the stream function ϕ into the complex plane,

$$\frac{\partial^2}{\partial z^2}\left\{\left(\frac{\partial^2\phi}{\partial z^2}\right)^{n-1}\left(\frac{\partial^2\phi}{\partial \bar{z}^2}\right)^n\right\} + \frac{\partial^2}{\partial \bar{z}^2}\left\{\left(\frac{\partial^2\phi}{\partial z^2}\right)^n\left(\frac{\partial^2\phi}{\partial \bar{z}^2}\right)^{n-1}\right\} = 0 \tag{3}$$

where $n = (1 + m)/2$, $0 < m < 1$, and ϕ is the stream function, z and $\bar{z}$ are the complex conjugate variables.

Expressing equation (2) in terms of the complex flow functions, the effective strain rate (in two-dimensional Cartesian coordinates) and the scalar-valued multiplier, gives

$$\dot{\tilde{\epsilon}} = \left(4\frac{\sqrt{1}}{3}\right)\left\{\frac{\partial^2\phi}{\partial z^2}\frac{\partial^2\phi}{\partial \bar{z}^2}\right\}^{1/2},$$

$$\dot{\lambda} = \frac{3}{2}\frac{\dot{\tilde{\epsilon}}}{\tilde{\sigma}} = \frac{3}{2\sigma_0}\left(4\sqrt{\frac{1}{3}}\right)^{1-m}\left\{\frac{\partial^2\phi}{\partial z^2}\frac{\partial^2\phi}{\partial \bar{z}^2}\right\}^{(1-m)/2} \tag{4}$$

Note that for $m = 1$ or $\dot{\lambda}$ = constant (perfectly viscous material, [3]), equation (3) reduces to the familiar biharmonic form. Solution of the biharmonic equation subject to the boundary conditions of plane-strain extrusion through a square-cornered die was illustrated in reference [5].

Summation Form Solution. Letting

$$\phi(z, \bar{z}) = \phi_1(z) + \phi_2(\bar{z}) \tag{5}$$

and denoting the second derivatives by

$$p = \frac{d^2\phi_1}{dz^2} \quad \text{and} \quad q = \frac{d^2\phi_2}{d\bar{z}^2} \tag{6}$$

upon substitution of equation (6) into equation (3) yields

$$\frac{d^2p^{n-1}}{dz^2} - Dp^n = 0 \quad \text{and} \quad \frac{d^2q^{n-1}}{d\bar{z}^2} + Dq^n = 0 \tag{7}$$

where D is a constant. The detailed derivation of equations (3) and (7) is given in [5].

Solutions for ϕ_1 and ϕ_2 are then given by

$$\left.\begin{aligned}\phi_1(z) &= 2(n-1)(2n-1)K\ln(z - A_0) + A_1 z + A_2 \\ \phi_2(\bar{z}) &= -2(n-1)(2n-1)K\ln(\bar{z} - K_0) + K_1\bar{z} + K_2\end{aligned}\right\} K = 1/D \tag{8}$$

where K, A_i, and K_i (i = 0–2) are constants.

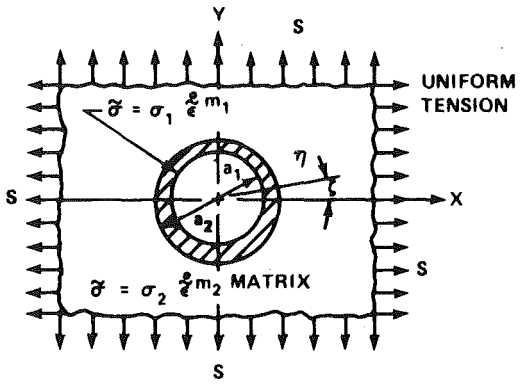

Fig. 1 Schematic diagram of problem

The stream function is given by letting $A_i = K_i = 0$ in equation (8)

$$\phi = 2m(1 - m)(K\ln z - K\ln\bar{z}) \tag{9}$$

Equation (9) can be rewritten as

$$\phi = 2m(1 - m)a_2{}^2K(\ln z - \ln\bar{z}) \tag{10}$$

where a_2 is the radius defined in Fig. 1.

Equation (8) is not valid for $m = 0.0$ and 1.0. For $m = 0$, the stream function is obtained as

$$\phi = 2\,\mathrm{Re}\left\{\frac{1}{A_0{}^2}\ln\frac{1}{A_0 z}\right\}$$

For $m = 1.0$, a perfectly viscous material, any biharmonic solution is valid. For $m \neq 1.0$ velocities, strain rates and stresses in the field are expressed in terms of the first and second derivatives of the stream function obtained from equation (10).

To find the stress component using the strain rates, the hydrostatic pressure is required. The hydrostatic pressure (negative mean stress) σ_p can be obtained from the equilibrium equation written in terms of the stream function gradients:

$$-\frac{\partial\sigma_p}{\partial x} + \frac{\partial}{\partial x}\left(\frac{1}{\dot{\lambda}}\frac{\partial^2\phi}{\partial x \partial y}\right) + \frac{\partial}{\partial y}\left\{\frac{1}{2\dot{\lambda}}\left(\frac{\partial^2\phi}{\partial y^2} - \frac{\partial^2\phi}{\partial x^2}\right)\right\} = 0$$

$$-\frac{\partial\sigma_p}{\partial y} - \frac{\partial}{\partial y}\left(\frac{1}{\dot{\lambda}}\frac{\partial^2\phi}{\partial x \partial y}\right) + \frac{\partial}{\partial x}\left\{\frac{1}{2\dot{\lambda}}\left(\frac{\partial^2\phi}{\partial y^2} - \frac{\partial^2\phi}{\partial x^2}\right)\right\} = 0$$

Differentiating the first equation with respect to y and the second with respect to x and adding yields

$$-2\frac{\partial^2\sigma_p}{\partial x \partial y} + \left(\frac{\partial^2}{\partial y^2} + \frac{\partial^2}{\partial x^2}\right)\left\{\frac{1}{2\dot{\lambda}}\left(\frac{\partial^2}{\partial y^2} - \frac{\partial^2}{\partial x^2}\right)\right\} = 0 \tag{11}$$

Transforming equation (11) to the complex plane gives

$$\frac{\partial^2\sigma_p}{\partial z^2} - \frac{\partial^2\sigma_p}{\partial \bar{z}^2} = 2ci\frac{\partial^2}{\partial z \partial \bar{z}}(p^{(1+m)/2}q^{(m-1)/2} + q^{(m+1)/2}p^{(m-1)/2}) \tag{12}$$

where

$$c = \frac{2\sigma_0}{3}\left(\frac{\sqrt{3}}{4}\right)^{1-m}$$

Substituting the second derivative of the stream function into equation (12) yields

$$\frac{\partial^2\sigma_p}{\partial z^2} - \frac{\partial^2\sigma_p}{\partial \bar{z}^2} = -2^{1+m}c\{b_0 m(1 - m)\} \times (1 - m^2)a_2{}^{2m}(z^{-(2+m)}\bar{z}^{-m} - z^{-m}\bar{z}^{-(2+m)}) \tag{13}$$

where $K = b_0 i$.

The solution of equation (13) is found as

$$\sigma_p = -(2)^{1+m}b_0 c\{b_0 m(1-m)\}^{m-1}(1 - m)^2\left(\frac{a_2}{z}\right)^m\left(\frac{a_2}{\bar{z}}\right)^m + A \tag{14}$$

Thus the velocity components in the horizontal and vertical direction are

$$u = i\left(\frac{\partial\phi}{\partial z} - \frac{\partial\phi}{\partial\bar{z}}\right)$$
$$= -4b_0m(1-m)a_2\left(\frac{a_2}{\eta}\right)\cos\zeta$$
$$v = -4b_0m(1-m)a_2\left(\frac{a_2}{\eta}\right)\sin\zeta \tag{15}$$

where $z = \eta e^{i\zeta}$.

The velocity field under biaxial tension or compression associated with a hollow cylindrical inclusion or hole has a symmetric plane. The horizontal velocity, u, is zero at $\zeta = \pi/2$ corresponding to the y-axis and the vertical velocity, v, vanishes at the x-axis ($\zeta = 0$). To satisfy this condition, the constant K is $K = b_0 i$.

The strain-rate components are

$$\dot{\epsilon}_x = -\dot{\epsilon}_y = i\left(\frac{\partial^2\phi}{\partial z^2} - \frac{\partial^2\phi}{\partial\bar{z}^2}\right)$$
$$= 4b_0m(1-m)\left(\frac{a_2}{\eta}\right)^2\cos 2\zeta$$
$$\dot{\epsilon}_{xy} = 4b_0m(1-m)\left(\frac{a_2}{\eta}\right)^2\sin 2\zeta \tag{16}$$

Substituting equations (14) and (16) into the constitutive equations, $\sigma_{ij} = (\dot{\epsilon}_{ij}/\dot{\lambda}) - \sigma_p\delta_{ij}$, the total stress components can be obtained. The components are

$$\sigma_x = (2)^{1+m}cb_0(1-m)\{b_0m(1-m)\}^{m-1}$$
$$\times\left(\frac{a_2}{\eta}\right)^{2m}\{m\cos 2\zeta + (1-m)\} + A$$
$$\sigma_y = (2)^{1+m}cb_0(1-m)\{b_0m(1-m)\}^{m-1} \tag{17}$$
$$\times\left(\frac{a_2}{\eta}\right)^{2m}\{-m\cos 2\zeta + (1-m)\} + A$$
$$\sigma_{xy} = (2)^{1+m}c\{b_0m(1-m)\}^m\left(\frac{a_2}{\eta}\right)^{2m}\sin 2\zeta$$

Transforming the velocities and stresses shown in equations (15) and (17) to cylindrical coordinates gives

$$u_r = 4b_0m(1-m)a_2\left(\frac{a_2}{\eta}\right)$$
$$u_\theta = 0 \tag{18}$$

and

$$\sigma_r = A + 2^{1+m}c\{b_0m(1-m)\}^{m-1}b_0(1-m)\left(\frac{a_2}{\eta}\right)^{2m}$$
$$\sigma_\theta = A + 2^{1+m}c\{b_0m(1-m)\}^{m-1}b_0(1-2m)(1-m)\left(\frac{a_2}{\eta}\right)^{2m}$$
$$\sigma_{r\theta} = 0 \tag{19}$$

Stress Function Solution. The stress analysis associated with a biaxial stress controlled system is performed using the stress function. The compatibility equation expressed in terms of the second derivatives with respect to x and y of the strain rate can be represented in terms of the stress function gradient by using the constitutive equations under a plane-strain condition. Substituting the stress function definitions, $\sigma_x = \psi_{,yy}$, $\sigma_y = \psi_{,xx}$, and $\sigma_{,xy} = -\psi_{,xy}$ into the compatibility equation, the resulting governing equation as derived in [4] is

$$\left(\frac{\partial^2}{\partial y^2} - \frac{\partial^2}{\partial x^2}\right)\left\{\frac{\dot{\lambda}}{2}\left(\frac{\partial^2\psi}{\partial y^2} - \frac{\partial^2\psi}{\partial x^2}\right)\right\} + \frac{\partial^2}{\partial x\partial y}\left(2\dot{\lambda}\frac{\partial^2\psi}{\partial x\partial y}\right) = 0 \tag{20}$$

The scalar multiplier $\dot{\lambda}$ is expressed in terms of the second derivatives with respect to the complex conjugate variables.

$$\dot{\lambda} = \frac{3}{2c_1}(4)^{(1-m)/m}\left(\frac{\partial^2\psi}{\partial\bar{z}^2}\right)^{(1-m)/2m}\Delta$$
$$\text{where}\quad \Delta = \left(\frac{\sqrt{3}}{2}\right)^{(1-m)/m}, \qquad c_1 = (\sigma_0)^{1/m} \tag{21}$$

and the governing equation (20) becomes

$$\frac{\partial^2}{\partial z^2}\left\{\left(\frac{\partial^2\psi}{\partial z^2}\right)^{(1-m)/2m}\left(\frac{\partial^2\psi}{\partial\bar{z}^2}\right)^{(1+m)/2m}\right\}$$
$$+\frac{\partial^2}{\partial\bar{z}^2}\left\{\left(\frac{\partial^2\psi}{\partial z^2}\right)^{(1+m)/2m}\left(\frac{\partial^2\psi}{\partial\bar{z}^2}\right)^{(1-m)/2m}\right\} = 0 \tag{22}$$

The solution of equation (22) may be obtained by assuming the stress function ψ in the form of either a summation or a product of the conjugate functions $\psi_1(z)$ and $\psi_2(\bar{z})$. When the solution cannot be separated by either the summation or the product form, equation (22) is solved by the mixed mode approach.

Product Solution. In this section, the stress function ψ is assumed to be the product of two complex functions that is,

$$\psi = \psi_1(z)\psi_2(\bar{z}) + Az\bar{z} \tag{23}$$

Substitution of this solution form into equation (23) yields

$$\left\{\psi_2(\bar{z})^\omega\left(\frac{\partial^2\psi_2}{\partial\bar{z}^2}\right)^{\omega+1}\right\}\frac{\partial^2}{\partial z^2}\left\{\psi_1{}^{\omega+1}\left(\frac{\partial^2\psi_1}{\partial z^2}\right)^\omega\right\}$$
$$+\left\{\psi_1{}^\omega\left(\frac{\partial^2\psi_1}{\partial z^2}\right)^{\omega+1}\right\}\frac{\partial^2}{\partial\bar{z}^2}\left\{\psi_2{}^{\omega+1}\left(\frac{\partial^2\psi_2}{\partial\bar{z}^2}\right)^\omega\right\} = 0 \tag{24}$$

where $\omega = (1-m)/2m$.

Equation (25) is assumed to be

$$\psi_1(z) = A(A_1 + A_0z)^\nu \tag{25}$$

where ν is determined subject to the following condition:

$$\psi_1{}^{\omega+1}\left(\frac{\partial^2\psi_1}{\partial z^2}\right)^\omega = D \tag{26}$$

the constant D is obtained from the boundary conditions. Substituting equation (25) into equation (26), ν and A are obtained as

$$\gamma = 1 - m$$
$$A = \left\{\frac{D}{m(1-m)A_0{}^2}\right\}^{(1-m)/2}\exp\left\{\frac{(1-m)}{2}\pi i\right\} \tag{27}$$

Hence, equation (26) can be rewritten as

$$\psi_1(z) = \left\{\frac{D}{m(1-m)A_0{}^2}\right\}^{(1-m)/2}\exp\left\{\frac{(1-m)}{2}\pi i\right\}(A_0z + A_1)^{1-m}$$
$$\psi_2(\bar{z}) = \left\{\frac{D}{m(1-m)K_0{}^2}\right\}^{(1-m)/2}\exp\left\{-\frac{(1-m)}{2}\pi i\right\}(K_0\bar{z} + K_1)^{1-m}$$

and

$$\psi = \left\{\frac{D}{m(1-m)}\right\}^{(1-m)}(r_0)^{-2(1-m)}$$
$$\times\{(A_0z + A_1)(K_0\bar{z} + K_1)\}^{1-m} + Az\bar{z} \tag{28}$$

The stress and strain components in the plane-strain field can be obtained.

If $A_1 = K_1 = 0$, equation (28) can be simplified further as

$$\psi = \left\{\frac{D}{m(1-m)}\right\}^{(1-m)}(z\bar{z})^{(1-m)} + Az\bar{z} \tag{29}$$

since A_0 and K_0 are complex conjugate integral constants.

The stress components, σ_x, σ_y, and σ_{xy} are obtained by using equation (29)

$$\sigma_x = -\left(\frac{\partial}{\partial z} - \frac{\partial}{\partial\bar{z}}\right)^2\psi = -2\left\{\frac{D}{m(1-m)}\right\}^{(1-m)}$$
$$\times(1-m)\eta^{-2m}(-m\cos 2\zeta - 1 + m) + A \tag{30}$$

$$\sigma_y = \left(\frac{\partial}{\partial z} + \frac{\partial}{\partial \bar{z}}\right)^2 \psi = 2\left\{\frac{D}{m(1-m)}\right\}^{(1-m)} \times (1-m)\eta^{-2m}(-m\cos 2\zeta + 1 - m) + A$$

$$\sigma_{xy} = 2\left\{\frac{D}{m(1-m)}\right\}^{(1-m)} m(1-m)\eta^{-2m}\sin 2\zeta \quad (30)$$

(*Cont.*)

The strain rates, derived from the Levy-Mises constitutive equations, are

$$\dot{\epsilon}_x = -\dot{\epsilon}_y = \frac{\sqrt{3}}{4c_1}(2\sqrt{3})^{1/m}\left\{\frac{D}{m(1-m)}\right\}^{(1-m)/m} \times m(1-m)^{1/m}(z\bar{z})^{-1}\left\{\frac{z}{\bar{z}} + \frac{\bar{z}}{z}\right\}$$

$$= \frac{\sqrt{3}}{2c_1}(2\sqrt{3})^{1/m}(D)^{(1-m)/m}m(1-m)\frac{\cos 2\zeta}{z\bar{z}}$$

$$\dot{\epsilon}_{xy} = -\frac{\sqrt{3}}{2c_1}(2\sqrt{3})^{1/m}(D)^{(1-m)/m}m(1-m)\frac{\sin 2\zeta}{z\bar{z}} \quad (31)$$

The velocity components u and v can be obtained by solving the equation defining the linear strain rate, given by

$$\dot{\epsilon}_x = \frac{\partial u}{\partial z} + \frac{\partial u}{\partial \bar{z}}$$

when this is done, the horizontal velocity, u, is given as

$$u = \frac{-\sqrt{3}}{2c_1}(2\sqrt{3})^{1/m}D^{(1-m)/m}m(1-m)\eta^{-1}\cos\zeta \quad (32)$$

The vertical velocity component, by similarity, is given by

$$v = \frac{-\sqrt{3}}{2c_1}(2\sqrt{3})^{1/m}D^{(1-m)/m}m(1-m)\eta^{-1}\sin\zeta \quad (33)$$

Equations (30)–(33) obtained from the stress function are identical to equations (15)–(17) obtained from the stream function.

Axially Symmetric Approach. The equal biaxial stress field corresponds to the axially symmetric problems subjected to a uniform external pressure. The dynamic and axially symmetric stress field subjected to a sudden step internal pressure or static pressure has been solved in [6]. Nadai [3] determined the stress concentration in a single hole for a strain-rate-hardening material. The states of the field obtained using the axially symmetric equilibrium equation will be compared in this section with those obtained from the complex stream and stress functions.

The equilibrium equation for a strain-rate-hardening material described by the power law under a plane-strain condition is given by

$$-\frac{\partial \sigma_p}{\partial \eta} + E\left\{\frac{\partial}{\partial \eta}\left(\frac{\partial u_r}{\partial \eta}\right)^m + \frac{2}{\eta}\left(\frac{\partial u_r}{\partial \eta}\right)^m\right\} = 0 \quad (34)$$

Using the incompressibility condition, the radial velocity and radial strain rates are obtained and given as

$$u_r = -4A/\eta$$

$$\dot{\epsilon}_r = 4A/\eta^2 \quad (35)$$

Substituting equation (35) into equation (34) the hydrostatic pressure can be found as

$$\sigma_p = 2^{1+m}c\left(\frac{A}{\eta^2}\right)^m + K_c$$

and the stress components are found from the constitutive equation. These are

$$\sigma_r = 2^{1+m}\left(\frac{c}{m}\right)\left(\frac{A}{\eta^2}\right)^m - K_c$$

$$\sigma_\theta = 2^{1+m}c\left(\frac{1-2m}{m}\right)\left(\frac{A}{\eta^2}\right)^m - K_c \quad (36)$$

where

$$c = \frac{2\sigma_0}{3}\left(\frac{\sqrt{3}}{4}\right)^{1-m}$$

Equations (35) and (36) are the same as those obtained from the complex conjugate stream function given in equations (18) and (19).

The constant, A, in equations (35) and (36) corresponds to $\{b_0 m(1-m)a_z{}^2\}$ in equations (18) and (19). As seen from the previous sections, the results obtained from the complex conjugate stream and stress function and the solution of the axially symmetric field equation are identical. This confirms the validity of the complex stress or stream function approach to nonlinear viscous material problems.

Boundary-Value Problem. Using the stream function solution transformed into cylindrical coordinates, a boundary-value problem is solved. The stress or strain rate and velocity distribution in composite cylinders comprised of nonlinear viscous materials is determined for different flow functions, σ_0, and different strain-rate-hardening exponents, m. The boundary stress is identical in the x and y-direction, consequently the field can be replaced by an axially symmetric field subjected to a uniform external pressure under a plane-strain condition. Specifically, the solution emphasizes the stresses, strain rates, and the velocities at the interface between two composite cylinders. The schematic illustrating the problem is shown in Fig. 1.

The material constants and the states of the field of the hollow cylindrical inclusion are described by subscript 1. The matrix is expressed by subscript 2. The constant c in equations (16), (18), and (19) for the inclusion is given by

$$\bar{c}_1 = \frac{2\sigma_1}{3}\left(\frac{\sqrt{3}}{4}\right)^{1-m_1}$$

and the constant for the matrix is denoted as

$$\bar{c}_2 = \frac{2\sigma_2}{3}\left(\frac{\sqrt{3}}{4}\right)^{1-m_2}$$

The boundary conditions of the problem are

1:	$u_{r1} = u_{r2}$		at	$\eta = a_2$
2:	$\sigma_{r2} = -s$	(tension)	at	$\eta \to \infty$
3:	$\sigma_{r1} = \sigma_{r2}$		at	$\eta = a_2$
4:	$\sigma_{r1} = 0$		at	$\eta = a_1$

(37)

where a_2 is the outside radius of the inner cylinder.

Using equation (18) and the first condition of equation (37), the relation between the two constants is

$$b_1 m_1(1-m_1) = b_2 m_2(1-m_2) \quad (38)$$

where b_i (i = 1–2) is the integral constant of the inner cylinder and matrix. From the second boundary condition and equation (19), A_2 can be determined by letting $\eta \to \infty$

$$A_2 = -s \quad \text{for tension} \quad (39)$$

where A_2 is the constant of the matrix in equation (19)

From the fourth boundary condition, A_1 is given as

$$A_1 = -2^{(1+m_1)}\bar{c}_1\{b_1 m_1(1-m_1)\}^{m_1}\frac{1}{m_1}\left(\frac{a_2}{a_1}\right)^{2m_1} \quad (40)$$

where A_1 is the constant of the inner cylinder in equation (19).

From the third boundary condition

$$\frac{1}{m_1}2^{(1+m_1)}\bar{c}_1\{b_1 m_1(1-m_1)\}^{m_1}\left\{1 - \left(\frac{a_2}{a_1}\right)^{2m_1}\right\} = 2^{1+m_2}\bar{c}_2\{b_2 m_2(1-m_2)\}^{m_2}\frac{1}{m_2} - s \quad (41)$$

Denoting

$$R = b_1 m_1(1-m_1) = b_2 m_2(1-m_2)$$

Equation (41) can be written as

$$R^{m_1} + \frac{1}{W_1}(W_2 R^{m_2} - s) = 0$$

where

$$W_1 = \bar{c}_1 \frac{2^{1+m_1}}{m_1}\left\{\left(\frac{a_2}{a_1}\right)^{2m_1} - 1\right\}$$

$$W_2 = \frac{\bar{c}_2}{m_2} 2^{1+m_2} \tag{41a}$$

Equation (41a) can be rearranged as

$$R^{m_1} + \frac{m_1}{\left\{\left(\frac{a_2}{a_1}\right)^{2m_1} - 1\right\}}\left(\frac{3}{2^{1+m_1}}\right)\left(\frac{4}{\sqrt{3}}\right)^{1-m_1}\left(\frac{s}{\sigma_1}\right)$$

$$\times\left\{\frac{(2)^{1+\alpha m_1}}{3}\left(\frac{\sqrt{3}}{4}\right)^{1-\alpha m_1}\left(\beta\frac{\sigma_1}{s}\right)\left(\frac{R}{\alpha m_1}\right)^{\alpha m_1} - \frac{1}{2}\right\} \tag{42}$$

where

$$\alpha = \frac{m_2}{m_1}, \quad \beta\frac{\sigma_2}{\sigma_1}$$

Equation (42) is a nonlinear equation. The root, R, is obtained numerically for various values of (a_2/a_1), α, and β. Once the value of R is found, the stress strain rate, the velocity for various combinations of the rate-hardening exponents and α and β for the inclusion and for the matrix can be determined. The solutions associated with the composite cylinders shown in Fig. 1 subjected to both uniform internal and external pressure can be obtained using the methods described in this paper.

Perfectly Viscous Material ($m = 1.0$). The equilibrium equation results in a biharmonic equation and the solution is

$$\phi_1(z) = \frac{a^2}{A_0}\ln\frac{a^2}{z}$$

$$\phi_2(\bar{z}) = \frac{a^2}{A_0}\ln\frac{a^2}{\bar{z}} \tag{43}$$

where $\phi(z, \bar{z}) = \phi_1(z) + \phi_2(\bar{z})$.

Using equation (43), the velocities, strain rates, and stresses for perfectly viscous materials can be found. The radial and hoop stress of the inside cylinder is found as

$$\sigma_r = \frac{-s}{\left\{\left(\frac{a_2}{a_1}\right)^2 + \left(\frac{\bar{c}_2}{\bar{c}_1}\right) - 1\right\}}\left\{\left(\frac{a_2}{a_1}\right)^2 - \left(\frac{a_2}{\eta}\right)^2\right\}$$

$$\sigma_\theta = \frac{-s}{\left\{\left(\frac{a_2}{a_1}\right)^2 + \left(\frac{\bar{c}_2}{\bar{c}_1}\right) - 1\right\}}\left\{\left(\frac{a_2}{a_1}\right)^2 + \left(\frac{a_2}{\eta}\right)^2\right\} \tag{44}$$

and the stresses for the matrix are given as

$$\sigma_r = -s\left\{1 - \left(\frac{\bar{c}_2}{\bar{c}_1}\right)\frac{1}{\left\{\left(\frac{a_2}{a_1}\right)^2 + \frac{\bar{c}_2}{\bar{c}_1} - 1\right\}}\left(\frac{a_2}{\eta}\right)^2\right\}$$

$$\sigma_\theta = -s\left\{1 + \left(\frac{\bar{c}_2}{\bar{c}_1}\right)\frac{1}{\left\{\left(\frac{a_2}{a_1}\right)^2 + \frac{\bar{c}_2}{\bar{c}_1} - 1\right\}}\left(\frac{a_2}{\eta}\right)^2\right\} \tag{45}$$

If $\bar{c}_1 = \bar{c}_2$, and $a_1 = a_2$ in equation (45), the problem is reduced to the problem of a hole in an infinite linear viscous material. The hoop stress-concentration factor is 2.0 at $\eta = a_2$. This corresponds to the linear elasticity solution at $\eta = a_2$. The solution corresponds to an axially symmetric problem with a uniform external pressure at $\eta \to \infty$.

Stress Around the Cylindrical Cavity. From equation (19) and the boundary condition, $\sigma_r = 0$ at $\eta = a_2$, the constants are found as

$$\{b_0 m(1-m)\}^m = -\frac{Am}{2^{1+m}c}$$

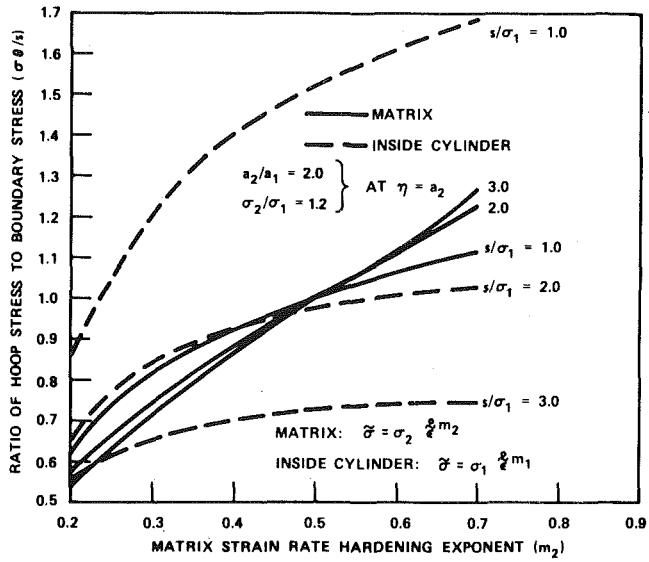

Fig. 2 Hoop stress at interface for various matrix strain-rate-hardening exponent and boundary stress ($m_1 = 0.1$)

and using the boundary condition, $\sigma_r = \sigma$ at $\eta \to \infty$, the constant, A is given as

$$A = \sigma \text{ (tension)}$$

Hence, the stress field associated with the cylindrical cavity is given as

$$\sigma_r = \sigma\left\{1 - \left(\frac{a_2}{\eta}\right)^{2m}\right\}$$

$$\sigma_\theta = \sigma\left\{1 - (1-2m)\left(\frac{a_2}{\eta}\right)^{2m}\right\} \tag{46}$$

The hoop stress at $\eta = a_2$ gives

$$K = \sigma_t/\sigma = 2m \tag{47}$$

The stress-concentration factor at the hole is $2m$ which agrees with Nadai's solution [3]. Nadai noted that the tangential stress is redistributed in a uniform manner at $m = 0.5$ and when the strain-rate-hardening exponent is smaller than 0.5, the hoop stress at the cavity becomes smaller than σ, the boundary stress.

The radial and hoop stress obtained by Nadai [3] for a hole in a rigid perfectly plastic material is

$$\sigma_r = \frac{2\sigma_0}{\sqrt{3}}\ln\frac{a}{\eta} \quad \text{and} \quad \sigma_\theta = \frac{2\sigma_0}{\sqrt{3}}\left(\ln\frac{a}{\eta} + 1\right)$$

which do not satisfy the condition that $\sigma_r = \sigma$ as $\eta \to \infty$. Nadai did mention however, that "the cases when m tends to zero are of no practical interest." The validity of the complex stream and stress function application to nonlinear viscous materials is illustrated by the boundary-value problem. The solutions obtained by applying the complex conjugate stream function are reduced to the linear viscous material case and to the case of a cavity in a nonlinear viscous material. These reduced solutions agree with existing solutions.

Results and Discussion

The numerical results of composite cylinders comprised of different nonlinear viscous materials are shown in Figs. 2–5. Figs. 2–5 illustrate the effect of the strain-hardening exponent and the boundary stress on the hoop stress-concentration factors and radial velocity at the interface of the two cylinders.

Fig. 2 presents the results for $\sigma_2/\sigma_1 = 1.2$, $a_2/a_1 = 2.0$, and for $m_1 < m_2$. The hoop stress-concentration factor for the inside cylinder, K_{11}, and the matrix K_{21}, for $m_2 < 0.5$ is inversely related to the boundary stress, s/σ_1. K_{21} is less than one for $m_2 < 0.5$ and is directly

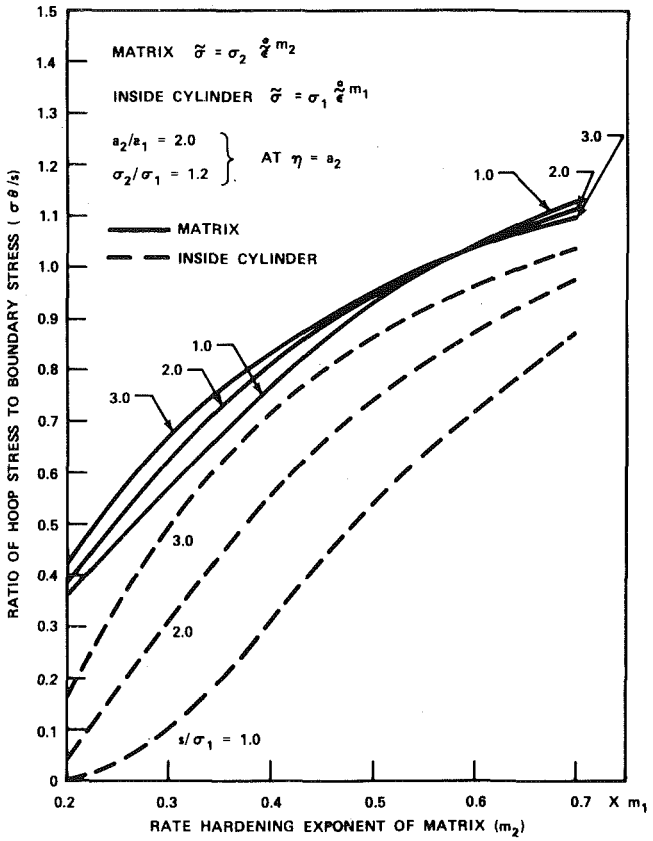

Fig. 3 Hoop stress at interface for various matrix strain-rate-hardening exponent and boundary stress ($m_1 = 0.9$)

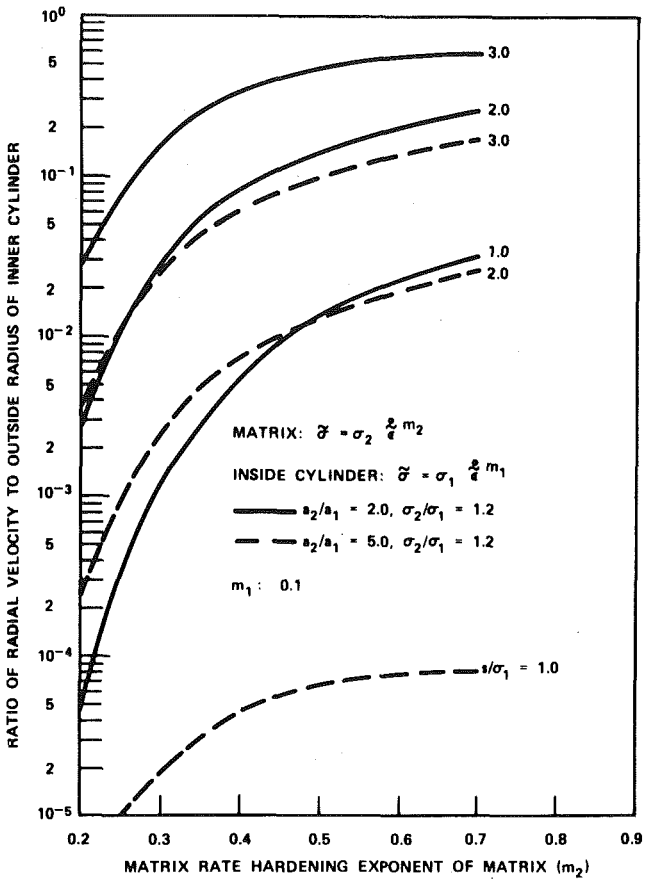

Fig. 4 The radial velocity at interface for various matrix strain-rate-hardening exponent, boundary stress, and geometry of inner cylinder ($m_1 = 0.1$)

proportional to the boundary stress for $m_2 > 0.5$. Fig. 2 shows the results for $\sigma_2/\sigma_1 = 1.2$, $a_2/a_1 = 2.0$, and $m_1 > m_2$. K_{11} and K_{21} are both proportional to the boundary stress for $m_2 < 0.5$. Therefore, the results shown in Fig. 1 are opposite to those shown in Fig. 3. When Figs. 2 and 3 are compared three common aspects are noted:

1 K_{11} and K_{21} are both proportional to the strain-rate-hardening exponent of the matrix, m_2.

2 At $m_2 = 0.5$, K_{21} is independent of σ_2/σ_1, a_2/a_1, and s/σ_1 and equals 1.0.

3 K_{21} is less than one for $m_2 < 0.5$.

The second and third items are consistent with the hoop stress concentration of a cavity in an infinite nonlinear viscous material shown in equation (46). The radial velocity, u_r, at the interface ($\eta = a_2$) for $m_1 < m_2$, $a_2/a_1 = 2.0$, and $a_2/a_1 = 5$ subjected to various boundary stresses is shown in Fig. 4. Fig. 5 presents the velocity for $m_1 > m_2$. The magnitude of the radial velocity is larger for $m_1 < m_2$ than for $m_1 > m_2$ when the boundary stress = 3.00. The converse is true for $s/\sigma_1 = 1.00$. When Fig. 4 is compared with Fig. 5 two common points should be noted:

1 The radial velocity increases with increased strain-rate-hardening exponents of the matrix.

2 As expected, the radial velocity is lower for both $m_1 > m_2$ and $m_1 < m_2$ for a stiff inclusion ($a_2/a_1 = 5$).

The results show both K_{11} and K_{21} for $m_1 = 0.1$ ($< m_2$) to be inversely related to σ_2/σ_1 for various values of a_2/a_1 and σ_2/σ_1 and both are nearly independent of σ_2/σ_1 at $m_2 = 0.7$ for various a_2/a_1-values. The effect of a_2/a_1 and σ_2/σ_1 for $m_1 = 0.9$ ($> m_2$) on K_{11} and K_{21} shows that K_{11} is independent of a_2/a_1 and σ_2/σ_1 and proportional to a_2/a_1 at $m_2 = 0.63$. K_{21} is independent of a_2/a_1 and σ_2/σ_1 for $m_2 = 0.18$ and is barely proportional to σ_2/σ_1 and inversely related a_2/a_1 for $m_2 = 0.63$.

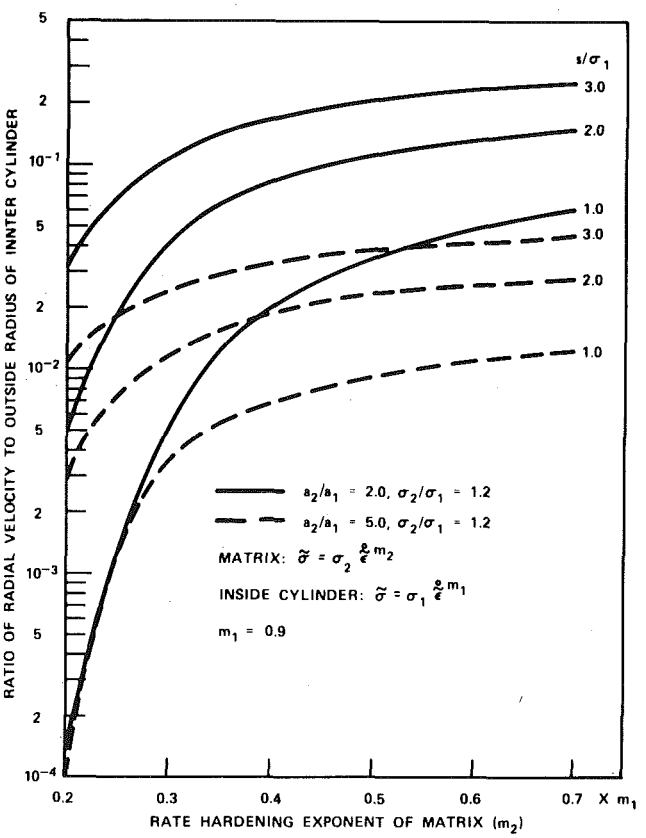

Fig. 5 The radial velocity at interface for various matrix strain-rate-hardening exponent, boundary stress, and geometry of inner cylinder

Conclusions

The following conclusions can be drawn from the analysis:

1 The complex stream and stress function approach is valid for nonlinear viscous materials described by the power law.

2 The dominant parameter affecting the stress-concentration factor at the interface between the inclusion and the matrix is the strain-rate-hardening exponent of the inclusion and the matrix rather than the value of a_2/a_1 or σ_2/σ_1.

References

1 McClintock, F. A., Kaplan, S. M., and Berg, C. A., "Ductile Fracture by Hole Growth in Shear Bands," *International Journal of Fracture Mechanics*, Vol. 2, 1966, p. 614.

2 McClintock, F. A., "A Criterion for Ductile Fracture by the Growth of Holes," ASME JOURNAL OF APPLIED MECHANICS, Vol. 35, 1968, p. 363.

3 Nadai, A., "On the Creep of Solid at Elevated Temperature," *Journal of Applied Physics*, Vol. 8, 1937, p. 418.

4 Shabaik, A. H., and Thomsen, E. G., "Theoretical Method for the Analysis of Metal-Working Problems," ASME *Journal of Engineering for Industry*, Vol. 90, May 1968, p. 343.

5 Lee, Y. S., and Patel, M. R., "An Analysis for Plane-Strain Plastic Deformation in Metal Working Process," ASME *Journal of Engineering for Industry*, Vol. 99, 1976, pp. 727–732.

6 Lee, Y. S., Patel, M. R., and Bohm, G. J., "Stress Analysis of the Strain-Rate-Hardening Material in Axially Symmetric Field," *International Journal of Mechanical Sciences*, Vol. 22, No. 11, 1980, pp. 661–672.

Z. Lisowski
Professor Dr. Hab. Inz.,
Technical University Kraków,
ul. Warszowska, 24,
31-155 Kraków
Poland

T. Stolarski
Dr. Inz.,
Technical University Gdańsk,
ul. Majakowskiego 11/12,
80-231 Gdonsk-Wrzeszcz,
Poland

An Analysis of Contact Between a Pair of Surface Asperities During Sliding

An analysis of friction junction formed by a pair of interacting hemispherically shaped surface asperities was carried out. Depending on the maximum geometrical interference of the asperities junction deformation can be elastic or plastic. Elastic junctions were analyzed using Hertz solution. Depending on whether the junction is welded or nonwelded it was assumed that the interfacial shear stress is constant and equal to or less than the bulk shear strength of the weaker material. Solution for the case of plastic junction was approximated by Green's slip-line field solution.

Introduction

The problem of contact of a pair of rough surfaces has been of interest to many scientists and engineers. It has long been realized that surfaces are rough on microscopic scale and that this causes the real area of contact to be extremely small compared to the nominal area.

The real contact area is a significant parameter in determining friction, wear and the thermal behavior of a pair of interacting surfaces. It is well understood that the real area of contact consists of a number of microcontacts. The problem of relating friction to the surface topography in most cases reduces to the determination of real contact area and studying the mechanism of mating microcontacts. Relation of the friction force to the normal load and the contact area is a classical problem. Amonton's law of friction that the friction force is directly proportional to the normal load and it is independent of the contact area is one of the earliest available theories in this respect.

Bowden, Moore, and Tabor [1] introduced the notion of adhesion at microcontacts formed by the interacting asperities. They explained friction by continued forming and shearing of such junction. This argument leads to the conclusion that the friction coefficient, given by the ratio of shear strength to the normal pressure, is a constant ($\approx$0.17), since for perfect adhesion the mean pressure is approximately equal to the hardness H_b and the shear strength is $\approx(1/6)H_b$. This value is rather low as compared with those observed in practical situations. With the notion of surface roughness and asperity interaction, investigations pertaining to geometrical description of asperities and the mechanism of junction deformation were promoted.

Archard [2] using the Hertz solution for elastic contact of spherical bodies showed that though for a single elastic junction the contact area is proportional to 2/3 power of normal load, nearly direct proportionality results in case of actual surfaces, where contact takes place at many points.

Plastic junction under combined normal and shear stress were analyzed by Green [3]. Green proposed slip-line field solutions for junctions of rigid plastic materials for plane-strain and plane-stress conditions. Various geometrical shapes were considered and some of the theoretical models were verified experimentally. It was also shown that a distinctive feature of steady sliding is that the two surfaces move parallel to each other and some limits on the validity of the theory were discussed and related to the failure of Amonton's law.

A further support to Green's solutions was provided by Greenwood and Tabor [4]. O'Connor and Johnson [5] studied experimentally the effect of tangential force, less than the limiting friction, on the deformation of interacting asperities and deformation of bulk bodies. The initial stages of junction deformation were investigated by Cocks [6]. He concluded that junctions do not break when sliding begins; instead the relative motion is accommodated by the plastic shear of underlying material in a direction somewhat inclined to the interface. The mechanism of formation and destruction of friction junctions, in relation to the physical and mechanical properties of the materials concerned, has been studied by Ainbinder and Prancs [7]. Edwards and Halling [8, 9] have provided an upper bound plasticity solution for interacting wedge-shaped asperities. With the assumption of a kinematically admissible velocity field they minimized the work dissipated in plastic deformation and frictional effects, to obtain the desired angles.

With the understanding that the contact of a pair of rough surfaces takes place only at a number of interacting asperities, study of individual asperity interaction is the primary objective of this paper.

Asperity Contact Model

The estimation of normal and friction forces carried by a pair of

Contributed by the Applied Mechanics Division for publication in the JOURNAL OF APPLIED MECHANICS.
Discussion on this paper should be addressed to the Editorial Department, ASME, United Engineering Center, 345 East 47th Street, New York, N. Y. 10017, and will be accepted until December 1, 1981. Readers who need more time to prepare a discussion should request an extension from the Editorial Department. Manuscript received by ASME Applied Mechanics Division, June, 1980.

rough surfaces in sliding contact is primarily dependent on the behavior of the individual junctions. Knowing the statistical properties of a rough surface and the mechanism at any junction, an estimate of the desired forces may be made. Thus an appropriate model of a junction in sliding contact is necessary. Furthermore, depending on the properties of surfaces in contact and the load to be supported by the junction, a general method for defining the type or class of a junction is essential. Hence, before modeling a junction, a systematic classification of junctions will be briefly presented.

Classification of Contacts. A number of models for a junction, formed by two interacting asperities, have been investigated in the available literature. Most of these investigations are limited to static contacts. In other words, very little or no sliding is assumed. In the case of a sliding contact the problem of solving for the friction and normal forces becomes extremely difficult. One of the possible ways of approaching the required solution is to consider the problem to be of a quasi-static nature. This is the basic assumption which will be made in determining the variation of loads carried by a junction as it goes through its life cycle.

After assuming a certain geometry for asperities in contact, is is simple to define two types of junctions, namely, elastic and plastic. For exceptionally smooth surfaces, the deformation may be purely elastic but for most surfaces, the contacts are plastic. Adhesion between mating asperities is one of the important properties which determines the frictional behavior of a pair of surfaces. That is, the friction coefficient will depend on the adhering properties of the contacting asperities. Depending on whether there is some adhesion or not we may introduce the concept of two further types of junctions, namely, welded junction and nonwelded junction. We can define these two types of junctions in terms of a stress ratio, β, the ratio of s, the shear strength of the junction to k, the shear strength of the weaker material.

$$\beta = s/k$$

For welded junction, the stress ratio,

$$\beta = s/k = 1,$$

i.e., the ultimate shear strength of the junction is equal to that of the weaker material.

For nonwelded junction, the stress ratio,

$$\beta = s/k < 1$$

A welded junction will have adhesion, i.e., the pair of asperities will be welded together upon contact, due to the adhesive forces. On the other hand in the case of a nonwelded junction, adhesive forces will be less important.

For any case, if the actual contact area is A then, the total shear force,

$$S = sA = \beta kA, \tag{1}$$

where $0 \leqslant \beta \leqslant 1$, depending on whether we have welded junction or nonwelded junction.

There have been no direct measurements of the strength of adhesive bounds between individual microscopic asperities. Current work with field-ion tips provides a method for simulating such interactions but even this is limited to the materials and environments which may be examined. At present, therefore, information on the strength of asperity junctions must be sought in macroscopic experiments. The most suitable source of data is to be found in the literature concerning pressure welding. Milner and Rowe [10] have pointed out that the deformation required to give significant adhesion is two orders of magnitude greater than the strain at which the elastic-plastic transition takes place. Thus the assumptions of elastic contacts and strong adhesive bounds seem to be incompatible. Therefore, it is assumed that elastic contacts lead to nonwelded junctions only for which $\beta < 1$. Plastic contacts, however, can lead to both welded and nonwelded junctions.

Geometrical Configuration of Contacting Asperities. Fig. 1 shows geometrical configuration of a pair of contacting asperities

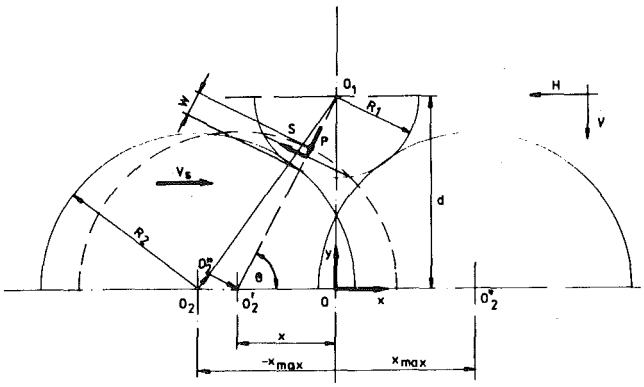

Fig. 1

schematically. Geometrically, a single asperity is idealized as a hemisphere of radius equal to the radius of the asperity curvature at its peak.

There is some experimental evidence [11] that the statistical correlation of radius of curvature at the peaks and the peak heights, for most rough surfaces is not significant. Thus, assuming identical radius of curvature distribution at all asperity heights will not introduce any serious error in further calculations. A junction is formed and destroyed as one hemisphere slides past the other at a given sliding velocity. For simplicity it will be further assumed that the center of the hemisphere in motion moves along a fixed horizontal line.

Elastic Contact. The Hertz solution is applicable in case of static contact of two elastic bodies. Therefore with the known geometry of contact the normal force and the area of contact can be determined. An estimate of friction force as sliding occurs is the main problem. With the assumption of quasi-static motion during the life cycle of a junction, the normal and friction forces at any time may be calculated separately. With the geometry of interacting asperities shown in Fig. 1 the deformation, as the center of lower asperity moves from O_2 to O_2' with respect to the upper asperity, may be divided in two distinct steps: compression according to the Hertz law from O_2 to O_2^* and subsequent sliding from O_2^* to O_2. At any position O_2' of the center of lower asperity, the normal and shear forces, P and S, respectively, can be estimated. These forces may be resolved in horizontal and vertical components and hence V and H are determined. The necessary calculations are performed as follows.

The Hertz solution for elastic contact of two spherical bodies of radii R_1 and R_2 is given by the following equations:

Total Normal Load

$$P = \frac{4}{3} E' w^{3/2} \sqrt{R_1 R_2/(R_1 + R_2)} \tag{2}$$

Area of Contact

$$A = \pi w[R_1 R_2/(R_1 + R_2)] \tag{3}$$

Here w is the geometrical interference between the two spheres and E' is given by the relation,

$$\frac{1}{E'} = \frac{1 - \nu_1^2}{E_1} + \frac{1 - \nu_2^2}{E_2}$$

where E_1, E_2, and ν_1, ν_2 are the Young's moduli and Poisson's ratios for the two materials.

By geometry shown in Fig. 1, the geometrical interference w, which is equal to the normal compression from O_2 to O_2^* is given by

$$w = (R_1 + R_2) - \sqrt{d^2 + x^2} \tag{4}$$

where d is the distance between the centers of two hemispheres in contact and x denotes the position of the moving hemisphere. By substitution of (4) into (2) and (3), the load P and area of contact A, at any time may be estimated. Now the inclination of load P to the horizontal θ is given by (see Fig. 1),

$$\sin\theta = \frac{d}{\sqrt{d^2 + x^2}}$$

$$\cos\theta = \frac{x}{\sqrt{d^2 + x^2}} \tag{5}$$

The friction force, depending on the type of junction under question may be determined by equation (1). Thus the total horizontal and vertical forces, H and V at any position x, of the sliding asperity, are determined,

$$V = P\sin\theta - S\cos\theta$$
$$H = P\cos\theta + S\sin\theta \tag{6}$$

Equations (1)–(6) can be solved for different values of d and β.

Elastic Limit of Junction Deformation. A limiting value of the geometrical interference w can be estimated for initiation of plastic flow. For Hertz solution, the maximum contact pressure occurs at the center of contact spot and is given by

$$q_0 = \frac{3}{2}\frac{P}{A}$$

The maximum shear stress occurs inside the material at a depth of approximately half the radius of the contact area and is equal to about $0.31q_0$ [12]. From the Tresca yield criterion the maximum shear stress for initiation of plastic deformation is $Y/2$, where Y is the tensile yield stress of the material under consideration. Thus

$$\frac{Y}{2} = 0.31\frac{3}{2}\frac{P}{A}$$

Substituting P and A, from equations (2) and (3) we get

$$w = 6.4\left(\frac{Y}{E'}\right)^2 R_1R_2/(R_1 + R_2)$$

Since Y is approximately equal to one third of the hardness for most materials, we have

$$w \approx 0.7\left(\frac{H_b}{E'}\right)^2\varphi,$$

where $\varphi = R_1R_2/R_1 + R_2$.

The foregoing equation gives the value of w for initiation of plastic flow. For fully plastic junction or a noticeable plastic flow, w will be rather greater than the value given by the previous relation. Thus the criterion for fully plastic junction can be given in terms of maximum geometric interference, by the relation

$$w_{\max} > w_p$$

and

$$w_p = \left(\frac{H_b}{E'}\right)^2\varphi \tag{7}$$

Hence, for the junction to be completely plastic, $w_{\max}$ must be greater than w_p.

Plastic Contact. An approximate solution for normal and shear stresses for plastic contacts can be determined through slip-line theory, where the material is assumed to be rigid plastic and nonstrain hardening. One of the well-known solutions of this type is due to Green [3] in which a slip-line field for two wedge-shaped asperities in contact has been suggested. This solution is reviewed in the Appendix. Green's solution is valid for a plane-strain problem and most surfaces fall within the geometrical limitations of the solution. For hemispherical asperities, the plane-strain assumption is not valid. However, in order to make the analysis feasible we will approximate the solution to our problem by the Green's plane-strain solution. Plastic deformation will be allowed in the softer material and the equivalent junction angle α will be determined by the geometry. Quasi-static sliding will be assumed and green's solution will be used at any time of the junction life.

The slip-line angle γ may be determined by velocity boundary conditions or the shear stress at the interface, as will be explained later in this section. Thus, knowing the angles α and γ, at any time the

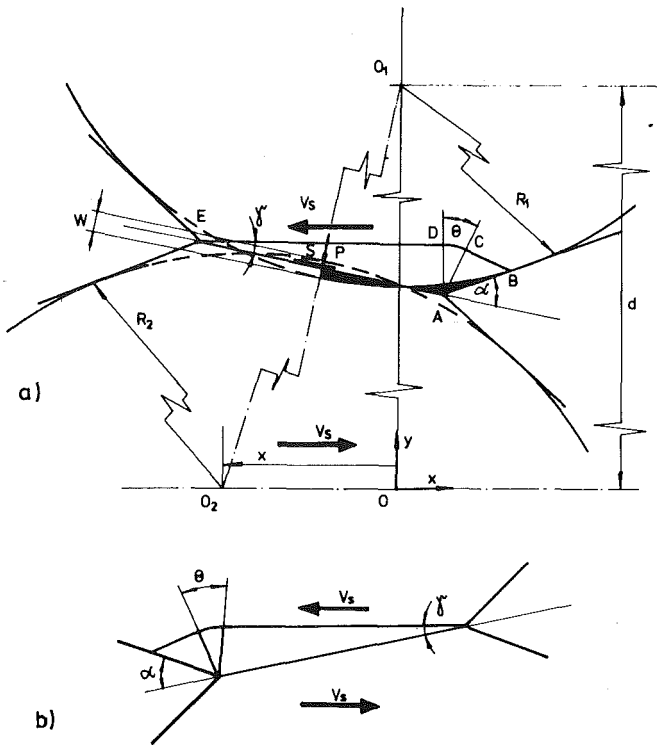

Fig. 2

stresses normal and tangential to the interface AE are given (see the Appendix),

$$p = k\left(1 + \sin 2\gamma + \frac{1}{2}\pi + 2\gamma - 2\alpha\right)$$
$$s = k\cos 2\gamma \tag{8}$$

Now assuming that the contact spot is circular with a radius a, even though Green's solution is strictly valid for plane strain, we get

$$P = p\pi a^2$$
$$S = s\pi a^2 \tag{9}$$

Radius a is determined by geometry as in the Appendix. Resolution of these forces in two fixed directions gives

$$V = P\cos\delta - S\sin\delta$$
$$H = P\sin\delta + S\cos\delta \tag{10}$$

where δ is the inclination of the interface to the sliding velocity. Thus V and H may be determined as a function of the position of the sliding asperity if all necessary angles are determined by geometry. We will consider the case of welded and nonwelded junctions separately.

Welded Junction. For welded junction the geometry shown in Fig. 2 will be assumed. For simplicity of the analysis the deformed material will be assumed to flow outside ways and the equivalent junction angle α will be determined by the minimum inclination of the line AB to the interface, when the incompressibility requirement for the materials is satisfied. A detailed calculation of α is given in the Appendix. Here it is sufficient to say that the minimum inclination of line AB is equal to that of a tangent to the spherical surface when the two shaded areas (see Fig. 2(a)) are equated in order to satisfy incompressibility.

Since no motion is allowed at the interface AE, the angle α is determined by the direction of velocity U, i.e.,

$$\gamma = \delta \tag{11}$$

Thus, knowing α by geometry and γ by equation (11), the required normal and tangential stresses may be calculated by equation (8). It is clear from the geometry of Fig. 2(a) that the interference w reaches

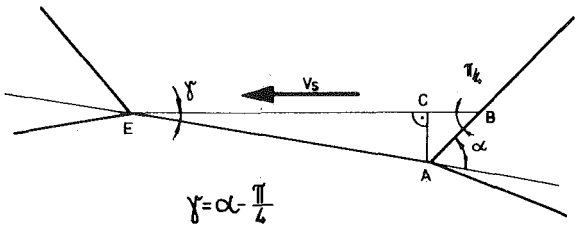

Fig. 3

a maximum value, when the center O_2 of the lower asperity reaches the central position O. As O_2 moves to the right of O, the junction will instantaneously go in tension because we are ignoring elasticity here. To allow for this tensile loading we rotate the slip-line field as shown in Fig. 2(b). Hence V and H through the whole life cycle of a welded junction may be determined.

During tensile loading of the junction, the maximum allowable stress will be limited by the adhesion strength. We denote this stress by p_a. When the normal stress at the interface, p, exceeds the bond strength p_a, the junction immediately breaks and the life of the junction is completed. Another failure mechanism which might occur during the junction life can be explained by the slip line geometry, shown in Fig. 2. When slip lines BC and DE both become parallel to the sliding velocity, i.e., when $\theta = 0$, the material will be sheared off at constant stresses along the straight slip line BE. Such a geometrical configuration is shown in Fig. 3. We assume that during the remainder of the junction life shear along BE occurs. The termination of junction will take place when the two asperities are separated during the sliding motion. Whether this failure mechanism will take place or not, will depend on the initial geometry of the interacting asperities, i.e., R_1, R_2, and w_{max}.

Nonwelded Junction. For the case of a nonwelded junction sliding at the interface is allowed and further it is assumed that the shear stress at the interface is constant. We ignore the flow of deformed material and approximate the junction angle α by the inclination of the tangent AB to the interface AE as shown in Fig. 4. With a geometrical interference w at any time the following geometrical relations may be derived (see the Appendix):

Contact Radius

$$a = \sqrt{\frac{2R_1R_2}{R_1 + R_2}}w,$$

and the angles

$$\alpha = \arcsin(a/R_2)$$

$$\delta = \frac{1}{2}\pi - \operatorname{arctg}(d/x) \tag{12}$$

Since we are assuming the shear stress s at the interface to be constant and less than the shear strength k of the weaker material, i.e., $\beta < 1$. This assumption is consistent with the one made by Green [3]. Thus, knowing the shear stress s, at the interface AE, from equation (8) we have

$$s = k\cos(2\gamma),$$

or

$$\gamma = \frac{1}{2}\arccos(s/k).$$

Hence, for $\beta < 1$,

$$\gamma = \frac{1}{2}\arccos\beta \tag{13}$$

After determining the equivalent junction angle from the geometry (equation (12)) and the angle γ from equation (13), the required stresses in the case of a nonwelded junction may be estimated. Now

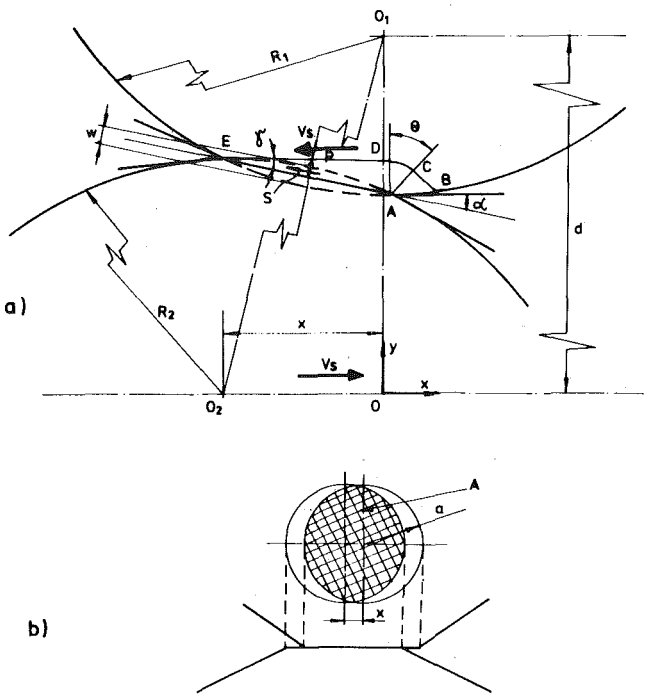

Fig. 4

V and H are determined by equations (9) and (10). After about half the life of a nonwelded junction, i.e., after O_2 moves to the right of O (see Fig. 4) and the interface becomes parallel to the direction of velocity, two possibilities must be considered:

Possibility 1. The junction instantaneously goes into tension and the solution is determined by a procedure similar to that used in the case of a welded junction, except that here the shear stress at the interface will remain constant.

Possibility 2. Another possibility might be that the two interacting bodies just slide off with the interface remaining horizontal, as shown in Fig. 4(b).

The normal compressive stress for Possibility 2 will be, in fact, a function of the elastic deformation in the contacting bodies. However, as the two bodies slide off, as shown in Fig. 4(b), the normal stress will increase, because the contact area is reduced and stresses on a part of the interface, which was originally in contact, are relieved. Moreover, this increased value of compressive stress will be limited by plastic stress obtained by slip-line field solution. Since the shear stress is constant and by geometry of Fig. 4(b) the equivalent junction angle α remains constant, the normal compressive stress given by the slip-line field solution will remain constant. Though this stress will be an upper bound for the actual normal stress, it will not be very unreasonable to assume that the normal stress during the process of sliding remains constant and is equal to the upper bound obtained by the plastic solution.

The area of contact for Possibility 1 is determined by equation (12). However for Possibility 2, by geometry of Fig. 4(b) we have

$$A = 2\left[a^2 \arccos\left(\frac{a-t}{a}\right) - (a-t)\sqrt{2at - t^2}\right.,$$

where

$$t = a - \frac{1}{2}x \tag{14}$$

Thus the total vertical load V and the horizontal force H may be determined from equations (8), (13), and (14). By substitution of α and γ in equation (8), the normal pressure p is determined, hence,

$$P = pA$$

$$S = sA = \beta kA,$$

here A is the area of contact given by (14) during the later half life of the nonwelded junction. If Possibility 1 takes place the forces V and H are determined by equations similar to equations (10). However for Possibility 2, since the interface remains horizontal,

$$V = P$$
$$H = S \tag{15}$$

This is valid for the later half life of the nonwelded junction. The junction life will be completed when the area of contact is reduced to zero.

Discussion of the Asperity Contact Model

It was assumed earlier that the stress s for a nonwelded junction is constant throughout the junction life and this constant value is less than the shear strength k, of the weaker material. However, for a welded junction the shear stress behaves as a cosine relation (equation (8)) and has a maximum value of k. During the asperity interaction the junction may therefore be nonwelded for part of its life and welded during the remainder of the life, depending on the interfacial shear stress. We can represent such a behavior of the plastic contact by assuming that the adhesion stress p_a is such that Possibility 2 of the nonwelded junction is relevant. Thus the normal stress remains compressive during the entire junction life for nonwelded junction solution, whereas the junction goes in tension and fracture takes place in case of a welded junction. As the life of the junctions starts, the shear stress required for a welded junction s_s is less than that for nonwelded junction s_w. Thus the junction will behave as welded and the shear stress

$$s = s_s.$$

When $s_s = s_w$ and later when $s_s > s_w$, the junction will behave as a nonwelded junction and the shear stress

$$s = s_w.$$

The nonwelded junction solution will be relevant until $s_s = s_w$ and $s_s > s_w$ during the remainder of the junction life. Thus the junction will once again tend to become welded. However, due to the limiting tensile stress p_a the tensile stress given by the welded junction solution may or may not be supported by the junction and therefore the junction life can terminate.

Conclusions

Junction deformation models for sliding interaction of hemispherical asperities have been considered. For elastic deformation the normal force and contact area are approximated by Hertz solution. The friction force is assumed to be proportional to the contact area, in other words a constant interfacial shear stress has been assumed. Depending on the interfacial characteristics this stress may be varied from any small value up the bulk shear stress of the weaker material and hence nonwelded and welded junctions are formulated.

Plastic junctions have been approximated by the plane-strain slip-line field solution proposed by Green. For a welded plastic junction no displacement is allowed at the interface and perfect welding is assumed. In case of nonwelded plastic junction interfacial sliding is allowed and a constant shear stress is assumed. The value of this shear stress, will again depend on the interfacial characteristics. Tension is allowed in the junctions until a limiting stress p_a, the adhesion stress, is reached. Beyond this failure takes place and the junction life is terminated.

With a known junction model and statistical description of the surface parameters, the overall average contact forces, area of contact, and contact resistance can be computed for different surface pairs with varying surface roughness.

References

1 Bowden, F. P., Moore, A. J. W., and Tabor, D., "The Ploughing and Adhesion of Sliding Metals," *Journal of Applied Physics*, Vol. 14, 1943, pp. 80–86.

2 Archard, J. F., "Elastic Deformation and the Laws of Friction," *Proceedings of the Royal Society*, London, Series A, Vol. 243, 1957, pp. 190–205.

3 Green, A. P., "Friction Between Unlubricated Metals. A Theoretical Analysis of Junction Model," *Proceedings of the Royal Society*, London, Series A, Vol. 228, 1955, pp. 191–204.

4 Greenwood, J. A., and Tabor, D., "Deformation Properties of Friction Junctions," *Proceedings of the Physical Society*, London, Vol. 58, 1955, pp. 609–619.

5 O'Connor, J. J., and Johnson, K. L., "The Role of Surface Asperities in Transmitting Tangential Forces Between Metals," *Wear*, Vol. 6, 1963, pp. 118–131.

6 Cocks, M., "Shearing of Junctions Between Metal Surfaces," *Wear*, Vol. 9, 1966, pp. 320–334.

7 Ainbinder, S. B., and Prancs, A. S., "On the Mechanisms of the Formation and Destruction of Adhesion Junctions Between Bodies in Friction Contact," *Wear*, Vol. 9, 1966, pp. 209–221.

8 Edwards, C. M., and Halling, J., "An Analysis of the Plastic Interaction of Surface Asperities and Its Relevance to the Value of the Coefficient of Friction," *Journal of the Mechanical Engineering Sciences*, Vol. 10, 1968, pp. 101–110.

9 Edwards, C. M., Halling, J., "Experimental Study of the Plastic Interaction of Model Surface Asperities During Sliding," *Journal of the Mechanical Engineering Sciences*, Vol. 10, 1968, pp. 121–129.

10 Milner, D. R., and Rowe, G. W., "Review of the Pressure Welding," *Metall. Rev.*, Vol. 7, 1962, 433–446.

11 Greenwood, J. A., and Williamson, J. B. P., "Contact of Nominally Flat Surfaces," *Proceedings of the Royal Society*, London, Series A, Vol. 295, 1966, pp. 300–321.

12 Timoshenko, S., and Goodier, J. N., *Theory of Elasticity*, McGraw-Hill, New York, 1951.

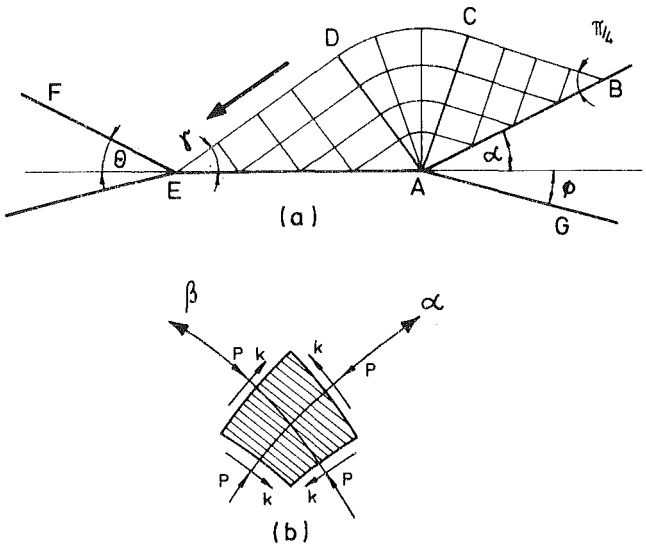

Fig. 5

APPENDIX

Fig. 5 shows the slip-line field suggested by Green [3]. The solution is determined by the junction angle α and the angle γ, which is determined by the velocity boundary condition. Using the notation shown in Fig. 5 for α and β-lines, it is easily seen that for motion from D to E, $BCDE$ is a β-line. The stress relations along the slip lines are given by

$$p + 2k\phi = \text{constant, along } \alpha\text{-line}$$
$$p - 2k\phi = \text{constant, along } \beta\text{-line} \tag{16}$$

where p is the hydrostatic pressure, k is the ultimate shear stress of the material as determined by the yield criterion and ϕ is the anticlockwise rotation of α-line from any fixed direction. In triangle ABC, $p = k$ and using (16) along CD we have

$$p_D - 2k(\pi + \gamma) = k - 2k(\pi - 1/4\pi - \alpha)$$

or

$$p_D = k(1 + 1/2\pi + 2\gamma - 2\alpha) \tag{17}$$

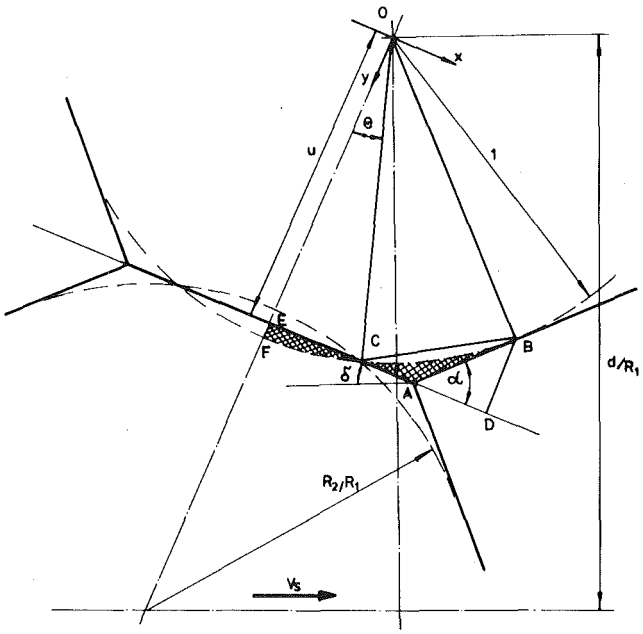

Fig. 6

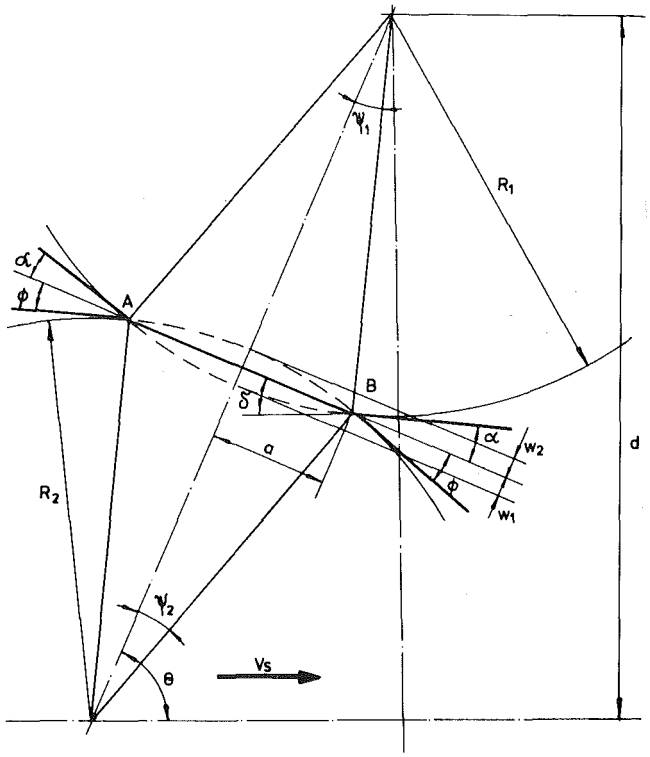

Fig. 7

The stresses p^* and s^*, normal and tangential to the interface AE may be determined by resolving the forces acting on ED and AD. Thus

$$p^* = p_D \cos^2\gamma + k \sin\gamma \cos\gamma + p_D \sin^2\gamma + k \sin\gamma \cos\gamma$$
$$s^* = -p_D \sin\gamma \cos\gamma + k \cos^2\gamma + p_D \sin\gamma \cos\gamma - k \sin^2\gamma$$

or

$$p^* = p_D + k \sin(2\gamma)$$
$$s^* = k \cos(2\gamma) \tag{18}$$

Substituting for p_D from (17) into (18) we get

$$p^* = k[1 + \sin(2\gamma) + 1/2\pi + 2\gamma - 2\alpha]$$
$$s^* = k \cos(2\gamma) \tag{19}$$

The limitation of this solution is imposed by the angle DAC which should be positive, i.e.,

$$\pi - (1/2\pi - \gamma) - (1/4\pi + \alpha) \geq 0$$
$$1/4\pi + \gamma - \alpha \geq 0$$
$$\gamma \geq \alpha - 1/4\pi \tag{20}$$

For most practical surfaces, the junction angle is very small as compared to $1/4\pi$. Therefore the lower limit of γ is zero. The upper limit is obtained when the field can be first extended to the sides EF or AG, i.e., when

$$\gamma = 1/4\pi + (\alpha - \phi), \quad \text{if } \phi > \theta$$
$$\gamma = 1/4\pi + (\alpha - \theta), \quad \text{if } \theta > \phi \tag{21}$$

The relevant geometrical parameters during plastic interaction of hemispherical asperities may be determined by simple geometrical relations. Since the geometry will differ slightly for welded and non-welded junctions, we consider these two cases separately.

Welded Junction

When two hemispherical asperities interact during sliding to form welded junction, such that complete welding is assumed at the interface and no interfacial displacement is allowed, we can assume that the deformed material flows outside ways as shown in Fig. 6. The equivalent junction angle α will be determined by satisfying the incompressibility requirement for the deforming material by equating the shaded areas. Furthermore α will be determined by the minimum angle which the line AB should make with the interface AE in order to satisfy incompressibility. Such a line will be tangent to the spherical surface. By the simple geometry

$$\text{area } CEF = \frac{1}{2}(\theta - \sin\theta \cos\theta) \tag{22}$$

If we denote the coordinates of any point with respect to the coordinate system shown in Fig. 6, the equation to the straight line AB is given by

$$y = mx + c$$

where

$$m = [(y_B - u)/(x_B - x_A)]$$

and

$$c = [(ux_B - y_B x_A)/(x_B - x_A)]$$

The area ABC is now given by the following integral:

$$ABC = \int_{y=y_B}^{u} \int_{x=\sqrt{1-y^2}}^{(y-c)/m} (dxdy).$$

Integrating the foregoing equation and rearranging it gives

$$ABC = \frac{1}{2}[x_A(u - \cos\alpha) + u(\sin\alpha - \sin\theta) + \theta - \alpha] \tag{23}$$

where

$$x_A = (1 - u\cos\alpha)/\sin\alpha. \tag{24}$$

Note that $u = \cos\theta$ and all the distances are measured in terms of the radius of the upper hemisphere R_1.

Substituting x_A in equation (8) and then equating the two areas gives the final equation for α

$$\alpha = \frac{2u - \cos\alpha(1 + u^2)}{\sin\alpha} \tag{25}$$

Equation (25) may be solved by Newton's iteration method and the

desired junction angle α may be computed. Knowing α, for any given value of u, the contact area is determined by evaluating the value of x_A from equation (24) which is the radius of the contact spot.

Nonwelded Junction

In this case the flow of the deformed material is neglected and the junction angle is determined by a tangent to the spherical surface at the point B (see Fig. 7). Thus

$$w_1(2R_1 - w_1) = a^2 \quad \text{and} \quad w_2(2R_2 - w_2) = a^2$$

or

$$w_1 = \frac{a^2}{2R_1} \quad \text{and} \quad w_2 = \frac{a^2}{2R_2}$$

Also, since, $w = w_1 + w_2$,

$$w = a^2\left[\frac{1}{2r_1} + \frac{1}{2R_2}\right]$$

Thus

$$a = \sqrt{2\varphi w} \quad \text{where} \quad \varphi = \frac{R_1R_2}{R_1 + R_2} \tag{26}$$

Also

$$\sin\theta = \frac{d}{R_1 + R_2 - w} \quad \text{or} \quad \theta = \arcsin\left[d/(R_1 + R_2 - w)\right] \tag{27}$$

Since $\delta = 1/2\pi - \theta$, we have

$$\delta = 1/2\pi - \arcsin\left[d/(R_1 + R_2 - w)\right] \tag{28}$$

Considering the sum of all angles at the point B on the line AB we get

$$1/2\pi - \psi_1 + 1/2\pi + \alpha = \pi$$

or

$$\alpha = \psi_1$$

But since by geometry

$$\psi_1 = \arcsin\left(a/R_1\right),$$

we have

$$\alpha = \arcsin\left(a/R_1\right) \tag{29}$$

where the radius of the contact spot, a, is given by equation (26).

M. P. Wnuk[1]

Department of Civil Engineering,
The Technological Institute,
Northwestern University,
Evanston, Ill. 60201

Stable Phase of Ductile Fracture in Two and Three Dimensions, Final Stretch Model

Analysis given here is based on the final stretch concept employed in conjunction with a line plasticity model as suggested by the author in 1972 [6] and in this Journal in 1974 [8]. Its objective is to provide the equations governing quasi-static extension of a tensile crack contained in either partially or in a fully yielded specimen. Differential equations defining the apparent material resistance developed during the early stages of a ductile fracture process are derived from a requirement that the "essential work of fracture" dissipated in a small volume immediately ahead of the crack front, or equivalently, the "final stretch," remains invariant in the process of ductile tear. The model suggests a certain near-tip distribution of displacements associated with a quasi-static Mode I crack such that the resulting strains are logarithmically singular at the crack tip. In contrast to the earlier work on this subject, here we impose no restrictions on the amount of plasticity which precedes the onset of crack growth and which accompanies spread of stable ductile fracture up to the point of global failure. The final results, which are illustrated in the diagrams of J-resistance curves, are analogous to the data obtained by other researchers on the basis of the incremental plasticity theory. Similarities between the present results and the solutions due to Hutchinson, Paris, and coworkers as well as the most recent data obtained by Shih and coworkers, are pointed out.

1 Introduction

Objective of the analysis given here has been to provide equations governing quasi-static crack extension in either partially yielded or in fully yielded specimens. The basic assumption made was that crack flank angle (or "crack tip opening angle," CTOA) remains constant during crack propagation. The experimental and numerical data available today seem to confirm such assumption. It has been also suggested (although not necessarily generally accepted) that the COD at which crack advances is typically about half or a quarter of the COD observed at the onset of crack growth. Such initial decrease and subsequent constancy of the COD during slow crack growth is implied by the solutions given in this investigation. Note that the assumed values of $\hat{\delta}$, which is a COD for a propagating crack, are usually about half of δ_i, the COD at which the initially blunted crack begins to propagate.

To make the problem susceptible to a mathematical treatment a major simplification has been imposed: a line-plasticity model of the DBCS type has been employed for description of a quasi-static crack. Such model, supplemented by the concept of final stretch (which in essence simulates the constancy of the CTOA), has been first suggested by this author in 1972, and then further developed by Wnuk [22, 23] and Smith [20]. Agreement of the end results of such highly idealized model with those obtained from the recent studies of Prandtl slip-line fields associated with a growing crack, cf. Rice and Sorensen [3] and Rice, Drugan, and Sham [5], is remarkable. Thus one is tempted to conclude that despite widely acknowledged deficiencies of one-dimensional modeling of near crack tip plastic stress and displacement fields, and despite somewhat unrealistic details inherent to this model, the gross features of the ductile fracture phenomenon are predicted correctly.

The objective of this paper is to discuss solutions, derived from a line-plasticity model supplemented by a concept of final stretch and extended to incorporate a nonsteady quasi-static motion of a crack. The restriction of the contained yielding is removed.

2 Final Stretch Criterion of Failure

Failure of a volume element located on the prospective path of the

[1] On leave from South Dakota State University, Brookings, S. D. 57007.

Contributed by the Applied Mechanics Division for presentation at the Winter Annual Meeting, Washington, D. C., November 15–20, 1981, of THE AMERICAN SOCIETY OF MECHANICAL ENGINEERS.

Discussion on this paper should be addressed to the Editorial Department, ASME, United Engineering Center, 345 East 47th Street, New York, N. Y. 10017, and will be accepted until December 1, 1981. Readers who need more time to prepare a discussion should request an extension from the Editorial Department. Manuscript received by ASME Applied Mechanics Division, December, 1979; final revision, September, 1980. Paper No. 81-WA/APM-5.

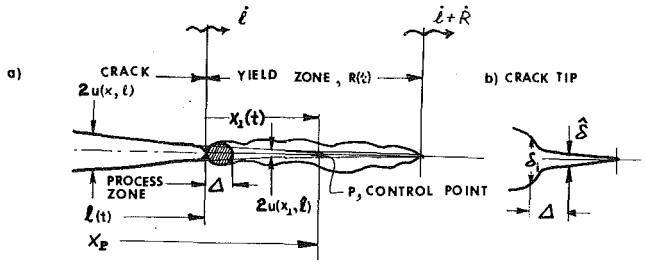

Fig. 1(*a*) Model of the crack and the associated structured end-zone consisting of the process zone (Δ) embedded within the yield zone (R); (*b*) Closeup view of the crack tip as it appears during the crack advancement; note the relations between the initiation COD, δ_i, the final stretch $\hat{\delta}$, and the process zone size Δ

crack front is linked to the incremental work dissipated within the process zone just prior to the collapse of this zone. If t denotes the instant at which the control element breaks down, then the incremental accumulation of damage occurs within the time interval $t - \delta t \leq \tau \leq t$, where the increment δt ($=\Delta/\dot{l}$) corresponds to the time used by the crack front to traverse its own process zone. Size of such hypothetical zone, over which an intensive straining occurs before the crack may advance, is characterized by the length Δ which is assumed to be a microstructural constant. The process zone is presumed in all the considerations which follow to be fully enveloped by the plastic zone R (this requirement is somewhat analogous to the Hutchinson-Paris condition restricting the size of the HRR zone to be small versus the extent of the yielded ligament).

The rate of damage accumulation is given by the product of the stress restraining separation of new surfaces, S, and the rate $\dot{u}$ at which these surfaces are being separated, observed at a certain fixed control point P (see Fig. 1). The integral of this product taken over the time interval δt represents the damage accumulated in the material element adjacent to the crack tip while it undergoes the final stages of straining preceding failure. Requiring that the prior-to-fracture work done at a fixed material point P, while the process zone of a microstructural dimension Δ passes through it, is a material constant, Wnuk [6, 8] postulated the failure condition

$$\hat{w}_\Delta = \int_{t-\delta t}^{t} S_p[x_1(\tau)]\dot{u}_p[x_1(\tau)]d\tau = \text{constant} \quad (=Y\hat{u}) \tag{1}$$

Symbol $x_1 = x_1(\tau)$ denotes the distance from the crack tip. Since point P is stationary while the crack front moves, this distance is time-dependent.

For a constant[2] restraining stress ($S \equiv$ yield stress, Y) the equation above reduces to the so-called "final stretch" condition proposed by Wnuk [6]

$$u(O, l + \Delta) - u(\Delta, l) = \hat{u} \tag{2}$$

The opening displacement $u = u(x_1, l)$ is regarded here to be a function of two variables, the time-dependent coordinate, x_1, and the current crack length l. On the right-hand-side of equation (2) we have the opening constant $\hat{u}$. According to the condition (2) for a continued crack extension an increment $\hat{\delta}$ ($=2\hat{u}$) of opening must be attained in a small segment Δ of yield zone immediately adjacent to the crack tip. From examination of Fig. 1 it becomes obvious that the second term in the LHS of equation (2) represents displacement ahead of a DBCS crack evaluated at the outer edge of the process zone, i.e., at the distance Δ from the physical tip of the crack whose current length is l. The first term in the LHS of equation (2) should be evaluated at the same point but when the crack tip has moved to the right and now coincides with the control point. We conclude, therefore, that the quantity $u(O, l + \Delta)$ is identical with the tip displacement when crack length equals $l + \Delta$, i.e., $u_{\text{tip}}(l + \Delta)$, while $u(\Delta, l)$ can be identified as a displacement prevailing a small distance away from the tip when crack length equals l, say $u_{\text{tip}+\Delta}(l)$. Note that we are using the current crack length as a time-like variable.

3 General Considerations—R-Curve for an Arbitrary Crack Configuration

When a ductile crack initiation occurs near or after general yield of the specimen, material resistance to cracking continues to rise steeply with crack advance. Such behavior of the material fracture toughness may be represented by either R-curve or a J_R-curve; both representations being equivalent between each other. Even if the initiation parameters, R_i or J_{IC}, are known from observations of the onset of crack growth, they alone are not sufficient means for predicting the instability which eventually terminates the process of slow stable cracking under fully plastic conditions. Therefore, it is necessary to devise a technique which would supply a more complete information regarding material response to propagation of ductile fracture, i.e., a resistance curve represented in (R, l) or in (J_R, l) plane if l denotes the current size of an advancing crack.

Let us now summarize the mathematical procedures required to obtain a resistance curve for a quasi-static crack. Discussion involves Mode I fracture, but it would remain equally valid for Modes II and III.

The essential feature of the analysis is the final stretch condition which presumes that the displacement accumulated at a fixed control point during the final act of fracture, i.e., during fracturing of a finite process zone adjacent to the crack front, remains a material property, say $\hat{u}$ (or $\hat{\delta} = 2\hat{u}$). All one needs in order to set up the final stretch equation is an expression for the displacement normal to the crack plane at a small distance from the tip of an advancing crack. Let this displacement be given as

$$[u(x_1, l)]_{x_1 \to 0} = u(O, l) - x_1 \left[\frac{\delta u(x_1, l)}{\delta x_1}\right]_{x_1 \to 0} + \ldots \tag{3}$$

or

$$[u(x_1, l)]_{x_1 \to 0} = C\{F(l) - x_1\Phi(x_1, l) + \ldots\} \tag{4}$$

where C is a constant, $C = 4Y/\pi E_1$, $u(O, l)$ is identical with the crack tip opening displacement, $u_t(l)$, while F and Φ are certain functions of the arguments shown. The modulus E_1 is identical with the Young modulus E for plane stress, while for plane strain it equals $(1 - \nu^2)^{-1}E$.

Note that the expansion of the kind (3) is *not* a Taylor series, since the derivative $\partial u(x_1, l)/\partial x_1$ becomes singular at $x_1 = 0$, while the derivative-like quotient[3] $\delta u/\delta x_1$ when evaluated at the point located a small distance ($x_1 = \Delta$) away from the crack tip ($x_1 = 0$), is finite. Substituting the forms (3) and (4) into the final stretch criterion for fracture (2) we obtain the differential equation which governs the growth of a quasi-static crack, i.e.,

$$(du_t/dl)_{x_1=\Delta} + [\delta u/\delta x_1]_{x_1=\Delta} = \hat{u}/\Delta \tag{5}$$

or

---

[2] Interestingly, other assumptions concerning the distribution of the restraining force S over the process zone lead to identical end results, i.e., the equation governing extension of a ductile fracture in its subcritical (stable) range, cf. Smith [20].

[3] Note that the symbol $[\delta u/\delta x_1]_{x_1=\Delta}$ used in equation (3) should not be interpreted as a partial derivative, although it is somewhat analogous to a partial derivative of the function $u(x_1, l)$. This point is brought out when the following two forms are compared:

$$\frac{\partial u(x_1, l)}{\partial x_1} = \lim_{x_1 \to 0}\left[\frac{u(O, l) - u(x_1, l)}{x_1}\right] \tag{a}$$

$$\Phi(\Delta, l) = C^{-1}\left[\frac{\delta u(x_1, l)}{\delta x_1}\right]_{x_1=\Delta} = C^{-1}\lim_{x_1 \to \Delta}\left[\frac{u(O, l) - u(x_1, l)}{x_1}\right] \tag{b}$$

in which the constant $C = 4Y/\pi E_1$. It is noted that for the displacement distribution $u(x_1, l)$ associated with a quasi-statically moving crack the form (*a*) is singular while the form (*b*) is not. Specific examples of function Φ are given in Section 4.

$$(dF/dl)_{x_1=\Delta} + \Phi(\Delta, l) = C^{-1}(\hat{u}/\Delta) \tag{6}$$

For a wide class of problems the function $F(l)$, which describes the opening displacement at the current crack tip, may be represented as follows:

$$F(l) = C^{-1}u_t(l) \equiv F[l, R(l)] = l\phi[R(l)/l] \tag{7}$$

Thus we assume that the nondimensional part of $F(l)$, i.e., the function ϕ, depends only on the ratio $R(l)/l$. This is true for a broad class of crack configurations. Confining our attention to this type of problems we may reduce the governing equation (6) a little further. At this point we should note that within the subcritical range of external loads imposed on the body containing a crack, the plastic zone size R, used here as a measure of the external field intensity, remains a function of the current crack length. This function, $R = R(l)$, is *a priori* unknown and it will be subject to determination. Following equation (7) we find

$$\frac{dF}{dl} = \frac{\partial F}{\partial l} + \frac{\partial F}{\partial R}\frac{dR}{dl} \tag{8}$$

If we now denote the ratio $R(l)/l$ by $x(l)$, then the partial derivatives in equation (8) can be evaluated as follows:

$$\frac{\partial F}{\partial l} = \phi - (d\phi/dx)x$$
$$\frac{\partial F}{\partial R} = d\phi/dx \tag{9}$$

When these expressions are substituted in equation (8) and then into equation (6), one obtains a nonlinear differential equation which defines the R-curve for a broad class of crack configurations, namely,

$$\frac{dR}{dl} = x(l) + \left(\frac{d\phi}{dx}\right)^{-1}\{M - \Phi(\Delta, l) - \phi(x)\}, \quad x(l) = R(l)/l \tag{10}$$

Here, the symbol M $(= \hat{u}/C\Delta = (\pi E_1/8Y)\,(\hat{\delta}/\Delta))$ denotes the tearing modulus, a material property required for characterization of ductile fracture process. If the material resistance is represented by the J-integral rather than by the function $R = R(l)$, the governing equation (6) simplifies considerably. This follows from the known relationship between the tip displacement $u(O, l)$ and the J-integral, namely,

$$J_R = (2nY)u(O, l) = (2nY)CF(l) = \kappa F(l) \tag{10a}$$

where the new constant $\kappa = 8nY^2/\pi E_1$ and n is a certain material sensitive coefficient whose value lies usually in the range 1 to 2.6. Obviously, the derivative dF/dl needed in evaluation of the difference $F(l + \Delta) - F(l)$, as implied by equation (2), becomes identical with the slope of the J- resistance curve, dJ_R/dl, within the accuracy of a numerical constant. Replacing dF/dl by $\kappa^{-1}dJ_R/dl$ in equation (6) we obtain an alternative representation for the apparent material toughness associated with the slow stable cracking process, i.e.,

$$\frac{dJ_R}{dl} = \kappa[M - \Phi(\Delta, l)] \tag{11}$$

or

$$\frac{dJ_R}{dl} = nY(\hat{\delta}/\Delta) - 2nYC\Phi(\Delta, l) \tag{11a}$$

This last equation is perhaps an easiest vehicle to generate the data pertaining to material resistance developed during the course of ductile fracture. If the "correction term" $2nYC\Phi(\Delta, l)$ is small versus the first term, a constant nY(CTOA) appearing on the left-hand-side of equation (11*a*), then the ductile tearing process obeys Paris' suggestion of constant slope dJ_R/dl, expected to be valid in highly ductile materials. Indeed, Smith [20] has shown that an assumption of finite specimen dimensions does not upset the general form of equation (11*a*), and he also pointed out to a possibility of having the second term in equation (11*a*) neglected when the amount of stable cracking is small. It appears to us that the conclusions of this kind may not yet be sufficiently justified and more numerical and experimental work is needed to verify the validity of such presumptions. It is also necessary to establish more precisely the restrictions under which approximations of the Paris type are valid. In particular it will become mandatory for anybody who would want to apply the analytical results of the theory given here for reduction and processing of the empirical data collected on the small laboratory specimens, to provide bounds on the minimum size of such specimens (otherwise it is impossible to test the validity of our equations). An analysis aimed at this end will be developed in a future paper.

To provide an evidence that the slope dJ_R/dl does not necessarily remain constant during slow stable crack extension, we have integrated numerically the governing equations (a different equation for each of the four configurations considered). The results are gathered and shown by the plots in Fig. 2. It is seen from this figure that neither is the slope of any of the J_R-curves constant, nor are such resistance curves a unique material property. Their shapes and slopes depend not only on the initial crack size but they are also influenced by the loading and crack configurations.

It is noteworthy that the point of transition from stable to unstable fracture can be predicted directly from equations (10) and (11). For the particular crack configurations considered here the partial derivatives $\partial R_A/\partial l$ and $J_A/\partial l$ (index "A" denotes outer field parameter) can be replaced by the ratios R_A/l and J_A/l, i.e.,

$$\frac{\partial R_A}{\partial l} = \frac{R_A}{l}, \quad \frac{\partial J_A}{\partial l} = \frac{J_A}{l} \tag{12}$$

At instability we have

$$\begin{cases} J_A = J_R \\ \partial J_A/\partial l = dJ_R/dl \end{cases} \quad \text{or} \quad \begin{cases} R_A = R \\ \partial R_A/\partial l = dR/dl \end{cases} \tag{13}$$

Recalling that $J_R/l = \kappa\phi$ and combining equations (12) with expressions (10) and (11) we arrive at the following equality which has to be satisfied when the global failure occurs

$$\{\Phi(\Delta, l) + \phi(R, l)\}_f = M \tag{14}$$

This equation contains two instability parameters l_f and R_f which are subject to determination. A second equation is therefore needed, and it is given by the top line in (13). One ought to point out that while the equations (10) and (11) describing material resistance curves are valid for an arbitrary crack configuration, the conditions at the terminal instability, as given by equations (12), are rather strongly dependent on the choice of specimen and loading configurations. In view of this the reader is reminded here that the instability locus defined by the expressions (14) applies only to the crack configurations for which the relations (12) are valid.

In closing let us point out that the only quantities needed to set up the governing equations for the problem considered, ϕ and Φ, can be derived, respectively, from (1) the expression for the crack-tip opening displacement for a given crack configuration, and (2) the gradient of the displacements in the immediate proximity of the crack tip, i.e.,

$$\phi(l) = (\pi E_1/4Y)(u_{\text{tip}}(l)/l) \text{ or } \phi = (\pi E_1/8nY^2)J(l)/l$$
$$\Phi(\Delta, l) = (\pi E_1/4Y)[\delta u(x_1, l)/\delta x_1]_{x_1=\Delta} \tag{15}$$

The predictive powers of the results given in this section, i.e., equations (10) and (11) are of rather sweeping generality. Verification of validity of these equations against physical reality will be an essential step in deciding in favor or against the model suggested here.

4 Examples of Solutions for 2*D* and 3*D* Crack Configurations

To illustrate the outcome of numerical solutions of the four differential equations involved in this study, Fig. 2 was constructed in which the J_R resistance curves are plotted for all the four configurations considered, i.e.,

$$2D \text{ crack} \begin{cases} (a) \text{ traction-free,} \\ (b) \text{ pressurized,} \end{cases}$$

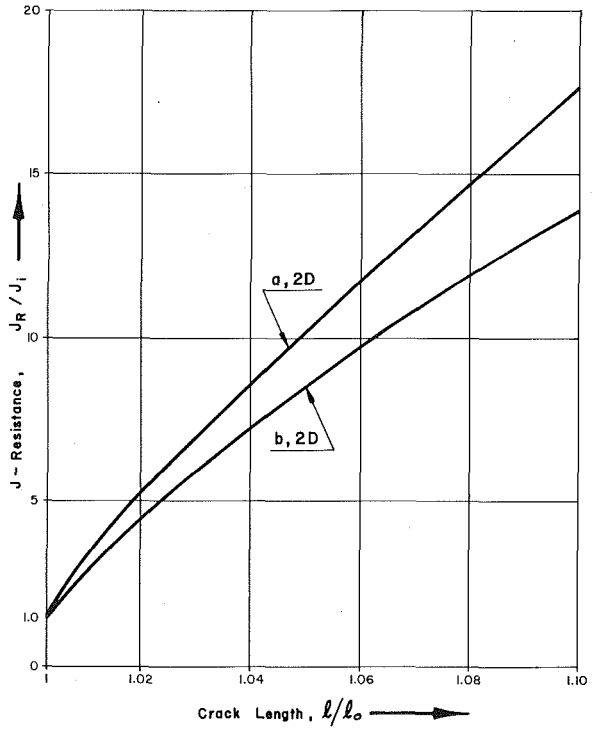

Fig. 2(*a*) *J*-resistance curves for a 2*D* crack subject to (*a*) tensile stress applied remotely from the crack, (*b*) hydrostatic pressure acting on the crack surface. Input data: tearing modulus, $M = 5$, initial crack length, $l_0 = 1000\Delta$, initial extent of the yield zone, $R_i = 10\Delta$.

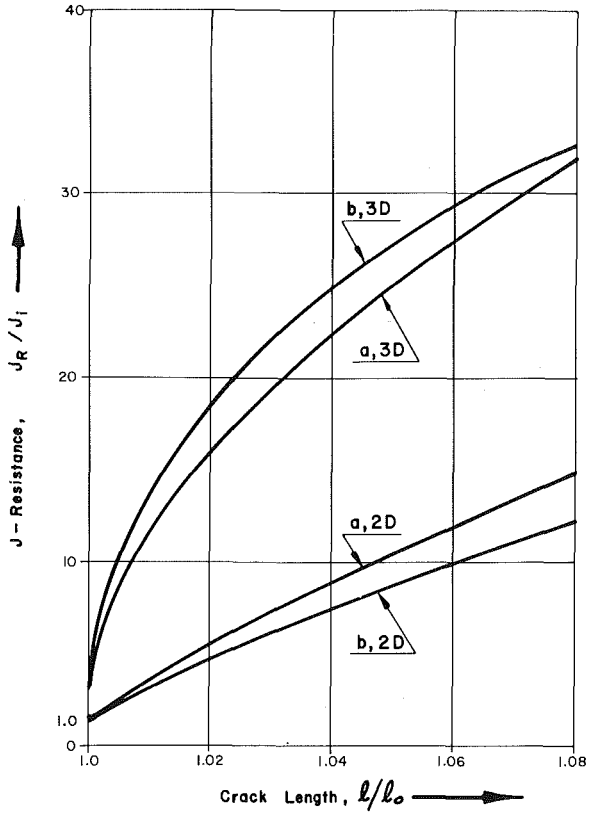

Fig. 2(*b*) *J*-resistance curves for the four configurations:

2*D* crack { (*a*) traction-free; (*b*) pressurized

3*D* crack { (*a*) traction-free; (*b*) pressurized

Input data: tearing modulus, $M = 5$, initial crack length, $l_0 = 1000\Delta$, initial extent of the yield zone, $R_i = 10\Delta$.

and

$$3D \text{ crack} \begin{cases} (a) \text{ traction-free,} \\ (b) \text{ pressurized.} \end{cases}$$

Material properties are chosen in the intermediate range so that the complete equations given in this text had to be used rather than their reduced forms.

The discrepancies between the respective J_R resistance curves are obvious upon examination of Fig. 2. A trend of an increased slope is noted when fracture initiates from a disk-shaped crack. Note also that for a vanishing plasticity, i.e., when $R/l \to 0$, the slope of an R-curve for a 3D crack, dR/dl becomes nearly infinite as then an R-curve degenerates to the step-like function which allows no stable crack growth, as it would be expected for the Griffith (brittle) limit.

The nonlinear differential equations which were employed to obtain the curves shown in Fig. 2 were derived from the basic condition for propagation of subcritical fracture, i.e., equation (6), applied to the four configurations just listed. All four equations are of the general form $g(l, R(l), dR/dl) = 0$, as given in the Appendices A and B, cf. equations (47) and (55) for a 2D crack, cases (a) and (b); and equations (68) and (73) for a 3D crack, case (a) and (b), respectively. Once these equations are integrated numerically for a given set of the initial data (l_0, R_i), the J_R-resistance curves can be obtained by replacing R and J_R, according to the following formulas:

$$J_R(l) = \kappa \begin{cases} [l \log (1 + R/l)] & (16a) \\ R\{1 + 2 \log [\sqrt{1 + (R/l)} + \sqrt{(R/l)}]\} & (16b) \end{cases}$$

for a 2D crack configuration ($\kappa = 2nYC = 8nY^2/\pi E_1$), and

$$J_R(l) = \kappa_1 \begin{cases} R/(1 + (R/l)) & (17a) \\ R\left[1 + (R/l) + \sqrt{\frac{R}{l}\left(2 + \frac{R}{l}\right)}\right] & (17b) \end{cases}$$

for a penny-shaped crack.

These relationships result from the simple formula, $J_R = (2nY)u_z(O, l)$, which connects the crack tip opening displacement with the material resistance to ductile fracture. The constant $\kappa_1 = (2nY)C_1 = 8nY^2(1 - \nu^2)/\pi E$ applies to a 3D crack configuration.

It might be of interest to note that the *ssy* and *lsy* limiting cases can be readily deduced from the basic equations given in the Appendices. For the 2D configuration (case a) one obtains

$$\frac{dR}{dl} = \begin{cases} M - \frac{1}{2} \log (4eR/\Delta), ssy, \Delta \ll R \ll l \\ \frac{R}{l}\left\{M - \frac{1}{2} \log \left(\frac{2R^2}{el\Delta}\right)\right\}, lsy, \Delta \ll R \gg l \end{cases} \quad (18)$$

The equivalent representation of the material resistance to crack growth (J_R versus l) leads to these forms[4] for a 2D crack, case a,

$$\frac{dJ_R}{dl} = \begin{cases} 4Y^2/\pi E_1) \log (J_{ss}/J_R), ssy \\ nY(\hat{\delta}/\Delta) - (4nY^2/\pi E_1) \log \left(\frac{2el}{\Delta}\right), lsy \end{cases} \quad (19)$$

Similarly, in the limiting cases of small scale yield (*ssy*) and large scale yield (*lsy*) one obtains for a 2D crack, case b,

[4] It should be noted that in the analogous equation given by Wnuk [23] and by Smith [20] the empirical constant n was assumed to be 1. Wnuk's [23] paper contains also a misprint due to which the base of the natural logarithm "e" appears in the denominator of the argument of the log-term present in the second of equations (4.4).

$$\frac{dR}{dl} = \begin{cases} M - \frac{1}{2}\log\left(\frac{4eR}{\Delta}\right), & ssy \\ \frac{1}{\log(4e^2R/l)}\left\{M - \frac{1}{2}\log\left(\frac{4eR}{\Delta}\right)\right\}, & lsy \end{cases} \tag{20}$$

$$\frac{dJ_R}{dl} = \begin{cases} \kappa\left\{M - \frac{1}{2}\log\left(\frac{4eJ_R}{\kappa\Delta}\right)\right\}, & ssy \\ \kappa\left\{M - \frac{1}{2}\log\left(\frac{l}{\Delta}\right) - x\right\}, & lsy \end{cases} \tag{21}$$

The nondimensional quantity x, which appears in the second equation written in the foregoing, is related to the material resistance J_R through the relation

$$\kappa x \log(4ex) = J_R/l \tag{21a}$$

Analogous reduction of the basic equations valid for an arbitrary R/l ratio, for the two limiting situations considered here, can be performed for the $3D$ configuration. The results are[5]

$$\frac{dR}{dl} = \begin{cases} M - \frac{1}{2}\log(8l/\Delta) + (l/2R) + 5/4, & ssy \\ \left(\frac{R}{l}\right)^2\left\{M - \frac{1}{2}\log\left(\frac{8l}{\Delta}\right)\right\} + \frac{2R}{l}, & lsy \end{cases} \quad \text{case } (a) \tag{22}$$

and

$$\frac{dR}{dl} = \begin{cases} M - \frac{1}{2}\log\left(\frac{8l}{\Delta}\right) + \frac{l}{2R} - \frac{1}{2}\sqrt{\frac{l}{2R}} + 1, & ssy \\ \frac{l}{4R}\left\{M - \left(\frac{R}{l}\right)^2\log\left(\frac{8l}{\Delta}\right)\right\} + \frac{R}{l}, & lsy \end{cases} \quad \text{case } (b) \tag{23}$$

If the J_R versus l representation is used, then for a $3D$ crack one obtains

$$\frac{dJ_R}{dl} = \kappa_1\begin{cases} \left[M - \frac{1}{2}\log\left(\frac{8l}{\Delta}\right) + \frac{1}{4}\left(\frac{J_R}{\kappa_1 l}\right)\right], & ssy \\ \left[M - \frac{1}{2}\log\left(\frac{8l}{\Delta}\right) + 1\right], & lsy \end{cases} \tag{24}$$

for the case (a), and

$$\frac{dJ_R}{dl} = \kappa_1\begin{cases} \left[M - \frac{1}{2}\log\left(\frac{8l}{\Delta}\right) + \frac{1}{2x} + \frac{1}{\sqrt{2x}} + \frac{5}{4}\right]_{x=J_R/\kappa_1 l}, & ssy \\ \left[M - x\log\left(\frac{8l}{\Delta}\right) + 2x^2\right]_{x=\sqrt{J_R/2\kappa_1 l}}, & lsy \end{cases} \tag{25}$$

for case (b).

Note that the relations, $x = J_R/\kappa_1 l$, for the ssy condition and, $x = (J_R/2\kappa_1 l)^{1/2}$, for the lsy condition are the limiting expressions obtained from the equation (b) in (17) when x assumes very small (ssy) and very large (lsy) values, respectively.

The new constant J_{ss}, which appears in the top equation in (19), denotes the steady-state level of the material resistance to cracking attained during a fully developed ductile tear process, i.e., when $dJ_R/dl \to 0$. Within the small scale yielding range the derivatives dJ_R/dl and dR/dl differ only by a constant factor. Setting, therefore, the slope dR/dl given by the top equation in (18) to zero, we obtain first the constant

$$R_{ss} = (\Delta/4)\exp(2M - 1) \tag{26}$$

and then the constant

$$J_{ss} = (2nY^2\Delta/\pi E_1)\exp\{(\pi E_1/4Yn)(\hat{\delta}/\Delta) - 1\} \tag{27}$$

Smith [20] considers only the case of limited amount of stable crack growth for which the terms other than the constant M in the corresponding lsy equations may be neglected. The J_R-resistance curve reduces then to a straight line.

$$J_R(\Delta l) = J_{IC} + nY(\hat{\delta}/\Delta)\Delta l, \; lsy \tag{28}$$

Such approximation becomes in fact equivalent to the Paris concept of constant slope of the resistance curve $(dJ_R/dl)_i$. It follows from equation (10) that when all the imposed restrictions are met the following equality should hold:

$$\frac{dJ_R}{dl} \equiv \left(\frac{dJ_R}{dl}\right)_i = nY(\hat{\delta}/\Delta) \tag{29}$$

or, in terms of the Paris' (T_J) and Shih's (T_δ) tearing moduli, we obtain

$$T_J = nT_\delta, \quad T_J = (E/\sigma_0^2)(dJ_R/dl)$$
$$T_\delta = (E/\sigma_0)(\hat{\delta}/\Delta) \text{ or } (E/\sigma_0)(\text{CTOA}) \tag{30}$$

Equality of this kind suggests an approach to testing the validity of the model discussed here. An independent study by Curry [24], aimed at evaluation of a J-resistance curve resulting from measurements obtained on a single edge notched bend specimen (SENB) loaded in four point (pure) bending, has shown that initial gradient of the J_R versus Δl curve is indeed given by an expression of type (29). Through application of Burns and McMeeking [25] expression which relates the bending moment to the J_R-integral computed for a slow crack growth test performed on a SENB specimen, Curry [24], predicts the initial slope of the resistance curve as

$$(dJ_R/dl)_i \simeq 1.7\sigma_0(\text{CTOA}) \tag{31}$$

If the crack opening angle (CTOA) is identified with the ratio of the final stretch to the process zone size, $\hat{\delta}/\Delta$, then formulas (31) and (29) are in agreement.

Curry [24] concludes that since the crack tip opening angle remains essentially constant during slow crack growth, the Paris tearing modulus T_J is also a constant; $T_J \alpha dJ_R/da \simeq (dJ_R/da)_i \alpha$ CTOA.

This need not be the case if the amount of slow crack growth prior to the terminal instability does not fulfill the restriction $\Delta l/l_0 \ll 1$. As shown by Wnuk [23] a substantial amount of postyield stable crack extension may precede the transition into an unstable fracture if the tearing modulus has sufficiently low value and/or when the yield point of a material is increased, e.g., due to cold-working or irradiation. Then, it appears that a more complete representation of the crack growth history is necessary, and it is provided by the closed form solutions of the "lsy" equations given by the bottom line in (18) and (19). These solutions for a center-cracked infinite width plate are

$$R(l) = R_i(l/l_0)^{1/2}\exp\left\{\frac{1}{2}(1 + 2\lambda_i)(1 - l_0/l)\right\}$$
$$J_R(l) = J_i + \left[J_i + \frac{\kappa l_0}{2}(1 + 2\lambda_i)\right]\left(\frac{l}{l_0} - 1\right) - \frac{\kappa l}{2}\log\left(\frac{l}{l_0}\right) \tag{32}$$

where $\kappa = 8nY^2/\pi E_1$ and

$$\lambda_i = \begin{cases} M + \frac{1}{2}\log\left(\frac{l_0\Delta}{2eR_i^2}\right), \text{ or} \\ M - (J_i/\kappa l_0) - (1/2)\log(2el_0/\Delta) \end{cases} \tag{33}$$

They suggest a *variable* tearing modulus, T_J, namely,

$$T_J = \frac{8n}{\pi}\omega\left(\frac{Y}{\sigma_0}\right)^2\left\{\frac{J_i}{\kappa l_0} + \lambda_i - \frac{1}{2}\log\left(\frac{l}{l_0}\right)\right\},$$
$$\omega = \begin{cases} 1 & \text{plane stress} \\ 1 - \nu^2 & \text{plane strain} \end{cases} \tag{34}$$

The plot of T_J versus the dimensionless crack length l/l_0 is given in Fig. 3. It shows that there may be a distinct variation in the tearing modulus (considered by Paris and his coworkers to be a material constant), and that the initially high value of T_J (see, e.g., Fig. 3) is followed by a gradual monotonic decrease with a tendency to level off

[5] If the terms of order lesser than l/R are omitted in the top equation in (22) and (23), then the material resistance in the small scale yielding range becomes insensitive to the loading configuration, as it would be expected (compare also the corresponding $2D$ solutions).

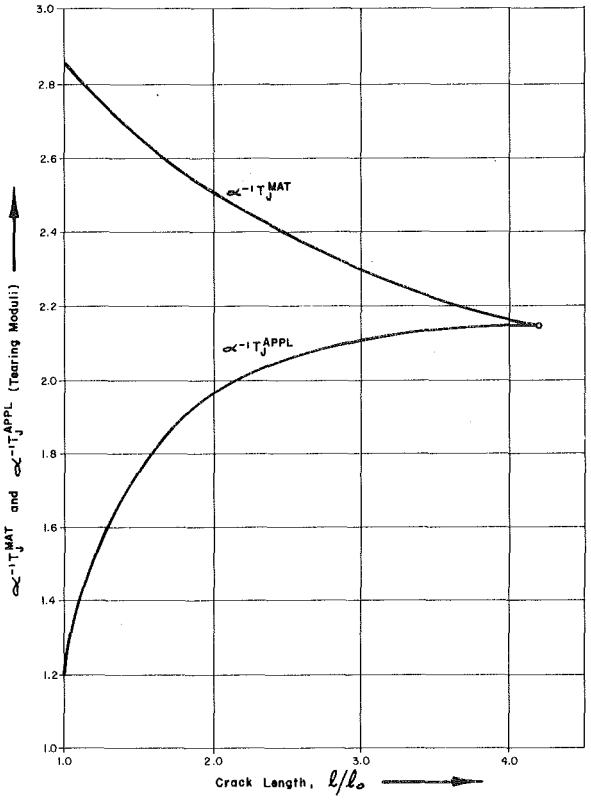

Fig. 3(*a*) Material and applied tearing moduli for the "*Isy*" case plotted versus the current crack length. The coefficient $\alpha = (8n\omega/\pi)\,(Y/\sigma_0)^2$ is about 41.7 when the constraint factor (Y/σ_0) is assumed to be 3, $\omega = 1 - \nu^2 = 0.91$, and the empirical factor $n \simeq 2$. With these values the initial tearing modulus $(T_J^{MAT})_I$ is about 119 while $(T_J^{APPL})_I$ is about 52. Other input data are as follows: $I_0 = 10\Delta$, $R_I = 35\Delta$, $M = 4.85$.

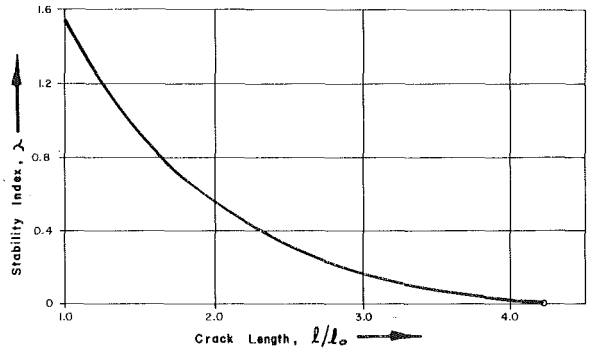

Fig. 3(*b*) Stability index λ (obtained as a difference between the two curves plotted in Fig. 3(*a*) shown as a function of the current crack length; little circle denotes the terminal instability point

prior to occurrence of the terminal instability. Perhaps it ought to be pointed out that the graph shown in Fig. 3 was obtained under an assumption of a constant crack tip opening angle (or $\hat{\delta}/\Delta$) throughout the slow crack growth phase of ductile fracture.

For comparison the quantity $(E/\sigma_0^2)\partial J_A/\partial l$ is added in Fig. 3. This entity is of the same dimension as the material tearing modulus T_J, but it reflects the amount of energy available for fracture (note the index "A" which emphasizes the "applied" nature of the J-integral, used in this context as an external field intensity). It has been suggested by Wnuk [23] that the difference

$$\lambda = (\pi E_1/8Y^2 n)[dJ_R/dl - \partial J_A/\partial l] \tag{35}$$

or

$$\lambda = (\pi\sigma_0^2/8Y^2 n)[T_{\mathrm{MAT}} - T_{\mathrm{APPL}}]$$

$$T_{\mathrm{MAT}} = (E/\sigma_0^2)(dJ_R/dl), \quad T_{\mathrm{APPL}} = (E/\sigma_0^2)(\partial J_A/\partial l) \tag{36}$$

be used as a measure of the "distance" of any given state encountered in the course of a ductile fracture from the state of terminal instability; this difference is plotted in lower half of Fig. 3. Indeed, when both entities T_{MAT} and T_{APPL} become equal, an unstable brittle-like fracture is imminent. For a stable crack extension the stability index λ is required to be a positive number, i.e., $T_{\mathrm{MAT}} > T_{\mathrm{APPL}}$.

References

1 Shih, C. F., deLorenzi, H. G., and Andrews, W. R., "Studies on Crack Initiation and Stable Crack Growth," Report No. 78CRD129, Power Generation and Propulsion Laboratory, General Electric Co., Schenactady, N. Y., 1978.

2 Paris, P. C., et al., "A Treatment of the Subject of Tearing Instability," U. S. Nuclear Regulatory Commission Report NUREG-0311 (available through National Technical Information Center, Springfield, Va., 1977.

3 Rice, J. R., and Sorensen, E. P., "Continuing Crack Tip Deformation and Fracture for Plane-Strain Crack Growth in Elastic-Plastic Solids," *Journal of the Mechanics and Physics of Solids*, Vol. 26, 1978, pp. 163–186.

4 Rice, J. R., "The Mechanics of Quasi-Static Crack Growth," Technical Report No. 63, Brown University, Providence, R. I., 1978.

5 Rice, J. R., Drugan, W. J., and Sham, T. L., "Elastic Plastic Analysis of Growing Cracks," Techn. Report No. 65, Brown University, Providence, R. I., presented at the 12th National Symposium on Fracture Mechanics at Washington University, St. Louis, Mo., May 1979.

6 Wnuk, M. P., "Accelerating Crack in a Viscoelastic Solid Subject to Subcritical Stress Intensity," *Proceedings of International Conference on Dynamic Crack Propagation*, Lehigh University, 1972, pp. 273–280.

7 Wnuk, M. P., "Prior to Failure Extension of Flaws in a Rate Sensitive Tresca Solid," ASTM STP 536, 1973, pp. 64–75.

8 Wnuk, M. P., "Quasi-Static Extension of a Tensile Crack Contained in a Viscoelastic-plastic Solid," ASME JOURNAL OF APPLIED MECHANICS, Vol. 41, 1974, pp. 234–242.

9 Kfouri, A. P., and Miller, K. J., "Crack Separation Energy Rates in Elastic-Plastic Fracture Mechanics," *Proceedings of the Institution of Mechanical Engineers*, Vol. 190, 1976, p. 571.

10 Andersson, H., *Journal of Mechanics and Physics of Solids*, Vol. 21, 1973, pp. 337–356.

11 Tilley, D. R., "Removal of the Singularity From the Numerical Solution to a Crack Problem," *Proceedings of the First International Conference on Numerical Methods in Fracture Mechanics*, Swansea, England, 1978, pp. 350–362.

12 Kanninen, M. E., et al., *Proceedings, ASTM Symposium on Elastic-Plastic Fracture*, Atlanta, 1977, ASTM-STP.

13 Clarke, G. A., et al., 1976, ibid.

14 Hutchinson, J. W., and Paris, P. C., "Stability Analysis of J-Controlled Crack Growth," ibid, 1977.

15 Griffis, C. A., and Yoder, G. R., "Initial Crack Extension in Two Intermediate-Strength Aluminum Alloys," ASME *Journal of Engineering Materials and Technology*, Vol. 98, 1978, pp. 152–158.

16 Garwood, S. J., PhD Thesis, Imperial College, London, 1977.

17 Willoughby, A. A., PhD Thesis, Imperial College, London, 1978.

18 Goodier, J. N., and Field, F. A., "Plastic Energy Dissipation in Crack Propagation," *Proceedings of the International Conference on Fracture of Solids*, eds., Drucker, D. D., and Gilman, J. J., Interscience, N. Y., 1963, pp. 103–118.

19 Smith, E., "The Invariance of the J versus Δc Curve for Plane Strain Crack Growth in Ductile Materials," to appear in *International Journal of Fracture Mechanics*, 1980.

20 Smith, E., "Some Observations on the Viability of Crack Tip Opening Angle as a Characterizing Parameter for Plane Strain Crack Growth in Ductile Materials," to appear in *International Journal of Fracture Mechanics*, 1980.

21 Rice, J. R., "Plastic Yielding at a Crack Tip," *Proceedings of 1st International Conference on Fracture Mechanics*, Sendai, eds., Yokobori, T., et al., 1965.

22 Wnuk, M. P., "Transition From Slow to Fast Fracture Under Postyield Conditions," *Proceedings of FCM3, Third International Conference on Mechanical Behavior of Materials*, Cambridge, England, Aug. 1978, Vol. 3, pp. 549–561.

23 Wnuk, M. P., "Occurrence of Catastrophic Fracture in Fully Yielded Components; Stability Analysis," *International Journal of Fracture Mechanics*, Vol. 15, 1979, pp. 553–581.

24 Curry, D. A., "Estimating a J-Resistance Curve for a Perfectly Plastic Material," *International Journal of Fracture Mechanics*, Vol. 15, 1979, pp. R59–R62.

25 Burns, S. J., and McMeeking, R. M., *International Journal of Fracture Mechanics*, Vol. 14, 1978, pp. R73–R76.

26 Olesiak, Z., and Wnuk, M. P., "Plastic Energy Dissipation Due to a Penny-Shaped Crack," *Rozprawy Inz. 3*, Vol. 14, 1966, p. 441, in Polish; English text, *International Journal of Fracture Mechanics*, Vol. 4, 1968, p. 383.

APPENDIX A

(a) 2D Traction-Free Crack. Equation describing an opening displacement ahead of a traction-free tensile crack extending in an infinite plate can be briefly written as

$$u_y(x_1, l) = cl\{\mathrm{I} - \mathrm{II}\}, \quad c = 2Y/\pi E_1 \tag{37}$$

where

$$\mathrm{I} = \log\frac{1+X}{1-X} - \log\frac{1+\epsilon+X}{1+\epsilon-X} = \log\frac{1-X^2+\epsilon(1+X)}{1-X^2+\epsilon(1-X)} \tag{38}$$

$$\mathrm{II} = \epsilon\log\frac{1+\epsilon+X}{1+\epsilon-X}, \quad X = X[x_1(l), R(l), l]$$

The entity may be expressed in terms of the R/l ratio, denoted by x, and a small quantity $\epsilon = x_1/l$ as follows:

$$S^2 = 1 - 2\chi\epsilon - \chi\epsilon^2, \quad \chi = (2x + x^2)^{-1}$$
$$S = 1 - \chi\epsilon - \frac{1}{2}\chi(1+\chi)\epsilon^2 + \ldots \tag{39}$$

Substitution of (39) into (38) leads to

$$\mathrm{I} = \log\frac{1+\chi+\ldots}{\chi(1+\epsilon+\ldots)} = \log\frac{1+\chi}{\chi} - \log(1+\epsilon+\ldots)$$
$$\mathrm{II} = \epsilon\log\frac{2+(1-\chi)\epsilon+\ldots}{(1+\chi)\epsilon+\ldots} = \epsilon\log\left[\frac{2}{(1+\chi)\epsilon} + \frac{1-\chi}{1+\chi} + \ldots\right] \tag{40}$$

It follows then that the expansions of these forms for $\epsilon \to 0$ are

$$\mathrm{I} = \log\frac{1+\chi}{\chi} - \epsilon + \ldots = 2\log(1+x) - \epsilon + \ldots$$
$$\mathrm{II} = \epsilon\log\left[\frac{2}{(1+\chi)\epsilon}\right] + \ldots = \epsilon\log\left[\frac{2x(1+x)}{\epsilon(1+x)^2}\right] + \ldots \tag{41}$$

Note that the second expression just shown contains a logarithmic factor $\log(1/\epsilon)$ which is typical for a quasi-static crack problem in any configuration. It reflects the singular behavior of *strains* when ϵ approaches zero. Of course, the product $\epsilon\log(1/\epsilon)$, which appears in the formula for the near tip *displacements*, vanishes when $\epsilon = 0$.

Combining expressions (41) with the equation (37) gives the desired near-tip displacement for a 2D traction-free crack

$$[u_y(x_1, l)]_{x_1\to 0} = 2cl\left\{\log(1+x) - \frac{\epsilon}{2}\log\left[\frac{2ex(2+x)}{\epsilon(1+x)^2}\right] + \ldots\right\}_{\epsilon=x_1/l} \tag{42}$$

Setting $\epsilon = 0$ one retrieves the tip displacement

$$u_y(O, l) = u_{\mathrm{tip}}(l) = (4Y/\pi E_1)l\log(1 + R/l) \tag{43}$$

Using this result the formula (42) can be written in an alternative form

$$[u_y(x_1, l)]_{x_1\to 0} = u_{\mathrm{tip}}(l) - (2Y/\pi E_1)\left(\frac{x_1}{l}\right)\log\left[\frac{2lex(2+x)}{x_1(1+x)^2}\right]_{x=x(l)} \tag{44}$$

or, if the notation of Section 5 is employed, one has

$$[u_y(x_1, l)]_{x_1\to 0} = C\{l\phi(x) - x_1\Phi(x_1, l)\}_{x=x(l)} \tag{45}$$

The coefficient $C = 2c = 4Y/\pi E_1$, while the functions $F(l)$ and $\phi(x_1, l)$ are obtained through a comparison of (45) and (42), namely,

$$\phi(x) = \log(1+x), \quad x = R(l)/l$$
$$\Phi(x_1, l) = \frac{1}{2}\log\left[\frac{2elx(2+x)}{x_1(1+x)^2}\right] \tag{46}$$

Hence, the application of the general result (6) yields the differential equation defining an R-curve

$$\frac{dR}{dl} = \frac{R}{l} + \left(1 + \frac{R}{l}\right)\left\{M - \frac{1}{2}\log\left[\frac{2eR(2l+R)}{l\Delta}\right]\right\} \tag{47}$$

(b) 2D Pressurized Crack. We begin with Rice's formula [21] which with our notation reads

$$u_y^{(p)}(x_1, l) = CR\{\sqrt{1 - x_1/R} - \mathrm{III} + \mathrm{IV}\}$$
$$\mathrm{III} = \frac{x_1}{2R}\log\left[\frac{1+(1-x_1/R)^{1/2}}{1-(1-x_1/R)^{1/2}}\right]$$
$$\mathrm{IV} = \log\frac{A+(1-x_1/R)^{1/2}}{A-(1-x_1/R)^{1/2}}$$
$$A = (1 + l/R)^{1/2}, \quad C = 4Y/\pi E_1 \tag{48}$$

Expansions of III and IV at the point $x_1 = 0$ give

$$\mathrm{III} = \frac{x_1}{2R}\log\left(\frac{4R}{x_1}\right) + \ldots$$
$$\mathrm{IV} = \log\frac{A+1-x_1/2R+\ldots}{A-1+x_1/2R+\ldots}$$
$$= \log\frac{A+1}{A-1} + \log\left[1 - \frac{A}{A^2-1}\left(\frac{x_1}{R}\right) + \ldots\right]$$
$$= \log\frac{A+1}{A-1} - \frac{A}{A^2-1}\left(\frac{x_1}{R}\right) + \ldots$$
$$= 2\log\left[\left(1+\frac{R}{l}\right)^{1/2} + \left(\frac{R}{l}\right)^{1/2}\right] - \frac{x_1}{l}\left(1+\frac{l}{R}\right)^{1/2} + \ldots \tag{49}$$

Replacing $\sqrt{1 - x_1/R}$ by $1 - x_1/2R$ and substituting (49) into the top equation in (48) we obtain

$$[u_y^{(p)}(x_1, l)]_{x_1\to 0} = CR\left\{1 + 2\log\left[\left(1+\frac{R}{l}\right)^{1/2} + \left(\frac{R}{l}\right)^{1/2}\right] - \frac{x_1}{2R}\log\left(\frac{4eR}{x_1}\right) - \frac{x_1}{l}\sqrt{1+l/R} + \ldots\right\} \tag{50}$$

Hence it follows

$$u_y^{(p)}(O, l) = u_{\mathrm{tip}}{}^{(p)}(l)$$
$$= (4Y/\pi E_1)R\left\{1 + 2\log\left[\left(1+\frac{R}{l}\right)^{1/2} + \left(\frac{R}{l}\right)^{1/2}\right]\right\}_{R=R(l)} \tag{51}$$

and

$$\phi(x) = x\{1 + 2\log[\sqrt{1+x} + \sqrt{x}]\}$$
$$\Phi(x_1, l) = (1/2)\log\left(\frac{4eR}{x_1}\right) + \sqrt{x(1+x)}$$
$$x(l) = R(l)/l \tag{52}$$

Application of equation (6) leads to the governing equation of the problem, namely,

$$\frac{dR}{dl} = h^{-1}\left\{M - \frac{1}{2}\log\left(\frac{4eR}{\Delta}\right) - \sqrt{x(1+x)} - \phi(x)\right\} + x$$
$$\phi(x) = x\{1 + 2\log[\sqrt{1+x} + \sqrt{x}]\}$$
$$h(x) = d\phi/dx = \frac{\phi}{x} + \sqrt{\frac{x}{1+x}} \tag{53}$$

For $x \ll 1$ equation (53) reduces to the small scale yielding limit

$$\frac{dR}{dl} = M - \frac{1}{2}\log\left(\frac{4eR}{\Delta}\right) \tag{54}$$

For $x \gg 1$ we obtain the other extreme, i.e., the large scale yielding case

$$\frac{dR}{dl} = [\log(4e^2R/l)]^{-1}\left\{M - \frac{1}{2}\log\left(\frac{4eR}{\Delta}\right)\right\} \tag{55}$$

APPENDIX B

(a) Traction-Free Penny-Shaped Crack. Using Olesiak and

Wnuk [26] solution for the displacements normal to the crack surface at a distance r_1 from the crack front

$$u_z(r_1, l) = C_1 \left(\frac{l}{m}\right) \left\{\frac{m^2-\rho^2}{\rho} F\left(\mu_2, \frac{m}{\rho}\right) + \rho E\left(\mu_2, \frac{m}{\rho}\right) - m^2 \sqrt{\frac{1-\rho^2}{1-m^2}}\right\}_{\rho \geq m} \quad (56)$$

Symbols F and E denote the incomplete elliptic integrals of the first and second kind, respectively. Other notations used are

$$m = \frac{l}{l+R}, \quad \rho = \frac{l+r_1}{l+R} = m(1+\epsilon), \quad \epsilon = r_1/l$$
$$\mu_2 = \sin^{-1}\left(\frac{1-\rho^2}{1-m^2}\right)^{1/2}, \quad C_1 = 4Y/\pi E(1-\nu^2) \quad (57)$$

For the distance r_1 approaching zero one may express the incomplete elliptic integrals F and E through a difference of the corresponding complete elliptic integrals $K(m/\rho)$ and $E(m/\rho, \pi/2)$ and certain corrective terms:

$$F\left(\mu_2, \frac{m}{\rho}\right) = K\left(\frac{m}{\rho}\right) - \Delta F$$
$$E\left(\mu_2, \frac{m}{\rho}\right) = E\left(\frac{m}{\rho}, \frac{\pi}{2}\right) - \Delta E \quad (58)$$

The corrective terms are defined as follows:

$$\Delta F = \int_{\pi/2-\bar{\epsilon}}^{\pi/2} \frac{d\psi}{\sqrt{1-\left(\frac{m}{\rho}\right)^2 \sin^2\psi}}, \quad \bar{\epsilon} = \sqrt{\frac{r_1}{R}}\sqrt{\frac{2l}{2l+R}}$$
$$\Delta E = \int_{\pi/2-\bar{\epsilon}}^{\pi/2} \sqrt{1-\left(\frac{m}{\rho}\right)^2 \sin^2\psi}\, d\psi \quad (59)$$

The lower limit in each integral was obtained by expanding the amplitude of the elliptic integrals involved, μ_2 into a power series of ϵ, i.e.,

$$\mu_2 = \frac{\pi}{2} - \frac{\sqrt{2}m}{\sqrt{1-m^2}}\epsilon^{1/2} + \ldots = \frac{\pi}{2} - \bar{\epsilon} + \ldots \quad (60)$$

Note that with $\bar{\epsilon} \to 0$ and $\rho \to m$ second of the foregoing integrals reduces to zero. The behavior of the first one needs to be investigated further, since its integrand becomes singular at $\rho \to m$. Such investigation reveals

$$\Delta F = \frac{l}{\sqrt{R(2l+R)}} + O(\epsilon^{1/2})$$
$$\Delta E = \frac{2r_1}{\sqrt{R(2l+R)}} + O(\epsilon^{3/2}) \quad (61)$$

This result does not contain a logarithmic term expected in this type of a problem. To extract the logarithmically singular terms inherent in the expressions (58) we apply formulas given by Gradstein and Rhyzik (Tables of Integrals, Moscow, 1971, Russian edition, p. 919) to obtain

$$K\left(\frac{m}{\rho}\right)\Big|_{\rho \to m} = \log\frac{4}{\sqrt{2\epsilon}} + \ldots$$
$$E\left(\frac{m}{\rho}\right)\Big|_{\rho \to m} = 1 + \frac{\epsilon}{2}\log(8/\epsilon) + \ldots \quad (62)$$

These results combined with (61) and substituted into equations (58) yield

$$\left[F\left(\mu_2, \frac{m}{\rho}\right)\right]_{\rho \to m} = \frac{1}{2}\log(8/\epsilon) - \frac{l}{\sqrt{R(2l+R)}} + O(\epsilon^{1/2})$$
$$\left[E\left(\mu_2, \frac{m}{\rho}\right)\right]_{\rho \to m} = 1 + \frac{\epsilon}{2}\log(8/\epsilon) - \frac{2l\epsilon}{\sqrt{R(2l+R)}} + O(\epsilon^{3/2}) \quad (63)$$

Observing now that

$$\frac{m^2-\rho^2}{\rho}\Big|_{\rho \to m} = (-2m)\epsilon + \ldots$$
$$-m^2[(1-\rho^2)/(1-m^2)]_{\rho \to m}^{1/2} = -m^2$$

and adding $(m^2-\rho^2)\rho^{-1}F$ with ρE we get

$$\left\{\frac{m^2-\rho^2}{\rho}F + \rho E\right\}_{\rho \to m} = m - \frac{m\epsilon}{2}\log(8/\epsilon) + m\epsilon + \ldots \quad (64)$$

Finally, the result just given is combined with the second of the expressions (63) to yield the desired expansion of the displacement $u_z(r_1, l)$, see equation (56), valid in the vicinity of crack tip, i.e.,

$$[u_z(r_1, l)]_{r_1 \to 0} = C_1 l \left\{1 - m - \frac{\epsilon}{2}\log(8/\epsilon) + \left(1 + \frac{m^3}{1-m^2}\right)\epsilon + \ldots\right\}_{\epsilon = r_1/l} \quad (65)$$

and

$$u_{\text{tip}}(l) = C_1 l(1-m) = C_1 l x(1+x)^{-1} \quad (65a)$$

If we agree to represent these relations by the general formula

$$[u_z]_{r_1 \to l} = C_1\{l\phi(x) - r_1\Phi(r_1, l)\} \quad (66)$$

it remains to define the functions ϕ and Φ. Comparison between (66) and (65) gives

$$\phi(x) = \frac{x}{1+x}$$
$$\Phi(r_1, l) = \frac{1}{2}\log(8l/r_1) - \left[1 + \frac{1}{x(1+x)(2+x)}\right] \quad (67)$$
$$x(l) = R(l)/l$$

These results combined with the equation (6) generate the differential equation of an R-curve valid for an arbitrary R/l ratio

$$\frac{dR}{dl} = (1+x)^2\left\{M - \frac{1}{2}\log(8l/\Delta)\right\} + f(x)$$
$$f(x) = 1 + 2x + \frac{1+x}{x(2+x)} \quad (68)$$

The limiting cases of the contained yielding and large scale plasticity are discussed in Section 4.

(b) Pressurized Penny-Shaped Crack. Examination of Olesiak and Wnuk's [26] formulas for the opening displacement $u_z(r_1, l)$ near the front of a pressurized penny-shaped crack reveals that the only difference between this solution and that for a traction-free crack, is the presence of a multiplicative factor

$$B = [1 + (1-m^2)^{1/2}]m^{-2} \quad (69)$$

which appears in front of the bracketed expression in equation (56). When m is replaced $(1+x)^{-1}$, the function B reads

$$B(x) = \{(1+x)[1 + x + \sqrt{x(2+x)}]\}_{x=R/l} \quad (70)$$

Thus, omitting the algebraic details, we can utilize the expression (65) which can be easily adapted for the considered crack and loading configuration, i.e.,

$$[u_z{}^{(p)}(r_1, l)]_{r_1 \to 0} = C_1 l B(x)\left\{1 - m - \frac{\epsilon}{2}\log(8/\epsilon) + \left(1 + \frac{m^3}{1-m^2}\right)\epsilon + \ldots\right\}_{\epsilon = r_1/l}$$
$$u_{\text{tip}}(l) = C_1 l B(x) x(1+x)^{-1} \quad (71)$$

These formulas imply

$$\phi(x) = x[1 + x + \sqrt{x(2+x)}]$$
$$\Phi(x_1, l) = (1+x)[1 + x + \sqrt{x(2+x)}]\{\tfrac{1}{2}\log(8l/\Delta) - H(x)\}$$
$$H(x) = 1 + [x(1+x)(2+x)^{-1}, \quad x(l) = R(l)/l \quad (72)$$

Application of the final stretch criterion gives now

$$\frac{dR}{dl} = \Phi_1(x)\left\{M - \frac{B(x)}{2}\log(8l/\Delta)\right\} + \Phi_2(x) \tag{73}$$

where the auxiliary functions Φ_1 and Φ_2 are defined as follows:

$$\Phi_1(x) = \frac{\sqrt{x(2+x)}}{(x+\sqrt{x(2+x)})(1+x+\sqrt{x(2+x)})}$$
$$\Phi_2(x) = x + \frac{\sqrt{x(2+x)}(1+x)^2}{x(2+x)(\sqrt{x(2+x)}+x)} \tag{73a}$$

In closing it should be noted that in order to obtain the correct limiting expressions for the *ssy* case the function $\phi(x)$ in (67) and (72) should be represented by a power series in which the term x^2 is retained, i.e.,

$$\phi(x)|_{ssy} = \begin{cases} x(1-x+\ldots), & \text{case } a \\ x(1+\sqrt{2x}+x+\ldots), & \text{case } b \end{cases} \tag{74}$$

which implies

$$J_R(l)|_{ssy} \simeq \begin{cases} \kappa R(1-x), & \text{case } a \\ \kappa R\left\{1+\frac{R}{l}+\sqrt{\frac{R}{l}\left(2+\frac{R}{l}\right)}\right\}, & \text{case } b \end{cases} \tag{75}$$

Differentiation of ϕ with respect to x reduces the order of the polynomials (74), and thus upon completion of the necessary calculations we find that the highest order term which survives is on the order of x^0, i.e., a constant. This constant is needed and should not be omitted.

Expansions of functions $\Phi_1(x)$, $B(x)$, and $\Phi_2(x)$ for $x \to 0$ are given as follows:

$$\Phi_1(x) = 1 - \tfrac{3}{2}\sqrt{2x} + \tfrac{5}{2}x + \ldots$$
$$B(x) = 1 + \sqrt{2x} + 2x + \ldots$$
$$\Phi_2(x) = \frac{1}{2x} + \frac{1}{2\sqrt{2x}} + 1 + \ldots \tag{76}$$

These relations were utilized in derivation of the top equations in (26) and in (29), valid in the limit of contained yielding.

J. Aboudi
Professor,
School of Engineering,
Tel Aviv University,
Ramat-Aviv, Israel

J. D. Achenbach
Professor,
Departent of Civil Engineering,
Northwestern University,
Evanston, Ill. 60201.
Fellow ASME.

Arrest of Mode III Fast Fracture by a Transition From Elastic to Viscoplastic Material Properties

The transient problem of arrest of a rapidly propagating Mode III crack has been investigated for a crack which initially propagates in an elastic solid, and then enters a region of viscoplastic material properties. The transition to the viscoplastic behavior is modeled by a gradual process which starts at a certain time at which the constitutive relations change in a timewise manner from elastic to elastic-viscoplastic. Both deceleration and complete arrest of the crack have been treated. The solution has been obtained numerically by a finite-difference procedure. Arrest of a crack in a perfectly elastic material has been treated as a special case. Several field quantities such as the effective plastic strain, plastic work, total strain, and crack surface displacement have been computed, and their relation to arrest criteria have been explored.

1 Introduction

The ultimate goal of fast-fracture studies is to analyze the conditions for prevention of rapid crack propagation. A prudent assumption is, however, that high rate fracture phenomena cannot always be prevented. Thus it is important to consider the conditions for arrest of a rapidly propagating crack tip.

Rapid crack propagation usually is an essentially brittle fracture process. In this paper we consider the case that a crack starts to propagate under brittle conditions, but then approaches an interface beyond which the material can yield considerably before rupturing. We investigate crack arrest as well as reduction of crack-tip speed as the crack-tip enters the region of plastic deformation.

In earlier work, which was concerned with rapid crack propagation in an elastic-viscoplastic material [1, 2] the authors have used a constitutive model which was proposed by Bodner and Partom [3]. This model does not require the statement of a separate yield criterion, nor is it necessary to consider loading and unloading separately. Plastic deformation always exists, but it is negligibly small when the material behavior should be essentially elastic.

In this paper we use the Bodner-Partom model for the material behavior in the region of elastic-viscoplastic behavior. Since the crack-tip speeds are high, and since considerable transient effects may occur when the region of plastic deformation is approached, the effect of inertia has been included in the analysis.

The constitutive equations for the elastic-viscoplastic region have been summarized in Section 2. The modeling of crack arrest as the plastic region is entered, and of penetration of the region of plastic deformation, is discussed in Section 3. The numerical method of analysis is discussed in some detail in Section 4. The last section is concerned with the discussion of the results, principally the plastic strains just ahead of the crack tip.

2 Constitutive Equations

In this section the governing equations for the Bodner-Partom model are briefly summarized.

In the usual manner the total rate of strain is expressed as the superposition of elastic (reversible) and plastic (irreversible) components

$$\dot{\epsilon}_{ij} = \dot{\epsilon}_{ij}^{(e)} + \dot{\epsilon}_{ij}^{(p)} \quad i, j = 1, 2, 3 \tag{1}$$

The elastic strain rates are related to the stress-rates by Hooke's law

$$\dot{\epsilon}_{ij}^{(e)} = \frac{1}{2\mu}\left(\dot{\sigma}_{ij} - \frac{\nu}{1-\nu}\dot{\sigma}_{kk}\delta_{ij}\right) \tag{2}$$

where μ is the shear modulus, ν is Poisson's ratio, and δ_{ij} is the Kronecker delta. It is assumed that the plastic deformations are incompressible, $\dot{\epsilon}_{kk}^{(p)} = 0$, and that the Prandtl-Reuss flow law holds. Thus

$$\dot{\epsilon}_{ij}^{(p)} = \dot{e}_{ij}^{(p)} = \Lambda s_{ij} \tag{3}$$

where s_{ij} and $\dot{e}_{ij}^{(p)}$ denote the deviators of the stress tensor and the plastic strain-rate tensor, respectively. Equation (3) can be squared to yield Λ in the form

$$\Lambda^2 = D_2^{(p)}/J_2 \tag{4}$$

Here

$$D_2^{(p)} = \tfrac{1}{2}\dot{e}_{ij}^{(p)}\dot{e}_{ij}^{(p)} \quad \text{and} \quad J_2 = \tfrac{1}{2}s_{ij}s_{ij} \tag{5a, b}$$

Contributed by the Applied Mechanics Division for publication in the JOURNAL OF APPLIED MECHANICS.
Discussion on this paper should be addressed to the Editorial Department, ASME, United Engineering Center, 345 East 47th Street, New York, N.Y. 10017, and will be accepted until December 1, 1981. Readers who need more time to prepare a discussion should request an extension from the Editorial Department. Manuscript received by the Applied Mechanics Division, September, 1980; final revision, February, 1981.

are the second invariants of the plastic strain-rate deviator and the stress deviator, respectively.

Following reference [3] we take the following relation between $D_2^{(p)}$ and J_2:

$$D_2^{(p)} = D_0^2 \exp\left[-(A^2/J_2)^n\right], \tag{6}$$

where

$$A^2 = \tfrac{1}{3} Z^2 [(n+1)/n]^{1/n} \tag{7}$$

The coefficient n is related to the steepness of the $D_2^{(p)} - J_2$ curve, D_0^2 is the limiting value of $D_2^{(p)}$ for very high stresses, and Z is an internal state variable referred to as the hardness of the material, which expresses its overall resistance to plastic flow. For isotropic work-hardening the evolution equation for Z is taken to depend on the amount of plastic (irreversible) work, W_p, which has been done on the material from a reference state. Specifically, Z is assumed to have the form

$$Z = Z_1 + (Z_0 - Z_1) \exp\left[-mW_p/Z_0\right] \tag{8}$$

where Z_0, Z_1, and m are appropriate parameters of the material, and the rate of plastic work can be expressed in the form

$$\dot{W}_p = \sigma_{ij}\dot{\epsilon}_{ij}^{(p)} = s_{ij}\dot{\epsilon}_{ij}^{(p)} = 2\Lambda J_2 \tag{9}$$

In equation (8), Z_0 is the initial hardness and Z_1 is the upper limit of Z. The hardness must have an upper limit, because otherwise $D_2^{(p)}$ would approach zero for large W_p, which would imply fully elastic behavior at appreciable strains.

In reference [3] the model was used to investigate tensile straining for a number of histories, that included straining at various rates, rapid changes of strain rate, unloading and reloading, and stress relaxation. The calculations were based on material constants chosen to represent commercially pure titanium. Theoretical and experimental results showed good agreement.

The system of governing equations is completed with the stress equations of motion

$$\sigma_{ij,j} = \rho\ddot{u}_i \tag{10}$$

where ρ is the mass density.

The Bodner-Partom theory is applied in this paper to a dynamic problem. It should be noted that its validity under dynamic conditions was examined in [4] where the response of elastic-viscoplastic beams subjected to dynamic loads was computed. Comparisons between theoretical and experimental dynamic deflections showed good agreement for relatively short response times.

The particular example of this paper is concerned with deformation in antiplane strain. Thus the only nonvanishing displacement component is $u_3(x_1, x_2, t)$, and the corresponding total strains are

$$\epsilon_{31} = \tfrac{1}{2} u_{3,1}\,; \quad \epsilon_{32} = \tfrac{1}{2} u_{3,2} \tag{11a, b}$$

The nonzero stress components follow from (1) and (2) as

$$\sigma_{31} = 2\mu(\epsilon_{31} - \epsilon_{31}^{(p)}), \quad \sigma_{32} = 2\mu(\epsilon_{32} - \epsilon_{32}^{(p)}) \tag{12a, b}$$

and the second invariant of the stress deviator reduces to

$$J_2 = \sigma_{31}^2 + \sigma_{32}^2 \tag{13}$$

Substitution of (11a, b) into (12a, b), and subsequent substitution of the results into (10) yields

$$(u_{3,11} + u_{3,22}) - 2(\epsilon_{31,1}^{(p)} + \epsilon_{32,2}^{(p)}) = \frac{1}{c_T^2}\ddot{u}_3 \tag{14}$$

where $c_T = (\mu/\rho)^{1/2}$ is the speed of elastic shear waves. The plastic strains are governed by the flow rule (3).

3 Arrest of a Rapidly Propagating Mode III Crack

We consider a semi-infinite Mode III crack which propagates in the center plane of a thick strip of height $2h$. The geometry is shown in Fig. 1. An interface (or a transition region) separates the strip into two

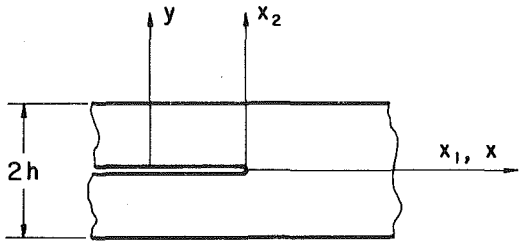

Fig. 1 Propagating crack in a strip

semi-infinite strips in which the constitutive behavior is elastic and elastic-viscoplastic, respectively. The crack originally propagates with a constant velocity v_0 in the elastic part of the strip in an essentially brittle fracture process. It is assumed that a steady-state situation relative to the moving crack tip has been established. As the region of viscoplastic constitutive behavior is approached, the steady-state process is terminated and a transient process starts.

Conceptually, it would be possible to model the interface between the elastic and viscoplastic parts as a discrete plane across which relevant stresses and displacements must be continuous. Since the computations are carried out relative to a coordinate system which moves with the crack tip, the presence of such an interface, which would be located a monotonically decreasing distance from the crack tip, creates some awkward complications in the numerical analysis. Even though the complications may not be unsurmountable, the authors have decided to model the transition into the viscoplastic region in an alternative manner, which approximates a transition region rather than a discrete interface. In this model it is assumed that at a certain time t (say $t = 0$) the constitutive behavior starts to change in a timewise manner from elastic to elastic-viscoplastic. Since time is measured relative to a coordinate system moving with the crack tip the change of the constitutive behavior with time can be considered as a change with the coordinate in the direction of crack propagation. At time $t = t_1$ the transition from elastic to viscoplastic has been completed. The time $t = 0$ corresponds to the time that the crack-tip region first becomes aware of plastic deformation ahead of the crack tip, while at the time $t = t_1$ the crack tip is completely surrounded by a plastic zone. In the time interval $0 \le t \le t_1$ the crack-tip speed may change its magnitude. Three cases have been considered:

1 The crack-tip speed does not change.
2 The crack tip is arrested.
3 The crack-tip speed changes from v_0 to v_f, where $v_f < v_0$.

In the latter two cases it is assumed that the velocity changes also take place in the time interval $0 \le t \le t_1$. The initial conditions in the strip for $t \le 0$ are given by the steady-state displacement distribution produced by a crack moving at a velocity v_0 in the x_1-direction in the center plane of an elastic strip, which is subjected to a tearing loads at its boundaries. For a constant displacement, W_0, on the faces at $x_2 = \pm h$, the displacement distribution within the strip has a closed-form expression which is given in reference [5]. The displacement field within the strip can also be obtained numerically by a very efficient method which was described in [1].

At time $t = 0$ the material starts to change gradually. The properties become elastic-viscoplastic with a constitutive behavior defined by equations (1)–(9). At the same time the crack-tip speed starts to decrease. The external loading does, however, not change, so that the boundary conditions on the faces of the strip remain of the form

$$u_3(x_1, \pm h, t) = W_0 \tag{15}$$

By virtue of antisymmetry it suffices to consider the upper half of the strip only. The boundary condition on the surface of the crack is

$$\sigma_{32}(x_1, 0, t) = 0 \quad \text{for} \quad -\infty < x_1 \le 0 \tag{16}$$

while the condition of displacement antisymmetry yields

$$u_3(x_1, 0, t) = 0 \quad \text{for} \quad x_1 > 0 \tag{17}$$

Let $v(t)$ denote the time-dependent velocity of the propagating crack tip. A system of (x_1, x_2, x_3) coordinates is now chosen to move with the crack tip. A stationary system (x, y, z) and the moving system (x_1, x_2, x_3) are related by

$$x_1 = x - \int_0^t v(s)ds, \quad x_2 = y, \quad x_3 = z \tag{18}$$

The time derivatives in the equation of motion and in the flow rule then reduce to

$$(\cdot) = \frac{\partial}{\partial t} - v\frac{\partial}{\partial x_1}; \quad (\cdot\cdot) = \frac{\partial^2}{\partial t^2} - 2v\frac{\partial^2}{\partial x_1 \partial t} + v^2\frac{\partial^2}{\partial x_1{}^2} - \frac{dv}{dt}\frac{\partial}{\partial x_1} \tag{19}$$

Consequently, in terms of the moving coordinates, the equation of motion (14) takes the form

$$(1 - v^2/c_T{}^2)u_{3,11} + u_{3,22} - 2(\epsilon_{31,1}{}^{(p)} + \epsilon_{32,2}{}^{(p)}) + 2\frac{v}{c_T{}^2}\frac{\partial}{\partial t}u_{3,1} + \frac{1}{c_T{}^2}\frac{dv}{dt}u_{3,1} = \frac{1}{c_T{}^2}\frac{\partial^2}{\partial t^2}u_3 \tag{20}$$

In the moving system the flow rule (3) is given by

$$\frac{\partial}{\partial t}\epsilon_{31}{}^{(p)} = v\epsilon_{31,1}{}^{(p)} + \Lambda\sigma_{31} \tag{21}$$

$$\frac{\partial}{\partial t}\epsilon_{32}{}^{(p)} = v\epsilon_{32,1}{}^{(p)} + \Lambda\sigma_{32}, \tag{22}$$

and equation (9) for the rate of plastic work reduces to

$$\frac{\partial}{\partial t}W_p = v(W_p)_{,1} + 2\Lambda J_2 \tag{23}$$

Equations (20)–(23) form a system of nonlinear differential equations for the variables $u_3(x_1, x_2, t)$, $\epsilon_{31}{}^{(p)}(x_1, x_2, t)$, $\epsilon_{32}{}^{(p)}(x_1, x_2, t)$, and $W_p(x_1, x_2, t)$ which govern the field induced by the motion of the crack in the elastic-viscoplastic medium.

When $D_0 = 0$ in (6), Hooke's law for a perfectly elastic material is obtained. The transition from the elastic state to the elastic-viscoplastic state during the time interval $0 \le t \le t_1$ is modeled by multiplying the parameter D_0 in (6) by an appropriate temporal function $G(t)$ which rises gradually from $G(0) = 0$ to $G(t_1) = 1$, and $G(t) = 1$ for $t > t_1$.

4 Numerical Solution

The system of equations (20)–(23) has been solved numerically by a finite-difference procedure which employs a grid of mesh sizes Δx_1 and Δx_2 in the x_1 and x_2-directions, respectively, and a time increment Δt. The procedure can be divided into three steps. In the first step equation (20) is integrated. Equations (21)–(23) are solved in the second step. In the third step the boundary conditions (16)–(17) are imposed.

In the integration of equation (20) the derivatives are replaced by their central difference approximations to yield an implicit three-level scheme of second-order accuracy, (i.e., the error resulting from the replacement of the differential equation (20) by its finite-difference approximation is of a second order in the spatial and temporal increments). The following system of equations in the unknown displacements at $t + \Delta t$ is obtained:

$$\begin{aligned}
&\epsilon_3 u_3(x_1 - \Delta x_1, x_2, t + \Delta t) + u_3(x_1, x_2, t + \Delta t) \\
&\quad - \epsilon_3 u_3(x_1 + \Delta x_1, x_2, t + \Delta t) = 2[1 - (c_T{}^2 - v^2)\epsilon_1{}^2 \\
&\quad - c_T{}^2\epsilon_2{}^2]u_3(x_1, x_2, t) - u_3(x_1, x_2, t - \Delta t) \\
&\quad + \epsilon_3[u_3(x_1 - \Delta x_1, x_2, t - \Delta t) - u_3(x_1 + \Delta x_1, x_2, t - \Delta t)] \\
&\quad + (c_T{}^2 - v^2)\,\epsilon_1{}^2[u_3(x_1 + \Delta x_1, x_2, t) + u_3(x_1 - \Delta x_1, x_2, t)] \\
&\quad + c_T{}^2\epsilon_2{}^2[u_3(x_1, x_2 + \Delta x_2, t) + u_3(x_1, x_2 - \Delta x_2, t)] \\
&\quad + \frac{dv}{dt}\epsilon_1\Delta t[u_3(x_1 + \Delta x_1, x_2, t) - u_3(x_1 - \Delta x_1, x_2, t)]/2 \\
&\quad - c_T{}^2\epsilon_1\Delta t[\epsilon_{31}{}^{(p)}(x_1 + \Delta x_1, x_2, t) - \epsilon_{31}{}^{(p)}(x_1 - \Delta x_1, x_2, t)] \\
&\quad - c_T{}^2\epsilon_2\Delta t[\epsilon_{32}{}^{(p)}(x_1, x_2 + \Delta x_2, t) - \epsilon_{32}{}^{(p)}(x_1, x_2 - \Delta x_2, t)] \qquad (24)
\end{aligned}$$

(*Cont.*)

where $\epsilon_1 = \Delta t/\Delta x_1$, $\epsilon_2 = \Delta t/\Delta x_2$, $\epsilon_3 = \epsilon_1 v/2$.

This system is tridiagonal so that a direct inversion algorithm can be employed and no iterations are needed. According to the three-level scheme (24) it is possible to compute the displacement u_3 at time $t + \Delta t$ if the field variables are known at time t and $t - \Delta t$ throughout the region.

In the second part of the numerical procedure the three differential equations (21)–(23) are solved. To this end we rewrite (21)–(23) in the form

$$\frac{\partial}{\partial t}\mathbf{U} = \mathbf{A}\mathbf{U}_{,1} + \mathbf{B} \tag{25}$$

where

$$\mathbf{U} = \begin{bmatrix} \epsilon_{31}{}^{(p)} \\ \epsilon_{32}{}^{(p)} \\ W_p \end{bmatrix}, \quad \mathbf{A} = v(t)\mathbf{I}, \quad \mathbf{B} = \begin{bmatrix} \Lambda & \sigma_{31} \\ \Lambda & \sigma_{32} \\ 2\Lambda & J_2 \end{bmatrix} \tag{26}$$

with $\mathbf{I}$ being the unit matrix. The quasi-linear system (25) is solved by the Lax-Wendroff method which is given in [6] for a homogeneous system ($\mathbf{B} = \mathbf{O}$). Here we generalize this method as follows:

$$\begin{aligned}
\mathbf{U}(x_1, x_2, t + \Delta t) &= \mathbf{U} + \Delta t\frac{\partial}{\partial t}\mathbf{U} + \frac{(\Delta t)^2}{2}\frac{\partial^2}{\partial t^2}\mathbf{U} + O(\Delta t^3) \\
&= \mathbf{U} + \Delta t(\mathbf{A}\mathbf{U}_{,1} + \mathbf{B}) + \frac{(\Delta t)^2}{2}\left(\mathbf{A}^2\mathbf{U}_{,11} + \frac{d\mathbf{A}}{dt}\mathbf{U}_{,1} + \mathbf{A}\mathbf{B}_{,1} + \frac{\partial\mathbf{B}}{\partial t}\right) + O(\Delta t^3) \qquad (27)
\end{aligned}$$

Let us define the operator Q by

$$\begin{aligned}
Q\mathbf{U} &= (1 - \mathbf{A}^2\epsilon_1{}^2)\mathbf{U}(x_1, x_2, t) \\
&\quad + \frac{1}{2}\left(\mathbf{A}^2\epsilon_1{}^2 + \mathbf{A}\epsilon_1 + \frac{1}{2}\frac{d\mathbf{A}}{dt}\epsilon_1\Delta t\right)\mathbf{U}(x_1 + \Delta x_1, x_2, t) \\
&\quad + \frac{1}{2}\left(\mathbf{A}^2\epsilon_1{}^2 - \mathbf{A}\epsilon_1 - \frac{1}{2}\frac{d\mathbf{A}}{dt}\epsilon_1\Delta t\right)\mathbf{U}(x_1 - \Delta x_1, x_2, t) \\
&\quad + \frac{1}{4}\mathbf{A}\epsilon_1\Delta t[\mathbf{B}(x_1 + \Delta x_1, x_2, t) - \mathbf{B}(x_1 - \Delta x_1, x_2, t)] \qquad (28)
\end{aligned}$$

Equation (27) can be spatially discretized in the form

$$\mathbf{U}(x_1, x_2, t + \Delta t) = Q\,\mathbf{U}(x_1, x_2, t) + \Delta t\,\mathbf{B}\left(x_1, x_2, t + \frac{\Delta t}{2}\right) + O(\Delta t^3) \tag{29}$$

In (29), $\mathbf{B}(x_1, x_2, t + \Delta t/2)$ can be approximated by $\frac{1}{2}[\mathbf{B}(x_1, x_2, t) + \mathbf{B}(x_1, x_2, t + \Delta t)]$. Hence $\mathbf{U}$ at time $t + \Delta t$ can be computed tentatively as

$$\overset{*}{\mathbf{U}}(x_1, x_2, t + \Delta t) = Q\,\mathbf{U}(x_1, x_2, t) + \Delta t\mathbf{B}(x_1, x_2, t) \tag{30}$$

This value is subsequently corrected according to

$$\overset{*}{\mathbf{U}}(x_1, x_2, t + \Delta t) = Q\,\mathbf{U}(x_1, x_2, t) + \frac{\Delta t}{2}[\mathbf{B}(x_1, x_2, t) + \overset{*}{\mathbf{B}}(x_1, x_2, t + \Delta t)] \tag{31}$$

where the asterisk on $\mathbf{B}$ means that this quantity is evaluated by using the predicted value given by (30).

According to (30)–(31) it is possible to compute the inelastic field variables by an explicit method of second-order accuracy whenever

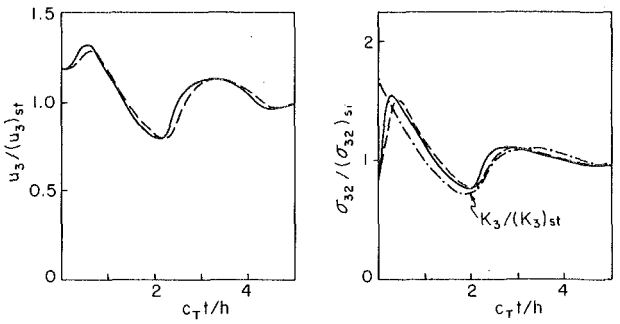

Fig. 2 Normalized displacements at $(-h/2, 0)$ and normalized stresses at $(\Delta x_1, 0)$ versus time for arrest ($v_f = 0$) of a propagating crack ($v_0/c_T = 0.8$) in an elastic strip. The rate of change of the crack-tip speed is given by equation (33), with $c_T t_1/h = 0.25$ (——) and $c_T t_1/h = 0.5$ (- - -). Also shown the normalized stress-intensity factor (- · -) for sudden crack arrest.

all the field variables are known at time t. In the special case of a stationary crack we have $\mathbf{A} = \mathbf{O}$, and the scheme (30)–(31) reduces to the improved Euler-Cauchy method for the numerical integration of ordinary differential equations.

The final part of the scheme consists of the application of the boundary conditions (16)–(17). Equation (16) is employed to determine the displacement along the surface of crack behind the tip in the form

$$u_3(x_1, 0, t) = u_3(x_1, \Delta x_2, t) - 2\Delta x_2 \epsilon_{32}^{(p)}(x_1, 0, t) \quad x_1 \leq 0 \quad (32)$$

5 Results

The method of solution has been applied to compute the fields generated by crack arrest as the crack tip enters titanium, for which the material parameters are, see [3]:

$$\mu = 0.44 \times 10^5 \text{N/mm}^2, \quad \rho = 4.87 \text{ gm/cm}^3, \quad Z_0 = 1150 \text{ N/mm}^2,$$

$$Z_1 = 1400 \text{ N/mm}^2, \quad D_0 = 10^4 \text{ sec}^{-1}, \quad m = 100 \text{ and } n = 1.$$

The height of the strip is chosen as $2h$ where $h = c_T/(5D_0)$, which means that an elastic shear wave will propagate a distance of $5h$ during the time interval D_0^{-1}.

The results presented in this paper have been obtained with the spatial increments $\Delta x_1/h = \Delta x_2/h = 0.05$ and the time increment $c_T \Delta t/h = 0.025$. The latter value fulfills the stability condition discussed in reference [6] for the Lax-Wendroff scheme (30)–(31), which in the present case can be written in the form $v\Delta t/\Delta x_1 \leq 1$. It also satisfies the stability condition for the scheme (25) discussed for an elastic problem in reference [7]. The applied displacements $\pm W_0$ on the two faces of the strip have been chosen as $W_0/h = 0.008$.

(1) Crack Arrest in a Perfectly Elastic Strip. We consider the case that the propagating crack tip changes its velocity at time $t = 0$ from a steady speed v_0 to the final value $v_f = 0$ over the time interval $0 \leq t \leq t_1$. The strip is assumed to be perfectly elastic. We consider the elastic strip because crack arrest problems in elastic materials are of great importance, and because results for the stress-intensity factor for sudden arrest of a crack in a strip have been given by Nilsson [8]. These results can be compared with our numerical solution for crack arrest over short time intervals $[0, t_1]$.

The time-dependent velocity is chosen in the form

$$v(t) = \begin{cases} (v_0 - v_f)[1 - \sin^2(\pi t/2t_1)] + v_f & 0 \leq t \leq t_1 \\ v_f & t > t_1 \end{cases} \quad (33)$$

from which the acceleration dv/dt can be determined.

In Fig. 2 we present the displacement on the faces of the crack at a distance $x_1 = -h/2$ behind the tip, versus the nondimensional time $c_T t/h$, for initial speed $v_0/c_T = 0.8$ and two values of t_1:$c_T t_1/h$ =0.25 and 0.5, respectively. Also shown in Fig. 2 are the normalized stresses σ_{32} at the closest grid point $(\Delta x_1, 0)$ directly ahead of the tip. The stresses are normalized with respect to the static value, $(\sigma_{32})_{st}$, achieved at the same point by a stationary crack in the strip. Also shown are the results of Nilsson for the normalized stress-intensity factor generated by sudden arrest of the crack. The stress-intensity factor is normalized with respect to the static value $(K_3)_{st} = \mu W_0 (2/h)^{1/2}$, for a stationary crack in the strip. Fig. 2 shows that the two time durations t_1 do not make a significant difference for the displacement, but it also shows that the maximum level of the stresses obtained at short times after arrest is initiated increases as the time duration t_1 decreases. For the case of sudden arrest, the results of Nilsson show a jump of about 1.72 at $t = 0$ after which a sudden decrease occurs. All results show that after short times the normalized quantities decrease rapidly and oscillate with decreasing amplitudes around unity. It should be noted that since the stresses are computed at the nearest point to the tip of the crack, they can be regarded as the asymptotic value of the near-tip stresses which are directly proportional to the stress-intensity factor. Accordingly the normalized stress near the tip can be directly compared with the normalized stress-intensity factor.

The displacements on the crack face at the point $(-h/2, 0)$ shown in Fig. 2 are normalized with respect to $(u_3)_{st}$—the static displacement for a stationary crack in the strip. It is readily seen that for both cases of $c_T t_1/h = 0.25$ and 0.5 the values of the normalized displacements equal unity when $c_T t/h \doteq 5$.

The aforementioned numerical results are given here for the arrest problem in which $v_f = 0$. It should be mentioned, however, that the present numerical method can be applied also to the more complicated case of steady propagation followed by nonsteady propagation of the crack tip. A short-time solution to this problem has been discussed recently by Nilsson [9].

In concluding this section we mention that by considering the case $v_f = v_0$ the steady-state solution for a propagating crack should be produced when the numerical scheme (24) is applied at $t > 0$. The procedure which was designed for transient phenomena then should provide time-independent results. This case forms a necessary test for the numerical method, and it was actually performed to yield excellent results.

(2) Crack Arrest in an Elastic-Viscoplastic Strip. The results of Fig. 2 show that arrest of a propagating crack in an elastic material induces high values of the stresses immediately after the arrest initiates. Accordingly, when the loads remain unchanged crack arrest requires changes of the material properties. As discussed in Section 3, we assume that the material properties change gradually from elastic to elastic-viscoplastic during the time interval $0 \leq t \leq t_1$. The specific change is represented by the function $G(t)$ (see Section 3) which is chosen here in the form

$$G(t) = \begin{cases} \sin(\pi t/2t_1) & 0 \leq t \leq t_1 \\ 1 & t > t_1 \end{cases} \quad (34)$$

The value of the t_1 was chosen to be equal to the time required for the crack tip to travel the length of the plastic zone ahead of the tip of a steadily moving crack tip in an elastic perfectly plastic material under small scale yielding conditions. The extension of the elastic-plastic boundary ahead of the crack tip is given by [10]: $(1/\pi)(K_3/\tau_0)^2$ where τ_0 is the yield stress in shear and K_3 is the stress intensity of the elastic field. For steady Mode III crack propagation in an elastic strip K_3 is given by [11]

$$K_3 = \mu W_0 [2(1 - v_0^2/c_T^2)^{1/2}/h]^{1/2} \quad (35)$$

Consequently, the duration time t_1 in (34) is approximated by

$$t_1 = (K_3/\tau_0)^2/[\pi v_0] \quad (36)$$

Adopting an offset rule by which the yield stress is determined at a permanent strain of 0.2 percent, we obtain for our material that the yield stress in shear is given approximately by $\tau_0/\mu = 0.008$. From (35)–(36) we obtain the following expression for t_1

$$c_T t_1/h = \frac{2}{\pi}(c_T/v_0)(1 - v_0^2/c_T^2)^{1/2}[(W_0/h)/(\tau_0/\mu)]^2 \quad (37)$$

It is assumed that as the material changes its properties during the time interval $[0, t_1]$, the velocity of the crack decreases according to

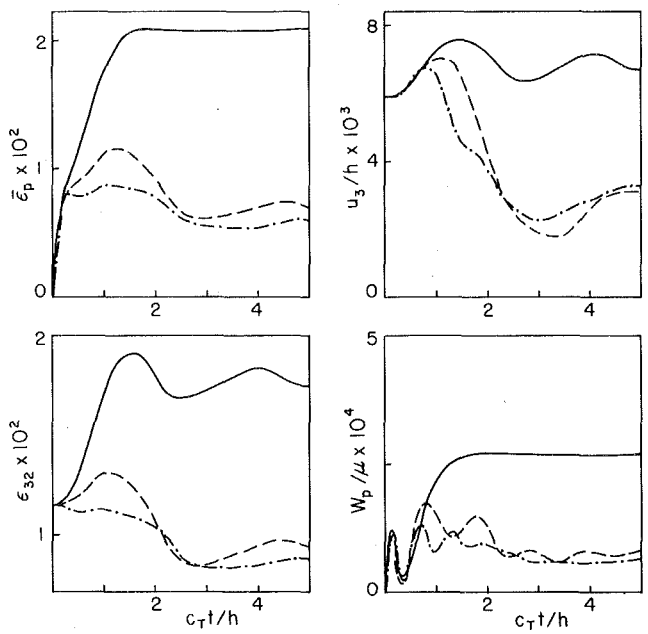

Fig. 3 Comparisons of crack-face displacement u_3 at $(-h/2, 0)$, and the effective plastic strain $\bar{\epsilon}_p$, the total strain ϵ_{32}, and the plastic work W_p, at $(\Delta x_1, 0)$ for $v_0/c_T = 0.5$ and three values of v_f/c_T: $v_f = 0$ (——), $v_f/c_T = 0.3$ (- - -), and $v_f/c_T = 0.5$ (-·-)

(33). In Fig. 3 the displacement on the crack face at distance $x_1 = -h/2$ behind the tip is shown together with the total strain ϵ_{32}, the plastic work W_p and the effective plastic strain $\bar{\epsilon}_p$ at the closest point $(\Delta x_1, 0)$ ahead of the crack tip. The rate of the effective plastic strain is defined by

$$\dot{\bar{\epsilon}}_p = [2\dot{\epsilon}_{ij}^{(p)}\dot{\epsilon}_{ij}^{(p)}/3]^{1/2} \tag{38}$$

With respect to the moving coordinates $\dot{\bar{\epsilon}}_p$ reduces to

$$\frac{\partial}{\partial t}\bar{\epsilon}_p = v(\bar{\epsilon}_p)_{,1} + 2\Lambda(J_2/3)^{1/2} \tag{39}$$

The plots in Fig. 3 are shown for an initial crack-tip speed $v_0/c_T = 0.5$, and for terminal velocities $v_f/c_T = 0$, 0.3 and 0.5, respectively. For these cases the value of t_1 in (33)–(34) has been computed from (37) as $c_T t_1/h = 1.1$.

It is of interest to mention that several functions $G(t)$ in addition to the one given by (34) have been used to represent the transition from the elastic to the viscoplastic state. The rise time t_1 in all these functions was kept constant and given by (37). It turns out that the resulting field after the transition has been completed was almost independent of the specific form of $G(t)$. This indicated that the specific representation of $G(t)$ is not important as long as the rise time is kept constant.

Several fracture criteria for continuing crack growth in ductile materials appear in the literature. This subject has recently been reviewed by Shih, et al. [12]. The crack opening displacement at a given distance behind the tip can be used as a growth criterion. Alternatively a strain-based fracture criterion can be used in Mode III crack propagation according to which crack growth can initiate or continue if ahead of the crack tip in the plastic zone the total strain ϵ_{32} achieves a critical value. Rice, et al. [13], proposed a criterion for continuing crack growth which requires that the amount of effective plastic strain, $\bar{\epsilon}_p$, accumulated near the tip be equal to or greater than a critical value. Here we investigate the stability of a crack using the foregoing criteria applied to the field variables shown in Fig. 3.

Let us first consider the time-dependent effective plastic strain. If the critical value of the effective plastic strain for continued crack propagation is very high (more that 2 percent say) then we readily observe that stopping of the crack should occur in all cases shown in Fig. 3 since this value is never achieved. Suppose next that the critical value would be achieved for crack arrest. Clearly, the crack will then not stop, but the crack-tip speed will presumably be reduced. The transient phenomena that take place during the change of crack-tip speed require extensive computations. It is, however, possible to obtain the final value of the crack-tip speed after the crack tip has entered the viscoplastic material, since at that velocity the steady-state plastic strain should just equal the critical value. Thus, referring to Fig. 3, if $(\bar{\epsilon}_p)_{cr}$ is 0.75 percent, the terminal velocity should be $v/c_T = 0.3$.

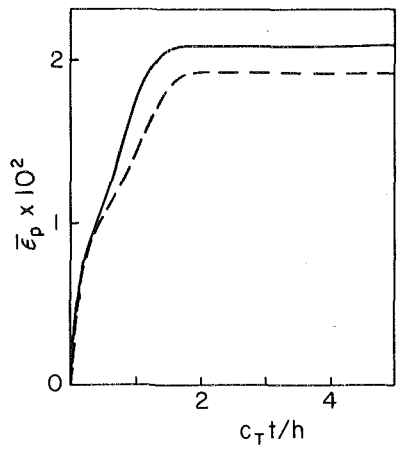

Fig. 4 Effective plastic strains ahead of the crack tip at $(\Delta x_1, 0)$ for crack arrest; $v_0/c_T = 0.5$ (——) and $v_0/c_T = 0.4$ (- - -)

Next, let us examine the criteria based on the crack-opening displacement and on the total strain measured ahead of the crack tip, respectively. These quantities are presented in Fig. 3, and they indicate that similar conclusions can be drawn about the stability of the crack as for the critical plastic strain criterion.

It is interesting to note that the dissipative plastic work W_p measured ahead of the crack tip can also be used as an equivalent criterion for crack growth as can be noted from Fig. 3.

For crack arrest the effective plastic strains, $\bar{\epsilon}_p$, accumulated at the closest point $(\Delta x_1, 0)$ ahead of the tip are compared in Fig. 4 for two initial velocities: $v_0/c_T = 0.4$ and 0.5. In each case t_1 in (33)–(34) has been computed from (36), giving $c_T t_1/h = 1.45$ and 1.1, respectively. The graphs show that crack arrest is more likely to occur for a crack propagating at a lower initial velocity, since the accumulated plastic strain will be lower. Similar conclusions can be drawn on the basis of the crack opening displacement, the total strain and the plastic work.

A check on the validity of our numerical method can be performed by comparing the long-time solution produced by the scheme (24), (30)–(31) (which is designed for a time-dependent problem) after the material changed its properties, with the steady-state solution of a propagating crack in the elastic viscoplastic strip which has been discussed in reference [1]. It turns out that for $v_0 = v_f = 0.8\, c_T$ the stress, strain, and displacement at time $c_T t/h = 5$ coincide with the steady-state solution at the same locations. It should be mentioned that as the initial steady velocity decreases the steady-state solution is recovered after longer times since as can be noticed from equation (37) the time required to establish the plastic zone ahead of the crack increases as v_0 decreases.

Acknowledgment

The work reported here was carried out in the course of research sponsored by the Office of Naval Research under Contract N00014-76-C0063.

References

1 Aboudi, J., and Achenbach, J. D., "Rapid Mode III Crack Propagation in a Strip of Viscoplastic Work-Hardening Material," *International Journal of Solids and Structures*, in press.

2 Aboudi, J., and Achenbach, J. D., "Numerical Analysis of Fast Mode

I Fracture of a Strip of Viscoplastic Work-Hardening Material," submitted for publication.

3 Bodner, S. R., and Partom, Y. "Constitutive Equations for Elastic-Viscoplastic Strain-Hardening Material," ASME JOURNAL OF APPLIED MECHANICS, Vol. 42, 1975, pp. 385–389.

4 Sperling, A., and Partom, Y., "Numerical Analysis of Large Elastic-Plastic Deformation of Beams Due to Dynamic Loading," *International Journal of Solids and Structures*, Vol. 13, 1977, pp. 865–876.

5 Field, F. A., and Baker, B. R., "Crack Propagation Under Shear Displacements," ASME JOURNAL OF APPLIED MECHANICS, Vol. 29, 1962, pp. 436–437.

6 Richtmyer, R. D., and Morton, K. W., *Difference Methods for Initial-Value Problems*, 2nd ed., Interscience, 1967.

7 Aboudi, J., "The Dynamic Stresses Induced by Moving Interfacial Cracks," *Compt. Meth. Appl. Mech. Eng.*, Vol. 10, 1977, pp. 303–310.

8 Nilsson, F., "A Suddenly Stopping Crack in an Infinite Strip Under Tearing Action," ASTM-STP 627, 1977, pp. 77–91.

9 Nilsson, F., "Steady Mode III Crack Propagation Followed by Nonsteady Growth," *International Journal of Solids and Structures*, Vol. 13, 1977, pp. 543–549.

10 Rice, J. R., "Mathematical Analysis in the Mechanics of Fracture," in *Fracture: An Advanced Treatise*, ed., Liebowitz, H., Vol. 2, Academic Press, 1968, pp. 191–311.

11 Sih, G. C., and Chen, E. P., "Moving Cracks in a Finite Strip Under Tearing Action," *The Journal of The Franklin Institute*, Vol. 290, 1970, pp. 25–32.

12 Shih, C. F., de Lorenzi, H. G., and Andrews, W. R., "Studies on Crack Initiation and Stable Growth," ASTM-STP 668, 1979, pp. 65–75.

13 Rice, J. R., Drugan, W. J., and Sham, T. L., "Elastic Plastic Analysis of Growing Cracks," Division of Engineering, Brown University, Technical Report 65, 1979.

B. L. Karihaloo[1]

L. M. Keer

Professor of Civil and Mechanical Engineering. Mem. ASME

S. Nemat-Nasser

Professor of Civil Engineering and Applied Mathematics. Mem. ASME

A. Oranratnachai

Postdoctoral Research Fellow.

Department of Civil Engineering, Northwestern University, Evanston, Ill. 60201

Approximate Description of Crack Kinking and Curving

An approximate description is given of the slightly out-of-plane growth of a straight crack under mixed-mode loading and in the presence of an in-plane stress. By using a perturbation technique, conditions are derived for the deviation of the crack from straightness. The allowance for the possible curvature of the quasi-statically growing crack, and the effect of the finite length of the main crack are included in the analysis, which retains second-order terms. In particular, it is shown that the curvature of the crack path depends on the in-plane stress and the derivatives of the stress-intensity factors with respect to the length of the main crack. The influence of the in-plane stress on the stability of the crack growth is also studied and the conclusions are the same as those reported by Cotterell and Rice.

Introduction

In a recent paper Cotterell and Rice [1] used a perturbation technique, originally proposed by Banichuk [4], and Goldstein and Salganik [3], to derive, among other things, the conditions necessary for slightly out-of-plane quasi-static growth of a semi-infinite straight crack under mixed-mode loading conditions. They also studied the stability of the crack growth under the influence of a nonsingular stress acting parallel to the crack plane. It was shown that the deviation of the quasi-statically growing crack that always occurred at a finite angle from the initial straight path resulted from the presence of a Mode II component in the externally applied loading.

As regards the dependence of the stability of the crack growth on the nonsingular stress term, T, representing the tensile stress acting parallel to the crack and appearing in the Irwin-Williams [5] crack tip stress field, it was shown that the straight path is stable for $T < 0$ and unstable for $T > 0$.

In [1] a strict first-order approximation was used in the analysis and the considered crack was semi-infinite. In the present analysis we include second-order terms in the governing integral equations and related field quantities. In addition, the effect of the crack length upon its extension is also investigated. We show in particular that crack curving can occur without kinking when $T = 0$ and when the Mode II stress-intensity factor is zero but its derivative with respect to the initial crack length is not.

Mathematical Analysis

We consider an infinite plane containing a crack such that its tips at $x = \pm a$ are located along the x-axis, as shown in Fig. 1, where the straight and the curved portions represent, respectively, the pre-existing crack and its extension. The deviation of the crack from the x-axis is described by the function $\lambda(x)$, which is assumed to be small relative to the extended length. The crack is opened by surface normal and shear tractions, T_n, T_s, which are necessary to remove the stresses due to external load (shown in Fig. 1).

Following [1], the stress field is expressed in terms of the analytic functions $\phi(z)$ and $\psi(z)$ [2] as

$$\begin{aligned} \sigma_{xx} + \sigma_{yy} &= 2[\phi(z) + \overline{\phi(z)}] \\ \sigma_{yy} - \sigma_{xx} - 2i\sigma_{xy} &= 2[z\overline{\phi'(z)} + \overline{\psi(z)}] \end{aligned} \tag{1}$$

where $z = x + iy$, $i = \sqrt{-1}$. Then the boundary condition on the crack is in the form

$$\phi(z) + \overline{\phi(z)} + e^{-2i\theta}[z\overline{\phi'(z)} + \overline{\psi(z)}] = T_n - iT_s \tag{2}$$

where θ is the angle made by the crack with the x-axis ($\theta = \lambda' \ll 1$). Introducing the analytic function,

$$\Omega(z) = \overline{\phi}(z) + z\overline{\phi}'(z) + \overline{\psi}(z), \tag{3}$$

equation (2) is written as

$$\phi(z) + \overline{\phi(z)} + e^{-2i\theta}[(z - \bar{z})\overline{\phi'(z)} + \Omega(\bar{z}) - \overline{\phi(z)}] = T_n - iT_s. \tag{4}$$

Following the method described in [1] we assume that there are two functions $F(z)$ and $W(z)$ which correspond to $\phi(z)$ and $\Omega(z)$, and whose boundary values are $F^{\pm}(t)$ and $W^{\pm}(t)$ on the upper and lower surfaces of a straight cut located along the x-axis and in between the crack tips; $\phi(z)$ and $\Omega(z)$ have their cut along the actual crack. The functions $F(z)$ and $W(z)$ can be written by the following perturbation scheme:

---

[1] On leave from the Department of Civil Engineering and Surveying, The University of Newcastle, N.S.W., 2308, Australia.

Contributed by the Applied Mechanics Division of THE AMERICAN SOCIETY OF MECHANICAL ENGINEERS, and presented at the 1981 Joint ASME/ASCE Applied Mechanics, Fluids Engineering, and Bioengineering Conference, University of Colorado, Boulder, Colo., June 22–27, 1981.

Discussion on this paper should be addressed to the Editorial Department, ASME, United Engineering Center, 345 East 47th Street, New York, N. Y. 10017, and will be accepted until December 1, 1981. Readers who need more time to prepare a discussion should request an extension from the Editorial Department. Manuscript received by ASME Applied Mechanics Division, June, 1979; final revision, September, 1980. Paper No. 81-APM-22.

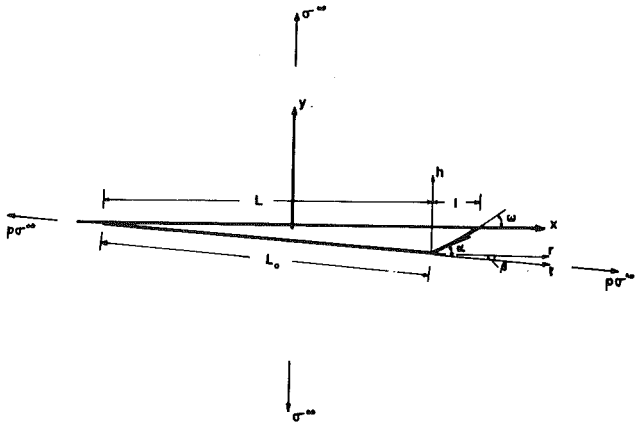

Fig. 1 Geometry of the straight crack and its kinked-curved extension, and the external loading

$$F(z) = F_0(z) + F_1(z) + F_2(z) + O(\lambda^3)$$
$$W(z) = W_0(z) + W_1(z) + W_2(z) + O(\lambda^3) \tag{5}$$

where $F_0(z)$ and $W_0(z)$ are $O(\lambda^0)$, $F_1(z)$ and $W_1(z)$ are $O(\lambda)$, and $F_2(z)$ and $W_2(z)$ are $O(\lambda^2)$. On the boundary of the crack at $z = t + i\lambda(t)$ the function $\phi(z)$ is given by

$$\phi^{\pm}(z) = F_0^{\pm}(t) + i\lambda\left[\frac{dF_0}{dz}\right]_t^{\pm} + F_1^{\pm}(t) + \tfrac{1}{2}(i\lambda)^2\left[\frac{d^2F_0}{dz^2}\right]_t^{\pm} + i\lambda\left[\frac{dF_1}{dz}\right]_t^{\pm} + F_2^{\pm}(t) + O(\lambda^3). \tag{6}$$

Since

$$\left[\frac{dF_0}{dz}\right]_t^{\pm} = \frac{dF_0^{\pm}(t)}{dt}, \qquad \left[\frac{dF_1}{dz}\right]_t^{\pm} = \frac{dF_1^{\pm}(t)}{dt}, \text{ etc.,}$$

equation (6) can be written as

$$\phi^{\pm}(z) = F_0^{\pm}(t) + i\lambda F_0^{\pm\prime}(t) + F_1^{\pm}(t) - \tfrac{1}{2}\lambda^2 F_0^{\pm\prime\prime}(t) + i\lambda F_1^{\pm\prime}(t) + F_2^{\pm}(t), \tag{7}$$

where the prime denotes the differentiation with respect to t. We can also express $\Omega^{\pm}(z)$ in terms of $W_0^{\pm}(t)$, $W_1^{\pm}(t)$, etc., in the same form as in equation (7). Using this expression and noting that, for small λ,

$$e^{-2i\theta} \approx 1 - 2i\lambda' - 2\lambda'^2 + O(\lambda^3), \tag{8}$$

equation (4) becomes

$$\begin{aligned} T_n - iT_s = {} & F_0^{\pm}(t) + W_0^{\mp}(t) + F_1^{\pm}(t) + W_1^{\mp}(t) \\ & + i\lambda[F_0^{\pm}(t) + W_0^{\mp}(t)]' + 2i\{\lambda[\overline{F}_0^{\mp}(t) - W_0^{\mp}(t)]\}' \\ & + F_2^{\pm}(t) + W_2^{\mp}(t) + 2\lambda'\{\lambda[\overline{F}_0^{\mp}(t) - W_0^{\mp}(t)]\}' \\ & - \tfrac{1}{2}\lambda^2[F_0^{\pm}(t) + W_0^{\mp}(t)]'' - 2[\lambda^2\overline{F}_0^{\mp\prime}(t)]' \\ & + i\lambda[F_1^{\pm}(t) + W_1^{\mp}(t)]' + 2i\{\lambda[\overline{F}_1^{\pm}(t) - W_1^{\mp}(t)]\}' + 2\lambda\lambda'\overline{F}_0^{\mp\prime} \end{aligned} \tag{9}$$

where only terms of the first and second order have been retained. It has been found in [1] that the angle of the kinked extension is proportional to the ratio of the Mode II to the Mode I stress-intensity factor (i.e., K_{II}/K_I); hence, for the case of the slightly deviated extension considered here the magnitude of T_s will be limited to within the first order of smallness. This limitation greatly simplifies the analysis to follow. Thus ordering the terms in equation (9) leads to

$$\lambda^0: \quad F_0^{\pm}(t) + W_0^{\mp}(t) = T_n \tag{10}$$

$$\lambda^1: \quad F_1^{\pm}(t) + W_1^{\mp}(t) = -iT_s - i\lambda[F_0^{\pm}(t) + W_0^{\mp}(t)]' - 2i\{\lambda[\overline{F}_0^{\mp}(t) - W_0^{\mp}(t)]\}' \tag{11}$$

$$\lambda^2: \quad F_2^{\pm}(t) + W_2^{\mp}(t) = -i\lambda[F_1^{\pm}(t) + W_1^{\mp}(t)]' - 2i\{\lambda[\overline{F}_1^{\mp}(t) - W_1^{\mp}(t)]\}' + \tfrac{1}{2}\lambda^2[F_0^{\pm}(t) + W_0^{\mp}(t)]'' + 2[\lambda^2\overline{F}_0^{\mp\prime}(t)]' - 2\lambda'\{\lambda[\overline{F}_0^{\mp}(t) - W_0^{\mp}(t)]\}' - 2\lambda\lambda'\overline{F}_0^{\mp\prime}. \tag{12}$$

The solution to equation (10) is

$$F_0(z) = W_0(z) = \frac{1}{2\pi(z^2 - a^2)^{1/2}}\int_{-a}^{a} T_n\frac{(a^2 - t^2)^{1/2}}{t - z}\,dt. \tag{13}$$

From equation (11) the boundary values of $[F_1(z) + W_1(z)]$ and $[F_1(z) - W_1(z)]$ are given by

$$[F_1(t) + W_1(t)]^+ + [F_1(t) + W_1(t)]^- = -2i(T_s + \lambda T_n') \tag{14}$$

and

$$[F_1(t) - W_1(t)]^+ - [F_1(t) - W_1(t)]^- = 0. \tag{15}$$

Therefore, $F_1(z) = W_1(z)$, which are given by

$$F_1(z) = W_1(z) = \frac{1}{2\pi(z^2 - a^2)^{1/2}}\int_{-a}^{a} -i(T_s + \lambda T_n')\frac{(a^2 - t^2)^{1/2}}{t - z}\,dt. \tag{16}$$

Using equations (13) and (16), equation (12) yields the boundary value of $[F_2(z) + W_2(z)]$

$$[F_2(t) + W_2(t)]^+ + [F_2(t) + W_2(t)]^- = 2\lambda T_s' + 4\lambda' T_s + 4(\lambda^2 T_n')' + \lambda^2 T_n'' \tag{17}$$

whose solution is

$$F_2(z) + W_2(z) = \frac{1}{2\pi(z^2 - a^2)^{1/2}}\int_{-a}^{a}[2\lambda T_s' + 4\lambda' T_s + 4(\lambda^2 T_n')' + \lambda^2 T_n'']\frac{(a^2 - t^2)^{1/2}}{t - z}\,dt. \tag{18}$$

At a point $z = a + r + i\omega r$, where $\omega = \lambda'(a)$ is the slope of the crack tip at $x = a$, the functions $F(z)$ and $W(z)$ are single-valued and $\sigma_{\omega\omega}$ and $\sigma_{r\omega}$ can be obtained from equation (9) as follows:

$$\begin{aligned} \sigma_{\omega\omega} - i\sigma_{r\omega} = {} & 2F_0(a + r) + 2F_1(a + r) + 2i\omega[r\overline{F}_0(a + r)]' \\ & - 2i\omega F_0(a + r) - 3\omega^2 r^2 F_0''(a + r) - 2\omega^2 r\overline{F}_0'(a + r) + 2i\omega r F_1'(a + r) \\ & + 2i\omega\{r[\overline{F}_1(a + r) - F_1(a + r)]\}' + F_2(a + r) + W_2(a + r) + O(\omega^3). \end{aligned} \tag{19}$$

By substituting equations (13), (16), and (18) into equation (19), the stress-intensity factors, K_I and K_{II}, are obtained as

$$\begin{aligned} K_I - iK_{II} &= \lim_{r\to 0}(1 + \omega^2)^{1/4}(2\pi r)^{1/2}(\sigma_{\omega\omega} - i\sigma_{r\omega}) \\ &= (1 + \omega^2)^{1/4}(\pi a)^{-1/2}\int_{-a}^{a}(q_I - iq_{II})\left(\frac{a + t}{a - t}\right)^{1/2}dt, \end{aligned} \tag{20}$$

where

$$q_I = (\tfrac{5}{8}\omega^2 - 1)T_n + \tfrac{3}{2}\omega\lambda T_n' - 2(\lambda^2 T_n')' + \left(\frac{3\omega}{2} - 2\lambda'\right)T_s - \lambda T_s' - \tfrac{1}{2}\lambda^2 T_n'' \tag{21}$$

$$q_{II} = -T_s - \frac{\omega}{2}T_n - \lambda T_n'. \tag{22}$$

Let L and l be the projections on the x-axis of the pre-existing crack (length L_0) and its extension, respectively. Let $t = a - l + r$ and assume the equation to the curved crack path in the form (see Fig. 1)

$$\lambda(r) = \begin{cases} h(r) - h(l), & 0 < r \le l \\ -\beta(L + r), & -L \le r \le 0 \end{cases} \tag{23}$$

where

$$h(r) = (\alpha - \beta)r + \eta r^{3/2} + \chi r^2, \tag{24}$$

$$\beta = h(l)/L, \tag{25}$$

and α, η and χ are constants to be determined from the ordering scheme.

After integration by parts and use of the Taylor expansion for $(1 + \omega^2)^{1/4}$, equation (20) can be written as

$$K_I = \frac{-1}{(\pi a)^{1/2}} \int_{-L}^{l} \left[\left(\lambda' - \frac{3\omega}{2}\right) T_s + (1 - \tfrac{3}{8}\omega^2 + \tfrac{3}{2}\omega\lambda') T_n\right] \times \left(\frac{L+t}{l-t}\right)^{1/2} dt - \frac{1}{(\pi a)^{1/2}} \int_{-L}^{l} (\tfrac{3}{2}\omega T_n - T_s) \frac{a\lambda}{(L+r)^{1/2}(l-r)^{3/2}} dr - \frac{1}{(\pi a)^{1/2}} \int_{-L}^{l} \frac{a}{2} T_n \left[\frac{5\lambda^2}{(L+r)^{1/2}(l-r)^{3/2}}\right]' dr - \frac{1}{(\pi a)^{1/2}} \int_{-L}^{l} T_n \left[\lambda\lambda' \left(\frac{a+t}{a-t}\right)^{1/2}\right]' dt \quad (26)$$

$$K_{II} = \frac{-1}{(\pi a)^{1/2}} \int_{-L}^{l} \left[T_s + \left(\frac{\omega}{2} - \lambda'\right) T_n\right] \left(\frac{L+r}{l-r}\right)^{1/2} dr + \frac{1}{(\pi a)^{1/2}} \int_{-L}^{l} \frac{a\lambda T_n\, dr}{(L+r)^{1/2}(l-r)^{3/2}} \quad (27)$$

where now and in the sequel prime is used to denote differentiation with respect to r.

To simplify equations (26) and (27), we resolve the components of the tractions in the directions of x and y-axes, whereupon

$$T_n = (1 - \lambda'^2)\sigma_{yy} + \lambda'^2\sigma_{xx} - 2\lambda'\sigma_{xy} + O(\lambda^3)$$
$$T_s = \lambda'(\sigma_{yy} - \sigma_{xx}) + (1 - 2\lambda'^2)\sigma_{xy} + O(\lambda^3). \quad (28)$$

For the case of crack extension the stress components on the boundary of the pre-existing crack are zero, and those on the extended portion can be derived from the stress field that exists along the prolongation of the pre-existing crack tip [4]. In the r, h-coordinates the stress components on the curved portion are expressed in the form

$$\sigma_{xx}(r,h) = \sigma_{xx}(r,0) + h\frac{\partial\sigma_{xx}(r,0)}{\partial y} + \frac{h^2}{2}\frac{\partial^2\sigma_{xx}(r,0)}{\partial y^2}$$
$$\sigma_{yy}(r,h) = \sigma_{yy}(r,0) + h\frac{\partial\sigma_{yy}(r,0)}{\partial y} + \frac{h^2}{2}\frac{\partial^2\sigma_{yy}(r,0)}{\partial y^2}$$
$$\sigma_{xy}(r,h) = \sigma_{xy}(r,0) + h\frac{\partial\sigma_{xy}(r,0)}{\partial y} + \frac{h^2}{2}\frac{\partial^2\sigma_{xy}(r,0)}{\partial y^2}. \quad (29)$$

Using the asymptotic expansion for the stress field together with its derivatives with respect to y near the tip of the main crack, equation (29) becomes

$$\sigma_{xx}(r,h) = \frac{-k_I}{(2\pi r)^{1/2}}\left(1 - \frac{9}{8}\frac{h^2}{r^2}\right) + \frac{3}{2}\frac{k_{II}}{\sqrt{2\pi r}}\frac{h}{r} - T - b_I\left(\frac{r}{2\pi}\right)^{1/2}\left(1 + \frac{3}{8}\frac{h^2}{r^2}\right) - \frac{3}{2}b_{II}\left(\frac{r}{2\pi}\right)^{1/2}\frac{h}{r} + O(\lambda^3)$$
$$\sigma_{yy}(r,h) = \frac{-k_I}{(2\pi r)^{1/2}}\left(1 + \frac{3}{8}\frac{h^2}{r^2}\right) - \frac{1}{2}\frac{k_{II}}{(2\pi r)^{1/2}}\frac{h}{r} - b_I\left(\frac{r}{2\pi}\right)^{1/2}\left(1 - \frac{h^2}{8r^2}\right) + b_{II}\left(\frac{r}{2\pi}\right)^{1/2}\frac{h}{2r} + O(\lambda^3)$$
$$\sigma_{xy}(r,h) = \frac{-k_I}{(2\pi r)^{1/2}}\left(\frac{h}{2r} + \frac{\beta}{2}\right) - \frac{k_{II}}{(2\pi r)^{1/2}} + T\beta + b_I\left(\frac{r}{2\pi}\right)^{1/2}\left(\frac{h}{2r} + \frac{\beta}{2}\right) - b_{II}\left(\frac{r}{2\pi}\right)^{1/2} + O(\lambda^3) \quad (30)$$

where k_I, k_{II} are the Mode I and Mode II stress-intensity factors and b_I, b_{II} are coefficients of terms proportional to square root in the Irwin-Williams expansion [5] (see the Appendix). For the stress state under consideration as shown in Fig. 1, $T = (p-1)\sigma^\infty$. The details required for the calculation of equation (30) are given in the Appendix.

Substituting $2a = L + l$ into equations (25) and (26), expanding $(L + r)^{1/2}$ and $(L + l)^{1/2}$ in terms of r/L and l/L, and assuming that l/L is a small quantity of the same order as λ/l, we obtain

$$K_I = -\left(\frac{2}{\pi}\right)^{1/2}\int_0^l T_n\left[1 - \frac{3}{8}\omega^2 + \frac{3}{2}\omega\lambda' + \frac{3\omega\lambda}{4(l-r)} + \lambda'^2 + \lambda\lambda'' + \frac{3\lambda\lambda'}{l-r} + \frac{15\lambda^2}{8(l-r)^2}\right]\frac{dr}{(l-r)^{1/2}} + \left(\frac{2}{\pi}\right)^{1/2} \quad (31)$$

$$\times \int_0^l \frac{T_n}{2L}(l-r)^{1/2}dr - \left(\frac{2}{\pi}\right)^{1/2}\int_0^l \frac{T_n}{8L^2}(3l^2 - 2lr - r^2)\frac{dr}{(l-r)^{1/2}} - \left(\frac{2}{\pi}\right)^{1/2}\int_0^l T_s\left[\lambda' - \frac{3}{2}\omega - \frac{\lambda}{2(l-r)}\right]\frac{dr}{(l-r)^{1/2}} \quad (31)\ (Cont.)$$

$$K_{II} = -\left(\frac{2}{\pi}\right)^{1/2}\int_0^l T_n\left[\frac{\omega}{2} - \lambda' - \frac{\lambda}{2(l-r)}\right]\frac{dr}{(l-r)^{1/2}} - \left(\frac{2}{\pi}\right)^{1/2}\int_0^l \frac{T_n}{2L}\left[\lambda' - \frac{\omega}{2} - \frac{\lambda}{2(l-r)}\right](l-r)^{1/2}dr - \left(\frac{2}{\pi}\right)^{1/2}\int_0^l T_s\left[1 - \frac{l-r}{2L}\right]\frac{dr}{(l-r)^{1/2}} \quad (32)$$

where terms only up to second order are retained.

Substituting equation (30) into equation (28), and the resulting expression into equations (31) and (32), equations (31) and (32) with the definition of λ in equation (23) become

$$K_I = \frac{1}{\pi}\int_0^l \left\{\frac{k_I}{r^{1/2}}\left(1 + \frac{3}{8}\frac{h^2}{r^2} - \frac{hh'}{r}\right) + \frac{k_{II}}{r^{1/2}}\left(\frac{h}{2r} - 2h'\right) + (2\pi)^{1/2}Th'^2 + b_I r^{1/2}\left(1 - \frac{h^2}{8r^2} + \frac{hh'}{r}\right) - b_{II}r^{1/2} \times \left(\frac{5\beta}{2} + \frac{h}{2r} + 2h'\right)\right\}\frac{dr}{(l-r)^{1/2}} + \frac{1}{\pi}\int_0^l \left(\frac{k_I}{r^{1/2}} + b_I r^{1/2}\right) \times \left\{\frac{\omega^2}{4} + \frac{\omega\eta}{4}(-3l^{1/2} + 33r^{1/2}) - \omega\chi(l-r) - \frac{1}{8}\chi^2(l-r)^2 + \frac{\eta^2}{32}\left[15l - 156(lr)^{1/2} + \frac{12r(7l^{1/2} - 11r^{1/2})}{l^{1/2} + r^{1/2}} + \frac{60r^2}{(l^{1/2} + r^{1/2})^2} + \frac{9}{4}t\right] + \frac{1}{8}\eta\chi(l-r)\left(3l^{1/2} - 12r^{1/2} + \frac{18r}{l^{1/2} + r^{1/2}}\right)\right\}\frac{dr}{(l-r)^{1/2}} + \frac{1}{\pi}\int_0^l \left\{\frac{k_I}{r^{1/2}}\left(\frac{h}{2r} + \frac{\beta}{2}\right) + \frac{k_{II}}{r^{1/2}} - (2\pi)^{1/2}T(h' + \beta) - b_I r^{1/2}\left(\frac{h}{2r} + \frac{\beta}{2}\right) + b_{II}r^{1/2}\right\}\left\{\eta\left[\frac{-7l - (lr)^{1/2} + 8r}{4(l^{1/2} + r^{1/2})}\right] - \frac{5\chi}{2}(l-r)\right\}\frac{dr}{(l-r)^{1/2}} - \frac{1}{2\pi L}\int_0^l \left[\frac{k_I}{r^{1/2}} + b_I r^{1/2}\right] \times (l-r)^{1/2}dr + \frac{1}{8\pi L^2}\int_0^l \frac{k_I}{r^{1/2}}(3l^2 - 2lr - r^2)\frac{dr}{(l-r)^{1/2}} \quad (33)$$

$$K_{II} = \frac{1}{\pi}\int_0^l \left\{\frac{k_I}{r^{1/2}} + \frac{k_{II}}{r^{1/2}}\left(\frac{h}{2r} - 2h'\right) + b_I r^{1/2} - b_{II}r^{1/2} \times \left(\frac{5\beta}{2} + \frac{h}{2r} + 2h'\right)\right\}\left[\frac{\eta}{4}\left(\frac{5l - (lr)^{1/2} - 4r}{l^{1/2} + r^{1/2}}\right) + \frac{3\chi}{2}(l-r)\right] \times \frac{dr}{(l-r)^{1/2}} + \frac{1}{\pi}\int_0^l \left\{\frac{k_I}{r^{1/2}}\left(\frac{h}{2r} + \frac{\beta}{2}\right) + \frac{k_{II}}{r^{1/2}} - (2\pi)^{1/2}T(h' + \beta) - b_I r^{1/2}\left(\frac{h}{2r} - \frac{\beta}{2}\right) + b_{II}r^{1/2}\right\}\frac{dr}{(l-r)^{1/2}} + \frac{1}{2\pi L}\int_0^l \left(\frac{k_I}{r^{1/2}} + b_I r^{1/2}\right)\left[\omega + \frac{\eta}{4}\left(\frac{-7l - (lr)^{1/2} + 8r}{l^{1/2} + r^{1/2}}\right) - \frac{5}{2}\chi(l-r)\right](l-r)^{1/2}dr - \frac{1}{2\pi L}\int_0^l \left\{\frac{k_I}{r^{1/2}}\left(\frac{h}{2r} + \frac{\beta}{2}\right) + \frac{k_{II}}{r^{1/2}} - (2\pi)^{1/2}T(h' + \beta) - b_I r^{1/2}\left(\frac{h}{2r} + \frac{\beta}{2}\right) + b_{II}r^{1/2}\right\}(l-r)dr. \quad (34)$$

Using equations (24) and (25), and noting that $\omega = h'(l)$, it follows that

$$K_I \approx k_I - \frac{3}{8}\alpha^2 k_I - \frac{3}{2}\alpha k_{II} + l^{1/2}\left(-\frac{9}{8}\alpha\eta k_I - \frac{9}{4}\eta k_{II} + 2\left(\frac{2}{\pi}\right)^{1/2}\alpha^2 T + \frac{31}{2\pi}\alpha\eta k_I + \ldots\right) \quad (35)$$

$$+ l\left[-k_I\left(\frac{1}{4L}+\frac{7}{4}\alpha\chi+\frac{15}{32}\eta^2\right)-3\chi k_{II}\right.$$
$$+\frac{11}{2}\left(\frac{2}{\pi}\right)^{1/2}\alpha\eta T+\frac{b_I}{2}-\frac{5}{4}\alpha b_{II}+\frac{86}{4\pi}\eta^2 k_I+\ldots\Big]$$
$$+ l^{3/2}\left[-\frac{5}{8}\eta\chi k_I+\left(\frac{2}{\pi}\right)^{1/2}T\left\{\eta^2\left(\frac{39}{16}-\frac{4}{\pi}\right)+7\alpha\chi\right\}\right.$$
$$\left.+\frac{21}{16}\alpha\eta b_I-\frac{13}{8}\eta b_{II}+\frac{653}{24\pi}\eta\chi+\ldots\right]+O(l^2) \quad (35)$$
(*Cont.*)

$$K_{II}\approx k_{II}+\frac{\alpha}{2}k_I+l^{1/2}\left[\frac{3}{4}\eta k_I-2\left(\frac{2}{\pi}\right)^{1/2}\alpha T+\ldots\right]+l\left[k_I\left(\frac{\alpha}{8L}+\chi\right)\right.$$
$$-\frac{k_{II}}{4L}-\frac{3\pi}{4}\left(\frac{2}{\pi}\right)^{1/2}\eta T-\frac{\alpha}{4}b_I+\frac{1}{2}b_{II}+\ldots\Big]+l^{3/2}\left[\frac{\eta}{16L}k_I\right.$$
$$\left.+\left(\frac{2}{\pi}\right)^{1/2}T\left(\frac{\alpha}{3L}-\frac{8\chi}{3}\right)-\frac{\eta}{8}b_I-\frac{8}{3\pi}\alpha b_I+\ldots\right]+O(l^2). \quad (36)$$

If α, η, and χ in equations (35) and (36) are set equal to zero the results become

$$K_I=k_I-\frac{k_I l}{4L}+\frac{b_I l}{2}+O(l^2), \quad (37)$$

$$K_{II}=k_{II}-\frac{k_{II}l}{4L}+\frac{b_{II}l}{2}+O(l^2). \quad (38)$$

We can identify the crack extension change (as $l\to 0$) of K_I and K_{II} as the following quantities:

$$-\frac{k_I}{4L}+\frac{b_I}{2}=\lim_{l\to 0}\frac{K_I-k_I}{l}\equiv\frac{\partial k_I}{\partial L_0}, \quad (39)$$

$$-\frac{k_{II}}{4L}+\frac{b_{II}}{2}=\lim_{l\to 0}\frac{K_{II}-k_{II}}{l}\equiv\frac{\partial k_{II}}{\partial L_0}, \quad (40)$$

the right-hand sides of which can be computed from the boundary conditions of the main crack. With these definitions equations (35) and (36) can be written in the form

$$K_I=k_I-\frac{3}{8}\alpha^2 k_I-\frac{3}{2}k_{II}\alpha$$
$$+l^{1/2}\left[-\frac{9}{8}\alpha\eta k_I-\frac{9}{4}\eta k_{II}+2\left(\frac{2}{\pi}\right)^{1/2}\alpha^2 T+\frac{31}{2\pi}\alpha\eta k_I+\ldots\right]$$
$$+l\left[\frac{\partial k_I}{\partial L_0}-k_I\left(\frac{7}{4}\alpha\chi+\frac{15}{32}\eta^2\right)-3\chi k_{II}+\frac{11}{2}\left(\frac{2}{\pi}\right)^{1/2}\alpha\eta T\right.$$
$$\left.-\frac{5}{2}\alpha\frac{\partial k_{II}}{\partial L_0}-\frac{5}{8}\frac{\alpha k_{II}}{L}+\frac{86}{4\pi}k_I\eta^2+\ldots\right]+O(l^{3/2}) \quad (41)$$

$$K_{II}=k_{II}+\frac{\alpha}{2}k_I+l^{1/2}\left[\frac{3}{4}\eta k_I-2\left(\frac{2}{\pi}\right)^{1/2}\alpha T+\ldots\right]$$
$$+l\left[\chi k_I+\frac{\partial k_{II}}{\partial L_0}-\frac{\alpha}{2}\frac{\partial k_I}{\partial L_0}-\frac{3}{2}\left(\frac{\pi}{2}\right)^{1/2}\eta T+\ldots\right]+O(l^{3/2}). \quad (42)$$

Following the discussion in [1] that the crack will extend in the direction of vanishing K_{II}, the ordered conditions for determining the constants α, η, and χ can be found as follows:

$$l^0: \quad k_{II}+\frac{\alpha}{2}k_I=0, \quad (43)$$

$$l^{1/2}: \quad \frac{3}{4}\eta k_I-2\left(\frac{2}{\pi}\right)^{1/2}\alpha T=0, \quad (44)$$

$$l^1: \quad \chi k_I+\frac{\partial k_{II}}{\partial L_0}-\frac{\alpha}{2}\frac{\partial k_I}{\partial L_0}-\frac{3}{2}\left(\frac{\pi}{2}\right)^{1/2}\eta T=0, \quad (45)$$

from which it follows that the terms in equation (24) are identified as[2]

$$\alpha\approx -2k_{II}/k_I \quad (46)$$

$$\eta\approx\frac{8}{3}\left(\frac{2}{\pi}\right)^{1/2}\alpha\frac{T}{k_I} \quad (47)$$

$$\chi\approx\alpha\left[4\frac{T^2}{k_I^2}+\frac{1}{2k_I}\frac{\partial k_I}{\partial L_0}+\frac{1}{2k_{II}}\frac{\partial k_{II}}{\partial L_0}\right]. \quad (48)$$

Discussion

By taking into account the length of the pre-existing crack it appears that the crack growth path depends not only on the in-plane uniform stress T, $T=(p-1)\sigma^\infty$, as concluded in [1] but also upon the derivatives with respect to the pre-existing crack length, L, of both Mode I and Mode II stress-intensity factors as indicated by equation (48). When $T=0$ we obtain from equations (46)–(48)

$$\alpha=-2k_{II}/k_I, \quad \eta=0, \quad \chi=(\alpha/2k_I)\partial k_I/\partial L_0+(\alpha/2k_{II})\partial k_{II}/\partial L_0,$$

and it follows from equation (24) that the crack path is a curved one whose curvature depends upon the derivatives of k_I, k_{II}, whereas in the absence of these additional terms, the extended portion would be predicted as a straight crack with angle α.

The initial angle of deviation from straightness α as given by equation (46) can be viewed as a parameter that characterizes the inhomogeneity in the system, which is unavoidable in an actual situation. Equation (24), together with equations (46)–(48), indicates that the slope of the crack extension increases with an increase in the value of $T>0$. If, however, $T<0$, the kinked crack has a tendency to revert to its original straight path; i.e., the crack growth is unstable when $T>0$, but stable otherwise. This conclusion is identical to that obtained in [1].

Consider now a loading condition for which $T=0$ and $k_{II}=0$, but $\partial k_{II}/\partial L_0\neq 0$. Then it follows from equations (46)–(48) and equation (24) that, in the r,h-coordinate system of Fig. 1, the crack path is given by

$$h=-\beta r-\left\{\frac{\partial k_{II}}{\partial L_0}\Big/k_I\right\}r^2+O(r^{5/2}),$$

so that without an initial kink the crack can have a smooth curved path in a nonhomogeneous stress field in which the Mode II stress-intensity factor, while zero at the tip of the pre-existing crack, gradually changes with distance away from the crack tip. Thermally induced crack curving of this kind has been observed experimentally by one of the authors (SN-N) in glass plates.

Acknowledgment

This work was supported by National Science Foundation Grant No. ENG77-22155 to Northwestern University. One of us (BLK) thanks the University of Newcastle, Australia, for granting him the study leave that enabled him to undertake the present project.

References

1 Cotterell, B., and Rice, J. R., "Slightly Curved or Kinked Cracks," *International Journal of Fracture Mechanics*, Vol. 16, 1980, pp. 155–169.

2 Muskhelishvilli, *Some Basic Problems on the Mathematical Theory of Elasticity*, Noordhoff, 1952.

3 Goldstein, R. V., and Salganik, R. L., "Brittle Fracture of Solids With Arbitrary Cracks," *International Journal of Fracture Mechanics*, Vol. 10, 1974, pp. 507–523.

4 Banichuk, N. V., "Determination of the Form of a Curvilinear Crack by Small Parameter Technique," *IZV. AN. SSR, M.T.T. (Mechanics of Solids)*, Vol. 7, 1970, pp. 130–137 (in Russian).

5 Williams, M. L., "On the Stress Distribution at the Base of a Stationary Crack," ASME JOURNAL OF APPLIED MECHANICS, Vol. 24, 1957, pp. 109–114.

6 Eftis, J., Subramonian, N., and Liebowitz, H., "Crack Border Stress and Displacement Equations Revised," *Journal of Engineering Fracture Mechanics*, Vol. 9, 1977, pp. 189–210.

APPENDIX

Stress Components and Their Derivatives Near a Crack Tip

Referring to Fig. 2 the stress components in the x, y-coordinates

[2] Equation (47) differs with the corresponding expression in Cotterell and Rice [1], their equation (45), by a factor of 2.

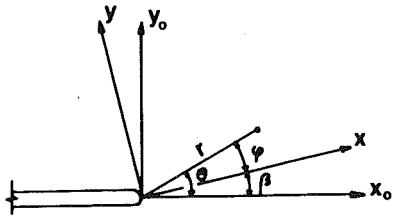

Fig. 2 Coordinate axes at the tip of a straight crack

can be expressed in terms of the polar stress components, σ_{rr}, $\sigma_{\theta\theta}$, and $\sigma_{r\theta}$ as follows:

$$\sigma_{xx}(x,y) = \sigma_{rr}\cos^2\phi + \sigma_{\theta\theta}\sin^2\phi - \sigma_{r\theta}\sin 2\phi,$$
$$\sigma_{yy}(x,y) = \sigma_{rr}\sin^2\phi + \sigma_{\theta\theta}\cos^2\phi + \sigma_{r\theta}\sin 2\phi,$$
$$\sigma_{xy}(x,y) = \tfrac{1}{2}(\sigma_{rr} - \sigma_{\theta\theta})\sin 2\phi + \sigma_{r\theta}\cos 2\phi. \tag{49}$$

Using the chain rule of differentiation and a transformation of coordinates, we obtain derivatives with respect to y in polar form as

$$\frac{\partial}{\partial y} = \sin\theta\frac{\partial}{\partial r} + \frac{\cos\theta}{r}\frac{\partial}{\partial\theta}$$
$$\frac{\partial^2}{\partial y^2} = \sin^2\theta\frac{\partial^2}{\partial r^2} + \frac{\sin 2\theta}{r}\left(\frac{\partial^2}{\partial r\partial\theta} - \frac{1}{r}\frac{\partial}{\partial\theta}\right) + \frac{\cos^2\theta}{r}\left(\frac{\partial}{\partial r} + \frac{1}{r^2}\frac{\partial^2}{\partial\theta^2}\right). \tag{50}$$

Hence, the stress components, σ_{xx}, σ_{yy}, σ_{xy}, along line Ox in Fig. 2 are

$$\sigma_{xx}(x,0) = \sigma_{rr}(x,\beta),$$
$$\sigma_{yy}(x,0) = \sigma_{\theta\theta}(x,\beta),$$
$$\sigma_{xy}(x,0) = \sigma_{r\theta}(x,\beta), \tag{51}$$

and their first and second derivatives with respect to y are in the form, using (49) and (50),

$$\frac{\partial\sigma_{xx}}{\partial y}(x,0) = \frac{1}{x}\left[\frac{\partial\sigma_{rr}}{\partial\theta} - 2\sigma_{r\theta}\right]_{r=x,\theta=\beta},$$
$$\frac{\partial\sigma_{yy}}{\partial y}(x,0) = \frac{1}{x}\left[\frac{\partial\sigma_{\theta\theta}}{\partial\theta} + 2\sigma_{r\theta}\right]_{r=x,\theta=\beta},$$
$$\frac{\partial\sigma_{xy}}{\partial y}(x,0) = \frac{1}{x}\left[\frac{\partial\sigma_{r\theta}}{\partial\theta} + \sigma_{rr} - \sigma_{\theta\theta}\right]_{r=x,\theta=\beta}. \tag{52}$$

$$\frac{\partial^2\sigma_{xx}}{\partial y^2}(x,0) = \frac{1}{x^2}\left[\frac{\partial^2\sigma_{rr}}{\partial\theta^2} + r\frac{\partial\sigma_{rr}}{\partial r} - 4\frac{\partial\sigma_{r\theta}}{\partial\theta} + 2(\sigma_{\theta\theta} - \sigma_{rr})\right]_{r=x,\theta=\beta},$$
$$\frac{\partial^2\sigma_{yy}}{\partial y^2}(x,0) = \frac{1}{x^2}\left[\frac{\partial^2\sigma_{\theta\theta}}{\partial\theta^2} + r\frac{\partial\sigma_{\theta\theta}}{\partial r} + 4\frac{\partial\sigma_{r\theta}}{\partial\theta} - 2(\sigma_{\theta\theta} - \theta_{rr})\right]_{r=x,\theta=\beta},$$
$$\frac{\partial^2\sigma_{xy}}{\partial y^2}(x,0) = \frac{1}{x^2}\left[\frac{\partial^2\sigma_{r\theta}}{\partial\theta^2} + r\frac{\partial\sigma_{r\theta}}{\partial r} + 2\frac{\partial}{\partial\theta}(\sigma_{rr} - \sigma_{\theta\theta}) - 4\sigma_{r\theta}\right]_{r=x,\theta=\beta}. \tag{53}$$

The asymptotic series representations of σ_{rr}, $\sigma_{\theta\theta}$, and $\sigma_{r\theta}$ are in the form (see [5, 6])

$$\sigma_{rr}(r,\theta) = \frac{k_I}{4\sqrt{2\pi r}}\left(5\cos\frac{\theta}{2} - \cos\frac{3\theta}{2}\right) + \frac{k_{II}}{4\sqrt{2\pi r}}\left(-5\sin\frac{\theta}{2} + 3\sin\frac{3\theta}{2}\right) + T\cos^2\theta + \frac{b_I}{4}\sqrt{\frac{r}{2\pi}}\left(3\cos\frac{\theta}{2} + \cos\frac{5\theta}{2}\right) + \frac{b_{II}}{4}\sqrt{\frac{r}{2\pi}}\left(3\sin\frac{\theta}{2} + 5\sin\frac{5\theta}{2}\right) + O(r), \tag{54}$$

$$\sigma_{\theta\theta}(r,\theta) = \frac{k_I}{4\sqrt{2\pi r}}\left(3\cos\frac{\theta}{2} + \cos\frac{3\theta}{2}\right) + \frac{k_{II}}{4\sqrt{2\pi r}}\left(-3\sin\frac{\theta}{2} - 3\sin\frac{3\theta}{2}\right) + T\sin^2\theta + \frac{b_I}{4}\sqrt{\frac{r}{2\pi}}\left(5\cos\frac{\theta}{2} - \cos\frac{5\theta}{2}\right) + \frac{b_{II}}{4}\sqrt{\frac{r}{2\pi}}\left(5\sin\frac{\theta}{2} - 5\sin\frac{5\theta}{2}\right) + O(r),$$

$$\sigma_{r\theta}(r,\theta) = \frac{k_I}{4\sqrt{2\pi r}}\left(\sin\frac{\theta}{2} + \sin\frac{3\theta}{2}\right) + \frac{k_{II}}{4\sqrt{2\pi r}}\left(\cos\frac{\theta}{2} + 3\cos\frac{3\theta}{2}\right) - T\sin\theta\cos\theta + \frac{b_I}{4}\sqrt{\frac{r}{2\pi}}\left(\sin\theta - \sin\frac{5\theta}{2}\right) + \frac{b_{II}}{4}\sqrt{\frac{r}{2\pi}}\left(-\cos\frac{\theta}{2} + 5\cos\frac{5\theta}{2}\right) + O(r).$$

(54) (*Cont.*)

Substituting (54) into (51)–(53) and making the approximation for small β (in fact β is of second order as discussed in the text), we arrive at

$$\sigma_{xx}(x,0) \simeq \frac{k_I}{\sqrt{2\pi x}} + \frac{k_{II}}{\sqrt{2\pi x}}\frac{\beta}{2} + T + b_I\sqrt{\frac{x}{2\pi}} + b_{II}\sqrt{\frac{x}{2\pi}}\frac{7\beta}{2} + O(x),$$

$$\sigma_{yy}(x,0) \simeq \frac{k_I}{\sqrt{2\pi x}} - \frac{k_{II}}{\sqrt{2\pi x}}\left(\frac{3\beta}{2}\right) + T\beta^2 + b_I\sqrt{\frac{x}{2\pi}} - b_{II}\sqrt{\frac{x}{2\pi}}\left(\frac{5\beta}{2}\right) + O(x),$$

$$\sigma_{xy}(x,0) \simeq \frac{k_I}{\sqrt{2\pi x}}\frac{\beta}{2} + \frac{k_{II}}{\sqrt{2\pi x}} - T\beta - b_I\sqrt{\frac{x}{2\pi}}\frac{\beta}{2} + b_{II}\sqrt{\frac{x}{2\pi}} + O(x). \tag{55}$$

$$\frac{\partial\sigma_{xx}}{\partial y}(x,0) \simeq -\frac{k_I}{\sqrt{2\pi x}}\left(\frac{3\beta}{4x}\right) - \frac{k_{II}}{\sqrt{2\pi x}}\left(\frac{3}{2x}\right) - \frac{b_I}{\sqrt{2\pi x}}\left(\frac{3\beta}{4}\right) + \frac{b_{II}}{\sqrt{2\pi x}}\left(\frac{3}{2}\right) + O(1),$$

$$\frac{\partial\sigma_{yy}}{\partial y}(x,0) \simeq \frac{k_I}{\sqrt{2\pi x}}\left(\frac{\beta}{4x}\right) + \frac{k_{II}}{\sqrt{2\pi x}}\left(\frac{1}{2x}\right) + \frac{b_I}{\sqrt{2\pi x}}\left(\frac{\beta}{4}\right) - \frac{b_{II}}{\sqrt{2\pi x}}\left(\frac{1}{2}\right) + O(1),$$

$$\frac{\partial\sigma_{xy}}{\partial y}(x,0) \simeq \frac{k_I}{\sqrt{2\pi x}}\left(\frac{1}{2x}\right) + \frac{k_{II}}{\sqrt{2\pi x}}\left(\frac{\beta}{4x}\right) - \frac{b_I}{\sqrt{2\pi x}}\left(\frac{1}{2}\right) - \frac{b_{II}}{\sqrt{2\pi x}}\left(\frac{7\beta}{4}\right) + O(1). \tag{56}$$

$$\frac{\partial^2\sigma_{xx}}{\partial y^2}(x,0) \simeq -\frac{k_I}{\sqrt{2\pi x}}\left(\frac{9}{4x^2}\right) + \frac{k_{II}}{\sqrt{2\pi x}}\left(\frac{3\beta}{8x^2}\right) + \frac{b_I}{\sqrt{2\pi x}}\left(\frac{3}{4x}\right) + \frac{b_{II}}{\sqrt{2\pi x}}\left(\frac{9\beta}{8x}\right) + O(x^{-1}),$$

$$\frac{\partial^2\sigma_{yy}}{\partial y^2}(x,0) \simeq \frac{k_I}{\sqrt{2\pi x}}\left(\frac{3}{4x^2}\right) + \frac{k_{II}}{\sqrt{2\pi x}}\left(\frac{3\beta}{8x^2}\right) - \frac{b_I}{\sqrt{2\pi x}}\left(\frac{1}{4x}\right) - \frac{b_{II}}{\sqrt{2\pi x}}\left(\frac{7\beta}{8x}\right) + O(x^{-1}),$$

$$\frac{\partial^2\sigma_{xy}}{\partial y^2}(x,0) \simeq -\frac{k_I}{\sqrt{2\pi x}}\left(\frac{9\beta}{8x^2}\right) - \frac{k_{II}}{\sqrt{2\pi x}}\left(\frac{9}{4x^2}\right) - 2T\frac{\beta}{x^2} - \frac{b_I}{\sqrt{2\pi x}}\left(\frac{3\beta}{8x}\right) + \frac{b_{II}}{\sqrt{2\pi x}}\left(\frac{3}{4x}\right) + O(x^{-1}). \tag{57}$$

K. Hayashi[1]
Visiting Scholar.

S. Nemat-Nasser
Professor of Civil Engineering and Applied Mathematics. Mem. ASME

Department of Civil Engineering, The Technological Institute, Northwestern University, Evanston, Ill. 60201

Energy-Release Rate and Crack Kinking Under Combined Loading

Based on the maximum energy-release-rate criterion, kinking from a straight crack is investigated under the plane strain condition. Solutions are obtained by the method that models a kink as a continuous distribution of edge dislocations. The energy-release rate is expressed as a quadratic form of the stress-intensity factors that exist prior to the onset of kinking, and the coefficients of this quadratic form are tabulated for various values of the kink angle. The examination of the results shows that Irwin's formula for the energy-release rate remains valid for any kink angle provided that the stress-intensity factors in the formula are taken equal to those existing at the tip of a vanishingly small kink.

Introduction

Crack kinking is of considerable importance in fracture mechanics, and many attempts have been made to study this phenomenon, beginning with the work of Erdogan and Sih [1], who used the maximum stress criterion. Sih [2] also proposed an approach known as the minimum strain-energy-density criterion. The predictions obtained from these two criteria are based on the near crack-tip field that exists prior to the onset of kinking. Besides these, there is the maximum energy-release-rate criterion which is a generalization of Griffith's original energy-release-rate criterion [3, 4], and which seems to stem from the fundamental mechanics principle of minimum potential energy. There are several analytical studies of the mixed mode fracture, that employ the maximum energy-release-rate criterion; i.e., the works of Hussain, Pu, and Underwood [5], Palaniswamy and Knauss [6], Gupta [7], and Wu [8–10]. Detailed discussions of [5, 6] are presented in [8]. Among these, the results in [10] are rather complete. Recently, closed-form expressions for the energy-release rate have been obtained by Wu [11], and Hayashi and Nemat-Nasser [12], assuming small kink angles.

The objective of this work is to investigate the kinking from a straight crack, on the basis of the maximum energy-release-rate criterion. To calculate the energy-release rate at the onset of kinking, the problem of a kinked crack with an infinitesimally small kink length is first solved by the method that models the kink as a continuous distribution of edge dislocations. This method is similar to that of Lo [13], and Karihaloo, Keer, and Nemat-Nasser [14], and is the same as that in [12]. Once the density functions of edge dislocations are obtained, the energy-release rate is readily determined with the aid of the near-tip stress field that exists prior to the onset of kinking.

Simple expressions are obtained, which relate the stress-intensity factors and the energy-release rate, where the expressions for the stress-intensity factors are linear combinations of those of the main crack, and therefore are identical to the expressions presented by Bilby and Cardew [15]. The energy-release rate is given by a quadratic form in stress-intensity factors of the main crack. Coefficients of these expressions are tabulated as functions of the kink angle. Once the crack problem without a kink is solved, then the stress-intensity factors and the energy-release rate can readily be evaluated for an infinitesimally small kink with the aid of the expressions presented here. The examination of these results shows that Irwin's formula for the energy-release rate is valid even at the inception of kinking for *any kink angle*, provided that the stress-intensity factors in the formula are taken to be those that exist at the tip of a vanishingly small kink. This fact was first suggested by Hussain, Pu, and Underwood in [5], but apparently had not been completely accepted [10], so that the validity of Irwin's formula had remained an unsettled question. The present work, therefore, should make it clear that Irwin's formula indeed holds at the inception of kinking for all kink angles; it clearly applies after kinking has taken place.

Statement of Problem and Basic Equations

Consider an elastic body with a kinked crack. The body is isotropic and in the state of plane strain under a set of uniform stresses applied far from the crack. The lengths of the main crack and the kink are denoted by $2a$ and l, respectively. The fixed rectangular Cartesian coordinate system x_α, shown in Fig. 1, is used; throughout this work Greek indices take on values 1, 2, and, unless otherwise stated, the usual summation convention is employed. A supplementary Cartesian coordinate system ζ_α is also used, as shown in Fig. 1. In what follows, the superscript 0 identifies functions in the supplementary coordinate system. The stress tensor at infinity, referred to the x_α-axes, is denoted by $\sigma^\infty_{\alpha\beta}$.

The boundary conditions of the problem are as follows:

[1] On leave from Department of Mechanical Engineering, Tohoku University, Sendai 980, Japan.

Contributed by the Applied Mechanics Division for publication in the JOURNAL OF APPLIED MECHANICS.

Discussion on this paper should be addressed to the Editorial Department, ASME, United Engineering Center, 345 East 47th Street, New York, N. Y. 10017, and will be accepted until December 1, 1981. Readers who need more time to prepare a discussion should request an extension from the Editorial Department. Manuscript received by ASME Applied Mechanics Division, June, 1980; final revision, October, 1980.

1 The surfaces of the main crack are free from tractions.
2 The surfaces of the kink are free from tractions.
3 The uniform stresses are given at infinity.

The kink is modeled as a continuous distribution of edge dislocations with Burgers' vector $b_\alpha(\zeta_1)$ referred to the ζ_α-axes. The elastic potential functions $\Phi(z)$ and $\Psi(z)$ of $z(=x_1+ix_2)$ [16], which satisfy Conditions 1 and 3, and the requirement for the single-valuedness of the displacement (for a circuit taken around the kinked crack) are given by [12]

$$\Phi(z)=\frac{\sigma_{11}^{\infty}+\sigma_{22}^{\infty}}{4}+\Phi_1^*(z)+i\lambda\int_0^l\frac{\beta(s)e^{i\omega}}{z-se^{i\omega}}ds+\int_0^l\Phi_2^*(z,s)ds,$$

$$\Psi(z)=\frac{\sigma_{22}^{\infty}-\sigma_{11}^{\infty}}{2}+i\sigma_{12}^{\infty}+\Psi_1^*(z)-i\lambda\times\int_0^l\left[\frac{\overline{\beta(s)}e^{-i\omega}}{z-se^{i\omega}}-\frac{s\beta(s)}{(z-se^{i\omega})^2}\right]ds+\int_0^l\Psi_2^*(z,s)ds, \quad (1)$$

where

$$\Phi_1^*(z)=\frac{\sigma_{22}^{\infty}-i\sigma_{12}^{\infty}}{2}[X(z)(z+a)-1], \quad (2)$$

$$\Phi_2^*(z,s)=-\frac{i\lambda}{2}\left[\beta(s)e^{i\omega}\left\{\frac{1}{z-se^{i\omega}}+\frac{1}{z-se^{-i\omega}}-\frac{X(z)}{X(se^{i\omega})}\frac{1}{z-se^{i\omega}}-\frac{X(z)}{X(se^{-i\omega})}\frac{1}{z-se^{-i\omega}}\right\}+\overline{\beta(s)}e^{-i\omega}s(e^{-i\omega}-e^{i\omega})\times\left\{\frac{1}{(z-se^{-i\omega})^2}-\frac{X(z)}{X(se^{-i\omega})}\times\frac{a+se^{-i\omega}}{se^{-i\omega}(se^{-i\omega}+2a)}\frac{1}{z-se^{-i\omega}}-\frac{X(z)}{X(se^{-i\omega})}\frac{1}{(z-se^{-i\omega})^2}\right\}\right], \quad (3)$$

$$\Psi_1^*(z)=-\Phi_1^*(z)+\overline{\Phi_1^*(\bar{z})}-z\Phi_1^{*\prime}(z), \quad (4)$$

$$\Psi_2^*(z,s)=-\Phi_2^*(z,s)+\overline{\Phi_2^*(\bar{z},s)}-z\Phi_2^{*\prime}(z,s), \quad (5)$$

$$X(z)=1/\sqrt{z(z+2a)}, \quad (6)$$

$$\lambda=\frac{E}{8\pi(1-\nu^2)}, \quad (7)$$

$$\beta=b_1+ib_2. \quad (8)$$

Here, E is Young's modulus, and ν Poisson's ratio. The branch of $X(z)$ is taken such that $X(z)\to 1/z$ as $|z|\to\infty$. An overbar is used to indicate the complex conjugate.

The density function $\beta(\zeta_1)$ is related to the displacement-discontinuities across the kink,

$$\beta(\zeta_1)=\frac{\partial}{\partial\zeta_1}([u_1^0]+i[u_2^0]), \quad (9)$$

where

$$[u_\alpha^0]=u_\alpha^0|_{\zeta_2\to 0+}-u_\alpha^0|_{\zeta_2\to 0-}. \quad (10)$$

Here, u_α^0 denotes the displacement vector referred to the ζ_α-axes.

Singular Integral Equations

The elastic potential functions given by (1) satisfy Conditions 1 and 3, and the requirement of the single-valuedness of the displacement. Only Condition 2 remains to be satisfied, and this leads to a system of singular integral equations whose unknown functions are the density functions $b_\alpha(\zeta_1)$.

The following nondimensional notation is introduced:

$$l=\frac{\tilde{l}}{a},\quad \xi=\frac{\zeta_1}{a},\quad r=\frac{s}{a},\quad t_{\alpha\beta}^0=\frac{\sigma_{\alpha\beta}^0}{\sigma_c},$$
$$t_{\alpha\beta}^{\infty}=\frac{\sigma_{\alpha\beta}^{\infty}}{\sigma_c},\quad B_\alpha(\xi)=\frac{b_\alpha(\zeta_1)}{\sigma_c/\lambda}, \quad (11)$$

where $\sigma_{\alpha\beta}^0$ is the stress tensor referred to the ζ_α-axes and σ_c is a representative stress for the system. Furthermore, set

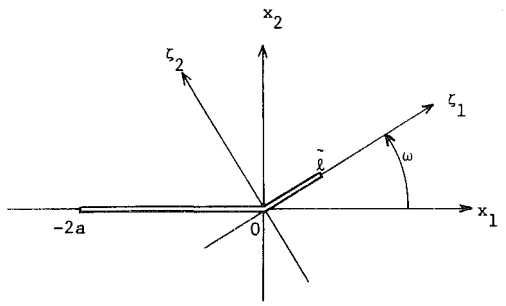

Fig. 1 Geometry and coordinate systems

$$x=\sqrt{\frac{\xi}{l}},\quad t=\sqrt{\frac{r}{l}},\quad \phi_\alpha(t)=\sqrt{r}\,B_\alpha(r). \quad (12)$$

For $\tilde{l}\ll a$, the basic integral equations then are[2]

$$\int_0^1 Q_{\beta\alpha}(x,t;\omega)\phi_\beta(t)dt=P_{\alpha\rho}(\omega)k_\rho+\sqrt{l}\,x(t_{11}^{\infty}-t_{22}^{\infty})R_\alpha(\omega),\quad 0<x<1, \quad (13)$$

where

$$P_{\alpha\rho}(\omega)=\frac{1}{2\sqrt{2}}\{C_{1\rho}(\omega)+C_{2\rho}(\omega)-C_{\alpha\rho}(\omega)\} \quad (14)$$

$$k_1=\tilde{k}_1/\sigma_c\sqrt{\pi a}=t_{22}^{\infty},\quad k_2=\tilde{k}_2/\sigma_c\sqrt{\pi a}=t_{12}^{\infty}, \quad (15)$$

$$R_1(\omega)=-\frac{1}{4}\sin 2\omega,\quad R_2(\omega)=\frac{1}{2}\sin^2\omega, \quad (16)$$

and $\tilde{k}_\alpha$ are the stress-intensity factors existing prior to kinking. The quantity $C_{\alpha\beta}(\omega)$ denotes the coefficients of the singular terms in the asymptotic expansion of the near-tip stress field of a straight crack, and is identical to those in the Irwin-Williams solution [17]:

$$C_{11}=\frac{1}{4}(3\cos\omega/2+\cos 3\omega/2),$$
$$C_{12}=-\frac{3}{4}(\sin 3\omega/2+\sin\omega/2),$$
$$C_{21}=\frac{1}{4}(\sin 3\omega/2+\sin\omega/2),$$
$$C_{22}=\frac{1}{4}(3\cos 3\omega/2+\cos\omega/2). \quad (17)$$

The kernels $Q_{\beta\alpha}$ are given by

$$Q_{\beta\alpha}=\frac{\delta_{\beta\alpha}}{x-t}+\frac{\delta_{\beta\alpha}}{x+t}+\frac{1}{2}k_{\beta\alpha}(x,t;\omega), \quad (18)$$

where

$$k_{\alpha1}+ik_{\alpha2}=\frac{d_{\alpha1}}{x+t}+\frac{d_{\alpha2}}{xe^{i\omega}+t}+\frac{xe^{i\omega}d_{\alpha3}}{(xe^{i\omega}+t)^2}+\frac{d_{\alpha4}}{xe^{-i\omega}+t}+\frac{xe^{-i\omega}d_{\alpha5}}{(xe^{-i\omega}+t)^2}+\frac{x^2e^{-2i\omega}d_{\alpha6}}{(xe^{-i\omega}+t)^3}, \quad (19)$$

and

$$d_{11}=-2,\quad d_{12}=-\cos\omega-2i\sin\omega,\quad d_{13}=i\sin\omega,$$
$$d_{14}=e^{-i\omega}(-\cos 2\omega+i\sin\omega\cos\omega),$$
$$d_{15}=-e^{-i\omega}\sin\omega(4\sin\omega+i\cos\omega),$$
$$d_{16}=2e^{-i\omega}\sin^2\omega,\quad d_{21}=-2i,\quad d_{22}=-i\cos\omega,\quad d_{23}=\sin\omega,$$
$$d_{24}=e^{-i\omega}(\sin\omega\cos\omega-i),\quad d_{25}=-e^{-i\omega}\sin\omega(\cos\omega+2i\sin\omega),$$
$$d_{26}=2ie^{-i\omega}\sin^2\omega. \quad (20)$$

[2] For $\tilde{l}\ll a$, $\sqrt{\zeta_1/2a}\,X(\zeta_1e^{i\omega})$, $\sqrt{s/2a}\,X(se^{i\omega})$, and $\sqrt{s/2a}\,X(se^{-i\omega})$ in the kernels of the integral equations can be expanded into the power series of $\zeta_1/2a$ or $s/2a$. Neglecting terms of the order higher than $0(\zeta_1/2a)$ and $0(s/2a)$ and taking into account (11) and (12), one arrives at (13).

It can be proved that the last term of the right-hand side of (13) makes no contribution to the solution as $l \to 0$.[3] Therefore, (13) can be reduced to two systems of integral equations,

$$\int_0^1 Q_{\beta\alpha}(x, t; \omega)\phi_{\beta 1}(t)\, dt = P_{\alpha 1}(\omega), \; 0 < x < 1, \tag{21}$$

$$\int_0^1 Q_{\beta\alpha}(x, t; \omega)\phi_{\beta 2}(t) dt = P_{\alpha 2}(\omega), \; 0 < x < 1. \tag{22}$$

The solution of (13) is given by

$$\phi_\beta(x) = k_\rho \phi_{\beta\rho}(x). \tag{23}$$

The second and third terms of the kernel $Q_{\beta\alpha}$ in (18), are unbounded as x and t approach zero simultaneously, and the singular behavior of the solution at $\xi = 0$ may no longer be described by $1/\sqrt{\xi}$. In order to study the singular behavior, it is necessary to examine the behavior of the integrals in (13) (or (21) and (22)) by the method proposed by Erdogan [18]. However, this examination is very tedious in the present case, so that here the singular behavior is estimated by using the asymptotic results presented by Bogy [19] for the fields associated with the vertex of a stress-free wedge, which, according to [19], behave as $1/d^\epsilon$ for a wedge angle larger than π and less than 2π, where d measures distance from the vertex and $\epsilon < 1/2$. In view of (9), this implies that $B_\alpha(\xi)$ is of the form,

$$B_\alpha(\xi) = \frac{B_\alpha^*(\xi)}{\xi^\epsilon \sqrt{l - \xi}}, \quad \epsilon < 1/2, \tag{24}$$

with a bounded function $B_\alpha^*(\xi)$. From (11), (12), (23), and (24), it is concluded that

$$\phi_\alpha(x) = \frac{k_\rho \psi_{\alpha\rho}(x)}{\sqrt{1 - x^2}}, \tag{25}$$

where $\psi_{\alpha\rho}(x)$ are bounded on the kink.

Stress-Intensity Factors and Energy-Release Rate

The stresses near $\zeta_1 = l$ on the ζ_1-axis, but not on the kink, are given by

$$t_{22}^0 - it_{12}^0 \sim i \int_0^l \frac{2(B_1 + iB_2)}{\xi - r}\, dr \sim \frac{2\pi i}{\sqrt{\xi - l}} \{k_\rho \psi_{1\rho}(1) + ik_\rho \psi_{2\rho}(1)\}. \tag{26}$$

The stress-intensity factors at the tip of the kink are defined as

$$K_I + iK_{II} = \lim_{\xi \to l+} \{\sqrt{2\pi(\xi - l)}\, (t_{22}^0 + it_{12}^0)_{\zeta_2 = 0}\}, \tag{27}$$

where the stress-intensity factors are nondimensionalized with respect to $\sigma_c\sqrt{\pi a}$. Then, for an infinitesimally small kink, it follows that

$$K_I + iK_{II} = -2\sqrt{2\pi}\{k_\rho \psi_{2\rho}(1) + ik_\gamma \psi_{1\gamma}(1)\}. \tag{28}$$

When a kink starts from the tip of a main crack under the plane strain condition, the change of the potential energy, ΔP, measured per unit thickness of the elastic body, is given by

$$\Delta P = \frac{1}{2} \int_{\Delta S} \sigma_{\alpha\beta}^{*0} \Delta u_\alpha^0 n_\beta^0 dS, \tag{29}$$

where ΔS denotes the newly created area by kinking, $\sigma_{\alpha\beta}^{*0}$ are the stresses acting on ΔS before the onset of kinking and referred to the ζ_α-axes, Δu_α^0 are the displacement increments due to kinking, and n_α^0 is the outward unit normal vector of ΔS. From (29), the energy-release rate, G, is given by

$$G = -\frac{\partial(\Delta P)}{\partial l}\bigg|_{l \to 0} = \lim_{l \to 0} \left\{ -\frac{1}{2l} \int_0^l \Sigma_{\alpha 2}(\zeta_1) \frac{\partial}{\partial \zeta_1} [u_\alpha^0] d\zeta_1 \right\}, \tag{30}$$

[3] Solution (13) can be expressed as the sum of two solutions. The first solution is determined from the first term of the right-hand side of (13) and is independent of l. The second solution is determined from the second term of the right-hand side of (13) and is proportional to $\sqrt{l}$.

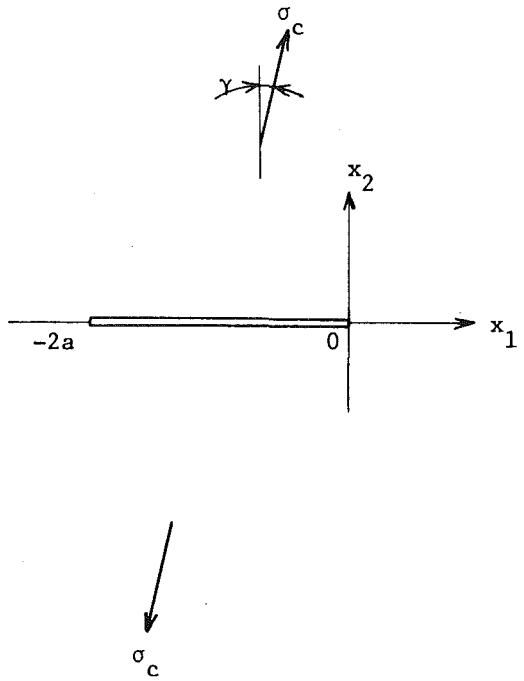

Fig. 2 A crack under unidirectional tension

where

$$\Sigma_{\alpha 2}(\zeta_1) = \int^{\zeta_1} \sigma_{\alpha 2}^{*0}(\zeta_1) d\zeta_1. \tag{31}$$

In deriving (30), the following conditions are used:

$$\Sigma_{\alpha\beta}(0) = 0, \quad [u_\alpha^0]_{\zeta = l} = 0. \tag{32}$$

Employing the Irwin-Williams expression for $\sigma_{\alpha\beta}^{*0}$, and using (9), (11), (12), (25), and (30), we arrive at

$$G^* \equiv \frac{G}{\frac{\pi a(1 - \nu^2)}{E} \sigma_c^2} = -32 k_\alpha k_\rho P_{\beta\alpha}(\omega) I_{\beta\rho}(\omega), \tag{33}$$

where

$$I_{\beta\rho}(\omega) = \int_0^1 \psi_{\beta\rho}(t) \frac{t}{\sqrt{1 - t^2}} dt. \tag{34}$$

Results and Discussion

The two sets of integral equations (21) and (22) are solved by the method developed by Gupta and Erdogan [20]. The discretized forms of (21) and (22) are

$$\frac{\pi}{2n + 1} \sum_{i=1}^{n} Q_{\beta\alpha}(x_j, t_i; \omega)\psi_{\beta 1}(t_i) = P_{\alpha 1}(\omega), \tag{35}$$

$$\frac{\pi}{2n + 1} \sum_{i=1}^{n} Q_{\beta\alpha}(x_j, t_i; \omega)\psi_{\beta 2}(t_i) = P_{\alpha 2}(\omega), \tag{36}$$

where

$$t_i = \cos\left(\frac{2i - 1}{4n + 2}\pi\right), \quad i = 1, 2, \ldots n,$$

$$x_j = \cos\left(\frac{\pi j}{2n + 1}\right), \quad j = 1, 2, \ldots n. \tag{37}$$

Equation (35) (or (36)) provides a system of $2n$ equations for the determination of the $2n$-values $\psi_{\beta 1}(t_i)$ (or $\psi_{\beta 2}(t_i)$).

For the numerical calculations, two cases, i.e., $n = 60$ and $n = 90$, have been examined. The discrepancy between the resulting two sets of stress-intensity factors (or the energy-release rate) becomes larger

Table 1 Maximum energy-release rate for unidirectional tension

$(\frac{\pi}{2}-\gamma)/\pi$	ω_c/π	G^*	K_I	K_{II}	$K_I^2+K_{II}^2$
0.025	-0.41169	0.00989	0.09942	0.00199	0.00989
0.050	-0.40269	0.04114	0.20279	0.00361	0.04114
0.750	-0.39367	0.09482	0.30788	0.00474	0.09482
0.100	-0.38442	0.17015	0.41242	0.00539	0.17012
0.125	-0.37453	0.26444	0.51423	0.00605	0.26447
0.150	-0.36411	0.37342	0.61106	0.00625	0.37343
0.175	-0.35317	0.49142	0.70096	0.00592	0.49139
0.200	-0.34141	0.61194	0.78220	0.00529	0.61186
0.225	-0.32835	0.72824	0.85338	0.00508	0.72828
0.250	-0.31414	0.83396	0.91318	0.00414	0.83392
0.275	-0.29825	0.92357	0.96106	0.00345	0.92365
0.300	-0.28022	0.99319	0.99659	0.00256	0.99319
0.325	-0.25970	1.04062	1.02014	0.00185	1.04070
0.350	-0.23598	1.06603	1.03248	0.00101	1.06602
0.375	-0.20836	1.07165	1.03522	0.00067	1.07168
0.400	-0.17620	1.06192	1.03051	0.00037	1.06196
0.425	-0.13894	1.04301	1.02129	0.00019	1.04304
0.450	-0.09645	1.02206	1.01098	0.00013	1.02207
0.475	-0.04938	1.00598	1.00298	0.00014	1.00597

Table 2 Maximum energy-release rate for crack-parallel shear

ω_c/π	G^*	K_I	K_{II}	$K_I^2+K_{II}^2$
-0.42080	1.51692	1.23119	0.02661	1.51655

as ω approaches π. However, this discrepancy is at most 1 percent for $\omega \leqq 0.8\pi$. The results presented next are obtained with $n = 90$.

In Tables 1 and 2, the critical kink angle, ω_c, the stress-intensity factors, and the energy-release rate are presented for the case of a unidirectional tension defined in Fig. 2 and for the case of a simple shear parallel to the main crack. The results in Table 1 agree well with those in [10]. The critical kink angle for the case of a simple shear parallel to the main crack is $-75.8°$. This value coincides with that predicted in [15], but is slightly at variance with the results in [6, 10].

From (28), the stress-intensity factors for an infinitesimally small kink are expressed as linear combinations of k_α, i.e., the stress-intensity factors existing prior to kinking,

$$K_I = K_{I\alpha}k_\alpha, \quad K_{II} = K_{II\alpha}k_\alpha, \tag{38}$$

where

$$K_{I\alpha} = -2\sqrt{2}\pi\,\psi_{2\alpha}(1), \quad K_{II\alpha} = -2\sqrt{2}\pi\,\psi_{1\alpha}(1). \tag{39}$$

In Table 3, $K_{I\alpha}$ and $K_{II\alpha}$ are presented.

From (33), the energy-release rate is expressed as a quadratic form of k_α,

$$G^* = C_{G11}k_1^2 + C_{G12}k_1k_2 + C_{G22}k_2^2, \tag{40}$$

where

$$C_{G11} = -32P_{\beta1}I_{\beta1},$$
$$C_{G12} = -32(P_{\beta1}I_{\beta2} + P_{\beta2}I_{\beta1}), \quad C_{G22} = -32P_{\beta2}I_{\beta2}. \tag{41}$$

Now, consider the following formula:

$$G^* = K_I^2 + K_{II}^2. \tag{42}$$

This formula is formally the same as Irwin's formula in which k_1 and k_2 are used instead of K_I and K_{II}. From (38) and (39),

$$G^* = C_{K11}k_1^2 + C_{K12}k_1k_2 + C_{K22}k_2^2, \tag{43}$$

where

$$C_{K11} = 8\pi^2\psi_{\rho1}(1)\psi_{\rho1}(1), \quad C_{K12} = 16\pi^2\psi_{\rho1}(1)\psi_{\rho2}(1),$$
$$C_{K22} = 8\pi^2\psi_{\rho2}(1)\psi_{\rho2}(1). \tag{44}$$

Table 3 Coefficients of (38); $K_{II1}(\omega) = -K_{II1}(-\omega)$, $K_{II2}(\omega) = K_{II2}(-\omega)$, $K_{I1}(\omega) = K_{I1}(-\omega)$, $K_{I2}(\omega) = -K_{I2}(-\omega)$

ω/π	K_{III}	K_{II2}	K_{I1}	K_{I2}
0.0	0.0	1.0	1.0	0.0
-0.04	-0.06251	0.98772	0.99410	0.18770
-0.08	-0.12320	0.95131	0.97655	0.37069
-0.12	-0.18029	0.89211	0.94794	0.54441
-0.16	-0.23219	0.81224	0.90913	0.70469
-0.20	-0.27751	0.71460	0.86127	0.84784
-0.24	-0.31514	0.60262	0.80579	0.97083
-0.28	-0.34430	0.48016	0.74427	1.07134
-0.32	-0.36449	0.35137	0.67837	1.14784
-0.36	-0.37560	0.22048	0.60981	1.19960
-0.40	-0.37782	0.09165	0.54024	1.22672
-0.44	-0.37159	-0.03116	0.47126	1.22996
-0.48	-0.35768	-0.14440	0.40426	1.21082
-0.52	-0.33705	-0.24495	0.34049	1.17129
-0.56	-0.31080	-0.33023	0.28095	1.11390
-0.60	-0.28024	-0.39818	0.22632	1.04149
-0.64	-0.24697	-0.44724	0.17664	0.95746
-0.68	-0.21803	-0.47259	0.12248	0.87185
-0.72	-0.17069	-0.49145	0.10537	0.75787
-0.76	-0.13673	-0.48255	0.07269	0.65584
-0.80	-0.10410	-0.45761	0.04716	0.55040

Table 4 Coefficients of the quadratic forms (40) and (43); $C_{K11}(\omega) = C_{K11}(-\omega)$, $C_{K12}(\omega) = -C_{K12}(-\omega)$, $C_{K22}(\omega) = C_{K22}(-\omega)$, $C_{G11}(\omega) = C_{G11}(-\omega)$, $C_{G12}(\omega) = -C_{G12}(-\omega)$, $C_{G22}(\omega) = C_{G22}(-\omega)$

ω/π	C_{K11}	C_{K12}	C_{K22}	C_{G11}	C_{G12}	C_{G22}
0.0	1.0	0.0	1.0	1.0	0.0	1.0
-0.04	0.99215	0.24970	1.01081	0.99215	0.24970	1.01081
-0.08	0.96884	0.48959	1.04238	0.96884	0.48959	1.04238
-0.12	0.93111	0.71044	1.09224	0.93111	0.71044	1.09224
-0.16	0.88043	0.90409	1.15633	0.88043	0.90409	1.15633
-0.20	0.81882	1.06381	1.22949	0.81882	1.06381	1.22949
-0.24	0.74864	1.18476	1.30565	0.74864	1.18476	1.30565
-0.28	0.67249	1.26411	1.37831	0.67249	1.26411	1.37831
-0.32	0.59304	1.30118	1.44099	0.59304	1.30118	1.44099
-0.36	0.51293	1.29745	1.48767	0.51293	1.29745	1.48767
-0.40	0.43461	1.25620	1.51321	0.43461	1.25620	1.51321
-0.44	0.36015	1.18240	1.51378	0.36015	1.18240	1.51378
-0.48	0.29135	1.08228	1.48692	0.29135	1.08228	1.48692
-0.52	0.22952	0.96274	1.43194	0.22952	0.96277	1.43194
-0.56	0.17552	0.83117	1.34982	0.17552	0.83117	1.34982
-0.60	0.12975	0.69461	1.24329	0.12975	0.69461	1.24329
-0.64	0.09221	0.55917	1.11674	0.09221	0.55920	1.11674
-0.68	0.06255	0.41965	0.98348	0.06227	0.42013	0.98329
-0.72	0.04024	0.32748	0.81587	0.04021	0.32748	0.81587
-0.76	0.02397	0.22729	0.66297	0.02397	0.22729	0.66297
-0.80	0.01307	0.14718	0.51236	0.01307	0.14718	0.51233

Table 5 Energy-release rate for crack-parallel shear

ω/π	W_u, [10, Table 1]	Present Result
0.2	1.2294	1.2294
0.4	1.5117	1.5132
0.6	1.2302	1.2433
0.8	0.4945	0.5123

The numerical results of (41) and (44) are given in Table 4. The coefficients C_{G11}, C_{G12}, and C_{G22} are exactly the same as C_{K11}, C_{K12}, and C_{K22}. Therefore, these data suggest that Irwin's formula remains valid for a large kink angle and for any in-plane loading, provided that the stress-intensity factors in the formula are taken to be those at the tip of an infinitesimally small kink. In [5] it has been suggested that (42) is valid for any kink angle but this has not been completely ac-

cepted; [10]. The results obtained in the present work, therefore, should remove any doubt that may have existed regarding the validity of Irwin's formula.

In Table 5, the energy-release rate for various kink angles under a shear parallel to the main crack is given together with those reported in [10], showing excellent agreement.

Based on the foregoing results, it is clear that, when k_α's are known, then the critical kink angle, the energy-release rate, and the stress-intensity factors can be evaluated using the data in Tables 3 and 4 without needing any additional information on the corresponding kinked crack problem.

Finally, it must be noted that the present results are not applicable to a loading condition which brings the surfaces of the main crack into contact. Under such a loading, the length of the contact zone changes due to kinking, and the formulation in the section, "Statement of Problem and Basic Equations," no longer holds. One possible approach to such a problem is to model the main crack together with the kink as a continuous distribution of edge dislocations. Then the problem is reduced to determining the density functions of edge dislocations and the length of the contact zone.

Acknowledgment

This work has been supported by National Science Foundation Grant No. ENG 77-22155 to Northwestern University.

References

1 Erdogan, F., and Sih, G. C., "On the Crack Extension in Plates Under Plane Loading and Transverse Shear," ASME *Journal of Basic Engineering*, Vol. 85, 1963, pp. 519–527.

2 Sih, G. C., "Introductory Chapter: A Special Theory of Crack Propagation," *Mechanics of Fracture 1*, Noordhoff, 1972.

3 Griffith, A. A., "The Phenomena of Rupture and Flow in Solids," *Philosophical Transactions of the Royal Society*, Vol. 221, Series A, 1921, pp. 163–198.

4 Griffith, A. A., "The Theory of Rupture," *Proceedings, First International Congress of Applied Mechanics*, Delft, 1924, pp. 55–63.

5 Hussain, M. A., Pu, S. L., and Underwood, J., "Strain-Energy-Release Rate for a Crack Under Combined Mode I and Mode II," ASTM-STP-560, 1974, pp. 2–28.

6 Palaniswamy, K., and Knauss, W. G., "On the Problem of Crack Extension in Brittle Solids Under General Loading," *Mechanics Today*, Vol. 4, ed., Nemat-Nasser, S., Pergamon Press, 1978, pp. 87–148.

7 Gupta, G. D., "Strain-Energy Release Rate for Mixed Mode Crack Problem," ASME Paper No. 76-WA/PVP-7, 1976.

8 Wu, C. H., "Elasticity Problems of Slender Z-Crack," *Journal of Elasticity*, Vol. 8, 1978, pp. 183–205.

9 Wu, C. H., "Maximum-Energy-Release-Rate Criterion Applied to a Tension-Compression Specimen With Crack," *Journal of Elasticity*, Vol. 8, 1978, pp. 235–257.

10 Wu, C. H., "Fracture Under Combined Loads by Maximum-Energy-Release-Rate Criterion," ASME JOURNAL OF APPLIED MECHANICS, Vol. 45, 1978, pp. 553–558.

11 Wu, C. H., "Explicit Asymptotic Solution for the Maximum-Energy-Release-Rate Problem," *International Journal of Solids and Structures*, Vol. 15, 1979, pp. 561–566.

12 Hayashi, K., and Nemat-Nasser, S., "Energy-Release Rate and Crack Kinking," *International Journal of Solids and Structures*, Vol. 17, 1981, pp. 107–114.

13 Lo, K. K., "Analysis of Branched Cracks," ASME JOURNAL OF APPLIED MECHANICS, Vol. 45, 1978, pp. 797–802.

14 Karihaloo, B. L., Keer, L. M., and Nemat-Nasser, S., "Crack Kinking Under Nonsymmetric Loading," *Engineering Fracture Mechanics*, Vol. 13, 1980, pp. 879–888.

15 Bilby, B. A., and Cardew, G. E., "The Crack With a Kinked Tip," *International Journal of Fracture*, Vol. 11, 1975, pp. 708–712.

16 Muskhelishvili, N. I., *Some Basic Problems in the Mathematical Theory of Elasticity*, Noordhoff, 1958.

17 Williams, M. L., "On the Stress Distribution at the Base of a Stationary Crack," ASME JOURNAL OF APPLIED MECHANICS, Vol. 24, 1957, pp. 109–114.

18 Erdogan, F., "Mixed Boundary-Value Problems in Mechanics," *Mechanics Today*, Vol. 4, ed., Nemat-Nasser, S., Pergamon Press, 1978, pp. 1–86.

19 Bogy, D. B., "Two Edge-Bonded Elastic Wedges of Different Materials and Wedge Angles Under Surface Tractions," ASME JOURNAL OF APPLIED MECHANICS, Vol. 38, 1971, pp. 377–386.

20 Gupta, G. D., and Erdogan, F., "The Problem of Edge Cracks in an Infinite Strip," ASME JOURNAL OF APPLIED MECHANICS, Vol. 41, 1974, pp. 1001–1006.

A. Golebiewska Herrmann
Acting Associate Professor
Mem. ASME

G. Herrmann
Professor and Chairman.
Fellow ASME

Division of Applied Mechanics,
Department of Mechanical Engineering,
Stanford University,
Stanford, Calif. 94305

On Energy-Release Rates for a Plane Crack

Considered is a plane crack in a homogeneous, static stress field. The component of the J_i integral normal to the plane of the crack (J_2) is shown not to be path-independent in the sense of the well-known J integral ($\equiv J_1$) parallel to the plane of the crack. The relation between the energy-release rate for rotation L and the integral J_2 is established. It is finally suggested that the integrals L and M may provide a more natural description of energy-release rates (or forces) for plane cracks, rather than the integrals J_1 and J_2.

Introduction

The by-now well-known J-integral of elastic fracture mechanics [1–3] has been related to potential energy-release rates associated with crack extension and has proved to be of great value in fracture testing. For a plane crack subjected to both far-field extension and in-plane shear, i.e., combined opening (Mode I) and sliding (Mode II), the J-integral, around the right crack tip, in terms of the stress-intensity factors K_I for Mode I and K_{II} for Mode II, is

$$J = (K_I^2 + K_{II}^2)/E \tag{1}$$

for plane stress. For plane strain, Young's modulus E has to be divided by $(1 - \nu^2)$, where ν is Poisson's ratio.

Actually the aforementioned expression for J is the component of a vector $\mathbf{J}_i$ $(i = 1, 2)$ in the plane of the crack (say $J \equiv J_1$).

One can also quite easily calculate J_2, the component of J_i normal to the crack plane, which was found to be (cf. e.g., [4, 5]) for the same crack tip

$$J_2 = -2K_IK_{II}/E \tag{2}$$

for plane stress, with a corresponding modification for plane strain as for J_1.

The J-integral (i.e., J_1) has been given a precise and clear physical significance as the rate of total potential energy-release per unit crack-tip advance. It is thus identical to Irwin's crack extension force. Attempts have been made to supply analogous physical interpretations for J_2 [4, 6] by postulating that the crack will skew and the tip advance either in the direction of the vector **J**, or by claiming that if the crack has advanced under an angle ϕ with respect to its plane, the energy release will be

$$G(\phi) = J_1 \cos\phi + J_2 \sin\phi$$

It is the purpose of this paper to examine energy-release rates of a single, plane, finite crack with traction-free surfaces in an infinite linearly elastic, uniformly stressed medium and to establish the role which J_2, as just given, plays in this connection. It will be shown, in particular, that J_2, as given by (2), is not path-independent and, in fact, is a function of the length of the crack enclosed by the line integral.

Only for some special applied stress fields, to be discussed in the sequel, does J_2 retain its value given by (2) and is path-independent in the sense of J_1. In that case, J_2 is connected to the L-integral in the same manner as J_1 is related to the M-integral, this latter result having been discussed recently by Freund [7]. (Here L and M-integrals refer to conservation laws found independently by Günther [8] and Knowles and Sternberg [9], which were interpreted as energy-release rates for a cavity by Budiansky and Rice [10].) The special results previously mentioned will follow from more general considerations in which a general homogeneous stress field is applied and a contour enclosing the crack completely is introduced.

Conservation Laws

Consider a two-dimensional deformation field referred to Cartesian coordinates x_1, x_2 described by the displacement $u_i = u_i(x_1, x_2)$. The J-integral has been defined as [1, 3]

$$J = \oint_C (W dx_2 - T_i u_{i,1} dl) \tag{3}$$

where C is a closed curve in the x_1, x_2 plane surrounding a crack tip, W is the strain-energy density and T_i is the traction (stress vector) acting on the outer side of C. As already mentioned, J is the x_1-component of the vector

$$J_k = \oint_C (W n_k - T_i u_{i,k})\, dl \qquad k = 1,2 \tag{4}$$

where n_i is the unit outward normal vector to C in the x_1, x_2 plane.

Other path-independent integrals established in [8, 9] in two dimensions are

$$L_3 \equiv L = \oint_C e_{3ij}(W x_j n_i - T_i u_j - T_k u_{k,i} x_j)\, dl \tag{5}$$

and

Contributed by the Applied Mechanics Division for presentation at the Winter Annual Meeting, Washington, D. C., November 15–20, 1981, of THE AMERICAN SOCIETY OF MECHANICAL ENGINEERS.

Discussion on this paper should be addressed to the Editorial Department, ASME, United Engineering Center, 345 East 47th Street, New York, N. Y. 10017, and will be accepted until December 1, 1981. Readers who need more time to prepare a discussion should request an extension from the Editorial Department. Manuscript received by ASME Applied Mechanics Division, September, 1980; final revision, January, 1981. Paper No. 81-WA/APM-3.

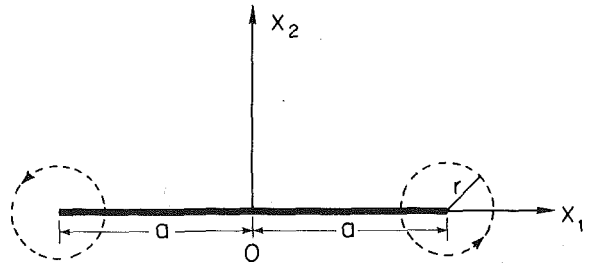

Fig. 1 Paths around crack tip

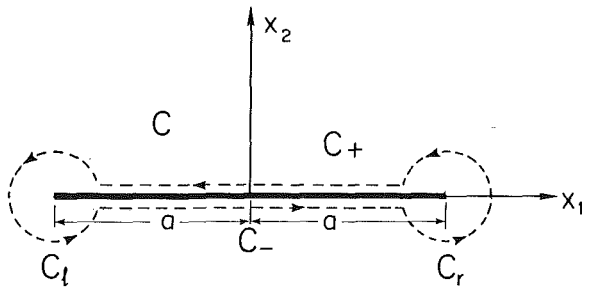

Fig. 2 Path enclosing the crack completely

$$M = \oint_C (W x_i n_i - T_k u_{k,i} x_i)\, dl \tag{6}$$

where e_{ijk} is the alternating tensor.[1]

The foregoing expressions, as taken from Budiansky and Rice [10], actually imply different definitions of the contour C. The path C of the J (J_1) integral has been introduced originally as one surrounding a crack tip and is path-independent as long as it does not enclose any other singularity, such as for instance the other tip of the same plane crack, while the contours in L and M are considered in the same paper [10] as surrounding the whole defect, i.e., crack, and not just a crack tip. As regards J_2, its value around a crack tip is to be calculated by expression (4), but its path-independence for cracks has, to authors' knowledge, never been established.

As mentioned, our aim here is to investigate the properties of J_2 and L in the presence of a plane crack by considering different contours. To avoid confusion, we will retain the notation J_k for contours around a crack tip, while if the integral (4) is taken around the complete crack, we shall call the corresponding value of the integral F_k.

We proceed to evaluate these integrals in the presence of a crack of length $2a$ placed as in Fig. 1 with respect to a system of coordinates 0, x_1, x_2 and subjected to far-field applied stresses σ^A_{11}, σ^A_{12}, σ^A_{22}. We choose the paths indicated in Figs. 1 and 2. To carry out the integration along circular paths of small radius r around crack tips, we can make use of the singular fields near crack tips (see, e.g., [11]).

The singular stress field and the singular displacement field near the right crack tip are of the form

$$\left.\begin{aligned} \sigma^m_{ij} &= K_m (2\pi r)^{-1/2} f^m_{ij}(\theta) \\ u^m_i &= (K_m/2E)(r/2\pi)^{1/2} f^m_i(\theta) \end{aligned}\right\} \begin{matrix} i, j = 1, 2 \\ m = \text{I, II} \end{matrix} \tag{7}$$

The specific dependence on θ is not relevant here, except the feature that all functions are either even or odd in θ, namely, $f^{\text{I}}_{22}, f^{\text{I}}_{11}, f^{\text{II}}_{21}, f^{\text{I}}_{1}$, and f^{II}_{2} are even in θ, while $f^{\text{I}}_{21}, f^{\text{II}}_{11}, f^{\text{II}}_{22}, f^{\text{I}}_{2}$, and f^{II}_{1} are odd in θ. We recall that for plane stress

$$W = \frac{1}{2E}(\sigma^2_{11} + \sigma^2_{22} - 2\nu\sigma_{11}\sigma_{22}) + \frac{(1+\nu)}{E}\sigma^2_{12} \tag{8}$$

Further

$$\begin{aligned} x_1 &= a + r\cos\theta & dx_1 &= -r\sin\theta\, d\theta \\ x_2 &= r\sin\theta & dx_2 &= r\cos\theta\, d\theta \\ n_1 &= \cos\theta & dl &= r\, d\theta \\ n_2 &= \sin\theta \end{aligned} \tag{9}$$

and

$$\begin{aligned} u_{i,1} &= u_{i,r}\cos\theta - \frac{1}{r}u_{i,\theta}\sin\theta \\ u_{i,2} &= u_{i,r}\sin\theta + \frac{1}{r}u_{i,\theta}\cos\theta \end{aligned} \tag{10}$$

In constructing the integrand, we have to be mindful of the fact that the total stress has contributions from Mode I and Mode II, while the regular stress field σ^A_{11} is negligible. Thus

$$\sigma_{ij} = \sigma^{\text{I}}_{ij} + \sigma^{\text{II}}_{ij} \tag{11a}$$

Similarly

$$u_i = u^{\text{I}}_i + u^{\text{II}}_i \tag{11b}$$

In noting the odd-even property of all functions involved, the integral (in θ) over a small circle with radius r, can now be easily evaluated from $-\pi$ to π.

The results for J_i of the crack tip $x_1 = a$ are, as already noted in the Introduction

$$\begin{aligned} J_1 &= (K^2_{\text{I}} + K^2_{\text{II}})/E; & K_{\text{I}} &= \sigma^A_{22}\sqrt{\pi a} \\ J_2 &= -2K_{\text{I}}K_{\text{II}}/E; & K_{\text{II}} &= \sigma^A_{12}\sqrt{\pi a} \end{aligned} \tag{12}$$

For the crack tip $x_1 = -a$ the sign of J_1 and J_2 is reversed.

We next consider possible contributions to F_1 and F_2 from the part of the contour along crack faces. We note that the term with T_i will not contribute to either integral, since the crack faces are traction-free. Thus the only possible contribution will be due to the term with W. From equation (4) we see that for $k = 1$ along crack faces $n_1 = 0$ and thus there will be no contribution to F_1. As regards F_2, the integral along the upper crack face in the $-x_1$ direction and along the lower crack face in the x_1 direction, to avoid misunderstandings, shall be denoted by F_{2a}. Thus

$$\begin{aligned} F_{2a} &= \int_{C+} W n_2 dl + \int_{C-} W n_2 dl \\ &= \int_{-a}^{a} (W_+ - W_-)\, dx_1 = \int_{-a}^{a} [W]\, dx_1 \end{aligned}$$

where $W_+ - W_- = [W]$ is found to be, by means of complex representation, and (8),

$$[W] = -4\sigma^A_{12}(\sigma^A_{11} - \sigma^A_{22})x_1(a^2 - x^2_1)^{-1/2}/E \tag{13}$$

It is observed that $[W]$ is an odd function of x_1, such that

$$F_{2a} = \int_{-a}^{a} [W] dx_1 = 0 \tag{14}$$

We note, thus, that the integral (4), taken along the closed path enclosing the crack completely, as in Fig. 2, leads to

$$F_1 = 0; \qquad F_2 = 0 \tag{15}$$

We postpone the discussion of the results obtained and proceed to evaluate the L-integral (as given by equation (5)) along the closed path of Fig. 2. Let us note that along circular paths the product $T_i u_j$ is independent of the radius; but dl is proportional to r and as $r \to 0$, the integral vanishes. Thus the only terms which contribute to L along circular paths are the same as those we had to consider in evaluating F_2, except that each is multiplied by x_j. We denote by L_R, L_L the contributions to L along the right and the left circular paths, respectively. We thus have, with J_2 given by equation (12)

$$L_R + L_L = -2aJ_2$$

[1] It is unfortunate that the foregoing definition, taken by Budiansky and Rice [10] from [9], implies the definition of a moment **M** of a force **P** as **P** × **r**, rather than the more customary **r** × **P**, which has been introduced in [8].

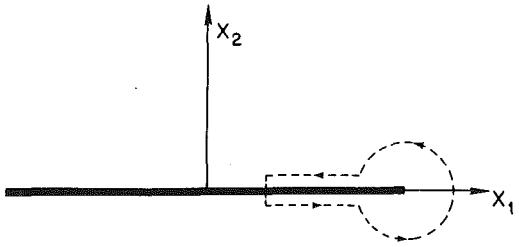

Fig. 3 Path to show path-dependence of J_2

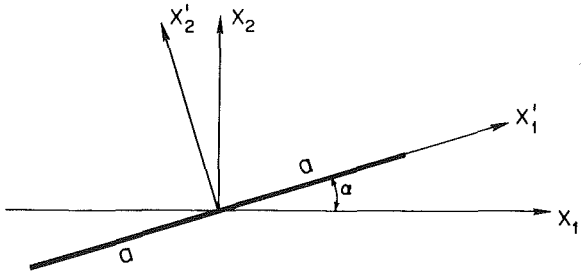

Fig. 4 Crack at angle α

Along crack faces the terms with T_i vanish and $n_1 = 0$, such that the only contribution to L, denoted by L_{2a}, is

$$L_{2a} = -\int_{-a}^{a} [W]x_1 dx_1 = 2\sigma_{12}^A(\sigma_{11}^A - \sigma_{22}^A)\pi a^2/E \tag{16}$$

or

$$L_{2a} = J_2 a + 2\sigma_{12}^A\sigma_{11}^A\pi a^2/E$$

The total L is

$$L = L_R + L_L + L_{2a} = 2\sigma_{12}^A(\sigma_{22}^A + \sigma_{11}^A)\pi a^2/E \tag{17}$$

or

$$L = -aJ_2 + 2\sigma_{12}^A\sigma_{11}^A\pi a^2/E = 2K_{II}(K_I + \sigma_{11}^A\sqrt{\pi a})a/E \tag{18}$$

or

$$L = -2aJ_2 + 2\sigma_{12}^A(\sigma_{11}^A - \sigma_{22}^A)\pi a^2/E \tag{19}$$

We are now ready to discuss the results obtained for the integrals J_2, F_2, and L. From expression (13) it is obvious that J_2 is not path-independent in the sense of J_1; namely, if we consider a path enclosing the crack tip, but not infinitesimal, the result will depend on the path selected. Thus J_2 as given by equation (12) holds only for infinitesimal paths surrounding the crack tip. Only if there would be no contributions to J_2 along crack faces, i.e., if $[W] = 0$, will J_2 become path-independent in the sense of J_1. From expression (13) we observe that this will be the case if $\sigma_{11}^A = \sigma_{22}^A$ or if $\sigma_{12}^A = 0$. The latter case, however, is of no interest to us in this study because J_2 and L vanish identically for $\sigma_{12}^A = 0$ (as can be seen from (12) and (17)).

As is known, J_1 is insensitive to the presence of σ_{11}^A. By contrast, from the foregoing discussion we see that J_2 is strongly affected by σ_{11}^A. It is noteworthy that $\sigma_{11}^A = 0$ does not correspond to the case of J_2 being path-independent. From expression (19) we observe that L cannot be expressed through J_2 completely, again because of the contribution to L along the crack faces. Thus, as J_2, L is not path-independent if a path is chosen as in Fig. 3.

We note, however, that for special applied stress fields just mentioned, namely,

$$\sigma_{11}^A = \sigma_{22}^A \tag{20}$$

L_{2a} will vanish and thus in this special case

$$L = -2aJ_2 \tag{21}$$

This result is analogous to the relation

$$M = 2aJ_1 \tag{22}$$

which holds for all homogeneous stress fields and which has been discussed in [7]. Let us emphasize that equation (22) formally expresses the equivalence of J_1 and M, i.e., the physical interpretation of one can be given in terms of the other. The translation of both crack tips in opposite directions described by J_1 for each crack tip is equivalent to self-similar expansion of the whole crack described by M. By contrast, the validity of equation (21) is restricted by condition (20) and in general L and J_2 are not equivalent. Thus their physical meaning must be different.

Crack Energies and Energy-Release Rates

Consider again a plane homogeneous stress field in an infinite body specified by components of stress σ_{11}^A, σ_{12}^A, and σ_{22}^A with respect to a Cartesian system of coordinates 0, x_1, x_2. A plane crack of length $2a$ with traction-free surfaces is placed into the field along the x_1-axis with its center at the origin 0. The insertion of the crack into the field induces a change U of total energy in the body which, as is known, is given by

$$U = \frac{1}{2}\int_{-a}^{a} \sigma_{2j}^A \Delta u_j(x_1)\, dx_1 \tag{23}$$

where $\Delta u_j(x_1)$ is the discontinuity in displacement across the crack and summation over j is implied. The evaluation of this integral yields, for plane stress

$$U = U_I + U_{II};\quad U_I = \pi a^2(\sigma_{22}^A)^2/E,\quad U_{II} = \pi a^2(\sigma_{12}^A)^2/E \tag{24}$$

For short, U may be referred to as the crack energy.

Let us assume next that, instead of being placed along the x_1-axis, the crack, with its center still at 0, is inserted at a *small* angle α with respect to x_1. The relevant system of coordinates is now 0, x_1' x_2' (see Fig. 4) and the stress field referred to this system is

$$\begin{aligned}
\sigma_{11}' &= \sigma_{11}\cos^2\alpha + 2\sigma_{12}\sin\alpha\cos\alpha + \sigma_{22}\sin^2\alpha \\
\sigma_{12}' &= -\sigma_{11}\sin\alpha\cos\alpha + \sigma_{12}(\cos^2\alpha - \sin^2\alpha) + \sigma_{22}\sin\alpha\cos\alpha \\
\sigma_{22}' &= \sigma_{11}\sin^2\alpha - 2\sigma_{12}\sin\alpha\cos\alpha + \sigma_{22}\cos^2\alpha
\end{aligned} \tag{25}$$

To evaluate U' we need to know only σ_{22}' and σ_{12}', which, for small α are

$$\begin{aligned}
\sigma_{22}' &= \sigma_{22} - 2\alpha\sigma_{12} \\
\sigma_{12}' &= \sigma_{12} + \alpha(\sigma_{22} - \sigma_{11})
\end{aligned} \tag{26}$$

Thus, since

$$U' = \pi a^2(\sigma_{22}'^2 + \sigma_{12}'^2)/E \tag{27}$$

we obtain

$$U' = \pi a^2[\sigma_{22}^2 + \sigma_{12}^2 - 2\alpha\sigma_{12}(\sigma_{11} + \sigma_{22})]/E \tag{28}$$

Now let us consider the difference $U' - U$ and divide it by α, which is to be interpreted as the energy release of a crack of length $2a$ per unit crack rotation. Thus $(U' - U)/\alpha \equiv G_R$ is the rotational energy-release rate, given by

$$G_R = -2\sigma_{12}^A(\sigma_{11}^A + \sigma_{22}^A)\pi a^2/E \tag{29}$$

We recall that for a single plane crack in an infinite body the applied components of stress σ_{22}^A and σ_{12}^A are related to the stress-intensity factors K_I and K_{II} of the singular stress field near the crack tips as

$$\sigma_{22}^A = \frac{K_I}{\sqrt{\pi a}},\qquad \sigma_{12}^A = \frac{K_{II}}{\sqrt{\pi a}} \tag{30}$$

We may thus write G_R also as

$$G_R = -2K_{II}(K_I + \sigma_{11}^A\sqrt{\pi a})a/E \tag{31}$$

This result can be readily generalized for an arbitrary angle ϕ with respect to the x_1-axis. The energy of a crack of length $2a$ in this configuration is

$$U = \frac{\pi a^2}{E}(\sigma_{22}'^2 + \sigma_{12}'^2) = \frac{\pi a^2}{E}[\sigma_{11}^2 \sin^2\phi + \sigma_{22}^2 \cos^2\phi + \sigma_{12}(\sigma_{12} - 2\sin\phi\cos\phi(\sigma_{11} + \sigma_{22}))] \quad (32)$$

and its derivative with respect to ϕ is

$$\frac{\partial U}{\partial \phi} \equiv G_\phi = \frac{\pi a^2}{E}[\sin 2\phi(\sigma_{11}^2 - \sigma_{22}^2) - 2\cos 2\phi\sigma_{12}(\sigma_{11} + \sigma_{22})] \quad (33)$$

The aforementioned expression for the rotational energy-release rate indeed reduces for $\phi = 0$ to G_R given by equation (29), which, up to the sign, is identical to L given by equation (17). This shows that L represents the rotational energy-release rate. This equivalence of L and G_R holds for any uniform stress field into which a crack is placed. Thus the relations between L and J_2 discussed in the previous section apply now to G_R and J_2.

Finally, we would like to express our results with respect to principal axes. If both the applied stress field and the crack (at angle γ), see Fig. 5, are referred to the principal axes x_1^p, x_2^p, then

$$U = \frac{\pi a^2}{E}[(\sigma_{11}^p)^2 \sin^2\gamma + (\sigma_{22}^p)^2 \cos^2\gamma] \quad (34)$$

and

$$\frac{dU}{ad\gamma} \equiv G_\gamma = \frac{\pi a}{E}\sin 2\gamma[(\sigma_{11}^p)^2 - (\sigma_{22}^p)^2] \quad (35)$$

We hence recognize the rotational energy-release rate G_R to be the sum of 2 additive contributions, namely,

$$G_R = (J_2 - 2K_{II}\sigma_{11}^A\sqrt{\pi a}/E)a \quad (36)$$

Thus the rotational energy-release rate G_R is identical to the value of the integral L, except for a change in sign, the latter having to do with the definition of L. Examining the rotational energy-release rate G_R (or L) in the form of equation (19), we remark again that J_2 contributes to this rate.

Concluding Remarks

On the basis of the foregoing analysis, it may be concluded that the integrals L and M provide a more natural description of energy-release rates (or forces) associated with plane cracks than the integrals J_1 ($\equiv$J) and J_2. If one considers a contour enclosing the whole crack completely, then in the case studied here (uniform applied stress field in the absence of the crack) both J_1 and J_2 vanish. If one considers a contour enclosing only one crack tip, then J_2 is not path-independent. Only for special applied fields for which $\sigma_{11}^A = \sigma_{22}^A$, does J_2 become path-independent in the same sense as J_1.

It is noted further that the energy release rate for rotation G_R may be used experimentally in a capacity analogous to J. Instead of following the standard procedure of changing the crack length in compliance tests, experiments could be performed by rotating the applied stress field with respect to the crack plane, keeping the crack length constant. Thus the procedure would be clearly nondestructive and would supply valuable information. This novel testing method will be discussed in a separate paper.

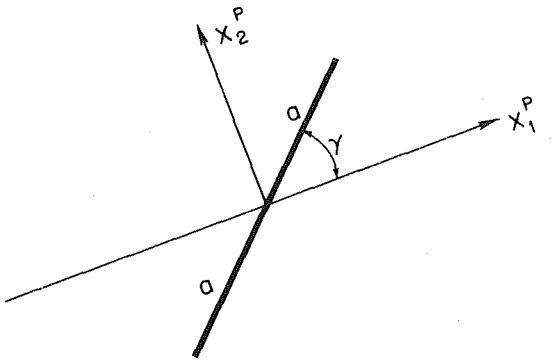

Fig. 5 Crack referred to principal axes

Acknowledgement

The authors are grateful to their Stanford colleague, Prof. D. M. Barnett and to Prof. J. R. Willis, visiting Stanford in 1980 from the University of Bath, England, for many valuable discussions. This work has been supported in part by AFOSR Grant F49630-79-C-0217 and EPRI Grant 609-1 to Stanford University.

References

1 Rice, J. R., "A Path-Independent Integral and the Approximate Analysis of Strain Concentration by Notches and Cracks," ASME JOURNAL OF APPLIED MECHANICS, Vol. 35, 1968, pp. 379–386.

2 Eshelby, J. D., "The Energy Momentum Tensor in Continuum Mechanics," *Inelastic Behavior of Solids*, ed., Kanninen, M. F., et al., McGraw-Hill, New York, 1970.

3 Rice, J. R., "Mathematical Analysis in the Mechanics of Fracture," *Fracture, An Advanced Treatise*, Vol. II, ed., Liebowitz, H., Academic Press, 1968, pp. 191–311.

4 Cherepanov, G. P., *Mechanics of Brittle Fracture*, Moscow, Publishing House "Nauka," 1974; English translation to be published by McGraw-Hill.

5 Bergez, D., "Determination of Stress-Intensity Factors by Use of Path-Independent Integrals," *Mechanics Research Communications*, Vol. 1, 1974, pp. 179–180.

6 Hussain, M. C., Pu, S. L., and Underwood, J., "Strain Energy Release Rate for a Crack Under Combined Mode I and Mode II," *Fracture Analysis, Proceedings of the 1973 National Symposium on Fracture Mechanics*, Part II, ASTM Special Technical Publication 560, 1973, pp. 2–28.

7 Freund, L. B., "Stress-Intensity Factor Calculations Based on a Conservation Integral," *International Journal of Solids and Structures*, Vol. 14, 1978, pp. 241–250.

8 Günther, W., "Über einige Randintegrale der Elastomechanik," *Abhandlungen der Braunschweigischen Wissenschaftlichen Gesellschaft*, Vol. XIV, Verlag Friedr. Vieweg & Sohn, Braunschweig, 1962.

9 Knowles, J. K., and Sternberg, E., "On a Class of Conservation Laws in Linearized and Finite Elastostatics," *Arch. Rat. Mech. Anal.*, Vol. 44, 1972, pp. 187–211.

10 Budiansky, B., and Rice, J. R., "Conservation Laws and Energy-Release Rates," ASME JOURNAL OF APPLIED MECHANICS, Vol. 40, 1973, pp. 201–203.

11 Lawn, B. R., and Wilshaw, T. R., *Fracture of Brittle Solids*, Cambridge University Press, 1975.

K. Hayashi[1]
Visiting Scholar.

S. Nemat-Nasser
Professor of Civil Engineering and Applied Mathematics. Mem. ASME

Department of Civil Engineering, The Technological Institute, Northwestern University, Evanston, Ill. 60201

On Branched, Interface Cracks

The problem of branched, external cracks in the interface between two elastic materials is considered under the plane strain condition. A small interface contact region is introduced in the vicinity of each crack tip in order to remove oscillatory singularities. The branches are replaced by continuous distribution of edge dislocations, and, with the aid of Muskhelishvili's potential method, the problem is reduced to a system of singular integral equations which are defined on the branches and the perfectly bonded region of the interface. The unknown functions of these integral equations are the shear stress acting on the bonded region, and the density functions of the edge dislocations. Stress-intensity factors of the interface cracks and branches are obtained numerically for several branch angles and branch lengths. Finally, the question of kinking from a tip of an interface crack is discussed with the aid of the results.

Introduction

The problem of a branched crack in a homogeneous material has received considerable attention in recent years; see, for example, Lo [1] who obtains the stress-intensity factor at the tip of a branched crack and also gives some account of other related work. The problem of a *branched crack* at the interface of two dissimilar materials, on the other hand, does not seem to have been addressed.

It is well known that the conventional formulation of interface cracks generally leads to oscillatory singularities that imply material overlap in the vicinity of the crack tips, as has been pointed out by England [2], and by Malyshev and Salganik [3]. This essential difficulty was first resolved by Comninou [4] who observed that the introduction of a very small region of frictionless contact at the neighborhood of each crack tip, removes the oscillatory singularity. Comninou's solution has since been successfully applied to a variety of interface problems; see, e.g., [5–10]. It has been shown by Achenbach, Keer, Khetan, and Chen [11], that the introduction of a small cohesive zone of a certain characteristic in the vicinity of the crack tip also serves to remove the corresponding oscillatory singularity; this is a generalization of the Dugdale-Barrenblatt model for application to interface crack problems.

The present paper deals with the problem of branched, external, interface cracks between two dissimilar half planes which are subjected to tensile loads applied perpendicularly to the interface far from the crack. The oscillatory singularities are removed by the introduction of frictionless contact regions near the tips of the interface crack. Each branch is replaced by a continuous distribution of edge dislocations, and the solution for an elastic half plane subjected to a point force is used in order to arrive at a system of singular integral equations whose unknown functions are the shear stress acting on the bonded region in the interface, and the density of edge dislocations on the branches. Numerical results for stress-intensity factors are obtained by the method of Erdogan, et al. [12], and Gupta and Erdogan [13], and the results are tabulated for several branch angles and branch lengths. Kinking of an interface crack is also discussed with the aid of these numerical results.

Statement of Problem

Let the elastic upper half plane S^+, with moduli μ_1 and ν_1, be bonded over a part, L_1, to the elastic lower half plane S^-, with moduli μ_2 and ν_2, where μ_ρ and ν_ρ, $\rho = 1, 2$, denote the shear modulus and the Poisson ratio, respectively. In addition, let L_4 and L_4' be two edge cracks extending into the lower half plane from certain points on the *unbonded* parts of the interface; see Fig. 1. Tensile loads of total magnitude N are applied at infinity, perpendicular to the interface, and, since N is assumed finite, the corresponding stresses vanish far away from the bonded part of the interface. Upon the load application, the external interface cracks open, except for small intervals, L_2 and L_2', near the ends where frictionless contacts are assumed in order to avoid oscillatory singularities. A fixed rectangular Cartesian coordinate system, with coordinate axes x_α, is used; Fig. 1. Throughout this work, Greek indices take on values 1, 2, and, unless otherwise stated, the usual summation convention on repeated indices is employed. A supplementary rectangular Cartesian coordinate system, ζ_α, is also used, as shown in Fig. 1. In what follows, the superscript 0 identifies functions in the ζ_α-coordinate system.

The boundary conditions of the problem are expressed in terms of the stress tensor, $t_{\alpha\beta}$, and the displacement vector, u_α, referred to the x_α-coordinate system, as follows:

(*a*) Tractions and displacements are continuous across $L_1(|x_1| < l)$:

[1] On leave from: Department of Mechanical Engineering, Tohoku University, Sendai 980, Japan.

Contributed by the Applied Mechanics Division of THE AMERICAN SOCIETY OF MECHANICAL ENGINEERS, and presented at the 1981 Joint ASME/ASCE Applied Mechanics, Fluids Engineering, and Bioengineering Conference, University of Colorado, Boulder, Colo., June 22–27, 1981.

Discussion on this paper should be addressed to the Editorial Department, ASME, United Engineering Center, 345 East 47th Street, New York, N. Y. 10017, and will be accepted until December 1, 1981. Readers who need more time to prepare a discussion should request an extension from the Editorial Department. Manuscript received by ASME Applied Mechanics Division, June, 1980; final revision, September, 1980. Paper No. 81-APM-20.

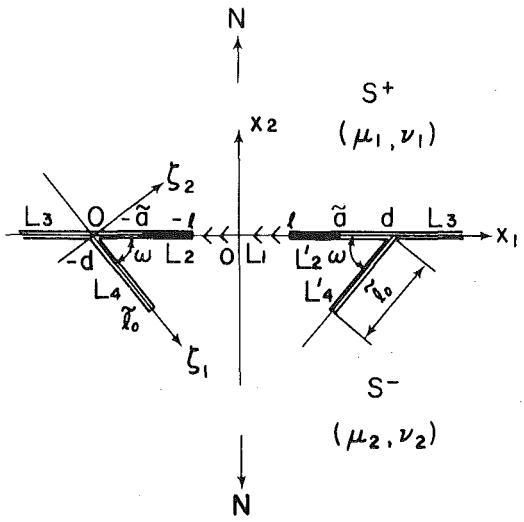

Fig. 1 Geometry and coordinate systems

$$t_{12}^{(1)} = t_{12}^{(2)}, \quad t_{22}^{(1)} = t_{22}^{(2)}, \tag{1}$$

$$u_{1,1}^{(1)} = u_{1,1}^{(2)}, \quad u_{2,1}^{(1)} = u_{2,1}^{(2)}. \tag{2}$$

(*b*) Two half planes are in frictionless contact over L_2 and $L_2'(l < |x_1| < \tilde{a})$:

$$t_{12}^{(1)} = t_{12}^{(2)} = 0, \qquad t_{22}^{(1)} = t_{22}^{(2)}, \tag{3}$$

$$t_{22}^{(1)} < 0, \qquad t_{22}^{(2)} < 0, \tag{4}$$

$$u_{2,1}^{(1)} = u_{2,1}^{(2)}. \tag{5}$$

(*c*) Tractions vanish along $L_3(|x_1| > \tilde{a})$:

$$t_{12}^{(1)} = t_{12}^{(2)} = 0, \quad t_{22}^{(1)} = t_{22}^{(2)} = 0. \tag{6}$$

(*d*) Tractions vanish on the surfaces of the branches $L_4(0 < \zeta_1 < \tilde{l}_0)$ and L_4':

$$t_{12}^{0(2)} = 0, \quad t_{22}^{0(2)} = 0. \tag{7}$$

(*e*) The resultant of the tractions along $L_1 + L_2 + L_2'$ is given:

$$\int_{-\tilde{a}}^{\tilde{a}} t_{22}^{(1)} dx_1 = \int_{-\tilde{a}}^{\tilde{a}} t_{22}^{(2)} dx_1 = N, \tag{8}$$

$$\int_{-l}^{l} t_{12}^{(1)} dx_1 = \int_{-l}^{l} t_{12}^{(2)} dx_1 = 0. \tag{9}$$

Here, superscripts 1 and 2 in parentheses denote functions defined in S^+ and S^-, respectively. The comma followed by an index denotes partial differentiation with respect to the corresponding coordinate.

Singular Integral Equations

The method of Green's function and two basic solutions for an elastic half plane, are employed; these are: the stress and displacement fields induced by a force which acts at a point on the free surface; and the fields induced by an interior edge dislocation.

When an elastic lower half plane is subjected to a force,[2] p_α, which is parallel to the x_α-axis and passes through point $(x_1 = \xi, x_2 = 0)$, the corresponding elastic potential functions, $\Phi(z)$ and $\Psi(z)$, of $z = x_1 + ix_2$, [14], are given by [15],

$$\Phi(z) = \frac{p_2 - i\,p_1}{2\pi i} \frac{1}{z - \xi}, \tag{10}$$

$$\Psi(z) = \frac{p_1}{\pi} \frac{1}{z - \xi} + \frac{p_2 - i\,p_1}{2\pi i} \frac{z}{(z - \xi)^2}. \tag{10 (Cont.)}$$

On the surface of the half plane, the x_1-displacement gradient is

$$u_{1,1} + iu_{2,1} = \frac{p_2 - i\,p_1}{4\mu} \left[\frac{\kappa + 1}{\pi i} \frac{1}{x_1 - \xi} + (\kappa - 1)\delta(x_1 - \xi) \right], \tag{11}$$

where μ is the shear modulus, $\kappa = 3 - 4\nu$, ν is Poisson's ratio, and $\delta(x_1 - \xi)$ denotes the Dirac delta function.

Consider next, an interior edge dislocation line running perpendicular to the z-plane through a point, $z = \bar{\alpha}$, in an elastic lower half plane. The Burgers vector of this edge dislocation makes an angle θ with the positive direction of the x_1-axis, and its magnitude is b. The corresponding elastic potential functions are

$$\Phi(z) = \frac{i\mu b}{\pi(\kappa + 1)} \left\{ \frac{e^{i\theta}}{z - \bar{\alpha}} - \frac{e^{i\theta}}{z - \alpha} - \frac{\alpha - \bar{\alpha}}{(z - \alpha)^2} e^{-i\theta} \right\},$$

$$\Psi(z) = -\frac{i\mu b}{\pi(\kappa + 1)} \left\{ \frac{e^{-i\theta}}{z - \bar{\alpha}} - \frac{\alpha e^{i\theta}}{(z - \bar{\alpha})^2} - \frac{e^{-i\theta}}{z - \alpha} + \frac{\alpha e^{i\theta}}{(z - \alpha)^2} + \frac{\alpha - \bar{\alpha}}{(z - \alpha)^2} e^{-i\theta} + \frac{2\alpha(\alpha - \bar{\alpha})}{(z - \alpha)^3} e^{-i\theta} \right\}. \tag{12}$$

The branched, interface crack system of Fig. 1 will now be formulated in terms of solutions (10)–(12). To this end, assume that the bimaterial is cut along the x_1-axis over L_1, and apply the necessary tractions as follows: For S^+, apply normal tractions $-p_2(\xi)$ on $L_1 + L_2 + L_2'$ and shear tractions $-p_1(\xi)$ on L_1, and for S^-, apply the same tractions but with opposite signs. Furthermore, on L_4 and L_4', distribute edge dislocations in such a manner as to preserve the symmetry with respect to the x_2-axis, and let $b_\alpha(\zeta_1)$ denote the Burgers vector of the edge dislocations on L_4 referred to the ζ_α-coordinate system.

The unknown functions, $p_\alpha(\xi)$ and $b_\alpha(\zeta_1)$, $\alpha = 1, 2$, must be such that the displacement continuity conditions (2) and (5), and the stress-free conditions (7) are satisfied. These requirements lead to the following integral equations:

$$\beta p_2(x_1) + \frac{1}{\pi} \int_{-l}^{l} \frac{p_1(\xi)}{\xi - x_1} d\xi + \frac{1 + \lambda}{4\pi\gamma} \int_0^{\tilde{l}_0} b_\alpha(\rho) f_{2\alpha}(x_1, \rho) d\rho = 0, \quad |x_1| < l, \tag{13}$$

$$\beta p_1(x_1) H(x_1) - \frac{1}{\pi} \int_{-\tilde{a}}^{\tilde{a}} \frac{p_2(\xi)}{\xi - x_1} d\xi - \frac{1 + \lambda}{4\pi\gamma} \int_0^{\tilde{l}_0} b_\alpha(\rho) f_{1\alpha}(x_1, \rho) dx_1 = 0, \quad |x_1| < \tilde{a}, \tag{14}$$

$$\int_0^{\tilde{l}_0} \frac{b_\alpha(\rho)}{\rho - \zeta_1} d\rho - \int_0^{\tilde{l}_0} b_\beta(\rho) h_{\alpha\beta}(\zeta_1, \rho) d\rho + \gamma \int_{-\tilde{a}}^{\tilde{a}} p_2(\xi) g_{\alpha 2}(\zeta_1, \xi) d\xi + \gamma \int_{-l}^{l} p_1(\xi) g_{\alpha 1}(\zeta_1, \xi) d\xi = 0, \quad 0 < \zeta_1 < \tilde{l}_0, \tag{15}$$

where

$$\gamma = \frac{1 + \kappa_2}{4\mu_2}, \quad H(x_1) = \begin{cases} 1 & \text{for } |x_1| < l \\ 0 & \text{for } |x_1| > l; \end{cases} \tag{16}$$

λ and β are Dundurs' parameters,

$$\lambda = \frac{\mu_1(\kappa_2 + 1) - \mu_2(\kappa_1 + 1)}{\mu_2(\kappa_1 + 1) + \mu_1(\kappa_2 + 1)}, \quad \beta = \frac{\mu_1(\kappa_2 - 1) - \mu_2(\kappa_1 - 1)}{\mu_2(\kappa_1 + 1) + \mu_1(\kappa_2 + 1)}; \tag{17}$$

functions $f_{\alpha\beta}(x_1, \rho)$, $g_{\alpha\beta}(\zeta_1, \xi)$, and $h_{\alpha\beta}(\zeta_1, \rho)$ are given in Appendix *A*.

Equation (14) can be viewed as a Cauchy singular equation for the unknown function $p_2(x_1)$. It can be solved formally by treating $p_1(x_1)$ and $b_\alpha(\zeta_1)$ as known functions, with $p_1(x_1)$ assumed singular at $x_1 = \pm l$ so that $p_2(x_1)$ is also singular at these points. Since it is assumed

[2] Since plane strain is assumed, p_α measures force per unit thickness normal to the plane.

that the two bodies are in the frictionless contact along L_2 and L_2', $p_2(x_1)$ must be bounded at $x_1 = \pm\tilde{a}$, and the solution of (14) is

$$p_2(x_1) = \frac{1+\lambda}{4\pi^2\gamma} w(x_1) \int_0^{l_0} b_\alpha(\rho) F_\alpha(x_1, \rho) d\rho - \frac{\beta}{\pi} w(x_1) \int_{-l}^{l} \frac{p_1(\xi)}{w(\xi)(\xi - x_1)} d\xi, \quad (18)$$

where $w(x_1)$ is the characteristic function of this singular integral equation, i.e.,

$$w(x_1) = \sqrt{\tilde{a}^2 - x_1^2}. \quad (19)$$

The functions $F_\alpha(x_1, \rho)$, $\alpha = 1, 2$, are given in Appendix B.

The solution (18) must comply with the following consistency condition [16]:

$$\pi\beta \int_{-l}^{l} \frac{p_1(\xi)}{w(\xi)} d\xi - \frac{1+\lambda}{4\gamma} \int_0^{l_0} \left\{ b_\alpha(\rho) \int_{-\tilde{a}}^{\tilde{a}} \frac{f_{1\alpha}(\xi,\rho)}{w(\xi)} d\xi \right\} d\rho = 0 \quad (20)$$

which is satisfied automatically, because, in view of symmetry, $f_{1\alpha}(\xi, \rho)$ and $p_1(\xi)$ are odd with respect to ξ.

Now, consider the following nondimensional notation:

$$a = \frac{\tilde{a}}{l}, \quad l_0 = \frac{l_0}{l}, \quad x = \frac{x_1}{l}, \quad t = \frac{\xi}{l}, \quad y = \frac{1}{l_0}\frac{\zeta_1}{l}, \quad s = \frac{1}{l_0}\frac{\rho}{l},$$

$$P(x) = \frac{p_2(x_1)}{N/l}, \quad Q(x) = \frac{p_1(x_1)}{N/l}, \quad B_\alpha(y) = \frac{b_\alpha(\zeta_1)}{\gamma N/l}, \quad (21)$$

and from (18) obtain

$$P(x) = \frac{1+\lambda}{4\pi^2} W(x) l_0 \int_0^1 B_\alpha(s) F_\alpha(x, l_0 s) ds - \frac{\beta}{\pi} W(x) \int_{-1}^{1} \frac{Q(t)}{W(t)(t-x)} dt, \quad (22)$$

where

$$W(x) = \sqrt{a^2 - x^2}. \quad (23)$$

Substituting from (18) into (13) and (15), and using (21), one arrives at

$$\int_{-1}^{1} \frac{Q(t)}{t-x} dt + \frac{\beta^2}{1-\beta^2} \int_{-1}^{1} \left\{ 1 - \frac{W(x)}{W(t)} \right\} \frac{Q(t)}{t-x} dt + \frac{1+\lambda}{4(1-\beta^2)} l_0 \int_0^1 B_\alpha(s) R_\alpha(x, l_0 s) ds = 0, \quad -1 < x < 1, \quad (24)$$

$$\int_0^1 \frac{B_\alpha(s)}{s-y} ds - l_0 \int_0^1 B_\beta(s) S_{\alpha\beta}(l_0 y, l_0 s) ds + \int_{-1}^{1} Q(t) T_\alpha(l_0 y, t) dt = 0, \quad 0 < y < 1. \quad (25)$$

The complementary condition (8) becomes

$$\frac{1+\lambda}{4\pi^2} l_0 \int_0^1 B_\beta(s) G_\beta(l_0 s) ds - \beta \int_{-1}^{1} \frac{tQ(t)}{W(t)} dt = 1. \quad (26)$$

The condition (9) is satisfied automatically because of the symmetry of $p_1(x_1)$ with respect to x_1. Functions $R_\alpha(x_1, \rho)$, $S_{\alpha\beta}(\zeta_1, \rho)$, $T_\alpha(\zeta_1, \xi)$, and $G_\alpha(\rho)$ are given in Appendix B.

Therefore, the problem has been reduced to solving the system of singular integral equations (24) and (25), compatible with condition (26).

Singular Behavior of Solutions

The integral equation (24) for the shear stress, $Q(x)$, is of the first kind. With the shear stress assumed unbounded at the end points, $x = \pm 1$, the characteristic function, $R(x)$, is chosen as

$$R(x) = \frac{1}{\sqrt{1-x^2}}. \quad (27)$$

Set

$$Q(x) = \frac{\psi(x)}{\sqrt{1-x^2}}, \quad (28)$$

where $\psi(x)$ ($|x| \le 1$) is bounded. Near the left end, $x = -1$, the shear stress $Q(x)$ is

$$Q(x) = \frac{\psi(-1)}{\sqrt{2(1+x)}} \quad \text{as} \quad x \to -1^+, \quad (29)$$

and the stress-intensity factor, $K_{II\,S}$, of the interface crack is

$$K_{II\,S} = \lim_{x_1 \to -l^+} \{\sqrt{2(l+x_1)}\, p_1(x_1)\} = \frac{N}{2l}\sqrt{l}\, 2\psi(-1). \quad (30)$$

The singularity of the normal stress, $P(x)$, near the ends of the bonded region results from the singular behavior of the second integral in (22) (or (18)), and, in view of (28), near the left end,

$$P(x) = -\beta \frac{\psi(-1)}{\sqrt{2(-1-x)}} \quad \text{as} \quad x \to -1^-. \quad (31)$$

Hence, near $x = -1$ the normal stress is related to the shear stress in such a manner that

$$\lim_{\epsilon \to 0^+} \left\{ \sqrt{\epsilon} P(-1+\epsilon) \right\} = -\beta \lim_{\epsilon \to 0^+} \{\sqrt{\epsilon} Q(-1+\epsilon)\}. \quad (32)$$

This feature was first predicted by Comninou [4], in connection with an interior, interface crack.

As is shown in Appendix B, the kernels, $S_{\alpha\beta}(l_0 y, l_0 s)$, in (25) are unbounded as y and t approach zero simultaneously, and, hence, the singular behavior of $B_\alpha(y)$ at $y = 0$ can not be described by $1/\sqrt{y}$. Here, this singular behavior is estimated with the aid of the results obtained by the asymptotic expansion approach near the vertex of a stress-free wedge; Bogy [17]. For a stress-free wedge with a wedge angle less than π, the stresses are regular at the vertex. Therefore, taking into account that the density functions of the edge dislocations are the derivatives of the crack-opening displacements with respect to ζ_1, set

$$B_\alpha(y) = \frac{\phi_\alpha(y)}{\sqrt{1-y^2}}, \quad (33)$$

where the functions $\phi_\alpha(y)$ ($0 \le y \le 1$) are bounded. The stresses near $\zeta_1 = 1$ on the $\zeta_1 -$ axis, but not on the branch, are given by

$$t_{22}^0 - i t_{12}^0 \sim \frac{1}{\pi}\frac{N}{2l} \int_0^1 \frac{B_2(s) + iB_1(s)}{s-y} ds \sim -\frac{N}{2l}\sqrt{l_0}\frac{\phi_2(1) + i\phi_1(1)}{\sqrt{2(\zeta_1 - l_0)}}. \quad (34)$$

The stress-intensity factors at the tip of the branch are defined as

$$K_I - iK_{II} = \lim_{\zeta_1 \to l_0^+} \{\sqrt{2(\zeta_1 - l_0)}\, (t_{22}^0 - i t_{12}^0)|_{\zeta_2 = 0}\}, \quad (35)$$

and are given by

$$K_I - iK_{II} = -\frac{N}{2l}\sqrt{l_0}\{\phi_2(1) + i\phi_1(1)\}. \quad (36)$$

Numerical Solution and Discussion

The set of integral equations (24) and (25), subject to the condition (26), is solved by the method of Erdogan, et al. [12], and Gupta and Erdogan [13]. Since $Q(x)$ is an odd function, the discretized forms of (24)–(26) are

$$\frac{1}{2n} \sum_{k=n+1}^{2n} \psi(t_k) \frac{2t_k}{t_k^2 - x_r^2} \left[1 + \frac{\beta^2}{1-\beta^2} \left\{ 1 - \frac{W(x_r)}{W(t_k)} \right\} \right] + \frac{1+\lambda}{4(1-\beta^2)} \frac{l_0}{2m+1} \sum_{i=1}^{m} \phi_\alpha(s_i) R_\alpha(x_r, l_0 s_i) = 0, \quad (37)$$

$$\frac{1}{2n} \sum_{k=n+1}^{2n} \psi(t_k) \{T_\alpha(l_0 y_j, t_k) - T_\alpha(l_0 y_i, -t_k)\} + \frac{1}{2m+1} \sum_{i=1}^{m} \frac{\phi_\alpha(s_i)}{s_i - y_j} - \frac{l_0}{2m+1} \sum_{i=1}^{m} \phi_\beta(s_i) S_{\alpha\beta}(l_0 y_j, l_0 s_i) = 0, \quad (38)$$

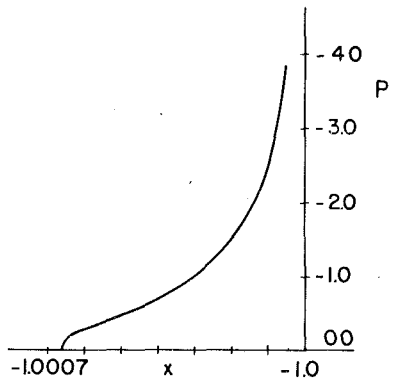

Fig. 2 Pressure distribution on the left contact region

Table 1 Stress-intensity factors, $K^*_{II\,S} = K_{II\,S}/\{\sqrt{\pi}N/(2l)\}$; $K^*_I = K_I/\{\sqrt{\bar{l}_0}\,N/(2l)\}$; $K^*_{II} = K_{II}/\{\sqrt{\bar{l}_0}N/(2l)\}$

ω	$\bar{l}_0/l$	$(d-l)/l$	$(\bar{a}-l)/l$	K^*_{IIS}	K^*_I	K^*_{II}
--	--	∞	0.639×10^{-3}	0.723	--	--
60°	0.10	0.10	0.138×10^{-3}	0.299	1.646	-0.175
	0.10	0.07	1.405×10^{-3}	0.094	1.681	-0.233
	0.05	0.05	0.381×10^{-3}	0.235	2.517	-0.131
	0.04	0.04	0.663×10^{-3}	0.220	2.873	-0.112
70°	0.10	0.10	0.146×10^{-3}	0.373	1.531	-0.297
	0.10	0.07	0.165×10^{-3}	0.189	1.586	-0.393
	0.05	0.05	0.254×10^{-3}	0.311	2.390	-0.361
	0.04	0.04	0.336×10^{-3}	0.293	2.745	-0.380
80°	0.10	0.10	0.170×10^{-3}	0.440	1.385	-0.403
	0.10	0.07	0.132×10^{-3}	0.287	1.447	-0.507
	0.05	0.05	0.233×10^{-3}	0.383	2.204	-0.547
	0.04	0.04	0.274×10^{-3}	0.366	2.547	-0.600

$$\frac{1+\lambda}{4\pi}\,\frac{l_0}{2m+1}\sum_{i=1}^{m}\phi_\alpha(s_i)G_\alpha(l_0 s_i) - \beta\frac{\pi}{n}\sum_{k=n+1}^{2n}\frac{t_k\psi(t_k)}{W(t_k)} = 1, \quad (39)$$

where

$$t_k = \cos\frac{2k-1}{4n}\pi, \quad (k = n+1, n+2, \ldots, 2n),$$

$$x_r = \cos\frac{r}{2n}\pi, \quad (r = n, n+1, \ldots, 2n-1),$$

$$s_i = \cos\frac{2i-1}{4m+2}\pi, \quad (i = 1, 2, \ldots, m),$$

$$y_j = \cos\frac{j}{2m+1}\pi, \quad (j = 1, 2, \ldots, m). \quad (40)$$

Equations (37)–(39) provide a system of $n + 2m + 1$ equations for the determination of the n-values of $\psi(t_k)$, the $2m$-values of $\phi_\alpha(s_i)$, and a. These equations are highly nonlinear in a and, here, have been solved by the usual inversion technique for a system of linear equations together with the Newton-Raphson method with $n = 90$ and $m = 50$, where condition (4) has been used as a guide in order to determine the solution.

According to the results of an asymptotic expansion approach presented in [4], the hoop stress around the tip of a two-dimensional crack in a flat interface of two materials is negative in the material with larger $\mu/(\kappa - 1)$. Only in the material with smaller $\mu/(\kappa - 1)$, can the hoop stress be positive, reaching a maximum value at the direction which makes an angle between 64° and 71° with the interface. Hence, in performing the numerical calculation, ω is set equal to 60°, 70°, and 80°. As to the material properties, fairly extreme values of Dundurs' parameters are used; i.e., $\lambda = 0.98$ and $\beta = 0.48$, which include the case $\nu_1 = \nu_2 \cong 0$, $\mu_1/\mu_2 \cong 100$.

In Table 1, the length of the contact region, $(\bar{a} - l)/l$, and the stress-intensity factors are presented for various lengths of the branch. In Fig. 2, the pressure distribution on the contact region is shown for $\omega = 60°$ and $\bar{l}_0/l = (d - l)/l = 0.04$. It is seen that the stress-intensity factor for the opening mode at the branch tip increases as the length of the branch becomes smaller. In the range of ω for which the calculation has been performed, the stress-intensity factor for the shear mode is always very small compared with that for the opening mode. It is also revealed that the stress-intensity factor of the interface crack, $K_{II\,S}$, decreases drastically, once a branch is formed near its tip.

Finally, let us discuss the phenomenon of kinking from an interface crack. If kinking from the tip of an interface crack is assumed, an oscillatory singularity occurs at the point of intersection of the kink and the interface [17]. Although the oscillatory singularity may have no influence on the overall stress field, since kinking is a local phenomenon, such a singularity must be eliminated somehow in order to be able to study the kinking process. Here, as a *tentative* measure, a small region of frictionless contact at the tip of the interface crack is introduced, where the length of this region is assumed to be of the order of the kink length during the initial growth stage. By setting $(d - l)/l$ equal to $\bar{l}_0/l$ and applying the Lagrange interpolation formula to the data in Table 1, one can estimate the limiting values of K^*_{II} as $\bar{l}_0/l \to 0$ for each branch angle, $\omega = 60°, 70°, 80°$. From these limiting values one can calculate the kink angle, ω_c, for which K^*_{II} at $\bar{l}_0/l = 0$ vanishes, and hence obtain the corresponding stress-intensity factor for the opening mode, K^*_{IC}. The results are $\omega_c \cong 60°$ and $K^*_{IC} = 4.9$. If the criterion of local symmetry is postulated to apply to an interface crack, then ω_c and K^*_{IC} are the critical kink angle and the stress-intensity factor at the onset of kinking.

Acknowledgment

This work has been supported by National Science Foundation Grant No. ENG77-22155 to Northwestern University.

References

1 Lo, K. K., "Analysis of Branched Crack," ASME JOURNAL OF APPLIED MECHANICS, Vol. 45, 1978, pp. 797–802.

2 England, A. H., "A Crack Between Dissimilar Media," ASME JOURNAL OF APPLIED MECHANICS, Vol. 32, 1965, pp. 400–402.

3 Malyshev, B. M., and Salganik, R. L., "The Strength of Adhesive Joints Using the Theory of Fracture," *International Journal of Fracture Mechanics*, Vol. 1, 1965, pp. 114–128.

4 Comninou, M., "The Interface Crack," ASME JOURNAL OF APPLIED MECHANICS, Vol. 44, 1977, pp. 631–636.

5 Comninou, M., "Interface Crack With Friction in the Contact Zone," ASME JOURNAL OF APPLIED MECHANICS, Vol. 44, 1977, pp. 780–781.

6 Comninou, M., "The Interface Crack in a Shear Field," ASME JOURNAL OF APPLIED MECHANICS, Vol. 45, 1978, pp. 287–290.

7 Comninou, M., and Dundurs, J., "A Closed-Form Crack Tip Terminating at an Interface," ASME JOURNAL OF APPLIED MECHANICS, Vol. 46, 1979, pp. 97–100.

8 Comninou, M., and Schmueser, D., "The Interface Crack in a Combined Tension-Compression and Shear Field," ASME JOURNAL OF APPLIED MECHANICS, Vol. 46, 1979, pp. 345–348.

9 Dundurs, J., and Comninou, M., "Some Consequences of the Inequality Conditions in Contact and Crack Problems," *Journal of Elasticity*, Vol. 9, 1979, pp. 71–82.

10 Keer, L. M., Chen, S. H., and Comninou, M., "The Interface Penny-Shaped Crack Reconsidered," *International Journal of Engineering Science*, Vol. 16, 1978, pp. 765–772.

11 Achenbach, J. D., et al., "Loss of Adhesion at the Tip of an Interface Crack," *Journal of Elasticity*, Vol. 9, 1979, pp. 397–424.

12 Erdogan, F., Gupta, G. D., and Cook, T. S., "Numerical Solution of Singular Integral Equations," *Methods of Analysis and Solutions of Crack Problems*, Sih, G. C., ed., Noordhoff, 1973.

13 Gupta, G. D., and Erdogan, F., "The Problem of Edge Cracks in an Infinite Strip," ASME JOURNAL OF APPLIED MECHANICS, Vol. 41, 1974, pp. 1001–1006.

14 Muskhelishvili, N. I., *Some Basic Problems in the Mathematical Theory of Elasticity*, Noordhoff, 1958.

15 Green, A. E., and Zerna, W., *Theoretical Elasticity*, Oxford, 1960.

16 Muskhelishvili, N. I., *Singular Integral Equations*, Noordhoff, 1953.

17 Bogy, D. B., "Two Edge-Bonded Elastic Wedges of Different Materials and Wedge Angles Under Surface Tractions," ASME JOURNAL OF APPLIED MECHANICS, Vol. 38, 1971, pp. 377–386.

APPENDIX A

Expressions for the functions $f_{\alpha\beta}(x_1, \rho)$, $g_{\alpha\beta}(\zeta_1, \xi)$ and $h_{\alpha\beta}(\zeta_1, \rho)$, $\alpha, \beta = 1, 2$, are given here, where an overbar is used to indicate the complex conjugate, and

$$\alpha = -d + \rho e^{i\omega}, \quad \eta = -d + \zeta_1 e^{-i\omega}.$$

Expressions for $f_{\alpha\beta}(x_1, \rho)$:

$$f_{22}(x_1, \rho) + if_{12}(x_1, \rho) = e^{-i\omega} f_1^*(x_1, \rho) + e^{i\omega} f_2^*(x_1, \rho),$$

$$f_{21}(x_1, \rho) + if_{11}(x_1, \rho) = ie^{-i\omega} f_1^*(x_1, \rho) - ie^{i\omega} f_2^*(x_1, \rho),$$

$$f_1^*(x_1, \rho) = -\frac{1}{x_1 - \bar{\alpha}} + \frac{1}{x_1 - \alpha} + \frac{2i\rho \sin \omega}{(x + \alpha)^2},$$

$$f_2^*(x_1, \rho) = -\frac{1}{x_1 + \bar{\alpha}} + \frac{1}{x_1 + \bar{\alpha}} - \frac{2i\rho \sin \omega}{(x_1 - \alpha)^2}.$$

Expressions for $g_{\alpha\beta}(\zeta_1, \xi)$:

$$g_{22}(\zeta_1, \xi) + ig_{12}(\zeta_1, \xi) = i\left\{-\frac{1}{\eta - \xi} + \frac{1}{\bar{\eta} - \xi} + \frac{2i\zeta_1 \sin \omega e^{2i\omega}}{(\bar{\eta} - \xi)^2}\right\},$$

$$g_{21}(\zeta_1, \xi) + ig_{11}(\zeta_1, \xi) = -\frac{1}{\eta - \xi} - \frac{1 - 2e^{2i\omega}}{\bar{\eta} - \xi} - \frac{2i\zeta_1 \sin \omega e^{2i\omega}}{(\bar{\eta} - \xi)^2}.$$

Expressions for $h_{\alpha\beta}(\zeta_1, \rho)$:

$$h_{22}(\zeta_1, \rho) + ih_{12}(\zeta_1, \rho) = -\frac{e^{i\omega}}{\bar{\eta} - \bar{\alpha}} + h_1^*(\zeta_1, \rho) + h_2^*(\zeta_1, \rho),$$

$$h_{21}(\zeta_1, \rho) + ih_{11}(\zeta_1, \rho) = ih_1^*(\zeta_1, \rho) - ih_2^*(\zeta_1, \rho),$$

$$h_1^*(\zeta_1, \rho) = -\frac{e^{-i\omega}}{2(\eta - \alpha)} - \frac{2i\rho \sin \omega \cos \omega}{(\bar{\eta} - \bar{\alpha})^2} + \frac{2i(\zeta_1 - \rho)\rho \sin \omega}{(\bar{\eta} - \bar{\alpha})^3} + \frac{e^{-i\omega}}{2}\left(\frac{1}{\bar{\eta} + \alpha} - \frac{1}{\bar{\eta} + \bar{\alpha}}\right) - \frac{i\rho \sin \omega e^{-i\omega}}{(\eta + \bar{\alpha})^2} + \frac{e^{i\omega}}{2}(\eta + \alpha)\left\{\frac{1}{(\bar{\eta} + \bar{\alpha})^2} - \frac{1}{(\bar{\eta} + \alpha)^2}\right\},$$

$$h_2^*(\zeta_1, \rho) = \frac{i\rho \sin \omega e^{i\omega}}{(\eta - \alpha)^2} + \frac{(\zeta_1 - \rho)e^{2i\omega}}{2(\bar{\eta} - \bar{\alpha})^2} + \frac{i\rho \sin 2\omega e^{2i\omega}}{(\bar{\eta} + \alpha)^2} + \frac{e^{i\omega}}{2}\left(\frac{1}{\eta + \bar{\alpha}} - \frac{1}{\eta + \alpha}\right) - \frac{2i\rho(\eta + \alpha) \sin \omega e^{3i\omega}}{(\bar{\eta} + \alpha)^3} + \frac{e^{3i\omega}}{2}\left(\frac{1}{\bar{\eta} + \alpha} - \frac{1}{\bar{\eta} + \bar{\alpha}}\right).$$

APPENDIX B

Expressions for functions $F_\alpha(x_1, \rho)$, $R_\alpha(x_1, \rho)$, $S_{\alpha\beta}(\zeta_1, \rho)$, $T_\alpha(\zeta_1, \xi)$, and $G_\alpha(\rho)$ are presented here, where the same notation as in Appendix A is employed.

Expressions for $F_\alpha(x_1, \rho)$:

$$F_\alpha(x_1, \rho) = \int_{-\tilde{a}}^{\tilde{a}} \frac{f_{1\alpha}(\xi, \rho)}{w(\xi)(\xi - x_1)} d\xi = \frac{\pi}{2i}\{F_\alpha^*(x_1, s) - \overline{F_\alpha^*(x_1, s)}\},$$

$$F_\alpha^*(x_1, \rho) = \frac{2}{X(\alpha)} A_{1\alpha 1}\left(\frac{1}{x_1 - \alpha} - \frac{1}{x_1 + \alpha}\right) + 2A_{1\alpha 2}(\alpha + d)\left\{\frac{1}{(x_1 - \alpha)^2} + \frac{1}{(x_1 + \alpha)^2}\right\},$$

$$A_{111} = \sin \omega + \frac{\alpha(\alpha + d)}{\alpha^2 - \tilde{a}^2} \sin \omega, \quad A_{112} = -\sin \omega,$$

$$A_{121} = \cos \omega + i\frac{\alpha(\alpha + d)}{\alpha^2 - \tilde{a}^2} \sin \omega, \quad A_{122} = -i \sin \omega,$$

$$X(\alpha) = \sqrt{\alpha^2 - \tilde{a}^2}.$$

Here, the branch of $X(\alpha)$ is taken such that $X(\alpha) \to \alpha$ as $|\alpha| \to \infty$.

Expression for $R_\alpha(x_1, \rho)$:

$$R_\alpha(x_1, \rho) = f_{2\alpha}(x_1, \rho) + \frac{\beta}{\pi} w(x_1) \int_{-\tilde{a}}^{\tilde{a}} \frac{f_{1\alpha}(\xi, \rho)}{w(\xi)(\xi - x_1)} d\xi = f_{2\alpha}(x_1, \rho) + \frac{\beta}{2i} w(x)\{F_\alpha^*(x_1, \rho) - \overline{F_\alpha^*(x_1, \rho)}\}.$$

Expressions for $S_{\alpha\beta}(\zeta_1, \rho)$:

$$S_{\alpha\beta}(\zeta_1, \rho) = h_{\alpha\beta}(\zeta_1, \rho) - \frac{1 + \lambda}{4\pi^2} \int_{-\tilde{a}}^{\tilde{a}} g_{\alpha 2}(\zeta_1, \xi) w(\xi) \times \int_{-\tilde{a}}^{\tilde{a}} \frac{f_{1\beta}(x_1, \rho)}{w(x_1)(x_1 - \xi)} dx_1 d\xi = h_{\alpha\beta}(\zeta_1, \rho) - \frac{1 + \lambda}{2}\{S_{\alpha\beta}^*(\zeta_1, \rho) + \overline{S_{\alpha\beta}^*(\zeta_1, \rho)}\},$$

$$S_{\alpha\beta}^*(\zeta_1, \rho) = \frac{1}{2} A_{\alpha\beta\lambda}\{B_{\alpha\beta\mu} r_{\lambda\mu}(\alpha, \eta) - \bar{B}_{\alpha\beta\mu} r_{\lambda\mu}(\alpha, \bar{\eta})\}, \quad (\alpha, \beta \text{ not summed}),$$

$$r_{11}(\alpha, \eta) = -\frac{1}{\eta + \alpha}\frac{Y(\alpha, \eta)}{X(\alpha)} + \frac{\eta + \alpha}{X(\alpha)Y(\alpha, \eta)},$$

$$r_{21}(\alpha, \eta) = (\alpha + d)\left\{\frac{1}{(\eta + \alpha)^2}\frac{Y(\alpha, \eta)}{X(\alpha)} - \frac{1}{\eta + \alpha}\frac{\alpha}{X(\alpha)^2} - \frac{\tilde{a}^2(\eta + \alpha)}{X(\alpha)^2 Y(\alpha, \eta) Z(\alpha, \eta)}\right\},$$

$$r_{12}(\alpha, \eta) = (\eta + d)\left\{\frac{1}{(\eta + \alpha)^2}\frac{Y(\alpha, \eta)}{X(\alpha)} - \frac{1}{\eta + \alpha}\frac{\eta}{X(\alpha)X(\eta)} - \frac{\tilde{a}^2(\eta + \alpha)}{X(\alpha)X(\eta)Y(\alpha, \eta)Z(\alpha, \eta)}\right\},$$

$$r_{22}(\alpha, \eta) = (\alpha + d)(\eta + d)\left\{-\frac{2}{(\eta + \alpha)^3}\frac{Y(\alpha, \eta)}{X(\alpha)} + \frac{1}{(\eta + \alpha)^2}\frac{Z(\alpha, \eta)}{X(\alpha)^2 X(\eta)} + \frac{\tilde{a}^2(\eta + \alpha)}{X(\alpha)^2 X(\eta) Y(\alpha, \eta)^2 Z(\alpha, \eta)}\right\},$$

$$Y(\alpha, \eta) = X(\alpha) + X(\eta),$$

$$Z(\alpha, \eta) = \alpha X(\eta) + \eta X(\alpha),$$

$$A_{2\alpha\beta} = A_{1\alpha\beta},$$

$$B_{111} = B_{121} = 0, \quad B_{112} = B_{122} = -e^{-i\omega} \sin \omega,$$

$$B_{211} = B_{221} = 1, \quad B_{212} = B_{222} = ie^{-i\omega} \sin \omega.$$

Expressions for $T_\alpha(\zeta_1, \xi)$:

$$T_\alpha(\zeta_1, \xi) = g_{\alpha 1}(\zeta_1, \xi) + \frac{\beta}{\pi}\frac{1}{w(\xi)} \int_{-\tilde{a}}^{\tilde{a}} \frac{w(x_1) g_{\alpha 2}(\zeta_1, x_1)}{x_1 - \xi} dx_1 = g_{\alpha 1}(\zeta_1, \xi) + \frac{\beta}{2i}\frac{1}{w(\xi)}\{T_\alpha^*(\zeta_1, \xi) - \overline{T_\alpha^*(\zeta_1, \xi)}\},$$

$$T_1^*(\zeta_1, \xi) = 2e^{-i\omega} \sin \omega \left\{\frac{1}{\eta - \xi}\frac{\eta(\eta + d)}{X(\eta)} - \frac{(\eta + d)X(\eta)}{(\eta - \xi)^2}\right\},$$

$$T_2^*(\zeta_1, \xi) = -\frac{1}{\eta - \xi}\left\{2X(\eta) + 2ie^{-i\omega} \sin \omega \frac{\eta(\eta + d)}{X(\eta)}\right\} + 2ie^{-i\omega} \sin \omega \frac{X(\eta)(\eta + d)}{(\eta - \xi)^2}.$$

Expressions for $G_\alpha(\rho)$:

$$G_\alpha(\rho) = \int_{-\tilde{a}}^{\tilde{a}} w(\xi) \int_{-\tilde{a}}^{\tilde{a}} \frac{f_{1\alpha}(x_1, \rho)}{w(x_1)(x_1 - \xi)} dx_1 d\xi = \frac{\pi^2}{2i}\{G_\alpha^*(\rho) - \overline{G_\alpha^*(\rho)}\},$$

$$G_\alpha^*(\rho) = 4\left\{1 - \frac{\alpha}{x(\alpha)}\right\}\left\{A_{1\alpha 1} - A_{1\alpha 2}\frac{\alpha + d}{X(\alpha)}\right\}.$$

S. Itou

Associate Professor,
Department of Mechanical Engineering,
Hachinohe Institute of Technology,
Hachinohe 031, Japan

Transient Response of a Finite Crack in a Half Plane Under Impact Load

Analytical investigation of a half plane weakened by a finite crack is considered. The crack is placed perpendicularly to the stress-free boundary of the half plane. The surfaces of the crack are loaded by a uniform pressure with Heaviside-function time dependence. In the Laplace transform domain, Fourier transformations are utilized to reduce the problem to the solution of a pair of dual integral equations which are solved by using the series expansion method. The Laplace inversion of the dynamic stress-intensity factors is carried out numerically.

1 Introduction

Recently, dynamic crack problems have received much attention. This is due to the fact that dynamic stress-intensity factors are of considerable importance not only in designing the various parts of a machine but also in the field of the development of terrestrial heat which closely concerns to the destruction of the earth's crust. Many investigations have been done for the dynamic crack problems. A recent book by Sih contains good reviews of a number of subjects [1]. However, most of the studies have been concerned mainly with a single crack in an infinite elastic medium.

In contrast to the foregoing works, analytical approaches to the transient crack problems including the effects of the boundaries were performed by Chen for an infinite strip with a centrally located crack [2, 3]. The dynamic response of a layered composite under normal and shear impact is also analyzed by assuming that the composite contains an initial flow in the matrix material [4]. Later, the same problem which was treated by Chen [3] is reworked by using a somewhat different approach [5]. The dynamic solutions of these problems are complicated by the presence of the other surface of the medium in addition to the crack surfaces. For this reason, such researches have generally been limited to the case that a crack is situated so as to achieve a geometrical symmetry with respect to the center line which intersects at a right angle to the crack surfaces. When a crack has not such a symmetry, the dynamic crack problem involves more difficulties in an analytical treatment.

In the present paper, the transient dynamic stress field in the vicinity of a Griffith crack in a half plane is determined. The crack is placed perpendicularly to the free surface of the half plane and is opened by internal pressure with the Heaviside-function time dependence. Fourier and Laplace transforms are applied and the problem is reduced to that of solving dual integral equations in the Laplace transform domain. To solve the equations, the crack surface displacement is expanded in a series of Jacobi polynomials. The unknown coefficients accompanied in that series are solved with the aid of the Schmidt method. The dynamic stress-intensity factors are defined in the transformed domain and are inverted numerically in the physical space with the method which is developed in reference [6] and used in references [2–5]. Numerical results are compared with those of the corresponding static values given by Isida [7].

2 Fundamental Equation

Consider an elastic half plane bounded in the x, y-plane by the line $x = h$ and a finite crack located along the x-axis from $-a$ to $+a$ as shown in Fig. 1.

When there are no body forces, we introduce two potentials ϕ and ψ for the Lamé solution of the equation of motion so that the components of displacement are given by

$$u = \phi_{,x} - \psi_{,y},$$
$$v = \phi_{,y} + \psi_{,x}, \tag{1}$$

where u and v are defined as the x and y-components of the displacement, respectively, and the indices following a comma indicate the partial differentiation with respect to the variable, e.g., $\phi_{,x} = \partial\phi/\partial x$.

The equations of motion in the plane state of strain are reduced to the forms

$$\phi_{,xx} + \phi_{,yy} = \frac{1}{c_L^2}\phi_{,tt}$$
$$\psi_{,xx} + \psi_{,yy} = \frac{1}{c_T^2}\psi_{,tt}, \tag{2}$$

Contributed by the Applied Mechanics Division for publication in the JOURNAL OF APPLIED MECHANICS.

Discussion on this paper should be addressed to the Editorial Department, ASME, United Engineering Center, 345 East 47th Street, New York, N.Y. 10017, and will be accepted until December 1, 1981. Readers who need more time to prepare a discussion should request an extension from the Editorial Department. Manuscript received by ASME Applied Mechanics Division, October, 1980.

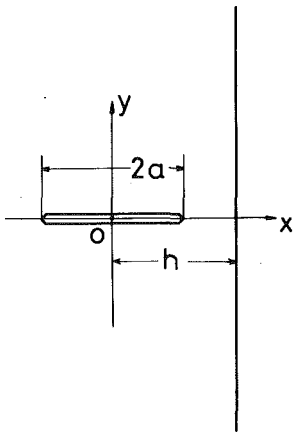

Fig. 1 Geometry and coordinate system

where the medium is assumed to be homogeneous and isotropic and $c_L = \{(\lambda + 2\mu)/\rho\}^{1/2}$, $c_T = (\mu/\rho)^{1/2}$ are the dilatational and shear wave velocities with λ and μ being the Lamé constants, ρ being the density of the material. The dynamic stress components are written in terms of ϕ and ψ as

$$\tau_{yy}/(2\mu) = -\phi_{,xx} + \tfrac{1}{2}\kappa^2(\phi_{,xx} + \phi_{,yy}) + \psi_{,xy},$$
$$\tau_{xx}/(2\mu) = -\phi_{,yy} + \tfrac{1}{2}\kappa^2(\phi_{,xx} + \phi_{,yy}) - \psi_{,xy},$$
$$\tau_{yx}/(2\mu) = \phi_{,xy} + \psi_{,xx} - \tfrac{1}{2}(\psi_{,xx} + \psi_{,yy}), \tag{3}$$

with

$$\kappa^2 = (c_L/c_T)^2, \tag{4}$$

where elastic constant κ^2 takes the value $2(1-\nu)/(1-2\nu)$ with ν denoting Poisson's ratio.

Equation (2) is to be solved subjected to zero initial conditions and the following boundary conditions:

$$\tau_{yy} = -P\,\mathrm{H}(t), \quad \text{for} \quad y = 0, \quad -a < x < a,$$
$$v = 0, \quad \text{for} \quad y = 0, \quad -\infty < x < -a, \quad a < x \leqq h,$$
$$\tau_{yx} = 0, \quad \text{for} \quad y = 0, \quad -\infty < x \leqq h, \tag{5}$$
$$\tau_{xx} = \tau_{yx} = 0, \quad \text{for} \quad x = h, \quad |y| < \infty, \tag{6}$$

where P is a constant and $\mathrm{H}(t)$ is the Heaviside unit step function. Because of the symmetry conditions in equations (5) and (6), it is possible to consider only the problem for the half plane, $y \geqq 0$.

3 Analysis

The Laplace transform of $f(t)$ is defined by the integral

$$f^*(s) = \int_0^\infty \exp(-st) f(t)dt. \tag{7}$$

The inverse Laplace transform is

$$f(t) = \frac{1}{2\pi i}\int_{\mathrm{Br}} \exp(st) f^*(s)ds, \tag{8}$$

where the integral is over the Bromwich path. Applying equation (7) to equation (2) results in

$$\phi^*_{,xx} + \phi^*_{,yy} = \frac{s^2}{c_L^2}\phi^*,$$
$$\psi^*_{,xx} + \psi^*_{,yy} = \frac{s^2}{c_T^2}\psi^*. \tag{9}$$

In the Laplace transform domain, equations (5) and (6) become

$$\tau^*_{yy} = -P/s, \quad \text{for} \quad y = 0, \quad -a < x < a, \tag{10a}$$
$$v^* = 0, \quad \text{for} \quad y = 0, \quad -\infty < x < -a, \quad a < x \leqq h, \tag{10b}$$
$$\tau^*_{yx} = 0, \quad \text{for} \quad y = 0, \quad -\infty < x \leqq h, \tag{10c}$$
$$\tau^*_{xx} = \tau^*_{yx} = 0, \quad \text{for} \quad x = h, \quad |y| < \infty. \tag{10d}$$

The solutions of equation (9) which are suitable for the present purpose have the forms

$$\phi^* = 2\int_0^\infty \{A_1^c(s,\xi)\cos(\xi x) + A_1^s(s,\xi)\sin(\xi x)\}\exp(-\gamma_1 y)d\xi + 2\int_0^\infty B_1(s,\zeta)\exp(\beta_1 x)\cos(\zeta y)d\zeta,$$
$$\psi^* = 2\int_0^\infty \{A_2^s(s,\xi)\sin(\xi x) + A_2^c(s,\xi)\cos(\xi x)\}\exp(-\gamma_2 y)d\xi + 2\int_0^\infty B_2(s,\zeta)\exp(\beta_2 x)\sin(\zeta y)d\zeta, \tag{11}$$

with

$$\gamma_1 = (\xi^2 + s^2/c_L^2)^{1/2},$$
$$\gamma_2 = (\xi^2 + \kappa^2 s^2/c_L^2)^{1/2},$$
$$\beta_1 = (\zeta^2 + s^2/c_L^2)^{1/2},$$
$$\beta_2 = (\zeta^2 + \kappa^2 s^2/c_L^2)^{1/2}, \tag{12}$$

where $A_1^c(s,\xi)$, $A_1^s(s,\xi)$, $A_2^s(s,\xi)$, $A_2^c(s,\xi)$, $B_1(s,\zeta)$, and $B_2(s,\zeta)$ are the unknown coefficients and to be determined from the boundary conditions.

The boundary conditions equation (10c) is satisfied by setting

$$A_2^s(s,\xi) = \xi\gamma_1 A_1^c(s,\xi)/(\xi^2 + \tfrac{1}{2}\kappa^2 s^2/c_L^2),$$
$$A_2^c(s,\xi) = -\xi\gamma_1 A_1^s(s,\xi)/(\xi^2 + \tfrac{1}{2}\kappa^2 s^2/c_L^2), \tag{13}$$

and equation (10d) can be satisfied if we choose $B_1(s,\zeta)$ and $B_2(s,\zeta)$ to be such that

$$B_1(s,\zeta) = -\frac{2}{\pi}\int_0^\infty [A_1^c(s,\xi)\{a_4 k_1(s)\cos(\xi h) - a_2 k_2(s)\sin(\xi h)\}/D + A_1^s(s,\xi)\{a_4 k_1(s)\sin(\xi h) + a_2 k_2(s)\cos(\xi h)\}/D]d\xi,$$
$$B_2(s,\zeta) = -\frac{2}{\pi}\int_0^\infty [A_1^c(s,\xi)\{a_1 k_2(s)\sin(\xi h) - a_3 k_1(s)\cos(\xi h)\}/D - A_1^s(s,\xi)\{a_1 k_2(s)\cos(\xi h) + a_3 k_1(s)\sin(\xi h)\}/D]d\xi, \tag{14}$$

with

$$a_1 = (\zeta^2 + \tfrac{1}{2}\kappa^2 s^2/c_L^2)\exp(\beta_1 h),$$
$$a_2 = -\beta_2\zeta\exp(\beta_2 h),$$
$$a_3 = -\beta_1\zeta\exp(\beta_1 h),$$
$$a_4 = (\beta_2^2 - \tfrac{1}{2}\kappa^2 s^2/c_L^2)\exp(\beta_2 h),$$
$$D = a_1 a_4 - a_2 a_3, \tag{15}$$
$$k_1(s) = \{\xi^2\gamma_1\gamma_2^2(\gamma_1^2 + \zeta^2) + \gamma_1(\gamma_2^2 + \zeta^2)(\xi^2 + \tfrac{1}{2}\kappa^2 s^2/c_L^2)(-\gamma_1^2 + \tfrac{1}{2}\kappa^2 s^2/c_L^2)\}/\{(\gamma_1^2 + \zeta^2)(\gamma_2^2 + \zeta^2)(\xi^2 + \tfrac{1}{2}\kappa^2 s^2/c_L^2)\},$$
$$k_2(s) = \xi\zeta\gamma_1(\gamma_2^2 - \gamma_1^2)/\{(\gamma_1^2 + \zeta^2)(\gamma_2^2 + \zeta^2)\}. \tag{16}$$

Now, we divide the Laplace transformed surface displacement v^{*0} into two parts

$$v^{*0} = v_e^{*0} + v_0^{*0}, \tag{17}$$

where v_e^{*0} and v_0^{*0} are even and odd functions of the x variable, and the superscript means that the values with it are those at $y = 0$. Equation (17) can be expressed by use of the Fourier transform as

$$v^{*0} = \frac{2}{\pi}\int_0^\infty \bar{v}_e^{*0}\cos(\xi x)d\xi + \frac{2}{\pi}\int_0^\infty \bar{v}_0^{*0}\sin(\xi x)d\xi, \tag{18}$$

with

$$\bar{v}_e^{*0} = \int_0^\infty v_e^{*0} \cos(\xi x)dx,$$

$$\bar{v}_0^{*0} = \int_0^\infty v_0^{*0} \sin(\xi x)dx. \quad (19)$$

Then, with the help of equation (18), we can represent $A_1^c(s,\xi)$ and $A_1^s(s,\xi)$ by

$$A_1^c(s,\xi) = 2\mu q(s,\xi)\bar{v}_e^{*0},$$

$$A_1^s(s,\xi) = 2\mu q(s,\xi)\bar{v}_0^{*0}, \quad (20)$$

with

$$q(s,\xi) = -(\xi^2 + \tfrac{1}{2}\kappa^2 s^2/c_L^2)/(\tfrac{1}{2}\kappa^2\pi s^2\gamma_1/c_L^2). \quad (21)$$

Finally, it can be easily shown that the mixed boundary values equation (10) yields to the following integral equations:

$$\tau_{yy}^{*0} = 4\mu \int_0^\infty \bar{v}_e^{*0}\Big\{f_1(\xi)\cos(\xi x) + \cos(\xi h)\int_0^\infty q(s,\xi)g_1(\xi,\zeta)d\zeta + \sin(\xi h)\int_0^\infty q(s,\xi)g_2(\xi,\zeta)d\zeta\Big\}d\xi$$

$$+4\mu \int_0^\infty \bar{v}_0^{*0}\Big\{f_1(\xi)\sin(\xi x) + \sin(\xi h)\int_0^\infty q(s,\xi)g_1(\xi,\zeta)d\zeta - \cos(\xi h)\int_0^\infty q(s,\xi)g_2(\xi,\zeta)d\zeta\Big\}d\xi = -P/s,$$

$$\text{for} \quad -a < x < a, \quad (22a)$$

$$v^{*0} = \frac{2}{\pi}\int_0^\infty \bar{v}_e^{*0}\cos(\xi x)d\xi + \frac{2}{\pi}\int_0^\infty \bar{v}_0^{*0}\sin(\xi x)d\xi = 0,$$

$$\text{for} \quad -\infty < x < -a, \quad a < x \leqq h, \quad (22b)$$

with

$$f_1(\xi) = -\{(\xi^2 + \tfrac{1}{2}\kappa^2 s^2/c_L^2)^2 - \xi^2\gamma_1\gamma_2\}/(\tfrac{1}{2}\kappa^2\pi s^2\gamma_1/c_L^2),$$

$$g_1(\xi,\zeta) = -\frac{2}{\pi}\{(-\beta_1^2 + \tfrac{1}{2}\kappa^2 s^2/c_L^2)\exp(\beta_1 x)a_4 - \beta_2\zeta\exp(\beta_2 x)a_3\}k_1(s)/D,$$

$$g_2(\xi,\zeta) = \frac{2}{\pi}\{(-\beta_1^2 + \tfrac{1}{2}\kappa^2 s^2/c_L^2)\exp(\beta_1 x)a_2 - \beta_2\zeta\exp(\beta_2 x)a_1\}k_2(s)/D. \quad (23)$$

To solve equation (22), we expand the even and odd components of the surface displacement by the following series, respectively,

$$2\mu v_e^{*0} = \sum_{m=1}^\infty c_m P_{2m-2}^{(1/2,1/2)}(x/a)(1 - x^2/a^2)^{1/2},$$

$$2\mu\, v_0^{*0} = \sum_{n=1}^\infty d_n P_{2n-1}^{(1/2,1/2)}(x/a)(1 - x^2/a^2)^{1/2}, \quad \text{for} \quad -a < x < a,$$

$$v_e^{*0} = v_0^{*0} = 0, \quad \text{for} \quad -\infty < x < -a, \quad a < x \leqq h, \quad (24)$$

where c_m and d_n are the unknown coefficients to be determined and $P_n^{(1/2,1/2)}(x)$ is a Jacobi polynomial. Substituting equation (24) into equation (19), we obtain

$$2\mu\bar{v}_e^{*0} = \sum_{m=1}^\infty c_m\sqrt{\pi}(-1)^{m-1}\Gamma(2m - \tfrac{1}{2})J_{2m-1}(\xi a)/\{(2m-2)!\xi\},$$

$$2\mu\bar{v}_0^{*0} = \sum_{n=1}^\infty d_n\sqrt{\pi}(-1)^{n-1}\Gamma(2n + \tfrac{1}{2})J_{2n}(\xi a)/\{(2n-1)!\xi\}, \quad (25)$$

where $\Gamma(x)$ and $J_n(x)$ are Gamma and Bessel functions, respectively. Therefore, we arrive at the system of equation by which the coefficients c_m and d_n can be obtained

$$\tau_{yy}^{*0} = \sum_{m=1}^\infty c_m r(m,x) + \sum_{n=1}^\infty d_n s(n,x) = -P/s, \quad \text{for} \quad -a < x < a, \quad (26)$$

with

$$r(m,x) = 2\sqrt{\pi}(-1)^{m-1}\frac{\Gamma(2m - \tfrac{1}{2})}{(2m-2)!}\Big[\int_0^\infty f_1(\xi)/\xi J_{2m-1}(\xi a)\cos(\xi x)d\xi + \int_0^\infty\Big\{1/\xi\, J_{2m-1}(\xi a)\cos(\xi h)\int_0^\infty h_1(\xi,\zeta)d\zeta\Big\}d\xi + \int_0^\infty\Big\{1/\xi\, J_{2m-1}(\xi a)\sin(\xi h)\int_0^\infty h_2(\xi,\zeta)d\zeta\Big\}d\xi\Big],$$

$$s(n,x) = 2\sqrt{\pi}(-1)^{n-1}\frac{\Gamma(2n + \tfrac{1}{2})}{(2n-1)!}\Big[\int_0^\infty f_1(\xi)/\xi\, J_{2n}(\xi a)\sin(\xi x)d\xi + \int_0^\infty\Big\{1/\xi\, J_{2n}(\xi a)\sin(\xi h)\int_0^\infty h_1(\xi,\zeta)d\zeta\Big\}d\xi - \int_0^\infty\Big\{1/\xi\, J_{2n}(\xi a)\cos(\xi h)\int_0^\infty h_2(\xi,\zeta)d\zeta\Big\}d\xi\Big], \quad (27)$$

and

$$h_1(\xi,\zeta) = q(s,\xi)g_1(\xi,\zeta)/2,$$

$$h_2(\xi,\zeta) = q(s,\xi)g_2(\xi,\zeta)/2. \quad (28)$$

The semi-infinite integrals in equation (27) with respect to variable ζ can be easily evaluated numerically because the integrands almost all decrease exponentially. The integrands put into braces { } decay with order of $\xi^{-3.5}$ because the function $h_1(\xi,\zeta)$ and $h_2(\xi,\zeta)$ behave as for a large value of ξ

$$h_1(\xi,\zeta) \to 0(\xi^{-2}),$$

$$h_2(\xi,\zeta) \to 0(\xi^{-2}). \quad (29)$$

Thereby, the double semi-infinite integrals in equation (27) can be evaluated numerically. The other integrals in equation (27) are rewritten as

$$\int_0^\infty f_1(\xi)/\xi\, J_{2m-1}(\xi a)\cos(\xi x)d\xi = \int_0^\infty\{f_1(\xi)/\xi - f_1(\delta)/\delta\}J_{2m-1}(\xi a)\cos(\xi x)d\xi + f_1(\delta)/\{\delta(a^2 - x^2)^{1/2}\}\cos\{(2m-1)\sin^{-1}(x/a)\},$$

$$\int_0^\infty f_1(\xi)/\xi\, J_{2n}(\xi a)\sin(\xi x)d\xi = \int_0^\infty\{f_1(\xi)/\xi - f_1(\delta)/\delta\}J_{2n}(\xi a)\sin(\xi x)d\xi + f_1(\delta)/\{\delta(a^2 - x^2)^{1/2}\}\sin\{2n\sin^{-1}(x/a)\}, \quad (30)$$

with

$$f_1(\delta)/\delta = \lim_{\xi\to\infty} f_1(\xi)/\xi = -(\kappa^2 - 1)/(\pi\kappa^2). \quad (31)$$

The function $\{f_1(\xi)/\xi - f_1(\delta)/\delta\}$ behaves as ξ^{-2} for a large ξ, so that the integrands in equation (30) decay with the order of $\xi^{-2.5}$ as ξ is increased and the integrals can be also evaluated numerically.

Thus equation (26) can be solved for coefficients c_m and d_n by the Schmidt method [8]. For brevity, we rewrite equation (26) as

$$\sum_{k=1}^\infty a_k E_k(x) = -v(x), \quad \text{for} \quad -a < x < a, \quad (32)$$

with

$$a_k = c_{(k-1)/2-1},$$

$$E_k(x) = r\{(k-1)/2 - 1, x\}, \quad \text{for} \quad k = 1, 3, 5, 7, \ldots,$$

$$a_k = d_{k/2},$$

$$E_k(x) = s(k/2, x), \quad \text{for} \quad k = 2, 4, 6, \ldots, \quad (33)$$

and

$$v(x) = P/s. \quad (34)$$

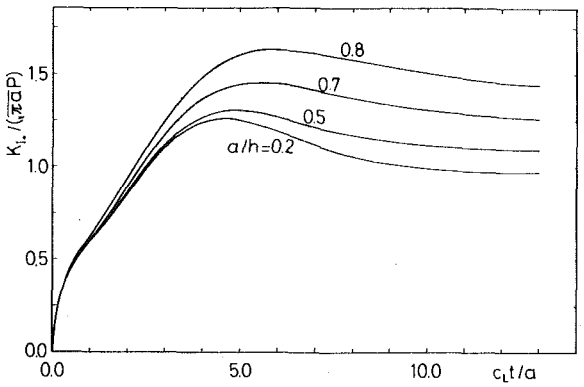

Fig. 2 Dynamic stress-intensity factor K_{I+} versus $c_L t/a$

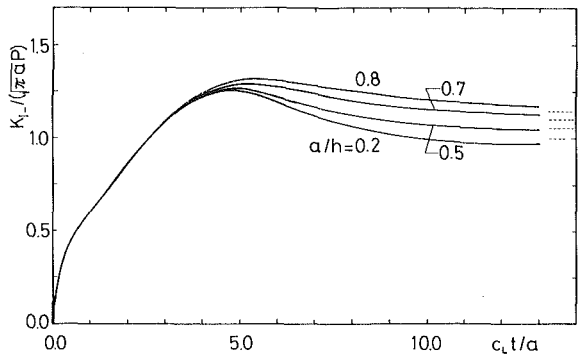

Fig. 3 Dynamic stress-intensity factor K_{I-} versus $c_L t/a$

A set of functions $Q_k(x)$ which satisfy the orthogonality condition

$$\int_{-a}^{a} Q_k(x)Q_l(x)dx = N_k\delta_{kl}, \quad N_k = \int_{-a}^{a} Q_k^2(x)dx, \tag{35}$$

can be constructed from the function, $E_k(x)$, such that

$$Q_k(x) = \sum_{i=1}^{k} \frac{M_{ik}}{M_{kk}} E_i(x), \tag{36}$$

where M_{ik} is the cofactor of the element d_{ik} of D_k, defined as

$$D_k = \begin{vmatrix} d_{11}\, d_{12} \ldots . d_{1k} \\ d_{21} \quad\quad\quad . \\ \vdots \quad\quad\quad \vdots \\ d_{k1} \ldots \ldots \quad d_{kk} \end{vmatrix}, \quad d_{ik} = \int_{-a}^{a} E_i(x)E_k(x)dx. \tag{37}$$

Using equations (32) and (36), we obtain

$$a_k = \sum_{j=k}^{\infty} q_j \frac{M_{kj}}{M_{jj}}, \tag{38}$$

with

$$q_j = \frac{-1}{N_j} \int_{-a}^{a} v(x)Q_j(x)dx. \tag{39}$$

4 Stress-Intensity Factor

The coefficients c_m, d_n are obtainable, so that the dynamic stress field is given. However, in fracture mechanics, it is of importance to determine stress τ_{yy} in the vicinity of the crack's tip. The stress along the line of the crack is given by the first equality in equation (26). The stress singularities at the tip of the crack come from the behavior of the integrands as the integration variable ξ has an infinite value. Therefore, in the Laplace transform domain, we can easily define the

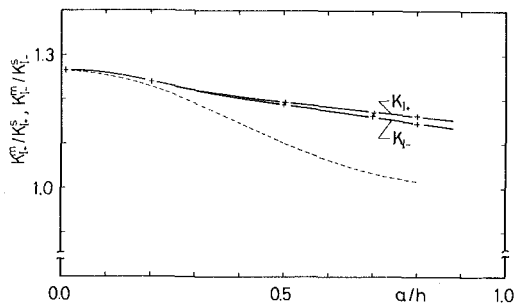

Fig. 4 Comparison of the dynamic stress-intensity factors with the corresponding static ones

stress-intensity factors for crack tip points $(a,0)$ and $(-a,0)$ by the formulas

$$\begin{aligned} K_{I+}^* &= \sqrt{2\pi(x-a)}\,\tau_{yy}^{*0}\,|_{x\to a+} \\ &= \frac{2(\kappa^2-1)}{\kappa^2\sqrt{a}}\left\{\sum_{m=1}^{\infty} c_m\,\Gamma\,(2m-\tfrac{1}{2})/(2m-2)!\right. \\ &\quad \left. + \sum_{n=1}^{\infty} d_n\,\Gamma\,(2n+\tfrac{1}{2})/(2n-1)!\right\}, \\ K_{I-}^* &= \sqrt{2\pi(-x-a)}\,\tau_{yy}^{*0}|_{x\to -a-} \\ &= \frac{2(\kappa^2-1)}{\kappa^2\sqrt{a}}\left\{\sum_{m=1}^{\infty} c_m\,\Gamma\,(2m-\tfrac{1}{2})/(2m-2)!\right. \\ &\quad \left. - \sum_{n=1}^{\infty} d_n\,\Gamma\,(2n+\tfrac{1}{2})/(2n-1)!\right\}. \end{aligned} \tag{40}$$

The Laplace inverse transformations in equation (40) are carried out by the numerical method given by Miller and Guy [6]. When the Laplace transform $f^*(s)$ can be evaluated at discrete points given by

$$s = (\beta + 1 + l), \quad l = 0, 1, 2, \ldots \tag{41}$$

we determine coefficients C_m from the following set of equations:

$$\delta' f^*\{(\beta+1+l)\delta'\} = \sum_{m=0}^{l} C_m\, l!/\{(l+\beta+1)(l+\beta+2) \ldots (l+\beta+1+m)(l-m)!\}, \tag{42}$$

where $\delta' > 0$ and $\beta > -1.0$. If coefficients are calculated up to C_{N-1}, an approximate value of $f(t)$ can be found as

$$f(t) = \sum_{m=0}^{N-1} C_m P_m^{(0,\beta)}\{2\exp(-\delta' t) - 1\}, \tag{43}$$

where $P_m^{(0,\beta)}(x)$ is a Jacobi polynomial and N is the number of terms employed. The parameters δ', β, and N are selected such that $f(t)$ can be best described within a particular range of time t.

5 Numerical Example and Results

Numerical calculations are done for Poisson's ratio $\nu = 0.25$. The semi-infinite numerical integrations in equation (27) with respect to the variable ζ and those with respect to the variable ξ are evaluated easily by using Simpson's method and Filon's method [9], respectively. To perform the Schmidt procedure, we adopt the first seven terms of the infinite series in equation (32). For a check of the accuracy, the values of $\Sigma_{k=1}^{7} a_k E_k(x)/(Pa/c_L)$ and $-v(x)/(a/c_L)$ are given in Table 1 for the case of $sa/c_L = 0.6$ and $a/h = 0.7$. From this it is clear that the Schmidt method is carried out satisfactorily. Using the values of $\beta = 0.0$, $\delta' = 0.2$, $N = 7$, we inverte the Laplace transforms numerically.

In Figs. 2 and 3, the results of K_{I+} and K_{I-} are plotted versus $c_L t/a$, in which the broken lines are the corresponding static values given by Isida [7]. The curve for $a/h = 0.0$ is omitted because, for the scale shown, the results for $a/h = 0.0$ and $a/h = 0.2$ are indistinguishable. In Fig. 4, the ratios of the peak values of K_{I+} and K_{I-} to the corre-

Table 1 Values of $\sum_{k=1}^{7} a_k E_k(x)/(Pa/c_L)$ and $-v(x)/(a/c_L)$ for $sa/c_L = 0.6$ and $a/h = 0.7$

x/a	$\sum_{k=1}^{7} a_k E_k(x)/(Pa/c_L)$	$-v(x)/(a/c_L)$
-1.00000	-1.6664	
-0.92857	-1.6666	
⋮	⋮	
0.00000	-1.6668	-1.6667
⋮	⋮	
0.92857	-1.6662	
1.00000	-1.6668	

sponding static values, namely, K_{I+}^m/K_{I+}^s and K_{I-}^m/K_{I-}^s are shown graphically, where the slender broken line shows the result for a centrally located crack in an infinite strip [5].

The maximum values of K_{I+} and K_{I-} are quite different, and K_{I+}^m is considerably larger than K_{I-}^m. However the value K_{I+}^m/K_{I+}^s is well coincident with that of K_{I-}^m/K_{I-}^s for the whole range of $a/h = 0.0 \sim 0.8$. Both of the ratios have the maximum for $a/h = 0.0$ and decrease according as the a/h ratio is increased. This means that the effect of inertia is predominant in the region of a small value of a/h, while the stress-intensity factors are more affected by the presence of the stress-free surface in the region of a larger value of a/h. Another useful result is that the values of K_{I+}^m/K_{I+}^s and K_{I-}^m/K_{I-}^s fall within the limits from 1.1 to 1.3 for $a/h = 0.0 \sim 0.8$.

Acknowledgments

The author wishes to acknowledge the extremely valuable suggestions offered by Prof. A. Atsumi of Tohoku University, which were given constantly throughout this work. Part of this research was financed to the Scientific Research Grant provided by the Ministry of Education, to which the author is eternally grateful.

References

1 Sih, G. C., ed., *Mechanics of Fracture 4, Elastodynamic Crack Problems*, Noordhoff International Publishing, Leyden, 1977.

2 Chen, E. P., "Impact Response of a Finite Crack in a Finite Strip Under Antiplane Shear," *Engineering Fracture Mechanics*, Vol. 9, 1977, pp. 719–724.

3 Chen, E. P., "Sudden Appearance of a Crack in a Stretched Finite Strip," ASME JOURNAL OF APPLIED MECHANICS, Vol. 45, 1978, pp. 277–280.

4 Sih, G. C., and Chen, E. P., "Normal and Shear Impact of Layered Composite With a Crack," ASME JOURNAL OF APPLIED MECHANICS, Vol. 47, 1980, pp. 351–358.

5 Itou, S., "Transient Response of a Finite Crack in a Strip With Stress-Free Edges," ASME JOURNAL OF APPLIED MECHANICS, Vol. 47, 1980, pp. 801–805.

6 Miller, M. K., and Guy, W. T., "Numerical Inversion of the Laplace Transform by Use of Jacobi Polynomials," *SIAM Journal of Numerical Analysis*, Vol. 3, 1966, pp. 624–635.

7 Isida, M., *Crack Problems in the Theory of Elasticity and Stress Intensity Factors* (in Japanese), Baifukan Press, Tokyo, 1976.

8 Morse, P. M., and Feshbach, H., *Methods of Theoretical Physics*, Vol. 1, McGraw-Hill, New York, 1958.

9 Åmemiya, A., and Taguchi, T., *Numerical Analysis and Fortran* (in Japanese), Maruzen, Tokyo, 1969.

J. D. Achenbach
Professor.
Fellow ASME

R. J. Brind
Postdoctoral Research Fellow.

Department of Civil Engineering,
Northwestern University,
Evanston, Ill. 60201

Elastodynamic Stress-Intensity Factors for a Crack Near a Free Surface

Elastodynamic Mode I and Mode II stress-intensity factors are presented for a subsurface crack in an elastic half space. The plane of the crack is normal to the surface of the half space. The half space is subjected to normal and tangential time-harmonic surface tractions. Numerical results show the variation of K_I and K_{II} at both crack tips, with the dimensionless frequency and the ratio a/b, where a and b are the distances to the surface from the near and the far crack tips, respectively. The results are compared with corresponding results for a crack in an unbounded solid.

Introduction

An homogeneous, isotropic, linearly elastic half space contains a subsurface crack perpendicular to the surface, as shown in Fig. 1. In this paper we examine the elastodynamic response of the cracked half space to the application at the surface of a uniform traction that varies harmonically with time. Attention will be directed toward the quantities that are of interest in fracture mechanics contexts, namely, the stress-intensity factors at the crack tips. We also compare the results with those for a Griffith crack in an unbounded medium subjected to the same incident wave motion.

In an earlier paper [1] the authors have considered the two-dimensional scattering of Rayleigh waves by a subsurface crack. There, the boundary-value problem for the scattered field was stated in mathematical terms and an integral representation for its solution derived. The problem was then reduced by standard methods to the solution of an uncoupled system of strongly singular integral equations which were solved numerically using a method due to Erdogan and Gupta [2]. Formulas were given for the far-field amplitudes of the waves in the scattered field and for the near-field quantities that we are concerned with here. The data in the integral equations were the values taken at the location of the crack by the stress components of the incident field, that is the elastodynamic solution in the absence of the crack. Thus the method described in [1] can be applied to the problem of this paper as well: the only modification required is to use the appropriate incident field. So in what follows only brief details of the equations which need to be solved will be given.

Contributed by the Applied Mechanics Division for publication in the JOURNAL OF APPLIED MECHANICS.

Discussion on this paper should be addressed to the Editorial Department, ASME, United Engineering Center, 345 East 47th Street, New York, N. Y. 10017, and will be accepted until December 1, 1981. Readers who need more time to prepare a discussion should request an extension from the Editorial Department. Manuscript received by the Applied Mechanics Division, October, 1980; final revision, February, 1981.

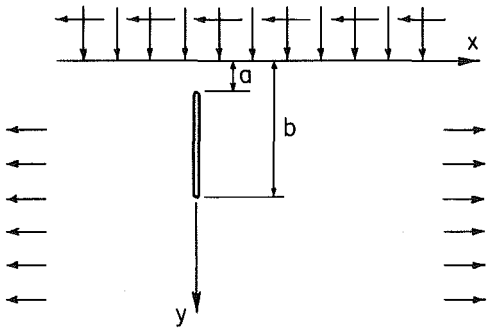

Fig. 1 Subsurface crack in prestressed half space

It is assumed that the faces of the crack do not interact with each other. This is a realistic assumption if the crack is actually a thin slit of finite width, or if a sufficiently large static prestress is applied which holds the crack in an open position as shown in Fig. 1.

Governing Equations

If the boundary conditions on the surface of the half space are

$$\sigma_{xy} = -\tau_0 e^{-i\omega t}, \quad \sigma_{yy} = -\sigma_0 e^{-i\omega t}, \tag{1a,b}$$

then the stress components of the incident field are calculated to be

$$\sigma_{xx}^{(i)} = \sigma_0(2k_L^2 - k_T^2)k_T^{-2} \exp(ik_L y) \tag{2}$$

$$\sigma_{xy}^{(i)} = -\tau_0 \exp(ik_T y), \tag{3}$$

where

$$k_\beta = \omega/c_\beta \quad \text{for} \quad \beta = L, T \tag{4}$$

$$c_L^2 = (\lambda + 2\mu)/\rho, \quad c_T^2 = \mu/\rho, \tag{5a, b}$$

and λ, μ are the Lamé constants, and ρ is the mass density. Now, it can be shown that, if the density functions, $d_x(y)$ and $d_y(y)$ satisfy the integral equations

$$-\sigma_{xx}^{(i)}(y') = \frac{\mu}{k_T^2} \int_a^b dy d_x(y) \Gamma_{x'x';xx}(0, y; 0, y') \tag{6}$$

$$-\sigma_{xy}^{(i)}(y') = \frac{\mu}{k_T^2} \int_a^b dy d_y(y) \Gamma_{x'y';xy}(0, y; 0, y') \tag{7}$$

together with the side conditions

$$\int_a^b dy d_i(y) = 0 \quad \text{for} \quad i = x, y \tag{8}$$

$$D_i(y) = d_i(y)(b - y)^{1/2}(y - a)^{1/2} \text{ is continuous in } [a, b], \tag{9}$$

then the elastodynamic field generated by the usual integral representation, equations (3.4a, b) of reference [1], satisfies all the required conditions and is the solution to the boundary-value problem we are seeking. Existence and uniqueness of the functions $d_x(y)$ and $d_y(y)$ can be proved, but these questions are not discussed here. The functions can be shown to have the physical interpretation of dislocation densities. The kernels of the integral equations are given by

$$\Gamma_{x'y';xy} = -\int_{\mathscr{C}} d\xi e^{i\xi(x'-x)} E(\xi, y) \times \frac{4\xi^2 \alpha_L \alpha_T e^{-\alpha_L y'} - (2\xi^2 - k_T^2)^2 e^{-\alpha_T y'}}{2\pi R(\xi)} + \int_{\mathscr{C}} d\xi (e^{i\xi(y-y')} + e^{i\xi(y+y')}) \times \frac{4\xi^2 \alpha_L \alpha_T e^{-\alpha_L |x-x'|} - (2\xi^2 - k_T^2)^2 e^{-\alpha_T |x-x'|}}{4\pi i \xi \alpha_T} \tag{10}$$

and

$$\Gamma_{x'x';xx} = -\int_{\mathscr{C}} d\xi e^{i\xi(x'-x)} F(\xi, y) \times \frac{(2\alpha_L^2 + k_T^2)(2\xi^2 - k_T^2) e^{-\alpha_L y'} - 4\xi^2 \alpha_L \alpha_T e^{-\alpha_T y'}}{2\pi R(\xi)} - \int_{\mathscr{C}} d\xi (e^{i\xi(y-y')} + e^{i\xi(y+y')}) \times \frac{(2\xi^2 - k_T^2)^2 e^{-\alpha_L |x-x'|} - 4\xi^2 \alpha_L \alpha_T e^{-\alpha_T |x-x'|}}{4\pi i \xi \alpha_L}, \tag{11}$$

where

$$E(\xi, y) = 4\xi^2 e^{-\alpha_L y} - (2\xi^2 - k_T^2)^2 \alpha_T^{-2} e^{-\alpha_T y} \tag{12}$$

$$F(\xi, y) = (2\alpha_L^2 + k_T^2)(2\xi^2 - k_T^2)\alpha_L^{-2} e^{-\alpha_L y} - 4\xi^2 e^{-\alpha_T y} \tag{13}$$

$$R(\xi) = (2\xi^2 - k_T^2)^2 - 4\xi^2 \alpha_L \alpha_T \tag{14}$$

$$\alpha_\beta = (\xi^2 - k_\beta^2)^{1/2} \quad \text{for} \quad \beta = L, T. \tag{15}$$

The integrands have poles at $\xi = \pm k_R$, where $k_R = \omega/c_R$ and c_R is the velocity of Rayleigh waves, and the branches are chosen so that Re $(\alpha_\beta) \geq 0$ for $\beta = L, T$, and $\xi \in \mathscr{C}$. The contour $\mathscr{C}$ in the complex plane is along the real axis and is indented above the pole and branch points in the left half plane and below those in the right, in order to satisfy the radiation condition.

The integral equations (6) and (7) together with the side conditions can be solved by standard methods, but the numerical evaluation of the kernels presents some difficulty. The expressions for the kernels involve terms which must be computed using a quadrature scheme on a deformed contour in the complex plane. For details we refer to [3, 2, and 1]. The displacement discontinuity $[u_i](y')$, $i = x, y$, and the stress-intensity factors can be calculated from the solutions to the discretized integral equations thus

$$[u_i](y') = \int_a^{y'} dy d_i(y), \quad i = x, y, \tag{16}$$

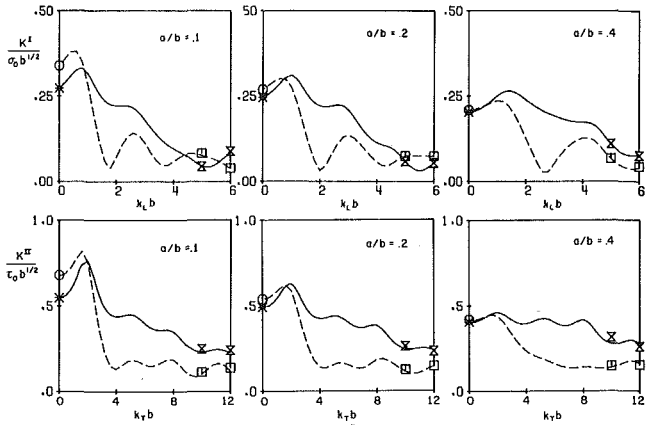

Fig. 2 Mode I and Mode II stress-intensity factors; - - - upper crack tip; —— lower crack tip; $\nu = \frac{1}{3}$; quasi-static approximation from [4]: ⊙, ∗; corresponding Griffith crack results: X, □

and

$$K_e^{\mathrm{I}} = \frac{\mu(k_T^2 - k_L^2)}{(b - a)^{1/2} k_T^2} |D_x(e)|, \quad e = a, b, \tag{17}$$

$$K_e^{\mathrm{II}} = \frac{\mu(k_T^2 - k_L^2)}{(b - a)^{1/2} k_T^2} |D_y(e)|, \quad e = a, b. \tag{18}$$

In the numerical computations Poisson's ratio was taken as $\nu = \frac{1}{3}$, and the two independent parameters were chosen to be $k_\beta b = \omega b/c_\beta$ and a/b.

Discussion of the Results

Deformations that are symmetric about the plane of the crack and those that are antisymmetric are independent of each other. In the present problem symmetric and antisymmetric deformations are induced by applied tractions that are normal and tangential, respectively, to the surface. Thus Mode II stress-intensity factors are generated by the shear tractions defined by equation (1a), and Mode I stress-intensity factors by the normal tractions defined by equation (1b).

Fig. 2 shows the variation of the Mode I and Mode II stress-intensity factors with the normalized frequencies $\omega b/c_L$ and $\omega b/c_T$, respectively, for three different crack configurations. The curves all show an increase to a peak and then an oscillatory decay as the frequency increases. In the limit $\omega b/c_\beta \to 0$ the near field can be approximated by the quasi-static field, and the incident field becomes uniform, i.e., $\sigma_{xx}^{(i)}$ and $\sigma_{xy}^{(i)}$ are constant on the crack. Cook and Erdogan [4] have presented results for the static problem of a subsurface crack opened by a constant pressure. They obtained these results from the solution of an integral equation which is actually the limit of equation (6) as $\omega b/c_L \to 0$. If the kernels of each of our equations (6) and (7) are examined, it can be shown that the limits are identical,

$$\lim_{\omega b/c_L \to 0} k_T^{-2} \Gamma_{x'x',xx}(0, y; 0, y') = \left(\frac{1}{(y - y')} + \frac{4yy' + y'^2 - y^2}{(y + y')^3}\right) \frac{1}{2\pi(1 - \nu)} = \lim_{\omega b/c_T \to 0} k_T^{-2} \Gamma_{x'y';xy}(0, y; 0, y'). \tag{19}$$

For static problems the results for the subsurface crack, opened by equal and opposite constant shear tractions acting on the two faces of the crack, can therefore be derived from the results for constant pressure. This is not true for dynamic problems. The stress-intensity factors presented in [4] are defined differently and are normalized with respect to different quantities, but they were multiplied by the appropriate factors and plotted as the symbols on the vertical axes in Fig. 2. The excellent agreement between the low frequency ap-

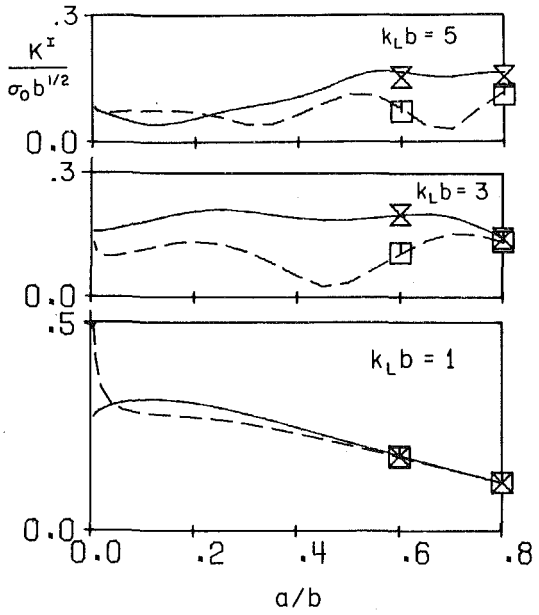

Fig. 3 Mode I stress-intensity factors versus a/b for three values of $\omega b/c_L$; - - - upper crack tip; —— lower crack tip; $\nu = \frac{1}{3}$; corresponding Griffith crack results: X, □

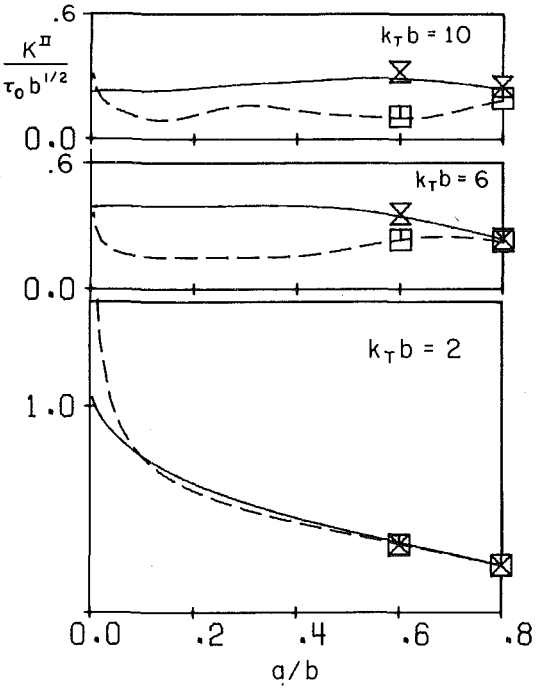

Fig. 4 Mode II stress-intensity factors versus a/b for three values of $\omega b/c_T$; - - - upper crack tip; —— lower crack tip; $\nu = \frac{1}{3}$; corresponding Griffith crack results: X, □

proximations and the results computed for small $\omega b/c_\beta$, provides a check on the solution of the integral equations and on the reliability of the evaluation of the kernels at low frequencies.

Figs. 3 and 4 show the variation of the stress-intensity factors with the nondimensional parameter a/b, for three fixed values of $\omega b/c_L$ in the Mode I case and of $\omega b/c_T$ in the Mode II case. The graphs show that the stress-intensity factors at the upper tip of a crack, that is gradually propagating towards a surface under the influence of vibrations excited at the free surface, suffer a sharp increase when the crack has almost broken the surface.

An example of the variation of the components of displacement discontinuity along the crack is given in Fig. 5. The profile is distorted

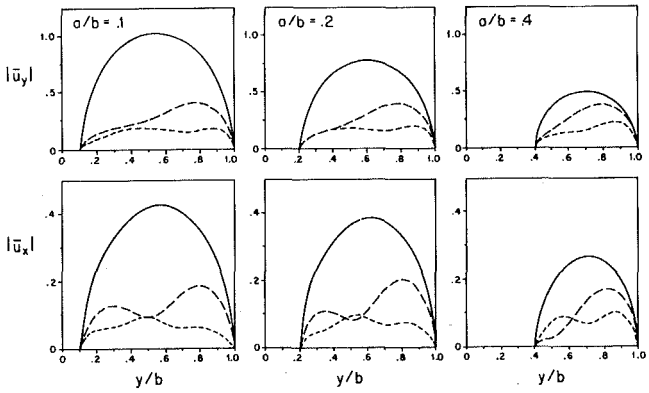

Fig. 5 Crack-opening displacements; tangential surface traction: $|\bar{u}_x| \equiv 0$, and $|\bar{u}_y|$ for $\omega b/c_T = 2$ (——), $\omega b/c_T = 6$ (- - -), and $\omega b/c_T = 10$ (- - - - -); $|\bar{u}_y| = \mu|[u_y]|/\tau_0 b$; normal surface traction: $|\bar{u}_y| \equiv 0$ and $|\bar{u}_x|$ for $\omega b/c_L = 1$ (——), $\omega b/c_L = 3$ (- - -), and $\omega b/c_L = 5$ (- · -); $|\bar{u}_x| = \mu|[u_x]|/\sigma_0 b$

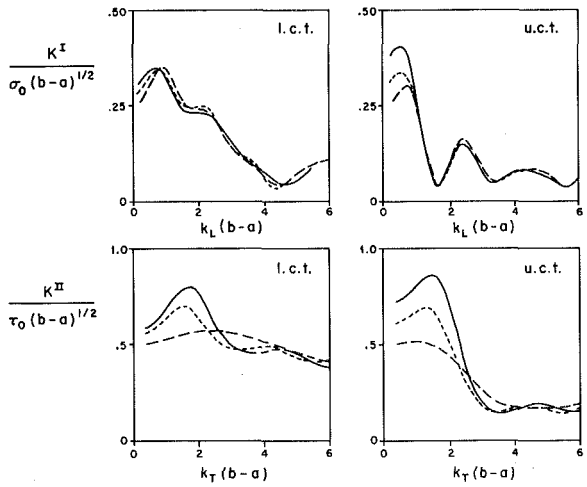

Fig. 6 Stress-intensity factors versus the dimensionless crack length for three values of a/b: —— $a/b = 0.1$, - - - - $a/b = 0.2$, and - - - $a/b = 1$ (crack in unbounded solid); uct = upper crack tip, lct = lower crack tip

from a symmetrical elliptic one, by the proximity of the free surface and the wave character of the incident field. At low frequency (long waves), i.e., at $k_L b = 1$ and $k_T b = 2$, the crack-opening displacement is almost elliptical for all three values of a/b.

It may be expected that the effect of the free surface diminishes as the crack moves away from it, i.e., as $k_\beta a = 2\pi a/\Lambda_\beta$ (where Λ_β = wavelength) becomes larger and/or a/b approaches unity. The stress-intensity factors should then approach the values for grazing incidence of L and T waves on a crack in an unbounded medium. Results for this problem can be obtained by noting that the kernels can be viewed as the sum of a source term and a term, which corresponds to its reflection in the free surface on which a condition of zero traction holds. If only the former term is retained and the integral equations are solved as before, then points which are indicated by symbols in Figs. 2–4, are obtained. The new integral equation is essentially that derived by Tan [5] for the treatment of normal incidence of elastic waves on a Griffith crack, but the numerical method of solution we use is different in that it preserves the correct form of the singularities of the solution at the crack tips.

To determine more precisely in what circumstances the effect of the free surface is negligible, the graphs of the stress-intensity factors of a Griffith crack in an unbounded medium were compared to those for subsurface cracks with various values of a/b. The Griffith crack is the limit of a subsurface crack as $k_\beta a \to \infty$ but $k_\beta(b-a)$ remains constant, or equivalently $a/b \to 1$ with $k_\beta(b-a)$ fixed. The results shown in Fig. 6 have therefore been plotted against and normalized

with respect to the crack length $(b - a)$. We expect that the subsurface crack curves will lie close to each other and to the Griffith crack curve, when the distance from the upper tip to the surface is large compared to either the crack length or the wavelength of the incident field. It appears that the condition, either that $a/b > 0.5$, or $k_L a > 0.25$ in the case of symmetric deformations and $k_T a > 0.5$ in the case of antisymmetric deformations, is sufficient to insure that the results do not depend greatly on the distance from the free surface to the nearest crack tip.

It is evident from Fig. 6 that the oscillations of the subsurface crack results about the curve for the Griffith crack are greater and persist for longer in the Mode II cases than the Mode I cases. It may be assumed that the oscillations about the infinite body curve are due primarily to the reflection of a diffracted body wave from the free surface. This body wave is primarily a longitudinal wave in the Mode I case and a transverse wave in the Mode II case, and so it seems that the latter is more significant.

Acknowledgment

This work was carried out in the course of research sponsored by the Air Force Office of Scientific Research under Grant AFOSR-78-3589-B to Northwestern University.

References

1 Achenbach, J. D., and Brind, R. J., "Scattering of Surface Waves by a Subsurface Crack," *Journal of Sound and Vibration*, in press.

2 Erdogan, F., and Gupta, G. D., "On the Numerical Solution of Singular Integral Equations," *Quarterly of Applied Mathematics*, Vol. 30, 1972, pp. 525–534.

3 Achenbach, J. D., Keer, L. M., and Mendelsohn, D. A., "Elastodynamic Analysis of an Edge Crack," ASME JOURNAL OF APPLIED MECHANICS, Vol. 47, 1980, pp. 551–556.

4 Cook, T. S., and Erodgan, F., "Stresses in Bonded Materials With a Crack Perpendicular to the Interface," *International Journal of Engineering Science*, Vol. 10, 1972, pp. 677–697.

5 Tan, T. H., "Scattering of Plane Elastic Waves by a Plane Crack of Finite Width," *Applied Scientific Research*, Vol. 33, 1977, pp. 75–100.

B. Paul
Professor of Mechanical Engineering,
Fellow ASME

J. Hashemi[1]
Research Fellow

Department of Mechanical Engineering,
University of Pennsylvania,
Philadelphia, Pa. 19104

Contact Pressures on Closely Conforming Elastic Bodies

A numerical method is developed for the determination of the contact pressure that arises when two elastic bodies with closely conforming non-Hertzian frictionless surfaces are pressed together. The method is a generalization of that recently developed by the authors for the case of antiformal contact, and includes a technique for automatically generating meshes that overlay the changing (load-dependent) contact patches. The method has been implemented in a computer program called CONFORM, and has been applied to problems of wheel and rail contact. The results have been verified by comparison with those generated by an independent program for the special case of relatively light wheel loading, where the contact is known a priori to be essentially counterformal. The results given herein for a relatively heavy (but realistic) wheel loading on the throat of the flange represent the first known solution for conformal contact between a railroad wheel and rail.

1 Introduction

Elastic contact stress problems are classified as Hertzian if they satisfy the following five conditions:

1 The bodies are homogeneous, isotropic, obey Hooke's law, and experience small strains and rotations (i.e., the linear theory of elasticity applies).

2 The contacting surfaces are frictionless.

3 The dimensions of the deformed contact patch remain small compared to the principal radii of the undeformed surfaces.

4 The deformations are related to the stresses in the contact zones as predicted by the linear theory of elasticity for half spaces (Boussinesq's influence functions are valid).

5 The contacting surfaces are continuous, and may be represented by second-degree polynomials (quadratic surfaces) prior to deformation.

Contact stress problems are also classified as follows:

(*a*) *Antiformal* (or *counterformal*), if Condition 3 is satisfied, or

(*b*) *Conformal*, if Condition 3 is violated.

Excellent surveys of recent research in the field of contact stresses have been provided by Kalker [1, 2]. From these surveys it will be seen that the vast bulk of such work starts from the assumption that the contact region is the ellipse predicted by Hertzian analysis. Even in Kalker's studies of the effects of friction on rolling creepage, both the contact pressure and the contact region are elliptical; i.e., the "contact pressure" problem is treated as Hertzian.

Until recently, there existed no general way of handling any non-Hertzian contact pressure problems. However, Singh and Paul [3] showed how to solve antiformal non-Hertzian problems using the so-called Simply Discretized (S.D.) method. This method was applied by them to relatively simple geometries. Later, Woodward and Paul [4] extended the S.D. method to the case of conformal problems, but Paul and Hashemi [5] developed a modification of the S.D. method by means of which they were able to solve antiformal contact problems for virtually arbitrary geometries. By means of a computer program COUNTACT [6] they found the first known solutions for realistic rail and wheel profiles in antiformal contact.

The present work represents an extension of the modified S.D. method to *conformal* problems with quite general geometries—including that of wheels and rails in closely conforming regions of the flange throat. Based upon this analysis, a computer program (called CONFORM) has been developed [7] and made available to the general public.

Additional references on related literature will be found in [3–5, 8].

In the next section, we formulate the integral equation governing conformal contact stress problems, and in Section 3, we show how the Modified Simply Discretized Method can be used to solve the integral equation. In Section 4 the determination of the initial candidate contact boundary is discussed. This is a necessary preliminary for the numerical method being used. In Section 5, methods are developed for mesh generation and true contact boundary determination which are more general and efficient than those used in the previously cited references. Section 6 discusses the influence functions used, and Section 7 briefly explains the organization of computer programs developed for this work. Examples are given in Section 8 and Conclusions are stated in Section 9.

---

[1] Now Assistant Professor at Abadan Institute of Technology, Abadan, Iran.

Contributed by the Applied Mechanics Division for publication in the JOURNAL OF APPLIED MECHANICS.

Discussion on this paper should be addressed to the Editorial Department, ASME, United Engineering Center, 345 East 47th Street, New York, N.Y. 10017, and will be accepted until December 1, 1981. Readers who need more time to prepare a discussion should request an extension from the Editorial Department. Manuscript received by the Applied Mechanics Division, July, 1980; final revision, January, 1981.

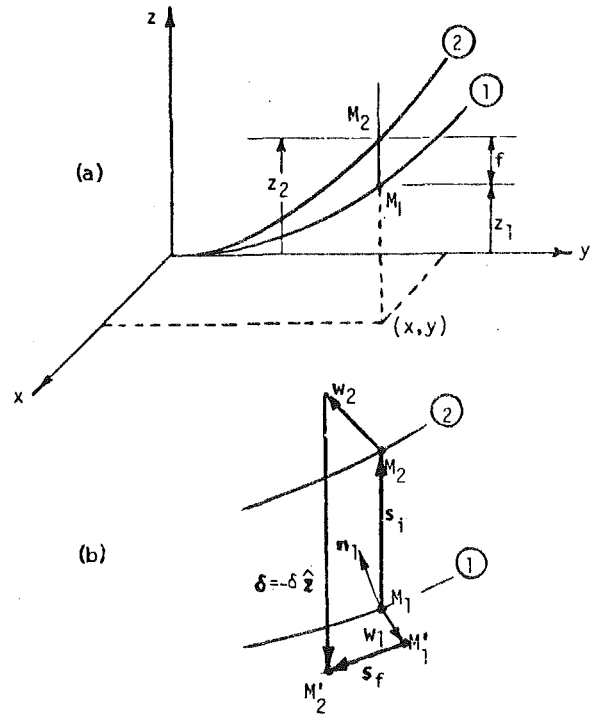

Fig. 1 The two bodies in contact under rigid body translation δ. (*a*) Curved lines are intersections of given surfaces with a plane through the *z*-axis. The line M_1M_2 is parallel to the *z*-axis, prior to deformation; (*b*) Enlargement of region near M_1 and M_2, showing the process of deformation.

2 Formulation of the Governing Integral Equation

Let two bodies of general, but closely conforming, shape be denoted as body 1 and body 2. Cartesian coordinate axes are set up with the initial contact point as common origin. Axes (x, y) lie in the tangent plane of the two surfaces at the initial contact point with the z-axis pointing into body 2.

The *initial separation* of points on the two bodies with common (x, y) coordinates is given by the known surface functions, z_1 and z_2, as (see Fig. 1):

$$f(x, y) = z_2(x, y) - z_1(x, y) \tag{1}$$

After the bodies are pressed together, the total displacement can be represented by a rigid-body motion plus a superposed deformation which decays rapidly with distance from the region of contact. In general, the rigid-body motion of body 2 relative to body 1 is defined by six parameters. For simplicity, we assume, at this point, that the rigid-body motion of body 2 relative to body 1 consists of a translation through distance δ in the negative direction of axis z. The quantity δ is called the *rigid-body approach*.

Let us consider two points M_1 and M_2 on the surfaces of bodies 1 and 2 with common coordinates (x, y) as in Fig. 1. The *initial separation vector* between the two points will be

$$\mathbf{s}_i = f(x, y)\hat{\mathbf{z}} \tag{2}$$

where $\mathbf{s}_i$ is the initial separation between point M_1 and M_2. $\hat{\mathbf{z}}$ is the unit normal vector in the z-direction, and $f(x, y)$ is given by (1). After deformation occurs, points M_1 and M_2 move to M_1' and M_2'.

If $\mathbf{w}_1$ and $\mathbf{w}_2$ represent the elastic displacement vectors of the points M_1 and M_2, then the separation vector after deformation becomes (see Fig. 1(*b*))

$$\mathbf{s}_f = \mathbf{s}_i + \mathbf{w}_2 - \mathbf{w}_1 - \delta\hat{\mathbf{z}} \tag{3}$$

For closely conforming surfaces, the normals to the two surfaces (at M_1 and M_2) differ very slightly in direction, and either of the two initial surfaces represents a good approximation to the deformed surface on which contact occurs. We will therefore assume that the contact patch lies on surface 1, and its unit normal vector $\mathbf{n}$ will be approximated by $\mathbf{n}_1$, the unit outward normal to surface 1.

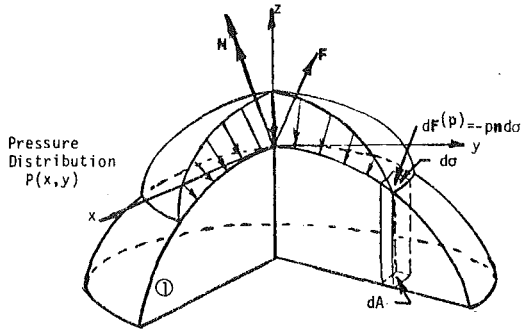

Fig. 2 Forces applied to body 1

Within the contact patch (by definition of contact), the component of separation $\mathbf{s}_f$ in the normal direction vanishes, i.e.,

$$\mathbf{s}_f \cdot \mathbf{n} = (f\,\hat{\mathbf{z}} + \mathbf{w}_2 - \mathbf{w}_1 - \delta\hat{\mathbf{z}}) \cdot \mathbf{n}_1 \approx 0 \tag{4}$$

or

$$w_2^n + w_1^n = (\delta - f)\, n_z \quad \text{(withing contact patch)} \tag{5}$$

where

$$w_1^n = -\mathbf{w}_1 \cdot \mathbf{n}_1$$

$$w_2^n = -\mathbf{w}_2 \cdot \mathbf{n}_2 = \mathbf{w}_2 \cdot \mathbf{n}_1$$

are the components of $\mathbf{w}_1$ and $\mathbf{w}_2$ along the inward normals to surfaces 1 and 2; note that $\mathbf{n}_2 \approx \mathbf{n}_1$, and n_z is the z-component of $\mathbf{n}_1$.

We consider the case of frictionless surfaces which develop a purely normal surface pressure p over the contact region σ. The displacement w_i^n for body i is related to the pressure on body i by the expression

$$w_1^n(\mathbf{r}) = \int_\sigma G_i(\mathbf{r}; \mathbf{r}')\, p(\mathbf{r}')\, d\sigma' \tag{6}$$

where the *influence function* $G_i(\mathbf{r}; \mathbf{r}')$ is the normal displacement of point $\mathbf{r}$ due to a unit normal force on body i at $\mathbf{r}'$.[2] Denoting the projection of area element $d\sigma'$ on the $x - y$ plane by

$$dA' \equiv n_z'\, d\sigma' \tag{7}$$

where n_z' is the z-component of $\mathbf{n}_1'$, we may write (6) in the form

$$w_i^n(\mathbf{r}) = \int_\Omega G_i(\mathbf{r}; \mathbf{r}')\, p(\mathbf{r}')\, \frac{dA'}{n_z'} \tag{8}$$

where Ω, the projection of σ on the $x - y$ plane, will henceforth be called the *contact region.*

Therefore, equation (5) becomes

$$\int_\Omega (G_1 + G_2)\, p(\mathbf{r}')\, \frac{dA'}{n_z'} = (\delta - f)\, n_z \tag{9}$$

For indentors of finite curvature, a physically meaningful solution requires that

$$\begin{aligned} p(x, y) &\geq 0 \quad \text{within } \Omega \\ p(x, y) &= 0 \quad \text{on } C \end{aligned} \tag{10}$$

where C is the boundary of the contact region Ω.

Equation (9) and condition (10) govern the conformal contact problem; they can be solved for $p(x, y)$ and C, if a value of δ is specified.

[2] The vector $\mathbf{r}(\mathbf{r}')$ locates a *field* (*source*) point. Quantities evaluated at a source point will be marked by primes: e.g., $p' = p(\mathbf{r}')$, but $p = p(\mathbf{r})$.

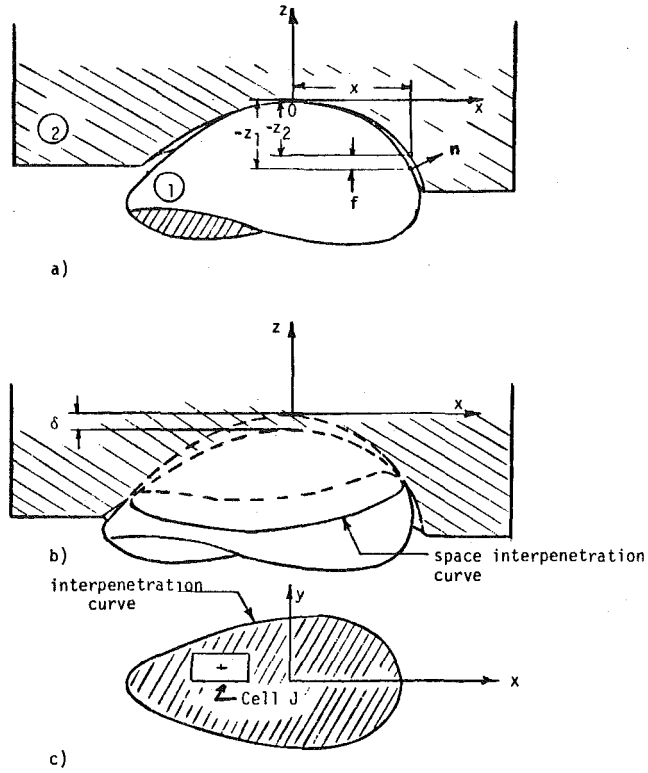

Fig. 3 Two bodies in conformal contact; (a) prior to deformation; (b) fictitious interpenetration; (c) initial candidate contact region

The resultant force $\mathbf{F}^{(p)}$ and moment $\mathbf{M}^{(p)}$ (due to the pressure on body 1), may be found (see Fig. 2) from the expressions

$$\mathbf{F}^{(p)} = -\int_\Omega p\mathbf{n}\, d\sigma \tag{11}$$

$$\mathbf{M}^{(p)} = -\int_\Omega \mathbf{r}\times p\mathbf{n}\, d\sigma \tag{12}$$

where $\mathbf{r} = (x, y, z)$, and $d\sigma = dA/n_z$. Thus the applied external force $\mathbf{F} = -\mathbf{F}^{(p)}$ and moment $\mathbf{M} = -\mathbf{M}^{(p)}$ are given by

$$\{F_x, F_y, F_z\} = -\int_\Omega p\{n_x, n_y, n_z\}\frac{dA}{n_z} \tag{13}$$

$$M_x = \int_\Omega (yn_z - zn_y)\, p\,\frac{dA}{n_z}$$

$$M_y = \int_\Omega (-x\, n_z + zn_x)\, p\,\frac{dA}{n_z}$$

$$M_z = \int_\Omega (xn_y - yn_x)\, p\,\frac{dA}{n_z} \tag{14}$$

3 Discretization of the Integral Equation

For a given rigid-body approach δ, equation (9) could be solved for the pressure field $p(x, y)$ if the region of integration Ω were known. We will begin by assuming a *candidate* contact region Ω. The projection, on the $x - y$ plane, of the intersection curve which would arise if surface 1 were displaced relative to surface 2, along the z-axis by distance δ, is called the *interpenetration curve* and is given (see Fig. 3) by

$$f(x, y) = z_2(x, y) - z_1(x, y) = \delta \tag{15}$$

If the region bounded by the interpenetration curve is chosen as the initial candidate region, equation (9) becomes an integral equation of the first kind, which we shall solve by the modified simply discretized method [5]. Let us discretize the region Ω of the integral equation into n subregions $\Omega_1, \Omega_2, \ldots, \Omega_n$, where the subregion Ω_j is called "cell j." Then, equation (9) reduces to

$$\int_{\Omega_1}(G_1 + G_2)\frac{p'dA'}{n_z'} + \int_{\Omega_2}(G_1 + G_2)\frac{p'dA'}{n_z'}\cdots + \int_{\Omega_n}(G_1 + G_2)\frac{p'dA'}{n_z'} = [\delta - f(x, y)]n_z(x, y) \tag{16}$$

If cell j is small enough so that $p(x', y')$ and $n_z(x', y')$ over that cell can be considered as constants p_j and n_z^j, then equation (16) reduces to

$$\int_\Omega (G_1 + G_2)\frac{p'dA'}{n_z'} \approx \sum_{j=1}^{n}\frac{p_j}{n_z^j}\int_{\Omega_j}(G_1 + G_2)\, dA' \approx [\delta - f(x, y)]\, n_z(x, y) \tag{17}$$

The term $(G_1 + G_2)$ will be singular within certain cells and must therefore be kept under the integral sign, at least for such cells.

To find the unknown values of p_j we select n field points (x_i, y_i) and write equation (17), for each of these points, in the form

$$\sum_{j=1}^{n} b_{ij}p_j = d_i \quad (i = 1, \ldots n) \tag{18}$$

where

$$b_{ij} = \frac{1}{n_z^j}\int_{\Omega_j}(G_1 + G_2)\, dA' \tag{19}$$

$$d_i = [\delta - f(x_i, y_i)](n_z)_i \tag{20}$$

If matrix $[b_{ij}]$ is nonsingular, equations (18) may be solved for the candidate pressures p_j. If these values of p_j do not satisfy conditions (10) we must modify the assumed contact region boundary C. The method used to choose and modify the boundary of Ω will be described in Section 5.

The influence functions used for the specific examples of rail and wheel considered in this paper are described in Section 6; for further discussion see [8].

The applied force and moment are obtained from equations (13) and (14) as

$$F_x = \sum_{j=1}^{n} p_j\left(\frac{n_x}{n_z}\right)_j$$

$$F_y = \sum_{j=1}^{n} p_j\left(\frac{n_y}{n_z}\right)_j A_j$$

$$F_z = \sum_{j=1}^{n} p_j A_j \tag{21}$$

$$M_x = \sum_{j=1}^{n} p_j\left[y - z\frac{n_y}{n_z}\right]_j A_j$$

$$M_y = \sum_{j=1}^{n} p_j\left[-x + z\frac{n_x}{n_z}\right]_j A_j$$

$$M_z = \sum_{j=1}^{n} p_j\,[(xn_y - yn_x)/n_z]_j\, A_j \tag{22}$$

where A_j is the area of cell j (in the x, y-plane).

4 Initial Candidate Contact Boundary

The initial candidate contact region will be chosen as the region insde the "interpenetration curve" defined in Section 3. General procedures for finding this curve are given in [9].

It was shown in [5] that for antiformal (but not necessarily Hertzian) contact, the actual contact region lies *inside* the interpenetration curve associated with a fixed approach. Similar reasoning shows [8] that, in the case of conformal contact problems, the true contact patch lies inside the interpenetration curve, provided that the influence

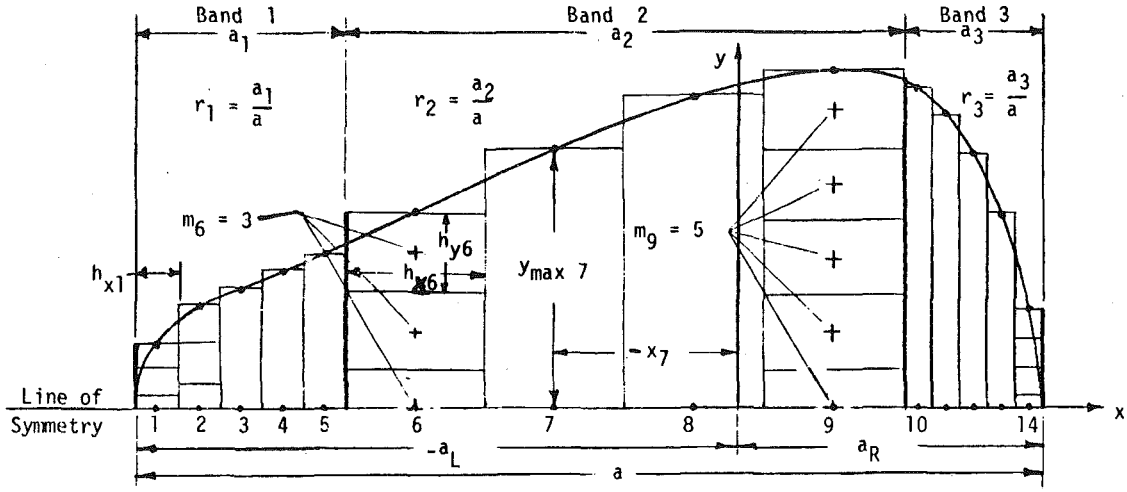

Fig. 4 Mesh arrangement for sample interpenetration curve. Bands are shown separated by heavy vertical lines. Band 1 is subdivided into 5 strips, band 2 into 4 strips, band 3 into 5 strips. Note that the x-axis is a line of symmetry, and only half of the contact patch is shown.

functions used for both bodies are *unidirectional*[3] over the initial candidate contact patch. Experience to date suggests that the interpenetration curve is a good candidate for the initial contact patch, for both conformal and antiformal contact.

5 Mesh Generation and Contact Boundary Determination

The method described in [5] for the mesh generation and boundary determination of antiformal problems has been improved and extended to the conformal problem. In the following, rectangular cells, with sides parallel to the x and y-axis are utilized, and the contact region is assumed to be symmetric about the x-axis (as it would be for a wheel axis parallel to the x-axis, and a rail axis parallel to the y-axis); consequently, only half of the contact region (see Fig. 4) needs to be discussed. Both the field points and source points will be chosen to lie at the centroids of the rectangular cells. The scheme of subdivision for a candidate contact region is as follows:

The x-diameter, which has known length a, may be divided into any number (n_b) of segments called *Bands*. A typical band (i) will be further divided into n_{si} segments called *strips*. Then the "horizontal" length h_{xi} of cells in band i will be given by

$$h_{xi} = a_i/n_{si} \tag{23}$$

where

$$a_i = r_i a \tag{24}$$

and r_i is a fixed positive ratio (less than 1) associated with band i, such that

$$\sum_i r_i = 1.$$

If we divide each half-strip j into a number of cells m_j, the "vertical" length h_y of each cell in that strip will be determined as

$$h_{yj} = y_{\max j}/m_j \tag{25}$$

where $y_{\max j}$ is the y-coordinate of the point on the boundary curve corresponding to the center line of half-strip$j$ (see Fig. 4).

If it is desired to have a field point on the x-axis, then we let

$$h_{yj} = y_{\max j}/(m_j - \tfrac{1}{2}) \tag{26}$$

The x-coordinate of the field points of all cells in the first strip will be obtained as

$$x_1 = a_L + \frac{h_{x1}}{2} \tag{27}$$

where a_L is the left-x-intercept of the boundary curve. Then the x-coordinate of the cell centroid in strip j becomes (for band 1):

$$x_j = x_{j-1} + h_{xj} \tag{28}$$

A similar procedure is followed for all subsequent bands.

Having unambiguously defined the cell arrangement, we may use equations (19) and (20) to evaluate b_{ij} and d_i. Then the unknowns p_j may be found by solving the linear equations (18).

If the current pressures p_j do not satisfy conditions (10), the diameter a and the ordinates $y_{\max j}$ are redefined by quadratic interpolation as described in [5], thereby determining a new candidate contact boundary C. The whole process is repeated until the conditions (10) are fully satisfied. This procedure has been tested on numerous cases (e.g., railroad wheels and rails, crowned rollers, cams, etc.) and has always terminated satisfactorily within approximately five iterations. As will be seen next, the geometry of a wheel-rail interface is about as complicated a case as one might find in any practical situation.

6 Influence Functions for Rail and Wheel Surface

One of the major difficulties in the solution of any contact problem is the determination of suitable Green's functions for the surfaces in contact. These "influence functions" relate the elastic displacements at a given point to a unit applied force at some other point. In contact problems, we are concerned with the elastic displacements of surface points due to a unit load applied anywhere on the surface of a body.

In *antiformal* contact of rail and wheel, the contact area is approximated by a plane, making it appropriate to use Boussinesq's influence function [10] for all surfaces. However, in *conformal* contact (where the contact surface is not approximately plane), it is generally necessary to find more individualized influence functions for each of the two surfaces in contact. For many realistic surfaces, the exact influence functions annot be found analytically; therefore, they must be generated numerically as in [4], or else be approximated by some convenient mathematical expressions.

A study of various exact and approximate influence functions has been described in [8]. Although, in principle, one may generate accurate influence functions for arbitrary surface geometries with the aid of three-dimensional finite-element programs, these studies indicate that the costs of such an approach for rail and wheel geometries are prohibitive at this time. The only exact solution (known to the authors) for the effects of a point load on a *curved* surface is that of Sternberg and Rosenthal [11]. This solution together with some finite-element solutions using the well-known program ANSYS provided benchmarks for the testing of various approximate influence

[3] An influence function will be described as *unidirectional* over a surface if a normal force applied to a point on the surface produces displacements at all points of the surface whose components in the direction of the applied force have the same sign everywhere.

functions. The results of this testing program are too copious to discuss here, but the overall conclusions are summarized next. It was found in [8] that for surfaces of negative Gaussian curvature (saddle surfaces) such as at point C in the rail-vehicle wheel of Fig. 5, the following expression gives a reasonable approximation to the normal displacement w_n at a surface point (x, y, z) due to a unit normal force at the surface point (x', y', z'):

$$w_n = \frac{(1-\nu)/\pi E}{[(x-x')^2 + (y-y')^2 + (z-z')^2]^{1/2}} \tag{29}$$

where E and ν are Young's modulus and Poisson's ratio.

For surfaces of positive Gaussian curvature (e.g., the sphere), it was found in [8] that some improvements could be made on the foregoing expression, but on balance equation (29) represents a reasonable compromise between accuracy and simplicity.

7 Computer Program "CONFORM"

The procedures just described have been incorporated into a FORTRAN computer program called CONFORM which stands for "*CONFORMal* contact." The program can treat all contact problems with one axis of symmetry in its contact patch. In rail-wheel problems there will always be at least one axis of symmetry (parallel to the wheel axis) for wheelsets at zero yaw angle. Complete information on the program is given in the User's Manual [7]. Additional background on the computational procedures used will be found in [8, 9].

8 Examples

To illustrate the method, we consider a problem of great practical interest; namely, the contact of the wheel of a metroliner railroad coach with a standard (140 lb per yard) rail. Both wheel and rail are made of steel with an elastic modulus of $E = 30 \times 10^6$ psi (2.068×10^{11} Pa) and Poisson's ratio of $\nu = 0.3$.

It is assumed that initial contact occurs at the point C in Fig. 5 where both the wheel and the rail profiles undergo jumps in curvature. The rail profile is described initially (from manufacturer's drawings) by a set of mutually tangent circular arc segments referred to Cartesian axes (x_r, z_r) fixed in the rail. Similarly, the segments of the wheel profile are referred to axes (x_w, z_w) fixed in the wheel. Complete dimensional data for the system are given in [7], but the circular arc segments on either side of point C (for both the rail and the wheel) which are needed for the present examples are specified as follows (dimensions in in.):

Body	*Radius*	*Coordinates of arc center*
rail	1.250	$x_r = 0.1612$, $z_r = -1.2715$
rail	0.375	$x_r = 1.0588$, $z_r = -0.5188$
wheel	1.280	$x_w = 1.0495$, $z_w = -1.3299$
wheel	0.378	$x_w = 1.5213$, $z_w = -0.5611$

The foregoing information is sufficient to uniquely define the wheel and rail profile referred to the local (ξ, ζ) coordinate system shown in Fig. 5, where the ζ axis is aligned with the common normal to wheel and rail at the initial contact point C. Details are given in [9] of geometric analysis needed to express the initial separation $(\zeta_{\text{wheel}} - \zeta_{\text{rail}})$ as a function of the orthogonal coordinates (ξ, η) in the common tangent plane at C.

For the contact point illustrated in Fig. 5, the problem could be either *antiformal* or *conformal* depending upon the magnitude of the applied load. In the first example, the applied load is relatively small so that the contact patch is antiformal and the accuracy and reliability of the program *CONFORM* can be verified versus program *COUNTACT* (see Fig. 6). In the second example, the load is so high that the problem is highly conformal and the deviation between the two programs is significant (see Fig. 7). The force component F and the normal approach δ mentioned later are measured in the direction of the ζ-axis. Complete input and output data are given in [7], but the major results are summarized as follows.

Example 1. Antiformal Case of Rail and Wheel Contact Stresses. Let the initial point of contact of rail and wheel be point C shown in Fig. 5. For $\delta = 0.0005$ in. the numerical solution was found

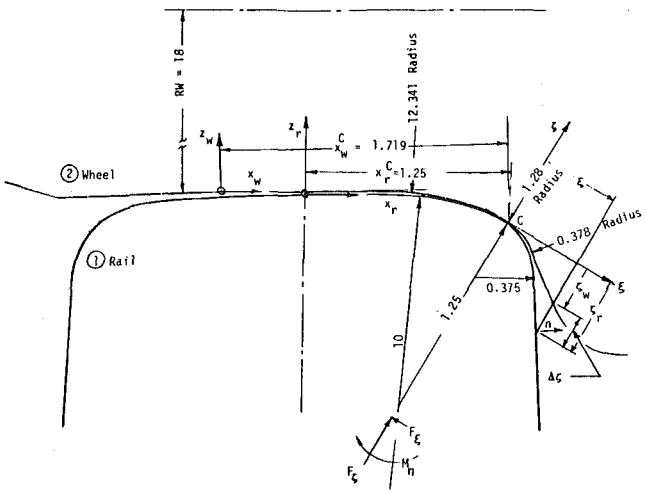

Fig. 5 Example of rail and wheel in conformal contact (unloaded case shown) Numerical data is for 140RE rail (AREA designation) and for SIG Metroliner wheel (SIG = Schweitzerische Industrie-Gesellschaft); dimensions in inches.

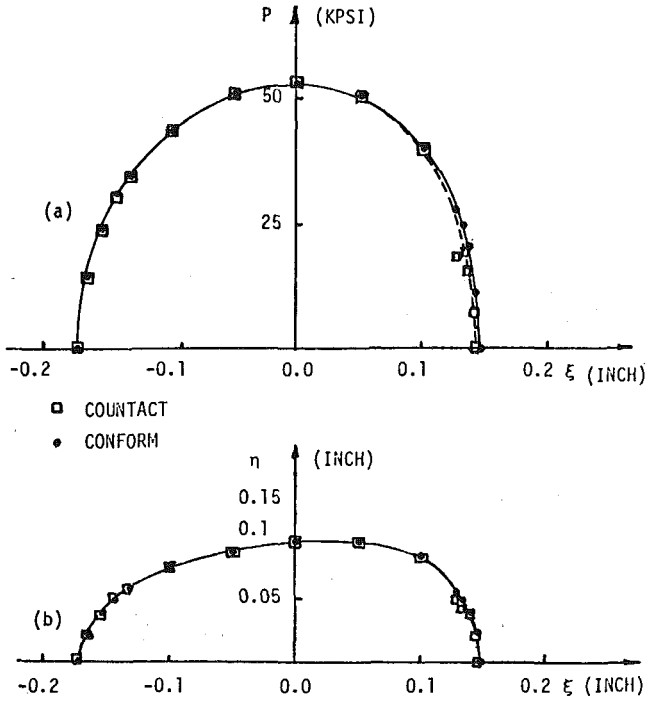

Fig. 6 Comparison of programs CONFORM and COUNTACT for $\delta = 0.0005$ in. (1.27×10^{-5}m). The corresponding forces are: $F = 1413$ lb (6.285 N) [CONFORM] $F = 1434$ lb (6.378 N) [COUNTACT] (*a*) Pressure distribution, (*b*) Contact patch.

by using the computer program "COUNTACT-1" [counterformal contact; see (5)] *and* also by program "CONFORM" (conformal contact). The contact region of Fig. 6(*b*) was divided into 42 cells.

The program CONFORM requires, as part of the input, the rigid-body approach δ, an initial candidate contact region, and the desired initial mesh arrangement. The output includes: pressure distribution, load (force and moment), and boundary of contact region.

A plot of pressure distribution along the ξ-axis is given in Fig. 6(*a*), and the upper half of the contact region is shown in Fig. 6(*b*) for both programs. Note that for the very light load applied (1413 lb), the contact patch is small and the problem is antiformal (but non-Hertzian). The excellent agreement between the predictions of programs COUNTACT and CONFORM, represents a validation of the latter program.

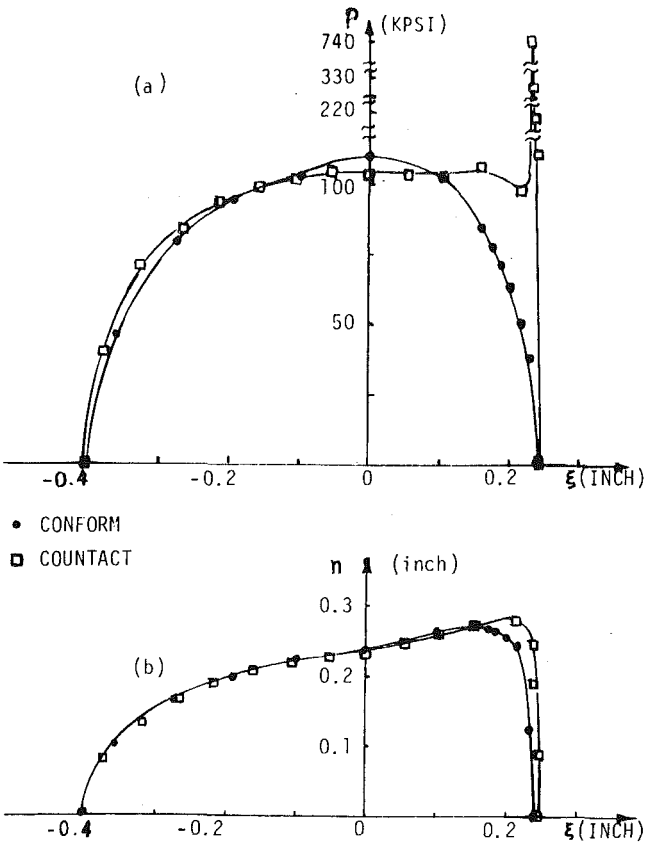

Fig. 7 Comparison of programs CONFORM and COUNTACT for $\delta = 0.003$ in. (7.62×10^{-5}m); $F = 20550$ lb (91400 N) [COUNTACT]; $F = 19000$ lb (84510 N) [CONFORM], (*a*) Pressure distribution, (*b*) Contact patch

Example 2. Conformal Case of Rail and Wheel Contact Stresses. For the same initial point of contact as in example 1, but for a higher load, the problems becomes conformal, and again the numerical solution of the problem was obtained by both *CONFORM* and *COUNTACT*, for $\delta = 0.003$ in. The plot of pressure distribution along the ξ-axis is shown in Fig. 7(*a*). The contact patch, shown in Fig. 7(*b*), was divided into 80 cells.

9 Conclusions

The modified simply discretized method of Paul and Hashemi [5] has been extended to conformal problems. Methods for automatic mesh generation and contact patch boundary determination have also been extended to conformal contact problems.

Computer program CONFORM, based on these ideas, has been described and numerical results were presented for selected examples.

The first numerical example demonstrates the accuracy of program CONFORM for the special case of non-Hertzian antiformal contact problems. The accuracy of program CONFORM for this class of problems was checked against the more specialized program COUNTACT, which is limited to strictly antiformal problems. Fig. 6 illustrates the validity of program CONFORM for this verifiable case.

The second example presents the first known solution to the conformal contact stress problem for geometry as complex as that of a realistic railhead and wheel making contact on the throat of the flange.

Fig. 7(*a*) illustrates how important it is to use program CONFORM for truly conformal cases, and that practical cases of conformal problems occur which cannot be adequately approximated by a procedure designed for antiformal cases.

Acknowedgment

The authors appreciate the support of the Federal Railroad Administration of the U. S. Department of Transportation, which sponsored this work under Contract DOT-0S-60144.

References

1 Kalker, J. J., "Review of Wheel-Rail Rolling Contact Theories," *The General Problem of Rolling Contact*, AMD-Vol. 40, eds., Browne, A. L., and Tsai, N. T., ASME, N.Y., 1980.

2 Kalker, J. J., "The Computation of 3D Rolling Contact With Dry Friction," *International Journal for Numerical Methods in Engineering*, Vol. 14, No. 9, 1979, p. 1293.

3 Singh, K. P., and Paul, B., "Numerical Solution of Non-Hertzian Elastic Contact Problems, "ASME JOURNAL OF APPLIED MECHANICS, Vol. 41, 1974, pp. 29–35.

4 Woodward, W., and Paul, B., "Contact Stresses for Closely Conforming Bodies—Application to Cylinders and Spheres," Technical Report No. 2, Dec. 1975, DOT-TST-77-48, Contract DOT-0S-400-3 (PB 271033/AS; available from National Technical Information Service, Springfield, Va. 22151.

5 Paul, B., and Hashemi, J., "An Improved Numerical Method and Computer Program for Counterformal Contact Stress Problems," ASME, *Computational Techniques for Interface Problems*, AMD-Vol. 40, eds., Park, K. C., and Gartling, D. K., 1978.

6 Paul, B., and Hashemi, J., "User's Manual for Program COUNTACT (*COUNT*erformal Cont*ACT* Stress Problems)," Technical Report, No. 4, Sept. 1977, FRA-ORD/78-27, (PB 286097/AS, available from National Technical Information Service, Springfield, Va. 22151.

7 Paul, B., and Hashemi, J., "User's Manual for CONFORM (*CONFOR-Mal* Contact Stress Problems," Technical Report No. 5, June 1978, FRA-ORD/78-40, (PB 288927/AS, available from National Technical Information Service, Springfield, Va. 22151.

8 Hashemi, J., and Paul, B., "Contact Stresses on Bodies With Arbitrary Geometry, Applications to Wheels and Rails," Report No. FRA-ORD/79-23, Technical Report No. 7, Apr. 1979 (PB 299409/AS, available from National Technical Information Service, Springfield, Va. 22151.

9 Paul, B., and Hashemi, J., "Contact Geometry Associated With Arbitrary Rail and Wheel Profiles," *Proc. of Symposium on the General Problem of Rolling Contact*, ASME, N.Y., 1980; also see Report No. FRA-ORD/78-41, Technical Report No. 6, 1979 (PB 80142656, available from National Technical Information Service, Springfield, Va. 22151.

10 Lur'e, A. I., *Three-Dimensional Problems of the Theory of Elasticity*, Interscience, N.Y., 1964.

11 Sternberg, E., and Rosenthal, F., "The Elastic Sphere Under Concentrated Loads," ASME JOURNAL OF APPLIED MECHANICS, Vol. 19, 1952, pp. 413–421.

M. Comninou
Associate Professor,
Department of Civil Engineering,
The University of Michigan,
Ann Arbor, Mich. 48109
Mem. ASME

J. Dundurs
Professor,
Department of Civil Engineering,
Northwestern University,
Evanston, Ill. 60201
Fellow ASME

J. R. Barber
Lecturer,
Department of Mechanical Engineering,
University of Newcastle upon Tyne,
Newcastle upon Tyne, NE1 7RU,
England

Planar Hertz Contact With Heat Conduction

The paper discusses the planar Hertz contact problem when the bodies are not only pressed together but also exchange heat by conduction. The nature of the problem and the results depend strongly on the direction of heat flow. If heat flows into the material with the larger distortivity, the common boundary conditions are sufficient to achieve a solution which satisfies the inequalities associated with a contact problem. For heat flowing in the opposite direction, the common boundary conditions by themselves lead to contradictions, but the difficulties can be overcome by introducing a zone of imperfect contact. The formulation is based on a suitable Green's function, and the problem is reduced to a singular integral equation which must be solved numerically.

Introduction

The common boundary conditions for thermoelastic contact are based on the ideas of perfect contact and perfect insulation. The first idea implies that the interface offers no resistance to heat flow in the regions with solid to solid contact. It is equivalent to an assumption that temperature is continuous across the contact interface. The second idea presumes that no heat is exchanged between the bodies in the separation zones where the solids are out of contact, or that the normal derivative of temperature vanishes in these zones. It is now known, however, that these boundary conditions may lead to mathematical dilemmas for steady-state heat conduction involving contact between bodies with geometrically smooth surfaces. The nature of the difficulties depends on the direction of heat flow: lack of existence for heat flowing into the material with the smaller distortivity (see the list of symbols for definition), and possible lack of uniqueness if heat flows into the material with the larger distortivity.

The difficulty with heat flowing into the material with the smaller distortivity was first noted by Barber [1] in treating the indentation of an elastic half space by a rigid sphere. If the sphere is cold, the contact tractions become tensile near the periphery of the contact region. It was subsequently proven by Barber [2] that the situation cannot be rectified by assuming a concentric array of contact and separation zones. Tensile contact tractions were also encountered by Panek and Dundurs [3] in analyzing the thermoelastic contact between bodies with wavy surfaces. It should be noted that the difficulty is not merely due to an insufficiency of the solution method, but that it is inherent to the problem. Thus Comninou and Dundurs [4] have shown by an asymptotic analysis that a direct transition from perfect contact to separation unavoidably leads to tensile contact tractions, as well as interpenetration of material.

It was conjectured by Dundurs and Comninou [5] on basis of a one-dimensional model that the lack of existence of solutions could be remedied by introducing a pressure-dependent resistance to heat flow in the contact zones. Indeed, it has recently been shown by Duvaut [6] that solutions satisfying the appropriate inequalities (negative normal tractions in the contact zones, and positive gaps in the separation zones) exist for physically realistic laws of the interface resistance. All contact problems are nonlinear because of the inequalities, but a pressure-dependent resistance makes the nonlinearities much stronger.

A modification of the idealized boundary conditions for heat flowing into the material with the smaller distortivity has been proposed by Barber [7]. It pays a penalty in that a new zone (imperfect contact) is needed, but avoids the strong nonlinearities that arise from a pressure-dependent resistance. Accordingly, the contact zone consists of two parts: a zone of perfect contact in which the common assumption of no thermal resistance holds, and a zone of imperfect contact in which the contact pressure vanishes and the contact interface offers some resistance to heat flow. One is led to these boundary conditions by considering a certain limit in the interface resistance, which must be a monotonically decreasing function of pressure [7]. An asymptotic analysis has revealed [4] that the inequalities are not violated at the transition from perfect to imperfect contact if heat flows into the material with the smaller distortivity.

The mathematical difficulties appear to be of the opposite nature when heat flows into the material with the larger distortivity. There

Contributed by the Applied Mechanics Division for publication in the JOURNAL OF APPLIED MECHANICS.
Discussion on this paper should be addressed to the Editorial Department, ASME, United Engineering Center, 345 East 47th Street, New York, N. Y. 10017, and will be accepted until December 1, 1981. Readers who need more time to prepare a discussion should request an extension from the Editorial Department. Manuscript received by ASME Applied Mechanics Division, July, 1980; final revision, January, 1981.

is evidence that, in such a case, the solutions are not necessarily unique. Thus, if two solids with flat surfaces are pressed together and prevented from bending away from each other globally, one possible steady state of heat conduction corresponds to the solids remaining in contact along the entire interface. It has recently been shown by Comninou and Dundurs [8] that it is also possible to construct solutions involving localized separation zones. A similar conclusion is also implicit in some of the previous results by Dundurs and Panek [9]. Moreover, a particularly simple demonstration of nonuniqueness has been given by Comninou and Dundurs [10] using the Aldo model [11]. Recent work by the authors [12] indicates, however, that it may not generally be possible to achieve uniqueness by introducing a resistance that depends on the pressure in the contact zones and on the gap size in the separation zones.

The situation when one of the contacting bodies has a sharp corner also has been studied [13], but the results are of no immediate interest for the Hertz contact considered, and the subject is mentioned merely for the sake of reference.

The indentation of an elastic half space by a rigid sphere has been treated by Barber for both cases when the sphere is hot and a direct transition from perfect contact to separation is possible [1], and when the sphere is cold and an intermediate zone of imperfect contact is necessary [7]. The same methods could be used to extend this work to two elastic spheres. The present article investigates the planar case of two elastic cylinders. This problem is of interest in its own right, but the main motivation is to provide more detailed results than is feasible in the three-dimensional case.

Mathematical Preliminaries

As it is customary in contact problems of the Hertz type, the geometric profiles of the bodies are approximated in the vicinity of the initial contact as surfaces of second degree, and the boundary conditions are written on their common tangent plane. In other words, the contacting solids are viewed as two elastic half spaces, except that their approximated shapes are incorporated in the boundary conditions to be imposed in the contact region and its immediate vicinity. In two dimensions, the bodies are parabolic cylinders that touch in the undeformed state along the line $x = z = 0$. The initial gap between the bodies, measured along the normal to the tangent plane $y = 0$, is

$$g_0(x) = \tfrac{1}{2}(K_1 + K_2)x^2 \tag{1}$$

where K_1 and K_2 are the curvatures of the cylinders reckoned positive for convexity to the outside. Therefore,

$$dg_0(x)/dx = Kx \tag{2}$$

with

$$K = K_1 + K_2 \tag{3}$$

being the mismatch in curvatures.

The formulation that enforces the required conformity between the bodies in their deformed states is based on a Green's function for interior thermoelastic contact [14]. It consists of a thermoelastic field (heat source and sink) and a purely elastic field (pair of concentrated forces). The advantage of this approach is that most of the boundary conditions pertaining to the problem are satisfied automatically, and that there only remains to find the source-sink and force-pair distributions which enforce a few remaining requirements in the contact zones. The boundary conditions that are automatically embedded in the formulation are continuity of heat flux, continuity of normal tractions, and vanishing shearing tractions at the interface. The full expressions for the field quantities associated with the Green's function are given in reference [14], and we repeat only the relations of immediate interest.

An isolated heat source-sink combination of strength λ acting at the point $(\xi, 0)$ leads to the following quantities at the interface:
Rate of Change of the Temperature Jump:

$$\frac{d\tau(x)}{dx} = \frac{d}{dx}[T_2(x,0) - T_1(x,0)] = \frac{\lambda}{\pi}\frac{k_1 + k_2}{k_1 k_2}\frac{1}{x - \xi} \tag{4}$$

Heat Flux Through the Interface:

$$q(x) = q_y{}^{(1)}(x,0) = q_y{}^{(2)}(x,0) = \lambda\delta(x - \xi) \tag{5}$$

Derivative of the Gap:

$$\frac{dg(x)}{dx} = \frac{d}{dx}[u_y{}^{(1)}(x,0) - u_y{}^{(2)}(x,0)] = \lambda(\delta_1 - \delta_2)\mathrm{H}(x - \xi) \tag{6}$$

Normal Tractions:

$$N(x) = \sigma_{yy}{}^{(1)}(x,0) = \sigma_{yy}{}^{(2)}(x,0) = 0 \tag{7}$$

where $\delta(\ )$ and $\mathrm{H}(\ )$ denote the Dirac and Heaviside functions. If a source-sink combination with the density $\Lambda(x)$ is distributed over a part of the contact interface, the corresponding relations follow from integration with respect to ξ, and

$$\frac{d\tau(x)}{dx} = \frac{1}{\pi}\frac{k_1 + k_2}{k_1 k_2}\int_{-\infty}^{\infty}\frac{\Lambda(\xi)d\xi}{x - \xi} \tag{8}$$

$$q(x) = \Lambda(x) \tag{9}$$

$$\frac{dg(x)}{dx} = (\delta_1 - \delta_2)\int_{-\infty}^{x}\Lambda(\xi)d\xi \tag{10}$$

$$N(x) = 0 \tag{11}$$

A pair of concentrated normal forces of magnitude f_y applied to each of the solids in a tensile direction gives [14]

$$\frac{d\tau(x)}{dx} = q(x) = 0 \tag{12}$$

$$\frac{dg(x)}{dx} = \frac{f_y}{2\pi M}\frac{1}{x - \xi} \tag{13}$$

$$N(x) = f_y\delta(x - \xi) \tag{14}$$

Integration with respect to ξ generates a distribution of interface normal tractions of intensity $F_y(\xi)$, and

$$\frac{d\tau(x)}{dx} = q(x) = 0 \tag{15}$$

Nomenclature

a = half length of perfect contact
b = half length of total contact
$F_y(x)$ = density of a force-pair distribution
f_y = magnitude of a discrete force pair
$g(x)$ = gap between the bodies
$g_0(x)$ = initial gap between the bodies
$\mathrm{H}(\ )$ = Heaviside step function
K = mismatch in curvatures
K_1, K_2 = curvatures of the bodies
k = conductivity
$M = 2\mu_1\mu_2/[\mu_1(\kappa_2 + 1) + \mu_2(\kappa_1 + 1)]$
$N(x)$ = normal tractions
O = order symbol
P = force transmitted between the bodies (per unit thickness)
Q = rate of heat flow between the bodies (per unit thickness)
$q(x)$ = heat flux through the interface
q_y = component of heat flux
T = temperature
u_y = component of displacement
x, y = coordinates
$\delta = \alpha(1 + \nu)/k$ = distortivity
$\delta(\ )$ = Dirac delta function
$\kappa = 3 - 4\nu$
$\Lambda(x)$ = density of heat source-sink distribution
λ = strength of a discrete source-sink
ν = Poisson's ratio
ξ = integration variable
τ = temperature jump across the interface

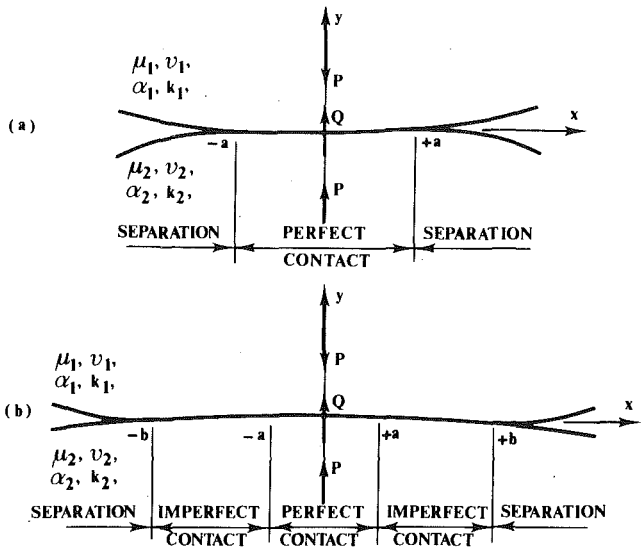

Fig. 1 Geometry of the contacting bodies

$$\frac{dg(x)}{dx} = \frac{1}{2\pi M}\int_{-\infty}^{\infty}\frac{F_y(\xi)d\xi}{x-\xi} \tag{16}$$

$$N(x) = F_y(x) \tag{17}$$

Heat Flowing Into the Material With the Larger Distortivity

If heat flows into the material with the larger distortivity ($\delta_1 > \delta_2$), the central zone of perfect contact can be bordered directly by zones of separation. The corresponding situation is indicated in Fig. 1(a), where the zone of perfect contact extends over the interval $(-a, a)$. The total force pressing the bodies together is denoted by P and the rate at which heat flows through the contact interval by Q ($Q > 0$). Both quantities are reckoned per unit thickness normal to the representative lamina.

As mentioned before, the boundary conditions of continuous heat flux, continuous normal tractions, and vanishing shearing tractions on $-\infty < x < \infty$ are automatically incorporated in the formulation by use of the Green's function [14]. If the source-sink and force-pair distributions are restricted to the interval $-a < x < a$, the separation zones $|x| < a$ are also insulated and free of normal tractions. Consequently, the remaining boundary conditions must only enforce that there be no temperature jump across the interface and the bodies must conform geometrically in the zone of perfect contact, or that

$$\frac{d\tau(x)}{dx} = 0, \quad -a < x < a \tag{18}$$

$$\frac{dg(x)}{dx} = 0, \quad -a < x < a \tag{19}$$

The last condition must only be enforced within an arbitrary constant.

In view of (8), the first boundary condition (18) yields the Cauchy singular integral equation

$$\int_{-a}^{a}\frac{\Lambda(\xi)d\xi}{\xi - x} = 0, \quad -a < x < a \tag{20}$$

with the auxiliary condition

$$\int_{-a}^{a}\Lambda(\xi)d\xi = Q, \quad Q > 0 \tag{21}$$

in which the total heat flux Q is considered as specified. The second boundary condition (19) leads on basis of (2), (10), and (16) to the integral equation

$$\int_{-a}^{a}\frac{F_y(\xi)d\xi}{\xi - x} = 2\pi M\left\{A + Kx + (\delta_1 - \delta_2)\int_{-a}^{x}\Lambda(\xi)d\xi\right\}, \quad -a < x < a \tag{22}$$

where A is an arbitrary constant. The integral equation (22) must be supplemented with the condition

$$\int_{-a}^{a}F_y(\xi)d\xi = -P, \quad P > 0 \tag{23}$$

specifying the total force P transmitted between the bodies. Moreover, the inequalities

$$N(x) < 0, \quad |x| < a \tag{24}$$

$$g(x) > 0, \quad a < |x| \tag{25}$$

must be obeyed by the solution to be constructed.

The solution of the first integral equation (20) together with the auxiliary condition (21) is well known [15]. Thus

$$\Lambda(x) = \frac{Q}{\pi}(a^2 - x^2)^{-1/2} \tag{26}$$

and the heat flux is square-root singular as predicted by the asymptotic analysis of the transition from perfect contact to separation [4].

Substituting (26) into (22)

$$\int_{-a}^{a}\frac{F_y(\xi)d\xi}{\xi - x} = 2\pi M\left\{A + Kx + \frac{Q}{\pi}(\delta_1 - \delta_2)\left(\sin^{-1}\frac{x}{a} + \frac{\pi}{2}\right)\right\} = f(x), \quad -a < x < a \tag{27}$$

Since $F_y(x)$ must be bounded, the consistency condition [15]

$$\int_{-a}^{a}\frac{f(\xi)d\xi}{(a^2 - \xi^2)^{1/2}} = 0 \tag{28}$$

must be satisfied. This yields

$$A + \tfrac{1}{2}(\delta_1 - \delta_2)Q = 0 \tag{29}$$

The solution of (27) is

$$F_y(x) = -\frac{2}{\pi}M(a^2 - x^2)^{1/2}\left\{Kx + \frac{Q}{\pi}(\delta_1 - \delta_2) \times \int_{-a}^{a}\frac{\sin^{-1}(\xi/a)d\xi}{(a^2 - \xi^2)^{1/2}(\xi - x)}\right\}, \quad -a < x < a \tag{30}$$

Applying the auxiliary condition (23) on (30), we obtain after some elementary integrations

$$\frac{P}{MKa^2} = \pi + \frac{4Q(\delta_1 - \delta_2)}{Ka} \tag{31}$$

The singular integral in (30) can be evaluated by the Lobatto-Chebyshev quadrature, as extended to Cauchy integrals by Theocaris and Ioakimidis [16]. Equation (30) is first put in a dimensionless form by the change of variables

$$\xi = ar, \quad x = as$$

The aforementioned quadrature then yields

$$\frac{F_y(s_i)}{MKa} = -\frac{2}{\pi}(1 - s_i^2)^{1/2}\left\{\pi + \frac{Q(\delta_1 - \delta_2)}{Ka}\frac{1}{n-1}\sum_{k=1}^{n}\frac{\lambda_k \sin^{-1} r_k}{r_k - s_i}\right\} \tag{32}$$

where

$$\lambda_k = \begin{cases}\frac{1}{2}, & k = 1, n\\ 1, & k = 2, \ldots, n-1\end{cases} \tag{33}$$

$$s_i = \cos\frac{(2i-1)\pi}{2(n-1)}, \quad i = 1, \ldots, n-1 \tag{34}$$

$$r_k = \cos\frac{(k-1)\pi}{n-1}, \quad k = 1, \ldots, n \tag{35}$$

The results obtained on this basis are discussed in a later section.

Heat Flowing Into the Material With the Smaller Distortivity

If heat flows into the material with the smaller distortivity ($\delta_1 < \delta_2$), the central zone of perfect contact must be bordered by zones of imperfect contact [4, 7] as indicated in Fig. 1(*b*). The zone of perfect contact is the interval $|x| < a$, the zones of imperfect contact occupy the intervals $a < |x| < b$. The boundary conditions that must be imposed beyond those satisfied automatically because of the Green's function approach are the same as for heat flow into the material with the larger distortivity, except that they apply to different intervals. Thus

$$\frac{d\tau(x)}{dx} = 0, \quad -a < x < a \tag{36}$$

$$\frac{dg(x)}{dx} = 0, \quad -b < x < b \tag{37}$$

As before, the boundary conditions must be supplemented with auxiliary conditions pertaining to the total rate of heat flow between the bodies and to the force pressing the bodies together. It should also be noted that now the source-sink distribution extends over the interval $-b < x < b$, while the force-pair distribution is restricted to the interval $-a < x < a$.

The boundary condition (36) yields

$$\int_{-b}^{b} \frac{\Lambda(\xi)d\xi}{\xi - x} = 0, \quad -a < x < a \tag{38}$$

and the associated auxiliary condition is

$$\int_{-b}^{b} \Lambda(\xi)d\xi = Q, \quad Q > 0 \tag{39}$$

The other boundary condition (37) gives

$$\int_{-a}^{a} \frac{F_y(\xi)d\xi}{\xi - x} = 2\pi M \left\{A + Kx + (\delta_1 - \delta_2) \times \int_{-b}^{x} \Lambda(\xi)d\xi\right\}, \quad -b < x < b \tag{40}$$

while

$$\int_{-a}^{a} F_y(\xi)d\xi = -P, \quad P > 0 \tag{41}$$

The solution must also satisfy the inequalities [4, 7]

$$N(x) < 0, \quad |x| < a \tag{42}$$

$$\Lambda(x)\tau(x) > 0, \quad a < |x| < b \tag{43}$$

$$g(x) > 0, \quad b < |x| \tag{44}$$

The essential task is to put the system of integral relations (38)–(41) into a form that is suitable for numerical evaluation. Consider first the Cauchy integral in (40). Integrating by parts

$$\int_{-a}^{a} \frac{F_y(\xi)d\xi}{\xi - x} = F_y(\xi) \log|\xi - x| \Big|_{\xi=-a}^{\xi=a} - \int_{-a}^{a} F_y'(\xi) \log|\xi - x| d\xi \tag{45}$$

It is known from the asymptotic analysis of the transition from perfect to imperfect contact that [4]

$$F_y(\xi) = O(a - |\xi|), \quad |\xi| \to a- \tag{46}$$

and consequently

$$\int_{-a}^{a} \frac{F_y(\xi)d\xi}{\xi - x} = -\int_{-a}^{a} F_y'(\xi) \log|\xi - x| d\xi \tag{47}$$

Substituting (47) into (40) and differentiating the resulting expression with respect to x, yields the integral equation

$$\int_{-a}^{a} \frac{F_y'(\xi)d\xi}{\xi - x} = 2\pi M \{K + (\delta_1 - \delta_2)\Lambda(x)\}, \quad -b < x < b \tag{48}$$

which then replaces (40).

From (48)

$$\Lambda(x) = \frac{1}{\delta_1 - \delta_2}\left\{\frac{1}{2\pi M}\int_{-a}^{a} \frac{F_y'(\xi)d\xi}{\xi - x} - K\right\}, \quad -b < x < b \tag{49}$$

and putting (49) into (38)

$$\frac{1}{2\pi M}\int_{-b}^{b} \frac{1}{\xi - x}\int_{-a}^{a} \frac{F_y'(\eta)}{\eta - \xi} d\eta d\xi - K \times \int_{-b}^{b} \frac{d\xi}{\xi - x} = 0, \quad -a < x < a \tag{50}$$

Using the Poincaré-Bertrand formula [15], the double integral in (50) becomes

$$\int_{-b}^{b} \frac{1}{\xi - x}\int_{-a}^{a} \frac{F_y'(\eta)}{\eta - \xi} d\eta d\xi = \int_{-a}^{a} F_y'(\eta)\int_{-b}^{b} \frac{d\xi}{(\xi - x)(\eta - \xi)} d\eta - \pi^2 F_y'(x) = \int_{-a}^{a} \frac{F_y'(\xi)}{\xi - x} \log\left|\frac{(b - x)(b + \xi)}{(b + x)(b - \xi)}\right| d\xi - \pi^2 F_y'(x) \tag{51}$$

Thus (50) reduces to

$$\int_{-a}^{a} \frac{F_y'(\xi)}{\xi - x} \log\left|\frac{(b - x)(b + \xi)}{(b + x)(b - \xi)}\right| d\xi - \pi^2 F_y'(x) = 2\pi MK \log\left|\frac{b - x}{b + x}\right|, \quad -a < x < a \tag{52}$$

which is a Fredholm integral equation of the second kind.

Once $F_y'(x)$ is determined, Λ is obtained from (49), and on basis of (8),

$$\frac{d\tau(x)}{dx} = -\frac{1}{\pi}\frac{k_1 + k_2}{k_1 k_2}\int_{-b}^{b} \frac{\Lambda(\xi)d\xi}{\xi - x}, \quad a < |x| \tag{53}$$

We need $d\tau(x)/dx$ in the interval $a < |x| < b$ to check the inequality. In terms of $F_y'(x)$

$$\frac{d\tau(x)}{dx} = \frac{1}{\pi}\frac{k_1 + k_2}{k_1 k_2}\frac{1}{\delta_1 - \delta_2}\left\{K \log\left|\frac{b - x}{b + x}\right| + \frac{1}{2\pi M}\int_{-a}^{a} \frac{F_y'(\xi)}{\xi - x} \log\left|\frac{(b - \xi)(b + x)}{(b + \xi)(b - x)}\right| d\xi\right\}, \quad a < |x| < b \tag{54}$$

and

$$\tau(x) = \frac{1}{\pi}\frac{k_1 + k_2}{k_1 k_2}\frac{1}{\delta_1 - \delta_2}\left\{K\left[(b + x)\log\left(1 + \frac{x}{b}\right) - (b - x)\log\left(1 - \frac{x}{b}\right) + (b - a)\log\left(1 - \frac{a}{b}\right) + (b + a)\log\left(1 + \frac{a}{b}\right)\right] + \frac{1}{2\pi M}\int_{a}^{x}\int_{-a}^{a} \frac{F_y'(\xi)}{\eta - \xi} \log\left|\frac{(b + \xi)(b - \eta)}{(b - \xi)(b + \eta)}\right| d\xi d\eta\right\}, \quad a < x < b \tag{55}$$

In the interval $-b < x < -a$, $\tau(x)$ follows from symmetry, while $F_y(x)$ is verified (numerically) to be even in x.

Finally

$$P = -\int_{-a}^{a} (a - \xi)F_y'(\xi)d\xi \tag{56}$$

and

$$Q = \frac{1}{\delta_1 - \delta_2}\left\{\frac{1}{2\pi M}\int_{-a}^{a} F_y'(\xi) \log\left|\frac{b + \xi}{b - \xi}\right| d\xi - 2Kb\right\} \tag{57}$$

In order to avoid iterations, we take a and b as given and compute the required values of P and Q.

Observing for the kernel in (52) that

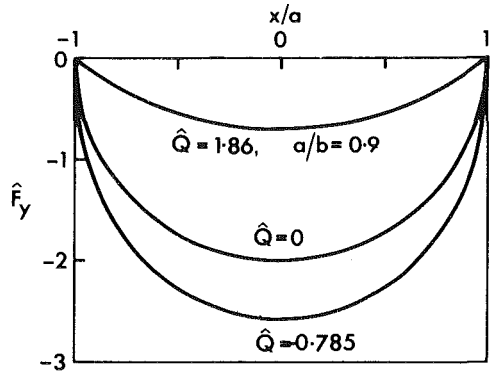

Fig. 2 Comparison of the normalized pressure distributions $\hat{F}_y = F_y/MKa$ for heat flow in different directions with $\hat{Q} = Q(\delta_2 - \delta_1)/Ka$

$$\lim_{x \to \xi} \left\{ \frac{1}{\xi - x} \log \frac{(b - x)(b + \xi)}{(b + x)(b - \xi)} \right\} = \frac{1}{b - \xi} + \frac{1}{b + \xi} \tag{58}$$

we use the same collocation (x) and integration points (ξ) to solve (52) numerically. The Lobatto quadrature [17] is convenient for the discretization. The discretized form of (52) according to this quadrature becomes

$$\sum_{j=1}^{n+2} W(r_i, r_j) Y(r_j) = 2\pi \log \left| \frac{1 - \lambda r_i}{1 + \lambda r_i} \right|, \quad i = 1, \ldots, n + 2 \tag{59}$$

where $Y(\xi) = F_y'(\xi)/MK$, $r = \xi/a$, $\lambda = a/b$ and

$$\begin{aligned} W(r_i, r_j) &= \frac{W_j^*}{r_i - r_j} \log \left| \frac{(1 - \lambda r_i)(1 + \lambda r_j)}{(1 + \lambda r_i)(1 - \lambda r_j)} \right| && \text{for } i \neq j \\ &= W_j - \pi^2 && \text{for } i = j \end{aligned} \tag{60}$$

$$W_1 = W_{n+2} = \frac{4\lambda}{(1 - \lambda^2)(n + 1)(n + 2)},$$

$$W_1^* = W_{n+2}^* = \frac{2}{(n + 1)(n + 2)} \tag{61}$$

$$W_{i+1} = \frac{2\lambda A_i}{(1 - z_i^2)(1 - \lambda^2 z_i^2)}, \quad W_{i+1}^* = \frac{A_i}{1 - z_i^2}, \quad i = 1, \ldots, n \tag{62}$$

Furthermore, z_i are the roots of the Jacobi polynomial $P_n^{(1,1)}(z_i) = 0$, A_i the corresponding coefficients and

$$r_{i+1} = z_i, (i = 1, \ldots, n), \quad r_1 = 1, \quad r_{n+2} = -1 \tag{63}$$

The roots z_i and the coefficients A_i are readily obtained by the Fortran program given in reference [18]. It may be noted that the Lobatto quadrature has the advantage of including the end points of the interval in the collocation points. The numerical calculations were performed with double precision, and $n = 40$ was used to obtain enough points for a graphical representation of the results.

The numerical evaluation of $\Lambda(x)$ requires the computation of an integral which is of the Cauchy type (singular) in the interval $|x| < a$. Although the Lobatto quadrature can still be applied in this interval as shown by Theocaris [19], we can no longer choose coinciding collocation and integration points. For best accuracy, the collocation points must be chosed as the roots of appropriate Legendre (or Jacobi) functions of the second kind. Since n is large in our case, the numerical scheme converges also well if we choose for collocation points the midpoints between the integration points. This avoids the need to calculate the zeroes of the aforementioned functions for which no program is available. Convergence was checked in the calculations by doubling n, and no difference was observed in the first eight digits that were printed out. The density $\Lambda(x)$ of the source-sink distribution has logarithmic singularities at $x = \pm a$. Extracting these singularities analytically before discretization did not affect the numerical results significantly.

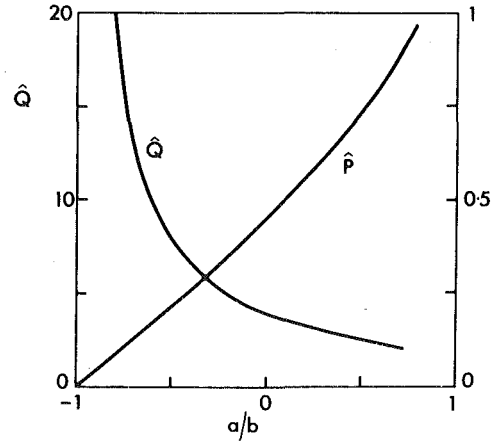

Fig. 3 Relation between a/b, the normalized applied force $\hat{P} = P/MKa^2$ and normalized total heat flow $\hat{Q} = Q(\delta_2 - \delta_1)/Ka$

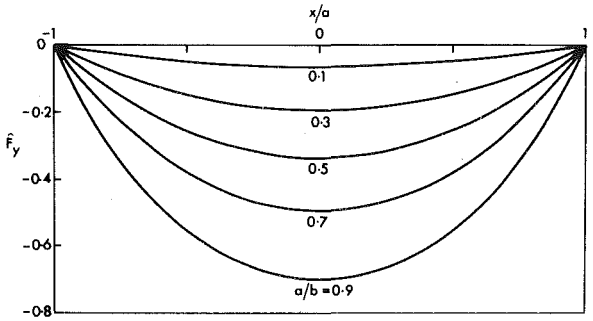

Fig. 4 Normalized pressure distributions $\hat{F}_y = F_y/MKa$ for heat flowing into the material with the smaller distortivity

The Lobbatto quadrature was also used for the evaluation of P, Q and the inner integral in $\tau(x)$. The ordinary trapezoidal rule was used to calculate $F_y(x)$ from $F_y'(x)$. The inequalities and symmetries were also verified numerically.

Results

Typical pressure distributions for heat flowing in either direction are shown in Fig. 2 where $\hat{Q}$ denotes $Q(\delta_2 - \delta_1)/Ka$ and $\hat{P} = P/MKa^2$. The pressure distribution for no heat flow is also included for comparison. It is seen from this figure that, in order to achieve the same extent a of perfect contact, a larger force P must be applied when heat flows into the material with the larger distortivity. It should be noted that the contact pressure distribution has a vertical slope for heat flowing into the material with the larger distortivity, but not for heat flow in the opposite direction. This is in conformity with the results from the asymptotic analysis [4].

Additional results for heat flowing into the material with the smaller distortivity are shown in Figs. 3–6. The relation between a/b, the applied force and total heat flow is shown in Fig. 3. The distribution of the contact pressure is shown in Fig. 4 for different values of a/b. The distribution of heat flux through the interface and the temperature discontinuity in the zone of imperfect contact are given in Figs. 5 and 6 for $a/b = 0.5$. In these figures $\hat{\Lambda} = \Lambda(\delta_2 - \delta_1)/K$ and $\hat{\tau} = \pi k_1 k_2 (\delta_2 - \delta_1)\tau/(k_1 + k_2)Ka$. It should be recalled from the asymptotic analysis [4] that the heat flux has a logarithmic singularity at the transition from perfect to imperfect contact.

References

1 Barber, J. R., "Indentation of the Semi-infinite Solid by a Hot Sphere," *International Journal of Mechanical Sciences*, Vol. 15, 1973, pp. 813–819.

2 Barber, J. R., "The Effect of Heat Flow on the Contact Area Between a Continuous Rigid Punch and a Frictionless Elastic Half Space," *Zeitschrift für angewandte Mathematik und Physik*, Vol. 27, 1976, pp. 439–445.

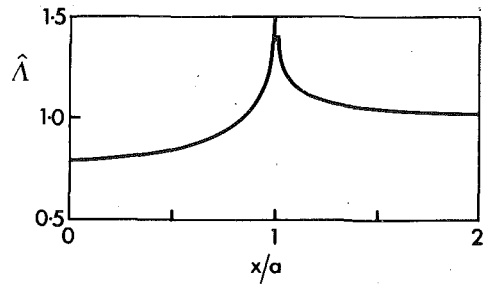

Fig. 5 Distribution of normalized heat flux $\hat{\Lambda} = \Lambda(\delta_2 - \delta_1)/K$ through the interface for $a/b = 0.5$

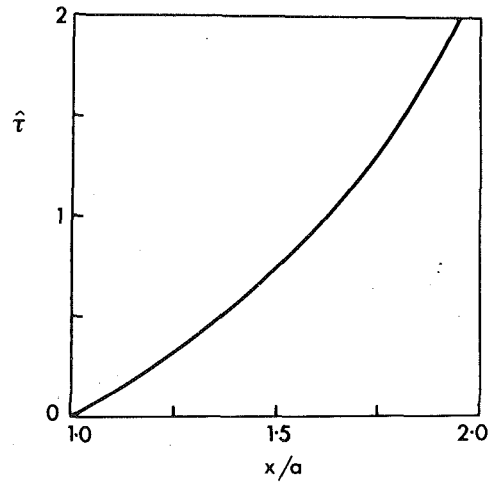

Fig. 6 Normalized temperature discontinuity $\hat{\tau} = \pi k_1 k_2(\delta_2 - \delta_1)\tau/(k_1 + k_2)Ka$ in the zone of imperfect contact for $a/b = 0.5$

3 Panek, C., and Dundurs, J., "Thermoelastic Contact Between Bodies With Wavy Surfaces," ASME JOURNAL OF APPLIED MECHANICS, Vol. 46, 1979, pp. 854–860.

4 Comninou, M., and Dundurs, J., "On the Barber Boundary Conditions for Thermoelastic Contact," ASME JOURNAL OF APPLIED MECHANICS, Vol. 46, 1979, pp. 849–853.

5 Dundurs, J., and Comninou, M., "On the Boundary Conditions in Contact Problems With Heat Conduction," *Developments in Theoretical and Applied Mechanics*, McNitt, R. P., ed., Virginia Polytechnic Institute and State University, 1976, pp. 3–11.

6 Duvaut, G., "Free Boundary Problem Connected With Thermoelasticity and Unilateral Contact," *Séminaire sur les problèmes à frontière libre*, Pavie, Sept.–Oct., 1979.

7 Barber, J. R., "Contact Problems Involving a Cooled Punch," *Journal of Elasticity*, Vol. 8, 1978, pp. 409–423.

8 Comninou, M., and Dundurs, J., "On Lack of Uniqueness in Heat Conduction Through a Solid to Solid Contact," ASME *Journal of Heat Transfer*, Vol. 102, 1980, pp. 319–323.

9 Dundurs, J., and Panek, C., "Heat Conduction Between Bodies With Wavy Surfaces," *International Journal of Heat and Mass Transfer*, Vol. 19, 1976, pp. 731–736.

10 Comninou, M., and Dundurs, J., "On the Possibility of History Dependence and Instabilities in Thermoelastic Contact," *Journal of Thermal Stresses*, Vol. 3, 1980, pp. 427–433.

11 Aldo, K. A. T., Private Communication.

12 Barber, J. R., Dundurs, J., and Comninou, M., "Stability Considerations in Thermoelastic Contact," ASME JOURNAL OF APPLIED MECHANICS, Vol. 47, 1980, pp. 871–874.

13 Comninou, M., and Dundurs, J., "Thermoelastic Contact Involving a Sharp Corner," *Wear*, Vol. 59, 1980, pp. 53–60.

14 Dundurs, J., and Comninou, M., "Green's Functions for Planar Thermoelastic Contact Problems—Interior Contact," *Mechanics Research Communications*, Vol. 6, 1979, pp. 317–321.

15 Muskelishvili, N. I., *Singular Integral Equations*, P. Noordhoff, Groningen, 1953.

16 Theocaris, P. S., and Ioakimidis, N. I., "On the Numerical Solution of Singular Integral Equations," *Quarterly of Applied Mathematics*, Vol. 29, 1972, pp. 525–534.

17 Kopal, Z., *Numerical Analysis*, Chapman and Hall, London, 1961.

18 Stroud, A. H., and Secrest, D., *Gaussian Quadrature Formulas*, Prentice-Hall, Englewood Cliffs, N.J., 1966.

19 Theocaris, P. S., "On the Numerical Integration of Cauchy-Type Singular Integral Equations," *Serdica Bulgaricae Mathematicae Publicationes*, Vol. 2, 1976, pp. 252–257.

J. R. Barber

Department of Mechanical Engineering,
University of Newcastle-upon-Tyne,
Newcastle-upon-Tyne NE1 7RU, England

Stability of Thermoelastic Contact for the Aldo Model

A perturbation method is used to investigate the stability of a simple one-dimensional rod model of thermoelastic contact which exhibits multiple steady-state solutions. A thermal contact resistance is postulated which is a continuous function of the contact pressure or separation. It is found that solutions involving substantial separation and/or contact pressures are always stable, but these are separated by unstable "imperfect contact" solutions in which one of the rods is very lightly loaded or has a very small separation. The results can be expressed in terms of the minimization of a certain energy function.

Introduction

A number of recent treatments of thermoelastic contact problems [1–3] have demonstrated that steady-state solutions are not necessarily unique if the hotter body has the lower thermal distortivity δ, defined by

$$\delta = \alpha(1 + \nu)/K \tag{1}$$

where α, ν, K are, respectively, the coefficient of linear thermal expansion, Poisson's ratio, and thermal conductivity.

In such cases, it is possible that some of the competing solutions are unstable, but if more than one are stable, the situation realized in practice will depend upon the history of heating and loading.

In an attempt to probe this question, Comninou and Dundurs [3] have considered a simplified thermoelastic contact system which they call the "Aldo Model." The three-dimensional contacting bodies are replaced by a large number of thin rods arranged normally to the interface and with frictionless and thermally insulated sides. This essentially constrains heat flow and load transfer to the normal direction.

Although this system is very much simpler than a real contact situation, it is sufficiently realistic to permit multiple solutions for the appropriate heat flow direction. Comninou and Dundurs have computed the total mechanical energies for these solutions, but these cannot be used to draw rigorous conclusions about stability, since the system is inherently nonconservative.

In this paper, the stability of steady-state solutions for the Aldo model will be investigated by an analysis of small transient perturbations. This method has already been successfully applied to the simpler problem of the one-dimensional rod confined between rigid walls at different temperatures [1] and leads to rigorous conclusions about stability which can be formulated in terms of an energy function.

Description of the Model

Comninou and Dundurs show that the cross section of the Aldo rods and the distribution of contacting and noncontacting rods over the interface do not influence the permissible steady-state solutions. In effect, a group of rods all in a similar state behaves as a single rod of proportionately greater cross-sectional area.

The essence of the Aldo model is therefore preserved if we consider the stability of a system of two rods of different cross-sectional areas A_1, A_2 as shown in Fig. 1.

The rods, both of length l, are rigidly joined at the top, where the temperature is maintained at zero. The other ends make contact with a rigid, perfectly conducting half space[1] at temperature T_0 (>0). The system is constrained so that only vertical displacements are permitted and a compressive contact force F is applied as shown.

As in the previous paper [1], we postulate the existance of a thermal contact reistance R_i (p_i, g_i) (i = 1, 2 for rods 1, 2, respectively) which depends on the pressure p_i between the rod and the half space, or on the gap g_i if the rod is not in contact. The stability of the system is not affected by the precise nature of this resistance function.

Steady-State Solution

Writing Q_i for the steady-state heat flux along rod i, and T_i for the temperature at the hot end, we have

$$Q_i = \frac{(T_0 - T_i)}{R_i} = \frac{A_i K T_i}{l} \tag{2}$$

and hence,

$$T_i = \frac{T_0}{(1 + A_i K R_i/l)} \tag{3}$$

[1] Comninou and Dundurs treat the contact of two systems of rods of different materials, but it is not anticipated that this more general case will introduce any qualitatively new features.

Contributed by the Applied Mechanics Division for publication in the JOURNAL OF APPLIED MECHANICS.

Discussion on this paper should be addressed to the Editorial Department, ASME, United Engineering Center, 345 East 47th Street, New York, N. Y. 10017, and will be accepted until December 1, 1981. Readers who need more time to prepare a discussion should request an extension from the Editorial Department. Manuscript received by ASME Applied Mechanics Division, July, 1980; final revision, January, 1981.

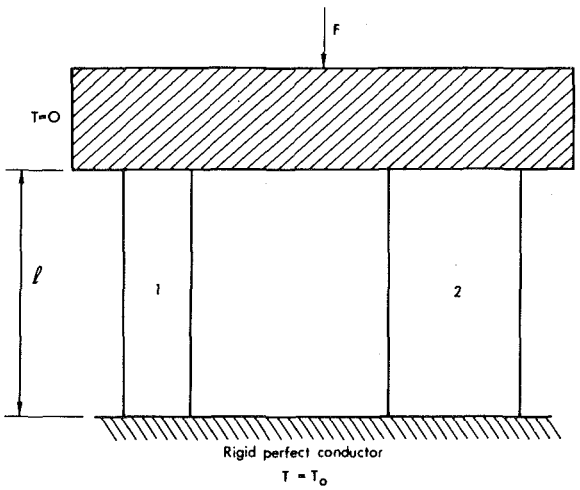

Fig. 1 The Aldo model

The unconstrained thermal expansion of the rod is therefore

$$u_i = \tfrac{1}{2}\alpha\, l\, T_i = u_0 fi \tag{4}$$

where $u_0 = \frac{1}{2}\alpha\, l\, T_0$ is the thermal expansion which would be developed if there were perfect thermal contact between the rod and the plane and

$$f_i = \frac{l}{(l + A_i K R_i)} \tag{5}$$

This function tends to zero when the gap g_i is large ($R_i \to \infty$) and to unity when the contact pressure p_i is large ($R_i \to 0$) as shown in Fig. 2. In general, ,the transition between these limits would be expected to occur over a relatively small range of g_i, p_i.

Three possible contact states for the system can be distinguished as follows:

(*i*) Rod 1 in Contact

$$p_2 = 0, \quad p_1 = F/A_1,$$

$$g_1 = 0, \quad g_2 > 0,$$

and

$$g_2 = u_0(f_1 - f_2) - Fl/A_1E \tag{6}$$

(*ii*) Both Rods in Contact

$$p_1, p_2 \geqslant 0,$$

$$g_1 = g_2 = 0,$$

and

$$u_0(f_1 - f_2) = (p_1 - p_2)l/E \tag{7}$$

(*iii*) Rod 2 in Contact

$$p_1 = 0, \quad p_2 = F/A_2,$$

$$g_2 = 0, \quad g_1 > 0,$$

and

$$g_1 = u_0(f_2 - f_1) - Fl/A_2E \tag{8}$$

We now define a piecewise continuous function x by the relations

$$x = g_2 + Fl/A_1E; \qquad g_2 > 0, \tag{9i}$$

$$= (p_1 - p_2)l/E; \qquad g_1 = g_2 = 0, \tag{9ii}$$

$$= -g_1 - Fl/A_2E; \qquad g_1 > 0 \tag{9iii}$$

In effect, x is the difference between the unconstrained thermal expansion of the two rods ($u_1 - u_2$). It is easily verified that this function is continuous at the transitions between the foregoing contact regimes. Furthermore, if equations (9*i*)–(9*iii*) are substituted into equations (6)–(8), respectively, the latter are all reduced to the form

$$(f_1 - f_2) = x/u_0 \tag{10}$$

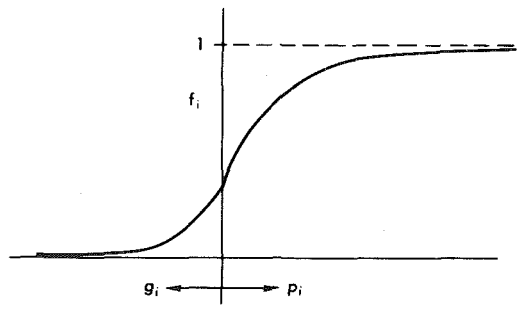

Fig. 2 Dependence of the function f_i on pressure (p_i) and gap (g_i)

Stability Analysis

In order to investigate the stability of the various solutions of equation (10), we examine the conditions under which a small perturbation from the steady state can grow exponentially with time.

The perturbation in temperature in the rods, ΔT_i, must satisfy the transient heat-conduction equation and the boundary condition

$$\Delta T_i(y) = 0 \quad \text{at} \quad y = 0 \tag{11}$$

where y is measured from the cold end. The appropriate exponentially growing solution is

$$\Delta T_i(y) = B_i\, e^{at} \sinh \lambda y \tag{12}$$

(see reference [1]), where

$$\lambda = (a/k)^{1/2} \tag{13}$$

a, B_i are constants, t is time, and k is the thermal diffusivity of the material.

The corresponding perturbation in heat input to the rod is

$$\Delta Q_i = -A_i k \frac{\partial T_i}{\partial y}(l) = -B_i A_i K \lambda\, e^{at} \cosh \lambda l \tag{14}$$

A second relationship between ΔT_i and ΔQ_i can be found by differentiating equation (2) to obtain

$$\Delta Q_i = -\frac{(T_0 - T_i)}{R_i{}^2}\frac{dR_i}{dx}\Delta x - \frac{\Delta T_i(l)}{R_i} \tag{15}$$

$$= -\frac{A_i K T_0}{(l + A_i K R_i) R_i}\frac{dR_i}{dx}\Delta x - \frac{\Delta T_i(l)}{R_i} \tag{16}$$

from equation (3).

We now solve equation (5) for R_i, obtaining

$$R_i = \frac{l}{A_i K}\left(\frac{1}{f_i} - 1\right) \tag{17}$$

and substitute into equation (16), from which

$$\frac{l}{A_i K}\left(\frac{1}{f_i} - 1\right)\Delta Q_i = \frac{T_0}{f_i}\frac{df_i}{dx}\Delta x - \Delta T_i(l). \tag{18}$$

The function x, defined by equations (9*i*)–(9*iii*) is the difference between the unconstrained thermal expansions of the two rods, ($u_1 - u_2$) and hence

$$\Delta x = \Delta u_1 - \Delta u_2 = \alpha \int_0^l \{T_1(y) - T_2(y)\}\, dy$$

$$= \alpha(B_1 - B_2)\, e^{at}(\cosh \lambda l - 1)/\lambda \tag{19}$$

from equation (12).

Two simultaneous equations can now be obtained by substituting

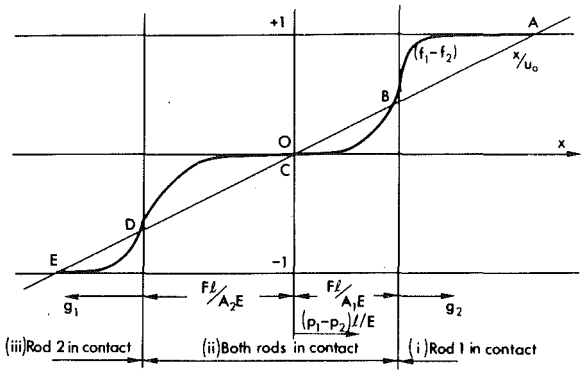

Fig. 3 Graphical solution of equation (10)

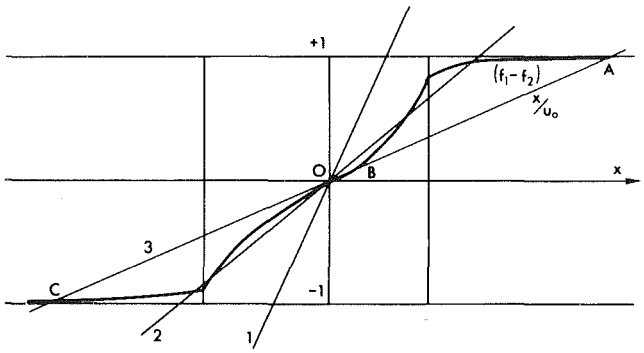

Fig. 4 Variation of contact resistance throughout the load range

for ΔQ_i, $\Delta T_i(l)$, Δx from equations (12), (14), (19) into equation (18), i.e.,

$$-B_1\left(\frac{1}{f_1}-1\right)z^2\cosh z = \frac{2u_0 f_1'}{f_1} \times (B_1 - B_2)(\cosh z - 1) - B_1 z \sinh z \quad (20)$$

and

$$-B_2\left(\frac{1}{f_2}-1\right)z^2\cosh z = \frac{2u_0 f_2'}{f_2} \times (B_1 - B_2)(\cosh z - 1) - B_2 z \sinh z \quad (21)$$

where

$$z = \lambda l \quad (22)$$

Finally, B_1,B_2 can be eliminated between these equations to give the characteristic equation for z (and hence a) which is

$$\frac{2u_0 f_1'(\cosh z - 1)}{(1-f_1)z^2\cosh z + f_1 z \sinh z} - \frac{2u_0 f_2'(\cosh z - 1)}{(1-f_2)z^2\cosh z + f_2 z \sinh z} = 1 \quad (23)$$

The perturbation (12) is unstable if, and only if, equation (23) has a root for which a and hence z^2 has a positive real part. This equation is investigated in the Appendix, where it is shown that

(*i*) There are no unstable complex roots and
(*ii*) Unstable real roots occur if, and only if,

$$(f_1' - f_2') > 1/u_0 \quad (24)$$

provided f_1, f_2 are monotonic functions of x.

Discussion

The relationship between the stability condition (24) and the steady-state solution equation (10) is illustrated graphically in Fig. 3.

The contact resistance is assumed to be continuous at the transition between contact and noncontact and hence $(f_1 - f_2)$ is a continuous function of x. This function is illustrated for the case in which the transition from perfect thermal contact to perfect insulation occurs over a small range of load or gap, in which case the curve passes nearly horizontally through the origin. This is probably a realistic physical assumption, but it is not necessary to the development of the argument.

Solutions of equation (10) are represented by the intersections (*ABCDE*) between the curve $(f_1 - f_2)$ and the straight line (x/u_0).

Furthermore, the stability criterion (24) shows that those solutions are stable for which the straight line crosses the curve from below when x is increasing. In view of the limits imposed on $(f_1 - f_2)$, it follows that

(*i*) There must be an odd number of solutions.
(*ii*) Stable and unstable solutions alternate with increasing x.
(*iii*) The outermost solutions are both stable.

The stable solutions *ACE* in Fig. 3 correspond to solutions in the contact regimes described as (*i*), (*ii*), (*iii*), respectively, given previously in this section. However, there are also two intermediate unstable solutions *BD* at which one rod carries most of the load while the other is either very lightly loaded or has a very small gap. We can define a limit to the contact resistance function R_i such that the change from thermal insulation to perfect thermal contact occurs over an infinitesimal range of gap or load. The function $(f_1 - f_2)$ will then correspond to states in which one rod is in perfect contact, carrying the total load F, while the other is in "imperfect contact" as defined by a similar limiting process in the treatment of problems with the reverse direction of heat flow [4]. The state of imperfect contact is defined by the conditions

$$p_i = 0; \quad g_i = 0; \quad 0 < f_i < 1 \quad (25)$$

These results support the hypothesis [5] that imperfect contact states are unstable when heat flows into the material of higher distortivity.

Fig. 3 has been drawn for a case in which all five intersections occur, but it is clear that if the straight line had a sufficiently large slope—corresponding to low values of u_0 and hence T_0—the only intersection would be *C*. In other words, when the temperature difference is small, the only permissible steady-state solution is that involving contact of both rods.

If the temperature is now increased, the slope of the straight line is reduced and, at some critical temperature, a pair of additional solutions such as *AB*—one stable, one unstable—will be introduced. The function $(f_1 - f_2)$ is not necessarily symmetrical about $x = 0$, since A_1 may differ from A_2. There will therefore generally be distinct temperature ranges with one, three and five solutions, respectively.

If the load F is increased, the two "steps" in $(f_1 - f_2)$ are displaced further from the origin. This has a similar effect to a reduction in temperature.

Fig. 4 illustrates a more general situation in which the contact resistances and hence $(f_1 - f_2)$ vary significantly over the entire load range, giving a nonzero slope near the origin (notice that $(f_1 - f_2)$ does not necessarily pass through the origin).

As temperature is increased, the same behavior is observed as in Fig. 3, with progression from one solution (line 1) to five solutions (line 2). However, with a further increase in temperature (line 3), the system passes into a new regime with three solutions. One of these (*B*) has both rods in contact but is *unstable*, whilst the other two (*AC*) involve contact at one rod only and are stable. In effect, Fig. 3 represents the limiting situation in which the temperature difference needed to initiate this new regime is very large.

Definition of an Energy Function

Following the same procedure as in reference [1], we can define an energy function

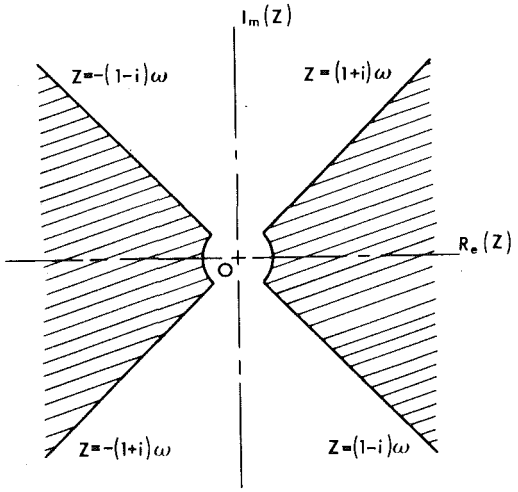

Fig. 5 Domain for unstable roots of equation (29)

$$U(x) = \frac{(A_1 + A_2)\,E}{l}\left[\int (f_1 - f_2)\,u_0 dx - \tfrac{1}{2}x^2\right] \tag{26}$$

The equation (10) for a steady-state solution can then be written

$$\partial U/\partial x = 0, \tag{27}$$

while the condition for instability (24) is

$$\partial^2 U/\partial x^2 < 0 \tag{28}$$

Thus $U(x)$ is stationary at all steady-state solutions, being a maximum if the solution is unstable and a minimum if it is stable.

The total mechanical energy for the system, calculated by Comninou and Dundurs [3] is not related to the function $U(x)$ and cannot be used to determine which solutions are stable. Indeed the aforementioned analysis shows that *all* the solutions which they consider—being those involving only perfect contact and separation—are stable. The only unstable solutions are those involving imperfect contact. These can be thought of as interposing higher energy barriers between the stable perfect contact/gap solutions.

References

1 Barber, J. R., Dundurs, J., and Comninou, M., "Stability Considerations in Thermoelastic Contact," ASME JOURNAL OF APPLIED MECHANICS, Vol. 47, 1980, pp. 871–874.

2 Comninou, M., and Dundurs, J., "On Lack of Uniqueness in Heat Conduction Through a Solid to Solid Interface," ASME *Journal of Heat Transfer*, Vol. 102, 1980, pp. 319–323.

3 Comninou, M., and Dundurs, J., "On the Possibility of History Dependence and Instabilities in Thermoelastic Contact," *Journal of Thermal Stresses*, Vol. 3, 1980, pp. 427–433.

4 Barber, J. R., "Contact Problems Involving a Cooled Punch," *Journal of Elasticity*, Vol. 8, 1978, pp. 409–423.

5 Comninou, M., and Dundurs, J., "On the Barber Boundary Conditions for Thermoelastic Contact," ASME JOURNAL OF APPLIED MECHANICS, Vol. 46, 1979, pp. 849–853.

APPENDIX

It is required to determine the conditions under which the equation

$$F(z) = \frac{2u_0 f_1'(\cosh z - 1)}{(1 - f_1)z^2 \cosh z + f_1 z \sinh z} - \frac{2u_0 f_2'(\cosh z - 1)}{(1 - f_2)z^2 \cosh z + f_2 z \sinh z} - 1 = 0 \tag{29}$$

has roots corresponding to values of z^2 with positive real part. In the z-plane, the corresponding zeros of $F(z)$ must lie in the two sectors shaded in Fig. 5 and bounded by the lines $z = \pm(1 + i)\,\omega$, the origin being excluded.

We first note that for the special case $f_1 = f_2 = 1; f_1' = f_2' = 0$, there are no such roots, since the only zeros of $F(z)$ correspond to

$$z \sinh z = 0 \tag{30}$$

and hence

$$z = 0 \pm in\pi \tag{31}$$

If we now allow f_1, f_2, f_1', f_2' to change continuously, the zeros will move continuously about the z-plane and will only be able to enter the unstable domain by crossing its boundaries.

(i) $z = (1 + i)\omega$. The first term in $F(\omega + i\omega)$ can be written

$$F_1(\omega) = \frac{2u_0 f_1'(A + iB)}{(C + iD)} = \frac{2u_0 f_1'(A + iB)\,(C - iD)}{(C^2 + D^2)} \tag{32}$$

where

$$\begin{aligned} &A = ch \cdot c - 1; \quad B = sh \cdot s; \\ &C = -2\omega^2(1 - f_1)\,sh \cdot s + \omega f_1(sh \cdot c - ch \cdot s); \\ &D = 2\omega^2(1 - f_1)\,ch \cdot c + \omega f_1(sh \cdot c + ch \cdot s); \end{aligned} \tag{33}$$

and $s = \sin\omega$, $c = \cos\omega$, $sh = \sinh\omega$, $ch = \cosh\omega$

If f_1 is monotonic, $u_0 f_1' > 0$ and the imaginary part of $F_1(\omega)$ has the same sign as

$$\begin{aligned} CB - AD &= 2\omega^2(1 - f_1)\,(-sh^2 s^2 - ch^2 c^2 + ch \cdot c) + \omega f_1(sh^2 cs \\ &\quad - s^2 shch - c^2 shch - ch^2 cs + sh \cdot c + ch \cdot s) \\ &= \omega^2(1 - f_1)(s^2 - sh^2 - (c - ch)^2) \\ &\quad + \omega f_1\,(s - sh)(ch - c) < 0, (\omega > 0); \quad 0 \leqslant f_1 \leqslant 1 \end{aligned} \tag{34}$$

By similar argument, it can be shown that the second term in $F(\omega + i\omega)$ also has a negative imaginary part, since the function $f_2(x)$ must satisfy $f_2 < 0$.

It follows that $F(\omega + i\omega)$ has a negative (and hence nonzero) imaginary part for all $\omega > 0$ and no roots of equation (29) can therefore cross the line $z = \omega + i\omega$.

(ii) $z = \omega + i\delta$. We next establish that no zeros can cross the line $z = \omega + i\delta$, where δ is small, and hence that all unstable roots are real.

Since $\delta \ll 1$, the corresponding forms of the coefficients in equation (32) are

$$\begin{aligned} &A = ch - 1; \quad B = \delta\, sh; \\ &C = \omega^2(1 - f_1)\,ch + \omega f_1 sh; \\ &D = \delta(1 - f_1)\,(2\omega ch + \omega^2 sh) + \delta f_1(sh + \omega ch) \end{aligned} \tag{35}$$

We therefore have

$$\begin{aligned} CB - AD &= (1 - f_1)(\omega^2 sh + 2\omega ch - 2\omega ch^2) \\ &\quad + \delta f_1\,(sh - \omega)(1 - ch) \\ &< 0\ (\omega > 0) \end{aligned} \tag{36}$$

as can be demonstrated by expanding in powers of ω.

A similar argument applied to the second term in $F(\omega + i)$ enables us to conclude that no zeros can cross $z = \omega + i$ if $f_1' > 0$ and $f_2' < 0$.

The function $F(z)$ is even in z and hence its zeros must be symmetrically disposed with respect to the real and imaginary axes. It is not therefore necessary to prove corresponding results for the remaining boundaries.

(iii) $z = \delta + i0$. The preceding arguments demonstrate that zeros can only enter the domain from the origin along the real axis and hence the stability boundary can be determined from the condition for a real root at $z = \delta + i0$, $\delta \ll 1$.

The function $F(z)$ can then be expanded in the form

$$F(\delta + i0) = u_0 f_1' - u_0 f_2' - 1 + 0(\delta^2) \tag{37}$$

and hence the stability boundary is defined by

$$u_0(f_1' - f_2') = 1 \tag{38}$$

The system is known to be stable for $f_1' = f_2' = 0$ and hence for instability we must have

$$u_0(f_1' - f_2') > 1. \tag{39}$$

G. Genta
Associate Professor.

M. Gola
Associate Professor.

Politecnico di Torino,
Torino, Italy

The Stress Distribution in Orthotropic Rotating Disks

The stress distribution in a rotating orthotropic disk of constant thickness with a central hole is obtained in closed form for the special case of a material satisfying a condition first studied by Wolf [9] in 1935. A more general analytical solution, proposed in 1973, is closely examined and discussed. The solution proposed in this paper, although limited to a particular kind of material, is successfully used to test the accuracy of the numerical procedures which solve a more generalized form of the problem.

Introduction

A closed-form solution for the stress distribution in cylindrically orthotropic rotating disks is available in the literature, at least with the plane-stress or plane-strain assumptions for simple disk shapes [1–3].

However no analytical solution exists for disks with a central hole and made from an orthotropic material, even for the case of constant thickness.

The aim of this paper is to develop a particular closed-form solution for the constant thickness disk with a central hole. Although this solution holds only for materials whose stiffness matrices are of a particular form, it can be used to demonstrate that the results obtained from an already existing analytical solution [4] are incorrect. It can also be used to check the accuracy of numerical methods.

Analysis

A rotating orthotropic disk can be regarded as a cylindrical body in which the stresses are constant in the direction of the generator.

In the case of a disk rotating about the z-axis, two stress functions F and ψ can be defined [5, 6], such that

$$\begin{aligned} \sigma_x &= (F)_{,yy} + U \\ \sigma_y &= (F)_{,xx} + U \\ \tau_{xy} &= -(F)_{,xy} \\ \tau_{xz} &= (\psi)_{,y} \\ \tau_{yz} &= -(\psi)_{,x} \end{aligned} \tag{1}$$

where the potential function of the body forces U is given by the following formula:

$$U = \tfrac{1}{2}\rho\omega^2(x^2 + y^2) \tag{2}$$

and ρ and ω are, respectively, the density of the material and the angular velocity.

The stress functions defined in (1) satisfy the equilibrium conditions

$$\begin{aligned} (\sigma_x)_{,x} + (\tau_{xy})_{,y} - (U)_{,x} &= 0 \\ (\tau_{xy})_{,x} + (\sigma_y)_{,y} - (U)_{,y} &= 0 \\ (\tau_{xz})_{,x} + (\tau_{yz})_{,y} &= 0 \end{aligned} \tag{3}$$

In order to lead to compatible displacements, F and ψ must satisfy a set of differential equations which, in the case of x and y-axes coinciding with the material's principal axes, reduce to:

$$\begin{aligned} \beta_{22}(F)_{,xxxx} + (2\beta_{12} + \beta_{66})(F)_{,xxyy} + \beta_{11}(F)_{,yyyy} \\ = -(\beta_{12} + \beta_{22})(U)_{,xx} - (\beta_{11} + \beta_{12})(U)_{,yy}; \end{aligned} \tag{4}$$

$$\beta_{44}(\psi)_{,xx} + \beta_{55}(\psi)_{,yy} = 0 \tag{5}$$

Equation (5) holds for the case of no external loads applied to the end surfaces of the cylinder.

In equations (4) and (5) the plane-strain elastic compliances

$$\beta_{ij} = S_{ij} - (S_{i3} \cdot S_{j3}/S_{33}) \tag{6}$$

are used to solve the problem in terms of generalized plane-strain state. The elastic compliances S_{ij} must be substituted for β_{ij} in the case of plane stress in which equation (4) only applies.

The Airy stress function F and the stress function ψ in equations (4) and (5) can be solved separately.

The boundary conditions on the lateral surfaces, which are assumed to be free from surface forces, are [5]

$$\begin{aligned} (F)_{,x} &= \int_0^s -U\frac{dx}{ds}ds + c_1 \\ (F)_{,y} &= \int_0^s -U\frac{dy}{ds}ds + c_2 \\ \psi &= c_3. \end{aligned} \tag{7}$$

If the disk is circular, with inner and outer radii, respectively, r_i and r_e, equations (7) reduce to

Contributed by the Applied Mechanics Division for publication in the JOURNAL OF APPLIED MECHANICS.

Discussion on this paper should be addressed to the Editorial Department, ASME, United Engineering Center, 345 East 47th Street, New York, N. Y. 10017, and will be accepted until December 1, 1981. Readers who need more time to prepare a discussion should request an extension from the Editorial Department. Manuscript received by ASME Applied Mechanics Division, December, 1979; final revision, November, 1980.

$$(F)_{,x} = \tfrac{1}{2}\rho\omega^2 r_e{}^2 x + c_1$$

$$(F)_{,y} = \tfrac{1}{2}\rho\omega^2 r_e{}^2 y + c_2 \quad \text{(outer boundary)}$$

$$\psi = c_3 \tag{7a}$$

$$(F)_{,x} = \tfrac{1}{2}\rho\omega^2 r_i{}^2 x + c_1'$$

$$(F)_{,y} = \tfrac{1}{2}\rho\omega^2 r_i{}^2 y + c_2' \quad \text{(inner boundary)}$$

$$\psi = c_3'. \tag{7b}$$

The constants c_i and c_i' are arbitrary and can be put equal to zero at least on one boundary.

The function ψ can be assumed to be of the form

$$\psi = C(x^2 + y^2 - r_e{}^2) \tag{8}$$

which satisfies the boundary conditions, giving $c_3 = 0$ and $c_3' = C(r_i{}^2 - r_e{}^2)$.

The constant C can be evaluated from equation (5), yielding $C = 0$. It follows:

$$\psi = 0 \tag{9}$$

and therefore also τ_{xz} and τ_{yz} are both equal to 0.

The following is a particular solution of equation (4) [7]:

$$F' = C_1(x^2 + y^2)^2. \tag{10}$$

Differentiating equation (10) the constant C_1 can be calculated from equation (4)

$$C_1 = \rho\omega^2(\beta_{11} + 2\beta_{12} + \beta_{22})/[12(\beta_{11} + \beta_{22}) + 4(2\beta_{12} + \beta_{66})]. \tag{11}$$

The problem of finding a general solution of the homogeneous equation (4) is a difficult one. The authors found a solution for the plane-stress problem, provided the elastic compliances of the material satisfy the equation

$$S_{11} + S_{22} - 2S_{12} - S_{66} = 0 \tag{12}$$

i.e., the material is of the type studied by De St. Venant [8] and Wolf [9].

Obviously in the case of plane-strain state, condition (12) becomes

$$\beta_{11} + \beta_{22} - 2\beta_{12} - \beta_{66} = 0. \tag{13}$$

Under condition (12) the solution of the homogeneous equation (4) was found to be

$$F'' = C_2(x^2 + y^2) + C_3 \ln (x^2 + y^2). \tag{14}$$

The complete Airy function F is therefore

$$F = C_1(x^2 + y^2)^2 + C_2(x^2 + y^2) + C_3 \ln (x^2 + y^2). \tag{15}$$

Constants C_2 and C_3 can be evaluated from the boundary conditions (7a) and (7b) in which all constants c_i and c_i' can be put equal to zero, yielding

$$C_2 = \left(\frac{\rho\omega^2}{4} - C_1\right)(r_e{}^2 - r_i{}^2)$$

$$C_3 = \left(C_1 - \frac{\rho\omega^2}{4}\right) r_e{}^2 r_i{}^2 \tag{16}$$

The stress state is therefore

$$\sigma_x = 2C_1(3y^2 + x^2) + 2C_2 + 2C_3(x^2 - y^2)/(x^2 + y^2)^2 - \tfrac{1}{2}\rho\omega^2(x^2 + y^2)$$

$$\sigma_y = 2C_1(3x^2 + y^2) + 2C_2 + 2C_3(y^2 - x^2)/(x^2 + y^2)^2 - \tfrac{1}{2}\rho\omega^2(x^2 + y^2)$$

$$\tau_{xy} = 4xy[-C_1 + C_3/(x^2 + y^2)^2]$$

$$\tau_{yz} = \tau_{xz} = 0 \tag{17}$$

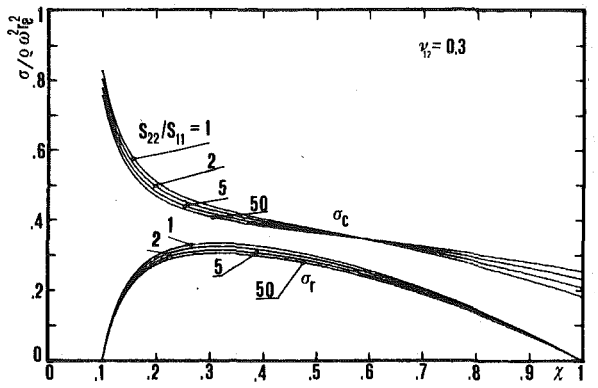

Fig. 1 Stress distribution in rotating disks with different values of the ratio S_{22}/S_{11}; the stress distribution is independent of angle θ since equation (12) is satisfied

σ_z can be calculated through the familiar equation

$$\sigma_z = -(S_{13}\sigma_x + S_{23}\sigma_y)/S_{33} \tag{18}$$

for the plane-strain case, while it is obviously equal to zero for the plane-stress case.

Transforming equation (17) into polar coordinates, and introducing the ratios $\beta = r_i/r_e$ and $\chi = r/r_e$, the complete stress distribution for the plane-stress case is

$$\sigma_r = \rho\omega^2 r_e{}^2 K_1\{1 + \beta^2 - \beta^2/\chi^2 - \chi^2\}$$

$$\sigma_c = \rho\omega^2 r_e{}^2\{K_1[1 + \beta^2 + \beta^2/\chi^2] - K_2\chi^2\}$$

$$\tau_{rc} = 0 \tag{19}$$

where

$$K_1 = \frac{2(S_{11} + S_{22}) + S_{66}}{6(S_{11} + S_{22}) + 4S_{12} + 2S_{16}} = \frac{3(S_{11} + S_{22}) - 2S_{12}}{8(S_{11} + S_{22})}$$

$$K_2 = \frac{S_{66} - 4S_{12}}{6(S_{11} + S_{22}) + 4S_{12} + 2S_{16}} = \frac{S_{11} + S_{22} - 6S_{12}}{8(S_{11} + S_{22})}. \tag{20}$$

If the material is isotropic, it follows that $S_{11} = S_{22} = 1/E$, $S_{12} = -\nu/E$; condition (12) is satisfied and the values of K_1 and K_2 are

$$K_1 = (3 + \nu)/8$$

$$K_2 = (1 + 3\nu)/8 \tag{21}$$

which give the usual stress distribution in isotropic constant thickness disks [10].

The stress distribution expressed by equation (19) is independent of angle θ. The nondimensional stress distribution in disks with a value of $\beta = 0.1$, built from materials with different ratios E_1/E_2, but all with $\nu_{12} = 0.3$ and all satisfying equation (12), is plotted in Fig. 1.

The independence of the stress distribution from angle θ for disks without a central hole, this time valid for any orthotropic material, was already proved by Chang [7, 11].

The maximum value of the circumferential stress

$$\sigma_{c\ \max} = \rho\omega^2 r_e{}^2\{K_1[2 + \beta^2] - K_2\beta^2\} \tag{22}$$

is found at the inner radius, and it is easy to check by comparing equation (22) with equation (18) in [7], that for $\beta \to 0$ the maximum stress in the disk with a central hole is twice the value of the maximum stress in the unpierced disk, which is exactly the same as if the material were isotropic. It is also easy to check that with $\beta \to 0$ the value of σ_c at the outer edge is the same in the two cases.

The displacements u and v in the x and y-directions can be easily calculated from equation (19) using the stiffness matrix of the material:

$$u = \rho\omega^2 x \left\{ K_1 \frac{r_e^2 r_i^2 (S_{11} - S_{12})}{x^2 + y^2} + K_3 \frac{x^2}{3} + K_4 y^2 + K_1 (r_e^2 + r_i^2)(S_{11} + S_{12}) \right\}$$

$$v = \rho\omega^2 y \left\{ K_1 \frac{r_e^2 r_i^2 (S_{22} - S_{12})}{x^2 + y^2} + K_5 x^2 + K_6 \frac{y^2}{3} + K_1 (r_e^2 + r_i^2)(S_{22} + S_{12}) \right\} \quad (23)$$

where

$$K_3 = \frac{-2S_{11}(S_{11} + S_{22}) + 4S_{12}^2 - S_{66}(S_{11} + S_{12})}{6(S_{11} + S_{22}) + 4S_{12} + 2S_{66}} = \frac{-3S_{11}(S_{11} + S_{22}) + S_{12}(6S_{12} + S_{11} - S_{22})}{8(S_{11} + S_{22})}$$

$$K_4 = \frac{2S_{12}(S_{11} - S_{22}) - S_{66}(S_{11} + S_{12})}{6(S_{11} + S_{22}) + 4S_{12} + 2S_{66}} = \frac{3S_{12}(S_{11} - S_{22}) - S_{11}(S_{11} + S_{22}) + 2S_{12}^2}{8(S_{11} + S_{22})}$$

$$K_5 = \frac{2S_{12}(S_{22} - S_{11}) - S_{66}(S_{22} + S_{12})}{6(S_{11} + S_{22}) + 4S_{12} + 2S_{66}} = \frac{3S_{12}(S_{22} - S_{11}) - S_{22}(S_{11} + S_{22}) + 2S_{12}^2}{8(S_{11} + S_{22})}$$

$$K_6 = \frac{-2S_{22}(S_{11} + S_{22}) + 4S_{12}^2 - S_{66}(S_{22} + S_{12})}{6(S_{11} + S_{22}) + 4S_{12} + 2S_{66}} = \frac{-3S_{22}(S_{11} + S_{22}) + S_{12}(6S_{12} - S_{11} + S_{22})}{8(S_{11} + S_{22})} \quad (24)$$

If $\beta \to 0$, the displacements in the disk with and without central hole coincide (equation (23) compared with equation (24) in [7]). In polar coordinates (r,θ) the expressions of the displacements in the radial direction u_r and in the circumferential direction u_c are

$$u_r = \rho\omega^2 r_e^3 \chi \{K_1(S_{11}\cos^2\theta + S_{22}\sin^2\theta - S_{12})\beta^2/\chi^2 + K_1(S_{11}\cos^2\theta + S_{22}\sin^2\theta + S_{12})(1 + \beta^2) + \chi^2[K_3\cos^4\theta/3 + (K_4 + K_5)\cos^2\theta + \sin^2\theta + K_6\sin^4\theta/3]\}$$

$$u_c = \rho\omega^2 r_e^3 \chi \{K_1(S_{22} - S_{11})(1 + \beta^2 + \beta^2/\chi^2) + \chi^2[(K_5 + K_3/3)\cos^2\theta + (K_6/3 - K_4)\sin^2\theta]\} \quad (25)$$

If the material is isotropic the first equation (25) gives the familiar formula for u_r [10], and the second gives $u_c = 0$.

Comparison With a Previous Analytical Solution

In a previous paper, doubts where cast on an existing analytical solution [4]; a comparison was made with results obtained via annular finite elements in which the displacement field was described by third-degree polynomials radially, and by trigonometric polynomials circumferentially [13].

The argument is strengthened here by the present closed-form solution. For a disk with $\beta = 0.1$ built in a grafite-epoxy composite (E_1 = 207 GN/m^2, E_2 = 5.17 GN/m^2, G_{12} = 4.98 GN/m^2, ν_{12} = 0.25) practically equal to the material referred to as M_1 in [4], a case is obtained which can be tested against the solution presented in [4] (Fig. 2).

The difference is evident, particularly because the solution in [4] is dependent also on angle θ while the present solution is not.

In Fig. 2 a numerical solution obtained with an improved version of the method described in [12–14] was also plotted.

The curves obtained in this way for various values of θ are all superimposed and not distinguishable from the one obtained from the present solution.

A possible explanation for the discrepancy between our results and those of [4] is the fact that, using a polar reference system, all derivatives of the elastic compliances S_i' related to the r and θ-directions

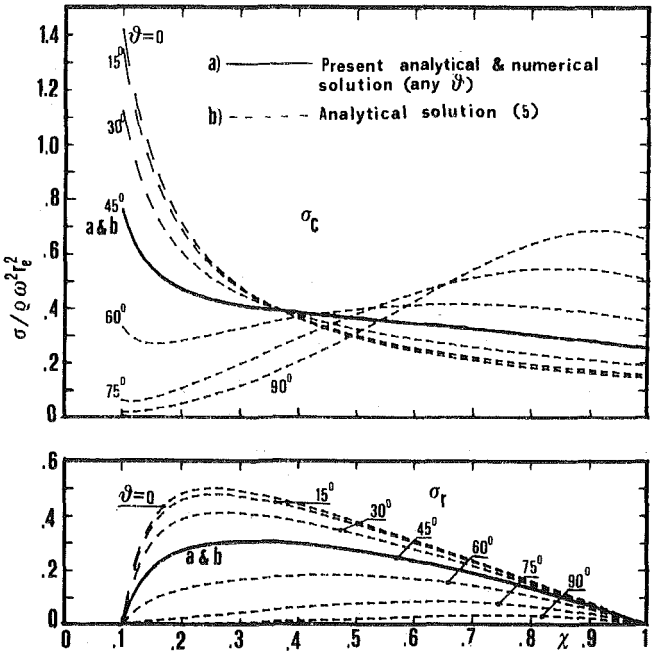

Fig. 2 Comparison of the present analytical solution with the analytical solution [4] and a numerical one; E_1 = 207 GN/m^2; E_2 = 5.17 GN/m^2; G_{12} = 4.98 GN/m^2, ν_{12} = 0.25; the correct solution is independent of θ

are there forgotten when the strains ϵ_r, ϵ_c, and γ_{rc} are differentiated with respect to θ. This also explains why at each radius the solution is identical to the solution relative to a cylindrically orthotropic material having the same elastic parameters found at that radius.

The correct expressions of the coefficients of equation (10) in [4], in reality should be

$$F_1 = S_{22}'; \quad F_2 = -2S_{26}'; \quad F_3 = S_{66}' + 2S_{12}';$$

$$F_4 = -2S_{16}'; \quad F_5 = S_{11}'; \quad F_6 = 2(n+1)S_{22}' + (S_{26}')_{,\theta}$$

$$F_7 = (n-1)(S_{66}' + 2S_{12}') - 3(S_{16}')_{,\theta}; \quad F_8 = S_{16}'(2-n) + 2(S_{11}')_{,\theta}$$

$$F_9 = -3nS_{26}' + (S_{66}')_{,\theta} + 2(S_{12}')_{,\theta};$$

$$F_{10} = -S_{11}' + n(S_{12}' + S_{22}' + nS_{22}') - (S_{16}')_{,\theta} - (S_{26}')_{,\theta}(1+n) + (S_{12}')_{,\theta\theta};$$

$$F_{11} = 2S_{16}' - (n-1)(n-2)S_{26}' - (1-n)(S_{66}')_{,\theta} + 2(S_{11}')_{,\theta} - (S_{16}')_{,\theta\theta};$$

$$F_{12} = -(n-1)S_{66}' - (n-2)(S_{11}' + S_{12}' - nS_{12}') + (S_{11}')_{,\theta\theta} + (S_{16}')_{,\theta}(3-n);$$

$$F_{13} = (1-n)(S_{11}' - nS_{12}') - n(S_{16}')_{,\theta} + (S_{11}')_{,\theta\theta};$$

$$F_{14} = (2-n)(S_{16}' + S_{26}' - nS_{26}') + (S_{16}')_{,\theta\theta} + (1-n)(S_{66}')_{,\theta};$$

$$p_\gamma = \rho\omega^2 h_0 b^n [6S_{22}' - 2S_{12}' - 3(S_{26}')_{,\theta} + (S_{12}')_{,\theta\theta}]. \quad (26)$$

This is necessary but not sufficient to obtain a solution, since major difficulties can come from the evaluation of the derivatives of the stress function (24) in [4], $(\phi)_{,\theta}$, $(\phi)_{,r\theta}$, $(\phi)_{,\theta\theta}$, due to the fact that the coefficients C_1, C_2, C_3, and C_4 are unknown functions of θ.

It should be noted that, curiously enough, the formulas given in [4] furnish the correct stress state, if the material satisfies condition (12), at $\theta = 45°$. In this same case however, the solution for the displacements doesn't hold; in fact, the fourth of equations (36) in [4] gives $u_c \to \infty$, except for the special case of isotropic material.

Generally Orthotropic Material

If the elastic compliances of the material do not satisfy equation

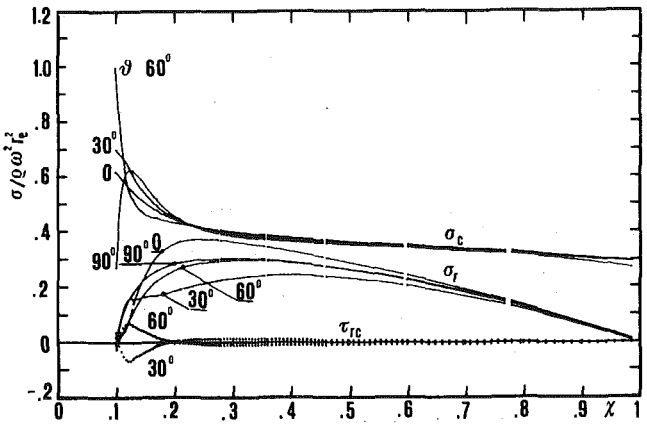

Fig. 3 Stress distribution in a constant thickness disk not satisfying equation (12); numerical solution; E_1 = 207 GN/m^2; E_2 = 5.17 GN/m^2; G_{12} = 9.96 GN/m^2, ν_{12} = 0.25.

(12), a solution to equation (5) could be attempted by the method of the characteristics [6]. Even if the characteristic equation is, in this case, particularly simple and its roots are pure imaginary numbers, the solution would involve anyway a considerable amount of effort [5, 6].

The present authors believe that a much better approach is in this case a numerical procedure, as the one already presented in [12–14]; in fact generally variable physical parameters, including thickness, can then be taken into account in a simple and very general computer program, that is conveniently tested against the analytical solution described in the present paper.

The stress state in a disk equal to the disk studied in Fig. 2, but having the value of elastic compliance S_{66} halved, is shown in Fig. 3. It can be seen now that, as the material does not satisfy equation (12), the stresses depend also on angle θ and the shear stresses are, therefore, not equal to zero.

Conclusion

While the analytical solution for the stress distribution of rotating disks without a central hole with constant thickness, is relatively simple [7, 11], in the case of pierced disks this leads to considerable analytical complications.

Examining the existing literature on the subject, and criticizing also some misleading conclusions [4], these authors have come to the conclusion that specially developed numerical procedures perform the task in a more efficient and general way [12–14].

Of course, the problem remains to evaluate the correctness of the numerical results; this could be done in the present work by testing them against the newly developed analytical solution which applies only to a particular kind of orthotropic material.

References

1 Morganthaler, G. F., and Bonk, S. P., "Composite Flywheel Stress Analysis and Material Study," *12th National SAMPE Symposium*, 1967.

2 Murthy, D. N. S., and Sherbourne, A. N., "Elastic Stresses in Anisotropic Disks of Variable Thickness," *International Journal of Mechanical Science*, 1970, Vol. 12, pp. 627–640.

3 Belingardi, G., and Genta, G., "Sull'analisi delle tensioni in dischi rotanti in materiale ortotropo sottoposti a variazione di temperatura," III Congresso Nazionale AIMETA, Cagliari, October 13–16, 1976 pp. III-26.1–III-26.18.

4 Lakshminarayana, H. V., and Srinath, H., "Elastic Stresses in Rotating Orthotropic Disks of Variable Thickness," *Journal of Strain Analysis*, Vol. 8, n. 3, 1973, pp. 176–181.

5 Lekhnitskii, S. G., *Theory of Elasticity of an Anisotropic Elastic Body*, Holden Day, New York, 1963.

6 Sendeckyj, G. P., "Some Topics in Anisotropic Elasticity," in *Composite Materials*, Vol. 7, Academic Press, New York, 1975, pp. 1–48.

7 Chang, C. I., "The Anisotropic Rotating Disk," *International Journal of Mechanical Science*, Vol. 17, 1975, pp. 397–402.

8 De St. Venant, B., "Memoire sur la distribution d'elasticité," *Journal des Math. Pures et Appl.*, S2, t8, 1863.

9 Wolf, K., *Zeitschrift für Angewaudte Mathematik und Mechanik*, Vol. 15, 1935, p. 249.

10 Giovannozzi, R., *Costruzione di macchine*, Patron, Bologna, 1963.

11 Chang, C. I., "A Closed-Form Solution for an Orthotropic Rotating Disk," ASME JOURNAL OF APPLIED MECHANICS, Vol. 4, 1974, pp. 1122–1123.

12 Belingardi, G., Genta, G., and Gola, M., "Una applicazione del principio dei lavori virtuali al calcolo di dischi rotanti in materiale anisotropo," V Congresso AIAS, Bari, 1977, pp. 15.1–15.12.

13 Belingardi, G., Genta, G., and Gola, M., "A Study of the Stress Distribution in Rotating Orthotropic Disks," *Composites*, Apr. 1979, pp. 77–80.

14 Genta, G., and Gola, M., "Volani in legno lamellare. Caratterizzazione del materiale, calcolo delle tensioni e prove di centrifugazione," VI Congresso AIAS, Brescia, 1978, pp. 275–286.

N. J. Hoff

Visiting Distinguished Professor (Adjunct),
Rensselaer Polytechnic Institute,
Troy, N. Y. 12181
Fellow ASME

Stress Concentrations in Cylindrically Orthotropic Composite Plates With a Circular Hole[1]

The equations governing the distribution of the stresses in a cylindrically orthotropic plate with a circular hole are solved for the case when the plate is subjected to uniform uniaxial traction. Closed-form solutions are given for the circumferential stresses along the edge of the hole.

Introduction

The inherent advantage of fiber-reinforced plastics is the possibility of arranging the fibers in such a manner as to optimize the load-carrying capacity of the composite structure. This purpose may be served by developing arrangements that reduce stress concentrations along the edge of a circular hole in a composite plate. An arrangement that may be capable of achieving this is one that results in a cylindrically symmetric plate with the origin of the system of coordinates at the center of the hole. It is believed that such plates can be manufactured by laying up tape, by filament winding, and probably also by weaving. The purpose of this paper is to calculate the stress-concentration factors for cylindrically symmetric plates with a central circular hole.

The first calculation of the effect of a circular hole on the stress concentration in a plate was published by Kirsch [1] in 1898. It dealt with isotropic plates and resulted in a stress-concentration factor (maximum circumferential stress along the edge of the hole divided by the value of the uniform uniaxial tensile stress at a large distance from the hole) of 3. This calculation can be found, for instance, in *Theory of Elasticity* by Timoshenko and Goodier [2]. A detailed summary of work dealing with stress concentrations along the edge of a hole is given by Lekhnitskii [3] for plates orthotropic with respect to a system of Cartesian coordinates. A concise report on the results of these investigations can be found in a book by Jones [4].

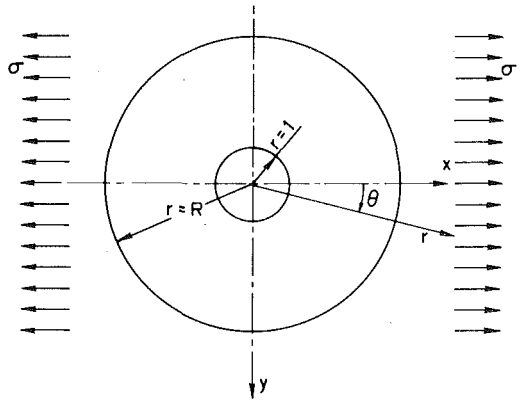

Fig. 1 Notation

In the present analysis, as in the calculations presented by Timoshenko and Goodier, a state of plane stress is assumed to prevail in the plate. At the outer radius R uniformly distributed tractions are applied to the plate in the direction of the x-axis, as indicated in Fig. 1.

Governing Equations

The conditions of equilibrium are satisfied if the stresses are derived from a stress function ϕ in accordance with the equations

$$\sigma_r = \frac{1}{r}\frac{\partial \phi}{\partial r} + \frac{1}{r^2}\frac{\partial^2 \phi}{\partial \theta^2} \tag{1a}$$

$$\sigma_\theta = \frac{\partial^2 \phi}{\partial r^2} \tag{1b}$$

$$\tau_{r\theta} = -\frac{\partial}{\partial r}\left(\frac{1}{r}\frac{\partial \phi}{\partial \theta}\right) \tag{1c}$$

The constitutive equation can be written in the form

[1] This work was carried out under Grant No. NGL 33-018-003 awarded to Rensselaer Polytechnic Institute by the Air Force Office of Scientific Research and the National Aeronautics and Space Administration (NASA Technical Officer: Leonard A. Harris).

Contributed by the Applied Mechanics Division for publication in the JOURNAL OF APPLIED MECHANICS, and was presented at the 1981 Joint ASME-ASCE Applied Mechanics, Fluids Engineering, and Bioengineering Conference, University of Colorado, Boulder, Colo., June 22–27, 1981 (No Preprints or number).

Discussion on this paper should be addressed to the Editorial Department, ASME, United Engineering Center, 345 East 47th Street, New York, N. Y. 10017, and will be accepted until December 1, 1981. Readers who need more time to prepare a discussion should request an extension from the Editorial Department. Manuscript received by the Applied Mechanics Division, December, 1980; final revision, February, 1981.

$$\begin{Bmatrix}\epsilon_r\\ \epsilon_\theta\\ \gamma_{r\theta}\end{Bmatrix} = \begin{vmatrix} S_{rr} & S_{r\theta} & 0\\ S_{r\theta} & S_{\theta\theta} & 0\\ 0 & 0 & S_{66}\end{vmatrix} \times \begin{Bmatrix}\sigma_r\\ \sigma_\theta\\ \tau_{r\theta}\end{Bmatrix} \tag{2}$$

The compatibility condition can be given as

$$\frac{\partial^2\epsilon_r}{\partial\theta^2} - r\frac{\partial\epsilon_r}{\partial r} + r\frac{\partial^2}{\partial r^2}(r\epsilon_\theta) - \frac{\partial^2}{\partial r\partial\theta}(r\gamma_{r\theta}) = T = 0 \tag{3}$$

The boundary conditions are

$$\sigma_r = \tau_{r\theta} = 0 \quad \text{when} \quad r = 1 \tag{4a, b}$$

$$\sigma_r = (\sigma/2)(1 + \cos 2\theta) \quad \text{when} \quad r = R \tag{4c}$$

$$\tau_{r\theta} = -(\sigma/2)\sin 2\theta \quad \text{when} \quad r = R \tag{4d}$$

The last two expressions are in agreement with

$$\sigma_x = \sigma \quad \sigma_y = \tau_{xy} = 0 \quad \text{when} \quad r = R \tag{5a–c}$$

Solution of the Equations

First, the solution will be sought for the changed boundary conditions

$$\sigma_r = \tau_{r\theta} = 0 \quad \text{when} \quad r = 1 \tag{6a, b}$$

$$\sigma_r = (\sigma/2)\cos n\theta \quad \text{when} \quad r = R \tag{6c}$$

$$\tau_{r\theta} = -(\sigma/2)\sin n\theta \quad \text{when} \quad r = R \tag{6d}$$

The solution can be written in the form

$$\phi = r^t \cos n\theta \tag{7}$$

where t is a constant. Substitution yields

$$\sigma_r = (t - n^2)r^{t-2}\cos n\theta \tag{8a}$$

$$\sigma_\theta = t(t-1)r^{t-2}\cos n\theta \tag{8b}$$

$$\tau_{r\theta} = n(t-1)r^{t-2}\sin n\theta \tag{8c}$$

The expressions for the strains become

$$\epsilon_r = [(t - n^2)S_{rr} + t(t-1)S_{r\theta}]r^{t-2}\cos n\theta \tag{9a}$$

$$\epsilon_\theta = [(t - n^2)S_{r\theta} + t(t-1)S_{\theta\theta}]r^{t-2}\cos n\theta \tag{9b}$$

$$\gamma_{r\theta} = n(t-1)S_{66}r^{t-2}\sin n\theta \tag{9c}$$

When these are substituted into the compatibility condition, the result is

$$T = S_{\theta\theta}r^{t-2}\cos n\theta\{t^4 - 4t^3 + (5 - \overline{S}_{rr} - n^2\overline{S})t^2 - 2(1 - \overline{S}_{rr} - n^2\overline{S})t + n^2[(n^2-2)(\overline{S}_{rr} + n^2\overline{S}) - (1-n^2)^2\overline{S}]\} = 0 \tag{10}$$

where

$$\overline{S}_{ab} = S_{ab}/S_{\theta\theta} \quad \overline{S} = 2\overline{S}_{r\theta} + \overline{S}_{66} \tag{11a, b}$$

The four roots of the equation

$$t^4 - 4t^3 + (5 - \overline{S}_{rr} - n^2\overline{S})t^2 - 2(1 - \overline{S}_{rr} - n^2\overline{S})t + n^2[(n^2-2)(\overline{S}_{rr} + n^2\overline{S}) - (1-n^2)^2\overline{S}] = 0 \tag{12}$$

can be written as

$$t_1 = 1 + \alpha, \quad t_2 = 1 - \alpha, \quad t_3 = 1 + \beta, \quad t_4 = 1 - \beta \tag{13a–d}$$

With these roots, equation (12) can also be given in the form

$$(t - t_1)(t - t_2)(t - t_3)(t - t_4) = 0 \tag{14}$$

Substitution from equations (13) results in

$$t^4 - 4t^3 + [6 - (\alpha^2 + \beta^2)]t^2 - 2[2 - (\alpha^2 + \beta^2)]t + [1 - (\alpha^2 + \beta^2) + \alpha^2\beta^2] = 0 \tag{15}$$

Equations (12) and (15) are identical if

$$1 - \overline{S}_{rr} - n^2\overline{S} = 2 - (\alpha^2 + \beta^2) \tag{16a}$$

$$5 - \overline{S}_{rr} - n^2\overline{S} = 6 - (\alpha^2 + \beta^2) \tag{16b}$$

$$n^2[(n^2-2)(\overline{S}_{rr} + n^2\overline{S}) - (1-n^2)^2\overline{S}] = 1 - (\alpha^2 + \beta^2) + \alpha^2\beta^2 \tag{16c}$$

from which follow the expressions

$$\alpha^2 + \beta^2 = 1 + \overline{S}_{rr} + n^2\overline{S} \quad \alpha^2\beta^2 = (n^2-1)^2\overline{S}_{rr} \tag{17a, b}$$

The two equations can be solved for α^2 and β^2. The result is

$$\alpha^2 = (\tfrac{1}{2})(1 + \overline{S}_{rr} + n^2\overline{S}) + \{(\tfrac{1}{4})(1 + \overline{S}_{rr} + n^2\overline{S})^2 - (n^2-1)^2\overline{S}_{rr}\}^{1/2} \tag{18a}$$

$$\beta^2 = (\tfrac{1}{2})(1 + \overline{S}_{rr} + n^2\overline{S}) - \{(\tfrac{1}{4})(1 + \overline{S}_{rr} + n^2\overline{S})^2 - (n^2-1)^2\overline{S}_{rr}\}^{1/2} \tag{18b}$$

where the square root should be taken with the positive sign.

The four roots of equation (12) are real if

$$(1 + \overline{S}_{rr} + n^2\overline{S})^2 > 4(n^2-1)^2\overline{S}_{rr} \tag{19a}$$

and

$$1 + \overline{S}_{rr} + n^2\overline{S} > 0 \tag{19b}$$

If the "greater than" signs are replaced with "equal" signs, the second equation represents a straight line, and the first one a curve with two branches in the $\overline{S} - \overline{S}_{rr}$ plane. They are shown in Fig. 2 for the case when $n = 2$.

If an equality sign held in (19a) we would have

$$\overline{S} = (\tfrac{1}{4})(\pm 6\sqrt{\overline{S}_{rr}} - 1 - \overline{S}_{rr}) \tag{19c}$$

provided $n = 2$. The curve has zeros at $\overline{S}_{rr} = 0.0294$ and 33.97, a vertical tangent at $\overline{S}_{rr} = 0$, a maximum of $\overline{S} = 2$ at $\overline{S}_{rr} = 9$, and it is tangent to the straight line $\overline{S} = 2\overline{S}_{rr}$. In agreement with inequalities (19a) and (19b), points lying above the upper branch of the curve represent plates for which the roots of equation (12) are real.

When inequalities (19) are satisfied, the following useful relations hold:

Nomenclature

A, B = integration constants in (64)
A_p = integration constants in (21)
D = denominator determinant given in (24)
$i = \sqrt{-1}$
n = integer
N_q = numerator determinant defined in (27)
p = exponent of r in stress function (55)
r = radial coordinate
R = outer radius of circular plate
S_{pq} = compliance
$\overline{S}_{pq}$ = relative compliance defined in (11a)
$\overline{S}$ = second fundamental parameter defined in (11b)
$\overline{S}_{rr}$ = first fundamental parameter defined in (11a)
t = exponent of r in stress function (7)
u = radial displacement
α, β = defined in (13)
$\gamma_{r\theta}$ = shear strain
ϵ_{pq} = strain component
θ = circumferential coordinate
σ = applied uniaxial stress
σ_{pq} = stress component
$\tau_{r\theta}$ = shear stress
ϕ = stress function

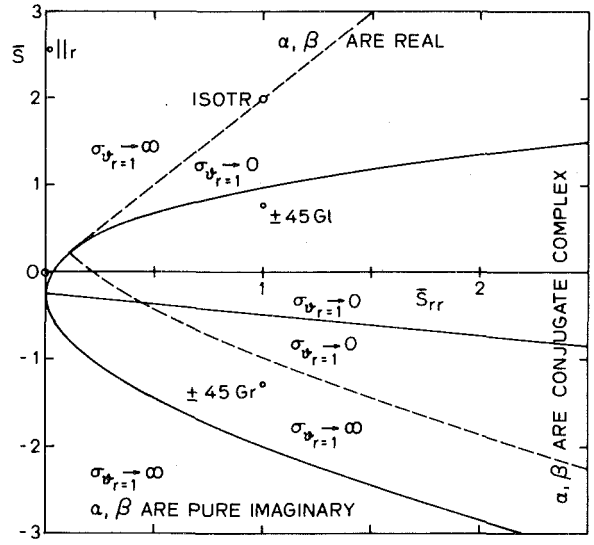

Fig. 2 Ranges of solution of equations for boundary conditions (6)

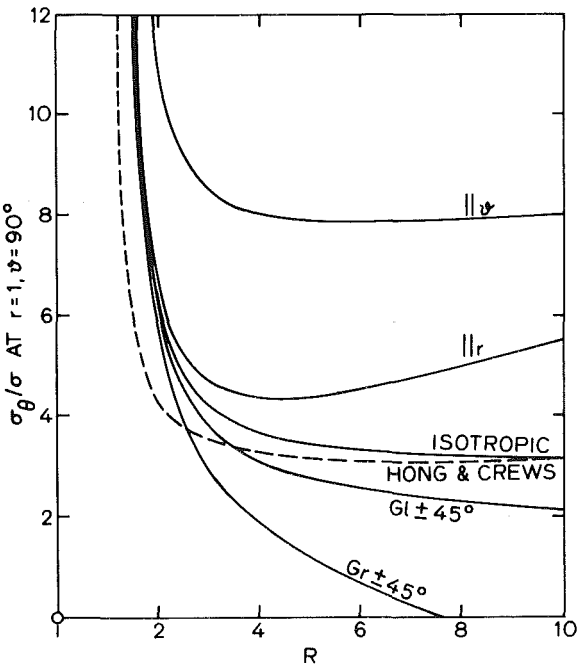

Fig. 3 Variations in stress-concentration factor with changing R and fiber arrangement (at $\theta = 90°$) for boundary conditions (4)

$$\alpha^2 + \beta^2 = 1 + \bar{S}_{rr} + n^2\bar{S} > 0 \tag{20a}$$

$$\alpha^2 - \beta^2 = \{(1 + \bar{S}_{rr} + n^2\bar{S})^2 - 4(n^2-1)^2\bar{S}_{rr}\}^{1/2} > 0 \tag{20b}$$

$$\alpha\beta = (n^2-1)\sqrt{\bar{S}_{rr}} > 0 \tag{20c}$$

$$(\alpha+\beta)^2 = 1 + \bar{S}_{rr} + n^2\bar{S} + 2(n^2-1)\sqrt{\bar{S}_{rr}} > 0 \tag{20d}$$

$$(\alpha-\beta)^2 = 1 + \bar{S}_{rr} + n^2\bar{S} - 2(n^2-1)\sqrt{\bar{S}_{rr}} > 0 \tag{20e}$$

The values of α and β can be calculated from equations (18), or from

$$2\alpha = \{1 + \bar{S}_{rr} + n^2\bar{S} + 2(n^2-1)\sqrt{\bar{S}_{rr}}\}^{1/2} + \{1 + \bar{S}_{rr} + n^2\bar{S} - 2(n^2-1)\sqrt{\bar{S}_{rr}}\}^{1/2} \tag{20f}$$

$$2\beta = \{1 + \bar{S}_{rr} + n^2\bar{S} + 2(n^2-1)\sqrt{\bar{S}_{rr}}\}^{1/2} - \{1 + \bar{S}_{rr} + n^2\bar{S} - 2(n^2-1)\sqrt{\bar{S}_{rr}}\}^{1/2} \tag{20g}$$

It follows that

$$\alpha > \beta > 0 \tag{20h}$$

$$\alpha + \beta > \alpha - \beta > 0 \tag{20i}$$

It is noted that in (20c) the positive sign for the square root was selected arbitrarily. The negative sign would be equally justified on the basis of (17b). If in (20c) the sign were changed, in (20f) and (20g) α would remain unchanged but β would become $-\beta$. This would still result in the same four roots as given in (13) except for their order.

Enforcement of the Boundary Conditions

The general expression for the stress function can be written as

$$\phi = \{A_1 r^{t_1} + A_2 r^{t_2} + A_3 r^{t_3} + A_4 r^{t_4}\} \cos 2\theta \tag{21}$$

where t_1, t_2, t_3, t_4 are the four roots of equation (12) and A_1, A_2, A_3, A_4 are constants of integration. The constants must be determined from boundary conditions (6). With $n = 2$ they give

$$\begin{array}{cccc} (-3+\alpha)A_1 & -(3+\alpha)A_2 & +(-3+\beta)A_3 & -(3+\beta)A_4 = 0 \\ \alpha A_1 & -\alpha A_2 & +\beta A_3 & -\beta A_4 = 0 \\ (-3+\alpha)R^{\alpha-1}A_1 & -(3+\alpha)R^{-(1+\alpha)}A_2 & +(-3+\beta)R^{\beta-1}A_3 & -(3+\beta)R^{-(1+\beta)}A_4 = (\sigma/2) \\ \alpha R^{\alpha-1}A_1 & -\alpha R^{-(1+\alpha)}A_2 & +\beta R^{\beta-1}A_3 & -\beta R^{-(1+\beta)}A_4 = -(\sigma/4) \end{array} \tag{22}$$

These equations can be simplified by subtracting the members of the second equation from those of the first, and the members of the fourth equation from those of the third. Next, the common multipliers -3 and R^{-1} can be factored out. The result is

$$\begin{aligned} A_1 + A_2 + A_3 + A_4 &= 0 \\ \alpha A_1 - \alpha A_2 + \beta A_3 - \beta A_4 &= 0 \\ R^\alpha A_1 + R^{-\alpha}A_2 + R^\beta A_3 + R^{-\beta}A_4 &= -R\sigma/4 \\ \alpha R^\alpha A_1 - \alpha R^{-\alpha}A_2 + \beta R^\beta A_3 - \beta R^{-\beta}A_4 &= -R\sigma/4 \end{aligned} \tag{23}$$

The equations can be solved with the aid of Cramer's rule. The denominator determinant is

$$D = \begin{vmatrix} 1 & 1 & 1 & 1 \\ \alpha & -\alpha & \beta & -\beta \\ R^\alpha & R^{-\alpha} & R^\beta & R^{-\beta} \\ \alpha R^\alpha & -\alpha R^{-\alpha} & \beta R^\beta & -\beta R^{-\beta} \end{vmatrix} \tag{24}$$

When evaluated, this becomes

$$D = 8\alpha\beta + (\alpha-\beta)^2(R^{\alpha+\beta} + R^{-(\alpha+\beta)}) - (\alpha+\beta)^2(R^{\alpha-\beta} + R^{-(\alpha-\beta)}) \tag{25}$$

or

$$D = 8\alpha\beta + 2(\alpha-\beta)^2 \cosh[(\alpha+\beta)\ln R] - 2(\alpha+\beta)^2 \cosh[(\alpha-\beta)\ln r] \tag{26}$$

The numerator determinants are

$$N_1 = [2\beta(1+\alpha)R^{-\alpha} + (1-\beta)(\alpha-\beta)R^\beta - (1+\beta)(\alpha+\beta)R^{-\beta}](-\sigma R/4) \tag{27a}$$

Table 1 Table of constants for Figs. 2 and 3

Fiber arrangement	$\bar{S}_{rr}$	$\bar{S}_{r\theta}$	$\bar{S}_{66}$	$\bar{S}$	α	β	Symbol
Fibers along r	0.068	-0.0204	2.6154	2.5746	3.3634	0.2326	||r
Fibers along θ	14.7059	-0.3	38.4615	37.8615	12.8979	0.892	||θ
Fibers at ±45° (graphite epoxy)	1	-0.83	0.3684	-1.2916	0.8416 +i1.5138	0.8416 -i1.5138	±45Gr
Fibers at ±45° (glass epoxy)	1	-0.39	1.56	0.78	1.6673 +i0.4690	1.6673 -i0.4690	±45Gℓ
Quasi-isotropic	1	-0.3	2.6	2	3	1	ISOTR.

$$N_2 = \{2\beta(1-\alpha)R^{\alpha} + (\alpha+\beta)(\beta-1)R^{\beta} + (\alpha-\beta)(1+\beta)R^{-\beta}\}(R\sigma/4) \quad (27b)$$

$$N_3 = \{(\alpha-\beta)(1-\alpha)R^{\alpha} + (\alpha+\beta)(1+\alpha)R^{-\alpha} - 2\alpha(1+\beta)R^{-\beta}\}(R\sigma/4) \quad (27c)$$

$$N_4 = \{-(1-\alpha)(\alpha+\beta)R^{\alpha} - (1+\alpha)(\alpha-\beta)R^{-\alpha} + 2\alpha(1-\beta)R^{\beta}\}(R\sigma/4) \quad (27d)$$

The coefficients of the stress function in (21) are

$$A_1 = N_1/D \quad A_2 = N_2/D \quad A_3 = N_3/D \quad A_4 = N_4/D \quad (28)$$

The circumferential stress can be written as

$$\sigma_\theta = \{A_1 t_1(t_1-1)r^{t_1-2} + A_2 t_2(t_2-1)r^{t_2-2} + A_3 t_3(t_3-1)r^{t_3-2} + A_4 t_4(t_4-1)r^{t_4-2}\}\cos 2\theta \quad (29)$$

At $r = 1$ the sum of the four contributions can be written in the following forms:

$$D\sigma_{\theta_{r=1}} = (\sigma R/2)(\alpha^2-\beta^2)\{\beta(1-\alpha)R^{\alpha} - \beta(1+\alpha)R^{-\alpha} - \alpha(1-\beta)R^{\beta} + \alpha(1+\beta)R^{-\beta}\}\cos 2\theta \quad (30a)$$

$$D\sigma_{\theta_{r=1}} = \sigma R(\alpha^2-\beta^2)\{\beta \sinh(\alpha \ln R) - \alpha\beta\cosh(\alpha \ln R) - \alpha \sinh(\beta \ln R) + \alpha\beta \cosh(\beta \ln R)\}\cos 2\theta \quad (30b)$$

$$D\sigma_{\theta_{r=1}} = \sigma R(\alpha^2-\beta^2)\left\{(\alpha+\beta)\cosh\frac{(\alpha+\beta)\ln R}{2}\sinh\frac{(\alpha-\beta)\ln R}{2} - (\alpha-\beta)\sinh\frac{(\alpha+\beta)\ln R}{2}\cosh\frac{(\alpha-\beta)\ln R}{2} - 2\alpha\beta\sinh\frac{(\alpha+\beta)\ln R}{2}\sinh\frac{(\alpha-\beta)\ln R}{2}\right\}\cos 2\theta \quad (30c)$$

$$D\sigma_{\theta_{r=1}} = (\sigma R/4)(\alpha^2-\beta^2)\{(\alpha+\beta)[R^{(\alpha+\beta)/2} + R^{-(\alpha+\beta)/2}] \times [R^{(\alpha-\beta)/2} - R^{-(\alpha-\beta)/2}] - (\alpha-\beta)[R^{(\alpha+\beta)/2} - R^{-(\alpha+\beta)/2}] \times [R^{(\alpha-\beta)/2} + R^{-(\alpha-\beta)/2}] - 2\alpha\beta[R^{(\alpha+\beta)/2} - R^{-(\alpha+\beta)/2}][R^{(\alpha-\beta)/2} - R^{-(\alpha-\beta)/2}]\}\cos 2\theta \quad (30d)$$

In Fig. 3, values of the stress-concentration factor are plotted against the outer radius R (note that the radius of the hole is unity) for a number of fiber arrangements. Inequalities (19a) and (19b) hold when all the fibers run circumferentially ($\|\theta$) or radially ($\|r$), and when the material is isotropic (or quasi-isotropic). In these cases, therefore, (25) and (30) are valid. However, the values of the ordinates in the figure are not those computed from these equations; to the values obtained from (25) and (30) have been added the circumferential stresses calculated for the case of uniform radial tensile loads which will be discussed later.

One more question to be answered is how the stress-concentration factor behaves as R approaches infinity. Because of inequalities (20i), equation (30d) becomes (α and β are real)

$$\frac{D\sigma_{\theta_{r=1}}}{\sigma\cos 2\theta} \to R(1/4)(\alpha^2-\beta^2)2\beta(1-\alpha)R^{(\alpha+\beta)/2}R^{(\alpha-\beta)/2} \quad \text{as} \quad R\to\infty \quad (31)$$

and (25) becomes

$$D \to (\alpha-\beta)^2 R^{\alpha+\beta} \quad \text{as } R\to\infty \quad (32)$$

The ratio of the two is

$$\frac{\sigma_{\theta_{r=1}}}{\sigma\cos 2\theta} = \frac{\beta}{2}\frac{(1-\alpha)(\alpha+\beta)}{\alpha-\beta}R^{1-\beta} \quad \text{when } R\gg 1 \quad (33)$$

$$\frac{\sigma_{\theta_{r=1}}}{\sigma\cos 2\theta} \to \begin{cases} 0 & \text{when} \quad \beta > 1 \\ -(1/2)(1+\alpha) & \text{when} \quad \beta = 1 \\ \infty & \text{when} \quad \beta < 1 \end{cases} \quad \text{as} \quad R\to\infty \quad (34)$$

When $\beta = 1$, (20c) yields (with $n = 2$)

$$\alpha = 3\sqrt{\bar{S}_{rr}} \quad \text{when} \quad \beta = 1 \quad (35)$$

and the stress-concentration factor becomes

$$\frac{\sigma_{\theta_{r=1}}}{\sigma\cos 2\theta} = -(1/2)(1+3\sqrt{\bar{S}_{rr}}) \quad \text{when} \quad \beta = 1 \quad (36)$$

Because of (20a) the condition of this is

$$\alpha^2+\beta^2 = 9\bar{S}_{rr} + 1 = 1 + \bar{S}_{rr} + 4\bar{S} \quad (37)$$

that is,

$$\bar{S} = 2\bar{S}_{rr} \quad (38a)$$

It is to be remembered, however, that in the derivation of (31) it was assumed that $\alpha > \beta$. This implies that

$$\bar{S}_{rr} > 1/9 \quad (38b)$$

in consequence of (35). But the straight line is tangent to the upper branch of the curve in Fig. 2. Hence, to the left of the point of tangency the stress-concentration factor tends to infinity as R increases beyond all bounds in the region of four real roots.

Equation (38a) is shown as a dotted straight line in Fig. 2. Above the line the stress-concentration factor tends to infinity as R approaches infinity; and between the straight line and the upper branch of the curve of Fig. 2 the stress-concentration factor tends to zero as R approaches infinity.

α and β Are Complex Numbers

It has already been stated that between the two branches of the curve of Fig. 2 the inequality holds

$$(1+\bar{S}_{rr}+4\bar{S})^2 < 4(n^2-1)^2\bar{S}_{rr} \quad (39)$$

The quantities of α and β and their useful combinations can be given in the form

$$\alpha^2 = (1/2)(1 + \overline{S}_{rr} + n^2\overline{S}) + i\{(n^2-1)^2\overline{S}_{rr} - (1/4)(1 + \overline{S}_{rr} + n^2\overline{S})^2\}^{1/2} \quad (40a)$$

$$\beta^2 = (1/2)(1 + \overline{S}_{rr} + n^2\overline{S}) - i\{(n^2-1)^2\overline{S}_{rr} - (1/4)(1 + \overline{S}_{rr} + n^2\overline{S})^2\}^{1/2} \quad (40b)$$

$$\alpha = (1/\sqrt{2})\{(n^2-1)\sqrt{\overline{S}_{rr}} + (1/2)(1 + \overline{S}_{rr} + n^2\overline{S})\}^{1/2} + (i/\sqrt{2})\{(n^2-1)\sqrt{\overline{S}_{rr}} - (1/2)(1 + \overline{S}_{rr} + n^2\overline{S})\}^{1/2} \quad (41a)$$

$$\beta = (1/\sqrt{2})\{(n^2-1)\sqrt{\overline{S}_{rr}} + (1/2)(1 + \overline{S}_{rr} + n^2\overline{S})\}^{1/2} - (i/\overline{2})\{(n^2-1)\sqrt{\overline{S}_{rr}} - (1/2)(1 + \overline{S}_{rr} + n^2\overline{S})\}^{1/2} \quad (41b)$$

$$\alpha + \beta = \sqrt{2}\{(n^2-1)\sqrt{\overline{S}_{rr}} + (1/2)(1 + \overline{S}_{rr} + n^2\overline{S})\}^{1/2} \quad (41c)$$

$$\frac{\alpha - \beta}{i} = \sqrt{2}\{(n^2-1)\sqrt{\overline{S}_{rr}} - (1/2)(1 + \overline{S}_{rr} + n^2S)\}^{1/2} \quad (41d)$$

$$(\alpha + \beta)^2 = 1 + \overline{S}_{rr} + n^2\overline{S} + 2(n^2-1)\sqrt{\overline{S}_{rr}} > 0 \quad (41e)$$

$$(\alpha - \beta)^2 = 1 + \overline{S}_{rr} + n^2\overline{S} - 2(n^2-1)\sqrt{\overline{S}_{rr}} < 0 \quad (41f)$$

$$\alpha^2 + \beta^2 = 1 + \overline{S}_{rr} + n^2\overline{S} \quad ((41g)$$

$$\frac{\alpha^2 - \beta^2}{i} = 2\{(n^2-1)^2\overline{S}_{rr} - (1/4)(1 + \overline{S}_{rr} + n^2\overline{S})^2\}^{1/2} \quad (41h)$$

$$\alpha\beta = (n^2-1)\sqrt{\overline{S}_{rr}} \quad (41i)$$

The expressions for the numerator and the denominator of the stress-concentration factor are

$$\frac{D\sigma_{\theta_{r=1}}}{\cos 2\theta} = \frac{-\sigma R}{2}\frac{\alpha^2 - \beta^2}{i}\left\{(\alpha+\beta)[R^{(\alpha+\beta)/2} + R^{-(\alpha+\beta)/2}] \times \sin\left(\frac{\alpha-\beta}{i}\frac{\ln R}{2}\right) - \frac{\alpha-\beta}{i}[R^{(\alpha+\beta)/2} - R^{-(\alpha+\beta)/2}]\cos\left(\frac{\alpha-\beta}{i}\frac{\ln R}{2}\right) - 2\alpha\beta[R^{(\alpha+\beta)/2} - R^{-(\alpha+\beta)/2}]\sin\left(\frac{\alpha-\beta}{i}\frac{\ln R}{2}\right)\right\} \quad (42)$$

$$D = 8\alpha\beta - \left(\frac{\alpha-\beta}{i}\right)^2[R^{\alpha+\beta} + R^{-(\alpha+\beta)}] - 2(\alpha+\beta)^2\cos\left(\frac{\alpha-\beta}{i}\ln R\right) \quad (43)$$

It is noted that all the combinations of α and β appearing in (42) and (43) are real and positive.

Again, it is of interest to investigate the behavior of the stress-concentration factor as R tends to infinity. In such a case the dominant terms in (42) and (43) are $RR^{(\alpha+\beta)/2}$ and $R^{\alpha+\beta}$, respectively, and their ratio determines the behavior at infinity:

$$\frac{\sigma_{\theta_{r=1}}}{\sigma\cos 2\theta} \sim R^{1-(\alpha+\beta)/2} \quad \text{as} \quad R \to \infty \quad (44)$$

The stress-concentration factor remains finite if

$$\alpha + \beta = 2 \quad (45)$$

From (41e) the condition of this being true is

$$1 + \overline{S}_{rr} + 4\overline{S} + 6\sqrt{\overline{S}_{rr}} = 4 \quad (46)$$

which can be solved for $\overline{S}$ to obtain

$$\overline{S} = (1/4)(3 - \overline{S}_{rr} - 6\sqrt{\overline{S}_{rr}}) \quad (47)$$

This equation is shown in Fig. 2 as a dotted line. Between this line and the upper boundary of the region of conjugate complex roots the stress-concentration factor tends to zero as R approaches infinity; and between the line and the lower boundary of the region of complex roots the stress-concentration factor increases beyond all bounds as R approaches infinity.

α and β Are Pure Imaginary Numbers

In the region of Fig. 2 below the lower boundary of the region of complex roots the following inequalities hold:

$$(1 + \overline{S}_{rr} + n^2\overline{S})^2 > 4(n^2-1)^2\overline{S}_{rr} \quad (48)$$

and

$$1 + \overline{S}_{rr} + n^2\overline{S} < 0 \quad (49)$$

The expressions for α and β are purely imaginary:

$$\alpha = i\left|(1/2)(1 + \overline{S}_{rr} + n^2\overline{S}) + \{(1/4)(1 + \overline{S}_{rr} + n^2\overline{S})^2 - (n^2-1)^2\overline{S}_{rr}\}^{1/2}\right|^{1/2} \quad (50a)$$

$$\beta = -i\left|(1/2)(1 + \overline{S}_{rr} + n^2\overline{S}) - \{(1/4)(1 + \overline{S}_{rr} + n^2\overline{S})^2 - (n^2-1)^2\overline{S}_{rr}\}^{1/2}\right|^{1/2} \quad (50b)$$

Thus the following useful combinations of α and β can be given

$$\alpha^2 + \beta^2 = 1 + \overline{S}_{rr} + n^2\overline{S} < 0 \quad (51a)$$

$$\alpha^2 - \beta^2 = \{(1 + \overline{S}_{rr} + n^2\overline{S})^2 - 4(n^2-1)^2\overline{S}_{rr}\}^{1/2} > 0 \quad (51b)$$

$$\alpha\beta = (n^2-1)\sqrt{\overline{S}_{rr}} > 0 \quad (51c)$$

$$(\alpha + \beta)^2 = 1 + \overline{S}_{rr} + n^2\overline{S} + 2(n^2-1)\sqrt{\overline{S}_{rr}} < 0 \quad (51d)$$

$$(\alpha - \beta)^2 = 1 + \overline{S}_{rr} + n^2\overline{S} - 2(n^2-1)\sqrt{\overline{S}_{rr}} < 0 \quad (51e)$$

$$\alpha + \beta = -i\left|1 + \overline{S}_{rr} + n^2\overline{S} + 2(n^2-1)\sqrt{\overline{S}_{rr}}\right|^{1/2} \quad (51f)$$

$$\alpha - \beta = i\left|1 + \overline{S}_{rr} + n^2\overline{S} - 2(n^2-1)\sqrt{\overline{S}_{rr}}\right|^{1/2} \quad (51g)$$

Alternate expressions for α and β follow:

$$2\alpha = -i\left|1 + \overline{S}_{rr} + n^2\overline{S} + 2(n^2-1)\sqrt{\overline{S}_{rr}}\right|^{1/2} + i\left|1 + \overline{S}_{rr} + n^2\overline{S} - 2(n^2-1)\sqrt{\overline{S}_{rr}}\right|^{1/2} \quad (51h)$$

$$2\beta = -i\left|1 + \overline{S}_{rr} + n^2\overline{S} + 2(n^2-1)\sqrt{\overline{S}_{rr}}\right|^{1/2} - i\left|1 + \overline{S}_{rr} + n^2\overline{S} - 2(n^2-1)\sqrt{\overline{S}_{rr}}\right|^{1/2} \quad (51i)$$

Substitution into (30d) and (26) yields

$$\frac{D\sigma_{\theta_{r=1}}}{\sigma} = -(\alpha^2 - \beta^2)R\left\{\frac{\alpha+\beta}{i}\cos\left(\frac{\alpha+\beta}{2i}\ln R\right)\sin\left(\frac{\alpha-\beta}{2i}\ln R\right) - \frac{\alpha-\beta}{i}\sin\left(\frac{\alpha+\beta}{2i}\ln R\right)\cos\left(\frac{\alpha-\beta}{2i}\ln R\right) - 2\alpha\beta\sin\left(\frac{\alpha+\beta}{2i}\ln R\right)\sin\left(\frac{\alpha-\beta}{2i}\ln R\right)\right\}\cos 2\theta \quad (52)$$

$$D = 8\alpha\beta + 2(\alpha-\beta)^2\cos\left(\frac{\alpha+\beta}{i}\ln R\right) - 2(\alpha-\beta)^2\cos\left(\frac{\alpha-\beta}{i}\ln R\right) \quad (53)$$

Again, all the combinations of α and β are real. But trigonometric functions of a real argument have values between -1 and $+1$; hence the numerator tends to infinity as R while the denominator remains finite when R approaches infinity. Consequently, the stress-concentration factor tends to infinity as R approaches infinity.

Solution of the Axisymmetric Part of the Problem

To solve the problem set in (1)–(4) completely, the axisymmetric part of the solution in which the boundary conditions are

$$\sigma_r = 0 \quad \text{when} \quad r = 1 \quad (54a)$$

$$\sigma_r = (\sigma/2) \quad \text{when} \quad r = R \quad (54b)$$

is also needed in addition to the solution derived for the boundary conditions given in (6). It is tempting to obtain the solution of this axisymmetric part from the general solution already derived by simply setting $n = 0$. When this is done, the following four expressions are obtained for the exponents p of the stress function

$$\phi = r^p: \quad (55)$$

$$p_1 = 1 + \sqrt{\overline{S}_{rr}} \quad p_2 = 1 - \sqrt{\overline{S}_{rr}} \quad p_3 = 2 \quad p_4 = 0 \quad (56)$$

The fourth expression corresponds to a trivial solution in which all the stresses are identically zero. But there remain three solutions whose integration constants must be determined from two boundary conditions. This can be done in more than one way, implying that the solution of the problem set is not unique.

The explanation of this anomaly is that in the axisymmetric case $p = 2$ is a spurious solution. Although it satisfies (12), it does not satisfy the proper compatibility condition of the axisymmetric problem. In the axisymmetric case

$$\epsilon_r = du/dr \quad \epsilon_\theta = u/r \tag{57a, b}$$

where u is the displacement in the radial direction. For the existence of a function u the condition must be satisfied

$$\epsilon_r = \frac{d}{dr}(r\epsilon_\theta) \tag{58}$$

which is the compatibility condition in terms of strains. In terms of the stress function the strains are

$$\epsilon_r = S_{rr}\sigma_r + S_{r\theta}\sigma_\theta = S_{rr}\frac{1}{r}\frac{d\phi}{dr} + S_{r\theta}\frac{d^2\phi}{dr^2} \tag{59a}$$

$$\epsilon_\theta = S_{r\theta}\sigma_r + S_{\theta\theta}\sigma_\theta = S_{r\theta}\frac{1}{r}\frac{d\phi}{dr} + S_{\theta\theta}\frac{d^2\phi}{dr^2} \tag{59b}$$

Substitution and differentiation yield the compatibility condition for the stress function ϕ:

$$S_{\theta\theta}\frac{d}{dr}\left(r\frac{d^2\phi}{dr^2}\right) - S_{rr}\frac{1}{r}\frac{d\phi}{dr} = 0 \tag{60}$$

Substitution of $\phi = r^2$ yields

$$S_{\theta\theta} - S_{rr} = 0 \tag{61}$$

which is true only for a restricted class of plates. In general, $p = 2$ is not a solution of the problem.

When the assumption $\phi = r^p$ is substituted into (60), the result is

$$p[(p-1)^2 S_{\theta\theta} - S_{rr}] = 0 \tag{62}$$

The solution is

$$p_1 = 1 + \sqrt{\bar{S}_{rr}} \quad p_2 = 1 - \sqrt{\bar{S}_{rr}} \quad p_3 = 0 \tag{63}$$

Since p_3 yields identically vanishing stresses, the complete solution of the axisymmetric problem can be written as

$$\phi = Ar^{1+\sqrt{\bar{S}_{rr}}} + Br^{1-\sqrt{\bar{S}_{rr}}} \tag{64}$$

The two boundary conditions are

$$(1 + \sqrt{\bar{S}_{rr}})A + (1 - \sqrt{\bar{S}_{rr}})B = 0 \tag{65a}$$

$$(1 + \sqrt{\bar{S}_{rr}})R^{-1+\sqrt{\bar{S}_{rr}}}A + (1 - \sqrt{\bar{S}_{rr}})R^{-1-\sqrt{\bar{S}_{rr}}}B = (\sigma/2) \tag{65b}$$

The solution of the two simultaneous equations is

$$A = \frac{1}{1 + \sqrt{\bar{S}_{rr}}}\frac{\sigma R/2}{R^{\sqrt{\bar{S}_{rr}}} - R^{-\sqrt{\bar{S}_{rr}}}} \tag{66a}$$

$$B = \frac{-1}{1 - \sqrt{\bar{S}_{rr}}}\frac{\sigma R/2}{R^{\sqrt{\bar{S}_{rr}}} - R^{-\sqrt{\bar{S}_{rr}}}} \tag{66b}$$

It follows then that

$$\sigma_\theta = \frac{d^2\phi}{dr^2} = \sqrt{\bar{S}_{rr}}\frac{\sigma}{2}\frac{R}{r}\frac{r^{\sqrt{\bar{S}_{rr}}} + r^{-\sqrt{\bar{S}_{rr}}}}{R^{\sqrt{\bar{S}_{rr}}} - R^{-\sqrt{\bar{S}_{rr}}}} \tag{67}$$

At the edge of the hole in the plate

$$\frac{\sigma_{\theta_{r=1}}}{\sigma} = \sqrt{\bar{S}_{rr}}\frac{R}{R^{\sqrt{\bar{S}_{rr}}} - R^{-\sqrt{\bar{S}_{rr}}}} \tag{68}$$

Since $\sqrt{\bar{S}_{rr}}$ is positive,

$$\sigma_{\theta_{r=1}}/\sigma = \sqrt{\bar{S}_{rr}}R^{1-\sqrt{\bar{S}_{rr}}} \quad \text{when} \quad R \gg 1 \tag{69}$$

Consequently

$$\lim_{R\to\infty}\frac{\sigma_{\theta_{r=1}}}{\sigma} \to \begin{cases} 0 & \text{when} \quad \bar{S}_{rr} > 1 \\ \sqrt{\bar{S}_{rr}} = 1 & \text{when} \quad \bar{S}_{rr} = 1 \\ \infty & \text{when} \quad \bar{S}_{rr} < 1 \end{cases} \tag{70}$$

At the outer edge of the circular plate

$$\frac{\sigma_{\theta_{r=R}}}{\sigma} = \frac{\sqrt{\bar{S}_{rr}}}{2}\frac{R^{\sqrt{\bar{S}_{rr}}} + R^{-\sqrt{\bar{S}_{rr}}}}{R^{\sqrt{\bar{S}_{rr}}} - R^{-\sqrt{\bar{S}_{rr}}}} \tag{71}$$

In the limit as R approaches infinity,

$$\lim_{R\to\infty}(\sigma_{\theta_{r=R}}/\sigma) = \sqrt{\bar{S}_{rr}}/2 \tag{72}$$

Discussion of Results

One of the interesting results of this investigation is that the four independent compliances S_{rr}, $S_{r\theta}$, $S_{\theta\theta}$, and S_{66} characterizing the elastic behavior of the plate can be combined into two relative compliance values $\bar{S}_{rr} = S_{rr}/S_{\theta\theta}$ and $\bar{S} = (1/S_{\theta\theta})(2S_{r\theta} + S_{66})$ in such a manner that the stress concentration at the edge of the hole depends only on the two new parameters. This is advantageous both in the computation and the presentation of the values of the stress-concentration factors.

A second interesting result is that a state of constant stress $\sigma_r = \sigma_\theta = C_1$ cannot exist in a cylindrically orthotropic circular plate subjected to constant uniaxial loading at its outer edge $r = R$, except in the special case when $S_{rr} = S_{\theta\theta}$. Such a constant stress would give rise to constant strains $\epsilon_r = (S_{rr} + S_{r\theta})C_1$ and $\epsilon_\theta = (S_{r\theta} + S_{\theta\theta})C_1$. But the constant radial strain implies radial displacements $u = \epsilon_r r + C_2$ from which the circumferential strain follows as $u/r = (S_{rr} + S_{r\theta})C_1 + C_2/r$. This can be equal to the circumferential strain calculated before only if $C_2 = 0$ and $S_{\theta\theta} = S_{rr}$, which proves the statement.

Next, it is perhaps unexpected that the limiting process in which R increases beyond all bounds can lead to vanishingly small or to indefinitely large stress concentrations along the edge of the hole. This is not so when the plate is orthotropic relative to a Cartesian system of coordinates or when it is isotropic. As a matter of fact, Kirsch's often quoted solution states that the maximum tensile stress at the edge of a hole in an isotropic plate has a value three times that of the applied stress at infinity.

An explanation of the unexpected behavior can be found in the values of the exponents of the radius in the expressions for the radial stresses. They are $-1 + \alpha$, $-1 - \alpha$, $-1 + \beta$, and $-1 - \beta$, when the load terms include the factor $\cos 2\theta$ or $\sin 2\theta$. In the region where α and β are real, they are positive by definition, and the second and fourth exponents are always negative. When $\alpha < 1$ or $\beta < 1$ the first and the third exponents, respectively, are also negative. But because $\alpha > \beta$, the condition of the simultaneous occurrence of three negative exponents can be given as $\beta < 1$.

When two exponents are positive and two negative in the general expression for the radial stress, the two solutions with negative exponents can be used to satisfy the boundary conditions at the edge of the hole ($r = 1$) and the two with positive exponents those at infinity ($r = R$, with $R \to \infty$) without any interaction between the two groups of solutions. When the edge of the hole is unloaded, this implies vanishing stresses at $r = 1$, and stresses of the order of magnitude of σ in a boundary layer near $r = R$. The stress-concentration factor for the edge of the hole is then zero.

On the other hand, if there are at least three solutions with negative exponents, and stresses of a magnitude σ are applied at $r = R$, at least one solution must have an integration constant of infinity to satisfy the boundary conditions at $r = R$ when R increases beyond all bounds. In such a case the stress-concentration factor at the edge of the hole is indefinitely large.

It has been shown that in the region of Fig. 2 where (12) has four real roots, the stress-concentration factor is finite when $\beta = 1$ (see (34)) which, in turn, implies that $\bar{S} = 2\bar{S}_{rr}$ (see (38)). If the value of $\bar{S}_{rr}$ is kept constant and that of $\bar{S}$ is increased beyond $2\bar{S}_{rr}$, both terms in the right-hand member of (18a) increase, and thus α also increases. But then β must decrease because the product $\alpha\beta$ remains constant in agreement with (20c). On the other hand, $\beta < 1$ implies indefinitely large stress-concentration factors according to (34b). Indeed, in the region above the line $\bar{S} = 2\bar{S}_{rr}$ in Fig. 2 indefinitely large stress-concentration factors were obtained for $R \to \infty$. A similar argument would show that below the straight line the stress-concentration factor tends to zero as R increases beyond all bounds.

In the range of conjugate complex values for α and β the stress-concentration factor is finite when $\alpha + \beta = 2$ implying the relationship (47) between $\overline{S}$ and $\overline{S}_{rr}$. It follows from (41c) that the value of $\alpha + \beta$ increases if $\overline{S}$ is increased beyond the value stipulated by (47) while $\overline{S}_{rr}$ is kept constant. But an increased value of $\alpha + \beta$ results in a negative exponent for R in (44) and thus the value of the stress-concentration factor approaches zero as R increases beyond all bounds. This again agrees with earlier findings as presented in Fig. 2. Below the line corresponding to (47) the value of $\alpha + \beta$ decreases when $\overline{S}$ is increased with $\overline{S}_{rr}$ remaining constant, the exponent of R in (44) becomes positive, and the stress-concentration factor of the infinite plate approaches infinity.

The situation is simpler in the case of axisymmetric loading. There one exponent in the expression for the stresses is $-1 - \sqrt{\overline{S}_{rr}}$ and is always negative. The other exponent, $-1 + \sqrt{\overline{S}_{rr}}$, is positive when $\overline{S}_{rr}$ is greater than unity; in this case two boundary layers exist and the stress-concentration factor approaches zero as R increases beyond all bounds. When $\overline{S}_{rr}$ is unity, the stresses are constant throughout the plate, and when $\overline{S}_{rr}$ is smaller than unity, the stress-concentration factor becomes indefinitely large as R increases beyond all bounds.

But infinite stress-concentration factors found for infinite plates should not dismay the engineer, because no one has yet built an infinite plate or has loaded one at infinity. What counts is the behavior in the finite range which is illustrated in Fig. 3.

In this figure four of the five full lines indicate slowly varying values for the stress-concentration factor in the practical range $3.5 \leq R \leq 10$, and the fifth full line shows low values for it. Below the value 3.5 for R the rapid rise in all the curves is a consequence of the rapidly decreasing cross-sectional area available to carry the load.

Of course, the solution obtained in this paper is rigorously valid only for the circular plate investigated. Similarly, the Kirsch solution holds rigorously only for the infinite isotropic plate. Whenever the stresses in a real plate of given shape and proportions are needed accurately, the actual article must be tested in the laboratory, a study must be made of a suitable model with the aid of photoelasticity, or a numerical investigation must be undertaken with the help of the finite-element method.

Such a study has already been carried out in the case of finite rectangular plates of varying proportions made of materials orthotropic with respect to a Cartesian system of coordinates. Of the many curves so obtained by Hong and Crews [5], only one is reproduced in Fig. 3; it is shown as a dotted line. It refers to an isotropic plate whose length is equal to twice its width. Between $R = 3.5$ and $R = 10$ the value of the stress-concentration factor is almost constant along this curve, and it differs little from the value obtained by Kirsch for the infinite plate. It is gratifying to observe that the dotted curve agrees very well with the isotropic curve of this investigation which is rigorously valid only for the circular plates. It appears, therefore, that the location and the shape of the outer boundary of the plate have much less effect on the stress-concentration factor than, for instance, the orientation of the fibers.

It is believed, therefore, that the stress-concentration factor along the edge of a circular hole in a finite plate of arbitrary (but reasonable) shape and size can be calculated from the equations here derived with a value of R between 3.5 and 10 if the elastic properties of the plate are cylindrically symmetric with respect to the center of the hole, and if great accuracy is not required for the value of the stress-concentration factor.

References

1 Kirsch, G., *VDI*, Vol. 42, 1898.

2 Timoshenko, S. P., and Goodier, J. N., *Theory of Elasticity*, 3rd ed., McGraw-Hill, New York, 1951, p. 90.

3 Lekhnitskii, S. G., *Anisotropic Plates* (translation by Tsai, S. W., and Cheron, T.,), Gordon and Breach Science Publishers, New York, 1968.

4 Jones, R. M., *Mechanics of Composite Materials*, Scripta Book Co., Washington, D.C., McGraw-Hill, New York, 1975.

5 Hong, C. S., and Crews, J. H., Jr., "Stress-Concentration Factors for Finite Orthotropic Laminates With a Circular Hole and Uniaxial Loading," NASA Technical Paper 1469, May 1979.

T. Kundu
A. K. Mal

Department of Mechanics and Structures,
University of California,
Los Angeles, Calif. 90024

Diffraction of Elastic Waves by a Surface Crack on a Plate

The interaction of time harmonic elastic waves with an edge crack in a plate is studied. The crack is assumed to be normal to the plate surface and its depth small compared to plate thickness. Only plane strain deformations are considered. The incident waves are assumed to be either plane body waves (compressional (P) or inplane shear (SV)) of arbitrary angle of propagation or surface Rayleigh waves propagating at right angles to the crack. For each incident wave type the complete high frequency diffracted field on the plate surface is calculated. Solution is obtained by the application of an asymptotic theory of diffraction. Application to ultrasonic inspection techniques is indicated.

Introduction

Study of the interaction of elastic waves with edge cracks is of considerable importance in a variety of engineering applications. In fracture mechanics the interest is in the stress concentration near the crack tip. In ultrasonic nondestructive testing the influence of crack length and direction of incidence on the diffracted wave pattern is of interest.

Solution of the problem is complicated by the presence of the free surface in addition to the crack surfaces and the associated sharp edges. As a consequence inspite of its engineering significance the problem has not been widely treated in the literature.

In a recent paper (Stone, Ghosh, and Mal [13]) the diffraction of antiplane shear waves by an edge crack was investigated. In [13] the problem was formulated in terms of a singular integral equation which was solved numerically for low and intermediate frequencies. At high frequencies the asymptotic solution was constructed from the solution of the well-known Sommerfield diffraction problem. It was shown that the asymptotic solution gives accurate results valid at surprisingly low frequencies (also see Achenbach and Gautesen [1]).

The inplane edge crack problem can be similarly formulated in terms of a system of coupled integral equations which can, in principle, be solved numerically to determine the response of the crack at any frequency. As in most elastodynamic problems, the numerical solution is likely to be unreliable at very high frequencies, and should therefore be supplemented by an asymptotic solution at high frequencies. Such a solution is presented here.

The inplane problem is considerably more complex than the antiplane one due to mode conversion of body waves on reflection as well as the presence of Rayleigh waves on the free surfaces. Fortunately at very high frequencies the problem can be decomposed into a number of canonical problems whose solutions are available in the literature. It is expected that the resulting solution will be valid in a frequency range which include some cases of practical importance.

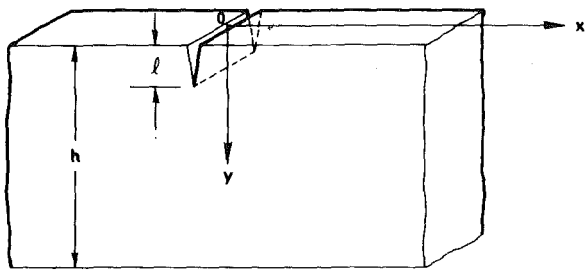

Fig. 1 Geometry of the problem

Theory

We locate a Cartesian coordinate system at the intersection of the crack with the plate surface, with the x-axis along the plate surface and normal to the crack surface (Fig. 1). The z-axis is taken along the length of the crack. Then the plate occupies the region $-\infty < x < \infty$, $0 < y < h$, $-\infty < z < \infty$ and the crack occupies the region, $x = 0 \pm$, $0 < y < l$, $-\infty < z < \infty$, where h is the plate thickness, l the crack depth. The incident waves are assumed to be polarized on the xy-plane, and all deformations are independent of z. Thus the problem can be formulated in two dimensions on the xy-plane. We further assume that the crack faces do not come into contact during motion.

The foregoing model corresponds to plane strain deformations of the plate. The formulations can be used, with minor modifications in plane stress situations (e.g., through cracks in thin plates, $-\infty < x < \infty$, $0 < y < h$, $-\epsilon < z < \epsilon$, ϵ small).

As indicated in the Introduction it is extremely difficult to obtain exact solutions of elastodynamic problems associated with the above geometry. At low frequencies numerical solutions via integral equation

Contributed by the Applied Mechanics Division for publication in the JOURNAL OF APPLIED MECHANICS.

Discussion on this paper should be addressed to the Editorial Department, ASME, United Engineering Center, 345 East 47th Street, New York, N. Y. 10017, and will be accepted until December 1, 1981. Readers who need more time to prepare a discussion should request an extension from the Editorial Department. Manuscript received by ASME Applied Mechanics Division, August, 1980; final revision, January, 1981.

Table 1

ν	R_0	T_0
0.25	$0.25\, e^{0.314i}$	$0.67\, e^{-1.31i}$
0.33	$0.4\, e^{0.6i}$	$0.6\, e^{-1.6i}$

formulations similar to that in [13] can in principle be obtained. At high frequencies application of ray theoretic considerations is a natural and promising approach.

In the ray theoretic approach the wave motion is constructed by calculating reflected, refracted, and diffracted waves from each individual surfaces and edges in the system by ignoring the presence of the others. In the present problem reflecting surfaces are the free surfaces of the plate ($x < 0, x > 0, y = 0; -\infty < x < \infty, y = h$) and the free surfaces of the crack ($x = 0 \pm, 0 < y < l$). The diffracting edges are the crack tip $x = 0, y = l$ and the two 90° corners $x = 0 \pm, y = 0$. Thus it is necessary that the solution of the following canonical problems be available.

(1) Reflection of Plane Harmonic Body Waves at a Free Surface. The solution of this problem is available in standard texts on elastodynamics (see, e.g., Eringen [4]). The results are expressed in terms of reflection coefficients $R_{PP}(\theta_0), R_{PS}(\theta_0), R_{SP}(\theta_0), R_{SS}(\theta_0)$ where the first index (P or S) indicates the incident wave type and the second index the reflected wave type. θ_0 is the angle of incidence. The expressions for these coefficients are given in [7].

(2) Diffraction of Body and Surface Waves by a Crack Tip. Since the effect of all other boundaries are ignored, the crack may be assumed to be semi-infinite. The solution to this half-plane diffraction problem has been given by Maue [11] for body wave incidence and by Freund [5] for Rayleigh wave incidence. The diffraction coefficients $D_{PP}(\theta, \theta_0), D_{PS}(\theta, \theta_0), D_{PR}{}^{\pm}(\theta, \theta_0), D_{SP}(\theta, \theta_0), D_{SS}(\theta, \theta_0), D_{SR}{}^{\pm}(\theta, \theta_0), D_{RP}(\theta), D_{RS}(\theta), D_{RR}{}^{\pm}$ are defined in the Appendix.

(3) Finally, the Transmission and Reflection of Body and Surface Waves by a Right-Angled Wedge. To the authors' knowledge no analytical solution of this problem is available in the literature. However excellent experimental data and numerical solutions for the reflection and transmission coefficients R_0, T_0 of the Rayleigh waves have been obtained for Poisson's ratios of $\frac{1}{3}$ and $\frac{1}{4}$ (see, e.g., Mal and Knopoff [10]; Fuyuki and Matsumoto [6]; Achenbach, Gautesen, and Mendelsohn [2]). These values are listed in Table 1.

Unfortunately none of the available results include estimates of the spatial and angular variations of the diffracted body waves at the corner. Clearly, they decay as $(k_j r)^{-1/2}$ at a distance r from the corner where k_j is the wavelength of either P or S waves. Further the decay becomes $O(k_j r)^{-3/2}$ on the free surfaces of the wedge. The amplitudes of the reflected and transmitted Rayleigh waves in Table 1 also indicate that very little of the incident wave energy is converted into body waves. Thus the diffracted body waves from the corner can be ignored for all practical purposes.

In the case of body wave incidence, all propagating body waves can be obtained by ray construction, except for one ray incident directly on the corner. Since all the incoming energy is carried away by the doubly reflected P and SV waves, this single ray can not produce any outgoing surface waves on the faces of the wedge. It can be further argued that there can be no scattered body waves propagating away from the corner, since any virtual source of body waves at the corner must also produce surface waves. Thus the only possible effect of the unaccounted for ray is a disturbance restricted to the immediate vicinity of the corner. The displacements produced by this disturbance in the far field must be of much lower order in magnitude than those due to the primary and secondary diffracted propagating waves included in the present analysis.

With prior knowledge of the solution of the three canonical problems described previously, an approximate solution of the edge crack problem at high frequencies can be constructed in a straightforward manner.

Edge Crack in a Half Plane. We first assume that the lower surface of the plate is at infinity; so that the crack is located in a uniform half plane $y > 0$. The influence of the lower surface of the plate will be included in the next section.

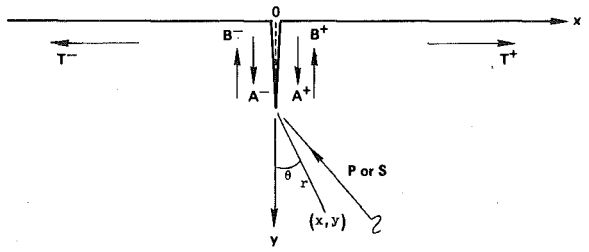

Fig. 2(*a*) Diffracted Rayleigh waves from body-waves incident on an edge crack

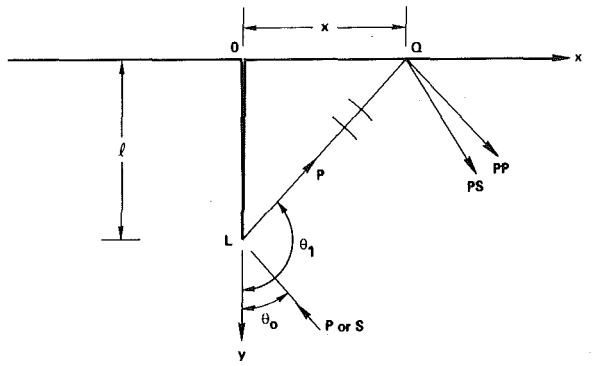

Fig. (2*b*) Reflection of diffracted body waves

Incident Body Waves (Figs. 2(*a*, *b*)). Let plane harmonic P or SV waves be incident on the crack at angle θ_0. The elastodynamic field due to the incident waves may be conveniently described by scalar potentials $\phi_0 e^{-i\omega t}, \psi_0 e^{-i\omega t}$,

$$\phi_0 = A_0 e^{-ik_1(x \cos\theta_0 + y \sin\theta_0)}$$

$$\psi_0 = B_0 e^{-ik_2(x \cos\theta_0 + y \sin\theta_0)} \tag{1}$$

where ω is the circular frequency and $k_j = \omega/c_j, j = 1, 2$; c_1, c_2 being the velocities of P and S waves in the medium. The time function $e^{-i\omega t}$ appears in all field quantities and will be suppressed.

If diffraction effects are ignored, approximate solutions for motion at all points in the medium can be immediately written down by means of the plane wave reflection coefficients $R_{PP}, R_{PS}, R_{SP}, R_{SS}$. The solution obtained in this manner is usually called the geometric solution following a terminology used in optics. The geometric solution can also be described by means of potentials ϕ_g and ψ_g, whose expressions can be easily written down. The displacement components due to the plane waves given by the geometric solution can be calculated from these expressions. These displacements are discontinuous across the boundaries between the various regions defining shadows of P and S waves. Diffracted waves from the corners at O and the edge at L must be added to the geometric solution in order that the total displacement field is continuous everywhere except on the crack OL.

We shall assume that the displacement components in the incident (and geometric) field are $O(1)$ in frequency. As indicated earlier the diffracted body waves are $O(k_j r)^{-1/2}$ at a distance r from the diffraction point. On the free surfaces the diffracted body waves are $O(k_j r)^{-3/2}$ while the diffracted surface (Rayleigh) waves are $O(1)$. The behavior of the diffracted surface waves imply that multiple reflection between O and L must be included in the solution even at extremely high frequencies. The situation is further complicated by the fact that each Rayleigh wave arriving at the crack tip L gives rise to diffracted body waves which are of same order in frequency as the primary diffracted body waves. It should be noted, however, that each successive reflection at O or L reduces the amplitude of the surface waves con-

siderably so that for practical purposes inclusion of one or two reflections would be sufficient. We include all reflections in the analysis, since they are the lowest order terms in the high frequency solution and return to the significance of multiple reflections later.

It is not necessary to retain the multiple reflection of body waves between O and L since they are two orders of magnitude smaller than those that are retained in the asymptotic solution. As indicated earlier, we also ignore the diffracted cylindrical body waves from the cornor O, since either they are small, or are higher order (on the free surfaces) than $(k_j r)^{-1/2}$.

In summary the diffracted field will be calculated by including

(a) Cylindrical body waves due to *primary* diffraction of incident and surface reflected plane waves at crack tip L.

(b) Surface (Rayleigh) waves generated by primary diffraction of incident and surface reflected plane waves at crack tip L.

(c) Diffracted surface waves due to multiple reflection and transmission of the surface waves described in (b) between O and L.

(d) Cylindrical body waves generated at L by all surface waves reaching L.

The resulting solution would be valid to $O(k_j r)^{-1}$, strictly at points on the free surface and approximately (but with small error) at points in the interior of the solid.

It is straightforward to write down the potentials due to the primary diffraction of the body waves at L. Denoting by ${\phi_{pr}}^d$, ${\psi_{pr}}^d$ the resulting potentials, it can be easily shown that for incident P waves

$$\begin{aligned}{\phi_{pr}}^d = A_0\{&D_{PP}(\pi+\theta,\theta_0) + R_{PP}(\theta_0)D_{PP}(\pi+\theta,\pi-\theta_0)\\ &+ R_{PS}(-\theta_0)D_{SP}(\pi+\theta,\pi-\theta_s)\}\frac{e^{i(k_1 r-\pi/4)}}{\sqrt{k_1 r}}\\ {\psi_{pr}}^d = A_0\{&D_{PS}(\pi+\theta,\theta_0) + R_{PP}(\theta_0)D_{PS}(\pi+\theta,\pi-\theta_0)\\ &+ R_{PS}(-\theta_0)D_{SS}(\pi+\theta,\pi-\theta_s)\}\frac{e^{i(k_2 r-\pi/4)}}{\sqrt{k_2 r}}\end{aligned} \quad (2)$$

where (r,θ) are measured from L, as shown in Fig. 2(a) and

$$\theta_s = \sin^{-1}(\sin\theta_0/\sigma)$$

Similar expressions can be easily written in the case of incident S waves. The displacement components ($u_r{}^d$, $u_\theta{}^d$) can be calculated from (2) by means of the relations

$$\begin{aligned}u_r{}^d &\simeq ik_1\phi^d\\ u_\theta{}^d &\simeq ik_2\psi^d\end{aligned} \quad (3)$$

The displacement components on each face of the crack after each successive reflection of the Rayleigh waves can in principle be written down in terms of the reflection coefficient R_0 at O and the reflection and transmission coefficients at L defined in the Appendix. The transmitted surface waves on $y=0$ and diffracted body waves from L due to each Rayleigh wave propagating on the crack faces in either direction can also be calculated. In order to carry out the details of this procedure we recall that for a Rayleigh wave propagating along a free surface, the surface displacement components normal and parallel to the surface differ by a multiplicative factor which is fixed for a given solid. Further, the two components of the displacement always differ in phase by $\pi/2$ and the sense of motion is retrograde elliptic. Thus, recalling that time-dependence $e^{-i\omega t}$ has been suppressed, the surface displacement vectors

$$\begin{pmatrix} i/\gamma_r \\ 1\end{pmatrix} e^{ik_r x};\quad \begin{pmatrix} i/\gamma_r \\ 1\end{pmatrix} e^{-ik_r x} \quad (4)$$

where γ_r is a constant defined in the Appendix and k_r is the Rayleigh wave number, represent Rayleigh waves propagating along the positive and negative x-directions in a half plane $-\infty < x < \infty, y < 0$. Then surface displacement on $y=0$ must be given by

$$T^+\begin{pmatrix} i/\gamma_r \\ 1\end{pmatrix} e^{ik_r x} \quad (5)$$

for $x > 0$ and by

$$T^-\begin{pmatrix} -i/\gamma_r \\ 1\end{pmatrix} e^{-ik_r x}$$

for $x < 0$, where $T^\pm$ are unknown complex constants.

Similarly the displacement on the crack surfaces $0 < y < l$ are given by

$$A^+\begin{pmatrix} 1 \\ i/\gamma_r\end{pmatrix} e^{ik_r y} + B^+\begin{pmatrix} 1 \\ -i/\gamma_r\end{pmatrix} e^{-ik_r(y-l)} \quad (6)$$

for $x = 0+$ and by

$$A^-\begin{pmatrix} -1 \\ i/\gamma_r\end{pmatrix} e^{ik_r y} + B^-\begin{pmatrix} -1 \\ -i/\gamma_r\end{pmatrix} e^{-ik_r(y-l)}$$

for $x = 0-$, where $A^\pm$, $B^\pm$ are unknown complex constants.

For an incident P wave the Rayleigh waves generated by primary diffraction at L and multiple reflection and transmission at O and L may be described by the system of linear equations

$$\begin{aligned}A^\pm &= R_0 B^\pm e^{ik_r l}\\ B^\pm &= D_{RR}{}^+ A^\mp e^{ik_r l} + D_{RR}{}^- A^\pm e^{ik_r l} + k_1 A_0 D_{PR}{}^\mp(\theta_0)e^{-ik_1 l\sin\theta_0}\\ T^\pm &= T_0 B^\pm e^{ik_r l}\end{aligned} \quad (7)$$

Similar equations result for incident S waves; only the term containing A_0 is changed into $k_2 B_0 D^\mp{}_{SR}(\theta_0)e^{-ik_2 l\sin\theta_0}$. Solution of the simultaneous equations (7) gives the unknowns $A^\pm$, $B^\pm$, $T^\pm$ in terms of known quantities,

$$\begin{aligned}A^\pm &= k_1 A_0 R_0 e^{ik_r l - ik_1 l\sin\theta_0}\{R_0 e^{2ik_r l}(D_{RR}{}^+ D_{PR}{}^\pm(\theta_0)\\ &\qquad - D_{RR}{}^- D_{PR}{}^\mp(\theta_0)) + D_{PR}{}^\mp(\theta_0)\}/\Delta\\ B^\pm &= k_1 A_0 e^{-ik_1 l\sin\theta_0}\{R_0 e^{2ik_r l}(D_{RR}{}^+ D_{PR}{}^\pm(\theta_0)\\ &\qquad - D_{RR}{}^- D_{PR}{}^\mp(\theta_0)) + D_{PR}{}^\mp(\theta_0)\}/\Delta\\ T^\pm &= k_1 A_0 T_0 e^{ik_r l - ik_1 l\sin\theta_0}\{R_0 e^{2ik_r l}(D_{RR}{}^+ D_{PR}{}^\pm(\theta_0)\\ &\qquad - D_{RR}{}^- D_{PR}{}^\mp(\theta_0)) + D_{PR}{}^\mp(\theta_0)\}/\Delta\end{aligned} \quad (8)$$

where

$$\Delta = (R_0 D_{RR}{}^- e^{2ik_r l} - 1)^2 - (R_0 D_{RR}{}^+ e^{2ik_r l})^2$$

It should be noted that if multiple reflection of the Rayleigh waves between O and L were ignored the surface displacments would be simply given by

$$\begin{aligned}B^\pm &\simeq k_1 A_0 D^\mp{}_{PR}(\theta_0)e^{-ik_1 l\sin\theta_0}\\ A^\pm &\simeq R_0 B^\pm e^{ik_r l}\\ T^\pm &\simeq T_0 B^\pm e^{ik_r l}\end{aligned} \quad (9)$$

The other terms in the resulting series expressions for $A^\pm$, $B^\pm$, $T^\pm$ in (8) give results of higher-order reflections between O and L.

The cylindrical body waves generated by secondary diffraction of the Rayleigh waves at L are given by the potentials ${\phi_{sec}}^d$, ${\psi_{sec}}^d$, where

$$\phi_{\text{sec}}{}^d = \{A^- D_{RP}(\theta) + A^+ D_{RP}(-\theta)\} \frac{e^{i(k_1 r - \pi/4)}}{\sqrt{k_1 r}}$$

$$\psi_{\text{sec}}{}^d = \{A^- D_{RS}(\theta) + A^+ D_{RS}(-\theta)\} \frac{e^{i(k_2 r - \pi/4)}}{\sqrt{k_2 r}} \tag{10}$$

The total diffracted body wave field given by

$$u^d \simeq ik_1 \phi^d = ik_1(\phi^d{}_{pr} + \phi^d{}_{\text{sec}})$$

$$v^d \simeq ik_2 \psi^d = ik_2(\psi^d{}_{pr} + \psi^d{}_{\text{sec}}) \tag{11}$$

is valid for large $(k_j r)$ to $O(k_j r)^{-1}$. In addition the diffracted Rayleigh waves on two sides of the crack are given by the surface displacements

$$T^+ \begin{pmatrix} i \\ \gamma_r \\ 1 \end{pmatrix} e^{ik_r x}; \quad T^- \begin{pmatrix} -i \\ \gamma_r \\ 1 \end{pmatrix} e^{-ik_r x} \tag{12}$$

(11) and (12) are the main results for P wave incidence. If the diffracted body waves are observed on the free surface $y = 0$, their amplitudes and phases will be different from those obtained from (11) due to reflection effects. In order to include these effects let the field point be located at $Q(x, 0)$, $x > 0$ (Fig. 2(*b*)).

At very high frequencies the x and y-components of the surface displacement at Q must be modified by the multiplicative factors are

$$1 + R_{PP}(\theta_1') - \frac{\sqrt{\sigma^2 - \sin^2\theta_1}\, R_{PS}(\theta_1')}{\sin\theta_1}$$

and

$$-1 + R_{PP}(\theta_1') - \tan\theta_1 R_{PS}(\theta_1') \tag{13}$$

Similarly, for S wave incidence the multiplicative factors are

$$1 - R_{SS}(\theta_1') - \tan\theta_1 R_{SP}(\theta_1')$$

and

$$1 + R_{SS}(\theta_1') + \frac{\sqrt{1 - \sigma^2 \sin^2\theta_1}\, R_{SP}(\theta_1).}{\sigma \sin\theta_1} \tag{14}$$

where

$$\sigma = k_2/k_1, \quad \theta' = \pi - \theta_1$$

The foregoing formulation can now be used to calculate high frequency displacements at almost all points on the surface of the medium for incident body waves.

Incident Rayleigh Wave. Let a Rayleigh wave with surface displacement

$$A_0 \begin{pmatrix} i/\gamma_r \\ 1 \end{pmatrix} e^{ik_r x}$$

be incident on the crack from the left side (Fig. 3). The situation is somewhat different from the body wave cases considered previously, since the Rayleigh waves are inhomogeneous waves and there is no primary diffraction at the crack tip at high frequencies. The displacement components can be calculated as before. It can be shown that the Rayleigh waves on the $+ve$ and $-ve$ faces of the crack are given by

$$A^+ \begin{pmatrix} 1 \\ i \\ \gamma_r \end{pmatrix} e^{ik_r y}; \quad B^+ \begin{pmatrix} 1 \\ -i \\ \gamma_r \end{pmatrix} e^{-ik_r(y-l)}$$

$$A^- \begin{pmatrix} -1 \\ i \\ \gamma_r \end{pmatrix} e^{ik_r y}; \quad B^- \begin{pmatrix} -1 \\ -i \\ \gamma_r \end{pmatrix} e^{-ik_r(y-l)}$$

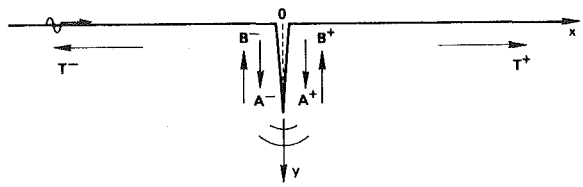

Fig. 3 Diffracted Rayleigh waves from incident surface wave on the edge crack

where

$$A^+ = R_0 T_0 T_L e^{2ik_r l}/\Delta$$

$$A^- = T_0 + R_0 T_0 \{R_0 e^{4ik_r l}(T_L{}^2 - R_L{}^2) + R_L e^{2ik_r l}\}/\Delta$$

$$B^+ = T_0 T_L e^{ik_r l}/\Delta$$

$$B^- = \{T_0 R_L e^{ik_r l} + R_0 T_0 e^{3ik_r l}(T_L{}^2 - R_L{}^2)\}/\Delta$$

$$\Delta = (R_0 R_L e^{2ik_r l} - 1)^2 - (R_0 T_L e^{2ik_r l})^2$$

and we have written $D^+{}_{RR} = T_L$; $D^-{}_{RR} = R_L$. Transmitted and reflected Rayleigh waves on the free surface are given by the displacement vectors

$$T^+ \begin{pmatrix} i \\ \gamma_r \\ 1 \end{pmatrix} e^{ik_r x} \tag{15}$$

for $x > 0$, and

$$T^- \begin{pmatrix} -i \\ \gamma_r \\ 1 \end{pmatrix} e^{-ik_r x} \tag{16}$$

for $x < 0$, where

$$T^+ = T_0{}^2 T_L e^{2ik_r l}/\Delta$$

$$T^- = R_0 + [T_0{}^2 e^{2ik_r l} R_L + R_0 T_0{}^2 e^{4ik_r l}(T_L{}^2 - R_L{}^2)]/\Delta$$

The influence of the successively reflected Rayleigh waves between L and O can be recovered as before by expanding Δ^{-1}. The diffracted body waves can also be calculated in a straightforward manner. The details of these calculations will be omitted.

The transmission and reflection coefficients T^+ and T^- are functions of $(k_r l)$ as might be expected. It can be easily seen however that they are both $O(1)$ in $k_r l$. Thus each of them oscillates about a constant value at all frequencies, so that even if $k_r l \to \infty$, i.e., the crack is infinitely long compared to the wavelength T^+ does not vanish. This result although somewhat unsatisfactory, is easily explained by the unrealistic two-dimensional nature of the model.

It should be further noted that if multiple reflection between L and O are ignored

$$|T^+| \simeq |T_0{}^2 T_L|$$

and

$$|T^-| \simeq |R_0|$$

For most materials $|T_0| \simeq 0.6$, $|T_L| \simeq 0.2$, and $|R_0| \simeq 0.3$. Thus

$$|T^+| \simeq 0.07, \qquad |T^-| \simeq 0.3$$

Clearly a very small amount of the incident energy is transmitted across the crack and the overall energy balance implies that most of the surface wave energy is converted into body waves by interaction with the crack.

Edge Crack in a Plate. The solution just described can be extended to the cases where the solid medium may contain other boundaries. The additional complications are only geometric and algebraic in nature.

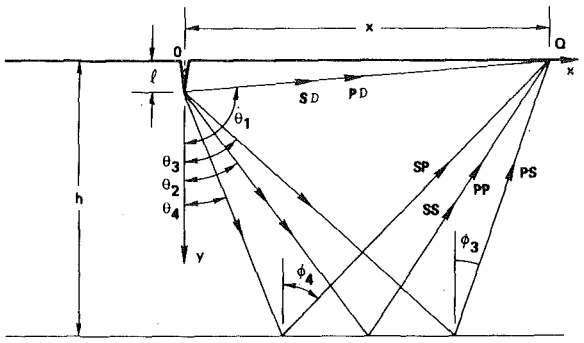

Fig. 4 Diffracted body waves from the crack tip

As an illustration of the foregoing we assume that the medium is bounded below by a free surface $-\infty < x < \infty, y = h, -\infty < z < \infty$. We seek solution under the restriction $k_j l \gg 1$ (waves short compared to plate thickness), and $l \ll h$.

We consider the motion generated by the diffracted waves at a point Q on the plate surface located at $(x, 0)$. The body wave ray paths between the crack tip L and Q are shown in Fig. 4. Other ray paths which include multiple interaction between the plate surfaces are ignored, although they can be included if necessary. Clearly the direct P or S waves must leave L at an angle θ_1, where

$$\theta_1 = \pi - \tan^{-1}(x/l) \tag{17}$$

in order to arrive at Q. The PP or SS wave leaves L at angle θ_2 where

$$x = (2h - l)\tan\theta_2 \tag{18}$$

Similarly the angles of the PS and SP are θ_3 and θ_4, respectively, where

$$x = (h - l)\tan\theta_3 + h\tan\phi_3$$
$$x = (h - l)\tan\theta_4 + h\tan\phi_4 \tag{19}$$

$$\sin\phi_3 = \frac{c_2}{c_1}\sin\theta_3$$
$$\sin\phi_4 = \frac{c_1}{c_2}\sin\theta_4 \tag{20}$$

It is to be noted that the angles $\theta_1, \theta_2, \theta_3, \theta_4$ are well defined for all $c_2/c_1 < 1$ so long as x, l, h are finite. For given values of c_2/c_1, x/l, h/l, θ_1 and θ_2 are calculated directly from (17) and (18) while θ_3 and θ_4 are most easily calculated by trial and error.

The effect of the bottom surface of the plate is to give two reflected body wave rays for each diffracted body wave incident on it. At high frequencies ($k_j h \gg 1$), these contributions can be calculated by simple plane wave reflection considerations.

Special attention must be paid to the diffracted body wave rays that propagate directly downward from L. No mode conversion (from P to S or vice versa) of these rays occur on reflection at the bottom surface of the plate. Since most of the energy in the diffracted ray is returned on reflection, the secondary diffraction at the crack tip from these reflected rays are relatively strong, thus significant Rayleigh waves on both sides of the crack are produced. These waves have same orders of magnitude as the primary diffracted body waves. The Rayleigh waves in turn are transmitted through the corners to create motion on the plate surface on either side of the crack. The motion due to these waves can be calculated from the results of the previous section by assuming incidence angle $\theta_0 = 0$.

The motion on either surface of the crack due to diffraction can be calculated by means of the procedure just described. For Rayleigh wave incidence the secondary diffracted Rayleigh waves previously discussed are the strongest distinguishing features in the surface motion for the plate problem as opposed to the half plane.

Numerical Results and Discussions. The normalized x-component of the displacement on the plate surface $y = 0$ due to various types of wave incidence is plotted against the dimensionless frequency $k_1 l$ in Figs. 5–8. The normalized displacement U is defined by

$$U = u(x, 0)/u^0(0, 0)$$

for Rayleigh wave incidence and by

$$U = u(x, 0)/|\mathbf{u}^0(0, 0)|$$

for body wave incidence. In all cases it is assumed that $h = 10l$, and

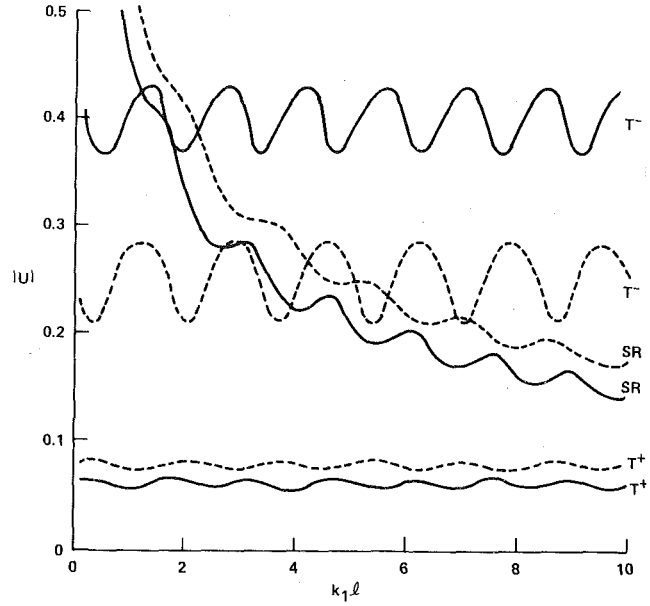

Fig. 5 Amplitudes of transmitted, reflected, and secondary shear converted Rayleigh waves for Poisson's ratios of $\frac{1}{3}$ (solid curves) and $\frac{1}{4}$ (dashed curves)

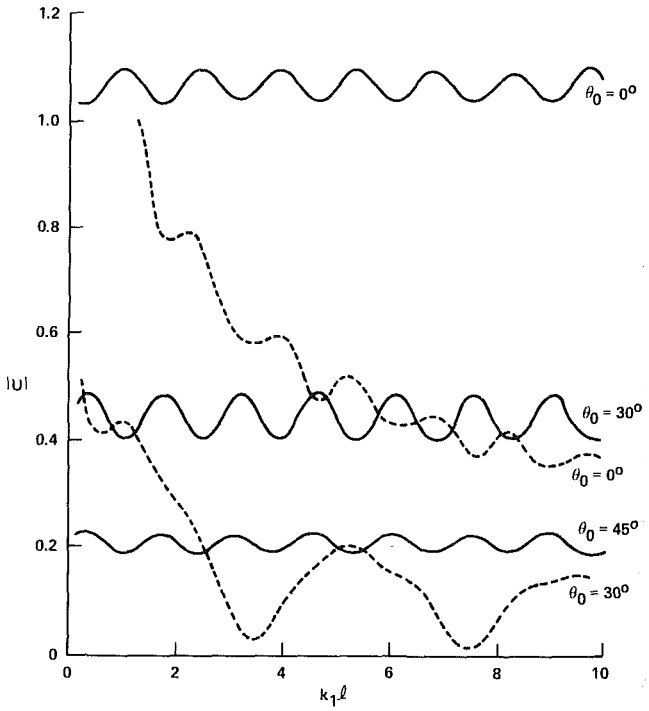

Fig. 6 Amplitudes of Rayleigh waves in $x > 0$ due to shear waves incidence at different angles; solid curves are for primary diffracted waves, dashed curves for secondary shear converted Rayleigh waves

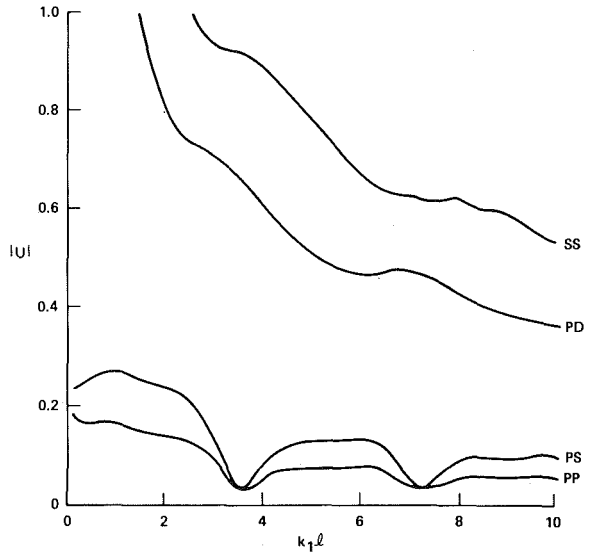

Fig. 7 The significant diffracted body waves at $x/l = 10$ due to incident shear wave at 30°; wave types are defined in Fig. 4

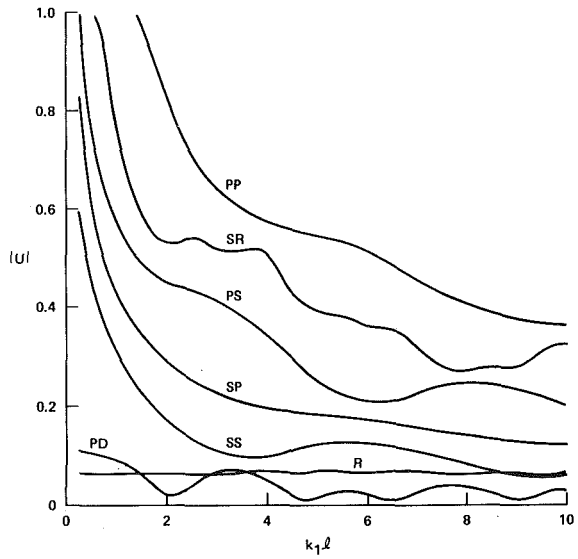

Fig. 8 Motion at $x/l = -10$ due to *P* wave incidence at 30°; *R* is primary diffracted Rayleigh wave, *SR* the secondary shear converted Rayleigh wave; diffracted body waves are defined in Fig. 4

that the Poisson's ratio of the plate material is $\frac{1}{3}$ (except in Fig. 5).

The surface displacements produced by transmitted, reflected, and secondary diffracted Rayleigh waves due to an incident Rayleigh wave are shown in Fig. 5 for two values of the Poisson's ratio. It can be seen that the reflection coefficients are significant, especially for $\nu = \frac{1}{3}$ and that the transmission coefficients are negligibly small. For $\nu = \frac{1}{3}$ the reflection and transmission coefficients oscillate about 0.3 and 0.07, respectively, values previously obtained by ignoring multiple reflection of the Rayleigh waves within the crack. The same is true for $\nu = \frac{1}{4}$.

It should be noted that the reflection and transmission coefficients $T^{\pm}$ are not influenced by the bottom surface of the plate. Hence, these coefficients are identical with those for an edge crack in a half plane. The half-plane problem has been considered in three recent papers by Achenbach and his colleagues [2, 3, 12]. Reference [2] contains the high frequency asymptotic solution for Rayleigh wave incidence. The reflection and transmission coefficients given in [2] are in basic agreement with $T^{\pm}$ shown in Fig. 5 for $\nu = \frac{1}{3}$.

The secondary Rayleigh waves shown in Fig. 5 are generated by the reflection of the diffracted S waves at the bottom surface of the plate and subsequent diffraction of these reflected waves at the crack tip L. Amplitudes of these waves decay with frequency and are symmetric with respect to the crack. Secondary Rayleigh waves are also generated by the reflection at $y = h$ of P waves from the virtual source at L. But the amplitudes of these secondary waves are negligibly small in all cases studied here, and therefore are not shown in Fig. 5. Amplitudes of the other body wave arrivals after reflection at the lower plate surface $y = h$ are also smaller than those of the transmitted Rayleigh waves and are not plotted in Fig. 5.

Figs. 6 and 7 contain representative results for shear wave incidence at different angles. Rayleigh waves produced by the interaction of the edge crack with shear waves incident at 0°, 30°, and 45° are shown in Fig. 6. Clearly, shear waves propagating parallel to the crack produces the strongest Rayleigh waves amongst all cases considered here. The secondary shear converted Rayleigh waves are also quite strong. The amplitudes of these waves decrease with increasing angle of incidence. The primary diffracted and reflected body waves arriving at a point $x/l = 10$ on the surface $y = 0$ due to S wave incidence at 30° are shown in Fig. 7. The notable features here are the strong reflected SS and direct PD waves for the diffraction point L. The diffracted body wave amplitudes are considerably smaller at other angles of incidence (including incidence parallel to the crack).

Body and surface waves of significant amplitude produced by incident P waves at 30° are plotted in Fig. 8. It can be seen that the field is dominated by reflected waves from the lower surface of the plate $y = h$.

Calculations of the diffracted field for other values of x/l were also carried out. The diffraction pattern was found to be similar except for the amplitude changes of the body waves caused by changes in distance between the virtual source and the field point.

The general conclusions that can be drawn from the present study are as follows:

1 The crack is an efficient reflector and poor transmitter of Rayleigh waves. The crack tip diffracted shear waves reflected from the opposite face of the plate directly below the crack produce relatively strong Rayleigh waves after secondary diffraction at the crack tip.

2 Both primary and secondary diffracted Rayleigh waves generated by incident shear waves are relatively strong at all angles of incidence, and especially for incidence parallel to the crack. Some of the body wave rays also carry significant energy.

3 Primary diffracted Rayleigh waves generated by incident P waves are small for all angles of incidence. The secondary shear converted Rayleigh waves and some of the body wave rays reflected off the lower surface of the plate have significant amplitudes for oblique incidence.

For Rayleigh wave incidence both the primary and secondary Rayleigh wave pulses have been observed and recorded in experiments involving plates containing long fatigue cracks (Tittman and Buck [14]). Fourier analysis of these pulses should exhibit the oscillatory behavior in their amplitudes as shown in Fig. 5. The period of oscillation is approximately related to the crack length through $k_r l = \pi$. It should also be possible to record the onset and pulse shape of some of the relatively strong body waves. These observations could be useful in the accurate determination of the geometrical properties of an edge crack.

Acknowledgment

This research was supported by the U. S. Department of Energy under Contract Number W-7405-ENG-48.

References

1 Achenbach, J. D., and Gautesen, A. K., "Geometrical Theory of Diffraction for Three-D Elastodynamics," *Journal of the Acoustical Society of America*, Vol. 61, 1976, pp. 413–421.

2 Achenbach, J. D., Gautesen, A. K., and Mendelsohn, D. A., "Ray Analysis of Surface Wave Interaction With an Edge Crack," *IEEE Trans. on Sonics and Ultrasonics*, Vol. SU-27, 1980, pp. 124–129.

3 Achenbach, J. D., Keer, L. M., and Mendelsohn, D. A., "Elastodynamic Analysis of an Edge Crack," ASME JOURNAL OF APPLIED MECHANICS, Vol. 47, 1980, pp. 551–556.
4 Eringen, A., *Elastodynamics*, Vol. II, New York, Academic Press, 1974–1975.
5 Freund, L. B., "The Oblique Reflection of a Rayleigh Wave From a Crack Tip," *International Journal of Solid Structures*, Vol. 7, 1971, pp. 1199.
6 Fuyuki, M., and Matsumoto, Y., "Finite Difference Analysis of Rayleigh Wave Scattering at a Trench," *Bulletin of the Seismological Society of America*, Vol. 70, 1980, pp. 2051–2069.
7 Kundu, T., "Diffraction Pattern of Elastic Waves by a Surface Crack," MS Thesis, 1980, UCLA,
8 Mal, A. K., "Rayleigh Waves From a Moving Thrust Fault," *Bulletin of the Seismological Society of America*, Vol. 62, 1972, pp. 751–762.
9 Mal, A. K., "Application of Continuum Mechanics," *Applied Mechanics Symposia*, Series of the ASME, Vol. AMD8, 1974, pp. 205–223.
10 Mal, A. K., and Knopoff, L., "Transmission of Rayleigh Waves at a Corner," *Bulletin of the Seismological Society of America*, Vol. 56, 1966, pp. 455–466.
11 Maue, A. W., "Die Bengung Elastigcher Wallen an der Halbebene," *Zeitschrift für Angewandte Mathematik und Mechanik*, Vol. 33, 1953, pp. 1–10.
12 Mendelsohn, D. A., Achenbach, J. D., and Keer, L. M., "Scattering of Elastic Waves by a Surface Breaking Crack," Wave Motion, Vol. 2, 1980.
13 Stone, S., Ghosh, M. L., and Mal, A. K., "Diffraction of Antiplane Shear Wave by an Edge Crack," ASME JOURNAL OF APPLIED MECHANICS, Vol. 47, 1980, pp. 359–362.
14 Tittman, B. R., and Buck, O., "Fatigue Life Time Prediction With the Aid of SAW NDE," *Journal of NDE*, 1980.

APPENDIX

The Diffraction Coefficients

For P wave incidence on the crack $x > 0, y = 0\pm$, the potentials in the incident and diffracted body wave field are related through the equations,

$$\phi^0 = e^{ik_1(\alpha_0 x + \beta_0 y)}, \quad \psi_0 = 0$$

$$\phi^d = D_{PP}(\theta, \theta_0) e^{i(k_1 r - \pi/4)}/\sqrt{k_1 r}$$

$$\psi^d = D_{PS}(\theta, \theta_0) e^{i(k_2 r - \pi/4)}/\sqrt{k_2 r}$$

where

$$\alpha_0 = \cos\theta_0, \quad \beta_0 = \sin\theta_0,$$

θ_0 is the angle between the incident ray and x-axis; (r, θ) the polar coordinates of the field point (x, y); D_{PP}, D_{PS} are the diffraction coefficients. Similarly, diffraction coefficients $D_{SP}(\theta, \theta_0)$, $D_{SS}(\theta, \theta_0)$ can be defined for S wave incidence. The diffracted Rayleigh displacement components are given by

$$\mathbf{u}^{dR}(x, 0+) = k_1 D_{XR}{}^{+}(\theta_0) \begin{pmatrix} i/\gamma_r \\ 1 \end{pmatrix} e^{ik_r x}$$

$$\mathbf{u}^{dR}(x, 0-) = k_1 D_{XR}{}^{-}(\theta_0) \begin{pmatrix} i/\gamma_r \\ -1 \end{pmatrix} e^{ik_r x}$$

The symbol X in the diffraction coefficients is either P or S depending on whether the incident wave is a P or S wave, and

$$k_r = \omega/c_r,$$

$$\gamma_r = \{2 - (c_r/c_2)^2\}/\{2\sqrt{1 - (c_r/c_2)^2}\}$$

For Rayleigh wave incidence we assume that the crack is located in $x < 0, y = 0$, and the waves are incident along the negative face of the crack $x < 0, y = 0-$. The displacement vector on the crack face due to the incident wave is

$$\mathbf{u}^0 = \begin{pmatrix} i/\gamma_r \\ -1 \end{pmatrix} e^{ik_r x}$$

The diffracted body waves in the far field are described by the potentials,

$$\phi^d \simeq \frac{D_{RP}(\theta)}{k_1} e^{i(k_1 r - \pi/4)}/\sqrt{k_1 r}$$

$$\psi^d \simeq \frac{D_{RS}(\theta)}{k_1} e^{i(k_2 r - \pi/4)}/\sqrt{k_2 r}$$

The reflected Rayleigh waves on the negative face of the crack and the transmitted Rayleigh waves on the positive face have associated displacement vectors $\mathbf{u}^r$ and $\mathbf{u}^t$ where

$$\mathbf{u}^r = D^{-}_{RR} \begin{pmatrix} -i/\gamma_r \\ -1 \end{pmatrix} e^{-ik_r x}$$

$$\mathbf{u}^t = D^{+}_{RR} \begin{pmatrix} -i/\gamma_r \\ 1 \end{pmatrix} e^{-ik_r x}$$

The expressions for the nondimensional diffraction coefficients are given in [7].

T. B. Moodie
Associate Professor,
Department of Mathematics.

J. B. Haddow
Professor,
Department of Mechanical Engineering.
Mem. ASME

A. Mioduchowski
Associate Professor,
Department of Mechanical Engineering.
Mem. ASME

R. J. Tait
Associate Professor,
Department of Mathematics.

University of Alberta,
Edmonton, Alberta, Canada T6G 2G8

Plane Elastic Waves Generated by Dynamical Loading Applied to Edge of Circular Hole

The generalized plane stress, or plane strain, elastodynamic problem of an unbounded body, subjected to sudden application of tractions at the surface of a circular hole, is considered. In general this problem involves three independent variables, two spatial coordinates, and time, but it is shown how the method of characteristics, for one spatial variable and time, can be applied when the dependent variables are expanded as Fourier series in terms of the polar angle θ. A numerical procedure is proposed for the method of characteristics and numerical results are obtained for a specific example.

Introduction

The plane problem of the response of an unbounded elastic body subjected to a suddenly applied, spatially uniform, application of loading at the surface of a circular hole has been studied extensively by Kromm [1], Selberg [2], and others. Kromm and Selberg used Laplace transform techniques to obtain their solutions, and Miklowitz [3], in solving a related problem of waves from a suddenly punched hole in a stretched plate, used an improved and more direct method of inversion of the Laplace transforms. The problems considered in [1–3] involve one spatial variable and time. Such problems can also be solved, numerically, by the method of characteristics as shown by Chou and Koenig [4]. In th is paper we are concerned with a generalization of the problem considered in [1, 2], which arises when a spatially nonuniform application of surface tractions is applied at the circular hole. Eringen [5] considered this generalization and also moving loads at the surface of the hole and indicated how solutions could be obtained by using integral transform methods, but did not give any numerical results. Ziv [6] has shown how the method of characteristics can be extended to analyze elastic wave propagation problems with two spatial variables, but again no numerical solutions were given. In this paper we present a different approach for the solution of a class of elastic wave propagation problems with two spatial variables. The dependent variables are represented by Fourier series in terms of the polar angle θ. Each "harmonic" of these variables is governed by a system of partial differential equations, which is hyperbolic. Such a system of equations and boundary conditions is not coupled with any other harmonic and has two independent variables, a spatial variable, and time. A solution is obtained by solving each system by the numerical method of characteristics, for one spatial variable and time. This gives the coefficients of the Fourier series for the dependent variables.

Haddow and Mioduchowski [7] used the method of near characteristics to obtain solutions to the problem of the unloading waves from a suddenly punched hole in a uniaxially stretched elastic plate. It has now become evident to us that this problem is a special case of the class of problems considered in this paper and that results can be obtained by the simpler procedure presented here.

Formulation of Problem

It is assumed that the plane elastic body is homogeneous and isotropic, although, with trivial modification a transversely isotropic body with the axis of isotropy in the direction of the axis of the hole can be considered. It is further assumed that the dimensions of the body in the plane are very large compared with the radius of the hole so that the body can be taken as unbounded and there are no reflected waves. The procedure presented is valid for both plane strain and generalized plane stress but the equations given are for generalized plane stress. Since the two independent elastic constants in these equations are taken as the shear modulus μ and Poisson's ratio ν, the plane strain equations can be obtained by replacing ν, in the plane stress equations, by $\nu/(1-\nu)$.

We take the origin of plane polar coordinates, r and θ, on the axis

Contributed by the Applied Mechanics Division for presentation at the Winter Annual Meeting, Washington, D. C., November 15–20, 1981, of THE AMERICAN SOCIETY OF MECHANICAL ENGINEERS.

Discussion on this paper should be addressed to the Editorial Department, ASME, United Engineering Building, 345 East 47th Street, New York, N. Y. 10017, and will be accepted until December 1, 1981. Readers who need more time to prepare a discussion should request an extension from the Editorial Department. Manuscript received by ASME Applied Mechanics Division, October, 1980; final revision, January, 1981. Paper No. 81-WA/APM-4.

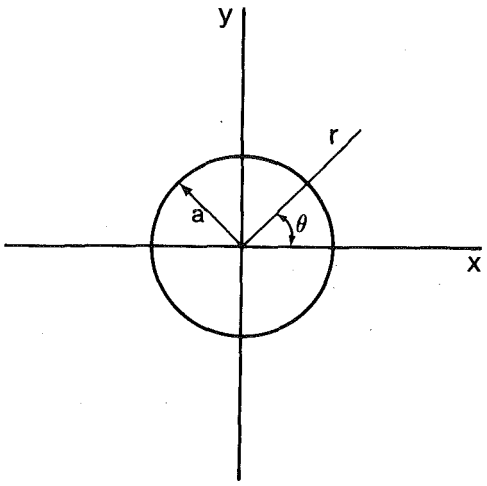

Fig. 1 Coordinate system

of the hole of radius a as shown in Fig. 1. Initially the body is at rest and unstressed so that

$$\sigma_r(r, \theta, t) = \sigma_\theta(r, \theta, t) = \tau_{r\theta}(r, \theta, t) = 0 \qquad r \geq a, t < 0 \quad (1)$$
$$u(r, \theta, t) = v(r, \theta, t) = 0$$

where σ_r, σ_θ, and $\tau_{r\theta}$ are the stress components in the usual notation, t is time and u and v are the radial and circumferential components of displacement, respectively. At $t = 0$ surface tractions

$$\sigma_r(a, \theta, t) = p(\theta, t)\,\mathrm{H}(t), \qquad (2)$$
$$\tau_{r\theta}(a, \theta, t) = \tau(\theta, t)\,\mathrm{H}(t),$$

are applied at $r = a$, where $\mathrm{H}(t)$ is the unit step function.

The equations of motion are

$$\frac{\partial \sigma_r}{\partial r} + \frac{1}{r}\frac{\partial \tau_{r\theta}}{\partial \theta} + \frac{(\sigma_r - \sigma_\theta)}{r} = \rho \frac{\partial^2 u}{\partial t^2}, \quad (3)$$

$$\frac{1}{r}\frac{\partial \sigma_\theta}{\partial \theta} + \frac{\partial \tau_{r\theta}}{\partial r} + \frac{2}{r}\tau_{r\theta} = \rho \frac{\partial^2 v}{\partial t^2}, \quad (4)$$

and the constitutive equations in terms of the shear modulus and Poisson's ratio are

$$\frac{\partial u}{\partial r} = \frac{(\sigma_r - \nu\sigma_\theta)}{2(1+\nu)\mu}, \quad (5)$$

$$\frac{u}{r} + \frac{1}{r}\frac{\partial v}{\partial \theta} = \frac{(\sigma_\theta - \nu\sigma_r)}{2(1+\nu)\mu}, \quad (6)$$

$$\frac{1}{r}\frac{\partial u}{\partial \theta} + \frac{\partial v}{\partial r} - \frac{v}{r} = \frac{\tau_{r\theta}}{\mu}. \quad (7)$$

Method of Characteristics

First we consider loading at $r = a$ which is symmetric about $\theta = 0$. Boundary conditions (2) may then be expressed as

$$\sigma_r(a, \theta, t) = P_0(t) + \sum_{n=1}^{\infty} P_n(t) \cos n\theta, \quad (8)$$

$$\tau_{r\theta}(a, \theta, t) = \sum_{n=1}^{\infty} S_n(t) \sin n\theta. \quad (9)$$

We seek a solution for the stresses and displacements in the form

$$\sigma_r = \sigma_r^{(0)}(r, t) + \sum_{n=1}^{\infty} \sigma_r^{(n)}(r, t) \cos n\theta, \quad (10)$$

$$\sigma_\theta = \sigma_\theta^{(0)}(r, t) + \sum_{n=1}^{\infty} \sigma_\theta^{(n)}(r, t) \cos n\theta, \quad (11)$$

$$\tau_{r\theta} = \sum_{n=1}^{\infty} \tau^{(n)}(r, t) \sin n\theta, \quad (12)$$

$$u = u^{(0)}(r, t) + \sum_{n=1}^{\infty} u^{(n)}(r, t) \cos n\theta, \quad (13)$$

$$v = \sum_{n=1}^{\infty} v^{(n)}(r, t) \sin n\theta. \quad (14)$$

Substituting equations (10)–(14) in equations (3)–(7), and equating coefficients of $\cos n\theta$, gives

$$\frac{\partial \sigma_r^{(n)}}{\partial r} + \frac{n\tau^{(n)}}{r} + \frac{(\sigma_r^{(n)} - \sigma_\theta^{(n)})}{r} = \rho \frac{\partial^2 u^{(n)}}{\partial t^2}, \quad (15)$$

$$\frac{\partial \tau^{(n)}}{\partial r} + \frac{2\tau^{(n)}}{r} - \frac{n}{r}\sigma_\theta^{(n)} = \rho \frac{\partial^2 v^{(n)}}{\partial t^2}, \quad (16)$$

$$\frac{\partial u^{(n)}}{\partial r} = \frac{(\sigma_r^{(n)} - \nu\sigma_\theta^{(n)})}{2\mu(1+\nu)}, \quad (17)$$

$$\frac{u^{(n)}}{r} + \frac{nv^{(n)}}{r} = \frac{(\sigma_\theta^{(n)} - \nu\sigma_r^{(n)})}{2\mu(1+\nu)} \quad (18)$$

$$-\frac{nu^{(n)}}{r} + \frac{\partial v^{(n)}}{\partial r} - \frac{v^{(n)}}{r} = \frac{\tau^{(n)}}{\mu} \quad (19)$$

for $n = 0, 1, 2 \ldots$

We note that $\tau^{(0)} = 0$ and $v^{(0)} = 0$, so for $n = 0$ equations (15)–(19) reduce from five equations to three, namely, equations (15), (17), and (18).

Comparing equations (8) and (9) with (10) and (12), gives

$$\sigma_r^{(n)}(a, t) = P_n(t), \quad (20)$$

$$\tau^{(n)}(a, t) = S_n(t). \quad (21)$$

If equations (17)–(19) are differentiated, partially with respect to time, equations (15)–(19) can be put in the form

$$\mathbf{A}\frac{\partial \mathbf{q}^{(n)}}{\partial t} + \mathbf{B}\frac{\partial \mathbf{q}^{(n)}}{\partial r} = \mathbf{b}^{(n)}, \quad (22)$$

where

$$\mathbf{A} = \begin{bmatrix} -\frac{1}{2(1+\nu)\mu} & \frac{\nu}{2(1+\nu)\mu} & 0 & 0 & 0 \\ -\frac{\nu}{2(1+\nu)\mu} & \frac{1}{2(1+\nu)\mu} & 0 & 0 & 0 \\ 0 & 0 & \frac{1}{\mu} & 0 & 0 \\ 0 & 0 & 0 & \rho & 0 \\ 0 & 0 & 0 & 0 & \rho \end{bmatrix}$$

$$\mathbf{B} = \begin{bmatrix} 0 & 0 & 0 & 1 & 0 \\ 0 & 0 & 0 & 0 & 0 \\ 0 & 0 & 0 & 0 & -1 \\ -1 & 0 & 0 & 0 & 0 \\ 0 & 0 & -1 & 0 & 0 \end{bmatrix},$$

$$\mathbf{q}^{(n)} = \begin{bmatrix} \sigma_r^{(n)} \\ \sigma_\theta^{(n)} \\ \tau^{(n)} \\ \dot{u}^{(n)} \\ \dot{v}^{(n)} \end{bmatrix}, \qquad \mathbf{b}^{(n)} = \begin{bmatrix} 0 \\ \frac{\dot{u}^{(n)}}{r} + \frac{n\dot{v}^{(n)}}{r} \\ -\frac{n\dot{u}^{(n)}}{r} - \frac{\dot{v}^{(n)}}{r} \\ \frac{(\sigma_r^{(n)} - \sigma_\theta^{(n)})}{r} + \frac{n\tau^{(n)}}{r} \\ \frac{2\tau^{(n)}}{r} - \frac{n\sigma_\theta^{(n)}}{r} \end{bmatrix},$$

and a superposed dot denotes differentiation with respect to time. Equation (22) represents a set of five linear first-order partial-differential equations. The system is hyperbolic and by using the stan-

dard techniques, given by Whitham [8], we obtain the characteristic directions,

$$\frac{dr}{dt} = \pm C_T, \quad \frac{dr}{dt} = \pm C_L, \quad \frac{dr}{dt} = 0,$$

and the relationships,

$$\pm \frac{d\dot{v}^{(n)}}{dt} - \frac{1}{\rho C_T}\frac{d\tau^{(n)}}{dt} = \frac{1}{r}\left\{\pm \frac{1}{\rho}(2\tau_{r\theta}^{(n)} - n\sigma_\theta^{(n)}) + C_T(n\dot{u}^{(n)} + \dot{v}^{(n)})\right\} \quad \text{on} \quad \frac{dr}{dt} = \pm C_T, \quad (23)$$

$$\pm \frac{d\dot{u}^{(n)}}{dt} - \frac{1}{\rho C_L}\frac{d\sigma_r^{(n)}}{dt} = \pm \frac{1}{r}\left\{\frac{1}{\rho}(\sigma_r^{(n)} - \sigma_\theta^{(n)} + n\tau^{(n)}) - \nu C_L(\dot{u}^{(n)} + n\dot{v}^{(n)})\right\} \quad \text{on} \quad \frac{dr}{dt} = \pm C_L, \quad (24)$$

$$\frac{1}{2(1+\nu)\mu}\left(\frac{d\sigma_\theta^{(n)}}{dt} - \nu\frac{d\sigma_r^{(n)}}{dt}\right) = \frac{1}{r}(\dot{u}^{(n)} + n\dot{v}^{(n)}) \quad \text{on} \quad \frac{dr}{dt} = 0, \quad (25)$$

where

$$C_T = \left(\frac{\mu}{\rho}\right)^{1/2} \quad \text{and} \quad C_L = C_T\left(\frac{2}{1-\nu}\right)^{1/2}$$

are the transverse and longitudinal wave speeds, respectively. When $n = 0$, equation (22) represents a set of three equations. The characteristic directions are then

$$\frac{dr}{dt} = \pm C_L \quad \text{and} \quad 0,$$

and the relations along the characteristics are equations (24) and (25). Henceforth we denote the characteristics with slopes $\pm C_T$, $\pm C_L$, and 0 as the $\pm\zeta_T$, $\pm\zeta_L$, and ζ_0 characteristics, respectively.

If the boundary conditions (1) and (2) have discontinuities with respect to time these discontinuities are propagated at speeds C_L and C_T, respectively. It may be deduced from those of equations (22) which are in conservation form that, for waves traveling radially outwards,

$$[\sigma_\theta^{(n)}] = \nu[\sigma_r^{(n)}], \quad (26)$$

$$[\sigma_r^{(n)}] = -\rho C_L[\dot{u}^{(n)}], \quad (27)$$

$$[\tau^{(n)}] = -\rho C_T[\dot{v}^{(n)}], \quad (28)$$

where the square brackets have the significance $[A] = A_2 - A_1$ and A_2 and A_1 are the values of A ahead of, and behind the wave front, respectively. Since the material of the body is homogeneous we deduce that discontinuities of $\sigma_r^{(n)}$ and $\tau^{(n)}$ travel in the (r, t)-plane along straight characteristics with slopes C_L and C_T, respectively.

If we consider loading at $r = a$ which is antisymmetric about $\theta = 0$ the boundary conditions (1) and (2) may be expressed in the form

$$\sigma_r(a, \theta, t) = \sum_{n=1}^{\infty} Q_n(t)\sin n\theta, \quad (29)$$

$$\tau_{r\theta}(a, \theta, t) = T_0(t) + \sum_{n=1}^{\infty} T_n(t)\cos n\theta. \quad (30)$$

The procedure followed is analogous to that for symmetric loading. The characteristic directions are the same, however, in the relations along the characteristics, n in equations (23)–(25) is replaced by $-n$. Also, $\sigma_r^{(0)} = 0, \sigma_\theta^{(0)} = 0$, and $u^{(0)} = 0$ so that for $n = 0$, the matrix equation (22) represents two equations and the relations along the ζ_T characteristics are equations (23) with n replaced by $-n$.

Nondimensionalization

We introduce the following nondimensionalization scheme:

$$(\bar{\sigma}_r^{(n)}, \bar{\sigma}_\theta^{(n)}, \bar{\tau}^{(n)}) = (\sigma_r^{(n)}, \sigma_\theta^{(n)}, \tau^{(n)})/\mu, \quad (\dot{\bar{u}}, \dot{\bar{v}}) = (\dot{u}, \dot{v})/C_T,$$

$$\bar{t} = C_T t/a, \quad \bar{C}_T = 1, \quad \bar{C}_L = C_L/C_T = (2/1-\nu)^{1/2}$$

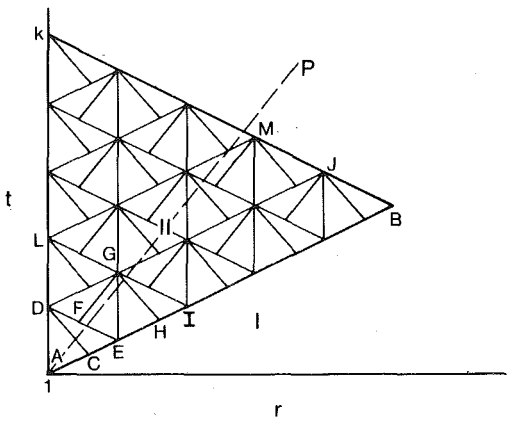

Fig. 2 Characteristic mesh

$$(\bar{u}, \bar{v}) = (u, v)/a, \quad \bar{r} = r/a, \quad \bar{a} = 1.$$

Henceforth we use nondimensional forms but for convenience we omit superposed bars. The nondimensional forms of the slopes of the characteristics are

$$\frac{dr}{dt} = \pm 1, \quad \frac{dr}{dt} = \pm\left(\frac{2}{1-\nu}\right)^{1/2}, \quad \frac{dr}{dt} = 0,$$

and the corresponding relations along the characteristics are

$$\pm \frac{d\dot{v}^{(n)}}{dt} - \frac{d\tau_{r\theta}^{(n)}}{dt} = \frac{1}{r}\{\pm(2\tau^{(n)} - n\sigma_\theta^{(n)}) + n\dot{u}^{(n)} + \dot{v}^{(n)}\}, \quad \text{on} \quad dr/dt = \pm 1, \quad (31)$$

$$\pm \frac{d\dot{u}^{(n)}}{dt} - \left(\frac{1-\nu}{2}\right)^{1/2}\frac{d\sigma_r^{(n)}}{dt} = \frac{1}{r}\left\{\pm(\sigma_r^{(n)} - \sigma_\theta^{(n)} + n\tau^{(n)}) - \left(\frac{2-\nu^2}{1-\nu}\right)^{1/2}(\dot{u}^{(n)} + n\dot{v}^{(n)})\right\} \quad \text{on} \quad \frac{dr}{dt} = \pm\left(\frac{2}{1-\nu}\right)^{1/2}, \quad (32)$$

$$\frac{1}{2(1+\nu)}\left[\frac{d\sigma_\theta^{(n)}}{dt} - \nu\frac{d\sigma_r^{(n)}}{dt}\right] = \frac{1}{r}(\dot{u}^{(n)} + n\dot{v}^{(n)}) \quad \text{on} \quad \frac{dr}{dt} = 0. \quad (33)$$

The nondimensional forms of equations (26)–(28) are

$$[\sigma_\theta^{(n)}] = \nu[\sigma_r^{(n)}], \quad (34)$$

$$[\sigma_r^{(n)}] = \left(\frac{2}{1-\nu}\right)^{1/2}[\dot{u}^{(n)}], \quad (35)$$

$$[\tau^{(n)}] = [\dot{v}^{(n)}]. \quad (36)$$

Again we note that the relations presented are for generalized plane stress and the plane strain relations can be obtained by replacing ν by $\nu/(1-\nu)$.

Solution of Problem

In this section we present the method of solution for loading, at $r = 1$, which is symmetric about $\theta = 0$, so that it can be represented by equations (8) and (9). The method of solution for the antisymmetric loading represented by equations (29) and (30) is similar but with the appropriate changes, for example, n replaced by $-n$ in equations (31)–(33).

The first step is to obtain the coefficients $P_n(t)$ and $S_n(t)$ in equations (8) and (9). It follows from equations (20) and (21) that this gives us prescribed data for $\sigma_r^{(n)}$ and $\tau^{(n)}$ on $r = 1$ in the (r, t) characteristic plane. We have five families of characteristics in the (r, t)-plane for $n \geq 1$. A numerical scheme for stepwise integration of such systems has been suggested by Whitham [8], however, this scheme was found to be inapplicable to the present problem. The characteristic mesh used is shown in Fig. 2 and is similar in form to the near characteristic mesh used in [7] but has a different significance.

In Fig. 2 only segments of the $\pm\zeta_T$ characteristics are shown except for the characteristic AP given by $r = t + 1$, which is shown as a

dashed line. Referring to Fig. 2 the characteristic AB given by $r = C_L t + 1$, where, in nondimensional form $C_L = (2/1-\nu)^{1/2}$, represents the wave front and divides the (r, t)-plane into two Regions I and II. It follows from equation (1) that in Region I all the field variables are zero. Along characteristic AB on Side II all the elements of the column matrix $\mathbf{q}^{(n)} = \{\sigma_r{}^{(n)}, \sigma_\theta{}^{(n)}, \tau^{(n)}, \dot{u}^{(n)}\}^T$, where the superscript T denotes the transpose, are known. If $P_n(0) = 0$ there is no discontinuity of any of the elements of $\mathbf{q}^{(n)}$ across AB so that $\mathbf{q}^{(n)} = 0$ on Side II of AB. If $P_n(0) \neq 0$ there is a jump $[\sigma_r{}^{(n)}(1, 0)]$ and the discontinuity $[\sigma_r{}^{(n)}(C_L t + 1, t)]$ is propagated along AB. It follows from the theory of propagation of wave fronts [9] that $[\sigma_r{}^{(n)}(C_L t + 1, t)] = [\sigma_r{}^{(n)}(1, 0)]\, r^{-1/2}$. The discontinuities $[\dot{u}^{(n)}]$ and $[\sigma_\theta{}^{(n)}]$ across AB are found from equations (34) and (35), and $\dot{v}^{(n)}$ and $\tau^{(n)}$ are continuous. It follows then that $\mathbf{q}^{(n)}$ is known on Side II of AB. If $P_n(t)$ is discontinuous at times other than $t = 0$ the discontinuities are propagated along the appropriate ζ_L characteristic. Similar remarks apply to discontinuities in $S_n(t)$ except that these discontinuities are propagated along ζ_T characteristics.

Referring to Fig. 2, the three unknowns $\sigma_\theta{}^{(n)}$, $\dot{u}^{(n)}$, $\dot{v}^{(n)}$ at D are found by solving the three simultaneous equations given by the finite difference: forms of equations (31)–(33) for the segments AD, CD, and ED of the ζ_0, $-\zeta_L$, $-\zeta_T$ characteristics through D. Next, the five unknowns, that is the elements of $\mathbf{q}^{(n)}$, at G are found by solving the five simultaneous equations given by the finite-difference forms of equations (31)–(33) for the segments DG, FG, EG, HG, and IG. The values of $\mathbf{q}^{(n)}$ at F and H are found by interpolation. The values of $\mathbf{q}^{(n)}$ at the other nodal points along the ζ_L characteristic DJ are found, successively, in a similar manner. The procedure is repeated for nodal points along LM and continued until point K is reached. If $S_n(0) \neq 0$, there is a jump $[\tau^{(n)}(1, 0)]$ and the discontinuity $[\tau^{(n)}(t + 1, t)]$ is propagated along the ζ_T characteristic AP. This discontinuity also decays as $r^{-1/2}$ and when the finite-difference forms of equations (31)–(33) are used in the numerical technique, account must be taken of the discontinuities for segments cut by the ζ_T characteristic AP.

The determination of the field $\mathbf{q}^{(0)} = \{\sigma_r{}^{(0)}, \sigma_\theta{}^{(0)}, \dot{u}^{(0)}\}^T$ is straightforward since only $\pm\zeta_L$ and ζ_0 characteristics are involved and the technique described by Chou and Koenig [4] is applicable.

We note that if $p(\theta, t)$ and $\tau(\theta, t)$ in equations (2) can be expressed in the forms

$$p(\theta, t) = p^*(\theta)\, f(t),$$
$$\tau(\theta, t) = \tau^*(\theta)\, f(t),$$

a simplification arises in the determination of the coefficients $P_n(t)$ and $S_n(t)$ in equations (8) and (9) since these can be expressed as

$$P_n(t) = P_n{}^* f(t),$$
$$S_n(t) = S_n{}^* f(t)$$

where $P_n{}^*$ and $S_n{}^*$ are constants.

Consideration of Special Cases

1 Waves From Suddenly Punched Hole in Plate Subjected to Uniaxial Tension. Solutions for the sudden punching of a circular hole in a thin plate subjected to uniaxial tension have been obtained by Haddow and Mioduchowski [7] who used the method of near characteristics and the details of the problem are given in [7]. This problem can be regarded as a special case of the class of problems considered here if we subtract the initial uniaxial tension $\sigma_y = s$. The boundary conditions are

$$\sigma_r(1, \theta, t) = -\frac{s}{2}(1 - \cos 2\theta)\, f(t), \tag{37}$$

$$\tau_{r\theta}(1, \theta, t) = -\frac{s}{2}\sin 2\theta\, f(t), \tag{38}$$

where

$$f(t) = \frac{t}{t^*}\{\mathrm{H}(t) - \mathrm{H}(t - t^*)\} + \mathrm{H}(t - t^*) \quad \text{and} \quad t^*$$

is the time to punch the hole as discussed in [7]. Consequently nonzero coefficients in equations (8) and (9) are

$$P_0 = -\frac{s}{2}f(t), \quad P_2 = \frac{s}{2}f(t),$$

$$S_2 = -\frac{s}{2}f(t).$$

A solution to the problem with quiescent initial conditions and boundary conditions (37) and (38) is readily obtained by the method described. The initial uniaxial tensile stress is then added to obtain a solution to the original problem. Results obtained are not presented but are identical to those in [7] but were obtained with substantially less computational effort than by the method of near characteristics.

2 Waves Due to Suddenly Applied Normal Stress on Part of Circumference. The problem that we now consider involves normal tractions at $r = 1$, which are symmetric about $\theta = 0$, and zero shearing traction. The numerical results which are given are for plane strain, so that ν is replaced by $\nu/(1 - \nu)$ in the governing equations. A step function application of loading is assumed at $r = 1, 0 \leq |\theta| \leq \alpha$, of the form

$$\sigma_r(1, \theta, t) = \frac{1}{2}\left(1 + \cos\frac{\pi\theta}{\alpha}\right)\mathrm{H}(t), \quad |\theta| \leq \alpha,$$
$$= 0, \quad \alpha < |\theta| \leq \pi, \tag{39}$$
$$\tau_{r\theta}(1, \theta, t) = 0. \tag{40}$$

The Fourier coefficients, in equations (8) and (9), which correspond to equations (39) and (40) are

$$P_0 = \frac{\alpha}{2\pi}\mathrm{H}(t),$$
$$P_n = \frac{\sin n\alpha}{n\alpha}\left(\frac{\pi}{\pi^2 - n^2\alpha^2}\right)\mathrm{H}(t), \quad n = 1, 2, \ldots$$
$$P_n = \frac{\alpha}{2\pi}\mathrm{H}(t), \quad n = \pi/\alpha,$$
$$S_n = 0, \quad n = 0, 1, 2 \ldots \tag{41}$$

The coefficients given by equations (41) were used in the procedure already described and results were obtained for $\alpha = 60°$, for the stresses. A nondimensional time increment, $\Delta t = 0.01$, that is $AD = 0.02$ in Fig. 2, was used in the finite-difference form of equations (31)–(33), and the series was terminated at $n = 14$. For smaller values of the semiangle α, more terms are required since convergence of the Fourier series representation of equation (39) is slower, the smaller the value of α. Numerical instability is encountered in the numerical scheme, described in the previous section, beyond a certain value of t which decreases as n increases and as the increment Δt is increased. For values of n up to 14 and with an increment $t = 0.01$ it was verified that the numerical values of $\sigma_r{}^{(n)}$, $\sigma_\theta{}^{(n)}$, and $\tau_{r\theta}{}^{(n)}$ obtained from the method of characteristics approached closely the equilibrium values and no instability occurred for $t < 7$. The equilibrium values were obtained from a special case of a solution obtained by Michell [10].

The variations of the stresses, with time, for several points are shown graphically in Figs. 3–6. Equilibrium values, obtained from the solution of Michell [10] are also shown, and the time-dependent stresses approach these as time increases.

It is interesting to note that the arrival times of the disturbance, for points not in the region $r = 1, 60° \geq |\theta|$, are clearly evident in the figures.

Miklowitz [11] has given a solution, based on transform methods, for the problem of a normal line load of unit intensity at the cavity-surface. We can approach this problem by taking

$$\sigma_r(1, \theta, t) = \frac{1}{2\alpha}\left(1 + \cos\frac{\pi\theta}{\alpha}\right)\mathrm{H}(t), \quad |\theta| \leq \alpha$$
$$= 0, \quad \alpha < |\theta| \leq \pi,$$
$$\tau_{r\theta}(1, \theta, t) = 0, \tag{42}$$

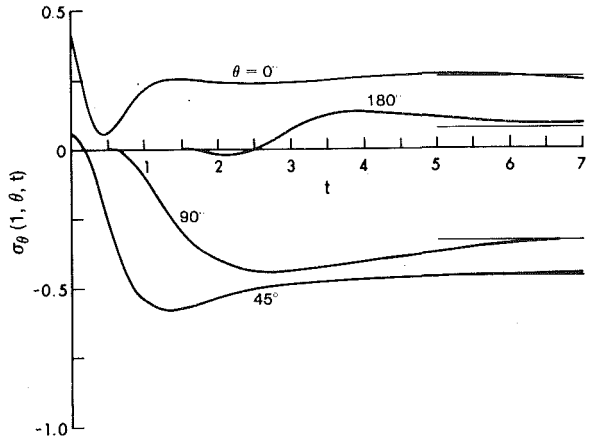

Fig. 3 Variation of nondimensional circumferential stress with nondimensional time at $r = 1$ for $\theta = 0°, 45°, 90°, 180°$

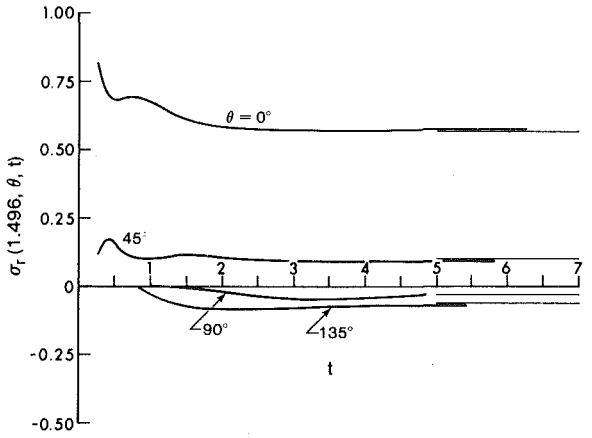

Fig. 4 Variation of radial stress with time at $r = 1.496$

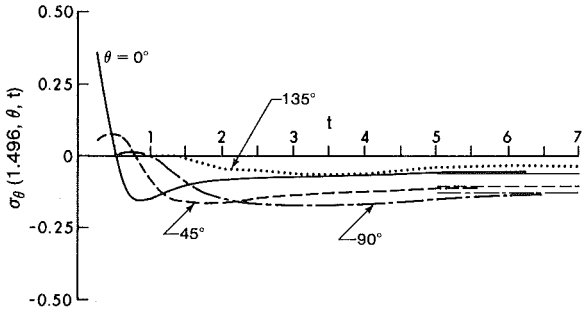

Fig. 5 Variation of circumferential stress with time at $r = 1.496$

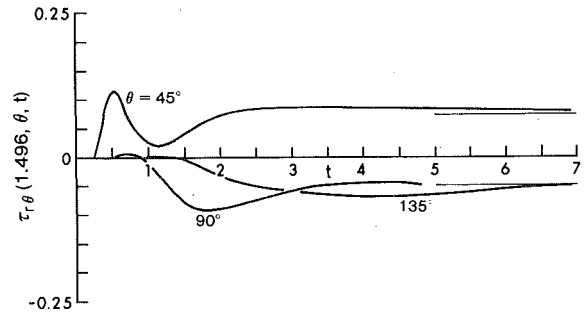

Fig. 6 Variation of shearing stress with time at $r = 1.496$

and letting α become small, however for small α, say $\alpha = 5°$ considerably more computational effort is required than for the example given. As α, in equation (42), approaches zero it is probable that an integral transform method with numerical inversion of the transforms, as described in [12], would require less computational time but more difficult analytical techniques. The method presented is not readily applicable to the limiting case of equation (42) as $\alpha \to 0$, which corresponds to a concentrated radial load of unit intensity, since the Fourier series (8) does not converge.

References

1 Kromm, A., "Zur Ausbreitung von Stosswellen in Kreislochschechen," *ZAMM*, Vol. 28, 1948, pp. 104–114.

2 Selberg, H. L., "Transient Compression Waves From Spherical and Cylindrical Cavities," *Archiv för Fysik*, Vol. 5, 1952, pp. 97–108.

3 Miklowitz, J., "Plane Stress Unloading Waves Emanating From a Suddenly Punched Hole in a Stretched Elastic Plate," ASME JOURNAL OF APPLIED MECHANICS, Vol. 27, 1960, pp. 165–171.

4 Chou, P. C., and Koenig, H. A., "A Unified Approach to Cylindrical and Spherical Elastic Waves by Method of Characteristics," ASME JOURNAL OF APPLIED MECHANICS, Vol. 33, 1966, pp. 159–167.

5 Eringen, A. C., "Propagation of Elastic Waves Generated by Dynamical Loads on Circular Cavity," ASME JOURNAL OF APPLIED MECHANICS, Vol. 28, 1961, pp. 218–222.

6 Ziv, M., "Two Spatial Dimensional Elastic Wave Propagation by the Theory of Characteristics," *International Journal of Solids and Structures*, Vol. 5, 1969, pp. 1135–1151.

7 Haddow, J. B., and Mioduchowski, A., "Waves From Suddenly Punched Hole in Plate Subjected to Uniaxial Tension Field," ASME JOURNAL OF APPLIED MECHANICS, Vol. 46, 1979, pp. 873–877.

8 Whitham, G. B., *Linear and Nonlinear Waves*, Wiley, 1974.

9 Keller, H., "Propagation of Stress Discontinuation in Inhomogeneous Elastic Media," *SIAM Review*, Vol. 6, 1964, pp. 356–382.

10 Michell, J. H., "On the Direct Determination of Stress in an Elastic Solid With Application to the Theory ol Plates," *Proceedings of the London Mathematical Society*, Vol. 31, 1899, pp. 100–124.

11 Miklowitz, J., *The Theory of Elastic Waves and Waveguides*, North-Holland, 1978.

12 Barclay, D. W., Moodie, T. B., and Haddow, J. B., "Analysis of Waves From Suddenly Punched Hole in an Axially Loaded Elastic Plate," *Wave Motion*, Vol. 3, 1981, pp. 105–113.

C.-Y. Wang
Professor,
Department of Mathematics,
Michigan State University,
E. Lansing, Mich. 48824

L. T. Watson
Associate Professor,
Department of Computer Science,
Virginia Polytechnic Institute
and State University,
Blacksburg, Va. 24061

Equilibrium of Heavy Elastic Cylindrical Shells

An originally circular, heavy elastic shell rests on a horizonal surface. The equilibrium shape is governed by the heavy elastica equations. The solutions depend heavily on the parameter B, which represents the relative importance of density and perimeter length to flexural rigidity. There are four distinct cases. A perturbation analysis is obtained for small B while a similarity solution exists for large B. The general solution is obtained by accurate numerical integration using a least change secant update quasi-Newton method and a new homotopy method.

Introduction

Consider a thin elastic originally circular cylindrical shell lying on a horizontal surface. Due to its own weight, the shell deforms into a noncircular shape (Fig. 1). The equilibrium of heavy elastic shells is important in the following areas: Thin shells intended for aquatic or space environments may not be able to support themselves on terrestrial ground. The shell may experience irreversible damage due to high local bending moments. On the other hand, the equilibrium shapes provide a means of testing the flexural rigidity of flimsy materials such as textile loops.

If the thickness of the shell is thin compared to its perimeter, the heavy elastica equations may be used to describe the equilibrium shape [1, 2]

$$EI\frac{d^2\theta}{ds'^2} = T\sin\theta + (F - \rho s')\cos\theta \tag{1}$$

$$\frac{dx'}{ds'} = \cos\theta, \quad \frac{dy'}{ds'} = \sin\theta \tag{2}$$

Here EI is the flexural rigidity, θ is the local angle of inclination, ρ is the weight per perimeter length of the material, s' is the arc length, x' and y' are Cartesian coordinates, T and F are the horizontal and vertical forces at $s' = 0$, respectively (Fig. 1). We normalize all lengths by the half perimeter length L

$$s = s'/L, \quad x = x'/L, \quad y = y'/L \tag{3}$$

Equations (1) and (2) become

$$\frac{d^2\theta}{ds^2} = A\sin\theta + (C - Bs)\cos\theta \tag{4}$$

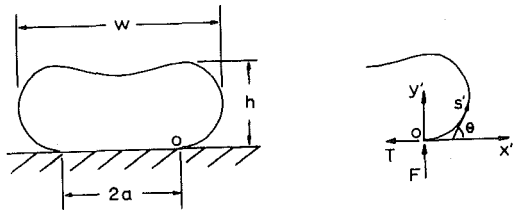

Fig. 1 The coordinate system

$$\frac{dx}{ds} = \cos\theta, \quad \frac{dy}{ds} = \sin\theta \tag{5}$$

where

$$A \equiv \frac{TL^2}{EI}, \quad B \equiv \frac{\rho L^3}{EI}, \quad C = \frac{FL^2}{EI} \tag{6}$$

Equations (4), (5) are strongly nonlinear and closed-form solutions do not exist.

The Boundary Conditions

The most important parameter is B, representing the importance of density and length to flexural rigidty. $B^{1/3}$ is the ratio of half perimeter length L to "bending length" $(EI/\rho)^{1/3}$. When B is zero, gravity has no effect and we expect the shape to be a perfect circle. As B increases we have the following four distinct cases (Fig. 2).

Case I. One Point Contacts Ground. In this case $F = \rho L$ or $C = B$. The boundary conditions are

$$s = 0, \quad \theta = x = \quad y = 0 \tag{7}$$

$$s = 1, \quad \theta = \pi, \quad x = 0 \tag{8}$$

The five unknowns are θ, $d\theta/ds$, x, y, A.

Case II. One Segment Contacts Ground. Let $2a$ be the contact width. The vertical force at $s = 0$ is then $\rho L(1 - a)$ or $C = (1 - a)B$. The six boundary conditions are

Contributed by the Applied Mechanics Division for publication in the JOURNAL OF APPLIED MECHANICS.
Discussion on this paper should be addressed to the Editorial Department, ASME, United Engineering Center, 345 East 47th Street, New York, N. Y. 10017, and will be accepted until December 1, 1981. Readers who need more time to prepare a discussion should request an extension from the Editorial Department. Manuscript received by ASME Applied Mechanics Division, September, 1980; final revisions, March, 1981.

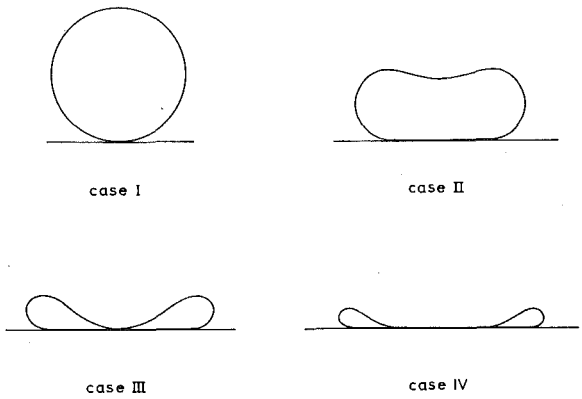

Fig. 2 The four cases

$$s = 0, \qquad \theta = d\theta/ds = x = y = 0$$
$$s = 1 - a, \quad x = -a, \quad \theta = \pi \tag{9}\ (10)$$

The six unknowns are θ, $d\theta/ds$, x, y, A, and a.

Case III. One Segment Plus One Point Contact Ground. The seven boundary conditions are

$$s = 0, \qquad \theta = d\theta/ds = x = y = 0$$
$$s = 1 - a, \quad x = -a, \quad y = 0, \quad \theta = \pi \tag{11}\ (12)$$

The seven unknowns are θ, $d\theta/ds$, x, y, A, a, and C.

Case IV. Two Segments Contact Ground. The seven boundary conditions are

$$s = 0, \quad \theta = d\theta/ds = x = y = 0$$
$$s = b, \quad y = d\theta/ds = 0, \quad \theta = \pi \tag{13}\ (14)$$

The seven unknowns are θ, $d\theta/ds$, x, y, A, b, and C.

Approximate Solution for Small B

When B is small, the effects of gravity are much smaller than the effects of stiffness. We expect Case I, small A, and the cylinder would be almost circular in shape. Let

$$B \equiv \epsilon \ll 1, \quad A \equiv \alpha\epsilon \tag{15}$$

where α is a constant of order unity. Equation (4) becomes

$$d^2\theta/ds^2 = \epsilon\alpha \sin\theta + \epsilon(1 - s)\cos\theta \tag{16}$$

We also perturb θ, x, y, and α

$$\theta = \theta_0(s) + \epsilon\theta_1(s) + \ldots \tag{17}$$
$$x = x_0(s) + \epsilon x_1(s) + \ldots \tag{18}$$
$$y = y_0(s) + \epsilon y_1(s) + \ldots \tag{19}$$
$$\alpha = \alpha_0 + \epsilon\alpha_1 + \ldots \tag{20}$$

Substitution into equations (5), (7), (8), and (16) yields the following successive equations:

$$\frac{d^2\theta_0}{ds^2} = 0, \quad \frac{dx_0}{ds} = \cos\theta_0, \quad \frac{dy_0}{ds} = \sin\theta_0 \tag{21}$$
$$\theta_0(0) = x_0(0) = y_0(0) = 0, \quad \theta(1) = \pi, \quad x_0(1) = 0 \tag{22}$$

The zeroth-order solution is the circle

$$\theta_0 = \pi s, \quad x_0 = \frac{\sin\pi s}{\pi}, \quad y_0 = \frac{1 - \cos\pi s}{\pi} \tag{23}$$

The first-order equations are

$$d^2\theta_1/ds^2 = \alpha_0 \sin\theta_0 + (1 - s)\cos\theta_0 \tag{24}$$
$$dx_1/ds = -\theta_1 \sin\theta_0, \quad dy_1/ds = \theta_1 \cos\theta_0 \tag{25}$$
$$\theta_1(0) = x_1(0) = y_1(0) = \theta_1(1) = x_1(1) = 0 \tag{26}$$

The solution is

$$\theta_1 = \frac{-3}{2\pi^3}\sin\pi s + \frac{1}{\pi^2}(s - 1)(\cos\pi s - 1), \quad \alpha_0 = -\frac{1}{2\pi} \tag{27}$$

$$x_1 = \frac{1}{4\pi^3}(s - 1)(\cos 2\pi s + 3 - 4\cos\pi s) + \frac{1}{\pi^4}(\sin\pi s - \frac{1}{2}\sin 2\pi s) \tag{28}$$

$$y_1 = \frac{1}{2\pi^4}\cos 2\pi s - \frac{1}{\pi^4}\cos\pi s + \frac{(s - 1)}{4\pi^3}\sin 2\pi s - \frac{(s - 1)}{\pi^3}\sin\pi s + \frac{s^2 - 2s}{4\pi^2} + \frac{1}{2\pi^4} \tag{29}$$

Now $d\theta/ds$ represents the local moment normalized by EI/L. We find from equations (23) and (27)

$$\left.\frac{d\theta}{ds}\right|_{\max} = \pi + \epsilon\left[\frac{-1}{2\pi^2}\cos\pi s - \frac{1}{\pi^2} + \frac{(1 - s)}{\pi}\sin\pi s\right]_{s=0.415393} + O(\epsilon^2)$$
$$= \pi + 0.0649225\,\epsilon + O(\epsilon^2) \tag{30}$$

$$\frac{d\theta}{ds}(0) = \pi - \frac{3}{2\pi^2}\epsilon + O(\epsilon^2) \tag{31}$$

$$\frac{d\theta}{ds}(1) = \pi - \frac{1}{2\pi^2}\epsilon + O(\epsilon^2) \tag{32}$$

The maximum height is at $s = 1$

$$h = \frac{2}{\pi} - \left(\frac{1}{4\pi^2} - \frac{2}{\pi^4}\right)\epsilon + O(\epsilon^2) \tag{33}$$

The maximum width is at $\theta = \pi/2$. Using equations (17), (23), and (27), we obtain the arc length at which it occurs.

$$s = \frac{1}{2} + \left(\frac{3}{2\pi^4} - \frac{1}{2\pi^3}\right)\epsilon + O(\epsilon^2) \tag{34}$$

Substitution of equation (34) into equations (18), (23), and (28) yields the maximum width

$$w \equiv 2x|_{\theta=\pi/2} = \frac{2}{\pi} + \left(\frac{2}{\pi^4} - \frac{1}{2\pi^3}\right)\epsilon + O(\epsilon^2) \tag{35}$$

The maximum height to maximum width ratio is

$$\frac{h}{w} = 1 - \left(\frac{1}{8\pi} - \frac{1}{4\pi^2}\right)\epsilon + O(\epsilon^2) \tag{36}$$

Similarity Solution for Large B

When B is very large the effect of rigidity is relatively small and we expect Case IV to occur. The problem is simplified further as follows. We multiply equation (4) by $d\theta/ds$ and integrate once to obtain

$$\frac{1}{2}\left(\frac{d\theta}{ds}\right)^2 = -A\cos\theta + C\sin\theta - B(s\sin\theta - y) + D \tag{37}$$

where D is a constant of integration. Using equations (13) and (14)

$$y = d\theta/ds = 0 \quad \text{at} \quad \theta = 0 \quad \text{and at} \quad \theta = \pi \tag{38}$$

we find

$$A = D = 0. \tag{39}$$

Thus equation (4) reduces to

$$d^2\theta/ds^2 = (C - Bs)\cos\theta \tag{40}$$

Now let

$$\bar{s} \equiv B^{1/3}s, \quad \bar{C} = B^{-2/3}C, \quad \bar{x} = B^{1/3}x, \quad \bar{y} = B^{1/3}y \tag{41}$$

which yields

$$d^2\theta/d\bar{s}^2 = (\bar{C} - \bar{s})\cos\theta \tag{42}$$
$$d\bar{x}/d\bar{s} = \cos\theta, \quad d\bar{y}/d\bar{s} = \sin\theta. \tag{43}$$

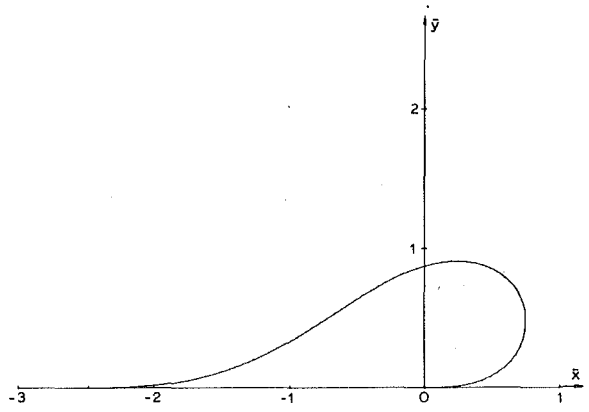

Fig. 3 The similarity shape for Case IV

The number of boundary conditions is thus reduced to five

$$\bar{s} = 0, \quad \theta = d\theta/d\bar{s} = \bar{x} = \bar{y} = 0 \tag{44}$$

$$\theta = \pi, \quad \bar{y} = 0 \tag{45}$$

since $d\theta/d\bar{s} = 0$ at $\theta = \pi, \bar{y} = 0$ is automatically satisfied by (37).

By trying different values of $\bar{C}$, we integrate equations (42)–(44) by the variable step Runge-Kutta algorithm until equation (45) is satisfied. We obtain

$$\bar{C} = 3.7450050 \tag{46}$$

The solution is similar, i.e., valid for all large B. The similarity shape is shown in Fig. 3. Other pertinent values are

$$\bar{x}_{\max} = 0.7572519, \quad \bar{x}_{\min} = -2.4844776 \tag{47}$$

$$\bar{y}_{\max} = 0.9065969, \quad \bar{s}_{\max} = 4.6833276 \tag{48}$$

The maximum moment, occurring at $\theta = \pi/2$, is

$$\left.\frac{d\theta}{d\bar{s}}\right|_{\max} = 2.5337470 \tag{49}$$

or

$$\left.\frac{d\theta}{ds}\right|_{\max} = 2.533747\, B^{1/3} \tag{50}$$

The maximum height is

$$h = 0.90660\, B^{-1/3} \tag{51}$$

The maximum width is

$$w = 1 + |x_{\min}| + 2x_{\max} - s_{\max}$$
$$= 1 - 0.68435\, B^{-1/3} \tag{52}$$

Similarly the base width is

$$w_{\text{base}} = 1 - 2.19885\, B^{-1/3} \tag{53}$$

The height to width ratio is

$$\frac{h}{w} = \frac{0.90660}{B^{1/3} - 0.68435} \tag{54}$$

Notice equations (50)–(54) are exact and are not expansions for large B. The similarity equations (42)–(45) were first integrated by Stuart [3] using a finite-difference algorithm. Stuart's values of $\bar{y}_{\max} = 0.9066$ and $\bar{s}_{\max} = 4.683459$ are extremely close to our equation (48).

Numerical Solution

For intermediate values of B, especially Cases II and III, numerical integration is necessary. We shall describe the numerical methods for Cases I, II, and III which are much more difficult than the previously discussed method for Case IV.

Table 1 Some representative numerical values; ℓ = free length/2

B	A	C	L/L
0.0000	0.00000	0.0000	1.00000
10.0000	-1.78903	10.0000	1.00000
18.3865	-3.68877	18.3865	1.00000
100.000	-11.0628	73.7308	0.737308
176.106	4.57499	121.978	0.692639
250.000	1.68826	150.045	0.673890
368.307	0.00000	192.424	0.653378
2000.00	0.00000	594.483	0.371716

For Case I, let

$$\upsilon_{\text{I}} = (A, \theta'(0)), \tag{55}$$

and $x(s;\upsilon_{\text{I}}), y(s;\upsilon_{\text{I}}), \theta(s;\upsilon_{\text{I}})$ be the solution to the initial value problem given by equations (4)–(5) with initial conditions (7) and (55). Then the two-point boundary-value problem equations (4), (5), (7), and (8) is equivalent to

$$F_{\text{I}}(\upsilon_{\text{I}}) = \begin{pmatrix} x(1;\upsilon_{\text{I}}) \\ \theta(1;\upsilon_{\text{I}}) - \pi \end{pmatrix} = 0 \tag{56}$$

Solving the nonlinear system equation (56) amounts to determining the correct parameters and initial conditions such that the boundary conditions are satisfied. The appropriate variables and nonlinear system for Case II are

$$\upsilon_{\text{II}} = (A, a) \tag{57}$$

$$F_{\text{II}}(\upsilon_{\text{II}}) = \begin{pmatrix} x(1-a;\upsilon_{\text{II}}) + a \\ \theta(1-a;\upsilon_{\text{II}}) - \pi \end{pmatrix} = 0; \tag{58}$$

and for Case III

$$\upsilon_{\text{III}} = (A, a, C) \tag{59}$$

$$F_{\text{III}}(\upsilon_{\text{III}}) = \begin{pmatrix} x(1-a;\upsilon_{\text{III}}) + a \\ y(1-a;\upsilon_{\text{III}}) \\ \theta(1-a;\upsilon_{\text{III}}) - \pi \end{pmatrix} = 0. \tag{60}$$

The notation $\upsilon, F(\upsilon)$ will be used generically to refer to any of the three cases equations (55)–(60).

Our methods require the Jacobian matrix $DF(\upsilon)$ of $F(\upsilon)$. For example, for $F_{\text{I}}(\upsilon_{\text{I}})$, this is

$$DF_{\text{I}}(\upsilon_{\text{I}}) = \begin{vmatrix} \dfrac{\partial x(1;\upsilon_{\text{I}})}{\partial A} & \dfrac{\partial x(1;\upsilon_{\text{I}})}{\partial(\theta'(0))} \\ \dfrac{\partial \theta(1;\upsilon_{\text{I}})}{\partial A} & \dfrac{\partial \theta(1;\upsilon_{\text{I}})}{\partial(\theta'(0))} \end{vmatrix} \tag{61}$$

Consider the initial value problem

$$\frac{dz_1}{ds} = \cos z_3, \quad \frac{dz_2}{ds} = \sin z_3, \quad \frac{dz_3}{ds} = z_4$$

$$\frac{dz_4}{ds} = A \sin z_3 + (C - Bs)\cos z_3$$

$$\frac{dz_5}{ds} = -z_7 \sin z_3, \frac{dz_6}{ds} = z_7 \cos z_3, \frac{dz_7}{ds} = z_8$$

$$\frac{dz_8}{ds} = Az_7 \cos z_3 + \sin z_3 - (C - Bs)z_7 \sin z_3 \tag{62}$$

$$z_1(0) = z_2(0) = z_3(0) = z_5(0) = z_6(0) = z_7(0) = z_8(0) = 0$$
$$z_4(0) = \upsilon_{1,2} \tag{63}$$

Then $z_5 = \partial x/\partial A$ and $z_7 = \partial\theta/\partial A$. The other partials of F are calculated similarly. These differential equations are solved by a very efficient variable order, variable step ODE algorithm, and computing these partials is not as expensive as it might appear.

The equation $F(\upsilon) = 0$ was solved by either a quasi-Newton or a new homotopy method, depending on the case and circumstances. These

two methods are described in the following. Whenever a quasi-Newton method converges, it is much more efficient than a homotopy method. However, even the best quasi-Newton algorithms sometimes fail, and then another algorithm, like the globally convergent homotopy algorithm proposed here, becomes necessary. Basically, our approach was to try the quasi-Newton first and then use the (much more expensive) homotopy algorithm wherever the quasi-Newton method failed.

Case I is fairly easy, and was solved entirely by the quasi-Newton method. Case II yields to quasi-Newton for $B < 100$, but for $B > 100$ it requires an initial estimate so close to the true solution as to be impractical (e.g., starting from the solution for $B = 100$, it failed for $B = 101$). The homotopy algorithm was used for Case II ($B > 100$), and most of Case III. Accurate B-values for the boundaries between the cases were determined by the secant method using quasi-Newton for the required function values. Essentially, quasi-Newton was used to home in on the case boundaries and homotopy was used in between the boundaries.

The quasi-Newton algorithm used was the code HYBRJ from the MINPACK package developed at Argonne National Laboratory. This method [4, 5] approximates the Jacobian matrix $DF(v)$ of $F(v)$ relatively cheaply, is reliable, robust, and does not require good initial estimates in general. Conceptually, a quasi-Newton algorithm operates as follows:

1 Start with an estimate B_0 of the Jacobian matrix and an estimate v_0 of the solution. For $i = 0, 1, 2, \ldots$, until convergence, do
2 Compute a search direction p_i by solving $B_i p_i = -F(v_i)$.
3 Compute the next approximation

$$v_{i+1} = v_i + t_i p_i, \tag{64}$$

where t_i is chosen to minimize $\|F(v_i + tp_i)\|$ in some "trust region" [4, 5].
4 Update the Jacobian approximation by

$$B_{i+1} = B_i + M, \tag{65}$$

where M is an easily and efficiently computed combination of rank one matrices, elementary matrices, and B_i. See Dennis and Moré [5] for the precise form of M.

The homotopy algorithm used was the code FIXPT from Watson and Fenner [6]. This powerful method is globally convergent (under farily general hypotheses) and thus does not require a close initial guess. Versions of the method have been previously applied to fluid mechanics [7], nonlinear complementarity [8], fixed point [9], and continuum mechanics problems [10]. The homotopy algorithm is applied to the nonlinear system of equations $F(v) = 0$. The theoretical justification of the algorithm requires fairly deep differential geometry, although the algorithm itself is deceptively simple. Thorough discussions of both the theory and some applications can be found in [6–11].

Define a homotopy map φ_w: $[0, 1) \times E^n \to E^n$ (where $n = 2$ or 3 depending on the case) by

$$\varphi_w(\lambda, v) = \varphi(w, \lambda, v) = \lambda F(v) + (1 - \lambda)(v - w). \tag{66}$$

The supporting theory [9] says that for almost all w (i.e., all w except possibly those in a set of Lebesgue measure zero), the Jacobian matrix $D\varphi_w$ of φ_w has full rank on

$$\varphi_w^{-1}(0) = \{(\lambda, v) | 0 \le \lambda < 1, \quad v \in E^n, \quad \varphi_w(\lambda, v) = 0\}, \tag{67}$$

the set of zeros of φ_w in λ, v space. The full rank condition implies that the zero set of φ_w consists of smooth disjoint curves which cannot just "stop" in the interior of $(0, 1) \times E^n$. The hope is that there is a zero curve γ of φ_w reaching from a trivial known solution (at $\lambda = 0$) to the desired solution (at $\lambda = 1$). Such a zero curve exists under fairly general hypotheses, but they are often difficult to verify for practical problems. Nevertheless, the homotopy method works well in practice.

The algorithm is conceptually simple: track the zero curve γ of φ_w emanating from $(0, w)$ until a point $(1, \bar{v})$ is reached. Then, by equation (66), $\bar{v}$ solves $F(v) = 0$, hence also the original two-point boundary-value problem. This algorithm differs significantly from standard continuation in that λ need not increase along γ, and there are never any "singular points" along γ [9]. The power of the algorithm derives from this ability of λ to both increase and decrease along γ, with turning points posing no special difficulty. Parameterize γ by arc length x so $\lambda = \lambda(r)$, $v = v(r)$ along γ. Then γ is the trajectory of the initial value problem

$$\frac{d}{dr}\varphi_w(\lambda(r), v(r)) = 0, \tag{68}$$

$$\left(\frac{d\lambda}{dr}\right)^2 + \left\|\frac{dv}{dr}\right\|^2 = 1, \tag{69}$$

$$\lambda(0) = 0, \quad v(0) = w, \tag{70}$$

where r is arc length along γ. Equation (68) is

$$D\varphi_w(\lambda(r), v(r)) \begin{pmatrix} \frac{d\lambda}{dr} \\ \frac{dv}{dr} \end{pmatrix} = 0, \tag{71}$$

where $D\varphi_w$ is the $n \times (n + 1)$ Jacobian matrix of φ_w. $D\varphi_w$ has full rank on the zero curve γ given parametrically by $\lambda(r), v(r)$. Thus the derivative $(d\lambda/dr, dv/dr)$ is calculated by numerically finding the kernel of $D\varphi_w$, and then using equation (69) and the continuity of the derivative [6, 9]. A sophisticated variable step, variable order ordinary differential equation solver (as in [12]) is used to solve equations (68)–(70), where the derivatives required by the ODE solver are calculated as just described. Such an ODE solver is very efficient [12], and considerable computational experience indicates that this approach is superior to schemes using Newton's method and/or simpler ODE techniques to track γ [9, 11].

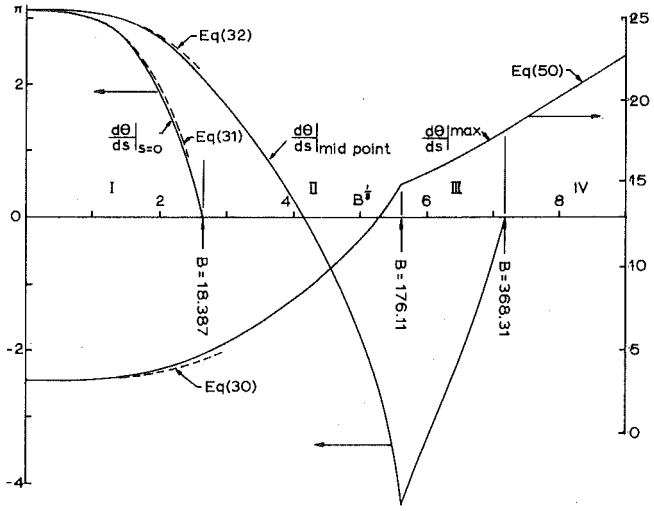

Fig. 4 Local bending moments as a function of $B^{1/3}$

Results and Discussion

The case boundaries are found to be

Case I	$0 \le B \le 18.38654$
Case II	$18.38654 \le B \le 176.10643$
Case III	$176.10643 \le B \le 368.30735$
Case IV	$368.30735 \le B \le \infty$

Fig. 4 shows some normalized local moments plotted against $B^{1/3}$, the ratio of half perimeter length to bending length. The corresponding case boundaries are at $B^{1/3} = 2.63937, 5.60521, 7.16809$. Notice that as B is increased, the slope of the moment curves show abrupt changes at the case boundaries.

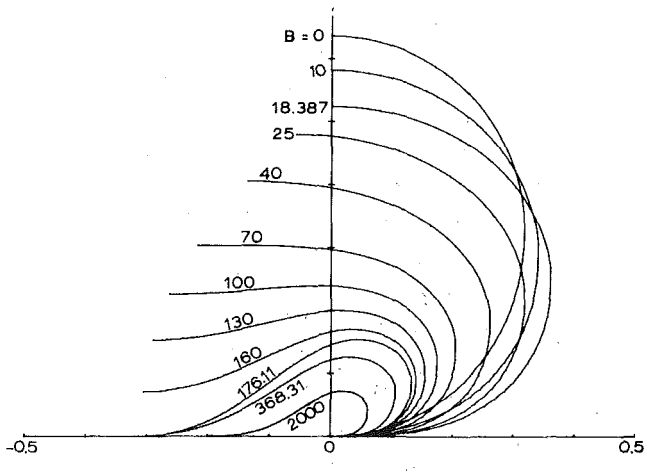

Fig. 5 The equilibrium shapes

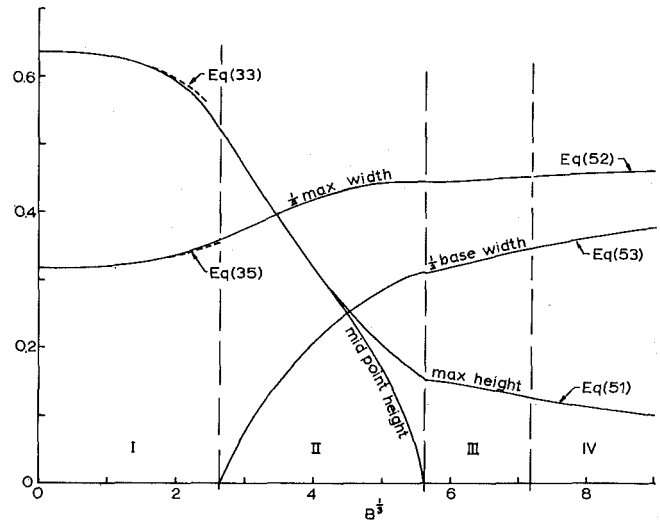

Fig. 6 The dimensions

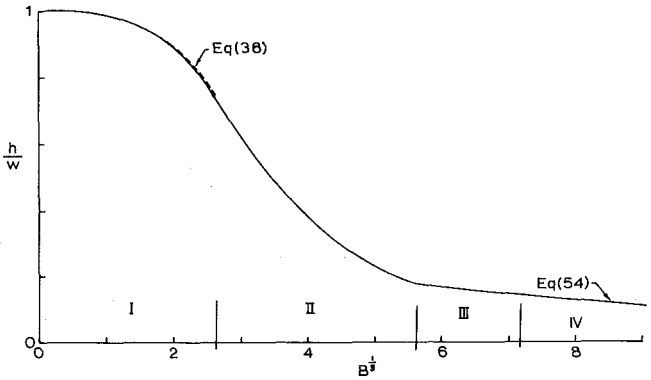

Fig. 7 The ratio of maximum height h to maximum width w as a function of $B^{1/3}$

Fig. 5 shows the integrated shapes for various B. Only the right half is shown since the configuration is symmetric. Fig. 6 shows the dimensions of the configurations. For $B^{1/3} \geq 4.12$ the midpoint height no longer represents the maximum height since the curvature becomes negative at the midpoint.

Fig. 7 is useful in the determination of the flexural rigidity of heavy elastic cylinders. Since maximum height h, maximum width w, perimeter length L, and density ρ can be easily measured, Fig. 7 yields EI, the flexural rigidity. Stuart [3] proposed a similar method, but his analysis can only be applied to Case IV, the extremely flimsy cylindrical shells.

From Figs. 4, 6, and 7, we see our approximate solutions for small B compare well with the exact numerical solution for almost the entire range of Case I. This is because the constant coefficients in our first-order solutions are small, thus extending the range of validity to values of B larger than unity.

References

1 Bickley, W. G., "The Heavy Elastica," *Philosophical Magazine*, Series 7, Vol. 17, 1934, pp. 603–622.

2 Frisch-Fay, R., *Flexible Bars*, Butterworths, Washington, D.C., 1962, Chapter 5.

3 Stuart, I. M., "A Loop Test for Bending Length and Rigidity," *British Journal of Applied Physics*, Vol. 17, 1966, pp. 1215–1220.

4 Moré, J. J., MINPACK documentation, Argonne National Laboratory, Argonne, Ill., 1979.

5 Dennis, J. E., and Moré, J. J., "Quasi-Newton Methods—Motivation and Theory," *SIAM Review*, Vol. 19, 1977, pp. 46–79.

6 Watson, L. T., and Fenner, D., "Chow-Yorke Algorithm for Fixed Points or Zeros of C^2 Maps, *ACM Trans. Math. Software*, Vol. 6, 1980, pp. 252–260.

7 Watson, L. T., Li, T. Y., and Wang, C. Y., "Fluid Dynamics of the Elliptic Porous Slider," ASME JOURNAL OF APPLIED MECHANICS, Vol. 45, 1978, pp. 435–436.

8 Watson, L. T., "Solving the Nonlinear Complementarity Problem by a Homotopy Method," *SIAM Journal of Control Optimization*, Vol. 17, 1979, pp. 36–46.

9 Watson, L. T., "A Globally Convergent Algorithm for Computing Fixed Points of C^2 Maps," *Appl. Math. Comput.*, Vol. 5, 1979, pp. 297–311.

10 Watson, L. T., and Yang, W. H., "Optimal Design by a Homotopy Method," *Applicable Anal.*, Vol. 10, 1980, pp. 275–284.

11 Watson, L. T., "An Algorithm That Is Globally Convergent With Probability One for a Class of Nonlinear Two-Point Boundary-Value Problems," *SIAM Journal Numer. Anal.*, Vol. 16, 1979, pp. 394–401.

12 Shampine, L. F., and Gordon, M. K., *Computer Solution of Ordinary Differential Equations: The Initial Value Problem*, Freeman, San Francisco, 1975.

T. J. R. Hughes
Associate Professor of Mechanical Engineering.
Assoc. Mem. ASME

T. E. Tezduyar
Research Assistant.

Division of Applied Mechanics,
Stanford University,
Durand Building, Room 252,
Stanford, Calif. 94305

Finite Elements Based Upon Mindlin Plate Theory With Particular Reference to the Four-Node Bilinear Isoparametric Element

Concepts useful for the development of Mindlin plate elements are explored. Interpolatory schemes and nodal patterns which are ideal according to the proposed criteria are found to be somewhat more complicated than desirable for practical applications. However, these ideas are found to be useful as starting points in the development of simpler elements. This is illustrated by the derivation of a new four-node bilinear quadrilateral which achieves good accuracy without ostensible defect.

1 Introduction

There has been considerable effort of late directed toward the development of improved plate and shell finite elements. Much of this effort has been focused upon theories which include transverse shear strain effects, for physical and computational reasons [22]. As a basis for the development of "displacement" plate elements of this type, the Mindlin theory [35] serves as the canonical starting point. Analogous, but generalized, theories may be used as the basis of shell element formulations. The "degeneration concept" is the terminology often applied to these ideas [1]. The literature on this topic, although mostly recent, has already become extensive. The interested reader may consult works among the following (incomplete) bibliography to familiarize himself with developments in this area: [6, 8, 9, 14–16, 19–25, 28, 29, 31, 37, 39–45, 49–52, 54, 56]. Although general improvement in element behavior is being sought, particular emphasis of late has been placed on reliability (i.e., making elements "fool proof") and simplicity. This latter requirement is an essential one in nonlinear analysis and especially in nonlinear transient analysis. Here, cost is the overriding consideration, and simple, inexpensive elements are actively sought after. Until fairly recently, there really was no plate or shell element which was sufficiently simple and inexpensive to be considered viable for large-scale nonlinear transient problems. However, the situation appears to be changing considerably as many efforts in the direction of simplicity have been performed (for a sampling of the literature on this topic, we may mention [3, 5, 7, 8, 17, 23–26, 28, 29, 31, 52, 54]). Progress is being made on many fronts, although a consensus favoring a particular approach is not yet in evidence. Efforts of ours in this area have employed reduced and selective integration techniques (see e.g., [22–26]), a topic which has generated considerable literature in recent years.

Unfortunately, efforts to develop effective simple elements (e.g., 3-node triangles, 4-node quadrilaterals) often engender conceptual complexity. To make simple functions and nodal patterns work well seems to require the use of special procedures, or "tricks," depending on one's viewpoint. These encumbrances are quite puzzling to the nonspecialist and even create controversy among specialists.

One of the purposes of this paper, is to attempt to provide some explanation why special techniques are necessary for the development of simple, effective elements within the context of Mindlin plate theory. Based upon an idea due to MacNeal [31], we propose criteria for the development of Mindlin plate elements. Interpreted strictly, not allowing for reduced/selective integration or allied procedures, the interpolation schemes suggested involve different order polynomials for displacement and rotation, and consequently different nodal patterns. Thus it may be argued that "natural" elements, from the standpoint of the performance criterion, are neither natural nor convenient from implementational and practical standpoints. It is thus no wonder that elements of this type have apparently not been investigated heretofore. The traditionally used alternative of equal-order interpolation, if to be optimally effective, requires additional embellishments. This is acknowledged by a weakened version of the criterion, which accommodates the use of special techniques, such as reduced/selective integration. This form is, in fact, the one used by MacNeal [31].

These thoughts are, at first, somewhat disconcerting since they seem to imply that elements which should work well, within the standard Ritz-Galerkin framework, are not practically desirable. However, it is felt that there are lessons to be learned from these elements in that they may serve as conceptual starting points for elements which are simpler than their progenitors. We use this idea to generate a new four-node quadrilateral which employs bilinear iso-

Contributed by the Applied Mechanics Division for publication in the JOURNAL OF APPLIED MECHANICS.

Discussion on this paper should be addressed to the Editorial Department, ASME, United Engineering Center, 345 East 47th Street, New York, N. Y. 10017, and will be accepted until December 1, 1981. Readers who need more time to prepare a discussion should request an extension from the Editorial Department. Manuscript received by the Applied Mechanics Division, December, 1980; final revision, February, 1981.

parametric shape functions for all dependent variables. The element possesses correct rank and thus cures the spurious zero-energy mode problem which has beleaguered our previous endeavors on four-node plates [22, 26]. The new element turns out to have some features in common with MacNeal's QUAD4 [31], although it is felt that several advantages are accrued in the present formulation. These are mentioned as follows:

The development of the element for the general quadrilateral configuration is different from MacNeal's and appears to preclude some of the complications alluded to in [31]. In particular, no special local Cartesian system is necessary for effectuating good element behavior, or for achieving an invariant formulation.

In nonlinear analysis, the entire strain and stress tensors need to be calculated at each evaluation point. A shortcoming of what may be described as the classical selective integration procedure is that different components are calculated at different points, thus precluding straightforward generalization to nonlinear analysis. Recently, a generalization of selective integration has been developed which enables the pointwise definition of all strain, and consequently stress, components [18, 23]. The present element was developed within this format and thus may be straightforwardly generalized to the nonlinear case. This does not appear to be the case for QUAD4, in which a complicated variant on the selective integration theme is employed.

We have avoided the use of any *ad hoc* modification to attain special behavior under certain circumstances. Robinson [45] has criticized QUAD4 on this point because of its tunable aspect ratio parameter whose value is selected to give acceptable test results in certain single element test cases. Although we are sympathetic of efforts to improve high aspect ratio behavior, *ad hoc* techniques of this kind, based on linear test cases, become suspect in generalizing to nonlinear analysis, and even in linear cases, improvement in one situation may result in deterioration in another. (An example of this phenomenon is presented in Section 5.6, "The Twisted Ribbon.") Presently, aspect ratio deterioration is an ubiquitous, but poorly understood finite-element phenomenon.

Another area in which we have opted for simplicity, compared with QUAD4, is in the calculation of bending strains. MacNeal develops a special selective integration procedure to accurately represent certain cubic bending modes. (Herein we refer to these as "Kirchhoff modes," see Section 2.) MacNeal goes on to show that full cubic behavior is unattainable, despite the introduction of a further complication, namely, modification of stiffness parameters via so-called "residual bending flexibility." Since an order-of-accuracy improvement is not achieved, it is felt that the additional complications are unwarranted. Admittedly, the price is not high in linear analysis; however, in nonlinear analysis it is not at all clear what can even be done along these lines. Consequently, standard procedures are employed herein to calculate bending strains.

An outline of the remainder of the paper is given as follows. In Section 2, criteria for designing effective Mindlin plate elements are discussed. A link between function approximation (i.e., order of accuracy) and special techniques, such as reduced/selective integration, is incorporated in the criteria. Element interpolatory schemes and nodal pattterns, suggested by these ideas, are presented.

Using one of the elements as a conceptual starting point, the new four-node bilinear quadrilateral plate is developed in Section 3. The only nonstandard feature of the development is the way transverse shear strains are interpolated, which is presented in detail in Section 3. In Section 4, implementational ideas are discussed. The special treatment of transverse shear strains manifests itself in the definition of the well-known "B-matrix" (i.e., strain-nodal displacement matrix) of finite-element theory. The modification falls within the framework presented in [18, 23]. In Section 4, numerical examples illustrate the good overall behavior of the element. Since it is now well known that plate/shell elements may behave well on one problem and pathologically on another, an extensive set of problem results is presented. The studies range from standard convergence tests to difficult problems, incorporating singular behavior, which tend to manifest element weaknesses. In addition, we consider a single-element test proposed by Robinson [45] as a critical measure of the performance of a plate bending element. Conclusions are presented in Section 6.

It is felt that some of the ideas presented herein significantly contribute to the understanding of plate element design and behavior. Many new element possibilities arise in the presentation which will no doubt be the objects of future studies. Furthermore, it is hoped that analogous concepts will be useful in the study of related problem areas, such as continuum elements for incompressible, and nearly incompressible, behavior (see, e.g., [4, 12, 18, 19, 32–34, 36, 38, 48]).

The new four-node bilinear element developed herein is a decent performer. The overall accuracy level of the element appears to be good, without any ostensible defect, and this is accomplished while retaining simplicity. Nevertheless, it is not claimed to be a panacea. For example, its aspect ratio behavior on some problems is disappointing. Perhaps further improvement may be made here. On balance, however, it appears as good as any four-node element we have seen, perhaps better. It is a common practice for the developers of elements to see only the virtues of their own work, and only the sins of others, so we shall not belabor this point, leaving it for the reader to decide what is most appropriate for his/her circumstances.

2 Criteria for Designing Effective Mindlin Plate Elements

The first criterion which shed some light on the design of Mindlin plate elements was the method of constraint counting. This was employed in the investigations of Malkus and Hughes [34], Hughes, Cohen, and Haroun [22], and several studies of Hinton, Zienkiewicz, and colleagues (see, e.g., [42, 55]). Although helpful in predicting the performance of many plate elements, for some time it has been known that an overly pessimistic assessment may be obtained in certain situations. Recently, Spilker and Munir [49–51] have proposed a modified constraint counting measure, called a "rotational constraint index," which has achieved better correlation for the performance of hybrid plate elements.

The criterion advocated herein is based upon the ideas originally presented by MacNeal [31] and employed by Parisch [39]. Thin plate behavior is governed by the classical Poisson-Kirchhoff theory. In this limiting situation the face rotations become equal to the slopes of the transverse displacement field. Analytically, the rotations are no longer independent kinematic variables, but become the derivatives of the transverse displacement field. To assess the ability of Mindlin-type plate elements to correctly handle limiting thin-plate behavior, we shall examine the Mindlin elements with respect to the modes of deformation emanating from the classical theory.

To be more precise, let us define a *Kirchhoff mode* by the relation

$$\theta_\alpha = w_{,\alpha} \tag{1}$$

where w is a given transverse displacement; θ_α is the x_α-rotation, $\alpha = 1, 2$; and a comma is used to denote partial differentiation (e.g., $w_{,\alpha} = \partial w/\partial x_\alpha$).

A *Kirchhoff mode of order m* will be one in which w is taken to be a complete mth-order polynomial, $P_m(x_1, x_2)$. An example of a complete polynomial is the quadratic polynomial

$$P_2(x_1, x_2) = C_1 + C_2x_1 + C_3x_2 + C_4{x_1}^2 + C_5x_1x_2 + C_6{x_2}^2 \tag{2}$$

where the C's are arbitrary coefficients.

Criterion 1. As a measure of the effectiveness of an element, we shall ask what order Kirchhoff mode the element is able to exactly interpolate. The higher the order, the greater the ability of the element to perform accurately in the thin-plate limit.

Criterion 2. A weakened version of the foregoing criterion, which accommodates reduced/selective integration and other procedures, asks for what order Kirchhoff mode is the strain energy calculated exactly. This is the form of the criterion employed by MacNeal [31] and Parisch [39]. Note that Criterion 1 implies Criterion 2.

Posing the criteria in terms of complete polynomials links up with order-of-accuracy concepts and may be useful in mathematical error analysis.

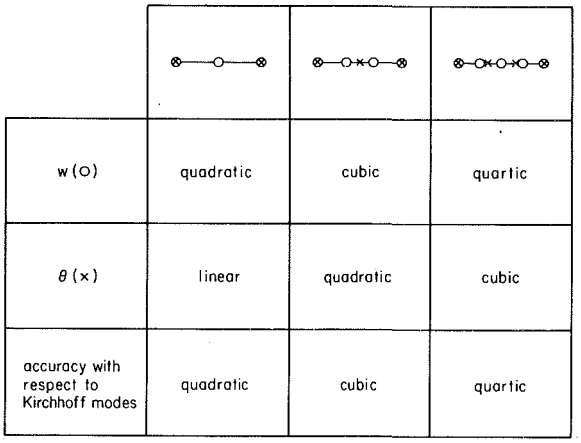

Fig. 1 Beam elements derived from the Kirchhoff-mode criterion

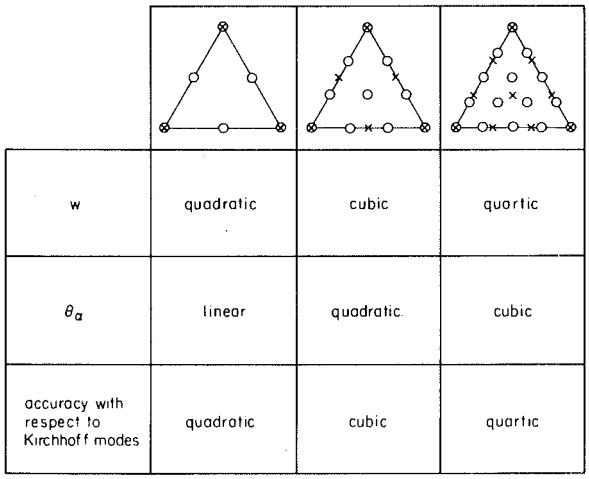

Fig. 2 Triangular plate elements derived from the Kirchhoff-mode criterion

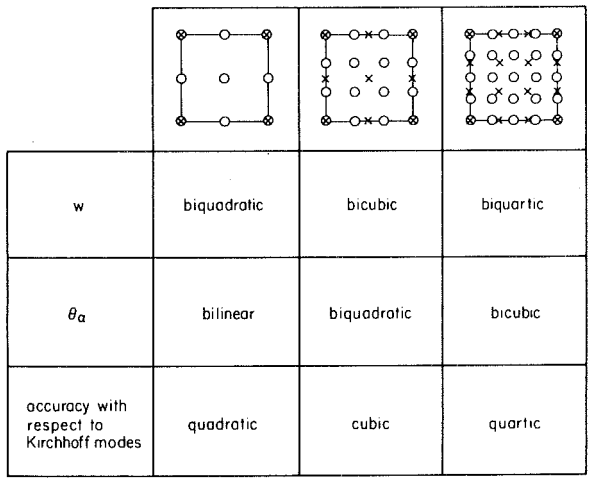

Fig. 3 Quadrilateral Lagrange plate elements derived from the Kirchhoff-mode criterion

Criterion 1 has the advantage that it suggests element interpolation schemes which may be effective. In this regard, it is immediately apparent that, according to Criterion 1, ideal interpolations may be devised by assuming w to be a polynomial one order higher than that assumed for the θ_α's. Before considering some detailed examples of this type, it is worth remarking that schemes like this have apparently not been tried before and would be somewhat inconvenient from an implementational standpoint.

As a starting point, let us consider some one-dimensional beam-type examples. The lowest order possibility is quadratic displacement and linear rotation. (Note that linear displacement, constant rotation, is inadmissible since the rotation would necessarily be discontinuous, in violation of the continuity requirements of the governing theory.) The nodal pattern is illustrated in Fig. 1. This element achieves quadratic accuracy according to Criterion 1. The center displacement degree of freedom is inconvenient, however. An element of equivalent accuracy, in the sense of Criterion 2, which exclusively uses linear interpolations, may be devised by employing the reduced integration concept (one-point Gaussian quadrature need be used). This element was introduced in [26] and has led to the simplest effective two-dimensional shell formulations [14, 24, 25, 54]. In the linear constant coefficient case it can be shown to be identical to the quadratic displacement, linear rotation beam. (The center displacement degree of freedom may be statically condensed to yield an identical stiffness matrix [2].) Here we have a primitive illustration of the success of the reduced/selective integration concept, in that an element possessing a convenient interpolatory scheme may be made to behave like one possessing a higher-order, inconvenient scheme.

The next beam example consists of cubic interpolation for displacement and quadratic interpolation for rotation. The nodal pattern is illustrated in Fig. 1. Again, the internal degrees of freedom are inconvenient in practice. Static condensation leads to the usual element stiffness of structural theory (see, e.g., [10, p. 333]). An equivalent element may be obtained with quadratic interpolations for both w and θ, in conjunction with reduced two-point Gaussian quadrature. Again, static condensation of the internal degrees of freedom leads to the usual stiffness of structural theory [2]. Higher-order examples of this type may be constructed similarly.

Analogous two-dimensional interpolatory schemes may be devised for triangles. The triangular family illustrated in Fig. 2 appears unique among two-dimensional element families in that the functions which constitute the rotational interpolations are obtained exactly from the derivatives of displacement—no more, no less. This is unlike the situation for a somewhat analogous family of quadrilaterals in which Lagrange interpolations are used, the displacement being one order higher than the rotation (see Fig. 3).[1] For this family of elements, the derivative of displacement contains more monomials than does the rotational interpolations. The classical Lagrange family of quadrilateral plate elements, in which identical interpolations are used for displacement and rotations (see Fig. 4), creates the opposite situation in that the rotational interpolation contains more monomials than does the derivative of displacement. That this situation is harmful has been suggested by Spilker and Munir [50]. Further research is required to determine the nature and extent of the problem when displacement and rotation fields fail to "match" according to the criteria. In any event, the triangular family of Fig. 2 appears canonical in this sense.

Of course, classical Lagrange-type interpolations, in which identical nodal patterns are employed for displacement and rotation (e.g., Fig. 4), are more easily implemented and applied than the new schemes suggested by the Kirchhoff modal criteria (i.e., Figs. 2 and 3). The behavior of Lagrangian elements has been shown to improve through use of the reduced/selective integration technique (unfortunately, so far at the expense of rank deficiency) [22, 42]. The excess rotational monomials are "filtered" by the lower-order quadrature resulting in higher-order behavior in the sense of Criterion 2. Thus we see again that convenient interpolations necessarily entail special procedures, such as reduced/selective integration and allied techniques, if they are to achieve optimal accuracy in practice. It has been argued that if high enough order interpolation (e.g., bicubic level) is used there is no need to employ reduced quadrature as adequate accuracy is

[1] In consideration of quadrilateral elements, for purposes of discussing Kirchhoff modal behavior, we shall assume a rectangular geometry.

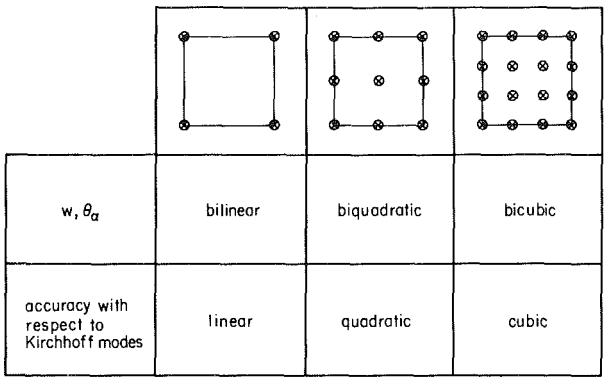

Fig. 4 Classical Lagrange plate elements

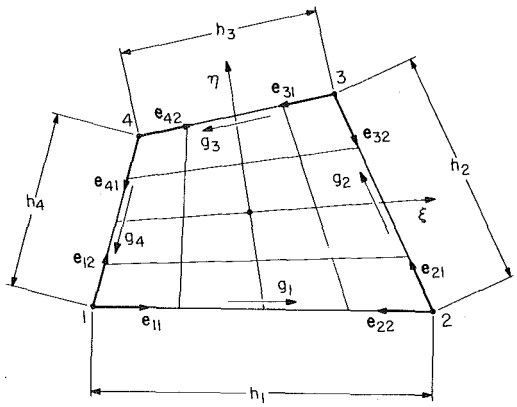

Fig. 5 Geometric and kinematic data for the four-node quadrilateral element

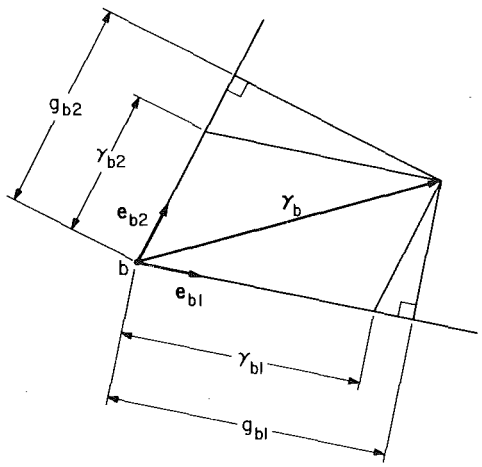

Fig. 6 Definition of nodal transverse shear strain vector

achieved. The fact remains, however, that the behavior of such elements with full quadrature is suboptimal and may be further improved by the use of appropriate reduced/selective integration techniques.

In passing, we may note that the behavior of serendipity interpolatory schemes [53] is similar to Lagrange schemes with respect to Kirchhoff modal behavior. Specifically, classical schemes, in which the same interpolations are used for displacement and rotation, result in excess rotational monomials, whereas schemes in which displacement is interpolated one order higher than rotation possess excess monomials in the displacement-derivative field.

It is interesting to note that by using different interpolations for displacement and rotation, the possibility arises of devising "matched" interpolations for quadrilaterals. As an example of this phenomenon we may mention the combination of nine-node biquadratic Lagrange interpolation for displacement with eight-node serendipity interpolation for rotation. (This scheme has in fact been used as the starting point for the development of a discrete-Kirchhoff element by Irons [27].)

In summary, the ideal interpolations, with respect to the proposed criteria, are not the most desirable from the practical standpoint. In the sequel we shall attempt to use the idea of "optimal interpolation" (roughly speaking, one order higher for displacement than rotation) as a basis for the design of a practically appealing four-node quadrilateral element which simultaneously achieves simplicity and accuracy without engendering rank deficiency.

3 The Four-Node Bilinear Isoparametric Element

The present version of the four-node bilinear isoparametric element is based upon the concepts described in the previous section. The *conceptual* starting point is the straight-edged quadrilateral element in which transverse displacement is interpolated via nine-node Lagrange shape functions and rotations are interpolated via four-node bilinear shape functions (see Fig. 3). This element achieves quadratic accuracy with respect to Kirchhoff modes. The idea is to calculate the transverse shear strains in a special way independent of the midside and center node displacement degrees of freedom. In this way, the element stiffness senses only the corner node transverse displacement degrees of freedom and, consequently, four-node bilinear shape functions may be used in place of the nine-node Lagrange shape functions in formulating the element arrays. Examination of the interpolations reveals that the midpoints of the sides are locations at which the transverse shear strain components parallel to the sides are independent of the aforementioned nodal values. These four scalar values will be used to define the transverse shear strains. The details of the procedure follow.

Definition of Element Transverse Shear Strains. Geometric and kinematic data is defined in Fig. 5. Note that the direction vectors have unit length (e.g., $\|\mathbf{e}_{11}\| = 1$, etc.). Let w_a and $\boldsymbol{\theta}_a$ denote the transverse displacement and rotation vector, respectively, associated with node a. Throughout, a subscript b will equal $a + 1$ modulo 4. That is

a	b
1	2
2	3
3	4
4	1

(3)

The definition of the element shear strains may be facilitated by the following steps:

1 For each element side define a shear strain component, located at the midpoint, in a direction parallel to the side, viz.,

$$g_a = (w_b - w_a)/h_a - \mathbf{e}_{a1} \cdot (\boldsymbol{\theta}_b + \boldsymbol{\theta}_a)/2. \tag{4}$$

2 For each node, define a shear strain vector (see Fig. 6 for a geometric interpretation of this process):

$$\boldsymbol{\gamma}_b = \gamma_{b1}\mathbf{e}_{b1} + \gamma_{b2}\mathbf{e}_{b2} \tag{5}$$

$$\gamma_{b2} = (1 - \alpha_b{}^2)^{-1}(g_{b2} - g_{b1}\alpha_b) \tag{6}$$

$$\gamma_{b1} = (1 - \alpha_b{}^2)^{-1}(g_{b1} - g_{b2}\alpha_b) \tag{7}$$

$$\alpha_b = \mathbf{e}_{b1} \cdot \mathbf{e}_{b2} \tag{8}$$

$$g_{b1} = g_b \tag{9}$$

$$g_{b2} = -g_a \tag{10}$$

3 Interpolate the nodal values by way of the bilinear shape functions (N_a's).

$$\boldsymbol{\gamma} = \sum_{a=1}^{4} N_a \boldsymbol{\gamma}_a \tag{11}$$

Remarks:

1 If the nodal transverse displacements and rotations are specified to consistently interpolate a constant transverse shear strain field, say $\bar{\gamma}$, then the preceding steps will result in $\gamma = \bar{\gamma}$. That is, constant transverse shear deformation modes are exactly representable in the general quadrilateral geometry.

2 In the rectangular configuration, the shear strains take on the following form (we assume the origin of coordinates coincides with the element center):

$$\gamma_1(x_2, x_2) = w_{,1}(0, 0) - \theta_1(0, 0) + x_2[w_{,12} - \theta_{1,2}(0, 0)] \quad (12)$$

$$\gamma_2(x_1, x_2) = w_{,2}(0, 0) - \theta_2(0, 0) + x_1[w_{,21} - \theta_{2,1}(0, 0)] \quad (13)$$

where $w_{,12} = w_{,21}$ = constant. In this case the linear variations of γ_1 with x_2 and γ_2 with x_1 may be clearly seen. Note that there are four scalar transverse shear strain modes. (This may be concluded in general from the foregoing steps 1–3 which amount to an interpolation of the four scalar parameters g_1, g_2, g_3, and g_4.) These modes include the two constant transverse shear modes, and the "hourglass" and "in-plane twist" modes (see [22] for a discussion), thus enabling the element to achieve correct rank. In the rectangular configuration, the transverse shear strain variation is equivalent to the selective integration scheme of MacNeal [31]. The generalizations to quadrilateral configurations differ somewhat.

3 The "constraint index" (as defined in [34]) for the present element is -1, which suggests failure in the thin-plate limit. As will be seen from the numerical examples, this is not the case, an illustration that the constraint index is sometimes overly pessimistic for plates.

4 To assess the effectiveness of the present element we employ the ideas of Section 2. Consider the rectangular configuration. It can be shown, with the aid of (12) and (13), that quadratic accuracy with respect to Kirchhoff modes is attained. This could be anticipated from the way the transverse shear strains were interpolated. The reduced/selective integration elements presented in [22, 26] effectively achieve the same end. However, they do not retain correct rank as does the present element.

5 Analogous procedures may be used to derive a three-node triangle employing linear shape functions. The conceptual starting point, in this case, is the triangle with quadratic w and linear θ_α's (see Fig. 2). Again, quadratic accuracy with respect to Kirchhoff modes is achieved in the sense of Criterion 2. If effective in practice, this element would represent one of the simplest effective elements ever devised for bending applications.

4 Implementation

In this section we consider the implementation of Mindlin plate elements in which the same interpolatory patterns are used for displacement and rotations. This is general enough to encompass our new four-node element. It suffices in the present circumstances to consider the simpler case of a homogeneous, isotropic, linearly elastic plate of constant thickness t.

Let A^e and s^e denote the area and boundary, respectively, of a typical element. Let $N_1, N_2, \ldots, N_n$ denote shape functions, where n is the number of element nodes.

The *element stiffness matrix*, $\mathbf{k}^e$, may be defined as follows:

$$\mathbf{k}^e = \mathbf{k}_b{}^e + \mathbf{k}_s{}^e \quad (14)$$

$$\mathbf{k}_b{}^e = \int_{A^e} \mathbf{B}^{b^T} \mathbf{D}^b \mathbf{B}^b dA \quad \text{bending stiffness} \quad (15)$$

$$\mathbf{k}_s{}^e = \int_{A^e} \bar{\mathbf{B}}^{s^T} \mathbf{D}^s \bar{\mathbf{B}}^s dA \quad \text{shear stiffness} \quad (16)$$

$$\mathbf{B}^b = [\mathbf{B}_1{}^b \mathbf{B}_2{}^b \ldots \mathbf{B}_n{}^b] \quad (17)$$

$$\bar{\mathbf{B}}^s = [\bar{\mathbf{B}}_1{}^s \bar{\mathbf{B}}_2{}^s \ldots \bar{\mathbf{B}}_n{}^s] \quad (18)$$

$$\mathbf{B}_a{}^b = \begin{bmatrix} 0 & N_{a,1} & 0 \\ 0 & 0 & N_{a,2} \\ 0 & N_{a,2} & N_{a,1} \end{bmatrix} \quad 1 \le a \le n. \quad (19)$$

The definition of $\bar{\mathbf{B}}_a{}^s$ is the essential ingredient in the development of an effective element. In the "normal" case, $\bar{\mathbf{B}}_a{}^s = \mathbf{B}_a{}^s$, which is defined by

$$\mathbf{B}_a{}^s = \begin{bmatrix} N_{a,1} & -N_a & 0 \\ N_{a,2} & 0 & -N_a \end{bmatrix} \quad 1 \le a \le n. \quad (20)$$

With this definition, some form of reduced/selective integration usually needs to be employed for success in the thin plate limit.

In the present formulation the reduced/selective-integration effect is accounted for directly in the definition of $\bar{\mathbf{B}}_a{}^s$ [18, 23]. For the transverse shear strain interpolations derived in the previous section, $\bar{\mathbf{B}}_a{}^s$ takes on the following form [recall the relation between subscripts a and b, see (3)]:

$$\bar{\mathbf{B}}_b{}^s = [\bar{\mathbf{B}}_{b1}{}^s \bar{\mathbf{B}}_{b2}{}^s \bar{\mathbf{B}}_{b3}{}^s] \quad 1 \le b \le 4 \quad (21)$$

$$\bar{\mathbf{B}}_{b1}{}^s = h_a{}^{-1}\mathbf{G}_a - h_b{}^{-1}\mathbf{G}_b \quad (22)$$

$$\bar{\mathbf{B}}_{b2}{}^s = (e_{b2}{}^1\mathbf{G}_a - e_{b1}{}^1\mathbf{G}_b)/2 \quad (23)$$

$$\bar{\mathbf{B}}_{b3}{}^s = (e_{b2}{}^2\mathbf{G}_a - e_{b1}{}^2\mathbf{G}_b)/2 \quad (24)$$

$$\mathbf{G}_a = (1 - \alpha_a{}^2)^{-1} N_a(\mathbf{e}_{a1} - \alpha_a \mathbf{e}_{a2}) - (1 - \alpha_b{}^2)^{-1} N_b(\mathbf{e}_{b2} - \alpha_b \mathbf{e}_{b1}) \quad (25)$$

$$\mathbf{e}_{b1} = \begin{Bmatrix} e_{b1}{}^1 \\ e_{b1}{}^2 \end{Bmatrix}, \text{ etc.} \quad (26)$$

The matrices $\mathbf{D}^b$ and $\mathbf{D}^s$, for the isotropic, linearly elastic, constant thickness case, take on the following forms (respectively):

$$\mathbf{D}^b = \frac{t^3}{12} \begin{bmatrix} 2\mu + \bar{\lambda} & \bar{\lambda} & 0 \\ & 2\mu + \bar{\lambda} & 0 \\ \text{symm.} & & \mu \end{bmatrix} \quad (27)$$

and

$$\mathbf{D}^s = \kappa t \mu \begin{bmatrix} 1 & 0 \\ 0 & 1 \end{bmatrix} \quad (28)$$

where $\bar{\lambda} = 2\lambda\mu/(\lambda + 2\mu)$, λ and μ are the Lamé parameters, and κ is a "shear correction factor," which is taken to be $\frac{5}{6}$ throughout.

The *external load vector*, $\mathbf{f}^e$, is given by

$$\mathbf{f}^e = \{f_I{}^e\} \quad (29)$$

$$f_I{}^e = \begin{cases} \int_{A^e} N_a F dA + \int_{s^e \cap s_2} N_a Q ds, & I = 3a - 2, \quad 1 \le a \le n \\ -\int_{A^e} N_a C_\alpha dA - \int_{s^e \cap s_2} N_a M_\alpha ds, & I = 3a + \alpha - 2, \quad 1 \le a \le n, \quad \alpha = 1, 2 \end{cases} \quad (30)$$

where F is the total applied transverse force per unit area, C_α is the total applied couple per unit area, Q is the applied shear force, M_α is the applied boundary moment, and s_2 is the portion of the plate boundary upon which forces and moments are prescribed.

The element stress resultants may be obtained from the following relations:

$$\begin{Bmatrix} m_{xx} \\ m_{yy} \\ m_{xy} \end{Bmatrix} = -\mathbf{D}^b \mathbf{B}^b \mathbf{d}^e \quad \text{bending moments} \quad (31)$$

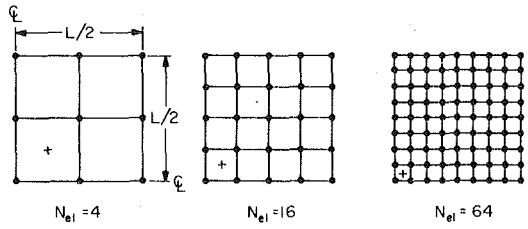

Fig. 7 Square plate meshes; due to symmetry, only one quadrant is discretized

$$\begin{Bmatrix} q_x \\ q_y \end{Bmatrix} = \mathbf{D}^s \mathbf{B}^s \mathbf{d}^e \quad \text{shear resultants} \tag{32}$$

where

$$\mathbf{d}^e = \{d_I{}^e\} \quad \text{element displacement vector} \tag{33}$$

$$d_I{}^e = \begin{cases} w_a, & I = 3a - 2, \quad 1 \le a \le n \\ \theta_{\alpha a}, & I = 3a + \alpha - 2, \quad 1 \le a \le n, \quad \alpha = 1, 2 \end{cases} \tag{34}$$

$$\theta_a = \begin{Bmatrix} \theta_{1a} \\ \theta_{2a} \end{Bmatrix}. \tag{35}$$

Remark. Generalization of the formulation to fully nonlinear analysis is straightforward by way of the procedures described in [18, 23].

5 Numerical Examples

All calculations were performed at the California Institute of Technology Computer Center on an IBM 3032 computer in double precision (64 bits per floating point word). Unless otherwise specified, a Poisson's ratio of 0.3, Young's modulus of 10.92×10^5, and geometric parameters $L = 10$ and $t = 0.1$ were used throughout.

In the context of Mindlin theory, two interpretations of the classical simply supported boundary condition are possible: SS_1, in which only the transverse displacement is set to zero; and SS_2, in which the transverse displacement and tangential rotation are set to zero. In applications to thin plates, SS_1 is generally preferable since it leads to convergent results when polygonal approximations of curved boundaries are employed. Nevertheless SS_2 corresponds to the simply supported condition of classical thin plate theory and may be safely employed for the analysis of polygonal, and in particular rectangular, plates. See [22] for a discussion of the treatment of simply supported boundary conditions and references to pertinent literature.

The following codes are used to denote the elements compared:

S1—This element employs 2×2 Gauss quadrature on the bending stiffness and one-point Gauss quadrature on the shear stiffness ("selective reduced integration"). It was originally proposed in [26] and has subsequently been studied extensively in [22] among other places. It possesses two spurious zero-energy modes [22, 26].

T1—This is the element developed herein; 2×2 Gauss quadrature it used on all terms. It possesses correct rank.

U1—This element employs one-point Gauss quadrature on all terms ("uniform reduced integration"). It was first proposed in [22] and studied therein. It possesses four spurious zero-energy modes.

In one case, the "twisted ribbon," we compare results with an element proposed by Robinson [45], dubbed LORA, and the MSC/NASTRAN element QUAD4 [31].

Despite the defects of S1 and U1 (i.e., spurious zero-energy modes) they behave well in many situations and are of interest because of their economy. With appropriate stabilization measures, such as so-called "hourglass" stiffness and viscosities, they hold significant potential in nonlinear analysis. See [11, 13, 30] for discussions of stabilization ideas employed in the continuum case.

In cases in which the dimensions enable the plate to be considered

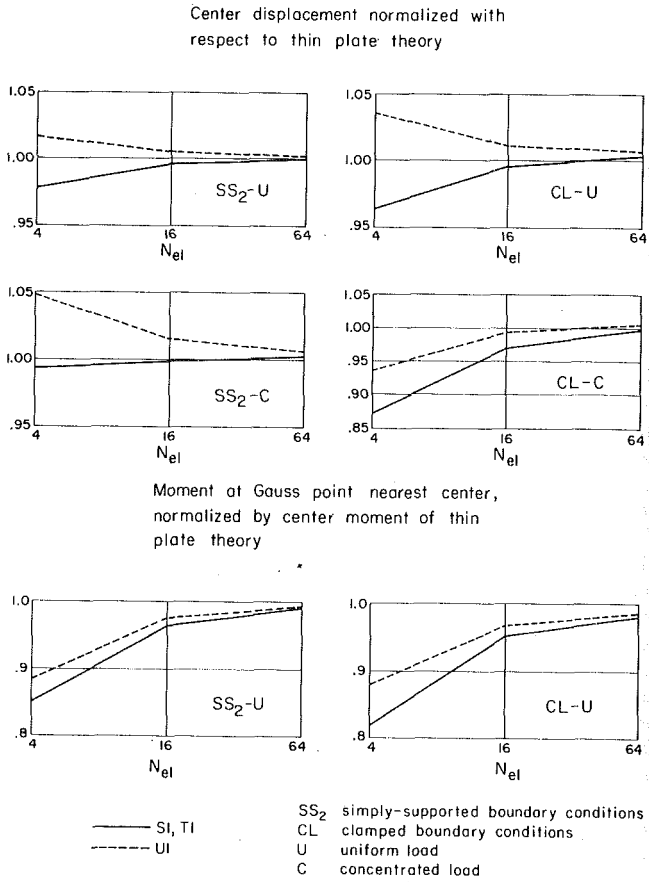

Fig. 8 Convergence study for thin square plate

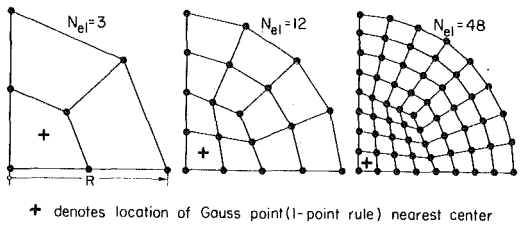

Fig. 9 Circular plate meshes; due to symmetry, only one quadrant is discretized

"thin," comparison is made with results of classical Poisson-Kirchhoff theory.

5.1 Thin Square Plate. This set of problems is perhaps the most common employed in testing plate element behavior. Meshes are depicted in Fig. 7 and results in Fig. 8. As may be seen, results for elements S1 and T1 are identical for plotting purposes. All elements perform well for this case.

5.2 Thin Circular Plate. These problems test the behavior of the elements in nonrectangular configurations. The radius $R = 5.0$. The meshes are shown in Fig. 9 and convergence results presented in Fig. 10. In this case, T1 is generally the best performer, although all elements perform well.

5.3 Thin Rectangular Plates. These problems test the response of the element to changes in planar aspect ratio. The meshes are shown in Figs. 11 and 12 and results are prsented in Figs. 13 and 14. In these cases, as in the case of the square plate study, the differences between S1 and T1 are indiscernible on the scale of the plots.

As may be seen from Figs. 13 and 14, by far the worst displacement results are obtained for the clamped-boundary, concentrated-load

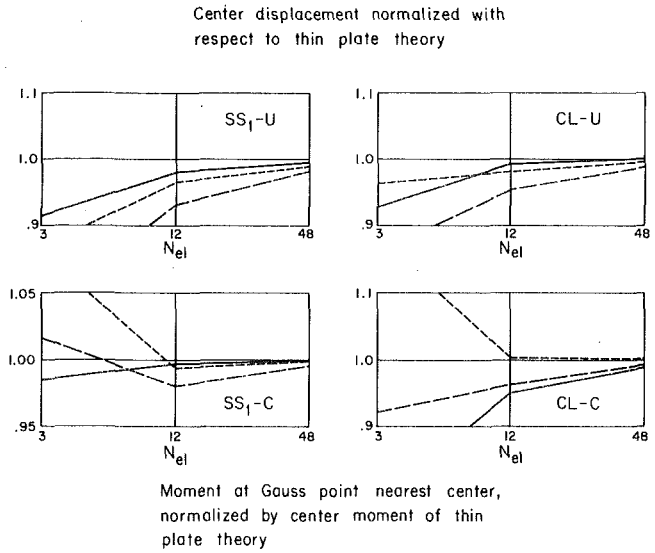

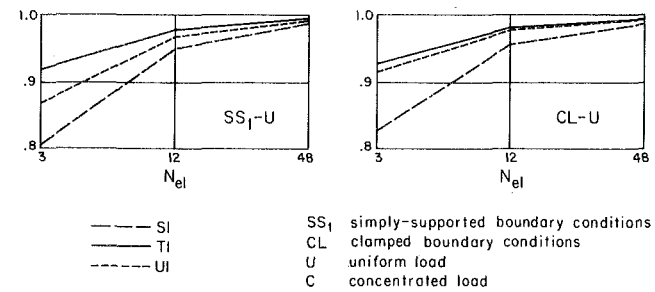

Fig. 10 Convergence study for thin circular plate

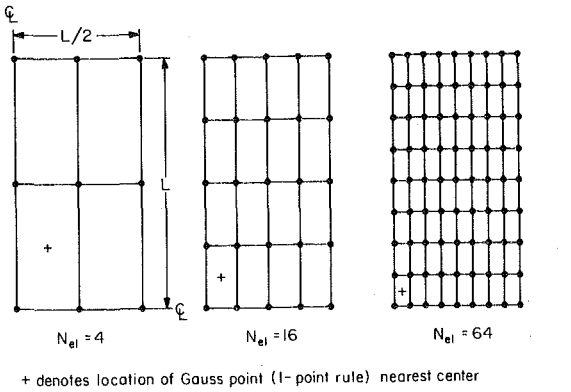

Fig. 11 Rectangular plate meshes (aspect ratio = 2); due to symmetry, only one quadrant is discretized

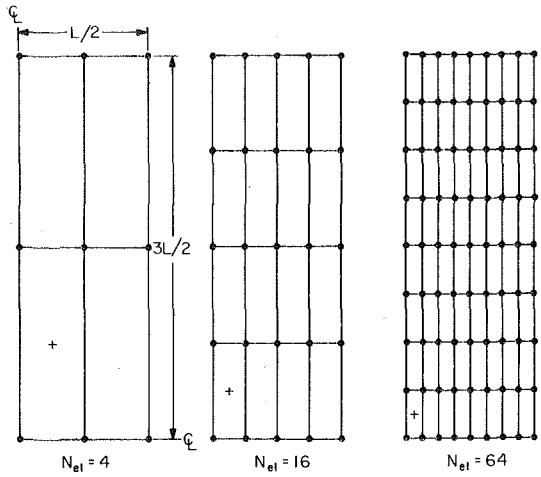

Fig. 12 Rectangular plate meshes (aspect ratio = 3); due to symmetry, only one quadrant is discretized

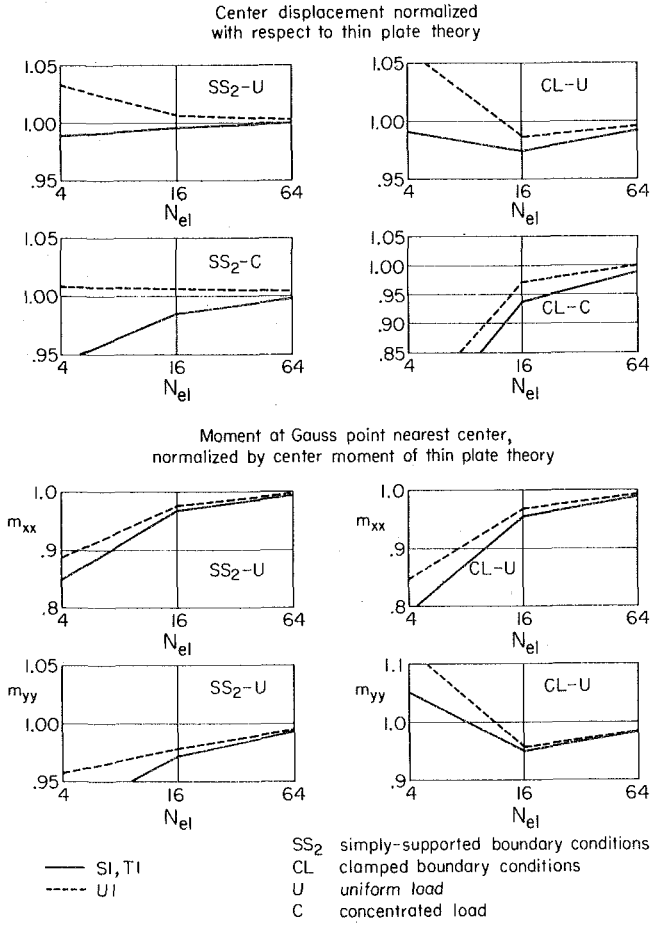

Fig. 13 Convergence study for thin rectangular plate (aspect ratio = 2)

case. (This same pattern is in evidence for the square plate, see Fig. 8.) Robinson [45] has selected this case to compare S1 with an element he proposes, and some others, on crude meshes. Furthermore, some of the data he presents for S1 shows the error to be approximately twice the actual amount. Nevertheless it must be admitted that there is deterioration of accuracy with planar aspect ratio, a common, but not well-understood phenomenon for virtually all finite elements.

5.4 Thin Rhombic Plate. The configuration and mesh are shown in Fig. 15. The length parameter $a = 100$. The plate is uniformly loaded and simply supported boundary conditions (SS_1) are employed. This problem is a difficult one since there is a singularity at the obtuse vertex. The analytical solution reveals that the x_1 and x_2 bending moments have *opposite* signs in the vicinity of the obtuse vertex. Many thin plate elements yield pathological results for this problem in that moments with the *same* sign are obtained (see [46, 47] for a discussion). Moment results are presented in Fig. 16. The general trend for each element is correct. However, the elements have a tendency to oscillate somewhat as may be seen. The worst oscillations are produced by U1. Considering that the mesh is not biased to favor the singularity, and that the problem is a numerically difficult one, the accuracy of the results obtained for S1 and U1 is considered to be fairly good.

5.5 Thick Circular Plate. This problem employs the same

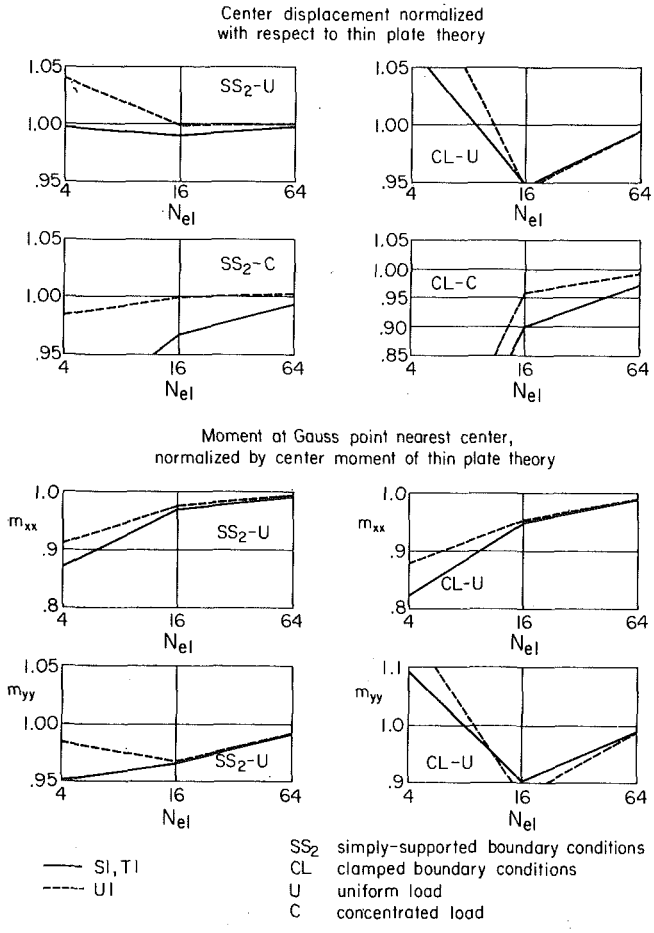

Fig. 14 Convergence study for thin rectangular plate (aspect ratio = 3)

48-element mesh as shown in Fig. 9, except the thickness is taken to be 2.0, and thus the plate may be considered "thick" ($R/t = 2.5$). It has been our experience that increasing thickness creates problems for rank-deficient elements [26]. An analytical solution obtained from Reissner's theory is used as a basis of comparison. The behavior under the load is singular and this gives rise to almost identical oscillatory patterns for elements S1 and U1 as may be seen in Fig. 17. On the other hand, element T1 produces very accurate results for this case.

5.6 Twisted Ribbon. Configurations, data and results for this problem are shown in Fig. 18. In each analysis, only one element is employed. Robinson [45] has proposed this as a critical single element test for plate bending elements. Comparisons are made with data presented in [45] for Robinson's element, LORA, and MacNeal's QUAD4 [31].

For Cases *A* and *C* (fully fixed boundary), comparison is made with respect to a benchmark analysis, reported upon in [45], involving sixteen high-precision elements. As may be seen, the results for our new element T1 are superior to the results for both LORA and QUAD4. Furthermore, no deterioration with increasing aspect ratio is detected. For this case, elements S1 and U1 exhibit pathological behavior due to rank deficiency (not shown).

It is interesting to note that Robinson [45], in advocating the use of LORA, has particularly emphasized its good behavior with respect to aspect ratio. Clearly, however, there is significant and inexplicable deterioration of LORA in Case B. Special emphasis has also been given to aspect ratio behavior by MacNeal [31] in the development of QUAD4. The technique employed is *ad hoc* and employs an adjustable parameter. Although improvement is noted in some situations, deterioration is encountered in others, as may be concluded from the comparison of T1 and QUAD4 in this example.

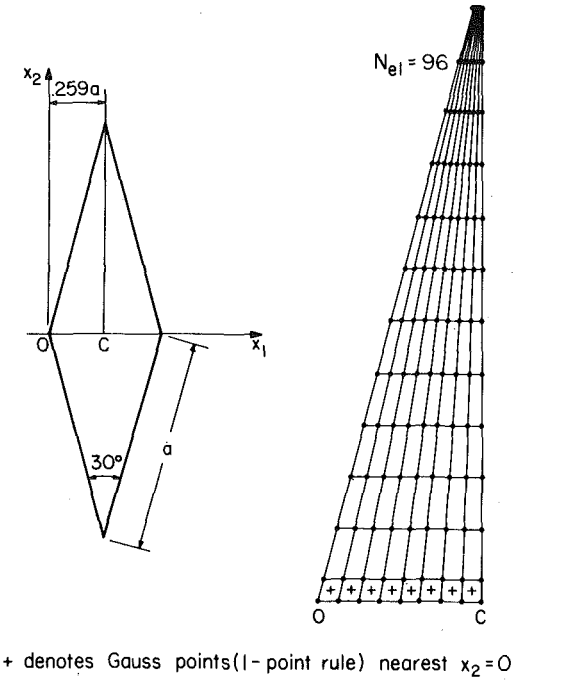

Fig. 15 Rhombic plate mesh; due to symmetry, only one quadrant is discretized

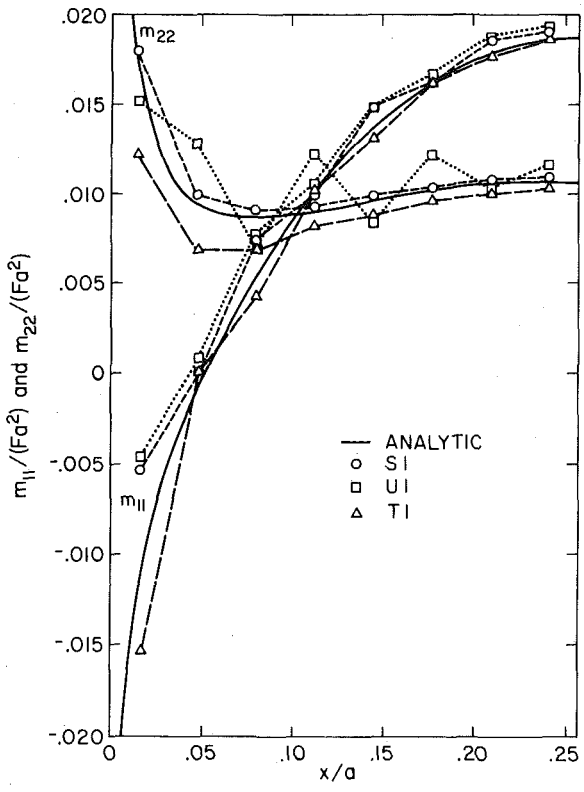

Fig. 16 Bending moments for rhombic plate

If only half the domain is modeled, and antisymmetrical boundary conditions are enforced (Cases *C* and *D*), the exact solution is one of pure twist. For these cases, S1 and T1 yield exact solutions, whereas U1 still behaves pathologically (not shown).

6 Conclusions

In this paper a new conceptual framework has been established for

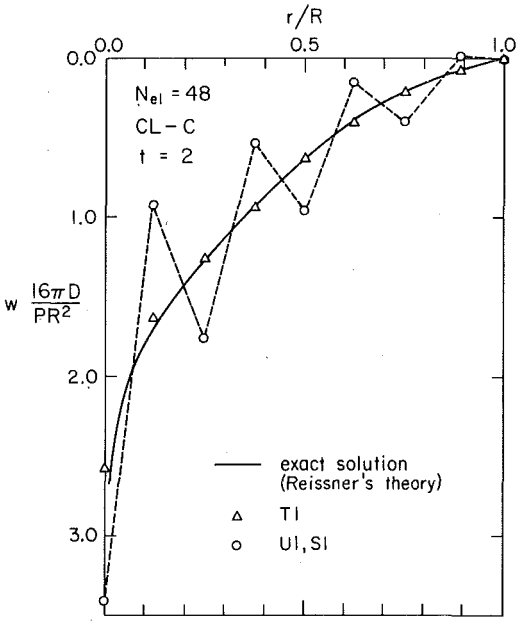

Fig. 17 Displacement results for thick circular plate

the development of plate elements based on Mindlin theory. The interpolatory patterns suggested have not been studied heretofore, but are somewhat more complicated than practical requirements presently dictate. It is proposed, however, that the ideas are useful in the development of more appealing elements, and this is illustrated by the development of a new four-node quadrilateral element employing bilinear isoparametric interpolation for all dependent variables. The element represents an improvement over past efforts of ours in that no spurious zero-energy modes are present. Simplicity is retained in the formulation and the element is shown to behave well on a variety of plate problems. The formulation enables straightforward generalization to nonlinear analysis, and appears to have some advantages over competing elements.

Considerable further work remains to be done in exploring the behavior of some of the new elements proposed herein. In addition, serious studies of aspect ratio effects and transverse shear resultants would be very helpful in improving the understanding of element response. Finally, the rigorous mathematical convergence analysis of elements of the type considered in this work, which is a delicate matter judging from related studies [38, 48], needs to be assiduously pursued to put matters on a sound footing.

Acknowledgment

We wish to thank the following individuals and organizations for providing support for our research: J. Crawford and T. Shugar of the Civil Engineering Laboratory, Port Hueneme, Calif., the National Science Foundation, and J. Carey of the Electric Power Research Institute, Palo Alto, Calif.

References

1 Ahmad, S., Irons, B. M., and Zienkiewicz, O. C., "Analysis of Thick and Thin Shell Structures by Curved Finite Elements," *International Journal for Numerical Methods in Engineering*, Vol. 2, 1970, pp 419–451.

2 Allik, H., Private Communication, 1976.

3 Argyris, J. H., and Dunne, P. C., "Postbuckling, Finite-Element Analysis of Circular Cylinders Under End Load," Report No. 224, Institut für Statik und Dynamik der Luft-und Raumfahrtkonstruktionen, University of Stuttgart, Germany, 1977.

4 Argyris, J. H., et al., "Large Natural Strains and Some Special Difficulties Due to Nonlinearity and Incompressibility in Finite Elements," *Computer Methods in Applied Mechanics and Engineering*, Vol. 4, 1974, pp. 219–278.

5 Argyris, J. H., et al., "A Simple Triangular Facet Shell Element With Applications to Linear and Nonlinear Equilibrium and Elastic Stability Problems," *Computer Methods in Applied Mechanics and Engineering*, Vol. 10, No. 3, Mar. 1977, pp. 371–403; Vol. 11, No. 1, Apr. 1977, pp. 97–131.

6 Bathe, K. J., and Bolourchi, S., "A Geometric and Material Nonlinear Plate and Shell Element," *Computers and Structures*, to appear.

7 Batoz, J. L., Bathe, K. J., and Ho, L. W., "A Search for the Optimum Three-Node Triangular Plate Bending Element," Report 82448-8, Massachusetts Institute of Technology, Cambridge, Mass., Dec. 1978.

8 Berkovic, M., "Thin Shell Isoparametric Elements," *Proceedings of the Second World Congress on Finite Element Methods*, Bournemouth, Dorset, England, Oct. 1978.

9 Bolourchi, S., "On Finite-Element Analysis of General Shell Structures,"

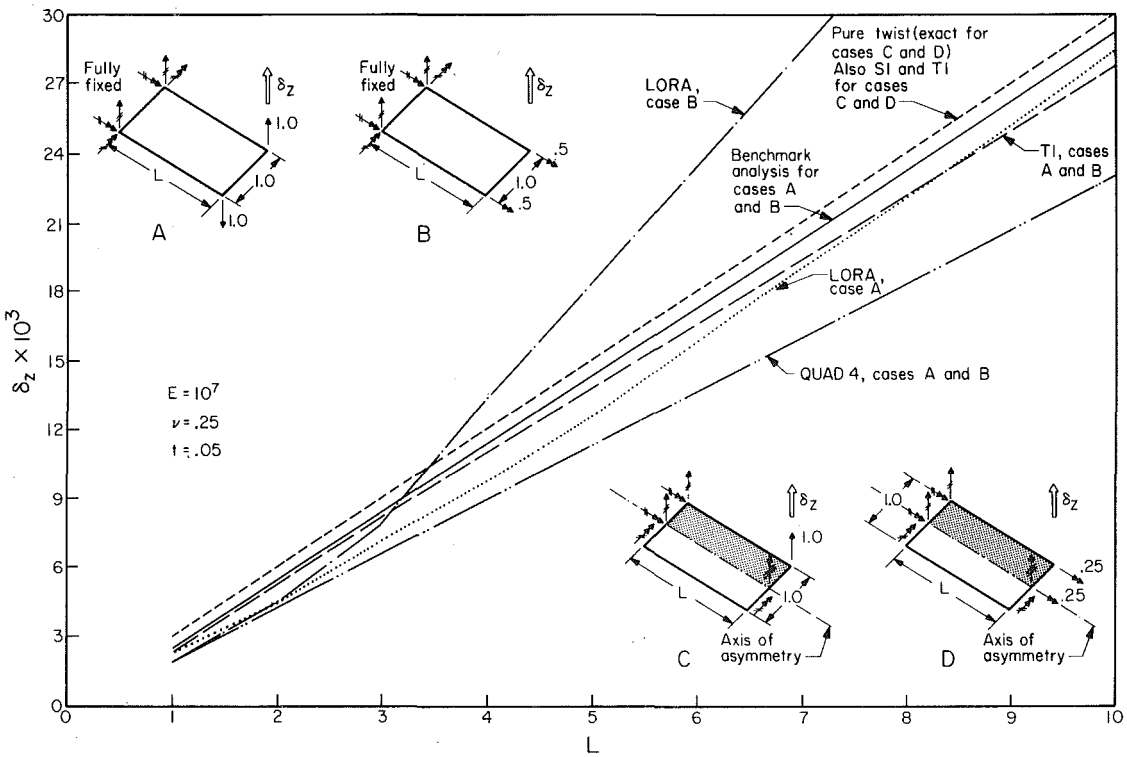

Fig. 18 Displacement results for the twisted ribbon; one element used in all cases

PhD Dissertation, Massachusetts Institute of Technology, Cambridge, Mass., May 1979.

10 Cook, R. D., *Concepts and Applications of Finite-Element Analysis*, John Wiley, New York, 1974.

11 Flanagan, D. P., and Belytschko, T., "A Uniform Strain Hexahedron and Quadrilateral With Orthogonal Hour Glass Control," preprint.

12 Fried, I., "Finite-Element Analysis of Incompressible Material by Residual Energy Balancing," *International Journal of Solids and Structures*, Vol. 10, 1974, pp. 993–1002.

13 Giroux, E. D., "HEMP User's Manual," University of California, Lawrence Livermore Laboratory, Report UCRL-51079, 1973.

14 Goudreau, G. L., "A Computer Module for One Step Dynamic Response of an Axisymmetric Plane Linear Elastic Thin Shell," Lawrence Livermore Laboratory Report No. UCID-17730, Feb. 1978.

15 Hinton, E., and Bicanic, N., "A Comparison of Lagrangian and Serendipity Mindlin Plate Elements for Free Vibration Analysis," *Computers and Structures*, Vol. 10, 1979, pp. 483–493.

16 Hinton, E., Salonen, E. M., and Bicanic, N., "A Study of Locking Phenomena in Isoparametric Elements," Third MAFELAP Conference, Brunel University, Oxbridge, 1978.

17 Horrigmoe, G., "Finite Element Instability Analysis of Free-Form Shells," Report 77-2, Division of Structural Mechanics, Norwegian Institute of Technology, University of Trondheim, Norway, May 1977.

18 Hughes, T. J. R., "Generalization of Selective Integration Procedures to Anisotropic and Nonlinear Media," *International Journal of Numerical Methods in Engineering*, Vol. 15, 1980, pp. 1413–1418.

19 Hughes, T. J. R., "Recent Developments in Computer Methods for Structural Analysis," *Nuclear Engineering and Design*, Vol. 57, No. 2, 1980, pp. 427–439.

20 Hughes, T. J. R., and Cohen, M., "The 'Heterosis' Finite Element for Plate Bending," *Computers and Structures*, Vol. 9, 1978, pp. 445–450.

21 Hughes, T. J. R., and Cohen, M., "The 'Heterosis' Family of Plate Finite Elements," *Proceedings of the ASCE Electronic Computations Conference*, St. Louis, Mo., August 6–8, 1979.

22 Hughes, T. J. R., Cohen, M., and Haroun, M., "Reduced and Selective Integration Techniques in the Finite Element Analysis of Plates," *Nuclear Engineering and Design*, Vol. 46, 1978, pp. 203–222.

23 Hughes, T. J. R., and Liu, W. K., "Nonlinear Finite Element Analysis of Shells: Part I. Three-Dimensional Shells," *Computer Methods in Applied Mechanics and Engineering*, to appear.

24 Hughes, T. J. R., and Liu, W. K., "Nonlinear Finite Element Analysis of Shells: Part II. Two-Dimensional Shells," *Computer Methods in Applied Mechanics and Engineerings*, to appear.

25 Hughes, T. J. R., Liu, W. K., and Levit, I., "Nonlinear Dynamic Finite Element Analysis of Shells," *Proceedings of the Europe-U.S. Workshop on Finite Element Methods in Structural Mechanics*, Bochum, West Germany, July 28–31, 1980.

26 Hughes, T. J. R., Taylor, R. L., and Kanoknukulchai, W., "A Simple and Efficient Element for Plate Bending," *International Journal for Numerical Methods in Engineering*, Vol. 11, No. 10, 1977, pp. 1529–1543.

27 Irons, B. M., "The Semiloof Shell Element," *Finite Elements for Thin Shells and Curved Members*, eds., Ashwell, D. G., and Gallagher, R. H., John Wiley, New York, 1976, Chapter 11, pp. 197–222.

28 Kanoknukulchai, W., "A Large Deformation Formulation for Shell Analysis by the Finite Element Method," PhD Thesis, University of California, Berkeley, Nov. 1978.

29 Kanoknukulchai, W., "A Simple and Efficient Finite Element for General Shell Analysis," *International Journal for Numerical Methods in Engineering*, Vol. 14, 1979, pp. 179–200.

30 Kosloff, D., and Frazier, G., "Treatment of Hourglass Patterns in Low Order Finite Element Codes," *Numerical and Analytical Methods in Geomechanics*, Vol. 2, 1978, pp. 57–72.

31 MacNeal, R. H., "A Simple Quadrilateral Shell Element," *Computers and Structures*, Vol. 8, 1978, pp. 175–183.

32 Malkus, D. S., "Finite Element Analysis of Incompressible Solids," PhD Dissertation, Boston University, Boston, Mass., 1975.

33 Malkus, D. S., "A Finite Element Displacement Model Valid for any Value of the Compressibility," *International Journal of Solids and Structures*, Vol. 12, 1976, pp. 731–738.

34 Malkus, D. S. and Hughes, T. J. R., "Mixed Finite Element Methods—Reduced and Selective Integration Techniques: A Unification of Concepts," *Computer Methods in Applied Mechanics and Engineering*, Vol. 15, No. 1, 1978, pp. 63–81.

35 Mindlin, R. D., "Influence of Rotatory Inertia and Shear on Flexural Motions of Isotropic, Elastic Plates," ASME JOURNAL OF APPLIED MECHANICS, Vol. 18, 1951, pp. 31–38.

36 Nagtegaal, J. C., Parks, D. M., and Rice, J. R., "On Numerically Accurate Finite Element Solutions in the Fully Plastic Range," *Computer Methods in Applied Mechanics and Engineering*, Vol. 4, 1974, pp. 153–178.

37 Noor, A. K., and Peters, J. M., "Mixed Models and Reduced/Selective Integration Displacement Models for Nonlinear Analysis of Curved Beams," *International Journal for Numerical Methods in Engineering*, to appear.

38 Oden, J. T., Kikuchi, N., and Song, Y. J., "Reduced Integration and Exterior Penalty Methods for Finite Element Approximations of Contact Problems in Incompressible Elasticity," TICOM 80-2, Texas Institute for Computational Mechanics, Univ. of Texas, Austin, 1980; submitted for review to *SIAM Journal of Numerical Analysis*.

39 Parisch, H., "A Critical Survey of the 9-Node Degenerated Shell Element With Special Emphasis on Thin Shell Application and Reduced Integration," *Computer Methods in Applied Mechanics and Engineering*, Vol. 20, 1979, pp. 323–350.

40 Pawsey, S. E., and Clough, R. W., "Improved Numerical Integration of Thick Shell Finite Elements," *International Journal for Numerical Methods in Engineering*, Vol. 3, 1971, pp. 545–586.

41 Pica, A., and Hinton, E., "Efficient Transient Dynamic Plate Bending Analysis With Mindlin Elements," *Earthquake Engineering and Structural Dynamics*, to appear.

42 Pugh, E. D. L., Hinton, E., and Zienkiewicz, O. C., "A Study of Quadrilateral Plate Bending Elements With 'Reduced' Integration," *International Journal for Numerical Methods in Engineering*, Vol. 12, No. 7, 1978, pp. 1059–1079.

43 Ramm, E., "A Plate/Shell Element for Large Deflection and Rotations," *Formulations and Computational Algorithms in Finite Element Analysis*, Bathe, K. J., Oden, J. T., and Wunderlich, W., eds., M.I.T. Press, Cambridge, Mass., 1977.

44 Reddy, J. N., "A Comparison of Closed-Form and Finite-Element Solutions of Thick, Laminated, Anisotropic Rectangular Plates," Report OU-AMNE-79-19, University of Oklahoma, Norman, Okla., Dec. 1979.

45 Robinson, J., "LORA—An Accurate Four Node Stress Plate Bending Element," *International Journal of Numerical Methods in Engineering*, Vol. 14, No. 2, 1979, pp. 296–306.

46 Rossow, M., "Efficient C^0 Finite-Element Solution of Simply Supported Plates of Polygonal Shape," ASME JOURNAL OF APPLIED MECHANICS, Vol. 44, 1977, pp. 347–349.

47 Sander, G., "Application of the Dual Analysis Principle," *Proceedings of the IUTAM Symposium*, Liege, Belgium, 1971, pp. 167–207.

48 Song, Y. J., Oden, J. T., and Kikuchi, N., "Discrete LBB Condition for RIP Finite Element Methods," TICOM 80-7, Texas Institute for Computational Mechanics, University of Texas, Austin, 1980, submitted for review to *SIAM Journal of Numerical Analysis*.

49 Spilker, R. L. and Munir, N. I., "The Hybrid-Stress Model for Thin Plates," *International Journal for Numerical Methods in Engineering*, Vol. 15, No. 8, Aug. 1980, pp. 1239–1260.

50 Spilker, R. L., and Munir, N. I., "A Serendipity Cubic-Displacement Hybrid-Stress Element for Thin and Moderately Thick Plates," *International Journal for Numerical Methods in Engineering*, Vol. 15, No. 8, Aug. 1980, pp. 1261–1278.

51 Spilker, R. L., and Munir, N. I., "A Hybrid-Stress Quadratic Serendipity Displacement Mindlin Plate Bending Element," *Computers and Structures*, to appear.

52 Taylor, R. L., "Finite Elements for General Shell Analysis," Preprints of the 5th International Seminar on Computational Aspects of the Finite Element Method, Berlin (West), Germany, August 20–21, 1979.

53 Zienkiewicz, O. C., *The Finite-Element Method*, 3rd ed., McGraw-Hill, London, 1977.

54 Zienkiewicz, O. C., et al., "A Simple Element for Axisymmetric Shells With Shear Deformation," *International Journal for Numerical Methods in Engineering*, Vol. 11, 1977, pp. 1545–1558.

55 Zienkiewicz, O. C., and Hinton, E., "Reduced Integration, Function Smoothing and Nonconformity in Finite Element Analysis," *Journal of The Franklin Institute*, Vol. 302, 1976, pp. 443–461.

56 Zienkiewicz, O. C., Taylor, R. L., and Too, J. M., "Reduced Integration Technique in General Analysis of Plates and Shells," *International Journal for Numerical Methods in Engineering*, Vol. 3, 1971, pp. 275–290.

L. M. Keer
Professor of Civil Engineering.
Mem. ASME

A. F. Mak

Department of Civil Engineering,
The Technological Institute,
Northwestern University,
Evanston, Ill. 60201

Loss of Contact in the Vicinity of a Right-Angle Corner for a Simply Supported, Laterally Loaded Plate[1]

The solutions to problems of laterally loaded, simply supported rectangular plates are classical ones that can be found in standard textbooks. It is found that forces directed downward must be present to prevent the corners of the plate from rising up during bending. The objective of the present analysis is to determine the extent to which such a plate will rise if the corner force is not present and the plate is unilaterally constrained. Rather than determine the solution for a rectangular plate, we consider a laterally loaded, simply supported plate which occupies a quarter space region. The plate is unilaterally constrained and may rise at the corner due to an absence of restraining force there. Using integral transform techniques appropriate to the quarter space for elastic plates, the region of lost contact is determined for a general loading. The special loading due to a concentrated force is given as an example.

Introduction

The solutions to problems of laterally loaded, simply supported rectangular plates are classical ones that can be found in standard textbooks [1], where it is shown that forces directed downward at the corners must be present to prevent the corners of the plate from rising up during bending. In the vicinity of a corner, therefore, if the plate is not solidly joined with the supporting members, then there will be a tendency of the plate to rise there.

It is clear that the problem is one of receding contact [2], since parts of the plate near the corners, if not constrained bilaterally, will bend away from the supports upon loading, resulting in a receding contact between the plate and the supporting structure. Since the contact is of the receding type, it can be predicted that the extent of contact between the plate and the supports is independent of the level of loading and that the support reactions are proportional to the load. Rectangular plates which are partially supported have been considered by Kiattikomol, et al., [3], by Stahl and Keer [4, 5], and rectangular plates which involve considerations of advancing contact have been considered by Dundurs, et al. [6].

The objective of the present analysis is to determine the extent to which a simply supported plate will rise in the vicinity of a right-angle corner if the force at the corner is not present. The support is viewed as a unilateral constraint allowing only upward motion of the plate. Rather than determine the solution for a rectangular plate, it is more revealing to consider instead a laterally loaded, simply supported plate that occupies a quarter infinite region, $x > 0, y > 0$. The analysis to a certain extent follows concepts from Sneddon's analysis of the elastic quarter space [7].

One could also develop a solution using the superposition of edge-point load solutions for half planes at right angles to each other with suitable symmetries. Although the exposition using that technique might be clearer, it is not clear that the path leading to integral equations (23) and (24) would be significantly eased.

Formulation

The problem concerning the lifting at the corner of a simply supported quarter infinite plate can be formulated as the sum of two solutions. The first is the solution to a laterally loaded, simply supported, quarter infinite plate in which the corner does not lift. For many cases a solution in closed form can be obtained and a specific example is given in the next section. The displacement corresponding to a problem of this type will be denoted as $w_0(x, y)$. The total displacement $w(x, y)$ can be represented as the sum

$$w(x, y) = w_0(x, y) + w_1(x, y) \tag{1}$$

where $w_1(x, y)$ represents the displacement solution required to insure that there is no loading on that region where the plate lifts from the support.

The equation governing w is

$$D\nabla^4 w = q \tag{2}$$

[1] This work was supported in part by the National Science Foundation, Grant CME-8006265.

Contributed by the Applied Mechanics Division for presentation at the Winter Annual Meeting, Washington, D. C., November 15–20, 1981, of THE AMERICAN SOCIETY OF MECHANICAL ENGINEERS.

Discussion on this paper should be addressed to the Editorial Department, ASME, United Engineering Center, 345 East 47th Street, New York, N. Y. 10017, and will be accepted until December 1, 1981. Readers who need more time to prepare a discussion should request an extension from the Editorial Department. Manuscript received by ASME Applied Mechanics Division, May, 1980; final revision, February, 1981. Paper No. 81-WA/APM-11.

where

$$D\nabla^4 w_0 = q,\ D\Delta^4 w_1 = 0,\ D = Eh^3/12(1-\nu^2), \qquad (3a\text{–}c)$$

and $q(x, y)$ is the applied load. The stress couples and resultants are

$$M_x = -D\left(\frac{\partial^2 w}{\partial x^2} + \nu\frac{\partial^2 w}{\partial y^2}\right) \qquad (4a)$$

$$M_y = -D\left(\frac{\partial^2 w}{\partial y^2} + \nu\frac{\partial^2 w}{\partial x^2}\right) \qquad (4b)$$

$$M_{xy} = -M_{yx} = D(1-\nu)\frac{\partial^2 w}{\partial x\,\partial y} \qquad (4c)$$

$$V_x = -D\frac{\partial}{\partial x}\left[\frac{\partial^2 w}{\partial x^2} + (2-\nu)\frac{\partial^2 w}{\partial y^2}\right] \qquad (5a)$$

$$V_y = -D\frac{\partial}{\partial y}\left[\frac{\partial^2 w}{\partial y^2} + (2-\nu)\frac{\partial^2 w}{\partial x^2}\right] \qquad (5b)$$

and the corner force R, at $x = 0, y = 0$, is given by

$$R = 2M_{xy}|_{x=0,y=0}. \qquad (6)$$

The boundary conditions for the lifting plate are (Fig. 1)

$$M_y = M_{y0} + M_{y1} = 0 \quad y = 0, \quad 0 < x \partial \infty \qquad (7a)$$

$$w = w_0 + w_1 = 0 \quad y = 0, \quad a < x < \infty \qquad (7b)$$

$$V_y = V_{y0} + V_{y1} = 0 \quad y = 0, \quad 0 < x < a \qquad (7c)$$

$$M_x = M_{x0} + M_{x1} = 0 \quad x = 0, \quad 0 < y < \infty \qquad (8a)$$

$$w = w_0 + w_1 = 0 \quad x = 0, \quad b < y < \infty \qquad (8b)$$

$$V_x = V_{x0} + V_{x1} = 0 \quad x = 0, \quad 0 < y < b. \qquad (8c)$$

Furthermore,

$$M_{xy} = 0 \quad x = 0, y = 0. \qquad (8d)$$

The boundary conditions for w_0 are the following:

$$w_0 = M_{y0} = 0 \quad y = 0, \quad 0 < x < \infty \qquad (9a)$$

$$w_0 = M_{x0} = 0 \quad x = 0, \quad 0 < y < \infty, \qquad (9b)$$

where w_0 satisfies (3a) and stress resultants having subscript "0" correspond to w_0. Similarly, w_1 satisfies (3b) and stress resultants having subscript "1" correspond to w_1. The remainder of the problem requires the determination of w_1 such that boundary conditions (7) and (8) are satisfied, including the corner condition (8d).

The lateral deflection w_1, appropriate for the region $x > 0, y > 0$, and satisfying equation (3), can be written in the following form:

$$D\,w_1(x,y) = \int_0^\infty \xi^{-2}\,[A(\xi) + \xi y B(\xi)]e^{-\xi y}\sin\xi x\,d\xi + \int_0^\infty \eta^{-2}\,[C(\eta) + \eta x D(\eta)]e^{-\eta x}\sin\eta y\,d\eta. \qquad (10)$$

Using equations (7) and (8) and assuming that w_0 and its corresponding stress resultants are known, one may determine boundary conditions on w_1 in terms of the assumed known solution w_0.

Differentiating equations (7b) and (8b) twice with respect to x and y, respectively, and integrating equations (7c) and (8c) with respect to x and y, respectively, leads, after use of equations (4), (5), (10), (7a), and (8a) to the following coupled equations:

$$\int_0^\infty B(\xi)\sin\xi x d\xi = 0 \quad a < x < \infty, \qquad (11)$$

$$\int_0^\infty D(\eta)\sin\eta y d\eta = 0 \quad b < y < \infty, \qquad (12)$$

$$-\int_0^\infty (1-\nu)(\eta x - 1)D(\eta)e^{-\eta x}d\eta - \int_0^\infty (3+\nu)B(\xi)\cos\xi x d\xi = \tilde{V}_y(x) + C_y; \quad 0 < x < a, \qquad (13)$$

$$-\int_0^\infty (1-\nu)(\xi y - 1)B(\xi)e^{-\xi y}d\xi - \int_0^\infty (3+\nu)D(\eta)\cos\eta y d\eta = \tilde{V}_x(y) + C_x \quad 0 < y < b, \qquad (14)$$

where $\tilde{V}_y(x) = \int V_{y0}(x)dx$ and $\tilde{V}_x(y) = \int V_{x0}(y)dy$ and C_y, C_x are constants of integration. We note that for many cases of simple loads the functions $\tilde{V}_x$ and $\tilde{V}_y$ can be found in closed form.

The corner force, R_1, is given as

$$R_1 = \left|2(1-\nu)\frac{\partial^2 w_1}{\partial x\,\partial y}\right|_{\substack{x=0\\y=0}} = -2(1+\nu)\int_0^\infty [B(s) + D(s)]ds. \qquad (15)$$

According to condition (8d), we must have

$$R = R_0 + R_1 = 0. \qquad (16)$$

Therefore,

$$\int_0^\infty [B(s) + D(s)]ds = R_0/2(1+\nu). \qquad (17)$$

Let $x = 0$ in (13) and $y = 0$ in (14), and if the resulting equations are summed, then we are led to the result

$$C_y + C_x = -R_0 - \tilde{V}_y(0) - \tilde{V}_x(0), \qquad (18)$$

where use has been made of equation (17).

At this point it is convenient to represent the transforms $B(\xi)$ and $D(\xi)$ as the following finite Fourier transforms:

$$B(\xi) = \int_0^a b(t)\sin\xi t\,dt, \quad D(\eta) = \int_0^b d(t)\sin\eta t\,dt. \qquad (19a,b)$$

Here we note that $b(t)$, $d(t)$ are related to the second derivatives of w with respect to x and y. These represent quantities which have the same singularities at a, b as do the moments there.

Substitution of equations (19) into equations (13) and (14) leads to the following coupled pair of singular integral equations (see, e.g., (7)):

$$-(1-\nu)\int_0^b \frac{t(x^2-t^2)}{(x^2+t^2)^2}d(t)dt - \frac{3+\nu}{2}\int_0^a b(t)\left[\frac{1}{t-x} + \frac{1}{t+x}\right]dt = \tilde{V}_y(x) + C_y \quad 0 < x < a \qquad (20)$$

$$-(1-\nu)\int_0^a \frac{t(y^2-t^2)}{(y^2+t^2)^2}b(t)dt - \frac{3+\nu}{2}\int_0^b d(t)\left[\frac{1}{t-y} + \frac{1}{t+y}\right]dt = \tilde{V}_x(y) + C_x \quad 0 < y < b. \qquad (21)$$

Let $x = 0$ and $y = 0$ in equations (20) and (21), respectively, and take the difference of these two equations to obtain

$$C_y - C_x = 4\int_0^b \frac{d(t)dt}{t} - 4\int_0^a \frac{b(t)dt}{t} - \tilde{V}_y(0) + \tilde{V}_x(0). \qquad (22)$$

Equations (18) and (22) are simultaneous equations for C_x and C_y. When they are determined and put into equations (20) and (21), the following equations are obtained, whose solutions will yield $b(t)$ and $d(t)$:

$$-\int_0^b \left[\frac{(1-\nu)t(x^2-t^2)}{(x^2+t^2)^2} + \frac{4}{t}\right]d(t)dt - \int_0^a \frac{(3+\nu)}{2}\left(\frac{1}{t-x} + \frac{1}{t+x}\right)b(t)dt = \tilde{V}_y(x) - \tilde{V}_y(0) - \frac{R_0(3+\nu)}{2(1+\nu)}, \quad 0 < x < a \qquad (23)$$

$$- \int_0^a \left[\frac{(1-\nu)t(y^2-t^2)}{(y^2+t^2)^2} + \frac{4}{t}\right] b(t)dt$$
$$- \int_0^b \left(\frac{3+\nu}{2}\right)\left(\frac{1}{t-y} + \frac{1}{t+y}\right) d(t)dt$$
$$= \tilde{V}_x(y) - \tilde{V}_x(0) - \frac{R_0}{2}\frac{(3+\nu)}{(1+\nu)}, \quad 0 < y < b. \quad (24)$$

Numerical Analysis

Equations (23) and (24) are prepared for numerical analysis by first extending the regions of integration to $-a < x < a$, $-b < y < b$ and introduce the following changes of variables and redefinition of $b(t)$ and $d(t)$:

$$t = as, \quad x = au, \quad b(as) = \bar{b}(s)\sqrt{1-s^2}$$
$$t = bq, \quad y = bz, \quad d(bq) = \bar{d}(q)\sqrt{1-q^2}, \quad (25)$$

where $\bar{b}(s)$ and $\bar{d}(q)$ are regular at ± 1. Here we note that the definition of $b(s)$, $d(q)$ in terms of $\bar{b}(s)$, $\bar{d}(q)$ imply that the moments of a, b are bounded there. This is in agreement with [6] where the related advancing contact problem was considered.

Equations (23) and (24) can thus be written in the following form:

$$\frac{1}{\pi}\int_{-1}^{1} \frac{\bar{b}(s)\sqrt{1-s^2}}{s-u} ds + \int_{-1}^{1} K(\alpha u, q)\bar{d}(q)\sqrt{1-q^2}\, dq = F_1(au), \quad -1 < u < 1 \quad (26)$$

$$\frac{1}{\pi}\int_{-1}^{1} \frac{\bar{d}(q)\sqrt{1-q^2}}{q-z} dq + \int_{-1}^{1} K(\alpha^{-1}z, s)\bar{b}(s)\sqrt{1-s^2} ds = F_2(bz), \quad -1 < z < 1 \quad (27)$$

where

$$K(\zeta,\mu) = \frac{2}{\pi(3+\nu)}\left[\frac{2}{\mu} + \left(\frac{1-\nu}{2}\right)\frac{\mu(\zeta^2-\mu^2)}{(\zeta^2+\mu^2)}\right] \quad (28a)$$

$$-\frac{1}{2}\pi(3+\nu)F_1(x) = \tilde{V}_y(x) - \tilde{V}_y(0) - \frac{R_0}{2}\frac{(3+\nu)}{(1+\nu)} \quad (28b)$$

$$-\frac{1}{2}\pi(3+\nu)F_2(y) = \tilde{V}_x(y) - \tilde{V}_x(0) - \frac{R_0}{2}\frac{(3+\nu)}{(1+\nu)}. \quad (28c)$$

and $\alpha = a/b$.

An important physical quantity is the displacement the plate undergoes near the corner of the plate as it lifts off the simple support. Using equations (13), together with (10) and (19), one obtains the following values for the edge displacements:

$$D\,w_1(x,0) = \frac{\pi}{1-\nu}\left\{\int_0^x b(t)t\,dt + \int_x^a b(t)x\,dt\right\}, \quad 0 < x < a$$
$$= \frac{\pi}{1-\nu}\int_0^a t\,b(t)dt, \quad x > a \quad (29a)$$

$$D\,w_1(0,y) = \frac{\pi}{1-\nu}\left\{\int_0^y d(t)t\,dt + \int_y^b d(t)y\,dt\right\}, \quad 0 < y < b$$
$$= \frac{\pi}{1-\nu}\int_0^b t\,d(t)dt, \quad y > b. \quad (29b)$$

Equations (29) require a rigid-body displacement term, w_c, to shift w_1 so that $w_1(x,0)$ and $w_1(0,y)$ are zero for $x > a$, $y > b$, respectively. Thus the additional condition

$$w_1(a,0) = w_1(0,b) = -w_c \quad (30)$$

is imposed, i.e.,

$$\int_0^a tb(t)dt = \int_0^b td(t)dt. \quad (31)$$

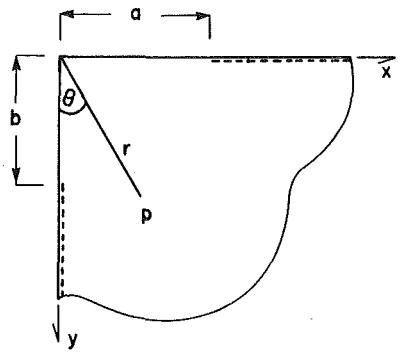

Fig. 1 A simply supported plate being loaded laterally by a concentrated force P acting at a position (R, θ). a and b denote the parts of the edges being lifted up

The Gauss-Chebyshev integration formula is applied to equations (26) and (27), which are then written as [8]

$$\sum_{i=1}^{n} \frac{1-s_i^2}{n+1}\left[\frac{\bar{b}(s_i)}{s_i-u_k} + \pi K(\alpha u_k, q_i)\bar{d}(q_i)\right] = G_1(u_k) \quad (32)$$

$$\sum_{i=1}^{n} \frac{1-q_i^2}{n+1}\left[\frac{\bar{d}(q_i)}{q_i-z_k} + \pi K(\alpha^{-1}z_k, s_i)\bar{b}(s_i)\right] = G_2(z_k) \quad (33)$$

where $G_1(u_k) = F_1(au_k)$, $G_2(z_k) = F_2(bz_k)$. Here,

$$s_i = q_i = \cos\left(\frac{i\pi}{n+1}\right), \quad i = 1, \ldots, n \quad (34a)$$

$$u_k = z_k = \cos\left(\frac{\pi}{2}\cdot\frac{2k-1}{n+1}\right), \quad k = 1, \ldots, n+1. \quad (34b)$$

Equation (31) becomes

$$\sum_{i=1}^{n} \{\alpha^2\bar{b}(s_i)s_i\bar{w}_i - \bar{d}(q_i)q_i\bar{w}_i\} = 0; \quad \bar{w}_i = \frac{\pi}{n+1}\sin^2\left(\frac{i\pi}{n+1}\right). \quad (35)$$

There are $2n+3$ equations arising from equations (32), (33), and (35) from which we wish to solve for n values each of $\bar{b}(s_i)$, $\bar{d}(q_i)$ and one value each of a and b. During the process of solution an even value of n was assumed, and the equations corresponding to $k = n/2 + 1$ in both (32) and (33) are identical equations and one can be discarded. The remaining $2n$ equations are then solved using an assumed value for α. The resulting $\bar{b}(s)$ and $\bar{d}(q)$ are put back into (35) and either one of the $(n/2+1)$th equations of (32), (33) for checking. A series of values for a and b are tried until the correct ones that simultaneously satisfy the checking equations are found.

Example—Concentrated Load. We consider a concentrated load located at a position (R, θ) as shown in Fig. 1. Solution to the simply supported quarter plane plate having a concentrated load at (R, θ) can be found by use of the solution to the concentrated load in an infinite plate along with the method of images. The resulting deflection is given by

$$w_0(x,y) = \frac{P}{8\pi D}\{[(x-\rho_1)^2 + (y-\rho_2)^2] \times \log[(x-\rho_1)^2 + (y-\rho_2)^2]^{1/2} + [(x+\rho_1)^2 + (y+\rho_2)^2]\log[(x+\rho_1)^2 + (y+\rho_2)^2]^{1/2} - [(x-\rho_1)^2 + (y+\rho_2)^2]\log[(x-\rho_1)^2 + (y+\rho_2)^2]^{1/2} - [(x+\rho_1)^2 + (y-\rho_2)^2]\log[(x+\rho_1)^2 + (y-\rho_2)^2]^{1/2}\} \quad (36)$$

where $\rho_1 = R\cos\theta$, $\rho_2 = R\sin\theta$. Using this solution for w_0, the corner force R_0 can be computed as

$$R_0 = 2D(1-\nu)\left.\frac{\partial^2 w_0}{\partial x\,\partial y}\right|_{\substack{x=0\\y=0}} = \frac{2P(1-\nu)}{\pi}\left[\frac{\rho_1\rho_2}{\rho_1^2+\rho_2^2}\right] \quad (37)$$

and the integrated values of the shears are found to be

Table 1 Values of a/R, b/R for different locations of concentrated load

θ \ ν	0.		0.125		0.250		0.375		0.5	
	a/R	b/R	a/R	b/R	a/R	b/R	a/R	b/R	a/R	b/R
$\pi/4$	0.829	0.829	0.788	0.788	0.742	0.742	0.692	0.692	0.632	0.632
$3\pi/16$	0.857	0.813	0.810	0.776	0.761	0.734	0.705	0.686	0.642	0.630
$\pi/8$	0.891	0.808	0.839	0.773	0.783	0.734	0.723	0.687	0.654	0.632
$\pi/16$	0.928	0.820	0.868	0.783	0.807	0.746	0.739	0.698	0.665	0.639
$\pi/32$	0.946	0.836	0.883	0.800	0.815	0.756	0.745	0.705	0.668	0.643
$\pi/512$	0.955	0.850	0.889	0.809	0.820	0.762	0.747	0.708	0.670	0.645

$$\tilde{V}_y(x) = \int V_{y0}(x)dx = \frac{-P}{\pi}\left\{\tan^{-1}\left(\frac{x+\rho_1}{\rho_2}\right) - \tan^{-1}\left(\frac{x-\rho_1}{\rho_2}\right) + (1-\nu)\rho_1\rho_2\left[\frac{\rho_1^2+\rho_2^2-x^2}{[(x+\rho_1)^2+\rho_2^2][(x-\rho_1)^2+\rho_2^2]}\right]\right\} \quad (38)$$

$$\tilde{V}_x(y) = \int V_{x0}(y)dx = \frac{-P}{\pi}\left\{\tan^{-1}\left(\frac{y+\rho_2}{\rho_1}\right) - \tan^{-1}\left(\frac{y-\rho_2}{\rho_1}\right) + (1-\nu)\rho_1\rho_2\left[\frac{\rho_1^2+\rho_2^2-y^2}{[(y+\rho_2)^2+\rho_1^2][(y-\rho_2)^2+\rho_1^2]}\right]\right\}. \quad (39)$$

Using these values, $G_1(u)$ and $G_2(z)$ in equations (32) and (33) are calculated as

$$G_1(u) = \frac{P}{\pi^2}\left(\frac{2}{3+\nu}\right)\left\{\left(\frac{1-\nu}{1+\nu}\right)\sin 2\theta - 2\theta + \theta_0 + \frac{(1-\nu)}{2}\frac{\left(1-\frac{a^2}{R^2}u^2\right)\sin 2\theta}{\left[\left(1+\frac{a^2}{R^2}u^2\right)^2 - \frac{4a^2}{R^2}u^2\sin^2\theta\right]}\right\} \quad (40)$$

$$G_2(z) = \frac{P}{\pi^2}\left(\frac{2}{3+\nu}\right)\left\{\frac{1-\nu}{(1+\nu)}\sin 2\theta + 2\theta - \pi + \theta_1 + \frac{(1-\nu)}{2}\frac{\left(1-\frac{b^2}{R^2}z^2\right)\sin 2\theta}{\left[\left(1+\frac{b^2}{R^2}z^2\right)^2 - \frac{4b^2}{R^2}z^2\cos^2\theta\right]}\right\} \quad (41)$$

$$\theta_0 = \tan^{-1}\left(\frac{au+\rho_1}{\rho_2}\right) - \tan^{-1}\left(\frac{au-\rho_1}{\rho_2}\right) \quad (42a)$$

$$\theta_1 = \tan^{-1}\left(\frac{bz+\rho_2}{\rho_1}\right) - \tan^{-1}\left(\frac{bz-\rho_2}{\rho_1}\right). \quad (42b)$$

Applying the numerical scheme just described, values for a/R and b/R can be computed for various locations of the concentrated load P and for different values of ν. Table 1 shows several such values that describe the locations of the loss of contact. In addition Fig. 2 shows the edge displacements near the corner of the lifting plate for some of these values.

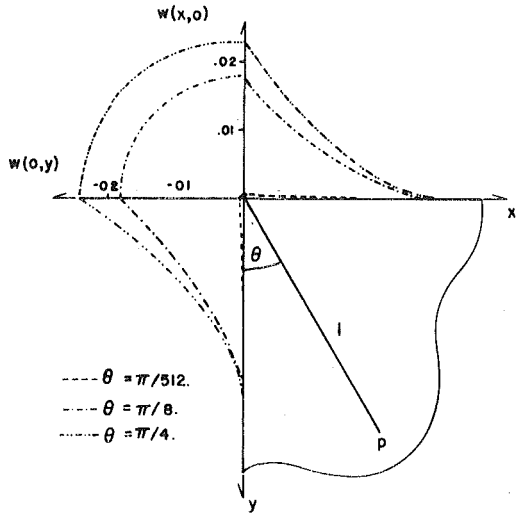

Fig. 2 The displacements of the edge near the corner for $\theta = \pi/512$, $\pi/8$, $\pi/4$, with ν being 0.25

Conclusion

Solutions are obtained for some cases of a quarter infinite, laterally loaded, simply supported plate having a unilateral constraint. The solution technique used here required the identification of certain limiting values of integral transforms related to the corner forces arising from the bilateral problem. Once this identification was established standard numerical solution techniques for such problems could be employed.

References

1 Timoshenko, S., and Woinowsky-Krieger, S., *Theory of Plates and Shells*, 2nd ed., McGraw-Hill, New York, 1959.

2 Dundurs, J., and Stippes, M., "Role of Elastic Constants in Certain Contact Problems," ASME JOURNAL OF APPLIED MECHANICS, Vol. 37, 1970, pp. 965–970.

3 Kiattikomol, K., Keer, L. M., and Dundurs, J., "Application of Dual Series to Rectangular Plates," *Journal of the Engineering Mechanics Division, ASCE*, Vol. 100, No. EM2, *Proceedings*, Paper 10486, Apr. 1974, pp. 433–444.

4 Stahl, B., and Keer, L. M., "Bending of a Uniformly Loaded Circular Plate With Mixed Boundary Conditions," *Journal of the American Institute of Aeronautics and Astronautics*, Vol. 10, 1972, pp. 739–743.

5 Stahl, B., and Keer, L. M., "Vibration and Buckling of a Rectanguar Plate With an Internal Support," *Quarterly Journal of Mechanics and Applied Mathematics*, Vol. 25, 1972, pp. 467–478.

6 Dundurs, J., Kiattikomol, K., and Keer, L. M., "Contact Between Plates and Sagged Supports," *Journal of the Engineering Mechanics Division, ASCE*, Vol. 100, No. EM2, Apr. 1974, pp. 445–456, *Proceedings*, Paper 10485.

7 Sneddon, I. N., "Fourier Transform Solutions of Quarter Plane Problems in Elasticity," File No. PSR-99/6, Applied Mathematics Research Group, North Carolina State University, May 1971.

8 Erdogan, F., Gupta, G. D., and Cook, T. S., "Numerical Solution of Singular Integral Equations," *Mechanics of Fracture*, Vol. 1, Sih, G. C., ed., Noordhoff International Publishing, Leyden, 1973, pp. 368–425.

E. Reissner

Department of Applied Mechanics
and Engineering Sciences,
University of California, San Diego,
La Jolla, Calif. 92093
Fellow ASME

On a One-Dimensional Theory of Finite Torsion and Flexure of Anisotropic Elastic Plates[1]

Equations for small finite displacements of shear-deformable plates are used to derive a one-dimensional theory of finite deformations of straight slender beams with one cross-sectional axis of symmetry. The equations of this beam theory are compared with the corresponding case of Kirchhoff's equations, and with a generalization of Kirchhoff's equations which accounts for the deformational effects of cross-sectional forces. Results of principal interest are:

1 The equilibrium equations are seven rather than six, in such a way as to account for cross-sectional warping.

2 In addition to the usual six force and moment components of beam theory, there are two further stress measures, (i) a differential plate bending moment, as in the corresponding linear theory, and (ii) a differential sheet bending moment which does not occur in linear theory.

The general results are illustrated by the two specific problems of finite torsion of orthotropic beams, and of the buckling of an axially loaded cantilever, as a problem of bending-twisting instability caused by material anisotropy.

Introduction

The principal purpose of the following is the derivation of a system of one-dimensional nonlinear beam equations for originally straight beams, as a rational consequence of a given *nonlinear* system of plate equations. The method of derivation and certain basic constitutivity assumptions are the same as those used previously for the problem of torsion and flexure within the framework of *linear* theory [3]. The present derivation is based on a system of nonlinear plate equations which represents a generalization of the Kirchhoff-von Karman system, in such a way that the effect of transverse shear deformation (which turns out to be more significant than anticipated) is included [1, 4].

The equations of the one-dimensional theory which is obtained here are compared with the corresponding classical Kirchhoff equations, and also with a direct generalization of Kirchhoff's equations in which account is taken of the deformational effects of cross-sectional forces, in addition to the deformational effects of cross-sectional moments [2].

The results of the present analysis which are thought to be of main interest are the following:

1 The equilibrium equations of the nonlinear beam theory are seven in number rather than six.

2 The relevant stress measures, in addition to force and moment components are (*i*) a differential *plate* bending moment, R_p, as known from linear theory, and (*ii*) what may be called a differential *sheet* bending moment, R_s, which does *not* occur in linear theory.

The meaning of the general results is illustrated by means of two specific problems. The first of these is the problem of finite torsion of an orthotropic beam, and the second the problem of Euler buckling of a cantilever beam as a problem of bending-twisting instability caused by material anisotropy. Both problems show a non-negligible effect of the two differential bending moments which are a part of this theory, over and above the conventional six force and moment components.

Equations of Nonlinear Plate Theory

We take as given a system of six equilibrium equations of the form [1]

[1] Supported by the Office of Naval Research.

Contributed by the Applied Mechanics Division for publication in the JOURNAL OF APPLIED MECHANICS.

Discussion on this paper should be addressed to the Editorial Department, ASME, United Engineering Center, 345 East 47th Street, New York, N. Y. 10017, and will be accepted until December 1, 1981. Readers who need more time to prepare a discussion should request an extension from the Editorial Department. Manuscript received by ASME Applied Mechanics Division, May, 1980; final revision, December, 1980.

$$N_{11,1} + N_{21,2} + p_1 = 0, \quad N_{12,1} + N_{22,2} + p_2 = 0, \quad N_{12} = N_{21}, \tag{1}$$

$$Q_{1,1} + Q_{2,2} - \kappa_{11}N_{11} - \kappa_{22}N_{22} - \kappa_{12}N_{12} - \kappa_{21}N_{21} + q = 0,$$

$$M_{11,1} + M_{21,2} - Q_1 + \gamma_1 N_{11} + \gamma_2 N_{21} + m_1 = 0, \tag{2}$$

$$M_{12,1} + M_{22,2} - Q_2 + \gamma_1 N_{12} + \gamma_2 N_{22} + m_2 = 0,$$

in conjunction with strain displacement relations

$$\kappa_{11} = \phi_{1,1}, \quad \kappa_{12} = \phi_{2,1}, \quad \kappa_{21} = \phi_{1,2}, \quad \kappa_{22} = \phi_{2,2},$$
$$\gamma_1 = \phi_1 + w_{,1}, \quad \gamma_2 = \phi_2 + w_{,2}, \tag{3}$$

$$\epsilon_{11} = u_{1,1} + w\phi_{1,1} - \tfrac{1}{2}\phi_1^2, \quad \epsilon_{22} = u_{2,2} + w\phi_{2,2} - \tfrac{1}{2}\phi_2^2,$$
$$\epsilon_{12} = u_{2,1} - \omega + w\phi_{2,1} - \tfrac{1}{2}\phi_1\phi_2,$$
$$\epsilon_{21} = u_{1,2} + \omega + w\phi_{1,2} - \tfrac{1}{2}\phi_1\phi_2, \tag{4}$$
$$\lambda_1 = \omega_{,1} - \tfrac{1}{2}\phi_1\phi_{2,1} + \tfrac{1}{2}\phi_2\phi_{1,1}, \quad \lambda_2 = \omega_{,2} + \tfrac{1}{2}\phi_2\phi_{1,2} - \tfrac{1}{2}\phi_1\phi_{2,2},$$

with (3) and (4) being consistent, via considerations of virtual work, with equations (1) and (2).[2]

We note that in the foregoing equations stress resultants N and Q and stress couples M, as well as body forces and moments and translational and rotational components of displacements are taken with respect to *body-fixed* directions, which in the undeformed state coincide with the cartesian axes x_1, x_2, and x_3.

A reduction to the Kirchhoff-von Karman theory takes place upon assuming, as part of a system of constitutive relations, that $\gamma_1 = \gamma_2 = 0$. Significantly, when this reduction is assumed the remaining system of equations seems no longer of sufficient generality so as to retain within its scope the possibility of leading to a system of one-dimensional equations which is general enough to allow a solution of the Prandtl-Michell lateral stability problem.

Constitutive Equations and Strain Displacement Relations for the Derivation of Beam Theory

The essence of our procedure for the derivation of a *conventional* system of one-dimensional equations depends on the assumption that only those components of strain which enable stresses acting over the *cross section* of the prospective beam to do work are of a non-negligible magnitude. If we consider x_1 as the direction of the axis of the beam we then have, as part of the constitutive equations of the plate, the system of rigidity conditions

$$\epsilon_{21} = \epsilon_{22} = \gamma_2 = \kappa_{21} = \kappa_{22} = \lambda_2 = 0, \tag{5}$$

with $N_{21}, N_{22}, Q_2, M_{21}$, and M_{22} now being reactive quantities,[3] and with the remaining constitutive equations being of the form

$$(N_{11},N_{12},Q_1,M_{11},M_{12}) = f(\epsilon_{11},\epsilon_{12},\epsilon_1,\kappa_{11},\kappa_{12}). \tag{6}$$

Leaving aside for now a stipulation of the form of (6) which will be used explicitly in what follows, we observe that equations (5) imply as expressions for displacements

$$\phi_2 = \phi_2(x_1), \quad \phi_1 = \phi_1(x_1), \quad \omega = \omega(x_1), \quad w = w(x_1) - x_2\phi_2, \tag{7}$$

$$u_2 = u_2(x_1) + \tfrac{1}{2}x_2\phi_2^2, \quad u_1 = u_1(x) - x_2(\omega - \tfrac{1}{2}\phi_1\phi_2), \tag{8}$$

and equations (7) and (8) in turn imply as expressions for the remaining components of strain, with differentiation with respect to x_1 now indicated by primes,

$$\kappa_{11} = \phi_1', \quad \kappa_{12} = \phi_2', \quad \gamma_1 = \phi_1 + w' - x_2\phi_2', \tag{9}$$

$$\epsilon_{11} = u_1' - \tfrac{1}{2}\phi_1^2 - x_2(\omega' + \tfrac{1}{2}\phi_1'\phi_2 - \tfrac{1}{2}\phi_2'\phi_1),$$
$$\epsilon_{12} = u_2' - \omega + w\phi_2' - \tfrac{1}{2}\phi_1\phi_2. \tag{10}$$

[2] The nonlinear strain displacement relations (4) have been derived in [1] by considerations which involved an element of speculativity. For an alternate systematic derivation see [4].

[3] We note the appearance of the quantity λ_2 in (5). The statical counterpart of λ_2 would be a moment component P_2 with axis perpendicular to the plate surface which, in the nature of a further constitutive stipulation, we do not consider here.

Equations (9) and (10), and therewith the constitutive equations (6), contain altogether *six* unknown one-dimensional displacement functions, $\phi_1, \phi_2, \omega, u_1, u_2, w$, and in order to complete the system of one-dimensional beam equations it is now only necessary to derive *six* one-dimensional equilibrium equations, as a consequence of the six plate equilibrium equations (1) and (2). If we do this we obtain a one-dimensional beam theory which is in effective agreement with the result in [2]. We will here, however, not proceed in this direction and, instead, consider a shortcoming of the foregoing which will then show the way to a generalization of the theory, involving a total of *seven* one-dimensional displacement functions and *seven* one-dimensional equilibrium equations.

The shortcoming of the results in (6) and (7) consists, in essence, of the fact that the bending strain measure κ_{11} and the rotational displacement ϕ_1 are independent of the *width* coordinate x_2, that is, the equations of the theory based on the assumption (5) do not make provision for the effect of *differential bending*. In looking for the cause of this excessive limitation we find that this cause is one of the constraint conditions in (5), namely, the condition $\kappa_{21} = 0$.

What follows is then based on leaving five of the six conditions in (5) as they are, while at the same time relaxing the sixth condition in the simplest way possible, by stipulating instead of the relation $\kappa_{21} = 0$ a relation

$$\kappa_{21} = \psi(x_1), \tag{5'}$$

with this relaxed condition then leading to a one-dimensional nonlinear beam theory which is significantly different from "conventional" Kirchhoff-type theories.

In evaluating the consequences of the assumption (5') it will be convenient to introduce the notation

$$\phi_1(x_1) = \phi, \quad \phi_2(x_1) = \theta, \quad u_1(x_1) = u, \quad u_2(x_1) = v. \tag{11}$$

Therewith we now obtain as expressions for displacement components

$$\phi_1 = \phi + x_2\psi, \quad \phi_2 = \theta, \quad w = w(x_1) - x_2\theta, \tag{12}$$

$$\omega = \omega(x_1) - \tfrac{1}{2}x_2\psi\theta, \quad u_2 = v + \tfrac{1}{2}x_2\theta^2,$$
$$u_1 = u - x_2(\omega + w\psi - \tfrac{1}{2}\phi\theta) + x_2^2\psi\theta, \tag{13}$$

with (12) and (13) agreeing with the previously derived equations (7) and (8) except for the additional terms with ψ.

Having equations (12) and (13) we obtain from (3) and (4) for the set of nonvanishing strain components

$$\kappa_{11} = \phi' + x_2\psi', \quad \kappa_{12} = \theta', \quad \kappa_{21} = \psi, \quad \gamma_1 = \phi + w' + x_2(\psi - \theta'), \tag{14}$$

and

$$\epsilon_{11} = u' + w\phi' - \tfrac{1}{2}\phi^2 - x_2[\omega' - \psi(\phi + w') + \tfrac{1}{2}(\theta\phi' - \phi\theta')] + x_2^2\psi(\theta' - \tfrac{1}{2}\psi),$$
$$\epsilon_{12} = v' - \omega + w\theta' - \tfrac{1}{2}\phi\theta. \tag{15}$$

Equilibrium Equations of Beam Theory

We now consider the plate equilibrium differential equations (1) and (2), with expressions for the components of strain which occur in them given by (14), with a view toward deducing altogether *seven* one-dimensional equilibrium equations.

As a step toward obtaining this one-dimensional system, we consider that we have as boundary conditions for two spanwise edges $x_2 = x_{21}$ and $x_2 = x_{22}$ of the plate

$$N_{21} = N_{22} = Q_2 = M_{21} = M_{22} = 0. \tag{16}$$

To make apparent the physical meaning of the various kinematical terms which will appear in the one-dimensional equations we introduce in equations (14) the defining relations

$$\phi' = \kappa_p, \quad \theta' = \kappa_t, \quad \phi + w' = \gamma_p. \tag{17}$$

With (16) and (17) we then obtain from equations (1) and (2) a system of *eight* integrated relations,

$$\begin{aligned} &\int N_{11}' + \int p_1 = 0, \quad \int N_{12}' + \int p_2 = 0, \\ &\int x_2 N_{11}' - \int N_{12} + \int x_2 p_1 = 0, \end{aligned} \tag{18}$$

$$\int Q_1' - \kappa_p \int N_{11} - \psi' \int x_2 N_{11} - (\kappa_t + \psi) \int N_{12} + \int q = 0, \tag{19}$$

$$\int x_2 Q_1' - \int Q_2 - \kappa_p \int x_2 N_{11} - \psi' \int x_2^2 N_{11} - (\kappa_t + \psi) \int x_2 N_{12} + \int x_2 q = 0, \tag{20}$$

$$\int M_{11}' - \int Q_1 + \gamma_p \int N_{11} - (\kappa_t - \psi) \int x_2 N_{11} + \int m_1 = 0, \tag{21}$$

$$\int M_{12}' - \int Q_2 + \gamma_p \int N_{12} - (\kappa_t - \psi) \int x_2 N_{12} + \int m_2 = 0, \tag{22}$$

$$\int x_2 M_{11}' - \int M_{21} - \int x_2 Q_1 + \gamma_p \int x_2 N_{11} - (\kappa_t - \psi) \int x_2^2 N_{11} + \int x_2 m_1 = 0, \tag{23}$$

In writing (18)–(23), as well as in what follows, we omit, to save space, the usual factor dx_2, and also the limits x_{21} and x_{22} in the definite integrals. The desired *seven* beam equations are derived from (18)–(23) in two steps. The first step consists in stipulating in equation (23), as part of the complete system of constitutive equations, the relation

$$\int M_{21} = \int M_{12}. \tag{24}$$[4]

The second step consists in the elimination of Q_2 from (20) and (22). The result of doing this is the one equation

$$\int (M_{12} - x_2 Q_1)' + \kappa_p \int x_2 N_{11} + \gamma_p \int N_{12} + \psi' \int x_2^2 N_{11} + 2\psi \int x_2 N_{12} + \int (m_2 - x_2 q) = 0, \tag{25}$$

in place of (20) and (22).

Therewith, and with the notation

$$\begin{aligned} &\int Q_1 = Q_p, && \int N_{12} = Q_s, && \int N_{11} = P, \\ &\int q_1 = q_p, && \int p_2 = q_s, && \int p_1 = p \end{aligned} \tag{26}$$

$$\begin{aligned} &\int M_{11} = M_p, && \int x_2 N_{11} = M_s, && \int M_{12} = T_M, \\ &\int m_1 = m_p, && \int x_2 p = m_s, && \int m_2 = t_M \end{aligned} \tag{27}$$

$$\begin{aligned} &\int x_2 Q_1 = -T_Q, && \int x_2 M_{11} = R_p, && \int x_2^2 N_{11} = R_s, \\ &-\int x_2 q = t_Q, && \int x_2 m_1 = r_p, && \int x_2^2 p_1 = r_s, \end{aligned} \tag{28}$$

where the subscripts p and s have been chosen to indicate the difference between *plate* and *sheet* action, we now rewrite the seven beam equilibrium differential equations in the form

$$P' + p = 0, \quad Q_s' + q_s = 0, \quad M_s' - Q_s + m_s = 0, \tag{29}$$

$$(Q_p - \psi M_s)' - \kappa_p P - \kappa_t Q_s + q_p = 0, \tag{30}$$

$$M_p' - \kappa_t M_s - (Q_p - \psi M_s) + \gamma_p P + m_p = 0, \tag{31}$$

$$T_M' + (T_Q + \psi R_s)' + \kappa_p M_s + \gamma_p Q_s + t_M + t_q = 0, \tag{32}$$

$$R_p' - \kappa_t R_s - T_M + (T_Q + \psi R_s) + \gamma_p M_s + r_p = 0. \tag{33}$$

The following observations may be made in regard to the appearance of the system (29)–(33).

1 We obtain a Kirchhoff-type system of the kind given in [2] by assuming $\psi = 0$ and by disregarding the seventh equation, (33). The additional assumption $\gamma_p = 0$ leads to an appropriately abbreviated version of the original Kirchhoff system. In saying this we take account of the fact that for beams of *narrow* cross section, as discussed here, the additional terms $\kappa_s Q_s$, $\kappa_p Q_p$, $\kappa_s N$, $\kappa_t Q_p$, $\kappa_t M_p$ which are included in the full version of equation (29) and the additional terms $\kappa_s T$ and $\kappa_s M_p$ which are included in the full version of equations (31) and (32) would be of negligible consequence.[5]

2 In order to obtain the term $\kappa_t M_s$ in equation (31), which term cannot be dispensed with, we had to make use of the term $\gamma_1 N_{11}$ in the plate equilibrium equations (2). What this seems to mean is that we *cannot* deduce an appropriate version of Kirchhoff's beam equations, as a consequence of the Kirchhoff-von Karman plate equations, without generalizing these plate equations first so as to account for the effect of transverse shear deformation.

3 The terms ψM_s and ψR_s in (30)–(33) account for sheet stress contributions to beam stress measures which, without explicit consideration of cross-sectional warping, would be due to plate stress action only.

Constitutive Equations for Beams

In deriving one-dimensional constitutive equations on the basis of a given system of constitutive equations for plates, in accordance with (6) or with generalizations of (6) in which account is taken of equation (5′), we limit ourselves here to cases of plate constitutive equations which are included in the following:

$$N_{11} = C_N \epsilon_{11}, \quad \epsilon_{12} = 0, \quad Q_1 = C_Q \gamma_1, \tag{34}$$

$$\begin{aligned} M_{11} &= D_B \kappa_{11} + D_{BT}(\kappa_{12} + \kappa_{21}), \\ M_{12} &= D_T(\kappa_{12} + \kappa_{21}) + D_{BT}\kappa_{11}. \end{aligned} \tag{35}$$

In this the coefficients C and D are given functions of x_1 and x_2. Furthermore,

$$\kappa_{11} = \kappa_p + x_2 \psi', \quad \kappa_{12} = \kappa_t, \quad \kappa_{21} = \psi, \quad \gamma_1 = \gamma_p + x_2(\psi - \kappa_t), \tag{36}$$

and, in accordance with (15),

$$\epsilon_{11} = \epsilon + x_2 \kappa_s + x_2^2 \psi(\kappa_t - \tfrac{1}{2}\psi), \quad \epsilon_{12} = \gamma_s + w\kappa_t - \tfrac{1}{2}\phi\theta, \tag{37}$$

where

$$\begin{aligned} \epsilon &= u' + w\kappa_p - \tfrac{1}{2}\phi^2, \quad \gamma_s = v' - \omega, \\ \kappa_x &= -\omega' + \psi\gamma_p + \tfrac{1}{2}(\phi\kappa_t - \theta\kappa_p). \end{aligned} \tag{38}$$

Introduction of equations (34)–(37) into the defining relations (26)–(28) then gives

$$P = \epsilon \int C_N + \kappa_s \int x_2 C_N + \psi(\kappa_t - \tfrac{1}{2}\psi) \int x_2^2 C_N, \tag{39}$$

$$M_s = \epsilon \int x_2 C_N + \kappa_s \int x_2^2 C_N + \psi(\kappa_t - \tfrac{1}{2}\psi) \int x_2^3 C_N, \tag{40}$$

$$R_s = \epsilon \int x_2^2 C_N + \kappa_s \int x_2^3 C_N + \psi(\kappa_t - \tfrac{1}{2}\psi) \int x_2^4 C_N, \tag{41}$$

$$Q_p = \gamma_p \int C_Q + (\psi - \kappa_t) \int x_2 C_Q, \tag{42}$$

$$-T_Q = \gamma_p \int x_2 C_Q + (\psi - \kappa_t) \int x_2^2 C_Q, \tag{43}$$

$$M_p = \kappa_p \int D_B + \psi' \int x_2 D_B + (\kappa_t + \psi) \int D_{BT}, \tag{44}$$

$$R_p = \kappa_p \int x_2 D_B + \psi' \int x_2^2 D_B + (\kappa_t + \psi) \int x_2 D_{BT}, \tag{45}$$

$$T_M = (\kappa_t + \psi) \int D_T + \kappa_p \int D_{BT} + \psi' \int x_2 D_{BT}. \tag{46}$$

In using (39)–(46) account has to be taken of the fact that the forces P and Q and moments M and T are components with respect to body fixed axes rather than with respect to the Cartesian axes x_i. Within the range of applicability of the present formulation, these differences are negligible for tangential force components and plate-normal moment components, but not for normal force components and tangential moment components. The relevant formulas are

$$V_3 = Q_p + \int (N_{11}\phi_1 + N_{12}\phi_2) = Q_p + P\phi + M_s\psi + Q_s\theta, \tag{47}$$

[4] The stipulation (24) is neither required, nor possible, in the event that we presuppose the additional constraint relation $\kappa_{21} = \psi = 0$, in which case equation (23) becomes a defining relation for $\int M_{21}$, in place of being a part of the differential equation system.

[5] A previous generalization of Kirchhoff's nonlinear beam theory, with three-dimensional theory equations as the point of departure, in which consideration of warping introduces a seventh equilibrium equation has been given by Wempner [5]. The present equations differ from equations which are included in Wempner's equations by the terms with ψ and γ_p in (30)–(32).

$$M_1 = T_M + T_Q + \int x_2(N_{11}\phi_1 + N_{12}\phi_2)$$

$$= T_M + T_Q + M_s\phi + R_s\psi + \tfrac{1}{2}R_s\theta, \quad (48)$$

where we have used the relation $\int x_2^2 N_{11}' - 2\int x_2 N_{12} = 0$, and with w in the integral as in equation (7)

$$M_2 = M_p + \int N_{11} w = M_p + Pw - M_s\theta. \quad (49)$$

Finite Torsion of Orthotropic Symmetrical Cross-Section Beam

We consider, as a relatively simple illustration of the use of the foregoing, a beam for which

$$D_{BT} = 0, \quad \int x_2 C_N = \int x_2 C_Q = \int x_2 D_B = \int x_2^3 C_N = 0, \quad (50)$$

with the only load being a torque M_1, as defined by (48).

By symmetry, we may assume that the only nonvanishing measures of strain are the quantities ϵ, κ_t, and ψ; and the only nonvanishing measures of stress the quantities T_M, T_Q, and R_s.

The relevant constitutive equations for this problem are then, in accordance with (39)–(46)

$$0 = \epsilon\int C_N + \psi(\kappa_t - \tfrac{1}{2}\psi)\int x_2^2 C_N, \quad (51)$$

$$R_s = \epsilon\int x_2^2 C_N + \psi(\kappa_t - \tfrac{1}{2}\psi)\int x_2^4 C_N, \quad (52)$$

and

$$T_Q = (\kappa_t - \psi)\int x_2^2 C_Q, \quad T_M = (\kappa_t + \psi)\int D_T, \quad (53)$$

with the applied torque equation (48) here reducing to the form

$$M_1 = T_M + T_Q + \psi R_s. \quad (54)$$

Equations (51)–(54) are, in effect, a system of three relations for the four quantities ϵ, ψ, κ_t, and R_s. The needed fourth relation is given by the *seventh* beam equilibrium equation, (33), which here becomes

$$T_M - T_Q + (\kappa_t - \psi)R_s = 0. \quad (55)$$

The result of principal interest which may be derived from the system (51)–(55) is a nonlinear torque-twist relation $M_1 = f(\kappa_t)$. In deriving this relation it is instructive to begin with a consideration of the case of negligible transverse shear deformation which results upon setting

$$\int x_2^2 C_Q = \infty, \quad \psi = \kappa_t, \quad (56)$$

with T_Q now being reactive and, in accordance with (55), such that $T_Q = T_M$.

We next obtain, from (51) and (52)

$$R_s\int C_N = \tfrac{1}{2}\kappa_t^2[\int C_N \int x_2^4 C_N - (\int x_2^2 C_N)^2], \quad (57)$$

and therewith, from (53) and (54), as expression for M_1

$$M_1 = 4\kappa_t\int D_T + \kappa_t^3 \frac{\int C_N \int x_2^4 C_N - (\int x_2^2 C_N)^2}{2\int C_N}. \quad (58)$$

For the case that $\int x_2^2 C_Q$ is not assumed to be infinite we have in place of (57)

$$R_s\int C_N = \psi(\kappa_t - \tfrac{1}{2}\psi)[\int C_N \int x_2^2 C_N - (\int x_2^2 C_N)^2]. \quad (59)$$

It now remains to determine ψ as a function of κ_t, through use of equations (55) and (53), that is from the relation

$$\psi(\int D_T + \int x_2^2 C_Q) + \kappa_t(\int D_T - \int x_2^2 C_Q) = (\psi - \kappa_t)R_s, \quad (60)$$

with the solution of this to be introduced into the torque expression

$$M_1 = \kappa_t(\int D_T + \int x_2^2 C_Q) + \psi(\int D_T - \int x_2^2 C_Q) + \psi R_s. \quad (61)$$

As the exact determination of ψ as a function of κ_t, by means of (59) and (60), now involves the solution of a cubic we limit ourselves here to an approximate determination, with (56) replaced by the stipulations,

$$\int D_T / \int x_2^2 C_Q \ll 1, \quad \psi = (1 + \delta)\kappa_t, \quad (62)$$

with $\delta \ll 1$. We obtain in this way an expression for M_1 which follows from (58) upon changing κ_t into $\kappa_t(1 - \frac{1}{2}\int D_T / \int x_2^2 C_Q)$.

Euler Buckling of Anisotropic Nonhomogeneous Cantilever

We consider a beam of length L which is acted upon at the end $x_1 = 0$ by an axial compressive force $P = -F$, with the line of action of this force coinciding with the elastic centroidal axis of the beam. We assume that the end $x_1 = L$ is fixed.

In view of our assumption that the x_1-axis is the line of centroids we have now $\int x_2 C_N = 0$, with the state of strain in the unbuckled state given, in accordance with (39) by $\epsilon = -F/\int C_N$. In view of (41) the state of stress in the unbuckled state involves in addition to P the stress measure R_s with a value

$$R_s = -\rho^2 F, \quad (63)$$

where $\rho^2 = \int x_2^2 C_N / \int C_N$.

Equilibrium equations for the problem of buckling follow from (30)–(33), with $Q_s = 0$ and $M_s = 0$, in the form

$$Q_p' + F\kappa_p = 0, \quad M_p' - Q_p - F\gamma_p = 0, \quad (64)$$

$$T_M' + T_Q' - \rho^2 F\psi' = 0, \quad R_p' - T_M + T_Q + \rho^2 F(\kappa_t - \psi) = 0, \quad (65)$$

where κ_p, κ_t, and γ_p are given in terms of displacements as in (17).

The four equations in (64) and (65) are associated with the five constitutive equations (42)–(46). With their help (64) and (65) may be transformed into four simultaneous equations for the four displacement variables ϕ, w, θ, ψ.

Boundary conditions for the system of buckling differential equations are the conditions of support

$$w(L) = \phi(L) = \theta(L) = \psi(L) = 0, \quad (66)$$

together with conditions of vanishing end moments,

$$M_p(0) = T_M(0) + T_Q(0) - \rho^2 F\psi(0) = R_p(0) = 0, \quad (67)$$

and together with a fourth loading condition which expresses the fact that the *direction* of the force F remains unchanged during buckling. It is simplest to express this condition for the built-in end of the beam, where it means the absence of a *transverse* force at the support, that is, we have in place of a fourth condition for $x_1 = 0$ a fifth condition for $x_1 = L$,

$$Q_p(L) = 0. \quad (68)$$

Buckling Equations for the Case of Negligible Transverse Shear Deformation. We assume that, effectively, $\int(1, x_2, x_2^2)C_Q = \infty$ and set $\gamma_p = 0$ and $\psi = \kappa_t$, with Q_p and T_Q now being reactive. The remaining constitutive equations (44)–(46) take on the form

$$M_p = \phi'\int D_B + \psi'\int x_2 D_B + 2\psi\int D_{BT}, \quad (68)$$

$$R_p = \phi'\int x_2 D_B + \psi'\int x_2^2 D_B + 2\psi\int x_2 D_{BT}, \quad (69)$$

$$T_M = 2\psi\int D_T + \phi'\int D_{BT} + \psi'\int x_2 D_{BT}, \quad (70)$$

and the four equilibrium equations in (64) and (65) reduce to two defining relations, $Q_p = M_p'$ and $T_Q = T_M - R_p'$, and to two differential equations

$$M_p'' + F\phi' = 0, \quad 2T_M' - R_p'' - \rho^2 F\psi' = 0. \quad (71)$$

The order of the system (71) may be reduced, through use of the second conditions in (66) and (67), in conjunction with (68), leaving as a fourth-order problem in terms of ϕ and ψ,

$$M_p' + F\phi = 0, \quad 2T_M - R_p' - \rho^2 F\psi = 0, \quad (72)$$

with the remaining boundary conditions being

$$\phi(L) = \psi(L) = \phi'(0) = \psi'(0) = 0. \quad (73)$$

Equations (72), when written with the help of (68)–(70), become

$$D_{b0}\phi'' + F\phi + D_{b1}\psi'' + 2D_{bt}\psi' = 0, \tag{74}$$

$$D_{b1}\phi'' - 2D_{bt}\phi' + D_{b2}\psi'' - 4D_t\psi + \rho^2 F\psi = 0, \tag{75}$$

with the coefficients in these equations defined by

$$D_{bn} = \int x_2^n D_B, \quad D_t = \int D_T, \quad D_{bt} = \int D_{BT}. \tag{76}$$

Equations (74) and (75) contain as special cases the problem of an orthotropic beam, upon setting $D_{bt} = 0$, and the problem of the beam with coincident centroid and shear center location, upon setting $D_{b1} = 0$. We will here give an exact solution of the former problem and an approximate solution to the latter.

Orthotropic Unsymmetrical Cross-Section Beam. Setting $D_{bt} = 0$ we may obtain the solution of (74) and (75) which satisfies all four boundary conditions in (73) by setting

$$\phi = A \cos \lambda x_1, \quad \psi = B \cos \lambda x_1, \tag{77}$$

with $\lambda = \pi/2L$. Equations (74) and (75) become, with (77), two simultaneous homogeneous equations for A and B. The vanishing of the determinant of this system gives as equation for the critical load F_c,

$$F_c = D_{b0}\lambda^2 \left[1 - \left(\frac{D_{b1}\lambda}{D_{b0}}\right)^2 \frac{D_{b0}}{4D_t + D_{b2}\lambda^2 - \rho^2 F_c}\right]. \tag{78}$$

Since, necessarily, $(D_{b1}\lambda/D_{b0})^2 \ll 1$ we must, for a numerically significant effect of the nonvanishing of D_{b1}, have that $D_t/D_{b0} \ll 1$. In general, this condition will not be satisfied for the class of narrow cross-section beams and so the effect of a nonvanishing D_{b1} is here negligible.

Anisotropic Symmetric Cross-Section Beam. We now set $D_{b1} = 0$ and attempt to determine the effect of a nonvanishing D_{bt} on the value of F_c. While it is possible to obtain an exact relation for F_c on the basis of (73)–(75), we will limit ourselves here to a simple approximate solution of the form (77), by assuming the effect of the term with D_{b2} in equation (75) to be negligible. Consistent with this we disregard the boundary conditions for ψ in (73). Equation (75) now gives

$$\psi = \frac{-2D_{bt}}{4D_t - \rho^2 F}\phi', \tag{79}$$

and (74) becomes therewith

$$\left(D_{b0} - \frac{4D_{bt}^2}{4D_t - \rho^2 F}\right)\phi'' + F\phi = 0. \tag{80}$$

The solution of (80), with boundary conditions in accordance with (73), gives an equation for F_c which can be written in the form

$$\frac{F_c}{D_{b0}\lambda^2} = 1 - \left(\frac{D_{bt}}{D_{b0}}\right)^2 \left(\frac{D_t}{D_{b0}} - \frac{\rho^2\lambda^2}{4}\frac{F_c}{D_{bo}\lambda^2}\right)^{-1} \approx 1 - \frac{D_{bt}^2}{D_t D_{b0}}, \tag{81}$$

with the simplified version of the result following from the fact that $D_t/D_{b0} = O(1)$ and, necessarily, $\rho^2\lambda^2/4 \ll 1$.

References

1 Reissner, E., "On the Equations of Non-Linear Shallow Shell Theory," *Studies Appl. Math.*, Vol. 48, 1969, pp. 171–175.

2 Reissner, E., "On One-Dimensional Large-Displacement Finite-Strain Beam Theory," *Studies Appl. Math.* Vol. 52, 1973, pp. 87–95.

3 Reissner, E., "On Torsion and Transverse Flexure of Orthotropic Elastic Plates," ASME JOURNAL OF APPLIED MECHANICS, Vol. 47, 1980, pp. 855–860.

4 Reissner, E., "On the Derivation of Two-Dimensional Strain Displacement Relations for Small Finite Deformations of Shear-Deformable Plates," to appear.

5 Wempner, G., *Mechanics of Solids*, 1973, pp. 352–400.

G. G. Adams
Assistant Professor.
Assoc. Mem. ASME

H. Manor
Visiting Associate Professor.

Department of Mechanical Engineering,
Northeastern University,
Boston, Mass. 02115

Steady Motion of an Elastic Beam Across a Rigid Step

An infinite elastic beam moves at constant speed across a frictionless rigid step. Steady-state solutions are obtained in closed form using both Euler-Bernoulli and Timoshenko beam models. With step height and speed as parameters, the noncontact regions, mode shapes, and foundation reactions are determined. The results show interesting qualitative as well as quantitative differences between the behavior of the Euler-Bernoulli and Timoshenko beams.

Introduction

Problems involving moving loads on elastic beams and strips have been the subject of many investigations. No attempt will be made to list and categorize all of them. Recently the behavior of such systems with unilateral constraints has been studied. In [1], Adams and Bogy determine the steady response of an elastic beam resting on a smooth rigid foundation and subject to a steadily moving load. Alternatively, that problem could be considered one of an elastic beam moving steadily along a rigid foundation and subjected to a stationary load. They determined the noncontact lengths, mode shapes, and foundation reactions as a function of load and speed. Related problems involving moving loads on elastic strips with one-sided constraints were studied by Adams [2, 3].

An elastic foundation which acts in compression only can be considered a generalization of a unilateral constraint (rigid foundation). In [4], Choros and Adams solve the problem of an infinite elastic beam resting on a tensionless Winkler foundation and subjected to a steadily moving load. They determine the minimum required loads in order to initiate separation of the beam from the foundation, as well as the liftoff regions and deflection curves. The solution of related problems involving elastic strips pressed against elastic half planes can be found in [5, 6].

In the present investigation, we determine the physical response of an infinitely long beam moving along a rigid foundation which has a step discontinuity. Such situations are encountered when an elastic medium, such as a computer tape, is pulled at high speed along a base with such a discontinuous configuration. Both Euler-Bernoulli and Timoshenko beam models are considered and solutions are obtained for both steady state and static cases. The method of solution is essentially to determine the solution of the appropriate differential equations of motion in terms of local coordinate systems, one for each contact and noncontact region. Then boundary and continuity conditions are applied separately to each noncontact region (pair of noncontact and contact regions for the Timoshenko beam). This leads to simplified forms for the displacement equations (displacement and rotation equations for the Timoshenko beam) which are finally matched together by continuity conditions at the step corner. Then by choosing one of the noncontact region lengths as if it were known and taking the step height as unknown, we obtain the desired solutions. This leads to a considerable reduction in algebraic complexity over the method of [1], especially for the Timoshenko beam. The results will be the noncontact regions, mode shapes and foundation reactions for a range of step height and speed.

Euler-Bernoulli Beam

(A) Problem Formulation. We consider an infinitely long elastic beam, resting under its own weight on a rigid step of height $\bar{h}$, and moving to the right with constant speed c (Fig. 1). Beginning with the partial differential equations of motion of an Euler-Bernoulli beam and transferring to a dimensionless coordinate system (x, y) fixed with respect to the stationary step, we obtain the following equations of motion:

$$y'''' + \omega^2 y'' = -1, \quad x \in \Omega \tag{1}$$

$$y = 0, \quad r(x) = 1, \quad x \in R - \Omega \tag{2}$$

where

$$y(x) = E\bar{y}(\bar{x} + ct)/\rho g\kappa^2, \quad x = (\bar{x} + ct)/\kappa,$$

$$r = \bar{r}/\rho gA, \quad \kappa = \sqrt{I/A}, \quad \omega = c/\sqrt{E/\rho}, \quad h = E\bar{h}/\rho g\kappa^2, \tag{3}$$

in which $\bar{y}$ is the transverse beam deflection, $\bar{r}$ is the foundation contact pressure, I is the second moment of the cross-sectional area (A), and ρ, E, g are the mass density, Young's modulus, and acceleration of gravity, respectively. R denotes the real line $(-\infty, \infty)$ and Ω the noncontact region(s). The corresponding dimensionless shear and moment are determined by

Contributed by the Applied Mechanics Division for presentation at the Winter Annual Meeting, Washington, D. C., November 15–20, 1981, of THE AMERICAN SOCIETY OF MECHANICAL ENGINEERS.

Discussion on this paper should be addressed to the Editorial Department, ASME, United Engineering Center, 345 East 47th Street, New York, N. Y. 10017, and will be accepted until December 1, 1981. Readers who need more time to prepare a discussion should request an extension from the Editorial Department. Manuscript received by ASME Applied Mechanics Division, November, 1980; final revision, February, 1981. Paper No. 81-WA/APM-7.

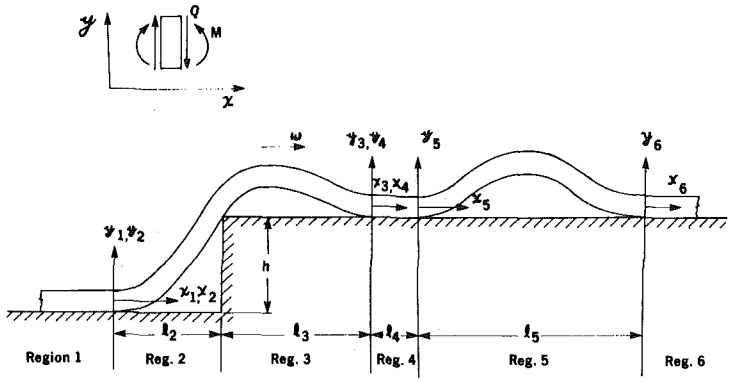

Fig. 1 An infinite elastic beam moving with constant speed across a rigid step

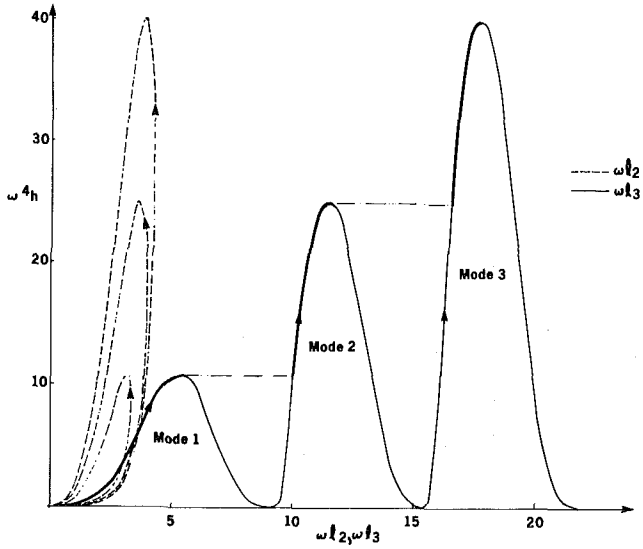

Fig. 2 Step height versus noncontact lengths for an Euler-Bernoulli beam

$$Q = \overline{Q}/\rho g A\kappa = y''', \quad M = \overline{M}/\rho g A\kappa^2 = y'' \tag{4}$$

No initial restrictions are placed upon the number of noncontact regions which may exist, or on their location with respect to the step. However, it was shown in [1] that multiple regions of noncontact must be "free mode" solutions which are decoupled from the noncontact regions surrounding the load. Their existence thus depends upon the history of loading and is not part of the steady problem. With this in mind we look for solutions with no more than one noncontact region on each side of the step. Referring to Fig. 1, region 4 extends to infinitely whereas regions 5 and 6 do not exist.

(B) Method of Solution. Although the equations of motion (1) and (2), subject to appropriate boundary and continuity conditions, could be solved directly, we will use the method of [4] which results in a considerable reduction in algebraic complexity. Writing the solution of (1) in terms of local coordinate systems, we obtain

$$\omega^4 y_2(x_2) = A_0 + A_1\omega x_2 + A_2\cos\omega x_2 + A_3\sin\omega x_2 - \tfrac{1}{2}\omega^2 x_2^2, \quad 0 < x_2 < l_2, \tag{5}$$

$$\omega^4 y_3(x_3) = B_0 + B_1\omega x_3 + B_2\cos\omega x_3 + B_3\sin\omega x_3 - \tfrac{1}{2}\omega^2 x_3^2, \quad -l_3 < x_3 < 0, \tag{6}$$

where l_2 and l_3 are the lengths of the two noncontact regions. The boundary conditions express the continuity of displacement, slope and moment and are given by

$$y_2(0) = 0, \quad y_2'(0) = 0, \quad y_2''(0) = 0, \tag{7}$$

$$y_3(0) = 0, \quad y_3'(0) = 0, \quad y_3''(0). \tag{8}$$

The continuity conditions between the two noncontact regions at the step are

$$y_2'(l_2) = y_3'(-l_3), \quad y_2''(l_2) = y_3''(-l_3) \tag{9}$$

$$y_2(l_2) = h, \quad y_3(-l_3) = 0 \tag{10}$$

Applying conditions (7), (8) to (5), (6), respectively, we obtain

$$\omega^4 y_2(x_2) = A_1(\omega x_2 - \sin\omega x_2) + 1 - \cos\omega x_2 - \tfrac{1}{2}\omega^2 x_2^2, \quad 0 < x_2 < l_2, \tag{11}$$

$$\omega^4 y_3(x_3) = B_1(\omega x_3 - \sin\omega x_3) + 1 - \cos\omega x_3 - \tfrac{1}{2}\omega^2 x_3^2, \quad -l_3 < x_3 < 0. \tag{12}$$

We now use $(10)_2$ obtaining

$$B_1 = (1 - \cos\omega l_3 - \tfrac{1}{2}\omega^2 l_3^2)/(\omega l_3 - \sin\omega l_3), \tag{13}$$

which expresses the unknown B_1 independently of both the step height h and the parameters of region 2. Applying $(9)_2$ and $(9)_1$ we find

$$A_1 = (\cos\omega l_3 - \cos\omega l_2 - B_1\sin\omega l_3)/\sin\omega l_2, \tag{14}$$

$$A_1(1 - \cos\omega l_2) + \sin\omega l_3 + \sin\omega l_2 = B_1(1 - \cos\omega l_3) + \omega(l_2 + l_3). \tag{15}$$

Equation (15) with (13), (14) represents a single transcendental equation which relates the two unknown lengths l_2 and l_3, and is independent of h. For each value of l_3 we solve for l_2 using standard iterative methods. The corresponding step height h can then be calculated by using $(10)_1$ which results in

$$\omega^4 h = A_1(\omega l_2 - \sin\omega l_2) + 1 - \cos\omega l_2 - \tfrac{1}{2}\omega^2 l_2^2 \tag{16}$$

A plot of $\omega^4 h$ versus ωl_2 and ωl_3 is given in Fig. 2, which is valid for any dimensionless speed ω.

We can also consider the possibility of a single noncontact region occurring by taking the limit as $l_3 \to 0$ in (13)–(15). This leads to

$$B_1 = 0, \quad A_1 = \tan(\omega l_2/2), \quad \tan(\omega l_2/2) = (\omega l_2/2),$$

$$y_2(x_2) = (\omega l_2/2)(\omega x_2 - \sin\omega x_2) + 1 - \cos\omega x_2 - \tfrac{1}{2}\omega^2 x_2^2,$$

which is the free mode solution [1] with $h = 0$. Thus all solutions with $h > 0$ have at least one noncontact region on each side of the step.

Having determined l_1, l_2, and h, we can now determine the corresponding beam deflections anywhere in the noncontact regions from (11)–(14). Typical configurations for each mode (1)–(3) are shown in Fig. 3 (*A–E*). In order for a solution to be physically admissible, it must have positive displacement everywhere in the noncontact regions. This is true of all the solutions given in Figs. 2 and 3.

The distributed foundation contact pressure is equal to unity in

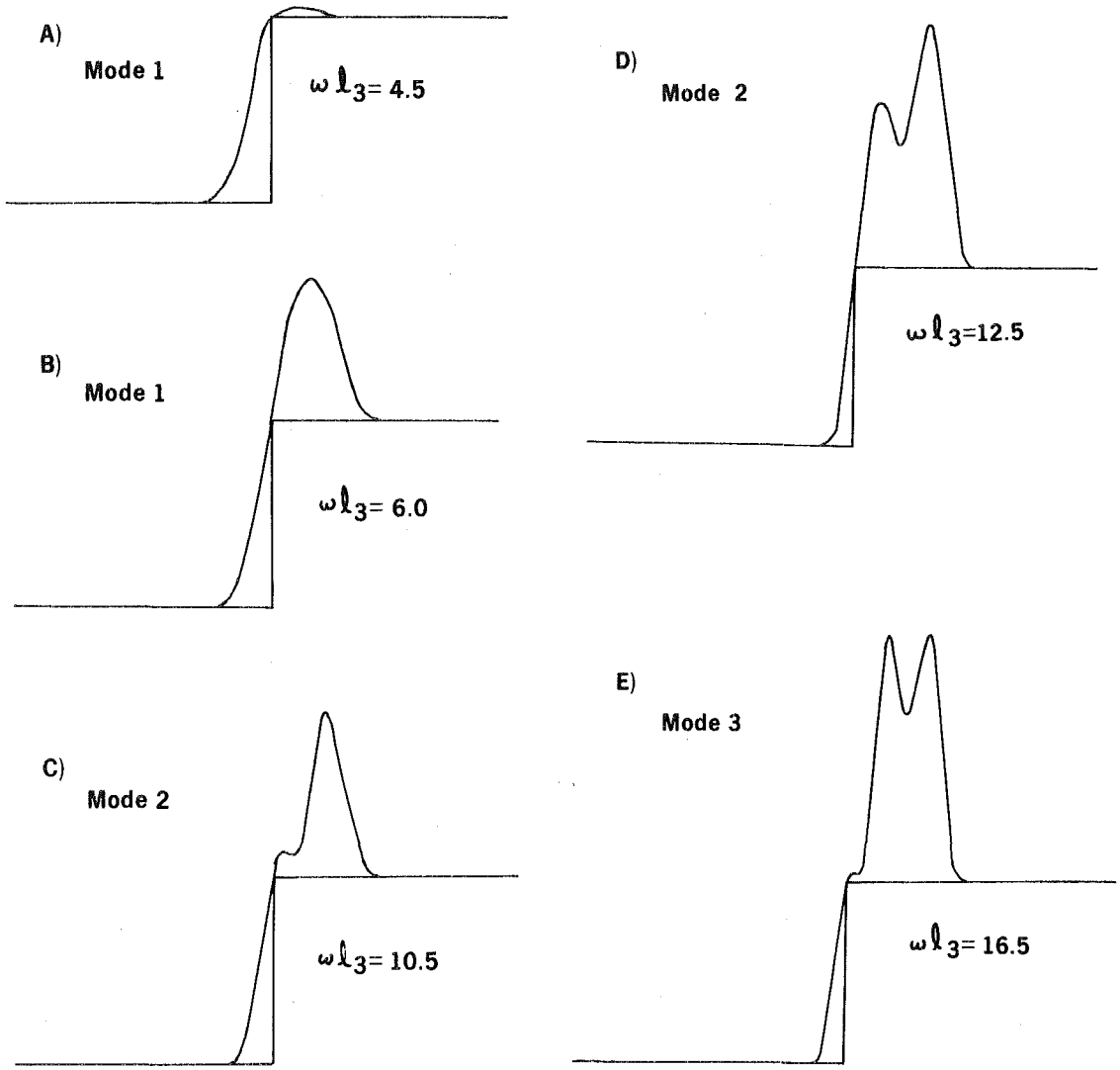

Fig. 3 (*A–E*) Typical Euler-Bernoulli beam deflection shapes, normalized in the vertical direction with respect to h and in the horizontal direction with respect to l_2

the contact region. However, concentrated reactions exist at the boundary of the noncontact regions and are found by determining the discontinuity in the internal shear force. The results are

$$\omega R_1 = A_1, \quad \omega R_4 = -B_1, \quad \omega R_h = B_1 \cos \omega l_3 - A_1 \cos \omega l_2 + \sin \omega l_2 - \sin \omega l_3, \quad (17)$$

where R_1, R_4, and R_h are the concentrated reactions at $x_2 = 0$, $x_3 = 0$, and $x_2 = l_2$, respectively. The results are shown in Fig. 4. In order for the solutions of Figs. 2 and 3 to be typically admissible it is necessary for R_1, R_4, and R_h to be positive, as shown in Fig. 4.

(*C*) Solution Choice and Discussion. We have shown only the first three solution types in Fig. 2; many others exist. The question then arises as to which solution is actually physically realized for a given value of $\omega^4 h$. The solution choice will be based upon an energy criterion. The energy functional V for the Euler-Bernoulli beam is given by

$$V = \tfrac{1}{2} \int_\Omega [(y'')^2 - \omega^2 (y')^2 + 2y] dx \quad (18)$$

in that stationary values of (18) yield (1). In (18) the first term represents the strain energy due to bending, the second term is from the kinetic energy and the last is the potential energy due to gravity. The solution of (18) is given by

$$\begin{aligned} 2\omega^5 V = {} & \tfrac{1}{2}(1 - A_1^2) \sin 2\omega l_2 + \tfrac{1}{2}(1 - B_1^2) \sin 2\omega l_3 - 4[A_1(1 - \cos \omega l_2) \\ & - B_1(1 - \cos \omega l_3)] + 2A_1 \sin \omega l_2 (A_1 + \sin \omega l_2 - \omega l_2) \\ & - 2B_1 \sin \omega l_3 (\sin \omega l_3 - \omega l_3 - B_1) - 2(\sin \omega l_3 + \sin \omega l_2) \\ & - 2\omega (l_3 \cos \omega l_3 + l_2 \cos \omega l_2) + 2\omega^2 (A_1 l_2^2 - B_1 l_3^2) \\ & - 2\omega^3 (l_3^3 + l_2^3)/3 + \omega l_2 (3 - A_1^2) + \omega l_3 (3 - B_1^2) \end{aligned} \quad (19)$$

Due to the dependence of the gravitational potential energy, which is measured with respect to $y_2 = h/2$, on the step height h, the expressions (18), (19) can only be used to compare the energies of configurations having the same value of $\omega^4 h$.

Without investigating the stability of the solutions, we take the actual solution as the one which, for given $\omega^4 h$, produces an absolute minimum in V. These solutions are the ones drawn in heavy lines (Fig. 2). It is not intended to reject other solutions, as multiple local minimums of the energy may exist. If so, the correct steady solution would have to be determined as an appropriate limit of the initial value problem.

Although physically we would specify step height, it is more convenient to discuss the results (Figs. 2–4) in terms of the length l_3. Mode 1 shows that as l_3 increases from zero, h increases from zero until it attains its maximum value for this mode and then decreases again to zero (Fig. 2). The length l_2 also increases from zero to a maximum value and then decreases to zero. It realizes its maximum

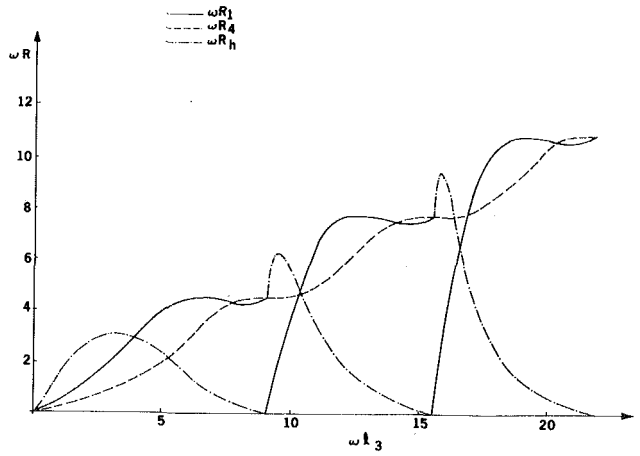

Fig. 4 Concentrated foundation reactions versus noncontact length ωl_3 for an Euler-Bernoulli beam

at a lower value of l_3 than that for which h was a maximum. So Mode 1 begins with h, l_2, and l_3 equal to zero and ends with h and l_2 equal to zero. The corresponding final value of l_3 is then the first free mode solution [1]. Mode 2 begins with the free mode solution and as it increases both h and l_2 increase with l_2 again reaching its maximum value first. They then decrease to zero with Mode 2 ending at the second free mode solution. Similarly Mode 3 begins with the second free mode solution and ends at the third free mode solution with h and l_2 varying as before.

The corresponding deflection shapes (Figs. 3, (A–E)) show that in all cases the transverse displacement increases monotonically from zero to h within region 2. In region 3 there are one, two and three local maximums for Modes 1, 2, and 3, respectively. The absolute maximum deflection as well as the overall deflection shape increases monotonically with l_3. The foundation reaction R_4 increases monotonically with the length l_3 (Fig. 4). However, for Mode 1, R_h increases from zero to a local maximum and then decreases to zero. In Modes 2 and 3, R_h begins at a finite value, increases, and then decreases to zero. The behavior of R_1 is as shown. Note that R_1 and R_h are both discontinuous at values of l_3 corresponding to the free mode solutions. This is because at these values the length l_2 approaches zero and R_1 becomes indistinguishable from R_h. The sum of R_1 and R_h is continuous at these points.

(D) Static Solutions. Solutions for a stationary beam can be easily obtained by setting $\omega = 0$ in (1). The method of solution is exactly the same as for the steady case and will be omitted for brevity. The results are

$$\begin{aligned} &y_2(x_2) = x_2^3(2l_3 - x_2)/24, \quad 0 < x_2 < l_2 \\ &y_3(x_3) = -x_3^3(l_3 + x_3)/24, \quad -l_3 < x_3 < 0 \\ &l_3 = (\sqrt{3} - 1)l_2, \quad h = (2\sqrt{3} - 3)l_2^4/24, \\ &R_1 = l_3/2, \quad R_4 = l_3/4, \quad R_h = l_2 + l_3/4. \end{aligned} \tag{20}$$

Solutions of this type are, of course, unique. The lengths l_2 and l_3 increase monotonically with the step height h.

Timoshenko Beam

(A) Problem Formulation. We now consider the same physical problem using Timoshenko beam theory which includes the effects of shear deformation and rotational inertia [7]. Writing the corresponding pair of partial differential equations of motion in terms of a dimensionless coordinate system (Fig. 1) fixed in space we obtain

$$\left.\begin{aligned} (1 - \omega^2)(1 - \omega_s^2)\phi''' + \omega_s^2\phi' &= -1 \\ y' &= \phi - (1 - \omega^2)\phi'' \end{aligned}\right\}, \quad x \in \Omega \tag{21}$$

and

$$\left.\begin{aligned} (1 - \omega^2)\phi'' - \phi &= 0, \quad y = 0 \\ r(x) &= 1 + \phi' \end{aligned}\right\}, \quad x \in R - \Omega \tag{22}$$

where

$$\begin{aligned} &y(x) = \alpha^4 E\bar{y}(\bar{x} + ct)/\rho g\kappa^2, \quad x = \alpha(\bar{x} + ct)/\kappa, \\ &\phi(x) = \alpha^3 E\bar{\phi}(x + ct)/\rho g\kappa, \quad \omega_s = c/\sqrt{G/\rho}, \quad \omega = c\sqrt{E/\rho}, \\ &\alpha = \sqrt{G/E} = \omega/\omega_s, \quad \kappa = \sqrt{I/A}, \end{aligned} \tag{23}$$

in which $\bar{\phi}$ is the rotation and G is the effective shear modulus. The dimensionless shear and bending moment are

$$M = \alpha^2\overline{M}/\rho g A\kappa^2 = \phi', \quad Q = \alpha\overline{Q}/\rho g A\kappa = (1 - \omega^2)\phi''. \tag{24}$$

(B) Method of Solution. (*i*) *Two Noncontact and Two Contact Regions.* In order to avoid the considerable algebraic complexity encountered in [1], we will apply a modification of the method of [4] to a Timoshenko beam. We obtain the solution of (21) in terms of local coordinates for each of the two noncontact regions (i = 2, 3)

$$\begin{aligned} &\phi_i(x_i) = A_i \sin px_i + B_i \cos px_i + C_i - x_i/\omega_s^2, \\ &y_i(x_i) = D_i + C_i x_i - x_i^2/2\omega_s^2 \\ &\qquad + [-A_i \cos px_i + B_i \sin px_i]/p(1 - \omega_s^2), \end{aligned} \tag{25}$$

and for each of the two contact regions (i = 1, 4)

$$\begin{aligned} &\phi_i(x_i) = A_i e^{-qx_i} + B_i e^{qx_i}, \quad y_i(x_i) = 0, \\ &r_i(x_i) = 1 + q(-A_i e^{-qx_i} + B_i e^{qx_i}) \end{aligned} \tag{26}$$

where

$$p = \omega_s q/\sqrt{1 - \omega_s^2}, \quad q = 1/\sqrt{1 - \omega^2}.$$

The boundary conditions to be applied at infinity are

$$\lim_{x_1 \to -\infty} \phi_1(x_1) = 0, \quad \lim_{x_4 \to \infty} \phi_4(x_4) = 0, \tag{27}$$

and those at the contact points of the noncontact region are

$$y_2(0) = 0, \quad y_3(0) = 0. \tag{28}$$

The following continuity conditions are now used:

$$\phi_1(0) = \phi_2(0), \quad \phi_1'(0) = \phi_2'(0), \quad \phi_1''(0) = \phi_2''(0), \tag{29}$$

$$\phi_3(0) = \phi_4(0), \quad \phi_3'(0) = \phi_4'(0), \quad \phi_3''(0) = \phi_4''(0). \tag{30}$$

By applying (27)–(30) we can determine the unknown constants pertaining to the regions to the left and to the right of the step in terms of B_1 and A_4, respectively.

There remains two unknown constants B_1, A_4 and two unknown lengths l_2 and l_3, which will be determined using the following four continuity conditions at the step:

$$y_2(l_2) = h, \quad y_3(-l_3) = 0, \quad \phi_2(l_2) = \phi_3(-l_3), \quad \phi_2'(l_2) = \phi_3'(-l_3). \tag{31}$$

Applying $(31)_{2,4,3}$ we obtain A_4, B_1 and a transcendental equation for l_2, l_3. Varying l_3 we can calculate corresponding values of l_2 by standard methods. For a given l_2 and l_3 the associated value of h is obtained from $(31)_1$.

The displacement and rotation at any point on the beam can now be obtained directly from (25). The corresponding foundation reactions are the distributed pressures given by

$$r_1(x_1) = 1 + qB_1 e^{qx_1}; \quad r_4(x_4) = 1 - qA_4 e^{-qx_4} \tag{32}$$

and the corresponding concentrated reaction

$$\begin{aligned} R_h &= [\phi_3''(-l_3) - \phi_2''(l_2)]/q^2 \\ &= A_4(q \cos pl_3 - p \sin pl_3)/q \\ &\quad + B_1(p \sin pl_2 - q \cos pl_2)/q \\ &\quad + p(\sin pl_2 + \sin pl_3)/\omega_s^2 q^2. \end{aligned} \tag{33}$$

Due to the inclusion of shear deformation the concentrated reaction at the step causes a discontinuous slope at that point.

(*ii*) *One Noncontact and Two Contact Regions.* At this point

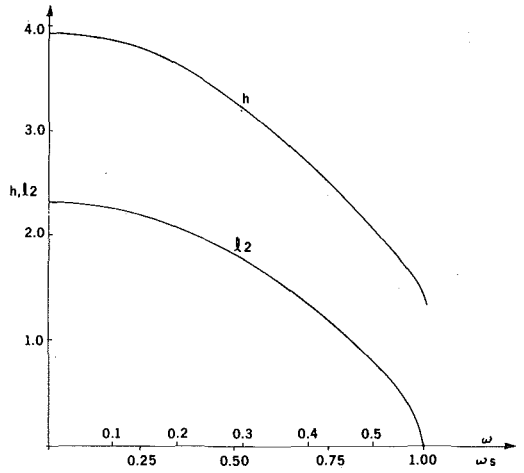

Fig. 5 Maximum step height and noncontact length versus dimensionless speed for a Timoshenko beam with $\alpha = 1/\sqrt{3}$ (rectangular cross section and Poisson's ratio of 0.25)

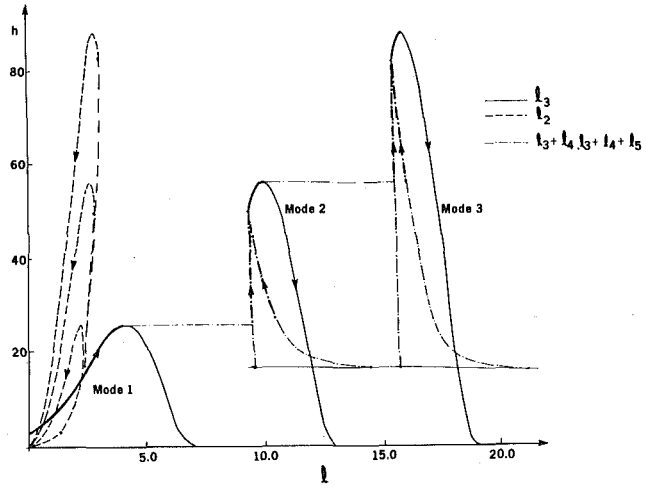

Fig. 6 Step height versus noncontact lengths at fixed speed $\omega = 0.4$ ($\alpha = 1/\sqrt{3}$)

we consider the possibility of a single noncontact region occurring with complete contact to the right of the step. This can be accomplished by eliminating regions 3, 5, and 6 in Fig. 1. Boundary and continuity conditions (27), $(28)_1$, (29), $(31)_1$ are still applicable and must be supplemented with

$$\phi_2(l_2) = \phi_4(0), \quad \phi_2'(l_2) = \phi_4'(0) \tag{34}$$

The resulting displacements, rotations, and step height are the same as before, with different expressions for B_1 and A_4. These are valid for any length l_2 provided that the conditions of positive displacement in the noncontact region and positive foundation reactions in the contact regions are satisfied. As h increases so does l_2 and the concentrated reaction at the step corner increases as expected. However the distributed pressure $(32)_2$ decreases because A_4 increases. Therefore, the maximum permissable step height h occurs when $A_4 = 1/q$. A graph showing the maximum value of h and the corresponding value of l_2 for which only a single noncontact region exists is shown as a function of dimensionless speed in Fig. 5. These limiting values agree with those obtained by taking an asymptotic expansions for small l_3. Note that the maximum value of h decreases with increasing speed.

Note that in the limit as $\omega_s \to 1$, the results in Fig. 5 show that $l_2 \to 0$, but h approaches a finite value. This can be verified directly by taking the limit as $\omega_s \to 1$ obtaining $l_2 = 0$ and $h = 2(1 - \alpha^2)$. The reason is that as the shear wave speed is approached, the discontinuous slope at the step corner, which results from shear deformation, increases without bound.

(iii) Two Noncontact and Three Contact Regions. Now let us consider the existence of a finite length contact region immediately to the right of the step corner (Fig. 1 without region 3). By applying the following conditions:

$$\begin{aligned} &\phi_4(l_4) = \phi_5(0), \quad &&\phi_4'(l_4) = \phi_5'(0) \quad &&\phi_4''(l_4) = \phi_5''(0), \\ &\phi_5(l_5) = \phi_6(0), \quad &&\phi_5'(l_5) = \phi_6'(0), \quad &&\phi_5''(l_5) = \phi_6''(0), \\ &y_5(0) = 0, \quad &&y_5(l_5) = 0, \end{aligned} \tag{35}$$

we obtain the solution for regions 4, 5, 6, where the length l_5 is given by

$$(pl_5/2) \cot (pl_5/2) = (1 + q\omega_s^2 l_5/2)/(1 - \omega_s^2). \tag{36}$$

There are an infinite number of solutions of (36); these are the free mode solutions encountered in [1]. Note that the behavior of the beam in the regions to the right of the step corner depends on only one parameter "l_4." The solutions for regions 1 and 2 are as before and are given strictly in terms of l_2 and B_1. Applying continuity of rotation and bending moment at the step corner

$$\phi_2(l_2) = \phi_3(-l_3) \quad \phi_2'(l_2) = \phi_3'(-l_3) \tag{37}$$

we eventually obtain B_1, l_4, and h.

The displacement and rotation of the beam at any point can now be determined from (25). The concentrated reaction at the step corner is given by

$$R_h = (l_5/2)e^{-ql_4} - B_1(q \cos pl_2 - p \sin pl_2)/q + (p/q^2\omega_s^2) \sin pl_2 \tag{38}$$

and the distributed reactions are

$$\begin{aligned} &r_1(x_1) = 1 + qB_1e^{qx_1}, \quad r_4(x_4) = 1 + (ql_4/2)e^{q(x_4 - l_4)}, \\ &r_6(x_6) = 1 - (ql_5/2)e^{-qx_6}. \end{aligned} \tag{39}$$

(iv) Three Noncontact and Three Contact Regions. Finally, we consider the possibility of all six regions occurring (Fig. 1). The solution can be obtained in a manner similar to the foregoing by applying appropriate boundary and continuity conditions. For brevity we have omitted all of the details. The essential effect of the extra noncontact region is to alter region 4 from one in which the rotation is exponentially decreasing to one in which it is exponentially increasing. This allows for new solutions in regions 1, 2, 3.

(C) Solution Choice and Discussion. In Fig. 6, we show a plot of step height h versus noncontact lengths as defined by l_2, l_3 for the case of two noncontact regions and l_2, $l_3 + l_4$ and $l_3 + l_4 + l_5$ for the case of three noncontact regions. These results are valid at a fixed speed of $\omega = 0.4$ for a beam with a rectangular cross section and Poisson's ratio equal to 0.25. Mode 1 begins with a finite value of h at $l_3 = 0$ due to the inclusion of shear deformation which allows only one noncontact region to exist for small values of h. As l_3 increases, h increases to a maximum and then decreases to zero leaving the first free mode solution. Typical displacement configurations for Mode 1 are shown in Fig. 7 (A, B). Unlike the Euler-Bernoulli beam, Mode 2 for the Timoshenko beam begins with three noncontact regions (Fig. 1) in which the noncontact region $i = 5$ is the first free mode. However as h approaches its minimum value, the distance l_4 approaches infinity. As h increases l_4 decreases to zero. At this point, two of the noncontact regions ($i = 3, 5$) coalesce forming a single noncontact region ($i = 3$) as the point $x_3 = 0$ is gently lifted off the smooth rigid foundation. Then h increases to a maximum value and decreases to zero leaving Mode 2 in the second free mode solution. A typical displacement configuration is shown in Fig. 7 (D). Mode 3 also begins with three noncontact regions, however, region 5 is the second free mode solution which is an infinite distance from the step corner. Note that both modes 2 and 3 begin with the same values of h, l_2, and l_3. This can be seen by taking the limit as $l_4 \to \infty$, obtaining $B_3 \to 0$.

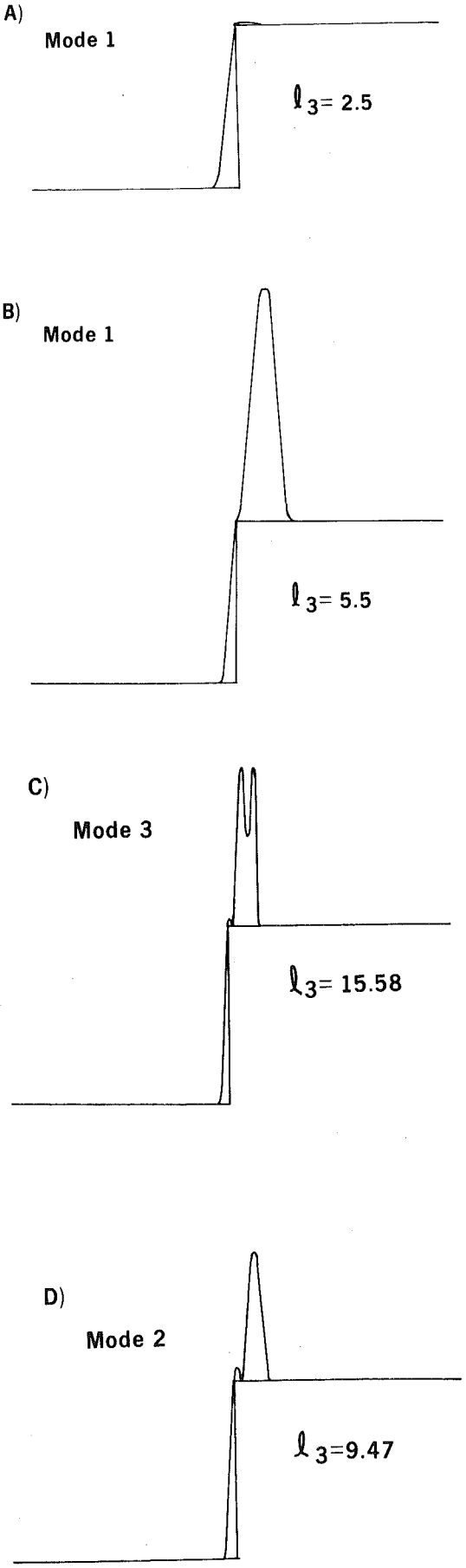

Fig. 7 (*A–D*) Displacement configurations for first three modes with $\omega = 0.4$, $\alpha = 1/\sqrt{3}$, normalized with respect to h and l_2

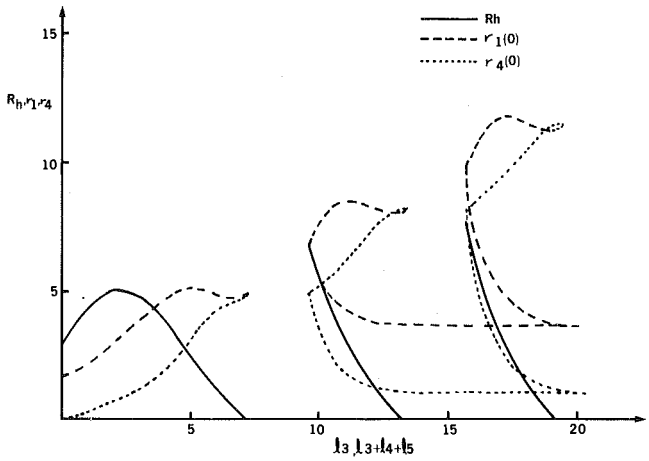

Fig. 8 Foundation reactions versus noncontact length $l_3(l_3 + l_4 + l_5$, for three noncontact regions) at fixed speed $\omega = 0.4$ ($\alpha = 1\sqrt{3}$)

Hence the displacement configurations in regions 1, 2, 3 are identical in the beginning stages of mode 2 or 3. The subsequent behavior of mode 3 is similar to that of mode 2 with the two noncontact regions ($i = 3, 5$) joining together and eventually ending with $h = 0$ and the third free mode solution. A representative deflection shape is shown in Fig. 7 (C). As with the Euler-Bernoulli beam, modes 1, 2, 3 correspond to one, two, and three local maximums, respectively, in the displacement shape.

We have also considered the possibility of a finite length contact region immediately to the right of the step. However, no solutions exist for the range of the parameters plotted in Fig. 6.

The results of Fig. 6 show that at fixed speed ω and step height h, many solutions exist. Following the same reasoning used for the Euler-Bernoulli beam, we form the energy functional

$$V = \tfrac{1}{2}\int_{-\infty}^{\infty} [(1-\omega^2)(\phi')^2 + (1-\omega^2)^2(\phi'')^2 - \omega^2(y')^2 + 2y]dx, \tag{40}$$

in which the first term represents the strain energy of bending and kinetic energy of rotation, the second term is strain energy due to shear deformation, the third term is the kinetic energy due to transverse motion, and the last term is due to gravity. This integral has been evaluated in closed form; however, the results are very lengthy and will not be given here. Those modes which result in an absolute minimum for V are shown in heavy lines in Fig. 6. Again we emphasize that many solutions exist; we have shown only the first three modes.

The foundation reactions $R_h, r_1(O), r_4(O)$ are plotted as a function of noncontact length l_3 in Fig. 8.

(*D*) Static Solutions. The solution for a stationary beam may be obtained either by taking an asymptotic expansion for small speeds, or by resolving the problem with $\omega = 0$ in (21), (22). For brevity we simply list the results

$$\phi_1(x_1) = B_1 e^{x_1}, \quad y_1(x_1) = 0, \quad r(x_1) = 1 + B_1 e^{x_1}$$

$$\phi_2(x_2) = B_1(1 + x_2 + x_2^2/2) - x_2^3/6,$$

$$y_2(x_2) = (B_1 + 1)x_2^2/2 + B_1 x_2^3/6 - x_2^4/24,$$

$$\phi_3(x_3) = A_4(1 - x_3 + x_3^2/2) - x_3^3/6$$

$$y_3(x_3) = (1 - A_4)x_3^2/2 + A_4 x_3^3/6 - x_3^4/24$$

$$\phi_4(x_4) = A_4 e^{-x_4}, \quad y_4(x_4) = 0, \quad r(x_4) = 1 - A_4 e^{-x_4}$$

in which

$$A_4 = (12 - l_3^2)/4(3 + l_3),$$

$$B_1 = -[A_4(1 + l_3) + (l_3^2 - l_2^2)/2]/(1 + l_2),$$

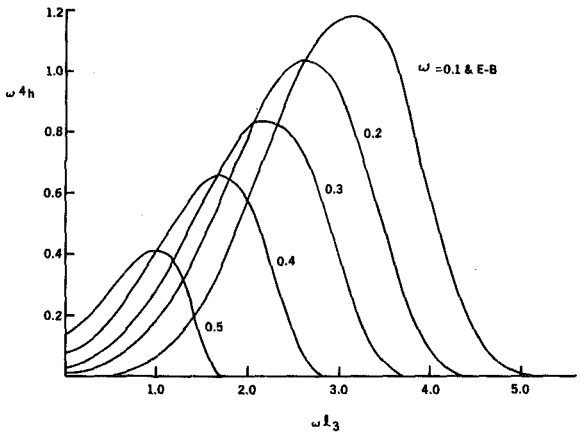

Fig. 9 Comparison of $\omega^4 h$ versus ωl_3 for first mode at different dimensionless speeds

$$h = l_2^2[(3 + l_2)B_1 + 3 - l_2^2/4]/6,$$

$$\frac{1 + l_2 + l_2^2/2}{1 + l_2} = -\frac{A_4(1 + l_3 + l_3^2/2) + (l_3^3 + l_2^3)/6}{A_4(1 + l_3) + (l_3^2 - l_2^2)/2},$$

$$R_h = A_4 - B_1 + l_3 + l_2,$$

where the foregoing is valid for two noncontact regions. For one noncontact region we have

$$B_1 = l_2^2\,(l_2 + 3)/12(1 + l_2 + l_2^2/4),$$

$$A_4 = l_2^2/2 - B_1(1 + l_2),$$

$$R_h = A_4 - B_1 + l_2$$

and the requirement of positive foundation reactions leads to $A_4 \leq 1$ and consequently $l_2^4 + 4l_2^3 - 24l_2 - 24 = 0$, which has a real positive root $l_2 = 2.3284$ and $h = 3.9604$.

Comparison of Results and General Discussion

In Fig. 9, we show a plot of $\omega^4 h$ versus ωl_3 for Mode 1 at different dimensionless speeds ω. Also shown are the corresponding results for the Euler-Bernoulli beam which are valid at any speed. Notice that the dimensionless variables x and y have been defined somewhat differently for the two beam theories (3), (23) which is why the Euler-Bernoulli results of Fig. 9 may appear to be different from those of Fig. 2. The results of the two theories agree to within graphing accuracy for $\omega = 0.1$ but begin to differ much more significantly at higher speeds. This behavior is not unexpected.

Using Euler-Bernoulli beam theory we always have two noncontact regions. Additional free mode noncontact regions can occur but are decoupled from the other regions. Using a Timoshenko beam, the results are more complex as has already been discussed. Free mode solutions can occur but are coupled to the other regions.

The nonuniqueness of the solution is characteristic of this as well as other problems [1–6]. This is due to the nonlinearity associated with the existence of noncontact regions, which allows different sets of initial conditions to result in different steady solutions. This type of nonuniqueness is different from that associated with, for example, a steadily moving lead on an infinite beam which is not supported by any foundation. In that case, different initial conditions can give rise to different steady solutions. However, the different steady solutions have different behaviors at infinity and hence each solution can be viewed as the solution of a different problem in which particular boundary conditions have been applied at infinity.

Also characteristic of this problem as well as [1–6] is that the response of these systems is not always continuous with increasing step height (load in [1–6]). At any finite speed there exists values of h for which there is a sudden change from one deflection configuration to another (e.g., the sudden change from Mode 1 to Mode 2 at $\omega^4 h = 10.681$, Fig. 2).

References

1 Adams, G. G., and Bogy, D. B., "Steady Solutions for Moving Loads on Elastic Beams With One-Sided Constraints," ASME JOURNAL OF APPLIED MECHANICS, Vol. 42, 1975, pp. 800–804.

2 Adams, G. G., "Moving Loads on Elastic Strips With One-Sided Constraints," *International Journal of Engineering Science*, Vol. 14, 1976, pp. 1071–1083.

3 Adams, G. G., "A Steadily Moving Load on an Elastic Strip Resting on a Rigid Foundation," *International Journal of Engineering Science*, Vol. 16, 1978, pp. 659–667.

4 Choros, J., and Adams, G. G., "A Steadily Moving Load on an Elastic Beam Resting on a Tensionless Winkler Foundation," ASME JOURNAL OF APPLIED MECHANICS, Vol. 46, 1979, pp. 175–180.

5 Adams, G. G., "An Elastic Strip Pressed Against an Elastic Half Plane by a Steadily Moving Force," ASME JOURNAL OF APPLIED MECHANICS, Vol. 45, 1978, pp. 89–94.

6 Adams, G. G., "Steady Solutions for a Moving Load on an Elastic Strip Resting on an Elastic Half Plane," *International Journal of Solids and Structures*, Vol. 15, 1979, pp. 885–897.

7 Timoshenko, S., "On the Correction for Shear in the Differential Equation for Transverse Vibrations of Prismatic Bars," *Philosophical Magazine*, Series 6, Vol. 41, 1921, pp. 744–746.

L. Jezequel

Assistant Professor,
Department of Mechanical Engineering,
Ecole Centrale de Lyon,
36 route de Dardilly,
Ecully, 69130, France

Response of Periodic Systems to a Moving Load

The motion of a beam or a plate resting on an elastic foundation and subjected to a moving load has been studied by numerous authors. But the extension of these studies to the case of periodic structures is difficult. In this paper, a method allowing the calculation at low numerical cost of periodically supported beams subjected to a moving force, is proposed. The interpretation of this method on the basis of the free-wave propagation equations in periodic structures has led to the definition of the predominant, so-called "primary," critical speeds. Individual examples were used to test the method. It was also possible to define the limits of a Winkler continuous model in representing the support reactions.

Introduction

Initial research into a steadily moving load on an infinite continuum was carried out by Schwedler [1] and Hovey [2]. These authors studied the steady-state response of an Euler-Bernoulli beam on a Winkler foundation. In recent years considerable attention has been paid to the problem of beams and plates subjected to moving loads [3–16]. The models of structural elements and foundations employed are increasingly complex but in all these studies the method of resolution adopted is identical. The deformation pattern is time invariant relative to a coordinate system moving with the load. By transforming the equilibrium equations to the moving coordinate and further by applying the Fourier transformation the solution is obtained. The inversion of the Fourier transform in conjunction with the integral contour is made problematic by the existence of real poles in the undamped cases. Double real poles are linked with a critical velocity for which displacement is unbounded. In their study of moving loads on an elastic plate strip, Adler and Reismann [11] present two methods for calculating response when the poles are real. The first is by introducing damping and the second is based on an application of the principle of causality by which the phase velocity is compared with the group velocity on the basis of the dispersion relations for free flexural waves.

The present work aims to study a traveling load on an infinite periodic system. Motions of vehicles on flexible guideways have been studied by Doran and Mingori [17], then by Chung and Genin [18] in the case of independent spans. This hypothesis eliminates the influence of wave propagation along the beam. For the calculation of the response of continuous, periodically supported beams to traveling loads, Smith and Wormley have proposed two methods [19]. The first, based on the Floquet principle, consists in calculating the Fourier transform of the displacement and the second only considers a finite number of spans before and after the moving load. Recently, Genin andChung [20] have proposed a numerical algorithm to analyze the dynamic response of the continuous guideway structure subjected to a moving vehicle. But all these numerical methods do not greatly advance the study of the solution near critical speeds where the waves are propagated at a great distance from the load. The introduction of damping facilitates the calculation but greatly influences the solution for high speeds and continuous guideways often have very low damping.

The method proposed in the first part of this study is analytical and takes into account the real phenomena of propagation. Critical speeds can thus be obtained as in the case of nonperiodical systems [1–16]. In the second part this method is discussed in the light of recent studies on free wave propagation in periodical structures. In particular the existence of bands of propagation and wave groups which result from reflections on the supports has been clearly demonstrated in references [21–30]. Mead has calculated the bounding frequencies of the propagation zones in terms of the receptance matrices of single elements [27, 28]. The work by this author on the response of a periodic beam to a uniform convected harmonic pressure field [25, 29] permits the justification of our method and the definition of the so-called "primary critical speeds." In the third part the conditions which permit the assimilation of the periodical supports to a foundation continuous model are specified. Individual examples are used in the last part to test the method.

Method Exposition

An Euler-Bernoulli infinite beam resting on elastic supports is taken as an example to demonstrate the method—Fig. 1. The stringers have a rotational stiffness K_r and a transverse elastic stiffness K_t and are spaced at an equal distance l apart. A concentrated force f is moving with a constant speed v in the positive x-direction. The origin of the fixed coordinate system coincides with one end of a span. The stringer situated at the point $x = Nl$ is subjected to a force F_N and a moment C_N, solely function of the speed v and the distance between the load and the support in steady state.

Contributed by the Applied Mechanics Division for publication in the JOURNAL OF APPLIED MECHANICS.

Discussion on this paper should be addressed to the Editorial Department, ASME, United Engineering Center, 345 East 47th Street, New York, N. Y. 10017, and will be accepted until December 1, 1981. Readers who need more time to prepare a discussion should request an extension from the Editorial Department. Manuscript received by the Applied Mechanics Division, May, 1980; final revision, April 1981.

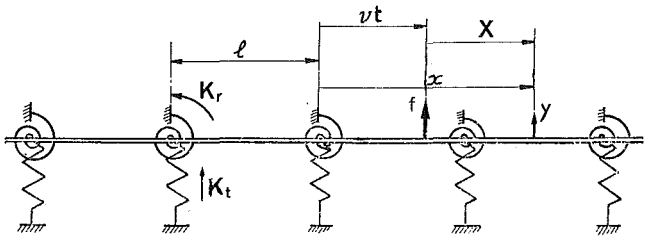

Fig. 1 Beam-type periodic structure subjected to a moving force

$$F_N = F(Nl - vt, v) \quad C_N = C(Nl - vt, v) \tag{1a,b}$$

The equilibrium equation for the bending theory of an Euler-Bernoulli beam is

$$EI\frac{\partial^2 y}{\partial x^2} = -M \tag{2}$$

In this notation E represents the elastic modulus, I is the moment of inertia of the beam, and y is the beam's deflection.

The derivative with respect to space of the bending moment M, considered as a generalized function, can be written

$$\frac{\partial M}{\partial x} = Q + \Pi(x)C(x - vt, v) \tag{3}$$

The transverse shear force Q is a generalized function. Π is a row of equal Dirac's delta functions

$$\Pi(x) = \sum_{N=-\infty}^{+\infty} \delta(x - Nl) \tag{4}$$

The derivative of the generalized function defined in equation (3) is

$$\frac{\partial^2 M}{\partial x^2} = r + \Pi(x)\left[F(x - vt, v) + \frac{\partial C}{\partial x}(x - vt, v)\right] + C(x - vt, v)\frac{d\Pi}{dx} \tag{5}$$

The distributed load r is constituted by the moving force f and transverse inertial forces

$$r = -m\frac{\partial^2 y}{\partial t^2} + f\delta(x - vt) \tag{6}$$

Equations (2), (5), and (6) give the differential equation for the bending of an infinite supported beam

$$EI\frac{\partial^4 y}{\partial x^4} + m\frac{\partial^2 y}{\partial t^2} = f\delta(x - vt) + \Pi(x)\left[(F(x - vt, v) + \frac{\partial C}{\partial x}(x - vt, v)\right] + C(x - vt, v)\frac{d\Pi}{dx} \tag{7}$$

In this last equation the flexural rigidity EI is taken to be constant. The equation for the displacement y in a coordinate system that moves with the load, is obtained by using a Galilean transformation.

$$\begin{cases} X = x - vt \\ Y = y \end{cases} \tag{8}$$

Supplementary terms appear in the equilibrium equation coming from the derivative with respect to time.

$$EI\frac{\partial^4 Y}{\partial X^4} + m\frac{\partial^2 Y}{\partial t^2} - 2mv\frac{\partial^2 Y}{\partial X \partial t} + mv^2\frac{\partial^2 Y}{\partial X^2} = f\delta(X) + \Pi\left[F(X, v) + \frac{dC}{dX}(X, v)\right] + \frac{\partial \Pi}{\partial X}C(X, v) \tag{9}$$

In a steady state the displacement at the coordinate X is a periodic time function. The period T depends on the speed of the moving load: $T = l/v$.

The solution $Y(X, t)$ can be found in the form of a Fourier series:

$$Y = A_0 + \sum_{j=1}^{\infty}[A_j \cos(2j\pi(X + vt)/l) + B_j \sin(2j\pi(X + vt)/l)] \tag{10}$$

The Fourier coefficients A_j and B_j are functions of v and X.

$$A_j = A_j(X, v) \quad B_j = B_j(X, v) \tag{11a,b}$$

The generalized function given in equation (4) and its derivative are periodic with period l and can be developed in a Fourier series:

$$\Pi = \frac{1}{l} + \frac{2}{l}\sum_{j=1}^{\infty}\cos(2j\pi(X + vt)/l) \tag{12}$$

$$\frac{\partial \Pi}{\partial X} = -\frac{4\pi}{l^2}\sum_{j=1}^{\infty} j \sin(2j\pi(X + vt)/l) \tag{13}$$

By incorporating equations (10), (12), and (13) in equation (9) and identifying the coefficients of the Fourier series, the following equations may be obtained

$$(F + C')/l + f\delta(X) = EIA_0'''' + mv^2A_0'' \tag{14}$$

$$(F + C')2/l = EI(A_j'''' + 4B_j'''p_j - 6A_j''p_j^2 - 4B_j'p_j^3 + A_jp_j^4) - \omega_j^2 mA_j + mv^2(A_j'' + 2B_j'p_j - A_jp_j^2) - 2mv(\omega_jB_j' - A_jp_j\omega_j) \tag{15}$$

$$-4\pi jC/l^2 = EI(B_j'''' - 4A_j'''p_j - 6B_j''p_j^2 + 4A_j'p_j^3 + B_jp_j^4) - \omega_j^2 mB_j + mv^2(B_j'' - 2A_j'p_j - B_jp_j^2) + 2mv(\omega_jA_j' + B_jp_j\omega_j) \tag{16}$$

with

$$\omega_j = 2\pi jv/l \quad p_j = 2\pi j/l \quad j \geq 1 \tag{17a,b}$$

where

$$(\ )' \equiv d(\ )/dX$$

The two supplementary equations which will enable us to determine the reactions C and F are obtained by imposing the force conditions at the supports

$$F_N = F(X, v) = -K_t y(X, t) \tag{18}$$

$$C_N = C(X, v) = -K_r\frac{\partial y}{\partial X}(X, t) \tag{19}$$

with

$$X = Nl - vt \tag{20}$$

By using equation (10) and these last three relationships we obtain

$$F(X, v) = -K_t\left[\sum_{j=0}^{\infty} A_j(X, v)\right] \tag{21}$$

$$C(X, v) = -K_r\left[\sum_{j=0}^{\infty} A_j'(X, v) + \sum_{j=1}^{\infty} p_jB_j(X, v)\right] \tag{22}$$

Equations (14)–(16), (21), and (22) can be solved by using the Fourier transformation with respect to X defined as

$$\bar{g} = \int_{-\infty}^{+\infty} g(X)e^{-ikX}\,dX \tag{23}$$

A system of linear equations is obtained

$$u_0\bar{A}_0 = f + (\bar{F} + ik\bar{C})/l \tag{24}$$

$$u_j\bar{A}_j - w_j\bar{B}_j = 2(\bar{F} + ik\bar{C})/l \quad j \geq 1 \tag{25}$$

$$w_j\bar{A}_j + u_j\bar{B}_j = -4\pi j\bar{C}/l^2 \quad j \geq 1 \tag{26}$$

$$\overline{F} = -K_t \sum_{j=0}^{\infty} \overline{A}_j \tag{27}$$

$$\overline{C} = -K_r \left[\sum_{j=0}^{\infty} ik\overline{A}_j + \sum_{j=1}^{\infty} p_j \overline{B}_j \right] \tag{28}$$

with

$$u_0 = EIk^4 - mv^2k^2 \tag{29}$$

$$u_j = EI(k^4 + 6p_j{}^2k^2 + p_j{}^4) - mv^2k^2 \quad j > 1 \tag{30}$$

$$w_j = ikp_j 4EI(k^2 + p_j{}^2) \quad j > 1 \tag{31}$$

An approximate solution is obtained if only a finite number of terms, n, is taken in equation (10).

The influence of this truncation will be studied in the following paragraph. After omitting the details one finally obtains the unknown functions $\overline{A}_0$, $\overline{A}_j$, and $\overline{B}_j$ as a solution of a linear system of order $2n + 1$

$$[H_{ij}] \begin{bmatrix} \overline{A}_0 \\ \overline{A}_1 \\ \overline{B}_1 \\ \cdot \\ \cdot \\ \cdot \\ \overline{A}_n \\ \overline{B}_n \end{bmatrix} = \begin{bmatrix} 2f \\ o \\ o \\ \cdot \\ \cdot \\ \cdot \\ o \\ o \end{bmatrix} \tag{32}$$

with

$$[H_{ij}] = \begin{bmatrix} 2u & & & & & \\ u_1 - w_1 & & & & & \\ w_1 \quad u_1 & & & & & \\ & \cdot & & & & \\ & & \cdot & & & \\ & & & \cdot & & \\ & & & & u_n - w_n & \\ & & & & w_n \quad u_n & \end{bmatrix} + [\alpha_{ij}] \tag{33}$$

$$\alpha_{ij} = \frac{2}{l} [(K_t - K_r k^2) c_i c_j - p_l p_m K_r d_i d_j + ikK_r(p_m c_i d_j - p_l c_j d_i)] \tag{34}$$

where

$$l = (2i - 1)/2 \quad m = (2j - 1)/2 \tag{35a,b}$$

$$c_1 = 1 \quad d_1 = 0 \tag{36a,b}$$

and for $j > 1$

$$c_j = (1 + (-1)^j)/2 \quad d_j = (1 - (-1^j)/2 \tag{37a,b}$$

The solutions are obtained by inversion of the matrix $[H]$

$$\begin{bmatrix} \overline{A}_0 \\ \overline{A}_1 \\ \overline{B}_1 \\ \cdot \\ \cdot \\ \cdot \\ \overline{A}_n \\ \overline{B}_n \end{bmatrix} = [H^{-1}] \begin{bmatrix} 2f \\ o \\ o \\ \cdot \\ \cdot \\ \cdot \\ o \\ o \end{bmatrix} \tag{38}$$

Functions $\overline{A}_j$ and $\overline{B}_j$ are rational algebraic fractions

$$\overline{A}_j = \frac{GA_j}{\Delta} \quad \overline{B}_j = \frac{GB_j}{\Delta} \tag{39a,b}$$

The symbol Δ stands for the determinant of the matrix $[H]$. It is a polynomial in k^2 whose real or complex roots are called k_l

$$\Delta(k^2{}_l) = 0 \quad 1 \le l \le 4(2n + 1) \tag{40}$$

These roots can be obtained as the solution of a nonlinear eigenvalue problem

$$[[E_0] + [E_1]k + [E_2]k^2 + [E_3]k^3 + [E_4]k^4]Z = 0 \tag{41}$$

Z is an eigenvector of order $2n + 1$. The matrices $[E_j]$ are constant and

If j is even:

$$[E_j] = [E_j]^T \tag{42a}$$

If j is odd:

$$[E_j] = -[E_j]^T \tag{42b}$$

The various methods of resolution are studied in reference [31, 32].

If the poles k_l are not real, functions A_j and B_j are obtained by contour integration using Cauchy's residue theorem in conjunction with Jordan's lemma [33]. For instance we have

$$A_j = (2\pi)^{-1} \int_{-\infty}^{+\infty} \overline{A}_j e^{+ikX} d = \begin{matrix} iSA_j{}^+, & X < 0 \\ -iSA_j{}^-, & X > 0 \end{matrix} \tag{43}$$

Where $SA_j{}^+$ and $SA_j{}^-$ denote the sum of the residues of $\overline{A}_j$ at its poles k_l in the upper and lower half plane, respectively. If the roots in equation (40) are real, an energy dissipation mechanism can be introduced into the equilibrium equation (7) or into the support reactions (18) and (19). The poles k_l have in this case an imaginary part and the undamped case is considered as a limit when the damping terms are made to vanish. In reference [11] a method of perturbation is proposed in order to define the half space concerned in the integral contour. When the polynomial $\Delta(k^2)$ has a double real root, the integral in equation (43) does not exist, not even in the sense of a Cauchy principal value. This case corresponds to an unbounded solution associated with a critical speed for the load. The introduction of damping makes it possible to obtain a physically acceptable solution.

When functions A_i and B_i are known, the displacement Y at any point can be calculated with equation (34). With the help of equations (8), (21), and (22) the support reactions can be calculated.

Justification of the Method in Terms of Wave Groups

To obtain the dispersion relations for free flexural waves propagating in the positive x-direction with frequency ω and wave number k, we assume

$$A_j = a_j e^{i(kx - vt)} \quad B_j = b_j e^{i(kx - vt)} \tag{44a,b}$$

This displacement is obtained by replacing v by ω/k in equation (10). By making cos and sin explicit, the wave group defined in references [24, 29] is obtained

$$y(x, t) = \sum_{j=0}^{\infty} [\gamma_j e^{i((k + 2\pi_j/l)x - \omega t)} + \mu_j e^{i((k - 2\pi_j/l)x - \omega t)}] \tag{45}$$

By substituting a_j, b_j, for $\overline{A}_j$, $\overline{B}_j$ and when $f = 0$ equation (32) corresponds to the free wave equation when a finite number of components, $2n + 1$, in the wave group is considered. The exact dispersion relations in periodic systems reveal the zones of propagation, references [21–30]. In Fig. 2 a plot of nondimensional wave number $K = kl/\pi$ versus frequency parameter Ω is shown over the first and second bands of free propagation in the case where $K_t = \infty$ and $K_r = 0$. The nondimensional frequency Ω is defined with respect to the first resonance frequency in a simply supported span $\Omega = \omega/\omega_0$. For a speed v of the moving load the response of the beam is the superimposition of the wave groups seen in equation (45) where k/v is substituted for ω. The solution corresponds to the intersection of the curves in Fig. 2 and a straight line of slope $1/V$. The nondimensional speed V is defined with respect to the Timoshenko critical speed

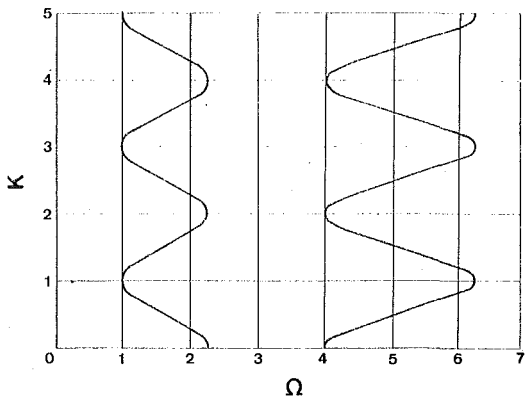

Fig. 2 The multivalued propagation constant curve versus frequency parameter ($K_t = \infty$, $K_r = 0$)

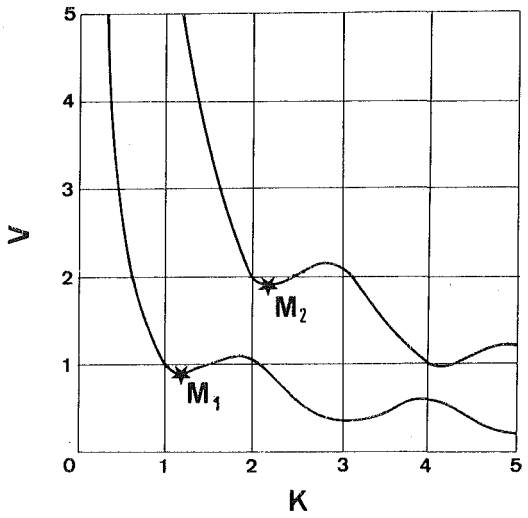

Fig. 3 Phase velocity versus wave number for $K_t = \infty$ and $K_r = 0$

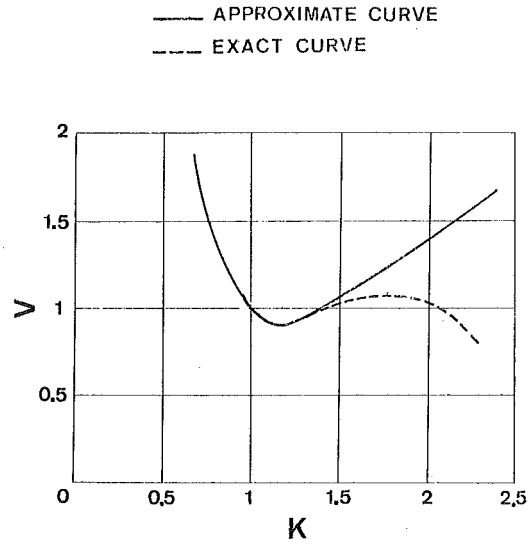

Fig. 4 Approximate dispersion curve for $n = 1$($K_t = \infty$, $K_r = 0$)

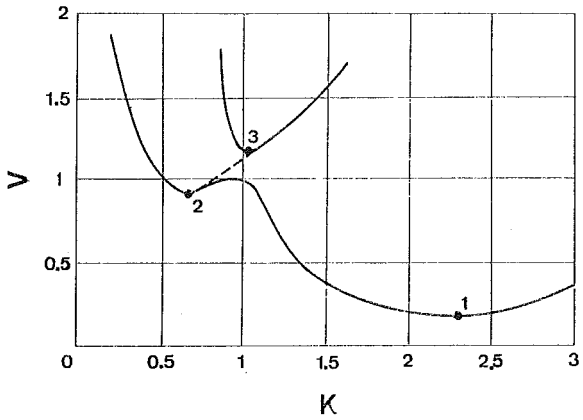

Fig. 5 Approximate dispersion curve for $R = 0.2$

$$V = v/v_0 = \frac{vl}{\pi}\left(\frac{m}{EI}\right)^{1/2}.$$

A plot of V versus K is shown in Fig. 3. Each continuous curve corresponds to a propagation zone. For a value of v there is an infinite number of k solutions, each being associated with a wave group. In the case of free propagation and coincidence effect with a convected pressure, Mead has shown that the greatest amount of flexural energy is transmitted by a component of the wave group, the wave number of which is considered as the "primary value" for a given frequency [25, 29]. Thus, for a load speed v, the predominant wave groups will be those which correspond to a k-value close to a "primary value." The minimum and maximum values of the curves in Fig. 3 are associated with critical load speeds defined in the preceding section. The primary value of nondimensional wave number K associated with each propagation band belongs to the interval $[N, N + 1]$ preceding the smallest value of the wave number K giving a minimum phase velocity. This minimum value corresponds to the so-called "primary critical speed" (points M_1 and M_2 in Fig. 3). The "nonprimary critical speeds" can be discounted as long as a low damping is introduced, since energy is difficult to transmit for such wave numbers. In the proposed method the number of components in a wave group is limited to $2n + 1$. Equation (40) is thus an approximate implicit relationship between the phase velocity v and real wave number k for free flexural waves propagating in the positive x-direction. The approximate solution is thus only valid for values of K even lower than n. Thus, if the solution in equation (10) is truncated at order n, only the primary critical speeds associated with the n first propagation bands can be approximated. Thus, in Fig. 4, in the case where $n = 1$, $K_r = 0$, $K_t = \infty$, the approximate dispersion relation is close to the exact curve traced in Fig. 3 for low wave numbers. As the primary critical speeds increase with the critical wave number, the low values of n correspond to the low load speeds v.

Transfer to a Continuous Foundation Model

Where $n = 1$ and $K_r = 0$, the characteristic equation (40) can be written in the following way:

$$\Phi(S, V) + R\Psi(S, V) = 0 \tag{46}$$

with

$$R = K_t l^3/(EI\pi^4) \quad S = K^2 \tag{47a,b}$$

Φ and Ψ are sixth and fourth-degree polynomials in the S. The calculation of the positive real poles in S gives the dispersion relationship of the free waves. For $R = 0.2$ the dispersion curves shown in Fig. 5 reveal three minimum phase speed values V_1, V_2, and V_3. The form of the curves varies according to the values of stiffness parameter R. For instance, the minimum value V_2 disappears for $R > 0.33$. When $K \to \infty$ the point P_1 associated with V_1 tends toward the point M_1 in Fig. 3. In the case where the stiffness $K_t l^2$ and K_r are less than the flexural rigidity EI, the reactions of the elastic supports can be expressed by a Winkler foundation model. In the proposed method this

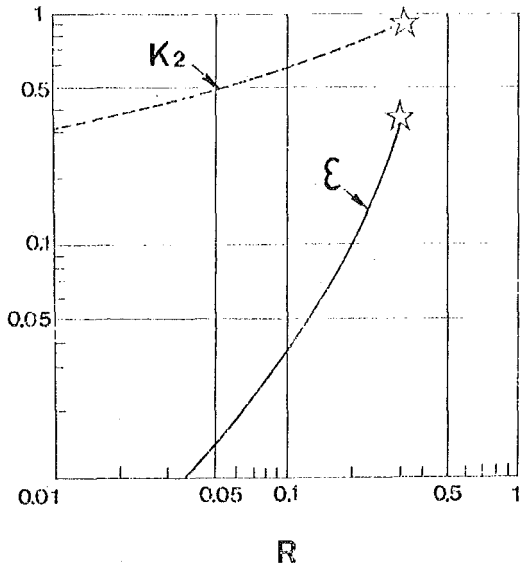

Fig. 6 Wave number K_2 and test function ϵ versus stiffness parameter R

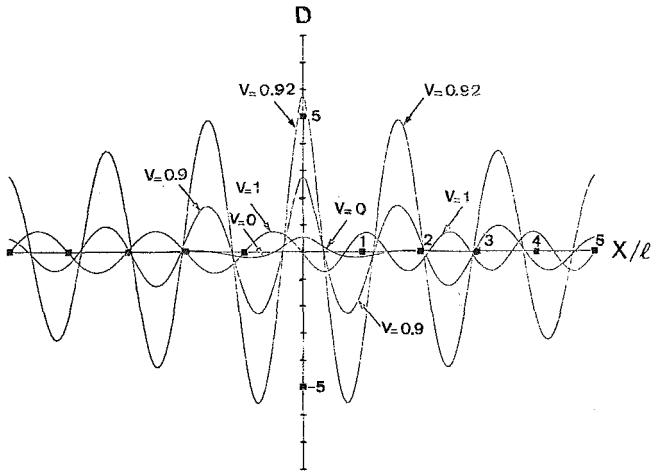

Fig. 7 Nondimensional beam deflection at midspan versus load distance for $R = \infty$

assumption is equivalent to discounting amplitude A_j and B_j for $j \geq 1$. The equilibrium equation is therefore reduced to the first diagonal term of the matrix equation (32)

$$[k^2(mv^2 - K_r/l) + EIk^4 + K_t/l]\overline{A}_0 = f \tag{48}$$

This equation is identical to that obtained in the case of an Euler-Bernoulli beam resting on a Winkler foundation with a distributed vertical load K_t/l and a distributed moment reaction K_r/l. The latter term has been proposed by Kerr to improve the stress analysis of railroad tracks [34]. The dotted curve in Fig. 5 corresponds to the dispersion curve for the Winkler continuous model with $K_r = 0$. For low values of K the phase speed V_2 is close to the critical speed of the Winkler model. The influence of periodical support spacing can be characterized by the ratio of A_1 and B_1 to the steady term A_0 associated with the wave group whose wave number is close to the critical value K_2

$$\epsilon = ((A_1^2 + B_1^2)/A_0^2)^{1/2} \tag{49}$$

ϵ increases rapidly beyond the value $R = 0.1$. In fact for such values of R, the critical wave number K_2 approaches 1—cf. Fig. 6—the stiffness parameter $R = 0.1$ appears to be the limit to the validity of the Winkler continuous model.

Results

In order to test the method we shall study the example of a simply supported beam on rigid supports ($K_r = 0, K_t = \infty$) and the Fourier series in equation (10) will be limited to the first order ($n = 1$).

The nondimensional beam deflection $D = y/y_0$ calculated at the center of a span for different values of nondimensional speed V are shown in Fig. 7—y_0 is the midspan deflection of a simple pinned end beam subjected to a static force f at midspan: $y_0 = fl^3/(48\,EI)$. In the static case ($V = 0$) the calculated value D_c is close to the exact value D_e:

$$D_e = 0.52452 \quad D_c = 0.53424$$

The equation (46) for $V = 0$ and $R = \infty$ has four complex roots

$$S_{1,2} = (K_{1,2})^2 = 0.829 \pm i\,0.833$$

$$S_{3,4} = (K_{3,4})^2 = 6.16 \pm i\,4.87$$

Since the zeros $K_{3,4}$ have a high value, their participation in the solution may be discounted for points at a distance from the load. The other zeros give a decreasing ratio for the support reaction θ_c which is practically real and very close to the exact value θ_e obtained by the three moment theorem

$$\theta_e = F_{N+1}/F_N = -0.26795$$

$$\theta_c = -0.27065\,(1 + i\,0.00394)$$

Fig. 4 shows that the calculated critical speed V_c is very close to the exact first primary critical speed V_e (Point M_1 in Fig. 3).

$$V_e = 0.92319 \quad V_c = 0.92519$$

The same is true for the nondimensional critical wave number K

$$K_e = 1.17322 \quad K_c = 1.16721$$

Conclusions

The proposed method has allowed us to calculate the critical speeds of a moving force on a periodic structure. The form of the solution and the convergence of the method have been justified on the basis of the free wave propagation equations. The motion could be interpreted as a superposition of wave groups and the "primary" critical speeds were defined. In the case of rigid supports, the static deflection and the first primary critical speed were calculated with high accuracy and low computer cost. The limitation to a finite number of wave-group components is analogous to modal truncation used in the Rayleigh-Ritz method. But the latter can only be applied in the case of finite structures. This study could be applied to more complex cases. For instance, it should allow the study of vehicles in motion on flexible guideways.

References

1 Schwedler, J. W., "On Iron Permanent Ways," *Proceedings, Institution of Civil Engineers*, London, 1882, pp. 95–118.

2 Hovey, B. K., *Beitrag zur Dynamik des geraden Eisenbahn-gleises*, Göttingen 1933.

3 Florence, A. L., "Traveling Force on a Timoshenko Beam," ASME JOURNAL OF APPLIED MECHANICS, Vol. 32, June 1965, pp. 351–358.

4 Steele, C. R., "The Timoshenko Beam With a Moving Load," ASME JOURNAL OF APPLIED MECHANICS, Vol. 35, Sept. 1968, pp. 481–488.

5 Achenbach, J. D., and Keshava, S. P., "Free Waves in a Plate Supported by a Semi-Infinite Continuum, ASME JOURNAL OF APPLIED MECHANICS, Vol. 34, June 1967, pp. 387–404.

6 Achenbach, J. D., Keshava, S. P., and Herrmann, G., "Moving Load on a Plate Resting on an Elastic Half Space," ASME JOURNAL OF APPLIED MECHANICS, Vol. 34, Dec. 1967, pp. 910–914.

7 Miles, J. W., "Response of a Layered Half Space to a Moving Load," ASME JOURNAL OF APPLIED MECHANICS, Vol. 33, Sept. 1966, pp. 680–681.

8 Wright, J. P., and Baron, M. L., "Exponentially Decaying Pressure Pulse Moving With Constant Velocity on the Surface of a Layered Elastic Material (Superseismic Layer, Subseismic Half Space)" ASME JOURNAL OF APPLIED MECHANICS, Vol. 37, Mar. 1970, pp. 141–153.

9 Sve, C., and Herrmann, G., "Moving Load on a Laminated Composite,"

ASME JOURNAL OF APPLIED MECHANICS, Vol. 41, Sept. 1974, pp. 663–667.

10 Yen, D. H. Y., and Chou, C. C., "Response of a Plate Supported by a Fluid Half Space to a Moving Pressure," ASME JOURNAL OF APPLIED MECHANICS, Vol. 37, Dec. 1970, pp. 1050–1054.

11 Adler, A., and Reismann, H., "Moving Loads on an Elastic Plate Strip," ASME JOURNAL OF APPLIED MECHANICS, Vol. 41, Sept. 1974, pp. 712–718.

12 Prasad, B., and Herrmann, G., "Response of a Laminated Beam to a Moving Load," *AIAA Journal*, Vol. 15, Oct. 1977, pp. 1424–1431.

13 Huang, C. C., "Traveling Loads on a Viscoelastic Timoshenko Beam," ASME JOURNAL OF APPLIED MECHANICS, Vol. 44, Mar. 1977, pp. 183–184.

14 Chonan, S., "Critical Velocity of a Load Moving on a Beam Supported by an Elastic Stratum," *Bulletin of the JSME*, Vol. 19, No. 132, June 1976, pp. 601–609.

15 Adams, G. G., and Bogy, D. B., "Steady Solutions for Moving Loads on Elastic Beams With One-Sided Constraints," ASME JOURNAL OF APPLIED MECHANICS, Vol. 42, Dec. 1975, pp. 800–804.

16 Choros, J., and Adams, G. G., "A Steadily Moving Load on an Elastic Beam Resting on a Tensionless Winkler Foundation," ASME JOURNAL OF APPLIED MECHANICS, Vol. 46, Mar. 1979, pp. 175–180.

17 Doran, A. L., and Mingori, D. L., "Periodic Motion of Vehicles on Flexible Guideways," ASME *Journal of Dynamic Systems, Measurement, and Control*, Vol. 99, Dec. 1977, pp. 268–276.

18 Chung, Y. I., and Genin, J., "Stability of a Vehicle on a Multispan Simply Supported Guideway," ASME *Journal of Dynamic Systems, Measurement, and Control*, Vol. 100, Dec. 1978, pp. 326–332.

19 Smith, C. C., and Wormley, D. N., "Response of Continuous Periodically Supported Guideway Beams to Traveling Vehicle Loads," ASME *Journal of Dynamic Systems, Measurement, and Control*, Vol. 97, Mar. 1975, pp. 21–29.

20 Genin, J., and Chung, Y. I., "Response of a Continuous Guideway on Equally Spaced Supports Traversed by a Moving Vehicle," *Journal of Sound and Vibration*, Vol. 67, No. 2, 1979, pp. 245–251.

21 Brillouin, L., *Wave Propagation in Periodic Structures*, Dover Publication, New York, Chapter 1, 1953.

22 Heckl, M., "Investigations on the Vibrations of Grillages and Other Simple Beam Structures," *Journal of the Acoustical Society of America*, Vol. 36, No. 7, 1964, p. 1335.

23 Lin, Y. K., and McDaniel, T. J., "Dynamics of Beam-Type Periodic Structures," ASME *Journal of Engineering for Industry*, Vol. 91, Nov. 1969, pp. 1133–1141.

24 Sen Gupta, G., "Natural Flexural Waves and the Normal Modes of Periodically Supported Beams and Plates," *Journal of Sound and Vibration*, Vol. 13, No. 1, 1970, pp. 89–101.

25 Mead, D. J., "Free Wave Propagation in Periodically Supported Infinite Beams," *Journal of Sound and Vibration*, Vol. 11, No. 2, 1970, pp. 181–197.

26 Mead, D. J., "A General Theory of Harmonic Wave Propagation in Linear Periodic Systems With Multiple Coupling," *Journal of Sound and Vibration*, Vol. 27, No. 2, 1973, pp. 235–260.

27 Mead, D. J., "Wave Propagation and Natural Modes in Periodic Systems: 1. Mono-Coupled Systems," *Journal of Sound and Vibration*, Vol. 40, No. 1, 1975, pp. 1–18.

28 Mead, D. J., "Wave Propagation and Natural Modes in Periodic Systems: 2. Multi-Coupled Systems, With and Without Damping," *Journal of Sound and Vibration*, Vol. 40, No. 1, 1975, pp. 19–39.

29 Mead, D. J., "Vibration Response and Wave Propagation in Periodic Structures," ASME *Journal of Engineering for Industry*, Aug. 1971, pp. 783–792.

30 Bansal, A. S., "Free Wave Motion in Periodic Systems With Multiple Disorders," *Journal of Sound and Vibration*, Vol. 60, 1978, pp. 389–400.

31 Wayland, H., *Quarterly of Applied Mathematics*, Vol. 2, 1945, pp. 277–306.

32 Guderly, K. G., "On Nonlinear Eigenvalue Problems for Matrices," *Journal of the Society of Industrial and Applied Mathematics*, Vol. 6, No. 4, Dec. 1958, pp. 335–353.

33 Moretti, G., *Functions of a Complex Variable*, Prentice-Hall, Englewood Cliffs, N. J., 1964, p. 147.

34 Kerr, A. D., "Improved Stress Analysis for Cross-Tie Tracks," ASCE *Journal of the Engineering Mechanics Division*, Vol. 105, Aug. 1979, pp. 539–548.

S. F. Masri
Professor.
Mem. ASME

G. A. Bekey
Professor.
School of Engineering,
University of Southern California,
Los Angeles, Calif. 90007

T. K. Caughey
Professor,
Division of Engineering
and Applied Science,
California Institute of Technology,
Pasadena, Calif. 91109

Optimum Pulse Control of Flexible Structures

A simple yet efficient active control method is presented for reducing the oscillations of distributed parameter systems subjected to arbitrary dynamic environments. Following determination that some specified response threshold has been exceeded, an open-loop control pulse is applied. The optimum pulse characteristics are determined analytically so as to minimize a non-negative cost function related to the structure energy. The proposed control method is shown to be reliable in consistently mitigating the response of realistic multidegree-of-freedom systems, whether linear or nonlinear, subject to arbitrary stochastic or deterministic excitation.

1 Introduction

Numerous studies have been conducted to investigate the use of passive vibration control techniques in structural systems (e.g., [1–10]), and in some cases actual hardware has been installed in representative building systems. However, while these devices are effective vibration controllers under certain conditions, they suffer from a limitation that is often inherent in most passive damping devices—the impracticality of applying the vibration control concept to existing structures. In many cases, these devices also suffer from the inability to substantially control the response of dynamic systems to nonstationary stochastic environments (such as those generated by winds or earthquakes) whose transient nature greatly reduces the efficiency of passive methods as compared to their efficiency under periodic excitation.

Analytical and experimental studies of impact vibration dampers [4] indicated that these nonlinear devices, which rely on the mechanism of momentum transfer and energy dissipation to accomplish their work, offer distinct advantages over conventional linear auxiliary mass dampers in attenuating the response of earthquake-excited structures [5].

However, due to the transient nature of the earthquake ground motion, the impulsive forces imparted by the impact damper to the primary structure do not always occur at the optimum time from the motion reduction point of view. A preliminary study indicated that the performance of the damper can be enhanced considerably by actively controlling the damper parameters to apply the generated impulsive forces at a time coinciding with the optimum phase relationship with respect to the excitation. The concept of using an auxiliary mass to generate an impact-induced impulsive force to counteract the motion of the primary structure (to which the damper is attached) can be extended to the direct use of external energy sources, as opposed to collision between two masses, to generate the needed impulsive actions.

A relatively recent method to simulate dynamic environments on test structures involves the use of a metal-cutting mandrel to generate prescribed pulse trains [11, 12]. In the course of a current study [13] to validate the concept of using pulse techniques to simulate the response of structures to arbitrary dynamic environments, a gas pulse generator is being built. This generator employs digital servo-controller and hydraulic actuators in conjunction with a gas storage system and a nozzle with a metered flow to furnish the needed thrust.

In view of the preceding discussion, an alternative approach to the exclusive reliance on passive methods to control the response of structures in dynamic environments such as earthquakes is to utilize active damping techniques. This paper is concerned with exploring the feasibility of using the soon-to-be-available portable gas pulse generators to actively control the response of structures during episodes of strong dynamic excitation.

1.1 Limitations of Active Control Techniques. The discipline of feedback control is an extremely active area of research and applications, as evidenced by the numerous books and technical journals devoted to the treatment of this subject. A recent survey [14] of just the optimal control of distributed-parameter systems contains over 260 references. While active control has been widely applied in many engineering areas and while some pioneering work has been done by Leipholz, Yao, and others [15–20] in the structural engineering area, they have yet to have meaningful applications in the active control of civil engineering structural systems to earthquake-like excitations.

Among the major difficulties encountered in the application of modern control techniques to building structural systems are the following:

Contributed by the Applied Mechanics Division for publication in the JOURNAL OF APPLIED MECHANICS.

Discussion on this paper should be addressed to the Editorial Department, ASME, United Engineering Center, 345 East 47th Street, New York, N. Y. 10017, and will be accepted until December 1, 1981. Readers who need more time to prepare a discussion should request an extension from the Editorial Department. Manuscript received by the Applied Mechanics Division, August, 1980; final revision, February, 1981.

1 Active control requires the ability to generate and apply large controlled forces to the structure.

2 Modern control theory often leads to feedback control laws, thus requiring on-line measurement (or estimation) of all the system state variables.

3 On-line control requires that both measurement and control be performed in real time.

4 Standard methods of control do not lend themselves readily to restricting the class of control signals to relatively narrow, high-energy pulses of the type suitable for active control of buildings and similar structures.

1.2 Proposed Active Control Strategy. Preliminary analytical and experimental studies by the authors [21] yielded promising results regarding the on-line pulse-control of building response under the action of nonstationary random excitations resembling typical earthquake ground motion.

The proposed control algorithm in [21] is designed to overcome the limitations of the existing controller design techniques. The algorithm requires a continuous monitoring of the state variables and the estimation of the energy content of the earthquake ground motion record. Following determination that some specified threshold has been exceeded, an open-loop pulse control is applied. The determination of the optimum pulse magnitude is based on a performance criterion which depends in a nonlinear way on both the deterministic and stochastic components of the response.

2 Pulse Control Method

2.1 Introduction. The proposed control method is applicable to arbitrary distributed systems with dynamic excitations which are directly applied or supplied through base motion. However, for the sake of clarity in explaining the procedure and illustrating its application, a base-excited building-like model of the type shown in Fig. 1 will be used.

The main idea behind the method is that the gradual rhythmic buildup of the structural response can be destroyed by applying pulses of suitable magnitude and proper direction at several locations distributed throughout the structure. Thus the control force need not be very large to completely counteract the massive amount of energy being applied to the structure; only a relatively small amount of control force is sufficient to interfere with orderly resonance phenomena which require many system periods to reach peak response levels.

Furthermore, in order to minimize the amount of control energy utilized, the control should be applied only when the structural response exceeds a certain threshold related to the resistance of the structure. Thus the control strategy requires that

1 The system be pulsed every time its response, which is monitored at several selected locations, crosses a threshold.

2 The minimum spacing between pulses be kept of the order T_1, the fundamental period of the structure.

3 The amplitudes of the pulses furnished by the controllers, which are placed at specific locations within the structure, are to be chosen so as to minimize an appropriate cost function.

2.2 Formulation. Consider the linear structure shown in Fig. 1, which is subjected to arbitrary base motion $S(t)$. The absolute displacement of location i is $x_i(t)$ and its relative motion with respect to the base is given by

$$y_i(t) = x_i(t) - S(t), \quad i = 1, 2, \ldots, n \tag{1}$$

In the context of earthquake engineering, the problem is to mitigate the damage to the structure resulting from excessive deformations $y_i(t)$, relative to the foundation which is undergoing an earthquake ground motion $S(t)$.

Assume that, on the basis of design considerations, threshold levels y_{r_i} $(i = 1, 2, \ldots, n)$ have been established for the locations whose motions are to be monitored. These levels will be used in conjunction with the control logic (to be discussed later) to trigger the controllers.

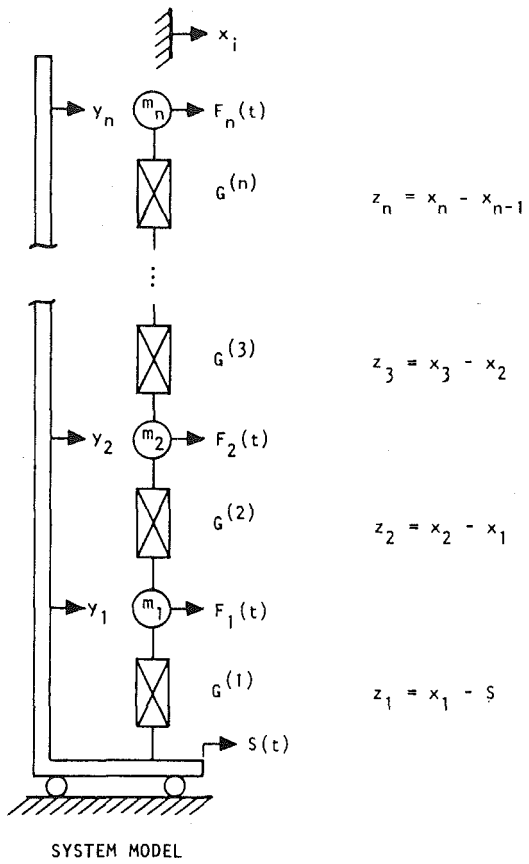

Fig. 1 System model

In the absence of control forces, the equation of motion of the system shown in Fig. 1 is

$$[m]\ddot{\mathbf{y}} + [c]\dot{\mathbf{y}} + [k]\mathbf{y} = -[m]\mathbf{e}\,\ddot{S}(t) \tag{2}$$

where $\mathbf{y}(t) = \text{col}\,(y_1, y_2, \ldots, y_n)$; $[m]$, $[c]$, and $[k]$ are mass, damping, and stiffness matrices, $\mathbf{e} = a$ unit vector of order $n = (1, 1, \ldots, 1)$, and $\ddot{S}$ = ground acceleration.

Assume that at time t_0 (Fig. 2), a decision has been made to trigger an array of pulse controllers located at selected points in the structure. The problem now is to select the optimum pulse characteristics so as to minimize an appropriate cost function. The control pulses to be used are constrained to satisfy the condition

$$P_i(t) = p_i p_0(t), \quad i = 1, 2, \ldots, n \tag{3}$$

where p_i is the amplitude of the pulse at location i, and $p_0(t)$ is an arbitrary time history. Note that equation (1) implies that (a) all the pulses are initiated at the same time and (b) they maintain a constant amplitude ratio, with respect to each other, every time a pulse is initiated.

In order to optimize (minimize) the motion of the system over a relatively short time segment T_{opt}, it will be assumed that the system motion consists of a stochastic component superimposed on top of a deterministic component. The pulse amplitudes are to be selected to minimize the deterministic (expected value) component of the motion.

Let

$$\mathbf{P}(t) = \mathbf{p}p_0(t) \tag{4}$$

where $\mathbf{p} = \text{col}\,(p_1, p_2, \ldots, p_n)$.

In order to account for the cases where controllers are to be applied only at certain locations NP, the reduced-order vector $\mathbf{P}_r$ is related to $\mathbf{p}$ by

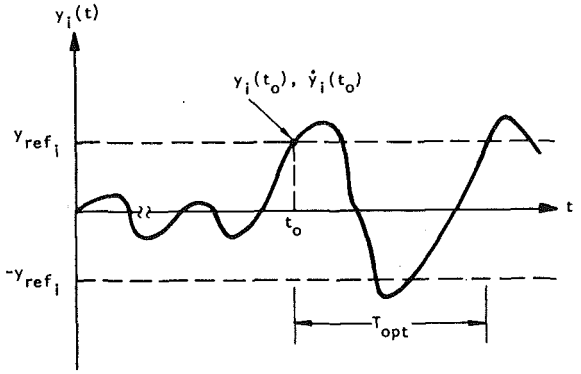

(a) System response at a typical location i

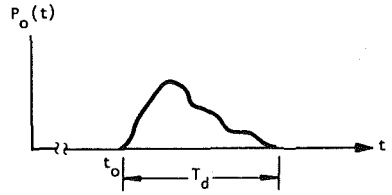

(b) Nominal pulse shape

(c) Pulse train amplitude at a typical location j

Fig. 2 Control algorithm parameters

$$\mathbf{p} = [w_2]\mathbf{P}_r \tag{5}$$

where $[w_2]$ is a constant matrix of order $n \times NP$, and $\mathbf{P}_r$ is a vector of order NP, containing the amplitude of the operating pulsers.

Neglecting the mean value of the earthquake excitation during the period t_0 to $T_0 = (t_0 + T_{opt})$, the system response is then given by the solution of

$$[m]\ddot{\mathbf{y}} + [c]\dot{\mathbf{y}} + [k]\mathbf{y} = \mathbf{p}(t) = \mathbf{p}p_0(t), \tag{6}$$

subject to the initial conditions

$$\mathbf{y}(t_0) \equiv \mathbf{y}_0, \quad \dot{\mathbf{y}}(t_0) = \dot{\mathbf{y}}_0. \tag{7}$$

Under the assumption that the damping matrix is proportional to $[m]$ and $[k]$, the modal approach will yield

$$\mathbf{y}(t) = [G_1(t)]\mathbf{y}(t_0) + [G_2(t)]\dot{\mathbf{y}}(t_0) - [G_4(t)][m]\mathbf{e} + [G_5(t)]\mathbf{p} \tag{8}$$

where

$$[G_1(t)] \equiv [\phi][U(t - t_0)][Q_1]$$

$$[G_2(t)] \equiv [\phi][V(t - t_0)][Q_1]$$

$$[G_3(t)] \equiv [\phi][H(t)][\phi]^T$$

$$[G_4(t)] \equiv \int_{t_0}^{t} [G_3(t - \tau)]\ddot{S}(\tau)d\tau$$

$$[G_5(t)] \equiv \int_{t_0}^{t} [G_3(t - \tau)]p_0(\tau)d\tau$$

$$[Q_1] \equiv [M]^{-1}[\phi]^T[m]$$

$[U]$, $[V]$, and $[H]$ are diagonal matrices with elements

$$u_{ii}(t) = \exp(-\zeta_i\omega_i t)\left[\left(\frac{\zeta_i}{\eta_i}\right)\sin\omega_i\eta_i t + \cos\omega_i\eta_i t\right]$$

$$v_{ii}(t) = \exp(-\zeta_i\omega_i t)\left[\frac{1}{\omega_i\eta_i}\sin\omega_i\eta_i t\right]$$

$$h_{ii}(t) = \frac{1}{M_i}v_{ii}(t)$$

$$\eta_i = \sqrt{1 - \zeta_i^2}, \quad \zeta_i = \frac{C_i}{C_{cr_i}} = \frac{C_i}{2\sqrt{K_iM_i}}$$

$$\omega_i = \sqrt{\frac{K_i}{M_i}}$$

$$[M] = [\phi]^T[m][\phi]$$

$$[C] = \alpha[M] + \beta[K] = [\phi]^T[c][\phi]$$

$$[K] = [\phi]^T[k][\phi]$$

$[\phi]$ = eigenvector matrix associated with $[m]^{-1}[k]$.

In view of the assumption that the ground excitation $\ddot{S}(t)$ can be treated during period T_{opt} as a zero-mean random process, then the expected value of $\mathbf{y}(t)$ as given by equation (8) will not depend on $\ddot{S}$. Hence

$$E[\mathbf{y}(t)] = [G_1(t)]\mathbf{y}_0 + [G_2(t)]\dot{\mathbf{y}}_0 + [G_5(t)]\mathbf{p} \tag{9}$$

Let the cost function to be minimized be

$$J(\mathbf{p}) = \int_{t_0}^{T_0} \epsilon^T(t)[w_1]\epsilon(t)dt \tag{10}$$

where $[w_1]$ is an arbitrary weighting matrix. If the strain or kinetic energy of the system is to be minimized, $[w_1]$ can be chosen as $[w_1] = [m]$ and $\epsilon(t) = E[\mathbf{y}(t)]$.

Making use of equations (5) and (8), equation (10) becomes

$$J(\mathbf{P}_r) = \int_{t_0}^{T_0} \{G_7(t) + 2\,\mathbf{G}_{10}{}^T(t)\mathbf{P}_r + \mathbf{P}_r{}^T[G_{11}(t)]\mathbf{P}_r\}dt \tag{11}$$

where

$$\mathbf{G}_6(t) \equiv [G_1(t)]\mathbf{y}_0 + [G_2(t)]\dot{\mathbf{y}}_0 - [G_4(t)][m]\mathbf{e}$$

$$G_7(t) \equiv \mathbf{G}_6{}^T[w_1]\mathbf{G}_6(t)$$

$$\mathbf{G}_8(t) \equiv [G_5(t)]^T[w_1]\mathbf{G}_6(t)$$

$$[G_9(t)] \equiv [G_5(t)]^T[w_1][G_5(t)]$$

$$\mathbf{G}_{10}(t) \equiv [w_2]^T[G_5(t)][w_1]\mathbf{G}_6(t)$$

$$[G_{11}(t)] \equiv [w_2]^T[G_9(t)][w_2]$$

For $J(\mathbf{P}_r)$ to have an extremum value,

$$\frac{\partial J}{\partial P_{r_k}} = 0, \quad k = 1, 2, \ldots, NP. \tag{12}$$

Application of equation (12) to (11) results in the optimum values of $\mathbf{P}_r$:

$$\hat{\mathbf{P}}_r = -[G_{13}]^{-1}\,\mathbf{G}_{12} \tag{13}$$

where

$$\mathbf{G}_{12} \equiv \int_{t_0}^{T_0} \mathbf{G}_{10}(t)dt$$

$$[G_{13}] \equiv \int_{t_0}^{T_0} [G_{11}(t)]dt$$

$$G_{14} \equiv \int_{t_0}^{T_0} G_7(t)dt$$

Note that, due to the assumption that the base excitation has a zero mean, the expected value of matrix $[G_4(t)]$ is zero.

For the special case of a single-degree-of-freedom system, equation (13) reduces to

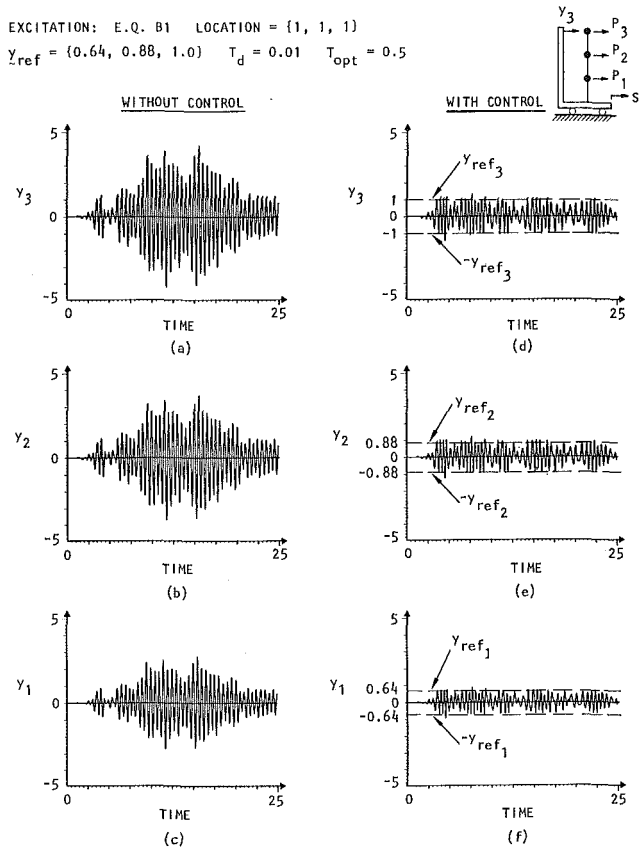

Fig. 3 Relative displacement

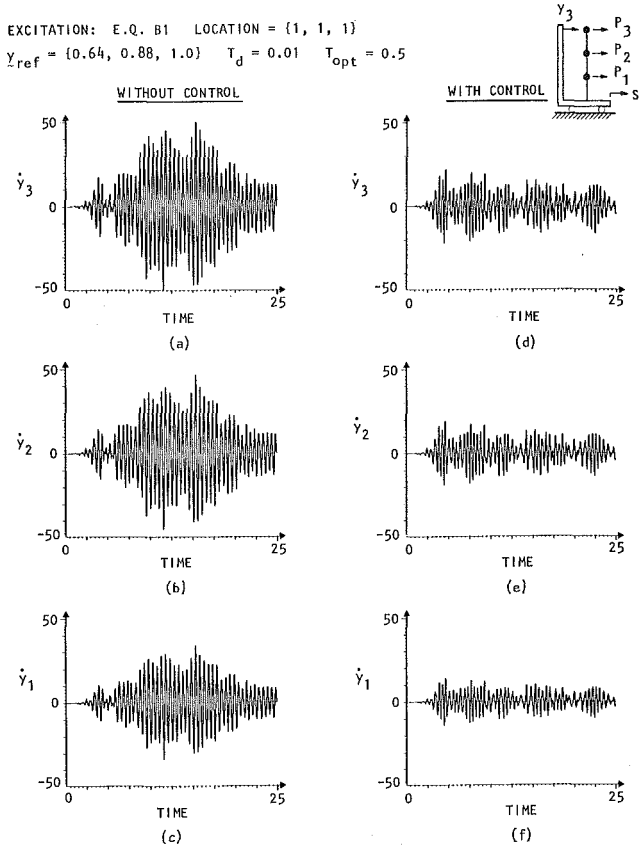

Fig. 4 Relative velocity response

$$\hat{P}_r = -\left[\int_{t_0}^{T_0} x_p{}^2(t)dt\right]^{-1} \times \left\{\int_{t_0}^{T_0} x_p(t)\,[u(t-t_0)y_0 + v(t-t_0)\dot{y}_0]dt\right\} \quad (14)$$

where

$$x_p(t) \equiv \int_{t_0}^{T_0} h(t-\tau)p_0(\tau)d\tau. \quad (15)$$

2.3 *Computational Considerations.* In view of the fact that on-line application of the control algorithm requires fast computation time, certain steps can be taken to reduce the computational tasks. For example, the matrices appearing in equation (13) contain many terms that depend only on the nominal pulse time history. Thus these terms can be evaluated just once and then stored for reuse whenever a pulse application is called for.

These ideas can be clarified by referring to equation (14) which applies to a SDOF system only. From this it is seen that once the nominal pulse shape $p_0(t)$ is selected (on the basis of physical considerations and limitations), the response term $x_p(t)$ appearing in equation (15) can be analytically evaluated and later used whenever needed.

Note from equation (14) that the optimum pulse amplitude is a function of two groups of terms: (*a*) the term $x_p(t)$, which depends on the particular choice of controller force $p_0(t)$, and (*b*) the bracketed group of terms, which depend on the system memory as reflected by terms $u(t)$ and $v(t)$, and on the "initial" conditions y_0 and $\dot{y}_0$ at the pulse initiation time t_0.

As a further simplification, the dynamic response of the structure due to the pulses with finite duration T_d can be accurately estimated on the basis of the impulsive response of the structure when subjected to an impulse of magnitude $\int_0{}^{Td} p_0(\tau)d\tau$.

3 Simulation of Control Strategy

Consider a model in the form of Fig. 1 of a three-story building frame that has been extensively analyzed, both analytically and experimentally [22, 23] at the University of California, Berkeley (UCB).

If this linear model of the UCB frame (henceforth referred to as model UCB-1) is subjected to a representative sample (earthquake B1) of a widely used set of artificial earthquakes [24] the relative displacement response of model UCB-1 without control will be as shown in Fig. 3(*a–c*). The three natural frequencies of model UCB-1 are ≈2, 6, and 10 Hz. Thus the time history segment shown in Fig. 3 corresponds to about 50 fundamental periods T_1 of the system.

Applying the control strategy just discussed to this structure with a threshold crossing level of $y_{ref_1} = \pm 0.44$, $y_{ref_2} = \pm 0.88$, and $y_{ref_3} = \pm 1.0$, the controlled response shown in Fig. 3(*d–f*) is obtained. This particular choice of $\mathbf{y}_{ref}$ corresponds to $\mathbf{y}_{ref} = d_3\boldsymbol{\phi}^{(1)}$ where $\boldsymbol{\phi}^{(1)} = \{0.64, 0.88, 1.0\}$ is the system eigenvector corresponding to the first mode, and d_3 (equal 1.0 in this example) is the scale factor corresponding to the absolute threshold level at the third (top) story. The pulse shape function $p_0(t)$ is rectangular and its duration is chosen equal to 0.01 sec, approximately equal to 2 percent of T_1, and the optimization time segment is taken as $T_{opt} = 0.5$ sec ≈ T_1. There is a sensor and a controller at each of the three mass locations.

It can be observed from Fig. 3 that the relative displacement at each location is closely bounded by the selected threshold levels, and that approximately the same percentage reduction is achieved at each location (each of the controlled locations has a peak response ≈35 percent of the corresponding uncontrolled response). Fig. 4 shows the relative velocity of the same structure with and without control under the same conditions shown in Fig. 3. The optimum pulse trains to be applied at the three locations are shown in Fig. 5.

Inspection of the results shown in Fig. 4 indicates that the peak relative velocity of each of the controlled locations is ≈40 percent of

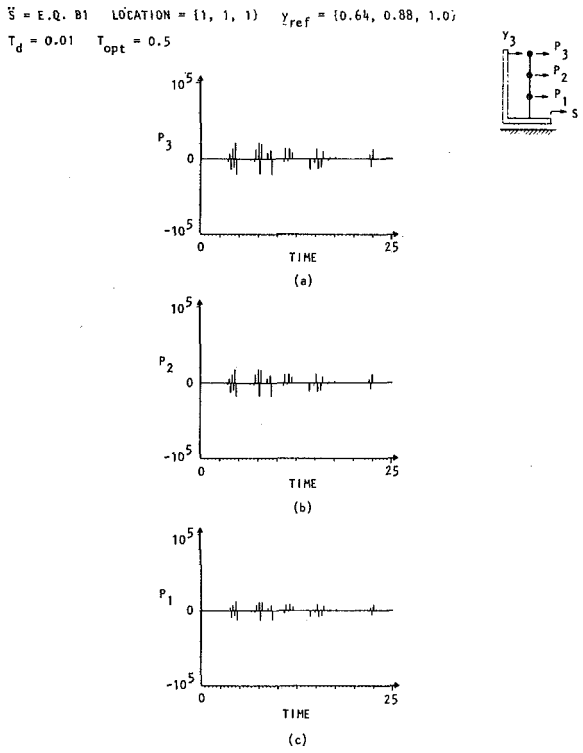

Fig. 5 Optimum pulse trains

the corresponding uncontrolled response. Also, it is seen from Figs. 3 and 4 that the percentage reduction in the rms level of the different response quantities is approximately the same as the corresponding reduction in peak levels.

It is seen from Fig. 5 that the amplitude ratios of the control pulses at the three locations are approximately equal to the corresponding ratios of the fundamental mode of vibration $\phi^{(1)}$. In fact, the average of the ratios for the 33 pulses applied in this case at each of the locations is {0.58, 0.84, 1.0}, which is fairly close to the ratios associated with $\phi^{(1)}$. In other words, the optimization scheme indicates that it is more efficient to apply the larger control forces at locations which can exert more control action by virtue of the amplification effects associated with the effective "moment arm" of each controller location.

The results of Figs. 6 and 7 illustrate the effects of adjusting the threshold level on the controlled response and the required pulse trains of model UCB-1, using the same excitation (E.Q. B1) and the same values for the rest of the control parameters shown in Figs. 3–5.

In the limiting case of $d_3 = 0$, the number of pulses used will be determined by the available control energy and can be constrained not to exceed a certain number of specifying T_{min}, the minimum spacing of the pulses. At the other extreme, if $d_3 = \infty$, the response will not be constrained and, consequently, no control action is called for. In between those two limits, the controlled response is seen to be held fairly closely to the governing threshold levels. Of course as the control limits are relaxed, there is less demand to take corrective action, thus less control force is needed. This fact is confirmed in the representative results shown in Fig. 7.

Since energy requirements are crucial for the feasibility of the proposed control method, determining the optimum pulse controller location for minimizing the needed control energy is an important

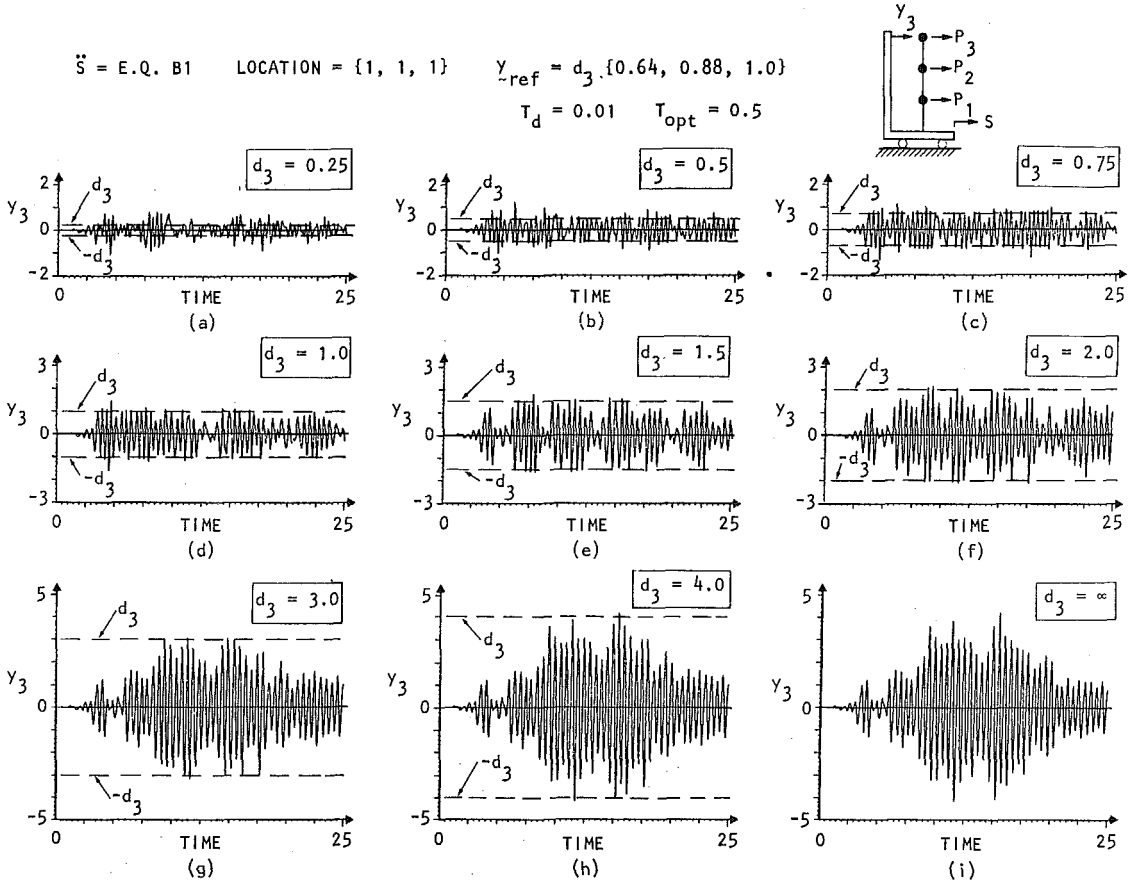

Fig. 6 Effects of threshold level on the controlled response of the UCB structure

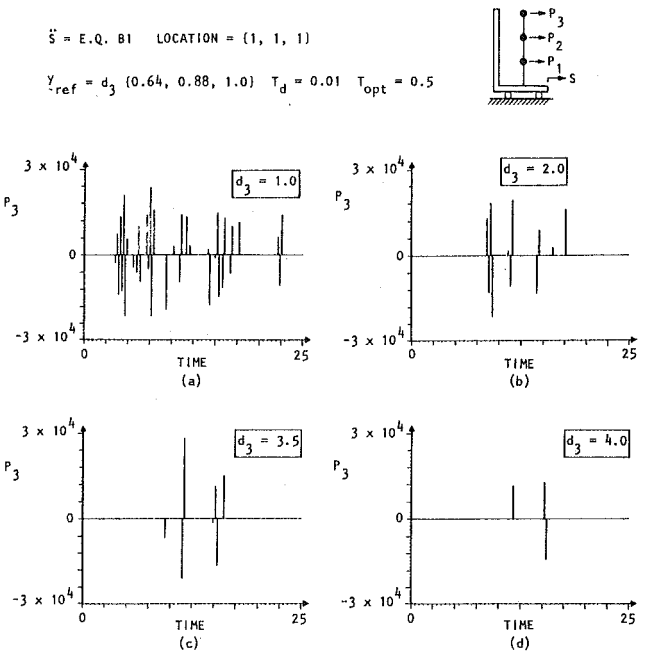

Fig. 7 Effects of threshold level on control pulse magnitude

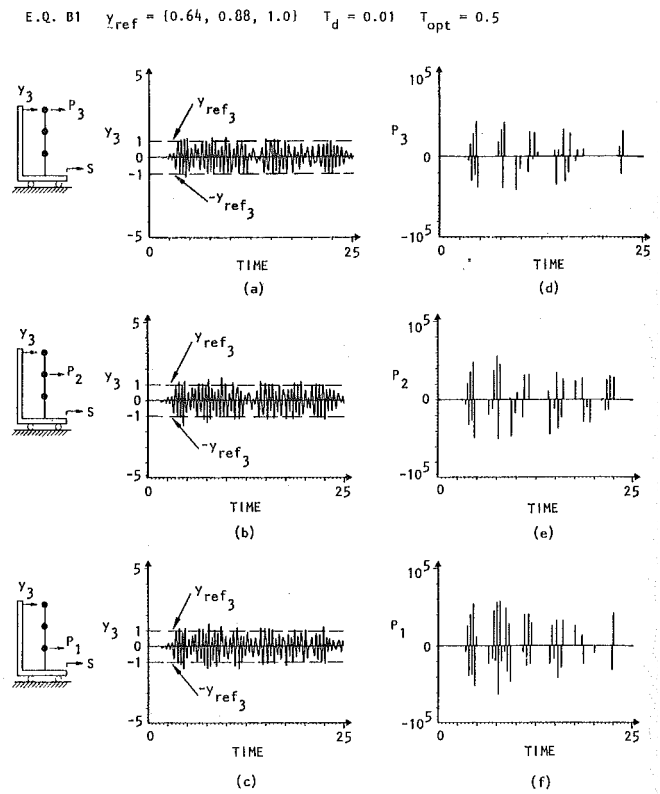

Fig. 8 Effects of single controller location on the response y_3

task. The results shown in Fig. 8 indicate the effects that can be obtained by using a single controller (instead of the three used previously). In Fig. 8(a) the controller is applied at the top floor (m_3); in Fig. 8(b) the controller is at the middle floor (m_2); and in Fig. 8(c) the controller is acting at the first floor (m_1).

Comparing the controlled response of the top floor in each of the three cases shown in Fig. 8 with its uncontrolled level, it is seen that approximately the same level of control can be achieved regardless of where the controller is applied. However, from the control energy point of view, there is a substantial difference in the requirements. The total impulse I applied by the controller used in Fig. 8(a–c) is $I_3 = 7.14 \times 10^3$ lb-sec, $I_2 = 10.2 \times 10^3$ lb-sec, and $I_1 = 12.5 \times 10^3$ lb-sec. These values compare with $I = 9.24 \times 10^3$ lb-sec used by the three controllers when applied simultaneously to the case shown in Figs. 3–5.

Thus it is clear that for this example structure, the optimum controller location is at m_3, and it is more energy-efficient to use one instead of three controllers. However, from the structural design point of view, it is more efficient to distribute the required control action over a large area of the structure.

Since the practical use of this method depends on determining some design parameters for the controller that can be derived from simulation studies, it is useful to investigate the response of model UCB-1 if its various control parameters are kept identical to those used in Fig. 3, and if it is then subjected to a variety of test excitations including stochastic as well as deterministic types.

The test excitation, comparison of the motion of m_3 with and without control, and the optimum pulse train at m_3 are given in reference [25] for each of the following cases:

1 Artificial earthquake A_1 [24].
2 Artificial earthquake D_1 [24].
3 Recorded ground motion corresponding to 1940 El Centro earthquake.
4 Stationary random excitation.
5 Swept-sine excitation.

The results shown in reference [25] together with Fig. 3 are indicative of the reliability of the proposed active control method in successfully limiting the structural response to predetermined levels, under a wide selection of text excitations.

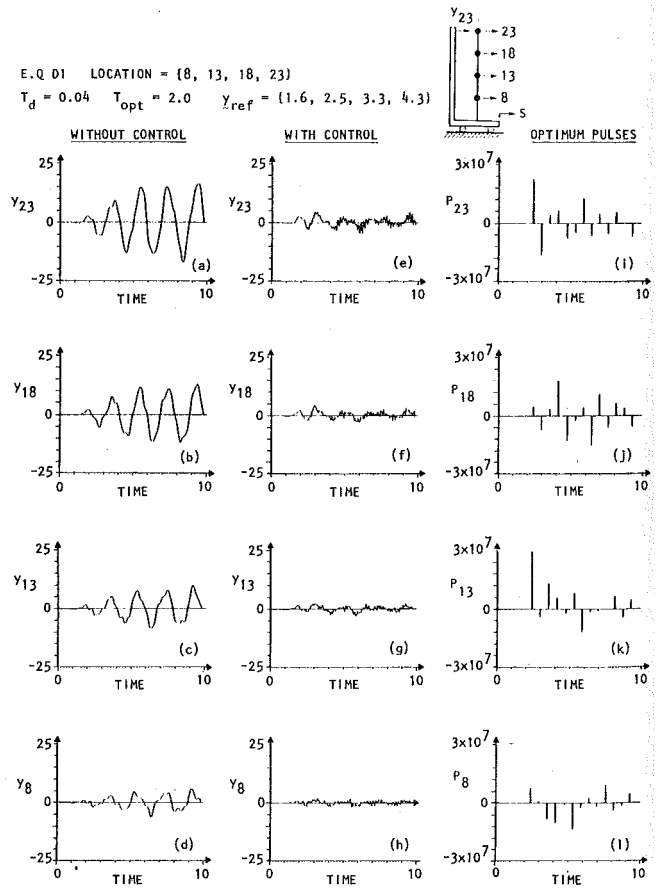

Fig. 9 Response of 25-DOF system under earthquake *D1*

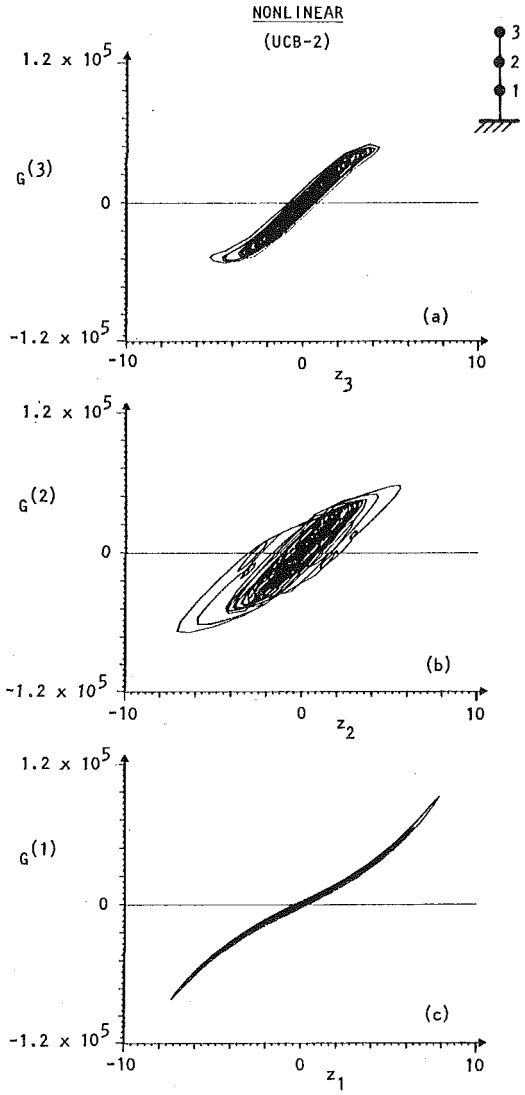

Fig. 10 Nonlinear system characteristics

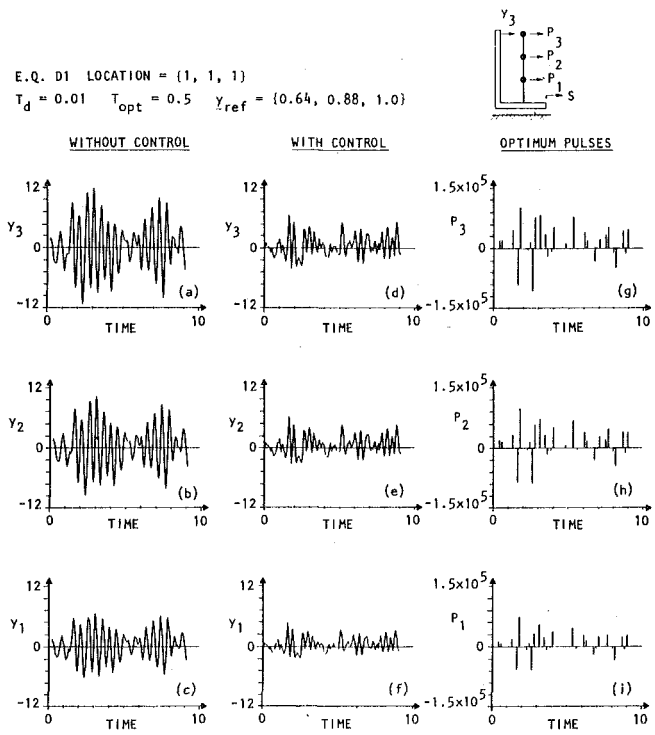

Fig. 11 Response of nonlinear 3-DOF System under earthquake $D1$

In order to illustrate the application of this method to more complicated structures, consider an example of 25 DOF building model which is representative of modern tall buildings [26].

Using earthquake D_1 as a hypothetical disturbance and placing threshold level detectors and controllers at locations 8, 13, 18, and 23, the control results shown in Fig. 9 are obtained. Note that substantial reduction is obtained in the response throughout the structure and the peak response levels are kept very close to the selected bounds. The optimum pulse trains shown in Figs. 9(i–l) confirm the expectation that it is more efficient to apply control forces at points that are farthest away from the point of fixity of the structure.

As a final example, consider a modified version of UCB-1 where it is assumed that the first restoring force element has a hardening-spring characteristic, the second element is hysteretic in nature, and the third element has a softening-spring nonlinearity. A plot of the restoring forces of the various elements of this structure versus their respective interstory displacement result in the nonlinear curves shown in Fig. 10. This structure will be referred to as UCB-2.

Subjecting structure UCB-2 to artificial earthquake D_1 and using equivalent linear properties to determine the optimum controller forces, results in the response shown in Fig. 11. It is clear that even though the control algorithm is devised for a linear distributed system, it is also successful in controlling the structural response of nonlinear systems provided reasonable equivalent linear properties are used to represent the nonlinear structure.

4 Summary and Conclusions

A simple yet efficient active control method is presented for reducing the oscillations of distributed parameter systems subjected to arbitrary deterministic or stochastic excitations.

This algorithm requires a continuous monitoring of the system state variables. Following the determination that some specified threshold has been exceeded, an open-loop control pulse is applied. The optimum pulse characteristics are determined analytically so as to minimize a non-negative cost function related to the structure strain energy and kinetic energy. The performance index is evaluated, and a control signal is calculated and applied for succeeding time intervals.

The determination of the optimum pulse magnitudes as well as the optimum spatial location of the controllers is based on a performance criterion which is linearly dependent on the deterministic (temporal mean) components of the response. The analytical solution for the optimum pulse characteristics uses the modal approach, and is shown to be computationally efficient and suitable for on-line implementation in controlling realistic structural systems.

Results of this investigation are applied to three example structures:

1 A linear model of a three-story frame that has been extensively investigated both experimentally and analytically by other researchers.

2 A linear mathematical model of a 25-story building which is representative of modern tall buildings.

3 A nonlinear three-degree-of-freedom system with components found in typical structures.

The test excitations used included several artificial earthquakes, an actual earthquake ground motion, stationary random excitation, and swept-sine signals.

It is shown that the proposed control method is reliable in consis-

tently mitigating the response of realistic structures subject to arbitrary dynamic environments.

Acknowledgment

This study was supported in part by a grant with the National Science Foundation. The authors appreciate the assistance of T. Dehghanyar in the computer studies and F. Safford and D. Oba in the preparation of the manuscript.

References

1 Martel, R. R., "The Effects of Earthquakes on Buildings With a Flexible First Story," *Bulletin of the Seismological Society of America*, Vol. 19, No. 3, 1929.

2 Caspe, M. S., "Earthquake Isolation of Multistory Concrete Structures," *Journal of the American Concrete Institute*, Vol. 67, No. 11, 1970.

3 Ikonomou, A. S., "The Earthquake Guarding System," *Technica Chronica*, Vol. 41, 1972.

4 Masri, S. F., "Steady-State Response of a Multidegree System With an Impact Damper," ASME JOURNAL OF APPLIED MECHANICS, Vol. 40, 1973, pp. 127–132.

5 Masri, S. F., and Yang, L., "Earthquake Response Spectra of Systems Provided With Nonlinear Auxiliary Mass Dampers," presented at 5WCEE, Paper No. 372, *Proceedings 5WCEE*, Rome, 1973.

6 Skinner, R. I., Beck, J. L., and Bycroft, G. N., "A Practical System for Isolating Structures From Earthquake Attack," *International Journal of Earthquake Engineering and Structural Dynamics*, Vol. 3, No. 3, 1975.

7 Robinson, W. H., and Greenbank, L. R., "An Extrusion Energy Absorber Suitable for the Protection of Structures During an Earthquake," *Earthquake Engineering and Structural Dynamics*, Vol. 4, 1976, pp. 251–259.

8 Megget, L. M., "Analysis and Design of a Base-Isolated Reinforced Concrete Frame Building," *Bulletin of the New Zealand Society for Earthquake Engineering*, Vol. 11, No. 4, 1978.

9 Derham, C. J., et al., "Natural Rubber Bearings for Earthquake Protection," Natural Rubber Technology, Vol. 8, Part 3, 1977; to appear in *Rubber Chemistry and Technology*, American Chemical Society, 1980.

10 Wiesner, K. B., "Tuned Mass Dampers to Reduce Building Wind Motion," Preprint 3510, ASCE Convention, Boston, Mass., April 2–6, 1979.

11 Safford, F. B., and Masri, S. F., "Analytical and Experimental Studies of a Mechanical Pulse Generator," ASME *Journal of Engineering for Industry*, Vol. 96, 1974, pp. 459–470.

12 Masri, S. F., Bekey, G. A., and Safford, F. B., "Optimum Response Simulation of Multidegree Systems by Pulse-Excitation," ASME *Journal of Dynamic Systems, Measurement, and Control*, Vol. 97, 1975, pp. 46–52.

13 National Science Foundation (NSF), *Feasibility of Force Pulse Generators for Earthquake Simulations*, NSF Grant PFR 77-15010, Washington, D. C., NSF, 1979.

14 Robinson, A. C., "A Survey of Optimal Control of Distributed-Parameter Systems," *Automatica*, Vol. 7, 1971, pp. 371–388.

15 Yao, J. T. P., "Concept of Structural Control," *Journal of the Structural Division*, ASCE, Vol. 98, No. ST7, July 1972, pp. 1569–1574.

16 Roorda, J., "Tendon Control in Tall Structures," *Journal of the Structural Division*, ASCE, Vol. 101, No. ST3, Mar. 1975, pp. 505–521.

17 Yang, J. N., "Application of Optimal Control Theory to Civil Engineering Structures," *Journal of the Engineering Mechanics Division*, ASCE, Vol. 101, No. EM6, Dec. 1975, pp. 819–838.

18 Martin, C., and Soong, T. T., "Modal Control of Multistory Structures," *Journal of the Engineering Mechanics Division*, ASCE, Vol. 102, No. EM4, Aug. 1976, pp. 613–623.

19 Abdel-Rohman, M., and Leipholz, H. H. E., "Structural Control by Pole Assignment Method," *Journal of the Engineering Mechanics Division*, ASCE, Vol. 104, No. EM5, Oct. 1978, pp. 1159–1175.

20 Leipholz, H. H. E., ed., *Structural Control*, North Holland SM Publications, 1980.

21 Masri, S. F., Bekey, G. A., and Udwadia, F. E., "On-Line Pulse Control of Tall Buildings," presented at International Union of Theoretical Mechanics Symposium on Structural Control, Waterloo, Ontario, Canada, June 4–8, 1979, published in *Structural Control*, Leipholz, H. H. E., ed., North-Holland Publishing Co. and SM Publications, 1980.

22 Clough, R. W., and Tang, D. T., "Earthquake Simulated Study of a Steel Frame Structure, Vol. I: Experimental Results," Report No. EERC 75-6, University of California, Berkeley, Apr. 1975.

23 Tang, D. T., "Earthquake Simulated Study of a Steel Frame Structure, Vol. II: Analytical Results," Report No. EERC 75-36, University of California, Berkeley, Oct. 1975.

24 Jennings, P. C., Housner, G. W., and Tsai, N. C., "Simulated Earthquake Motions," California Institute of Technology Report, 1968.

25 Masri, S. F., Bekey, G. A., and Caughey, T. K., "Optimum Pulse Control of Flexible Structures," University of Southern California Report USC-CE-8101, Jan. 1981.

26 Blume, J. A., Newmark, N. M., and Corning, L. H., "Design of Multistory Reinforced Concrete Buildings for Earthquake Motions," Portland Cement Association, Skokie, Ill., 1961.

A. Maewal

Assistant Professor,
Department of Engineering and Applied Science,
Yale University,
New Haven, Conn. 06520

Nonlinear Harmonic Oscillations of Gyroscopic Structural Systems and the Case of a Rotating Ring

Two related problems are investigated in order to study via a simple example the influence of gyroscopic forces on nonlinear harmonic oscillations of rotationally symmetric shell structures. First, the amplitude frequency equations are calculated for circumferentially traveling waves in a circular ring rotating about its geometrical axis. The results show that in the range of rotational speeds considered the backward traveling waves exhibit hardening type of response, whereas for the forward traveling waves there is a transition from hardening to softening type of behavior as the rotational speed increases. The second part of the paper is devoted to an analysis of interaction between the two traveling waves which is expected at low angular speeds. The results, valid for arbitrary shells of revolution, reveal the existence of secondary bifurcation points on the branches corresponding to the traveling waves, and the response on the secondary branches is found to be close to standing waves which do not appear at all as solutions of the linear free-vibration problem for the rotating shell.

Introduction

Due to Coriolis acceleration the linear problems of free vibrations of shells of revolution rotating about their geometrical axis admit only circumferentially traveling wave type of solutions. Motivated by the need for an elucidation of this phenomenon of disappearance of standing wave solutions of the linear problem even for arbitrarily small but nonvanishing speeds of rotation, this paper is devoted to an investigation of the effect of gyroscopic forces on steady nonlinear harmonic oscillations of elastic structures. Although the methods developed herein for our purposes are quite general, we have utilized them for analysis of an inextensible circular ring due to obvious reasons of simplicity.

The earliest investigation of the influence of rotation on vibration of a shell is apparently due to Bryan [1] who was interested in the beat phenomenon that occurs due to small difference between the frequencies of forward and backward traveling waves in a shell rotating at relatively small angular speeds. Although Carrier's study [2] is the most comprehensive one on the linear vibration of a rotating ring, there are some other treatments which include illuminating accounts of technical applications such as aircraft engine shells [3] and electromagnetic shields for superconducting electrical machines for power generation [4] wherein the influence of gyroscopic forces on vibration of shells is an important consideration for engineering design.

In this paper we first derive the amplitude frequency equations for the traveling waves in a rotating ring on the basis of a perturbation technique which is an application of the Lyapunov-Schmidt method [5]. For the limiting case of vanishing rotational speed our results complement the earlier analyses [6, 7] of standing waves in an elastic ring. Insofar as the amplitude frequency equation is concerned, our results indicate that for the stationary ring the traveling wave solutions are significantly different from the standing wave solution, and for the rotating ring the forward and backward traveling waves exhibit markedly different nonlinear charcteristics.

Another aspect of the problem that we have addressed in the sequel is the interaction that occurs between the two traveling waves at low speeds of rotation of the ring. Application of the Lyapunov-Schmidt method to the interaction problem for rotationally symmetric structures yields results which are quite general and, even for the case of stationary shells, have been obtained hirtherto in the context of specific examples only [e.g., 8]. The picture that emerges from our analysis—and which, retrospectively, is not quite unexpected—is the following. For the undamped free-vibration problems of rotationally symmetric stationary shells there are four solution branches, two corresponding to traveling waves, and the rest to the standing waves. Due to Coriolis acceleration, mode-splitting occurs in rotating shells and only traveling waves occur as solutions of the linear problem. However, when nonlinearities are taken into account, secondary bifurcation points appear on one of the branches corresponding to the

Contributed by the Applied Mechanics Division for presentation at the Winter Annual Meeting, Washington, D. C., November 15–20, 1981, of THE AMERICAN SOCIETY OF MECHANICAL ENGINEERS.

Discussion on this paper should be addressed to the Editorial Department, ASME, United Engineering Center, 345 East 47th Street, New York, N. Y. 10017, and will be accepted until December 1, 1981. Readers who need more time to prepare a discussion should request an extension from the Editorial Department. Manuscript received by ASME Applied Mechanics Division, June, 1980; final revision, February, 1981. Paper No. 81-WA/APM-2.

traveling waves, and the solution branches that emanate from the secondary bifurcation points approach asymptotically the standing wave solutions for large values of amplitude of oscillation.

Formulation

We use the theory of an inextensible[1] circular ring derived by Budiansky [9] and write the governing equations by first defining a functional

$$V(q) = V_2(q) + V_3(q) + V_4(q) \tag{1}$$

where

$$V_2(q) = \frac{1}{2}\int_0^{2\pi} [(v' - w'')^2 + 2\nu(w + v')]d\theta, \tag{2}$$

$$V_3(q) = \frac{1}{2}\int_0^{2\pi} \nu[(w + v')^2 + (w' - v)^2]d\theta, \tag{3}$$

$$V_4(q) = \frac{1}{2}\int_0^{2\pi} (v' - w'')^2\,(v - w')^2 d\theta, \tag{4}$$

which represent the strain energy of the ring appropriately augmented to account for the inextensibility condition. In (2)–(4), w and v denote, respectively, the radial and circumferential displacements, both nondimensionalized by the ring radius R; ν is the Lagrange multiplier associated with the inextensibility condition, q represents the triple $(v, w, \nu)^T$ and superposed primes denote differentials with respect to θ. With the definitions just given the equilibrium equations for a ring rotating at a steady speed $\tilde{\Omega}$ and oscillating at a frequency $\tilde{\omega}$ can be written in a coordinate frame rotating with the ring in a variational form as

$$\delta V(q) + \int_0^{2\pi} [a_r \delta w + a_\theta \delta v]d\theta = 0, \tag{5}$$

where

$$a_r = \omega^2 \ddot{w} - \Omega^2 (1 + w) - 2\omega\Omega\dot{v}, \tag{6}$$

$$a_\theta = \omega^2 \ddot{v} - \Omega^2 v + 2\omega\Omega\dot{w}, \tag{7}$$

are the acceleration components. The dots in (6), (7) denote derivatives with respect to the time coordinate nondimensionalized by using the frequency of oscillation, and

$$(\Omega, \omega) = (\tilde{\Omega}, \tilde{\omega})\rho h R^4/D, \tag{8}$$

where ρ, h, and D denote, respectively, the density ring thickness, ring thickness, and the bending stiffness, and $\delta V(q)$ is the first variation of the functional with respect to q.

It is easily shown that the equation (5) has a time-independent solution

$$\nu_0 = \Omega^2, \quad v_0 = w_0 = 0. \tag{9}$$

We shall now investigate nonlinear steady harmonic oscillations about the steady solution (9). For this purpose we write

$$q = q_0 + q^*, \tag{10}$$

where q_0 denotes the triple $(w_0, v_0, \nu_0)^T$, etc. The equations governing q^* are obtained by substituting (9), (10) into (5) and the result of this procedure can be written succintly (in Koiter's notation [10] for homogeneous functionals and their derivatives) in the form

$$R(q, \delta q) \equiv P_{11}(q, \delta q) + P_{21}(q, \delta q) + P_{31}(q, \delta q) + \omega G_{11}(\dot{q}, \delta q) + \omega^2 M_{11}(\ddot{q}, \delta q) = 0 \tag{11}$$

where superposed star has been dropped from q^* for notational convenience, and

$$P_{11}(q, \delta q) = \delta V_2(q) + \frac{1}{2}\Omega^2\delta\int_0^{2\pi} [(w + v')^2 + (w' - v)^2]d\theta - \Omega^2\int_0^{2\pi} [w\delta w + v\delta v]d\theta, \tag{12}$$

$$P_{21}(q, \delta q) = \delta V_3(q), \quad P_{31}(q,\delta q) = \delta V_4(q), \tag{13}$$

$$G_{11}(q, \delta q) = \int_0^{2\pi} 2\Omega[-\dot{v}\delta w + \dot{w}\delta v]d\theta, \tag{14}$$

$$M_{11}(\ddot{q}, \delta q) = \int_0^{2\pi} [\ddot{w}\delta w + \ddot{v}\delta v]d\theta. \tag{15}$$

It is evident that of the bilinear functionals introduced above, P_{11} and M_{11} are symmetric, whereas G_{11} is antisymmetric with respect to the arguments. Moreover, although (11) has been derived in the context of a specific example, insofar as it requires that the first variation of the transitional strain energy be balanced by the acceleration of the structure, it is applicable, with appropriate definitions of q and various functionals, to the general problem of oscillation of a rotating structure. We shall first describe, for the solution of the general problem, a procedure that results from the application of the Lyapunov-Schmidt method and which is only a slight modification of the development given in an earlier paper [6]. The technique will then be utilized for the precise problem which has motivated the analysis presented in the next section.

Asymptotic Analysis for the General Case

Since we seek time periodic solutions of (11), the equation has to be complemented by the periodicity conditions

$$q(0) = q(2\pi), \quad \dot{q}(0) = \dot{q}(2\pi), \tag{16}$$

where the spatial dependence of q has been suppressed for brevity of notation. Thus, in the time domain, we have a two-point nonlinear boundary-value problem in which the frequency of oscillation ω appears as a parameter. Equations (11), (16) have the trivial solution for all values of ω and the condition for the existence of bifurcation points on the trivial solution branch yields the equations for the natural frequencies and free vibration modes of the structure, to wit

$$\omega_0^2 M_{11}(\ddot{u}, \delta q) + \omega_0 G_{11}(\dot{u}, \delta q) + P_{11}(u, \delta q) = 0, \tag{17a}$$

$$u(0) = u(2\pi), \quad \dot{u}(0) = \dot{u}(2\pi). \tag{17b}$$

which is the linear part of the original equations (11), (16). Equation (17) has the solutions (with overbar denoting the complex conjugate)

$$u = y\,e^{it}, \quad \bar{u} = \bar{y}e^{-it} \tag{18}$$

where y, whose components are functions of spatial coordinates only, is the free-vibration mode. It satisfies the quadratic eigenvalue problem

$$-\omega_0^2 M_{11}(y, \delta q) + i\omega_0 G_{11}(y, \delta q) + P_{11}(y, \delta q) = 0, \tag{19a}$$

$$T_{11}(y, \bar{y}) = 1, \tag{19b}$$

The condition (19b) is basically a normalization condition in terms of the first variation T_{11} of a functional T_2. As in [10], choice of T_2 is arbitrary except that it is required to be positive-definite.

Since the subsequent analysis is similar to one presented in [6], with the modifications arising due to the presence of gyroscopic terms, we shall only outline the steps leading to the amplitude frequency equation near any natural frequency ω_0 which is such that (i) the associated eigenmode is unique within a sign and (ii) none of the other natural frequencies is an integral multiple of ω_0.

The solution of (11) is first written in the form

$$q = (\alpha y e^{it} + \text{c.c.}) + z, \int_0^{2\pi} e^{-it} T_{11}(z, \bar{y})dt = 0, \tag{20}$$

where α is the (complex) amplitude of oscillation and "c.c." denotes the complex conjugate of the term immediately preceding it. When

[1] The introduction of the inextensibility condition introduces errors of the order of the square of the thickness to radius ratio, as is shown in [7].

(20) is substituted into (11), the resulting equation can be written in terms of two equivalent ones:

$$\omega_0^2 M_{11}(\ddot{z}, \delta q) + \omega_0 G_{11}(\dot{z}, \delta q) + P_{11}(z, \delta q) = \tilde{R}\ (q, \delta q) - \left\{\frac{1}{2\pi} e^{it} T_{11}(y, \delta q) \int_0^{2\pi} e^{-it} \tilde{R}(q, \bar{y})\, dt + \text{c.c.}\right\} \quad (21a)$$

$$\int_0^{2\pi} e^{-it} \tilde{R}(q, \bar{y})\, dt = 0, \quad (21b)$$

where

$$-\tilde{R}(q, \delta q) = (\omega^2 - \omega_0^2) M_{11}(\dot{q}, \delta q) + (\omega - \omega_0) G_{11}(\dot{q}, \delta q) + P_{21}(q, \delta q) + P_{31}(q, \delta q), \quad (22)$$

with q given by (20). Equation (20) is merely a decomposition of the solution in terms of the natural mode of oscillation and its orthogonal component, whereas (21) reflects the same decomposition for the equation itself, following the Lyapunov-Schmidt method [5]. It is evident that when (11) is decomposed in the form of (21), secular terms are automatically eliminated from (21a). Thus the latter equation can be solved in an asymptotic series in the amplitude of oscillation and $(\omega - \omega_0)$. This solution when substituted into (21b) yields the desired amplitude frequency equation. The lowest order solution of (21a) which allows one to obtain the essential character of the nonlinear solution near ω_0 is given by

$$z = (\alpha^2 e^{2it} z^{(2)} + \text{c.c.}) + \alpha\bar{\alpha} z^{(0)}. \quad (23)$$

In (23), $z^{(2)}$ and $z^{(0)}$ are obtained from the solution of the linear time-independent problems

$$-4\omega_0^2 M_{11}(z^{(2)}, \delta q) + 2i\omega_0 G_{11}(z^{(2)}, \delta q) + P_{11}(z^{(2)}, \delta q) + P_{21}(y, \delta q) = 0, \quad (24)$$

$$P_{11}(z^{(0)}, \delta q) + P_{111}(y, \bar{y}, \delta q) = 0. \quad (25)$$

These equations (23), (25) are simply obtained by expanding the quadratically nonlinear term (21a), (22). Substitution of (23) into (21b) yields the desired result

$$-(\omega^2 - \omega_0^2)\, m\alpha + (\omega - \omega_0) g\alpha + \gamma_1 \alpha^2 \bar{\alpha} = 0, \quad (26)$$

where

$$m = M_{11}(y, \bar{y}), \quad (27a)$$

$$g = iG_{11}(y, \bar{y}), \quad (27b)$$

$$\gamma_1 = 2P_{21}(\bar{y}, z^{(2)}) + P_{111}(y, \bar{y}, z^{(0)}) + P_{211}(y, \bar{y}, \bar{y}). \quad (27c)$$

The aforementioned analysis could be carried through without any significant changes even if damping and a time periodic forcing function were present. In such a case equation (11) is modified to

$$R(q, \delta q) + \mu C_{11}(\dot{q}, \delta q) = \xi\{F_{11}(f, \delta q) e^{it} + \text{c.c.}\} \quad (28)$$

where μ and ξ are scalar measures of damping and applied force, respectively, with both the measures assumed to be small. The lowest order result which contains all the significant terms turns out to be

$$-(\omega^2 - \omega_0^2) m\alpha + (\omega - \omega_0) g\alpha + i\mu c\alpha + \gamma_1 \alpha^2 \bar{\alpha} = \zeta, \quad (29)$$

where

$$c = C_{11}(y, \bar{y}), \quad \zeta = \xi F_{11}(f, \bar{y}). \quad (30)$$

In summary, in order to obtain the response of a rotating structure one has to solve the eigenvalue problem (19) and linear boundary-value problems (24), (25). These solutions can be used to obtain the numerical coefficients in the response equation (29) by utilizing (27), (30). This procedure shall now be illustrated by an analysis of the rotating circular ring problem formulated in an earlier section.

Amplitude Frequency Equation for Traveling Waves in a Rotating Ring

We first calculate the natural modes of a rotating ring by using (12), (14), (15), and (19), which yield

$$L(\omega_0, \partial_\theta; \Omega) y = 0, \quad (31)$$

where L is the matrix differential operator defined by

$$[L] = -\omega_0^2 \begin{bmatrix} 1 & 0 & 0 \\ 0 & 1 & 0 \\ 0 & 0 & 0 \end{bmatrix} + i\omega_0\Omega \begin{bmatrix} 0 & -2 & 0 \\ 2 & 0 & 0 \\ 0 & 0 & 0 \end{bmatrix} - \begin{bmatrix} -\partial_\theta^4 & \partial_\theta^3 & -1 \\ -\partial_\theta^3 & \partial_\theta^2 & \partial_\theta \\ -1 & -\partial_\theta & 0 \end{bmatrix} + \Omega^2 \begin{bmatrix} -\partial_\theta^2 & 2\partial_\theta & 0 \\ -2\partial_\theta & -\partial_\theta^2 & 0 \\ 0 & 0 & 0 \end{bmatrix} \quad (32)$$

On substitution of

$$y = (1, iB_1, C_1)^T e^{in\theta} \equiv Y e^{in\theta}, \quad n = 2, 3 \ldots, \quad (33)$$

equation (31) yields the matrix eigenvalue problem

$$L(\omega_0, in; \Omega) Y = 0. \quad (34)$$

The solution of (34) is found to be

$$\omega_0 = \frac{2n\Omega}{n^2 + 1} \pm \omega_{sn} \sqrt{1 + \frac{\Omega^2}{n^2 + 1}}, \quad (35a)$$

$$B_1 = 1/n, \quad (35b)$$

$$C_1 = \omega_0^2 + n^2 - n^4 + (2 - n^2)\Omega^2 - 2\omega_0\Omega/n, \quad (35c)$$

where ω_{sn} is the natural frequency of the stationary ring associated with a given circumferential wave number and is given by

$$\omega_{sn}^2 = n^2(n^2 - 1)^2/(n^2 + 1). \quad (35d)$$

It is evident from (20), (33), (35) that due to rotational effects there are two different natural frequencies, one positive and other negative, corresponding to a given value of circumferential wave number n, and these frequencies correspond to traveling waves, since, in terms of the dimensional variables,

$$\tilde{w} = e^{i(n\theta + \omega_0 \tilde{t})}, \text{ etc.} \quad (36)$$

This result is in contrast to the stationary case wherein both the traveling waves have the same frequencies.

Further computations require the calculation of the forcing terms in (24), (25). On using (3), (13), (33), (35) these turn out to be

$$P_{21}(y, \delta q) = \int_0^{2\pi} [\delta w G_1 + i\, \delta v\, G_2 + \delta v\, G_3]\, e^{2in\theta} d\theta, \quad (37a)$$

where

$$G_1 = 2nC_1(n - B_1), \quad (37b)$$

$$G_2 = -C_1(n - B_1), \quad (37c)$$

$$G_3 = -(n - B_1)^2/2, \quad (37d)$$

and

$$P_{111}(y, \bar{y}, \delta q) = \int_0^{2\pi} (n - B_1)^2\, \delta v d\theta. \quad (37e)$$

From (24), (36) and (25), (37) it follows that

$$z^{(2)} = (A_2, iB_2, C_2)^T e^{2in\theta} \equiv Z^{(2)} e^{2in\theta}, \quad (38)$$

$$z^{(0)} = (A_0, iB_0, C_0)^T = Z^{(0)}, \quad (39)$$

where

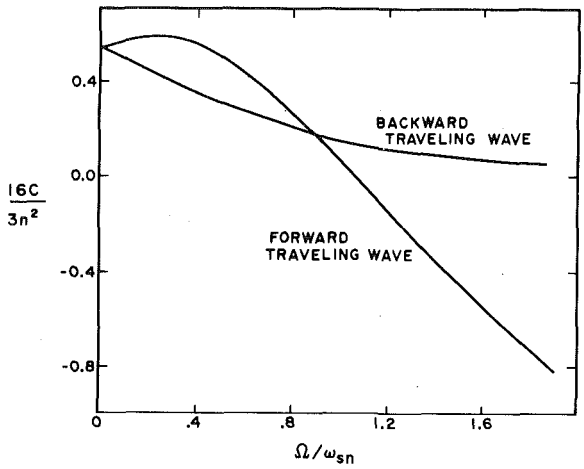

Fig. 1 The coefficient of the nonlinear term in the amplitude frequency equation (44) for a rotating ring; circumferential wave number $n = 2$

$$L(2\omega_0, 2in; \Omega)\, Z^{(2)} + (G_1, iG_2, G_3)^T = 0, \tag{40}$$

$$L(0, 0; \Omega)\, Z^{(0)} + (0, 0, [n - B_1]^2)^T = 0, \tag{41}$$

and $L(\omega_0, \partial_\theta; \Omega)$ is defined by (32). Equations (40), (41) are linear algebraic equations which can be solved readily. The solutions of these equations together with (4), (13), (27), (36)–(39) yield

$$\frac{\gamma_1}{2\pi} = 2(A_2G_1 + B_2G_2 + C_2G_3) + 2\,(n^2 - 1)^4/n^2. \tag{42}$$

The other constants in the amplitude frequency equation (26) are

$$\frac{m}{2\pi} = (1 + B_1^2), \quad \frac{g}{2\pi} = 4\Omega B_1, \tag{43}$$

which are obtained from (27), (33), (35). It is convenient to put the final result in the form

$$\frac{\omega}{\omega_0} = 1 - \frac{2(A_2G_1 + B_2G_2 + C_2G_3) + 2(n^2 - 1)^4/n^2}{4\omega_0[4\Omega B_1 - 2\omega_0(1 + B_1^2)]} A^2$$
$$= 1 + C\,A^2 \tag{44}$$

which follows from (26). Furthermore, in (44) we have set

$$A^2 = 4\alpha\bar{\alpha} \tag{45}$$

which is the square of the amplitude of oscillation.

We have used the sequence of linear algebraic equations leading to (44) to compute the coefficient C which determines the essential effect of including the nonlinearity. Typical results for $n = 2$ are given in Fig. 1. Numerical results were also obtained for other values of cricumferential wave number ($2 \le n \le 10$) in the range of rotational speeds $0 \le \Omega \le 2\omega_{sn}$. The results are qualitatively similar in that for the forward traveling wave the nonlinearity coefficient C defined by (44) is positive at zero and low rotational speeds and then changes sign as the speed increases, whereas for the backward traveling wave the nonlinearity is always of the hardening type. (Note that $\omega_0 < 0$ for forward traveling wave and $\omega_0 > 0$ for backward traveling wave, cf. (36).) These numerical results also indicate that for a stationary ring $C \simeq (3/16)\, n^2$ for large values of the circumferential wave number (see Table 1) which is the reason why the quantity $16C/(3n^2)$ has been plotted in Fig. 1.

The result for traveling waves in stationary ring is in sharp contrast to what was obtained earlier [6,7] for standing wave pattern, for which the coefficient in amplitude frequency equation (36) was found to be approximately given by $C \simeq -n^4/8$ for large values of n. It is evident, therefore, that the interaction between the two traveling waves which gives rise to the significantly different nonlinear character of the standing wave pattern plays an important role in the determination of nonlinear dynamic response of the ring and, generally, of geometrical similar rotationally symmetric shells of revolution. Further, it is also expected that the interaction would give rise to qualitatively interesting behavior in such structures even when they are rotating about their axis of symmetry. The aforementioned considerations have motivated the analysis of the next section.

Table 1 The coefficient in the amplitude frequency equation (44) for traveling waves in a stationary ring

n	$16\ C/3n^2$
2	.550
3	.776
4	.868
5	.914
6	.940
7	.955
8	.966
9	.973
10	.978

A Mode Interaction Analysis for Slowly Rotating Shells of Revolution

In what follows we consider the general equation of motion (11) under the restriction that the rotational speed Ω which is implicitly contained in the functional associated with the gryoscopic forces and in the strain-energy functionals is sufficiently small. Moreover, we restrict our attention to rotationally symmetric shells for which all the functionals in (11) are of the type

$$\int_0^{2\pi} F(q)d\theta$$

where F represents any of the functionals and q is dependent on θ,t and one other spatial coordinate subsequently referred to as the axial coordinate, and all the components of q are periodic with respect to θ. Since (11) is a variational statement, it implicitly includes any natural boundary conditions at the ends of the shell and requires that all the admissible variations satisfy the imposed kinematic conditions. As a result, at $\Omega = 0$, the equations for natural frequencies and natural modes for (11),

$$\omega_0^2\, M_{11}(\ddot{u}, \delta q) + P_{11}(u, \delta q) = 0, \tag{46a}$$

$$\int_0^{2\pi} T_2(u)dt \neq 0 \tag{46b}$$

have for the same value of ω_0 the following *four* linearly independent solutions

$$\hat{y}\, e^{in\theta}\, e^{it}, \bar{\hat{y}}\, e^{-in\theta}\, e^{it}, \hat{y}\, e^{in\theta}\, e^{-it}, \bar{\hat{y}}\, e^{-in\theta}\, e^{-it}$$

where components of $\hat{y}$ are independent of both θ and t but are functions of the axial coordinate. These functions satisfy the linear eigenvalue problem

$$-\omega_0^2\, M_{11}(y, \delta q) + P_{11}(y, \delta q) = 0, \tag{47a}$$

$$T_{11}(y, \bar{y}) = 1, \tag{47b}$$

where $y = \hat{y}\, e^{\pm in\theta}$. To obtain the solution of the nonlinear problem we write

$$q = (\alpha y e^{it} + \text{c.c.}) + (\beta \bar{y} e^{it} + \text{c.c.}) + z, \tag{48a}$$

$$\int_0^{2\pi} e^{-it} T_{11}(z, \bar{y}) dt = \int_0^{2\pi} e^{-it} T_{11}(z, y) dt = 0. \tag{48b}$$

The decomposition (48a) is similar to (20) except that the multiplicity of solutions of (47) has been taken into account. Further, just as in (21), (22), we decompose (11) into *three* equivalent equations

$$\omega_0^2 M_{11}(\ddot{z}, \alpha q) + P_{11}(z, \delta q) = \hat{R}(q, \delta q) - \frac{1}{2\pi}\left\{e^{it} T_{11}(y, \delta q) \int_0^{2\pi} e^{-it} \hat{R}(q, \bar{y}) dt + \text{c.c.}\right\} - \frac{1}{2\pi}\left\{e^{it} T_{11}(\bar{y}, \delta q) \int_0^{2\pi} e^{-it} \hat{R}(q, y) dt + \text{c.c.}\right\} \tag{49a}$$

$$\int_0^{2\pi} e^{-it} \hat{R}(q, \bar{y}) dt = 0, \tag{49b}$$

$$\int_0^{2\pi} e^{-it} \hat{R}(q, y) dt = 0, \tag{49c}$$

where

$$-\hat{R}(q, \delta q) = (\omega^2 - \omega_0^2) M_{11}(\ddot{q}, \delta q) + \omega G_{11}(\dot{q}, \delta q) + P_{21}(q, \delta q) + P_{31}(q, \delta q), \tag{50}$$

and the difference between (49a), (50) on the one hand and (21a), (22) on the other arises due to the fact that now we are seeking a perturbation solution about $\Omega = 0$ as well. Once again it is easily shown that (49a) does not contain any secular terms so that its solution z can be obtained as an asymptotic series in the amplitudes of the two traveling waves, $(\omega - \omega_0)$ and Ω. The solution adequate for the purpose of extracting the essential nonlinear behavior is given by

$$z = (\alpha^2 z_{11}^{(2)} e^{2it} + \text{c.c.}) + \alpha\bar{\alpha} z_{11}^{(0)} + (\beta^2 z_{22}^{(2)} e^{2it} + \text{c.c.}) + \beta\bar{\beta} z_{22}^{(0)} + (\alpha\beta z_{12}^{(2)} e^{2it} + \text{c.c.}) + (\alpha\bar{\beta} z_{12}^{(0)} + \text{c.c.}), \tag{51}$$

where various time independent quantities are given by solutions of

$$-4\omega_0^2 M_{11}(z_{11}^{(2)}, \delta q) + P_{11}(z_{11}^{(2)}, \delta q) + P_{21}(y, \delta q) = 0, \tag{52a}$$

$$P_{11}(z_{11}^{(0)}, \delta q) + P_{111}(y, \bar{y}, \delta q) = 0, \tag{52b}$$

$$-4\omega_0^2 M_{11}(z_{22}^{(2)}, \delta q) + P_{11}(z_{22}^{(2)}, \delta q) + P_{21}(\bar{y}, \delta q) = 0, \tag{53a}$$

$$P_{11}(z_{22}^{(0)}, \delta q) + P_{111}(\bar{y}, y, \delta q) = 0, \tag{53b}$$

$$-4\omega_0^2 M_1(z_{12}^{(2)}, \delta q) + P_{11}(z_{12}^{(2)}, \delta q) + P_{111}(y, \bar{y}, \delta, q) = 0, \tag{54a}$$

$$P_{11}(z_{12}^{(0)}, \delta q) + P_{111}(y, y, \delta q) = 0. \tag{54b}$$

Further simplification is achieved on noting that

$$y = \hat{y} e^{in\theta}$$

so that on examination of nonhomogeneous terms in (52)–(54) one finds that

$$z_{22}^{(2)} = \bar{z}_{11}^{(2)} = \hat{z}_{11}^{(2)} e^{-2in\theta}, \quad z_{22}^{(0)} = z_{11}^{(0)} = \hat{z}_{11}^{(0)}, \tag{55a}$$

and

$$z_{12}^{(2)} = \hat{z}_{12}^{(2)}, \quad z_{12}^{(0)} = \hat{z}_{12}^{(0)} e^{2in\theta}. \tag{55b}$$

In (55) the terms with superposed caret are independent of θ and t, but are functions of the axial coordinate. We now substitute (48a) in (49b,c), and use (55) with the fact that in evaluation of the functionals in (49b,c) one has to integrate in the domain $0 \le \theta \le 2\pi$. These considerations lead to the remarkably simple result

$$-m(\omega^2 - \omega_0^2)\alpha + \omega g \alpha + \gamma_1 \alpha^2 \bar{\alpha} + \gamma_2 \beta\bar{\beta}\alpha = 0, \tag{56a}$$

$$-m(\omega^2 - \omega_0^2)\beta - \omega g \beta + \gamma_1 \beta^2 \bar{\beta} + \gamma_2 \alpha\bar{\alpha}\beta = 0, \tag{56b}$$

where

$$m = M_{11}(y, \bar{y}), \quad g = iG_{11}(y, \bar{y}), \tag{57a,b}$$

$$\gamma_1 = P_{111}(z_{11}^{(2)}, \bar{y}, \bar{y}) + P_{111}(z_{11}^{(0)}, y, \bar{y}) + P_{211}(y, \bar{y}, \bar{y}) \tag{58a}$$

$$\gamma_2 = P_{111}(z_{11}^{(0)}, y, \bar{y}) + P_{111}(z_{12}^{(2)}, y, \bar{y}) + P_{111}(z_{12}^{(0)}, \bar{y}, \bar{y}) + 2P_{211}(y, \bar{y}, \bar{y}). \tag{58b}$$

Equations (56a,b) are the desired coupled amplitude frequency equations for the (complex) amplitudes α and β of the two traveling waves which have the same frequency when $\Omega = 0$ and when nonlinearities are not taken into account. To compute the constants in these equations one has to solve the four linear boundary value problems (52), (54). Since these problems as previously stated are in terms of vanishing of first variations of functionals, their solutions depend upon the imposed boundary conditions which are implicitly contained in the variational statements (52), (54). It is worthwhile to note here that for the case of a stationary shell if one sets

$$\alpha = a + ibe^{i\psi}, \quad \beta = a - ibe^{i\psi}$$

one can obtain from (56) the amplitude frequency equations of the type derived by Ginsberg [8] for the special case of a circular cylindrical shell. Moreover, addition of damping and forcing terms in the original equation (11) changes the final form of the amplitude frequency equation only to the extent that two more easily computable terms have to be added to each of (56a,b) just as in (29). Though these terms are expected to endow interesting qualitative features to the dynamic response curves as in [8] we restrict our discussion to the case of undamped free vibration only.

Solutions of the Amplitude Frequency Equations. We first dispose of the case of the stationary shell wherein $g = 0$. It is seen from (56) that there are only four solution

$$\omega^2 = \omega_0^2 + \gamma_1 \alpha\bar{\alpha}/m, \quad \beta = 0, \tag{59a}$$

$$\omega^2 = \omega_0^2 + \gamma_1 \beta\bar{\beta}/m, \quad \alpha = 0, \tag{59b}$$

$$\omega^2 = \omega^2{}_0 + (\gamma_1 + \gamma_2)\alpha\bar{\alpha}/m, \quad \beta = \pm\alpha, \tag{59c}$$

the first two of which correspond to traveling waves and the rest to standing wave patterns. As is generally true for free-vibration problems the phase of these solutions is arbitrary.

For the slowly rotating shell ($g \neq 0$) two solutions of (56) are immediately obvious

$$\omega^2 = \omega_0^2 + \frac{\omega_0 g}{m} + \gamma_1 \alpha\bar{\alpha}/m, \quad \beta = 0, \tag{60a}$$

$$\omega^2 = \omega_0^2 - \frac{\omega_0 g}{m} + \gamma_1 \beta\bar{\beta}/m, \quad \alpha = 0, \tag{60b}$$

which represent traveling waves whose frequencies at zero amplitudes differ due to gyroscopic forces, as expected. Another set of solutions of (56) occurs when both α and β are nonzero in which case the solutions satisfy

$$-2(\omega^2 - \omega_0^2)m + (\gamma_1 + \gamma_2)\left(\frac{A^2}{4} + \frac{B^2}{4}\right) = 0, \tag{61a}$$

$$2\omega_0 g + (\gamma_1 - \gamma_2)\left(\frac{A^2}{4} - \frac{B^2}{4}\right) = 0, \tag{61b}$$

where

$$\alpha\bar{\alpha} = \frac{A^2}{4}, \quad \beta\bar{\beta} = \frac{B^2}{4}. \tag{62}$$

If g is positive, it follows from (61b) that real solutions of (61) exist for

$$(i) \quad \frac{B^2}{4} > \frac{2\omega_0 g}{\gamma_1 - \gamma_2}, \quad (\gamma_1 - \gamma_2 > 0), \tag{63a}$$

or for

$$(ii) \quad \frac{A^2}{4} > \frac{2\omega_0 g}{\gamma_2 - \gamma_1}, \quad (\gamma_1 - \gamma_2 < 0). \tag{63b}$$

Thus, in Case (i) there is a secondary bifurcation point on the branch given by (60b), occurring at

$$\frac{\tilde{B}^2}{4} = \frac{2\omega_0 g}{\gamma_1 - \gamma_2}, \quad \tilde{\omega}^2 = \omega_0{}^2 + \frac{\gamma_1 + \gamma_2}{\gamma_1 - \gamma_2}\frac{g\omega_0}{m}, \quad \tilde{A} = 0. \qquad (64a)$$

In Case (*ii*) the secondary bifurcation point occurs on the branch (60*a*) at[2]

$$\frac{\tilde{A}^2}{4} = \frac{2\omega_0 g}{\gamma_2 - \gamma_1}, \quad \tilde{\omega}^2 = \omega^2{}_0 + \frac{\gamma_1 + \gamma_2}{\gamma_2 - \gamma_1}\frac{g\omega_0}{m}, \quad \tilde{B} = 0. \qquad (64b)$$

A similar analysis for $g < 0$ reveals that secondary bifurcation point occurs at one and only one of the two traveling wave solution branches. Of course, the secondary branches are given by simultaneous solutions of (61*a*,*b*). From (61*b*) it is concluded that along the secondary branches, for $g > 0$,

$$(i) \qquad \frac{A}{2} \simeq \pm\frac{B}{2}\left[1 - \frac{4\omega_0 g}{(\gamma_1 - \gamma_2)B^2}\right], \qquad (65a)$$

or

$$(ii) \qquad \frac{B}{2} \simeq \pm\frac{A}{2}\left[1 - \frac{4\omega_0 g}{(\gamma_2 - \gamma_1)A^2}\right], \qquad (65b)$$

so that for large amplitudes these branches asymptotically approach the standing wave solutions along which $A = \pm B$.

We conclude this section by noting that, based on (56), a number of qualitatively different free-vibration response curves in the A, B, ω space can be drawn with the differences depending on the relative magnitudes and signs of the coefficients γ_1 and γ_2. For the sake of brevity, however, we shall present the result only for the case of a rotating ring.

Mode Interaction in a Slowly Rotating Ring

The analysis of mode interaction in a rotating ring on the basis of the procedure derived in the last section begins with the solution of the eigenvalue problem (47) specialized to the functionals given by (12), (15). The solution is similar to that of (31), i.e.,

$$y = (1, iB_{10}, C_{10})^T e^{in\theta}, \qquad (66a)$$

$$\omega_0{}^2 = \omega_{sn}{}^2, \qquad (66b)$$

where B_{10}, C_{10}, and ω_0 are given by (35) with $\Omega = 0$.

Similarly, the solution of the higher-order problems corresponding to (52), (54) are of the form (55), with

$$\hat{z}_{11}{}^{(2)} = (A_{11}{}^{(2)}, iB_{11}{}^{(2)}, C_{11}{}^{(2)})^T, \text{ etc.}, \qquad (67)$$

The quantities $\hat{z}_{11}{}^{(2)}$, $\hat{z}_{11}{}^{(0)}$, $\hat{z}_{12}{}^{(2)}$, and $\hat{z}_{12}{}^{(0)}$ in (55) satisfy

$$L(2\omega_0, 2in;\, 0)\, \hat{z}_{11}{}^{(2)} + (G_{10}, i\,G_{20}, G_{30})^T = 0, \qquad (68a)$$

$$L(0, 0;\, 0)\, \hat{z}_{11}{}^{(0)} + (0, 0, \{n - B_{10}|^2)^T = 0, \qquad (68b)$$

$$L(2\omega_0, 0;\, 0)\, \hat{z}_{12}{}^{(2)} + (0, 0, \{n - B_{10}|^2)^T = 0, \qquad (69a)$$

$$L(0, 2in;\, 0)\, \hat{z}_{12}{}^{(0)} + 2(G_{10}, iG_{20}, G_{30})^T = 0, \qquad (69b)$$

where G_{i0}, $i = 1, 2, 3$ are given by (37*b*–*d*) with C_1 and B_1 replaced by C_{10} *and* B_{10} and the matrix L is defined by (32). Finally, equations (57), (58) furnish

$$\frac{\gamma_1}{2\pi} = 2(B_{10} - n)^2\,(-n\,B_{10} + n^2)^2 + 2\,(G_{10}A_{11}{}^{(2)} + G_{20}B_{11}{}^{(2)} + G_{30}C_{11}{}^{(2)}), \qquad (70a)$$

$$\frac{\gamma_2}{2\pi} = -4(n - B_{10})^4\,\omega_0{}^2 + 2\,(G_{10}A_{12}{}^{(0)} + G_{20}B_{12}{}^{(0)} + G_{30}C_{11}{}^{(0)}) + 4(B_{10} - n)^2\,(-n\,B_{10} + n^2)^2, \qquad (70b)$$

and m and g in (56) are given by (43). In (70) we have used the explicit solutions of (68*b*) and (69*a*) but $A_{11}{}^{(2)}$, $B_{11}{}^{(2)}$, etc. in these equations are given by (68*a*) and (69*b*). Thus the coefficients γ_1 and γ_2 can be obtained through a sequence of linear algebraic calculations which are best done numerically. The results are given in Table 2. A typical free-vibration response curve, which exhibits the type of characteristics described in the last section has been shown in Fig. 2. In this figure the coordinates have been chosen so that the plots are independent of speed of rotation and valid for small nonvanishing values of Ω.

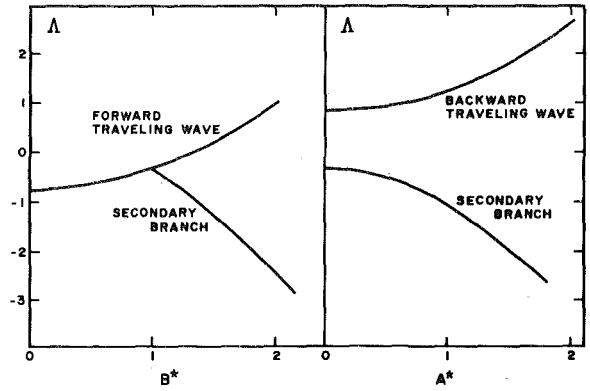

Fig. 2 Free-vibration response curves for a rotating ring ($n = 2$), [$\Lambda = (\omega/\omega_0 - 1)/(\Omega/\omega_0)$, $(A^*, B^*) = (A, B)/\tilde{B}$, with $\tilde{B}$ defined by (64)]

Table 2 The coefficients in the amplitude frequency equation (56) for the mode interaction problem for a circular ring

n	$\gamma_1/2\omega_0^2 m$	$\gamma_2/2\omega_0^2 m$
2	1.650	-0.0432×10^2
3	5.240	-0.781×10^2
4	10.420	-3.457×10^2
5	17.134	-9.764×10^2
6	25.363	-2.187×10^3
7	35.100	-4.241×10^3
8	46.341	-7.451×10^3
9	59.086	-1.218×10^4
10	73.331	-1.883×10^4

Concluding Remarks

Perturbation procedures based on the Lyapunov-Schmidt method have been presented in this paper for the analysis of nonlinear harmonic oscillations of structural systems with gyroscopic forces and the techniques have been illustrated by analyses of the simple, yet nontrivial, problem of a rotating ring. The procedure for mode-interaction analysis of rotationally symmetric structures appears to be particularly useful for further applications to shells of revolution as it can provide a basis for efficient computational schemes for solution of a class of problems which have not been treated before in a general framework.

References

1 Bryan, G. H., "On the Beats in the Vibrations of Revolving Cylinder or Bell," *Proceedings of the Cambridge Philosophical Society*, Vol. VII, 1890, pp. 101–111.

2 Carrier, G. F., "On the Vibrations of the Rotating Ring," *Quarterly of Applied Mathematics*, Vol. VII, 1945, pp. 235–245.

3 Macke, H. J., "Traveling Wave Vibration of Gas Turbine Engine Shells," ASME *Journal of Engineering for Power*, Vol. 88, 1966, pp. 179–187.

4 Shevchuk, G. J., and Thullen, P., "Flexural Vibrations of Rotating Electromagnetic Shields," *Journal of Mechanical Design*. Vol. 101, 1979, pp. 133–137.

5 Vainberg, M. M., and Tregonin, V., *Theory of Branching of Solutions of Nonlinear Equations*, Nordhoff, Holland, 1974.

6 Maewal, A., and Nachbar, W., "Lyapunov-Schmidt Method for Analysis of Postbuckling Behavior and Steady Nonlinear Harmonic Oscillations of

[2] It can be verified that $(\tilde{A}, \tilde{B}, \tilde{\omega})$ defined by (64*a*) satisfy both (60*b*) and (61) and similar result holds for Case (*ii*).

Conservative Structures," Eighth U.S. National Congress of Applied Mechanics, UCLA, 1978.

7 Simmonds, J. G., "Accurate Nonlinear Equations and a Perturbation Solution for the Free Vibrations of a Circular Elastic Ring," ASME JOURNAL OF APPLIED MECHANICS, Vol. 46, 1979, pp. 156–160.

8 Ginsberg, J. H., "Large Amplitude Forced Vibrations of Simply Supported Thin Cylindrical Shells," ASME JOURNAL OF APPLIED MECHANICS, Vol. 40, 1973, pp. 471–477.

9 Budiansky, B., "Theory of Buckling and Postbuckling Behavior of Elastic Structures," *Adv. Appl. Mech.*, Vol. 14, 1974, pp. 2–65.

10 Koiter, W. T., "On Stability of Elastic Equilibrium," Thesis, Delft, 1945 (English translation available as AFFDL-TR-70-25-1970).

C. S. Hsu

Professor of Applied Mechanics,
Department of Mechanical Engineering,
University of California,
Berkeley, Calif. 94720
Fellow ASME

A Generalized Theory of Cell-to-Cell Mapping for Nonlinear Dynamical Systems

The simple theory of cell mapping and the associated algorithm presented in [1, 2] have been found to form a very effective tool for the global analysis of nonlinear systems. In this paper we generalize the theory by allowing the mapping of a cell to have multiple image cells with appropriate individual mapping probabilities. This generalized theory will be able to deal with very fine and complicated global behavior patterns, if they exist, in a more attractive way without having to utilize extremely small cell sizes. It is found that such a generalized cell mapping can be identified with a Markov chain and the well-developed mathematical theory of Markov chains can be immediately applied. Similar to the simple theory of [1], the generalized cell mapping theory is also eminently suited as a theoretic base for computer alogorithms which will be needed when dealing with systems involving a very large number of cells.

1 Introduction

In [1] a primitive theory of cell-to-cell mapping has been introduced. In essence, the cell-to-cell mapping of that theory is described by

$$\mathbf{Z}(n+1) = \mathbf{C}(\mathbf{Z}(n)) \tag{1}$$

where, without any loss of generality, the cell vector $\mathbf{Z}$ can be taken to be integer-valued, and $\mathbf{C}$ is an integer-valued vector cell mapping. By confining the total number of cells to be treated finite, a very simple algorithm has been devised for studying the global properties of nonlinear systems [2]. The algorithm is easy to implement and has been found to be very effective.

The theory offered in [1] is a simple one. However, it is also a coarse one. When it is applied to point mapping systems or to systems governed by ordinary differential equations, it could not disclose the fine structural details of the global behavior if they exist, unless the cell size is taken to be very small. In this paper we offer a generalized cell mapping theory by bringing into the theory certain new ingredients. When compared with the simple theory of [1] the new theory is much more complex, but, on the other hand, it will have the capability of describing any intricate global behavior in a more satisfying manner. Just like the theory in [1] the new theory also lends itself well as a theoretical base for computer implementation.

The theory offered here is believed to use an entirely new approach to the global analysis of nonlinear systems. In this regard, it is indeed *unusually fortunate* that the analytical techniques required to develop this theory are found readily available in the mathematics literature in the form of Markov chains. After presenting the basic ideas of the generalized cell mapping theory we summarize some results on Markov chains. Thereafter, we discuss a few simple examples involving very few cells in order to illustrate the idea and application of the theory. Our ultimate aim is of course to analyze systems with very large number of cells. This will require a special algorithm similar to the one presented in [2].

2 New Ingredients: Multiple Mapping Image Cells and Their Probabilities

The basic idea of the cell mapping theory presented in [1, 2] is that a cell $\mathbf{Z}(n)$ is mapped by the mapping $\mathbf{C}$ into a *single* image cell $\mathbf{Z}(n$

Contributed by the Applied Mechanics Division for presentation at the Winter Annual Meeting, Washington, D. C., November 15–20, 1981, of THE AMERICAN SOCIETY OF MECHANICAL ENGINEERS.

Discussion on this paper should be addressed to the Editorial Department, ASME, United Engineering Center, 345 East 47th Street, New York, N. Y. 10017, and will be accepted until December 1, 1981. Readers who need more time to prepare a discussion should request an extension from the Editorial Department. Manuscript received by ASME Applied Mechanics Division, February, 1981; final revision, April 1981. Paper No. 81-WA/APM-25.

+ 1). In the *generalized* theory we remove this restriction. Instead, we allow the mapping of a cell $\mathbf{Z}(n)$ to have several possible image cells, each image cell having a definite fraction of the total possibility. In other words, if the system is at cell $\mathbf{Z}(n)$ when $t = n$, the state at the next evolution step $t = n + 1$ can be at $\mathbf{Z}^{(1)}(n + 1)$ with probability $p^{(1)}$, at $\mathbf{Z}^{(2)}(n + 1)$ with probability $p^{(2)}$, and so forth. Of course, we must have $\Sigma_i p^{(i)} = 1$ where the sum covers all the possible image cells. With these new ingredients it is no longer adequate to specify the state of the system to be at a certain cell $\mathbf{Z}(n)$ at $t = n$. Rather, the state of the system should be described by the probabilities according to which the state of the system may be found in various cells.

Now let us formalize the foregoing notion in mathematical terms. Let $\mathbf{S}$ be a closed set of cells of interest. In application of the theory we shall always deal with a finite number of cells. However, for the general discussion in this section, we take $\mathbf{S}$ to be a denumerable set. Moreover, we assume that the cells are labeled[1] $1, 2, \ldots, N$ according to an appropriate procedure, with N possibly being infinite.

Cell Probability Vector. Let $\zeta_i(n)$ denote the probability of the state of the system being in cell i at $t = n$. The vector $\zeta(n)$ with components $\zeta_i(n)$, $i = 1, 2, \ldots, N$, will be called the *cell probability vector* or simply *probability vector.*

Transition Probability Matrix. Let p_{ij} denote the probability of cell j being mapped to cell i in one mapping step. The matrix $\mathbf{P}$ with components p_{ij} will be called the *transition probability matrix*, or *mapping probability matrix*, or simply *mapping matrix.*

In general, $\mathbf{P}$ may depend upon n, the time of the mapping step. In this paper we consider, however, only cell mappings whose transition probability matrices are independent of n. These may be appropriately called *stationary cell mappings.*

It is evident that $\zeta_i(n)$ and p_{ij} have the following properties:

$$\zeta_i(n) \geqq 0, \tag{2}$$

$$\sum_{i \in \mathbf{S}} \zeta_i(n) = 1, \tag{3}$$

$$p_{ij} \geqq 0, \tag{4}$$

$$\sum_{i \in \mathbf{S}} p_{ij} = 1. \tag{5}$$

We can now describe the generalized cell mapping by the following evolution equation:

$$\zeta(n + 1) = \mathbf{P}\zeta(n). \tag{6}$$

For a specific evolution we need to have the initial cell probability vector $\zeta(0)$. Once $\zeta(0)$ is given the subsequent evolution is simply given by

$$\zeta(n) = \mathbf{P}^n\zeta(0) \tag{7}$$

Thus one sees that the mapping matrix $\mathbf{P}$ completely controls the whole evolution process. For this reason it is helpful to examine $\mathbf{P}$ more closely. Besides the properties (4) and (5), one notes that there can be no zero columns in $\mathbf{P}$. There can however be zero rows. A zero ith row means that cell i is not accessible from any cell of $\mathbf{S}$; therefore, $\zeta_i(n) = 0$ for $n = 1, 2, \ldots$. For any column, say the jth, the nonzero elements represent the possible image cells of cell j under the mapping. Because of (4) and (5) $\mathbf{P}$ is a so-called non-negative matrix and the largest value any of its elements can take is 1. There are special properties for matrices of this kind; they will be discussed further later.

It is now of interest to examine the simple theory presented in [1, 2] within the framework of the generalized one. It can readily be seen that the simple theory is nothing but a special case of the new one with two special features. One is that the transition probability matrix has only *one* nonzero element in each column and the other is that the cell probability vector has also only *one* nonzero element. These nonzero elements always have the magnitude 1.

3 A Simple Example

Before proceeding further it might be instructive to look at a concrete simple example of such generalized cell mapping systems in order to gain some acquaintance with them. One of the basic purposes of developing the theory of cell mapping is to use it to study the global behavior of nonlinear point mapping systems or systems governed by ordinary differential equations. As an example, let us consider the one-dimensional point mapping

$$\mathbf{G}: \quad x(n + 1) = sx(n)\left\{1 - \frac{x(n)}{4}\right\} \tag{8}$$

and see how a corresponding generalized cell mapping system can be created. The point mapping (8) has been used in the study of population dynamics. It has very complex behavior despite the simple nature of its nonlinearity [3, 4].

For definiteness of discussion let us take the cell size h to be 0.04. Let us further assume that we are only interested in the system behavior when the state variable x remains in the range $-0.02 \leqq x < 4.02$. Following the idea given in [2] we introduce a "*sink cell*," to be labeled number 0, to cover $x < -0.02$ and $x \geqq 4.02$. For the "*regular cells*," [2], covering the range of interest, the labeling of the cells will be as follows. Cell i will cover

$$\left(i - \frac{3}{2}\right) \times 0.04 \leqq x < \left(i - \frac{1}{2}\right) \times 0.04. \tag{9}$$

Thus there will be 101 regular cells covering $(-0.02, 4.02)$. Altogether we will deal with 102 cells labeled $0, 1, 2, \ldots, 101$.

The transition probability matrix for this cell mapping can now be determined in the following manner. First, consider the sink cell, cell #0. Since once the system gets into the sink cell we are no longer interested in the further evolution of the system, the sink cell is assumed to be mapped into itself, i.e., cell #0 is mapped into cell #0 with 100 percent probability. For cell #1 its end points $x = -0.02$ and $x = 0.02$ are mapped by (8) to $x = -0.0201s$ and $x = 0.0199s$. Again, for the sake of definiteness, let us take a specific value of s, say $s = 2.7$. Then the terminal points of cell #1 are mapped into $x = -0.05427$ and $x = 0.05373$. It is seen that this image range of cell #1 covers a part of the sink cell $(-0.05427, -0.02)$, cell #1 itself $(-0.02, 0.02)$, and a part of cell #2 $(0.02, 0.05373)$. Thus cell #1 has three image cells, namely, 0, 1, 2. To apportion the probabilities of mapping among these cells, different schemes may be used. The simplest one, and also the one to be used in this example, is to approximate the mapping in this small interval by a linear one determined by the end points of the cell and to apportion[2] the probabilities according to the percentages of the total image range which are occupied by the image cells. This leads to the following:

$$\text{Cell \#1 to Cell \#0:} \quad p_{0,1} = \frac{-0.02 - (-0.05427)}{0.05373 + 0.05427} = 0.3173$$

$$\text{Cell \#1 to Cell \#1:} \quad p_{1,1} = \frac{0.02 - (-0.02)}{0.05373 + 0.05427} = 0.3704$$

$$\text{Cell \#1 to Cell \#2:} \quad p_{2,1} = \frac{0.05373 - 0.02}{0.05373 + 0.05427} = 0.3123$$

In this manner the image cells of the other regular cells and the corresponding mapping probabilities can be determined, leading to the following matrix $\mathbf{P}$.

[1] In some instances we may elect to label the cells $0, 1, 2, \ldots, N - 1$.

[2] This method of apportioning the probabilities will be referred to in the future as the "*linear interpolation method.*"

$j=$	0	1	2	.	.	50	51	.	.	100	101
$i=0$	1	0.3173	0	.	.	0	0	.	.	0	0.3173
1	0	0.3704	0	.	.	0	0	.	.	0	0.3704
2	0	0.3123	0.0593	.	.	0	0	.	.	0.0593	0.3123
3	0	0	0.3779	.	.	0	0	.	.	0.3779	0
4	0	0	0.3779	.	.	0	0	.	.	0.3779	0
5	0	0	0.1849	.	.	0	0	.	.	0.1849	0
.	.	.	.	.	.	.	.	.	.	.	.
.	.	.	.	.	.	.	.	.	.	.	.
68	0	0	0	.	.	1	1	.	.	0	0
.	.	.	.	.	.	.	.	.	.	.	.
101	0	0	0	.	.	0	0	.	.	0	0

(10)

By this process the point mapping (8) is recast into a generalized cell mapping and the solution of (8) is to be reinterpreted in the form of (7) with **P** given by the previous table.

4 Markov Chains

For a generalized cell mapping the dynamical properties of the system are entirely contained in the transition probability matrix **P**. Our task is therefore to examine **P** and to discover in what manner **P** controls the global behavior. In this connection it is indeed remarkable and fortunate to find that there is already a body of mathematical development which can be used directly for this purpose. This is the *theory of Markov chains*.[3] There are many excellent reference books on this subject; here we cite [5–7]. It is easily seen that mathematically our generalized cell mappings can be identified with Markov chains. In what follows we shall summarize, without citing any proofs, some of the known results of Markov chains which are found useful for our purpose. The summary is provided here because it is believed that this is the first time the theory of Markov chains is being employed in the global analysis of nonlinear oscillation problems and that some of the readers might not be familiar with this subject matter. In order not to complicate the discussion unnecessarily, we restrict the treatment in the remainder of this paper to *finite Markov chains*. The total number of the cells in **S** is now assumed to be finite.

First, let us dispose of a preliminary item of terminology. For Markov chains the state space **S** is a denumerable set of discrete states and one sees in the literature the usage of "from state i to state j." However, in our application of the theory of Markov chains to dynamical systems, we often need refer to certain originating systems for which the state space is a continuum of state. In order not to use the same word "state" in two different contexts in one problem, we shall use the name *cells* as the elements of the space for Markov chains, hence the usage like "from cell i to cell j."

A Dilemma. In reporting and applying the results of Markov chains we do face a serious dilemma with regard to the usage of a key notation. In most of the mathematics books on Markov chains the transition probability p_{ij} is defined as the probability of transition from cell i to cell j, and the cell probability vector is taken to be a row vector $\mathbf{a}(n)$. With this notation a Markov chain is represented by

$$\mathbf{a}(n+1) = \mathbf{a}(n)\mathbf{P}. \tag{11}$$

i.e., a step of evolution is equivalent to a *post multiplication* by **P**. However, in the theory of oscillations one usually takes the state vector to be a column vector, and invariably uses *premultiplication* when applying an operator, leading to a form like (6). To follow that convention it is necessary to define p_{ij} as the probability of mapping from cell j to cell i, as is given in Section 2. We have adopted this notation because this paper is intended to serve in the field of vibration and dynamical systems and, therefore, it is desirable to have a notation consistent with the common usage in that field. The reader is alerted to exchange the roles of the rows and the columns in the transition probability matrix when he compares the results cited in this paper with those given in the mathematical literature of Markov chains.

n-Step Transition Probabilities. The n-step transition probability $p_{ij}^{(n)}$ is defined as the probability of being in cell i after n steps, starting from cell j. It can be shown that $p_{ij}^{(n)}$ is the (i,j)th element of $\mathbf{P}^n$. Evidently, we have

$$p_{ij}^{(m+n)} = \sum_k p_{ik}^{(m)} p_{kj}^{(n)} \tag{12}$$

Here, $p_{ij}^{(0)}$ is taken to be δ_{ij}, the Kronecker symbol. In the theory of Markov chains a matrix having the properties (4) and (5) is called a *stochastic matrix*. One can easily see that if **A** and **B** are two stochastic matrices then **AB** is also one. Hence, all $\mathbf{P}^n$ with non-negative integer power n are stochastic matrices.

Following Chung [5], we say cell j *leads* to cell i, symbolically $j \to i$, if and only if there exists a positive m such that $p_{ij}^{(m)} > 0$. The cells i and j are said to *communicate* if and only if $j \to i$ and $i \to j$; this will be denoted by $i \leftrightarrow j$. The property of communicativeness can be used to divide the cells into disjoint subsets called classes. Two cells belong to the same class if and only if they communicate. A cell which does not communicate with any other cells is said to form a class by itself. The notation $C(i)$ is used to denote the class containing the cell i. We now describe the classification of the cells. Again we rely on [5–7].

Essential and Inessential Cells. A cell that communicates with every cell it leads to is called *essential*; otherwise *inessential*, [5]. It can be shown that an essential cell cannot lead to an inessential cell. The property of being essential or inessential is a class property.

Period. If $i \to i$, the greatest common divisor of the set of positive n such that $p_{ii}^{(n)} > 0$ is called the period of i and denoted by d_i, [5]. For cells which do not lead to themselves the period is not defined. The property of having a period equal to d is a class property, i.e., all the cells in one class have the same period.

Definitions of $f_{ij}^{(n)}$ and f_{ij}^*. Given that the system starts from cell j, the probability that it will be in cell i for the first time at the nth step is denoted by $f_{ij}^{(n)}$. Given that the system starts from cell j, the probability that it will be in cell i at least once is denoted by f_{ij}^*. Evidently,

$$f_{ij}^* = \sum_{n=1}^{\infty} f_{ij}^{(n)}. \tag{13}$$

We also have the following results relating $p_{ij}^{(n)}$ to $f_{ij}^{(n)}$ and f_{ij}^*:

$$p_{ij}^{(n)} = \sum_{k=1}^{n} p_{ii}^{(n-k)} f_{ij}^{(k)} \tag{14}$$

$$f_{ij}^* = \lim_{N\to\infty} \left\{ \sum_{n=1}^{N} p_{ij}^{(n)} \Big/ \sum_{n=0}^{N} p_{ii}^{(n)} \right\} \tag{15}$$

Persistent and Transcient Cells, [6]. A cell i is called *persistent* or *transcient* according as $f_{ii}^* = 1$ or <1. The properties of being essential or inessential and of being persistent and transcient are based upon different notions, but they are related. Thus one can show that an inessential cell is transcient and persistent cells are essential.

Expected Return Time. For a persistent cell j we define its *expected return time* as

[3] The theory of Markov chains is, of course, related to the theory of graphs.

$$\mu_j = \sum_{n=1}^{\infty} n f_{jj}^{(n)} \tag{16}$$

Decomposition Into Groups. As stated before, the property of communicating can be used to divide the cells into groups. All the essential cells can be formed into isolated groups (or classes) $\mathbf{B}_1, \mathbf{B}_2, \ldots, \mathbf{B}_k$ such that the cells in one and the same group communicate but those belonging to different groups do not. These isolated groups will be called *persistent groups*. The inessential cells can also be formed into groups $\mathbf{B}_{k+1}, \mathbf{B}_{k+2}, \ldots, \mathbf{B}_{k+m}$ according to the procedure that the system can go from the group $\mathbf{B}_{k+h}$, $h = 1, 2, \ldots, m$, to one of the groups $\mathbf{B}_1, \mathbf{B}_2, \ldots, \mathbf{B}_{k+h}$, but cannot go to the groups with a higher subscript designation such as $\mathbf{B}_{k+h+1}, \ldots, \mathbf{B}_{k+m}$. These groups composed of inessential cells will be called *transcient groups*. Corresponding to this decomposition into persistent and transcient groups is the possibility of interchanging rows and columns in the transition probability matrix so that it will take the form

$$\mathbf{P} = \begin{bmatrix} \mathbf{P}_1 & \mathbf{0} & . & \mathbf{0} & \mathbf{T}_{1,k+1} & . & \mathbf{T}_{1,k+m} \\ \mathbf{0} & \mathbf{P}_2 & . & \mathbf{0} & \mathbf{T}_{2,k+1} & . & \mathbf{T}_{2,k+m} \\ . & . & . & . & . & . & . \\ \mathbf{0} & \mathbf{0} & . & \mathbf{P}_k & \mathbf{T}_{k,k+1} & . & \mathbf{T}_{k,k+m} \\ \mathbf{0} & \mathbf{0} & . & \mathbf{0} & \mathbf{Q}_{k+1} & . & \mathbf{T}_{k+1,k+m} \\ . & . & . & . & . & . & . \\ \mathbf{0} & \mathbf{0} & . & \mathbf{0} & \mathbf{0} & \mathbf{0} & \mathbf{Q}_{k+m} \end{bmatrix} \tag{17}$$

where $\mathbf{P}_1, \mathbf{P}_2, \ldots, \mathbf{P}_k, \mathbf{Q}_{k+1}, \ldots, \mathbf{Q}_{k+m}$ are square matrices and $\mathbf{T}_{1,k+1}, \ldots, \mathbf{T}_{k+m-1,k+m}$ are, in general, rectangular. Once the system is in a persistent group, say $\mathbf{B}_j$, $j = 1, 2, \ldots, k$, it remains in that group forever. Thus a persistent group $\mathbf{B}_j$ is by itself a Markov chain and its transition probability matrix given by $\mathbf{P}_j$ is a stochastic matrix having the properties (4) and (5). $\mathbf{Q}_{k+j}$, $j = 1, 2, \ldots, m$, is associated with the transcient group $\mathbf{B}_{k+j}$. These are not stochastic matrices because, although they satisfy (4), they satisfy

$$\sum_i q_{ij} \leqq 1 \tag{18}$$

instead of (5). These matrices are sometimes referred to as *substochastic matrices*. The matrices $\mathbf{T}_{ij}$, $i = 1, \ldots, k$; $j = k+1, \ldots, k+m$, describe the manner by which the transcient groups are mapped into the persistent groups. In a similar manner, the matrices $\mathbf{T}_{ij}$, $i = k+1, \ldots, k+m-1$; $j = k+2, \ldots, k+m$, describe the transition from transcient groups to transcient groups of lower subscript designation. These $\mathbf{T}$ matrices will be called *transit matrices*. Sometimes when there is no advantage to have distinct transcient groups $\mathbf{B}_{k+1}, \mathbf{B}_{k+2}, \ldots, \mathbf{B}_{k+m}$, we shall lump them together and call it the transcient group $\mathbf{B}_{k+1}$ with a substochastic matrix $\mathbf{Q}_{k+1}$. In that case the number of transit matrices will be simply k; they will be denoted by $\mathbf{T}_{1,k+1}, \mathbf{T}_{2,k+1}, \ldots, \mathbf{T}_{k,k+1}$. In actual application of Markov chains to the global analysis of nonlinear systems we usually will be dealing with a very large number of cells and there would be no attempt to put the transition probability matrix in the form of (17). However, to describe and to discuss the properties of Markov chains this representation is of immense help. Therefore, for easy reference we shall call (17) the *normal form* of the transition probability matrix. We also note here that the cells within each persistent group communicate; therefore, each persistent group cannot be further decomposed and is sometimes referred to as *irreducible* or *indecomposable*.

If the mapping matrix $\mathbf{P}$ is in its normal form, then the general global behavior of the cell mapping is quite clear. If the system starts in a persistent group $\mathbf{B}_j$, i.e., $\zeta_i(0) = 0$ for $i \notin \mathbf{B}_j$, then the system remains forever in $\mathbf{B}_j$. If the system starts from a transcient group $\mathbf{B}_j$, then the system eventually gets out of that group completely. It will settle into the persistent groups as the evolution proceeds. The final probability distribution of the system among the various persistent groups occupied by the system depends upon the matrices $\mathbf{Q}$'s and $\mathbf{T}$'s and the initial probability vector $\zeta(0)$.

In essence, given $\mathbf{P}$ the global property of a Markov chain is found by studying $\lim p_{ij}^{(n)}$ as $n \to \infty$. The probability distribution $p_{ij}^{(n)}$ among the i cells gives us the long term behavior of the system with cell j as the starting cell. In this connection two simple results are immediate.

Theorem 1, [5]. If i is a transcient cell, then for every j

$$\lim_{n\to\infty} p_{ij}^{(n)} = 0. \tag{19}$$

Theorem 2, [5]. If i and j are two persistent cells but belong to two different persistent groups, then

$$p_{ij}^{(n)} = 0, \quad p_{ji}^{(n)} = 0 \quad \text{for every } n. \tag{20}$$

In the next three sections we examine $\lim p_{ij}^{(n)}$ as $n \to \infty$ for other cases where i is a persistent cell and j is either a persistent or a transcient cell.

5 Absorbing Cells and Acyclic Groups

A cell i for which $p_{ii} = 1$ form a persistent group by itself. It will be called an *absorbing cell.*

Next, we consider persistent groups composed of more than one cell. Each persistent group $\mathbf{B}$ has a period d. In this section we study persistent groups of period 1. These groups will be called *acyclic*[4] *groups* and the cells in these groups *acyclic cells.* Persistent groups of period $d \geqq 2$ will be discussed in the next section; they will be called *periodic groups* and their cells *periodic cells.* As stated in the last section, a persistent group may be taken as a finite Markov chain by itself. We shall state below certain properties of an acyclic group in this context.

Theorem 3, [6]. Let $\mathbf{P}$ be the transition probability matrix for an irreducible persistent acyclic finite Markov chain with a cell space $\mathbf{S}$. Then for each $i \in \mathbf{S}$, $\lim p_{ij}^{(n)}$ as $n \to \infty$ approaches a limit which is independent of j.

Let the limit be called the *limiting probability distribution* and be denoted by p_i. Then it can be shown that

$$p_i = \lim_{n\to\infty} p_{ij}^{(n)} = \frac{1}{\mu_i} > 0 \tag{21}$$

where μ_i is the expected return time for cell i. This most important result can also be discussed from the point of view of eigenvalues and eigenvectors of $\mathbf{P}$. First, let us call an eigenvalue of a matrix the *dominant one* if it is of multiplicity one and it is larger than any other eigenvalue in absolute value.

Theorem 4, [6]. The transition probability matrix $\mathbf{P}$ for an irreducible persistent acyclic finite Markov chain has an eigenvalue equal to 1 and, moreover, this eigenvalue is dominant. The normalized right-eigenvector associated with this eigenvalue is equal to the limiting probability distribution $\mathbf{p} = \{p_i\}$. Thus

$$\mathbf{p} = \mathbf{P}\mathbf{p} \quad \text{or} \quad p_i = \sum_{j=1}^{N} p_{ij} p_j \tag{22}$$

$$p_i > 0 \quad \text{for all } i, \quad \sum_{i=1}^{N} p_i = 1 \tag{23}$$

where the second equation of (23) is the normalization condition.

With these two theorems at hand we can elaborate further the properties of an irreducible acyclic Markov chain. Theorem 3 states that

$$\lim_{n\to\infty} \mathbf{P}^n = \begin{bmatrix} p_1 & p_1 & . & p_1 \\ p_2 & p_2 & . & p_2 \\ . & . & . & . \\ p_N & p_N & . & p_N \end{bmatrix} \tag{24}$$

i.e., the limit of $\mathbf{P}^n$ as $n \to \infty$ is a matrix with identical columns.

[4] In [6] these are called aperiodic groups. However, since we have in mind to apply the theory of Markov chains to dynamical systems we believe it is more desirable to avoid the word aperiodic and adopt the name acyclic as is done in [7].

Moreover, all components are positive. With $\mathbf{P}^n$ possessing this property (7) implies immediately that no matter what is the initial probability vector $\xi(0)$, the probability vector $\xi(n)$ eventually approaches the limiting probability distribution $\mathbf{p}$ as $n \to \infty$. Before concluding this section we mention here another result which is instructive in understanding the persistent groups.

Theorem 5, [6]. The multiplicity of the eigenvalue 1 of the transition probability matrix of a finite Markov chain is equal to the number of the irreducible persistent groups (acyclic and periodic) of the chain.

6 Periodic Persistent Groups

Next, we consider periodic groups. Each periodic group, being a persistent group, may be taken as a Markov chain.

Theorem 6, [5, 6]. Let j be a member of a periodic group $\mathbf{B}$ of period d. Then to every member $i \in \mathbf{B}$ there corresponds a unique residue class r modulo d such that $p_{ij}^{(n)} > 0$ implies that $n = r$ (modulo d).

In other words, the member cells of an irreducible periodic group $\mathbf{B}$ of period d can be divided into d disjointed *subgroups* $\mathbf{B}_1, \mathbf{B}_2, \ldots, \mathbf{B}_d$ such that from $\mathbf{B}_h$, $h = 1, 2, \ldots, d-1$, the system goes to $\mathbf{B}_{h+1}$ and from $\mathbf{B}_d$ it goes back to $\mathbf{B}_1$. Let the number of cells in $\mathbf{B}_h$ be N_h. Then the foregoing result implies that the transition probability matrix for this periodic group may be put in the form

$$\mathbf{P} = \begin{bmatrix} \mathbf{0} & \mathbf{0} & . & \mathbf{0} & \mathbf{P}_{1,d} \\ \mathbf{P}_{2,1} & \mathbf{0} & . & \mathbf{0} & \mathbf{0} \\ \mathbf{0} & \mathbf{P}_{3,2} & . & \mathbf{0} & \mathbf{0} \\ . & . & . & . & . \\ \mathbf{0} & \mathbf{0} & . & \mathbf{P}_{d,d-1} & \mathbf{0} \end{bmatrix} \tag{25}$$

where all the diagonal block matrices are zero square matrices, $\mathbf{P}_{2,1}$ a matrix of order $N_2 \times N_1$, $\mathbf{P}_{3,2}$ a matrix of order $N_3 \times N_2 \ldots$, and $\mathbf{P}_{1,d}$ of order $N_1 \times N_d$.

This cyclic behavior means that $\mathbf{R} = \mathbf{P}^d$ (with components r_{ij}) maps each subgroup into itself. Therefore, $\mathbf{R}$ is the transition probability matrix of a Markov chain for which the subgroups $\mathbf{B}_1, \mathbf{B}_2, \ldots, \mathbf{B}_d$ become now d irreducible acyclic groups. Based upon this one can show the following.

Theorem 7, [6]. Let $\mathbf{P}$ be the transition probability matrix of an irreducible periodic persistent Markov chain with period d. Let $\mathbf{R} = \mathbf{P}^d$. Then

$$\lim_{n\to\infty} r_{ij}^{(n)} = \frac{d}{\mu_i} \quad \text{if } i \text{ and } j \text{ belong to the same subgroup } \mathbf{B}_h, \tag{26}$$

$$\lim_{n\to\infty} r_{ij}^{(n)} = 0 \quad \text{otherwise.} \tag{27}$$

where μ_i is expected return time for cell i using $\mathbf{P}$.

A slightly more general result which is also useful for our purpose is the following. Let $\mathbf{C}_r(j)$ be the residue class r discussed in Theorem 6.

Theorem 8, [5]. If i is a persistent cell with period d and expected return time μ_i and if j belongs to the same irreducible persistent group as i so that $i \in \mathbf{C}_r(j)$, then

$$\lim_{n\to\infty} p_{ij}^{(nd+r)} = \frac{d}{\mu_i} \tag{28}$$

and

$$p_{ij}^{(n)} = 0 \quad \text{if} \quad n \neq r \text{ (modulo } d). \tag{29}$$

We note here that for an irreducible periodic Markov chain, unlike for the acyclic groups, $\lim p_{ij}^{(n)}$ as $n \to \infty$ does not converge. It converges only along a properly chosen subsequence. This leads to consider the limit of the Cesaro average of $p_{ij}^{(n)}$, [5, 6].

Theorem 9, [5]. Let $\mathbf{P}$ be the transition probability matrix of an irreducible persistent finite Markov chain. Then

$$\lim_{n\to\infty} \frac{1}{n} \sum_{k=1}^{n} p_{ij}^{(k)} = \frac{1}{\mu_i} \tag{30}$$

The properties of periodic groups are also intimately governed by the eigenvalues of $\mathbf{P}$. We cite here the following two theorems.

Theorem 10, [6]. The dth roots of unity are eigenvalues of the transition probability matrix of an irreducible periodic Markov chain. Moreover, each of these eigenvalues is of multiplicity one and there are no other eigenvalues of modulus one.

Theorem 11, [6]. Let $\mathbf{P}$ be the transition probability matrix of a Markov chain. Then any eigenvalue of $\mathbf{P}$ of modulus 1 is a root of unity. The dth root of unity are eigenvalues of $\mathbf{P}$ if and only if $\mathbf{P}$ has a persistent group of period d. The multiplicity of each collection of dth roots of unity is the number of persistent groups of period d.

7 Evolution From Transcient Cells

In the last two sections we have seen how to evaluate $\lim p_{ij}^{(n)}$ as $n \to \infty$ when i and j are persistent cells. In this section we examine the case where j is a transcient cell. Before doing so, it is however helpful to introduce some new quantities. Let the period of cell i be d. For every integer r, $f_{ij}^*(r)$ is defined as, [5],

$$f_{ij}^*(r) = \sum_{\substack{n=1 \\ n\equiv r(\mathrm{mod}\ d)}}^{\infty} f_{ij}^{(n)} \tag{31}$$

Evidently, one has

$$\sum_{r=1}^{d} f_{ij}^*(r) = f_{ij}^*. \tag{32}$$

Theorem 12, [5]. If i is a persistent cell with period d_i and expected return time μ_i and if j is a transcient cell, then for every r

$$\lim_{n\to\infty} p_{ij}^{(nd_i+r)} = f_{ij}^*(r)\frac{d_i}{\mu_i} \tag{33}$$

where

$$f_{ij}^*(r) \geqq 0 \quad \text{and} \quad \sum_{r=1}^{d_i} f_{ij}^*(r) \leqq 1. \tag{34}$$

Again, instead of using a subsequence of $p_{ij}^{(n)}$, we can consider the Cesaro limit of the full sequence and in fact obtain a general result.

Theorem 13, [5]. The Cesaro limit

$$\lim_{n\to\infty} \frac{1}{n} \sum_{k=1}^{n} p_{ij}^{(k)} = \pi_{ij} \tag{35}$$

exists for every i and j and

$$\pi_{ij} = \frac{f_{ij}^*}{\mu_i} \tag{36}$$

provided that we define $\mu_i = \infty$ in case cell i is transcient.

One may also study the evolution from a transcient cell by making use of the transit matrix $\mathbf{T}$ and the matrix $\mathbf{Q}$ in the following normal form of the transition probability matrix $\mathbf{P}$.

$$\mathbf{P} = \begin{bmatrix} \mathbf{P}_1 & \mathbf{0} & . & \mathbf{0} & \\ \mathbf{0} & \mathbf{P}_2 & . & \mathbf{0} & \\ . & . & . & . & \begin{bmatrix}\mathbf{T}\end{bmatrix} \\ \mathbf{0} & \mathbf{0} & . & \mathbf{P}_k & \\ \mathbf{0} & \mathbf{0} & . & \mathbf{0} & \mathbf{Q} \end{bmatrix} \tag{37}$$

Theorem 14, [6]. Let $\mathbf{N} = (\mathbf{I} - \mathbf{Q})^{-1}$. Then the sum of the elements of the jth column of $\mathbf{N}$ gives the *expected adsorption time* of the jth transcient cell to be absorbed into the persistent groups.

Theorem 15, [6]. Let $\mathbf{N} = (\mathbf{I} - \mathbf{Q})^{-1}$. Then the (i, j)th element of $\mathbf{TN}$ is the probability of being absorbed into the persistent cell i from the transcient cell j.

As a matter of notation, we denote by ν_j the *expected absorption time* of a transcient cell j being absorbed into the persistent groups. The *absorption probability* from a transcient cell j into a persistent cell i will be denoted by α_{ij}.

8 Analysis of Simple Examples

We are now ready to apply the theory of Markov chains to the generalized cell mapping. In this paper we present only the studies

of mappings involving very small numbers of cells so that the ideas and the results of the evolution of the systems can be perceived directly and easily without the aid of a computer. Our main purpose is to demonstrate the use of Markov chains as tools for global analysis of our cell mapping systems. Five problems will be analyzed using the same point mapping system (8). The range of interest of the state variable x is taken to be from -0.2 to 4.2. Eleven regular cells, labeled 1 to 11, will be used; the cell size is therefore 0.4. The 0th cell is the sink cell covering $x < -0.2$ and $x \geqq 4.2$. In the five problems the parameter s will be varied, but all the generalized cell mappings will be created by using the *linear interpolation method.*

Problem 1. We take $s = 2.5$. The transition probability matrix of the mapping is easily found and it will have an appearance similar to (10) except with only 12 cells. This matrix **P** can be put in a normal form as shown by the table (38) below where all the unfilled elements below the diagonal are zero. One readily finds that besides the obvious absorbing cell at cell 0, cell 7 is also an absorbing cell. These two are the only persistent cells. The remaining 10 cells are all transcient. Starting from any of the transcient cells the system moves eventually toward one or both of the absorbing cells 0 and 7. Using Theorem 15, one can find all the absorbing probabilities α_{ij}:

Normal form of **P**:

Row cell #	Column Cell Number 0	7	6	5	4	3	2	1	11	10	9	8
0	1	0	0	0	0	0	0	0.325	0.325	0	0	0
7		1	1	1	0.188	0	0	0	0	0	0	0.188
6			0	0	0.812	0.125	0	0	0	0	0.125	0.812
5				0	0	0.667	0	0	0	0	0.667	0
4					0	0.208	0.344	0	0	0.344	0.208	0
3						0	0.500	0	0	0.500	0	0
2							0.156	0.275	0.275	0.156	0	0
1								0.400	0.400	0	0	0
11									0	0	0	0
10										0	0	0
9											0	0
8												0

(38)

α_{ij}	$j = 1$	2	3	4	5	6	8	9	10	11
$i = 0$	0.542	0	0	0	0	0	0	0	0	0.542
7	0.458	1	1	1	1	1	1	1	1	0.458

(39)

These values indicate that starting from any of the transcient cells 2, 3, 4, 5, 6, 8, 9, 10 the system moves eventually to cell 7. Starting from cell 1 or 11 the system will eventually go to the sink cell 0 with a probability 0.542 and to cell 7 with a probability 0.458. One can also use Theorem 14 to compute the expected absorption times ν_j for each transcient cell j.

$j =$	1	2	3	4	5	6	8	9	10	11
$\nu_j =$	3.137	3.208	2.169	1.812	1	1	1.812	2.169	3.208	3.137

(40)

The interpretation of ν_1 and ν_{11} are not immediate because cells 1 and 11 are absorbed into two different absorbing cells. The meaning of the other ν_j's is simple; for example, the expected (or mean) absorption time from cell 2 into cell 7 is 3.208 steps.

Next, we may try to see how these results from this cell mapping reflect the properties of the point mapping (8) with $s = 2.5$.

(*i*). Equation (8) is known to have an asymptotically stable $P - 1$ point[5] at $x^* = 2.4$ which is located in cell 7. Thus an asymptotically stable $P - 1$ point of the point mapping is replaced now for the cell mapping by an absorbing cell.

(*ii*). For equation (8) all points in the range $0 < x < 4$ are known to converge eventually to the $P - 1$ point at $x^* = 2.4$. Here we find correspondingly that all cells 2–6, 8–10 are absorbed into cell 7. Concerning the absorption time, consider cell 2. According to (8), of all the points on the segment (0.2, 0.6) occupied by cell 2 those in the lower 16.24 percent part take 4 steps to get into cell 7 while those in the upper 83.76 percent take only 3 steps, resulting in an average of 3.162 steps. The present cell mapping gives $\nu_2 = 3.208$, only 1.5 percent off despite the coarse cells used.

(*iii*). Cell 1 occupies $(-0.2, 0.2)$. According to (8), half of the points in this range will move to $x^* = 2.4$ while the other half toward $x = -\infty$, which is in the sink cell. Here the cell mapping calculation gives $\alpha_{0,1} = 0.542$ and $\alpha_{7,1} = 0.458$. The deviations of these values from 0.5 and 0.5 as required by the point mapping can be shown to be due to the large cell size used here.

Problem 2. For this problem we take $s = 2.95$. The mapping matrix **P** can again be put in a normal form as shown in (41). Here we find that cell 0 is an absorbing cell as it should be. Cells 7 and 8 now form an acyclic persistent group and the limiting probability distribution is given by

$$p_7 = 0.451, \quad p_8 = 0.549. \tag{42}$$

Normal form of **P**:

Row cell number	Column Cell Number 0	7	8	Transcient cells
0	1	0	0	
7	0	0	0.821	**T**
8	0	1	0.179	
Transcient cells	**0**	**0**	**0**	**Q**

(41)

The other cells are all transcient cells. Their absorption probabilities and expected absorption times are as follows:

[5] For this terminology the reader is referred to [1 or 4].

α_{ij}	$j=1$	2	3	4	5	6	9	10	11
$i=0$	0.539	0	0	0	0	0	0	0	0.539
7	0.171	0.371	0.018	0.821	0	0	0.018	0.371	0.171
8	0.290	0.629	0.982	0.179	1	1	0.982	0.629	0.290

(43)

$j=$	1	2	3	4	5	6	9	10	11
$\nu_j=$	2.657	2.478	1.982	1	1	1	1.982	2.478	2.657

(44)

Again let us compare the result with those of the point mapping analysis. (8) has an asymptotically stable $P-1$ point at $x^* = 2.644$. This point is located in cell 8 covering (2.6, 3.0) but it is also very near to cell 7 covering (2.2, 2.6). Thus the asymptotically stable $P-1$ point for the point mapping is replaced for the cell mapping by an acyclic group.[6] As a matter of fact, the limiting probability distribution for this group as given by (42) is a very good reflection of the location of x^* in the combined range of cells 7 and 8. Of all the transcient cells, cells 1 and 11 are eventually absorbed into the sink cell and the acyclic group, but all the other transcient cells are absorbed only into the acyclic group.

$$\begin{bmatrix} p_5 \\ p_6 \\ p_7 \\ p_9 \end{bmatrix} = \begin{bmatrix} 0.148 \\ 0.505 \\ 0.347 \\ 0 \end{bmatrix} \quad \text{for even steps.} \tag{46}$$

(*Cont.*)

For the case starting from cell 9 the *limiting* behavior is again given by (46) except that the conditions of odd steps and even steps should be exchanged. The cells 1–4, 8, 10, 11 are transcient. Their absorption probabilities and expected absorption times are as follows:

α_{ij}	$j=1$	2	3	4	8	10	11
$i=0$	0.535	0	0	0	0	0	0.535
5	0.144	0.320	0.148	0	0	0.320	0.144
6	0.093	0.178	0.505	0	0	0.178	0.093
7	0.225	0.494	0.347	0.979	0.979	0.494	0.225
9	0.003	0.008	0	0.121	0.021	0.008	0.003

(47)

$j=$	1	2	3	4	8	10	11
$\nu_j=$	2.734	2.919	1	4.132	4.132	2.919	2.734

(48)

Problem 3. Here we take $s = 3.3$. The normal form of **P** is given by

Row cell number	Column Cell Number 0	5	6	7	9	Transcient cells
0	1	0	0	0	0	
5	0	0	0	0	0.148	
6	0	0	0	0	0.505	**T**
7	0	0	0	0	0.347	
9	0	1	1	1	0	
Transcient cells	**0**	**0**	**0**	**0**	**0**	**Q**

(45)

Besides the sink cell as a persistent group of a single cell, there is a periodic persistent group of period 2 composed of cells 5, 6, 7, and 9. The *limiting* behavior of the system starting from cell 5, 6 or 7, or any combination of them is as follows:

$$\begin{bmatrix} p_5 \\ p_6 \\ p_7 \\ p_9 \end{bmatrix} = \begin{bmatrix} 0 \\ 0 \\ 0 \\ 1 \end{bmatrix} \quad \text{for odd steps,} \tag{46}$$

Having α_{ij} of (47) and the "limiting" probability distribution of (46) at our disposal, the long term probability distribution of the system among the persistent cells can be ascertained easily if the starting transcient cell is known.

With $s = 3.3$ the point mapping (8) has an asymptotically stable $P-2$ solution consisting of $x^*(1) = 1.918$ and $x^*(2) = 3.294$, which are located in cells 6 and 9, respectively. Thus an asymptotically stable $P-2$ solution of the point mapping is replaced by a periodic persistent group of period 2 for the cell mapping. Globally for the point mapping every point in $0 < x < 4$ is eventually mapped into the $P-2$ solution. For the cell mapping we have the same general result. The transcient cells 2–4, 8 and 10 are mapped eventually to the periodic group while cells 1 and 11 are mapped into the sink cell 0 and the periodic persistent group.

Problem 4. In this problem we take again $s = 3.3$ as in Problem 3, but in creating the generalized cell mapping we use $\mathbf{G}^2$, instead of simply **G** of the mapping (8). The matrix **P** can be put in the following form:

Row cell number	Column Cell Number 0	6	9	Transcient cells
0	1	0	0	
6	0	1	0	**T**
9	0	0	1	
Transcient cells	**0**	**0**	**0**	**Q**

(49)

Here, we find three absorbing cells 0, 6, and 9. All the other cells are transcient. Their absorption probabilities and expected absorption times are as follows:

[6] Here, the reader may wish to refer to the discussion on pseudo periodic cells given in [1].

α_{ij}	$j=1$	2	3	4	5	7	8	10	11
$i=0$	0.617	0	0	0	0	0	0	0	0.617
6	0.211	0.727	0	0.533	1	1	0.533	0.727	0.211
9	0.172	0.273	1	0.467	0	0	0.467	0.273	0.172

(50)

$j=$	1	2	3	4	5	7	8	10	11
$\nu_j=$	2.035	2.720	1	3.813	2.203	2.203	3.813	2.720	2.035

(51)

For the point mapping the $P-2$ points for **G** are, of course, $P-1$ points for $\mathbf{G}^2$. Thus it is interesting and satisfying to see that the cells in which the two $P-2$ points of **G** lie become two absorbing cells of the cell mapping generated by using $\mathbf{G}^2$. The α_{ij} and ν_j data from Problems 3 and 4 cannot be compared against each other because the data in Problem 4 ignore the history of evolution (or location of the system in the cell space **S**) at all the odd number steps.

Problem 5. Here we take $s = 3.58$. The normal form of **P** is given by

Column Cell Number

Row cell number	0	3	4	5	6	7	8	9	10	Transcient cells
0	1	0	0	0	0	0	0	0	0	
3	0	0	0	0	0	0	0	0	0.279	
4	0	0	0	0	0	0	0	0	0.349	
5	0	0	0	0	0	0	0	0	0.349	
6	0	0.436	0	0	0	0	0	0.436	0.023	**T**
7	0	0.466	0	0	0	0	0	0.466	0	
8	0	0.098	0.550	0	0	0	0.550	0.098	0	
9	0	0	0.450	0.497	0	0.497	0.450	0	0	
10	0	0	0	0.503	1	0.503	0	0	0	
Transcient cells	**0**	**0**	**0**	**0**	**0**	**0**	**0**	**0**	**0**	**Q**

(52)

In this case we find that beside the sink cell as a persistent group of a single cell, there is a *huge* acyclic persistent group consisting of cells from #3 to #10. These cells cover the range $0.6 \leqq x < 3.8$, which is 80 percent of the important range $0 \leqq x < 4$. This acyclic persistent group has the following limiting probability distribution:

$i=$	3	4	5	6	7	8	9	10
$p_i=$	0.060	0.074	0.074	0.116	0.119	0.147	0.196	0.214

(53)

There are only 3 transcient cells, #1, #2, and #11. Their absorption probabilities and expected absorption times are as follows:

α_{ij}	$j=1$	2	11
$i=0$	0.534	0	0.534
3	0.187	0.279	0.187
4	0.135	0.349	0.135
5	0.135	0.349	0.135
6	0.009	0.023	0.009
7	0	0	0
8	0	0	0
9	0	0	0
10	0	0	0

(54)

$j=$	1	2	11
$\nu_n=$	1.774	1	1.774

(55)

Again let us compare the results of this *crude* cell mapping approximation with those of the point mapping analysis. According to [3], with $s = 3.58$ the system (8) seems to have a "chaotic" behavior. Corresponding to that, we have here a very large acyclic persistent group. Interestingly, this generalized cell mapping technique gives readily the limiting probability distribution of the group which indicates, on a long term basis, the probability by which the system occupies a particular cell in that acyclic persistent group. This kind of information seems to be difficult to obtain otherwise.

9 Global Properties of Generalized Cell Mappings

In this section, we discuss the manner by which the global properties of generalized cell mappings can best be described. We also discuss the relations between the properties of point mappings and the cell mappings derived from them. Let $\mathbf{B}_h$ be a persistent group and j any cell in **S**. We denote by $\alpha(\mathbf{B}_h, j)$ the *group absorption probability* of j into $\mathbf{B}_h$. Evidently, if j does not lead to any member of $\mathbf{B}_h$, $\alpha(\mathbf{B}_h, j) = 0$. If j is a member of $\mathbf{B}_h$, $\alpha(\mathbf{B}_h, j) = 1$. We also have

$$\alpha(\mathbf{B}_h, j) = \sum_{i \in \mathbf{B}_h} \alpha_{ij} \tag{56}$$

For each persistent group $\mathbf{B}_h$ we can define its *domain of attraction*, $\mathbf{D}_h$, as the set of all cell j such that $\alpha(\mathbf{B}_h, j) > 0$. If there are k persistent groups then there will be k domains of attraction, $\mathbf{D}_h$, $h = 1, 2, \ldots, k$. However, we must note here that since a transcient cell may eventually be absorbed into several persistent groups, it may belong to several domains of attraction. In other words, the domains of attraction may not be disjointed. For this reason the concept of domains of attraction may not be as useful for cell mappings as in the classical study of nonlinear oscillations. It is our current thinking that for cell mappings it is more sensible simply to use the *group absorption probability* distribution $\alpha(\mathbf{B}_h, j)$, $h = 1, 2, \ldots, k$ and j all transcient cells, to *describe* the global behavior of the system. For a given starting cell, j, $\alpha(\mathbf{B}_h, j)$, $h = 1, 2, \ldots, k$, give the absorption probability distribution of the system among the persistent groups. We have, of course,

$$\sum_{h=1}^{k} \alpha(\mathbf{B}_h, j) = 1 \tag{57}$$

This paper being introductory in nature for the generalized cell mappings, we are not in a position to offer here a set of rigorous and general mathematical results relating the behavior of a point mapping to the behavior of the derived cell mapping. Nevertheless, we could make some plausible general inferences. One might expect the following when the cells are sufficiently small:

1 An asymptotically stable $P-1$ point of the point mapping will, in general, be replaced by an absorbing cell containing that point or replaced by an acyclic group of persistent cells in the neighborhood of that $P-1$ point.

2 An asymptotically stable $P-K$ solution of the point mapping will, in general, be replaced by a periodic group of persistent cells of period K for the cell mapping. These periodic cells either contain or are in the neighborhoods of the $P-K$ points of that $P-K$ solution.

3 Let L, k, and K be positive integers such that $L = kK$. Let $\mathbf{G}$ denote the point mapping. Let the cell mapping be created by using $\mathbf{G}^k$. Then, an asymptotically stable $P-L$ solution for the point mapping $\mathbf{G}$ will, in general, be replaced by k periodic groups of persistent cells of period K. If the period K has the value of 1, then the groups are either absorbing cells or acyclic groups.

4 In general, an unstable $P-K$ solution for the point mapping will not have its counterpart in the cell mapping. Because of the diffusive nature of the evolution of the probability distribution near the $P-K$ points of that solution, all the cells containing these $P-K$ points can be expected to become transcient cells.

5 For a point mapping system which seems to have a "chaotic" motion covering a part of the state space, the corresponding generalized cell mapping is likely to have a large persistent group covering the same part of the space. Depending upon the nature of the chaotic motion, the persistent group could be acyclic or periodic.

6 For a point mapping the domains of attraction for its asymptotically stable periodic solutions are disjointed. However, they can intertwine around each other in a very fine and complicated way. Consider a cell j. If several domains of attraction of the point mapping traverse this cell j, then for the derived cell mapping the system, starting from cell j, is likely to be absorbed into the corresponding periodic groups. The absorption probability distribution among these groups is likely to reflect the extents by which the cell j is covered by these various traversing domains of attraction. Here lies the attractiveness of the cell mapping approach. By using $\alpha(\mathbf{B}_k, j)$ to describe the global behavior, one obliviates the need to search for ever finer structure of the global behavior of the point mapping in a seemingly never ending process.

7 When using a derived cell mapping to ascertain the properties of a point mapping, the accuracy can be expected to increase with smaller cell sizes and with the use of higher-order interpolation formulas in computing the transition probability matrix.

10 Concluding Remarks

In the paper we have presented the basic ideas of a generalized theory of cell mappings. In the development the theory of Markov chains is used as the basic tool of analysis. Our main aim is to use this generalized theory of cell mapping to study the global behavior of nonlinear systems governed by point mappings or by ordinary differential equations. For that purpose we envision to employ a huge number of cells and the methods used to analyze the problems in Section 8 will no longer be viable. More effective algorithms akin to that presented in [2] will be needed. That topic is, however, outside the scope of this introductory paper.

Acknowledgment

This material is based upon work supported by the National Science Foundation under Grant No. CME-8019274.

References

1 Hsu, C. S., "A Theory of Cell-to-Cell Mapping Dynamical Systems," ASME JOURNAL OF APPLIED MECHANICS, Vol. 47, 1980, pp. 931–939.

2 Hsu, C. S., and Guttalu, R. S., "An Unravelling Algorithm for Global Analysis of Dynamical Systems: An Application of Cell-to-Cell Mappings," ASME JOURNAL OF APPLIED MECHANICS, Vol. 47, 1980, pp. 940–948.

3 May, R. M., "Biological Populations With Nonoverlapping Generations: Stable Points, Stable Cycles, and Chaos," *Science*, Vol. 186, 1974, pp. 645–647.

4 Hsu, C. S., and Yee, H. C., "Behavior of Dynamical Systems Governed by A Simple Nonlinear Difference Equation," ASME JOURNAL OF APPLIED MECHANICS, Vol. 42, 1975, pp. 870–876.

5 Chung, K. L., *Markov Chains With Stationary Transition Probabilities*, 2nd ed., Springer-Verlag, New York, 1967.

6 Isaacson, D. L., and Madsen, R. W., *Markov Chains: Theory and Applications*, Wiley, New York, 1976.

7 Romanovsky, V. I., *Discrete Markov Chains*, Wolters-Noordhoff Publishing, Groningen, The Netherlands, 1970.

Journal of Applied Mechanics

Design Data and Methods

Buckling of Polar Orthotropic Annular Plates Under Uniform Inplane Compressive Forces

G. K. Ramaiah[1]

The problem of buckling of polar orthotropic annular plates under various types of inplane compressive forces along the radial edges has been analyzed in detail by the Rayleigh-Ritz method for eight different combinations of clamped, simply supported, and free boundary conditions. Accurate estimates of critical buckling loads have been obtained for various values of hole ratios and for various values of rigidity ratios. The numerical results are presented in the form of data sheets for direct use by the design engineers.

Nomenclature

a, b = radii of inner and outer edges, respectively

C, S, F = clamped, simply supported, and free edge conditions, respectively

$D = Eh^3/12(1 - \nu^2)$

$D_r = E_r h^3/12(1 - \nu_r \nu_\theta)$

$D_\theta = E_\theta h^3/12(1 - \nu_r \nu_\theta)$

$D_{r\theta} = Gh^3/12$

$D_1 = \nu_\theta D_r = \nu_r D_\theta$

E_r, E_θ = Young's moduli in radial and tangential directions, respectively

G = shear modulus

h = thickness of plate

$k = (E_\theta/E_r)^{1/2} = (D_\theta/D_r)^{1/2}$

n = number of nodal diameters

p_i, p_0 = uniform inplane radial forces along the inner and outer edges, respectively

r, θ = polar coordinates of a point in midplane of the plate

T = potential energy due to inplane forces during bending

u_i, v_i = admissible functions

V = strain energy due to bending

$W(r, \theta)$ = lateral displacement

ν_r, ν_θ = Poisson's ratio in radial and tangential directions, respectively

$\sigma_r, \sigma_\theta, \sigma_{r\theta}$ = prebuckling membrane stresses

Introduction

In reference [1], Mansfield considered the buckling of an isotropic infinite plate supported along two concentric circles and subjected to an uniform radial compression or radial tension along the inner circle. He ingeneously interpreted these solutions for a finite isotropic annular plate—in which radial and hoop stresses vary inversely as the square of the distance from the center—with a member of requisite tensile stiffness supporting the outer circle. The class of problems considered by Mansfield [1] is unusual in the sense that exact solutions are available in terms of elementary functions despite the fact that the stresses are varying throughout the plate. It is difficult to obtain such exact solutions in a general case of loading conditions along the radial edges and the problem becomes even more complicated if the analysis is to be carried out for polar orthotropic annular plates. Such an analysis is of much practical utility and it assumes added significance due to recent developments in composites [2].

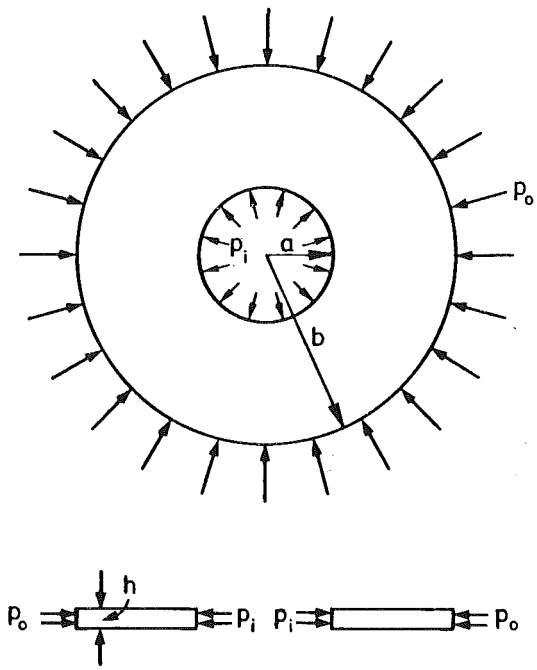

Fig. 1 Annular plate under uniform compressive forces

In the present paper, the problem of buckling of polar orthotropic annular plates under various types of inplane compressive forces along the inner and/or outer edges has been analyzed in detail by the Rayleigh-Ritz method with simple polynomials as admissible functions. Accurate estimates of critical buckling loads have been obtained for various values of hole ratios, for various values of rigidity ratios and for different combinations of clamped, simply supported and free

[1] Institut für Mechanik, Technische Hochschule Darmstadt, D-6100 Darmstadt, West Germany.

Manuscript received by ASME Applied Mechanics Division, November, 1980; final revision, March, 1981.

boundary conditions. Some numerical investigations have also been carried out to study the influence of Poisson's ratio ($=\nu_\theta$) on the critical buckling loads of the plate under internal compression. The entire numerical results are presented neatly in the form of data sheets for direct use by the design engineers.

Mathematical Analysis

A thin annular plate of uniform thickness h subjected to uniform inplane compressive forces p_i and p_0 along the inner and outer edges of radii a and b, respectively, is considered (see Fig. 1). The material of the plate is assumed to be homogeneous and polar orthotropic. The prebuckling membrane stresses in such a plate are given by [3]

$$\left.\begin{aligned} \sigma_r &= Ar^{k-1} + Br^{-k-1} \\ \sigma_\theta &= k(Ar^{k-1} - Br^{-k-1}) \end{aligned}\right\} \quad \text{and} \quad \left.\begin{aligned} \\ \sigma_{r\theta} &= 0 \end{aligned}\right\} \tag{1}$$

in which $k = (D_\theta/D_r)^{1/2}$ and A and B are constants to be determined from the stress conditions along the inner and outer edges. These constants are

$$\left.\begin{aligned} A &= -\frac{p_0 b^{k+1} - p_i a^{k+1}}{b^{2k} - a^{2k}} \\ B &= \frac{(p_0 a^{k-1} - p_i b^{k-1})\,(ab)^{k+1}}{b^{2k} - a^{2k}} \end{aligned}\right\} \tag{2}$$

It is assumed that the plate buckles in n circumferential waves and the lateral deflection $W(r, \theta)$ is expressed as

$$W(r, \theta) = W_n(r) \cos(n\theta + \epsilon) \tag{3}$$

Within the limitations of small deflection thin plate theory, the expressions for the strain energy V of bending and the potential T due to midplane forces during bending are given by

$$V = \frac{\pi}{2}(1 + \delta_{0n}) \int_a^b \left[D_r \left(\frac{d^2W_n}{dr^2}\right)^2 + 2\frac{D_1}{r}\frac{d^2W_n}{dr^2}\left(\frac{dW_n}{dr} - \frac{n^2}{r}W_n\right) + \frac{D_\theta}{r^2}\left(\frac{dW_n}{dr} - \frac{n^2}{r}W_n\right)^2 + 4D_{r\theta}\frac{n^2}{r^2}\left(\frac{dW_n}{dr} - \frac{W_n}{r}\right)^2 \right] r\,dr \tag{4}$$

$$T = \frac{\pi}{2}(1 + \delta_{0n})h \left[\int_a^b \left\{ \sigma_r \left(\frac{dW_n}{dr}\right)^2 + \sigma_\theta \left(\frac{n}{r}W_n\right)^2 \right\} r\,dr \right] \tag{5}$$

in which $\delta_{00} = 1$ and $\delta_{0n} = 0$ for $n \neq 0$ and other symbols are as defined earlier in the list of symbols.

In order to apply the Rayleigh-Ritz method, the mode shape $W_n(r)$ in radial direction is expressed as

$$W_n(r) = \sum_{i=1}^{\infty} A_i v_i(r) \tag{6}$$

in which $v_i(r)$ are chosen admissible functions satisfying the relevant geometric boundary conditions such that they are linearly independent and form a complete set. $A_i (i = 1, 2, 3, \ldots)$ are linear parameters to be determined from the stationary condition $\delta(V + T) = 0$ for arbitrary variations of these parameters. This process leads to a set of homogeneous, linear, algebraic equations in the A_i's. For nontrivial solutions of this set of equations, one derives the necessary characteristic equations for the determination of eigenloads.

For large values of a/b and in particular when both the edges are clamped, the direct application of the Rayleigh-Ritz method with large number of simple polynomials as admissible functions has been found [4, 5] to lead to an ill-conditioned set of equations and round-off errors predominate in the numerical work. To overcome this difficulty in the computational work, the energy integrals V and T have been expressed in more convenient forms by using in succession the transformations proposed and effectively utilized earlier in references [4, 5]. Upon obtaining the modified expressions for V and T, the mode shape $w(y)$ is assumed as $w(y) = \Sigma_{i=1}^{\infty} B_i u_i(y)$ in which $u_i(y)$ are chosen admissible functions. The Rayleigh-Ritz method as described earlier is applied to obtain the characteristic equations for the accurate determination of eigenloads. It may be mentioned here that the analysis modified by using the transformation $n \geq 2$ also yields accurate estimates for $n = 0$ and $n = 1$ for large values of hole ratios.

Table 1 Admissible functions, $W_n(r) = v_0(r)(A_1 + A_2 r + A_3 r^2 + \ldots)$; $w(y) = u_0(y)(B_1 + B_2 y + B_3 y^2 + \ldots)$

Boundary condition		Designation	$v_0(r)$	$u_0(y)$
Outer	Inner			
Free	Simply supported	FS	(r-a)	y
Simply supported	Free	SF	(b-r)	(1-y)
Free	Clamped	FC	$(r-a)^2$	y^2
Clamped	Free	CF	$(b-r)^2$	$(1-y)^2$
Simply supported	Simply supported	SS	(b-r)(r-a)	y(1-y)
Simply supported	Clamped	SC	$(b-r)(r-a)^2$	$y^2(1-y)$
Clamped	Simply supported	CS	$(b-r)^2(r-a)$	$y(1-y)^2$
Clamped	Clamped	CC	$(b-r)^2(r-a)^2$	$y^2(1-y)^2$

Note: w is related to the mode W_n through the transformations given earlier.

n	First transformation	Second transformation
0	$W(r) = w(r)$	$y = (r^2 - a^2)/(b^2 - a^2)$
1	$W_1(r) = r\,w\,(r)$	$y = (r - a)/(b - a)$
≥ 2	$W_n(r) = r^2 w(r)$	$y = (r - a)/(b - a)$

Numerical Results and Conclusions

Admissible functions $v_i(r)$ in the direct analysis and $u_i(y)$ in the modified analysis were chosen to be simple least-order polynomials in r and y, respectively (see Table 1). Direct analysis was used for $a/b \leq 0.5$ and modified analysis for $a/b > 0.5$ by taking five terms in the Rayleigh-Ritz method. The Poisson's ratio ν_θ and the parameter $D_{r\theta}/D_r$ were fixed at 0.3 and 0.35, respectively. The parameter a/b was varied from 0.1 to 0.9 in steps of 0.1 for values of D_θ/D_r equal to 0.5, 0.8, 1.0, 1.25, 2.0, and 5.0. All computations were carried out with double precision arithmetic (about 16 significant digits) on an IBM 370/168 digital computer available at THD.

It is to be noted that T is a function of two parameters p_0 and p_i. By assuming a particular value for p_0 or p_i or p_0/p_i, T becomes a function of a single parameter. In the present investigations, the following cases of loading have been considered:

(*i*) $p_i = 0$.
(*ii*) $p_0 = p_i = p$.
(*iii*) $p_0 b^2 = p_i a^2$.
(*iv*) $p_0 = 0$.

The estimates of critical buckling load parameter (defined appropriately in the table heading) together with the corresponding number of circumferential waves ($= n$) in the critical buckling mode are presented in Tables 2–5. The numerical results are presented in such a way that they are complete and are self-explanatory.

In view of the earlier experience [4, 5] with regard to convergence and accuracy of solutions by the present method of analysis, the numerical results reported here are believed to be quite accurate. The accuracy of critical buckling loads [4, 5] in the isotropic case has recently been established by several investigators [6–9] using different techniques. The present estimates of critical buckling loads for isotropic plates are found to agree very well with the corresponding exact values reported by Yamaki [10] in the $p_0 = p_i = p$ case and by Mansfield [1] in the $p_0 b^2 = p_i a^2$ case. To further assess the accuracy

Table 2 Estimates of critical buckling load parameter ($= p_0 b^2 h/D_r$) of polar orthotropic annular plates under uniform compressive forces along the outer edge ($p_i = 0$); $\nu_\theta = 0.3$, $D_\theta/D_r = 0.35$

a/b	Values of D_θ/D_r						Values of D_θ/D_r					
	0.5	0.8	1.0	1.25	2.0	5.0	0.5	0.8	1.0	1.25	2.0	5.0
	(1) SF case:						(2) FS case:					
0.1	2.082	3.277	3.983	4.832	7.148	15.52	1.035	1.184	1.273	1.403	1.757	3.107
	(0)	(0)	(0)	(0)	(0)	(0)	(1)	(1)	(1)	(1)	(1)	(1)
0.2	1.668	2.611	3.335	4.415	6.865	15.47	1.279	1.480	1.608	1.777	2.264	4.147
	(0)	(0)	(0)	(0)	(0)	(0)	(1)	(1)	(1)	(1)	(1)	(1)
0.3	1.412	2.433	3.105	3.938	6.362	15.22	1.412	1.743	1.904	2.108	2.713	4.222
	(0)	(0)	(0)	(0)	(0)	(0)	(0)	(1)	(1)	(1)	(1)	(2)
0.4	1.242	2.154	2.763	3.524	5.798	14.61	1.242	2.006	2.196	2.435	3.152	4.263
	(0)	(0)	(0)	(0)	(0)	(0)	(0)	(1)	(1)	(1)	(1)	(2)
0.5	1.121	1.947	2.500	3.193	5.283	13.69	1.121	1.947	2.500	2.777	3.602	4.515
	(0)	(0)	(0)	(0)	(0)	(0)	(0)	(0)	(0)	(1)	(1)	(2)
0.6	1.031	1.790	2.297	2.934	4.854	12.67	1.031	1.790	2.297	2.934	4.062	5.214
	(0)	(0)	(0)	(0)	(0)	(0)	(0)	(0)	(0)	(0)	(1)	(2)
0.7	0.961	1.666	2.138	2.728	4.507	11.72	0.961	1.666	2.138	2.728	4.507	6.658
	(0)	(0)	(0)	(0)	(0)	(0)	(0)	(0)	(0)	(0)	(0)	(2)
0.8	0.905	1.568	2.010	2.564	4.226	10.93	0.905	1.568	2.010	2.564	4.228	9.239
	(0)	(0)	(0)	(0)	(0)	(0)	(0)	(0)	(0)	(0)	(0)	(2)
0.9	0.859	1.487	1.906	2.430	4.003	10.31	0.859	1.487	1.906	2.430	4.003	10.31
	(0)	(0)	(0)	(0)	(0)	(0)	(0)	(0)	(0)	(0)	(0)	(0)
	(3) CF case:						(4) FC case:					
0.1	8.238	11.77	13.95	16.58	23.81	49.29	2.003	2.149	2.231	2.366	2.722	4.127
	(0)	(0)	(0)	(0)	(0)	(0)	(1)	(1)	(1)	(1)	(1)	(1)
0.2	8.671	11.70	13.60	15.99	23.06	49.05	3.111	3.302	3.373	3.470	3.712	4.385
	(0)	(0)	(0)	(0)	(0)	(0)	(1)	(2)	(2)	(2)	(2)	(2)
0.3	11.08	13.39	14.96	16.96	23.13	48.30	4.406	4.446	4.472	4.570	4.693	4.942
	(0)	(0)	(0)	(0)	(0)	(0)	(2)	(2)	(2)	(2)	(2)	(2)
0.4	13.26	17.22	18.55	20.25	25.50	48.09	6.349	6.349	6.348	6.349	6.357	6.425
	(0)	(0)	(0)	(0)	(0)	(0)	(2)	(2)	(2)	(2)	(2)	(2)
0.5	22.86	24.59	25.76	27.23	31.77	51.31	9.601	9.599	9.598	9.597	9.596	9.621
	(0)	(0)	(0)	(0)	(0)	(0)	(2)	(2)	(2)	(2)	(2)	(2)
0.6	28.35	31.56	33.51	35.37	41.03	60.74	14.79	14.90	14.98	15.07	15.33	16.15
	(3)	(3)	(2)	(2)	(2)	(1)	(3)	(3)	(3)	(3)	(3)	(2)
0.7	36.87	41.36	43.69	46.46	53.94	77.34	23.77	24.77	25.10	25.35	26.10	26.70
	(5)	(5)	(4)	(4)	(3)	(2)	(5)	(5)	(4)	(4)	(4)	(3)
0.8	54.03	60.72	64.70	68.71	79.40	111.6	41.74	44.79	46.35	47.65	50.46	54.97
	(9)	(8)	(7)	(7)	(6)	(5)	(9)	(8)	(7)	(7)	(6)	(5)
0.9	106.1	119.8	127.5	136.0	157.2	216.8	94.67	104.9	110.2	115.8	128.6	156.4
	(21)	(18)	(17)	(16)	(14)	(11)	(21)	(18)	(17)	(16)	(14)	(11)

Table 2 Continued

(5) SC case:

0.1	19.88 (0)	21.44 (1)	22.14 (1)	23.29 (1)	26.18 (1)	36.62 (1)
0.2	27.77 (1)	28.99 (1)	29.77 (1)	30.76 (1)	33.60 (1)	44.13 (1)
0.3	38.19 (2)	39.32 (2)	40.07 (2)	41.02 (2)	43.82 (2)	54.77 (2)
0.4	51.48 (3)	53.26 (3)	54.44 (3)	55.91 (3)	58.62 (2)	68.33 (2)
0.5	68.30 (5)	72.47 (4)	74.14 (4)	76.21 (4)	81.01 (3)	94.10 (3)
0.6	92.36 (8)	99.39 (7)	103.0 (6)	106.9 (6)	115.2 (5)	134.7 (3)
0.7	130.7 (12)	143.1 (10)	149.9 (10)	156.5 (9)	172.6 (8)	208.4 (6)
0.8	205.6 (20)	228.2 (17)	240.5 (16)	253.8 (15)	285.4 (13)	361.1 (10)
0.9	427.7 (43)	480.1 (38)	509.1 (36)	541.0 (34)	619.0 (30)	822.1 (23)

(6) CS case:

0.1	31.39 (1)	34.90 (1)	37.17 (1)	39.99 (1)	48.06 (1)	77.25 (1)
0.2	39.88 (2)	43.16 (2)	45.34 (2)	48.08 (2)	56.06 (2)	86.33 (2)
0.3	49.77 (3)	53.97 (2)	55.73 (2)	57.94 (2)	64.60 (2)	91.22 (2)
0.4	61.64 (4)	67.36 (3)	69.62 (3)	72.43 (3)	80.95 (3)	107.2 (2)
0.5	77.62 (6)	84.55 (5)	88.78 (5)	92.99 (4)	103.2 (4)	133.0 (3)
0.6	100.4 (8)	111.9 (8)	116.4 (7)	122.3 (6)	137.6 (5)	176.2 (4)
0.7	137.9 (12)	153.3 (11)	161.5 (10)	170.9 (9)	192.9 (8)	251.0 (6)
0.8	212.1 (20)	237.4 (18)	251.4 (17)	266.7 (16)	304.1 (14)	402.6 (11)
0.9	433.7 (44)	488.4 (39)	518.9 (36)	552.6 (34)	636.2 (30)	860.2 (24)

(7) SS case:

0.1	14.16 (0)	16.87 (0)	18.05 (1)	19.18 (1)	22.34 (1)	33.53 (1)
0.2	18.27 (0)	20.23 (0)	21.52 (0)	22.74 (1)	25.65 (1)	37.37 (1)
0.3	25.34 (0)	26.91 (0)	27.77 (1)	28.75 (1)	31.67 (1)	42.99 (1)
0.4	36.06 (2)	37.21 (2)	37.98 (2)	38.94 (2)	41.73 (1)	52.55 (1)
0.5	49.55 (3)	51.19 (3)	52.29 (3)	53.66 (3)	56.31 (2)	66.23 (2)
0.6	68.24 (5)	71.75 (5)	73.71 (4)	75.46 (4)	80.71 (4)	93.26 (3)
0.7	97.64 (9)	104.3 (8)	108.0 (7)	112.0 (7)	120.9 (6)	143.0 (4)
0.8	154.9 (15)	168.1 (13)	175.4 (12)	183.1 (12)	201.7 (10)	247.3 (8)
0.9	324.3 (34)	356.2 (30)	373.9 (28)	393.5 (27)	441.5 (23)	566.5 (18)

(8) CC case:

0.1	38.71 (2)	42.25 (2)	44.53 (2)	47.42 (2)	55.74 (2)	84.30 (1)
0.2	50.19 (3)	53.83 (2)	55.69 (2)	58.01 (2)	64.89 (2)	91.68 (2)
0.3	62.39 (4)	67.71 (3)	70.25 (3)	73.41 (3)	82.86 (3)	107.8 (2)
0.4	77.48 (5)	83.53 (5)	87.11 (4)	93.17 (4)	105.1 (3)	134.2 (3)
0.5	97.39 (7)	108.2 (6)	113.8 (6)	120.7 (6)	134.7 (5)	173.3 (4)
0.6	126.2 (10)	141.6 (9)	150.0 (8)	158.8 (8)	180.2 (7)	233.4 (5)
0.7	173.3 (15)	196.1 (13)	208.7 (12)	222.3 (12)	254.7 (10)	337.0 (8)
0.8	266.6 (24)	303.9 (22)	324.4 (20)	346.9 (19)	402.0 (17)	544.7 (13)
0.9	544.6 (53)	624.7 (44)	669.2 (44)	718.7 (42)	840.8 (37)	1168 (29)

Notes:
1 Value in ( ) denotes the number of circumferential waves (=n) in the critical buckling mode.
2 Vijayakumar and Joga Rao [11] have reported data for orthotropic plates but only for axisymmetric modes ($n = 0$) and that too for $a/b = 0.5$ only.
3 Uthgenannt and Brand [12] have reported some numerical results for the axisymmetric modes ($n = 0$) in the two cases of SF and CF.
4 When $D_\theta/D_r = 1.0$, the value for $a/b = 0.1$ in the SC case should read 22.24 and for $a/b = 0.3$ in the SS case should read 27.77.

Table 3 Estimates of critical buckling load parameter ($= pb^2h/D_r$) of polar orthotropic annular plates under uniform equal compressive forces along inner and outer edges ($p_o = p_i = p$); $\nu_\theta = 0.3$, $D_{r\theta}/D_r = 0.35$

a/b	Values of D_θ/D_r						Values of D_θ/D_r					
	0.5	0.8	1.0	1.25	2.0	5.0	0.5	0.8	1.0	1.25	2.0	5.0
	(1) SF case:						(2) FS case:					
0.1	2.007 (0)	3.199 (0)	3.918 (0)	4.762 (0)	7.094 (0)	15.50 (0)	1.029 (1)	1.179 (1)	1.277 (1)	1.397 (1)	1.751 (1)	3.101 (1)
0.2	1.484 (0)	2.352 (0)	3.249 (0)	4.102 (0)	6.344 (0)	15.26 (0)	1.248 (1)	1.446 (1)	1.578 (1)	1.740 (1)	2.223 (1)	4.097 (1)
0.3	1.151 (0)	2.016 (0)	2.601 (0)	3.338 (0)	5.575 (0)	14.38 (0)	1.151 (0)	1.644 (1)	1.800 (1)	1.995 (1)	2.580 (1)	4.323 (2)
0.4	0.931 (0)	1.632 (0)	2.109 (0)	2.713 (0)	4.581 (0)	12.59 (0)	0.931 (0)	1.632 (0)	1.970 (1)	2.188 (1)	2.848 (1)	4.456 (2)
0.5	0.777 (0)	1.358 (0)	1.751 (0)	2.248 (0)	3.781 (0)	10.44 (0)	0.777 (0)	1.358 (0)	1.751 (0)	2.248 (0)	3.037 (1)	4.762 (2)
0.6	0.664 (0)	1.156 (0)	1.487 (0)	1.905 (0)	3.180 (0)	8.601 (0)	0.664 (0)	1.156 (0)	1.487 (0)	1.905 (0)	3.163 (1)	5.357 (2)
0.7	0.578 (0)	1.003 (0)	1.288 (0)	1.646 (0)	2.731 (0)	7.222 (0)	0.578 (0)	1.003 (0)	1.288 (0)	1.646 (0)	2.731 (0)	6.293 (1)
0.8	0.510 (0)	0.884 (0)	1.134 (0)	1.446 (0)	2.389 (0)	6.215 (0)	0.510 (0)	0.884 (0)	1.134 (0)	1.446 (0)	2.389 (0)	6.215 (0)
0.9	0.455 (0)	0.788 (0)	1.010 (0)	1.288 (0)	2.122 (0)	5.471 (0)	0.455 (0)	0.788 (0)	1.010 (0)	1.288 (0)	2.122 (0)	5.471 (0)
	(3) CF case:						(4) FC case:					
0.1	7.513 (0)	10.96 (0)	13.17 (0)	15.83 (0)	23.22 (0)	49.07 (0)	1.995 (1)	2.142 (1)	2.238 (1)	2.359 (1)	2.716 (1)	4.123 (1)
0.2	6.868 (0)	9.259 (0)	10.91 (0)	13.04 (0)	19.71 (0)	46.61 (0)	3.061 (1)	3.257 (1)	3.387 (1)	3.550 (1)	3.985 (2)	4.414 (2)
0.3	7.403 (0)	9.030 (0)	10.16 (0)	11.62 (0)	16.33 (0)	38.81 (0)	4.411 (1)	4.647 (1)	4.799 (2)	4.718 (2)	4.779 (2)	5.038 (2)
0.4	8.893 (0)	10.06 (0)	10.89 (0)	11.93 (0)	15.21 (0)	30.73 (0)	6.337 (1)	6.604 (1)	6.760 (2)	6.701 (2)	6.669 (2)	6.631 (2)
0.5	11.77 (0)	12.68 (0)	13.29 (0)	14.07 (0)	16.49 (0)	27.29 (0)	9.263 (0)	9.687 (1)	9.883 (1)	10.03 (2)	9.999 (2)	9.935 (2)
0.6	17.33 (0)	18.05 (0)	18.54 (0)	19.15 (0)	21.01 (0)	28.98 (0)	14.60 (0)	15.07 (0)	15.39 (0)	15.68 (1)	16.03 (2)	16.31 (2)
0.7	29.52 (0)	30.11 (0)	30.51 (0)	31.00 (0)	32.50 (0)	38.69 (0)	26.24 (0)	26.69 (0)	26.98 (0)	27.35 (0)	28.35 (1)	29.45 (2)
0.8	64.36 (0)	64.85 (0)	65.18 (0)	65.59 (0)	66.83 (0)	71.85 (0)	59.84 (0)	60.25 (0)	60.52 (0)	60.86 (0)	61.90 (0)	64.79 (2)
0.9	251.3 (0)	251.7 (0)	252.0 (0)	252.4 (0)	253.4 (0)	257.6 (0)	242.9 (0)	243.3 (0)	243.5 (0)	243.8 (0)	244.8 (0)	248.7 (0)

Table 3 Continued

	(5) SC case:						(6) CS case:					
0.1	19.29 (0)	21.19 (1)	22.04 (1)	23.07 (1)	26.00 (1)	36.52 (1)	29.75 (0)	33.61 (1)	35.90 (1)	38.72 (1)	46.86 (1)	76.32 (1)
0.2	25.98 (0)	27.64 (0)	28.69 (1)	29.69 (1)	32.61 (1)	43.37 (1)	35.58 (0)	39.37 (0)	41.40 (1)	43.85 (1)	51.20 (1)	80.24 (1)
0.3	35.55 (0)	36.96 (0)	37.89 (0)	39.06 (0)	41.86 (1)	52.62 (1)	45.33 (0)	48.01 (0)	49.82 (0)	52.11 (0)	58.25 (1)	83.39 (1)
0.4	50.16 (0)	51.39 (0)	52.21 (0)	53.24 (0)	56.10 (1)	66.55 (1)	60.62 (0)	62.65 (0)	64.02 (0)	65.74 (0)	70.97 (0)	91.54 (1)
0.5	74.31 (0)	75.41 (0)	76.14 (0)	77.06 (0)	79.81 (0)	89.82 (1)	85.97 (0)	87.58 (0)	88.66 (0)	90.02 (0)	94.12 (0)	111.0 (0)
0.6	116.8 (0)	117.8 (0)	120.5 (0)	121.3 (0)	123.8 (0)	133.3 (1)	132.4 (0)	133.8 (0)	134.7 (0)	135.8 (0)	139.1 (0)	152.6 (0)
0.7	215.3 (0)	216.2 (0)	216.8 (0)	217.6 (0)	219.8 (0)	228.9 (0)	232.4 (0)	233.5 (0)	234.2 (0)	235.2 (0)	237.9 (0)	249.1 (0)
0.8	492.2 (0)	493.1 (0)	493.6 (0)	494.3 (0)	496.4 (0)	504.7 (0)	516.4 (0)	517.4 (0)	518.0 (0)	518.8 (0)	521.1 (0)	530.6 (0)
0.9	1996 (0)	1997 (0)	1997 (0)	1998 (0)	2000 (0)	2007 (0)	2042 (0)	2042 (0)	2043 (0)	2044 (0)	2046 (0)	2054 (0)
	(7) SS case:						(8) CC case:					
0.1	13.28 (0)	15.98 (0)	17.70 (0)	18.88 (1)	22.08 (1)	33.36 (1)	39.27 (2)	42.80 (1)	45.05 (1)	47.79 (1)	55.62 (1)	83.76 (1)
0.2	15.77 (0)	17.62 (0)	18.84 (0)	20.37 (0)	24.48 (1)	36.14 (1)	51.43 (2)	54.36 (2)	56.29 (2)	58.69 (2)	65.76 (2)	92.84 (2)
0.3	20.26 (0)	21.63 (0)	22.56 (0)	23.71 (0)	27.22 (0)	39.23 (1)	69.32 (3)	72.88 (2)	74.60 (2)	76.74 (2)	83.10 (2)	107.9 (2)
0.4	27.44 (0)	28.53 (0)	29.26 (0)	30.16 (0)	32.97 (0)	44.32 (1)	96.55 (4)	99.86 (3)	102.0 (3)	104.7 (3)	111.5 (2)	134.7 (2)
0.5	39.47 (0)	40.37 (0)	40.97 (0)	41.73 (0)	44.02 (0)	53.45 (0)	140.3 (5)	145.0 (4)	147.4 (4)	150.4 (3)	157.0 (3)	181.1 (2)
0.6	61.65 (0)	62.42 (0)	62.93 (0)	63.58 (0)	65.51 (0)	73.41 (0)	220.7 (6)	227.8 (5)	231.0 (5)	234.8 (4)	242.5 (5)	265.6 (3)
0.7	109.6 (0)	110.3 (0)	110.7 (0)	111.3 (0)	113.0 (0)	119.7 (0)	394.0 (9)	406.4 (7)	411.4 (7)	416.5 (6)	427.1 (5)	453.0 (4)
0.8	246.7 (0)	247.3 (0)	247.7 (0)	248.2 (0)	249.6 (0)	255.5 (0)	889.2 (15)	915.3 (12)	926.5 (11)	936.7 (10)	955.9 (8)	990.7 (5)
0.9	986.9 (0)	987.5 (0)	987.8 (0)	988.2 (0)	989.5 (0)	994.8 (0)	3561 (31)	3665 (25)	3708 (23)	3746 (21)	3813 (17)	3904 (11)

Notes:

1 Value in ( ) denotes number of circumferential waves (= n) in the critical buckling mode.

2 Yamaki [10] has reported values of $(\rho b^2 h/D)^{1/2}$ for isotropic plates in all these cases.

3 Vijayakumar and Joga Rao [11] have reported data for orthotropic plates but only for the axisymmetric modes ($n = 0$) and that too for $a/b = 0.5$ only.

4 Uthgenannt and Brand [12] have also reported some numerical results for the axisymmetric modes in the four cases of SF, CF, SS and CC.

Table 4 Estimates of critical buckling load parameter ($= p_1 a^2 h/D_r$) of polar orthotropic annular plates. Loading condition $p_0 b^2 = p_1 a^2$ (radial compression): $\nu_\theta = 0.3$, $D_{r\theta}/D_r = 0.35$

a/b	Values of D_θ/D_r						Values of D_θ/D_r					
	0.5	0.8	1.0	1.25	2.0	3.0	0.5	0.8	1.0	1.25	2.0	3.0
	(1) SF case:						(2) FS case:					
0.1	0.348	0.669	0.910	1.246	2.424	8.268	0.348	0.669	0.880*	0.985*	1.301*	2.574*
0.2	0.374	0.685	0.910	1.210	2.229	7.650	0.374	0.685	0.910	1.134*	1.514*	3.093*
0.3	0.388	0.695	0.910	1.191	2.109	6.796	0.388	0.695	0.910	1.191	1.690*	3.346*
0.4	0.396	0.701	0.910	1.179	2.032	6.115	0.396	0.701	0.910	1.179	1.862*	3.803*
0.5	0.402	0.704	0.910	1.171	1.983	5.639	0.402	0.704	0.910	1.171	1.983	4.116*
0.6	0.406	0.707	0.910	1.166	1.950	5.320	0.406	0.707	0.910	1.166	1.950	4.484*
0.7	0.408	0.708	0.910	1.163	1.930	5.114	0.408	0.708	0.910	1.163	1.930	4.811*
0.8	0.409	0.709	0.910	1.161	1.918	4.991	0.409	0.709	0.910	1.161	1.918	4.991
0.9	0.410	0.710	0.910	1.160	1.912	4.928	0.410	0.710	0.910	1.160	1.912	4.928
	(3) CF case:						(4) FC case:					
0.1	0.577	0.915	1.165	1.501	2.650	8.284	0.935	1.374	1.689 (1) 1.693 (0)	1.826 (1) 2.414 (0)	2.291 (1) 3.798 (0)	3.751 (1) 13.32 (0)
0.2	0.959	1.299	1.541	1.858	2.906	8.147	1.598	2.001	2.291	2.667 (1) 2.678 (0)	3.153 (1) 3.993 (0)	5.121 (1) 5.225 (2)
0.3	1.585	1.928	2.165	2.472	3.457	8.212	2.499	2.892	3.166	3.522	4.298 (1) 4.678 (0)	6.197 (2) 6.587 (1)
0.4	2.664	3.010	3.246	3.548	4.493	8.839	3.910	4.295	4.558	4.896	5.937 (1) 5.960 (0)	7.913 (2) 8.456 (1)
0.5	4.647	4.996	5.232	5.531	6.453	10.50	6.330	6.709	6.966	7.291	8.296	10.97 (2) 11.27 (1)
0.6	8.656	9.007	9.244	9.541	10.45	14.29	10.97	11.34	11.59	11.91	12.88	16.29 (1) 16.56 (2)
0.7	16.08	16.44	16.66	16.97	19.67	23.58	21.42	21.79	22.04	22.35	23.29	27.14 (1) 27.17 (0)
0.8	47.23	47.59	47.83	48.13	49.02	52.66	52.39	52.96	53.21	53.51	54.43	58.17 (0)
0.9	216.9	217.3	217.5	217.8	218.7	222.3	228.3	228.7	228.9	229.2	230.1	233.8

Table 4 Continued

(5) SC case:

0.1	3.899	4.633	5.185	5.864	8.191	20.19
0.2	8.496	9.302	9.852	10.55	12.75	22.75
0.3	15.45	16.27	16.82	17.52	19.66	28.85
0.4	26.65	27.46	28.00	28.69	30.77	39.43
0.5	46.09	46.89	47.42	48.09	50.12	58.39
0.6	83.56	84.36	84.89	85.54	87.51	95.47
0.7	168.4	169.2	169.7	170.3	172.2	179.9
0.8	422.0	422.8	423.3	423.9	425.8	433.3
0.9	1656	1656	1657	1658	1659	1667

(6) CS case:

1.938	2.352	2.640	3.012	4.199	9.619
4.842	5.313	5.632	6.038	7.293	12.74
9.890	10.41	10.76	11.20	12.53	18.15
18.77	19.33	19.71	20.18	21.60	27.45
35.18	35.77	36.17	36.67	38.17	44.28
68.32	68.95	69.37	69.89	71.47	77.81
146.1	141.8	147.2	147.8	149.4	156.0
386.0	386.7	387.2	387.7	389.4	396.2
1779	1780	1780	1781	1783	1789

(7) SS case:

0.1	1.350	1.731	2.001	2.353	3.496	8.874
0.2	3.066	3.476	3.757	4.118	5.254	10.40
0.3	5.915	6.345	6.637	7.006	8.148	13.13
0.4	10.76	11.21	11.51	11.88	13.04	17.91
0.5	19.48	19.94	20.24	20.63	21.79	26.60
0.6	36.72	37.18	37.50	37.86	39.05	43.82
0.7	76.45	76.92	77.23	77.62	78.80	83.54
0.8	197.1	197.5	197.8	198.2	199.4	204.1
0.9	887.9	888.4	888.7	889.1	890.3	895.0

(8) CC case:

5.434	6.356	7.001	7.832	10.51	23.61
12.74	13.83	14.57	15.51	18.42	31.25
24.44	25.63	26.43	27.44	30.52	43.56
44.04	45.29	46.13	47.19	50.38	63.60
79.07	80.37	81.23	82.32	85.60	98.96
148.1	149.4	150.3	151.4	154.8	168.2
307.1	308.4	309.3	310.5	313.8	327.4
789.6	791.0	791.9	793.0	796.4	810.0
3553	3554	3555	3557	3560	3574

Notes:
1 Value in ( ) denotes the number of circumferential waves (= n) in the critical buckling mode; when no value is given, $n = 0$ corresponds to critical buckling mode.
2 * $n = 1$ corresponds to the critical buckling mode.
3 The corresponding data in the isotropic case have been reported by Mansfield [1] in all cases except in the two cases of SC and CS.
4 Axisymmetric ($n = 0$) eigenloads in SF and FS cases are identical and in the isotropic case $(p_i a^2 h/D) = (1 - \nu^2)$ for all hole sizes [1]. For $a/b \to 1$, the axisymmetric buckling load for the orthotropic plates in these two cases can be approximately calculated from $(p_i a^2 h/D_r) \simeq (D_\theta/D_r) - \nu_\theta^2$.

for orthotropic plates, the present estimates of critical buckling loads are compared with the corresponding estimates reported by Elishakoff and Charmats [6] and are found to agree very well.

It can be seen from the data in Tables 2–5 that for all values of compressive force p_0/p_i, hole ratios a/b and rigidity ratios D_θ/D_r the axisymmetric mode always corresponds to the critical buckling mode in the SF case. This behavior is also exhibited by the data in the CF case for a/b less than about 0.5. In the remaining cases, the plate buckles first either axisymmetrically or asymmetrically depending upon the value of p_0/p_i, a/b, D_θ/D_r and the boundary conditions. The number of circumferential waves (=n) in the critical buckling mode increases with increasing values of p_0/p_i, a/b as well as increasing order of geometric constraints at the edges. With regard to the influence of D_θ/D_r, it is to be noted first that there is a limitation on the variation of D_θ/D_r. For structural materials satisfying volume criterion, analysis for $\nu_\theta > D_\theta/D_r$ has no physical validity or physical significance [4, 11]. In the physical valid range of D_θ/D_r it is found that an increase in the value of D_θ/D_r generally leads to a decrease in the number of circumferential waves (=n) in the critical buckling mode in all cases except in the two cases of FS and FC (and that too up to certain values of a/b).

In Table 6, some additional data on tensile critical buckling load in the $p_0 b^2 = p_i a^2$ (radial tension) case of loading are presented in the four cases of SC, CS, SS, and CC. The corresponding estimates for isotropic plates were earlier obtained by Mansfield [1] in the two cases of SS and CC. It is found from these data and the data in the other four cases (not reported here) that the axisymmetric mode never corresponds to the critical buckling mode for plates under radial tension. On the other hand, the axisymmetric mode always corresponds to the critical buckling mode for plates under internal compression ($p_0 = 0$) because the hoop stress is tensile all along the radial line. In a general case of compressive loading condition, it can be shown that the hoop stress

$$\sigma_\theta = k\left(-\frac{p_0 b^{k+1} - p_i a^{k+1}}{b^{2k} - a^{2k}} r^{k-1} - \frac{p_0 a^{k-1} - p_i b^{k-1}}{b^{2k} - a^{2k}} (ab)^{k+1} r^{-k-1}\right)$$

is tensile everywhere if

$$p_0/p_i \ge 2\left(\frac{a}{b}\right)^{k+1}\left(\frac{b^{2k}}{b^{2k} + a^{2k}}\right).$$

Hence, for load ratios satisfying this condition one would expect the plate to buckle first axisymmetrically for all boundary conditions. The present extensive numerical investigations confirm, in general, the validity of the foregoing restriction for all boundary conditions except in the two cases of FS and FC. In these two cases for $p_0 b^2 = p_i a^2$ loading, the mode with one nodal diameter corresponds to the critical buckling mode for small hole sizes even in the isotropic case ($k = 1$, see Table 4). This behavior is not exhibited in the results reported by Mansfield [1]. It may, however, be mentioned here that there exists a corresponding behavior in the free flexural vibrations problem (unloaded plate) in the sense that the mode with one nodal diameter corresponds to the fundamental mode of vibration for hole ratios less than about 0.3 in these two cases of FS and FC.

In order to understand the plate behavior properly, it is useful to have the information on the influence of ν_θ on the critical buckling load. For this purpose, estimates of $p_i a^2 h/D_r$ for plates under internal compression have been obtained for $\nu_\theta = 0.2$, 0.3, and 0.4 and $D_\theta/D_r = 0.5$, 1.0, and 2.0 (see Table 7). It is interesting to observe from this data that a decrease in ν_θ increases the value of the critical buckling load for isotropic as well as orthotropic plates in all cases except in the two cases of inner edge clamped and the outer edge either simply supported or free. In the CC case, ν_θ has no influence on the value of $p_i a^2 h/D_r$ but as D_r contains ν_θ, the buckling load depends on ν_θ.

In the context of the present work, it is pertinent to mention the recent handbook of structural stability [13] brought out by the Column Research Committee of Japan. This work contains an excellent

Table 5 Estimates of critical buckling load parameter ($= p_l a^2 h/D_r$) of polar orthotropic annular plates under uniform inplane compressive forces along the inner edge ($p_0 = 0$), $\nu_\theta = 0.3$, $D_{r\theta}/D_r = 0.35$

a/b	Value of D_θ/D_r						Value of D_θ/D_r					
	0.5	0.8	1.0	1.25	2.0	5.0	0.5	0.8	1.0	1.25	2.0	5.0
	(1) SF case:						(2) FS case:					
0.1	0.397	0.758	1.028	1.393	2.622	8.347	Axisymmetric eigenloads are					
0.2	0.465	0.849	1.124	1.486	2.678	8.307	identical in SF and FS cases.					
0.3	0.522	0.932	1.218	1.587	2.771	8.270						
0.4	0.574	1.011	1.309	1.691	2.888	8.270						
0.5	0.621	1.085	1.399	1.797	3.024	8.342						
0.6	0.665	1.157	1.488	1.904	3.172	8.498						
0.7	0.706	1.226	1.574	2.010	3.328	8.735						
0.8	0.746	1.293	1.658	2.115	3.490	9.044						
0.9	0.784	1.357	1.740	2.218	3.654	9.411						
	(3) CF case:						(4) FC case:					
0.1	0.608	0.961	1.219	1.565	2.732	8.332	1.301	1.910	2.385	3.057	5.568	21.18
0.2	1.055	1.423	1.683	2.022	3.127	8.441	2.548	3.233	3.732	4.403	6.724	19.64
0.3	1.812	2.196	2.461	2.801	3.882	8.898	4.527	5.282	5.813	6.508	8.795	20.63
0.4	3.137	3.557	3.829	4.175	5.251	10.05	7.896	8.717	9.282	10.01	12.32	23.43
0.5	5.694	6.110	6.390	6.744	7.829	12.49	14.06	14.95	15.55	16.31	18.69	29.39
0.6	10.94	11.37	11.66	12.02	13.13	17.72	26.53	27.48	28.12	28.92	31.39	41.96
0.7	23.55	23.99	24.29	24.66	25.76	30.36	55.96	56.97	57.66	58.50	61.07	71.74
0.8	63.23	63.69	63.99	64.37	65.53	70.17	147.4	148.5	149.2	150.1	152.8	163.7
0.9	298.1	298.6	298.9	299.3	300.5	305.2	682.9	684.0	684.8	685.7	688.5	699.9
	(5) SC case:						(6) CS case:					
0.1	4.548	5.449	6.086	6.922	9.684	24.09	2.024	2.449	2.745	3.125	4.333	9.799
0.2	11.20	12.31	13.06	14.03	17.06	30.73	5.281	5.776	6.111	6.536	7.842	13.44
0.3	22.76	24.04	24.90	25.99	29.34	43.80	11.26	11.82	12.19	12.66	14.08	19.97
0.4	43.39	44.82	45.77	46.97	50.63	65.96	22.29	22.90	23.31	23.83	25.37	31.65
0.5	82.31	83.86	84.90	86.20	90.14	106.3	43.52	44.18	44.63	45.18	46.85	53.56
0.6	162.6	164.3	165.4	166.8	171.0	188.1	87.93	88.64	89.12	89.71	91.50	98.65
0.7	354.9	356.6	357.8	359.3	363.7	381.6	195.4	196.1	196.6	197.2	199.1	206.7
0.8	958.4	960.3	961.6	963.1	967.8	986.8	535.4	536.2	536.7	537.4	539.4	547.4
0.9	4518	4520	4522	4523	4528	4548	2556	2557	2557	2558	2560	2568
	(7) SS case:						(8) CC case:					
0.1	1.446	1.852	2.137	2.508	3.706	9.225	5.980	6.985	7.680	8.578	11.44	25.16
0.2	3.522	3.984	4.301	4.706	5.971	11.58	15.19	16.45	17.31	18.40	21.73	36.01
0.3	7.277	7.792	8.140	8.580	9.932	15.72	31.29	32.77	33.76	35.00	38.77	54.39
0.4	14.16	14.73	15.10	15.58	17.03	23.07	60.26	61.90	63.00	64.38	68.53	85.45
0.5	27.37	27.98	28.39	28.90	30.46	36.81	115.1	116.9	118.1	119.6	124.1	142.3
0.6	54.95	55.61	56.05	56.60	58.26	64.96	228.8	230.7	231.9	233.6	238.5	257.9
0.7	121.6	122.3	122.8	123.3	125.1	132.2	500.9	503.9	504.3	506.1	511.2	531.6
0.8	332.3	333.0	333.5	334.1	336.0	343.4	1357	1359	1359	1362	1367	1389
0.9	1583	1584	1585	1585	1587	1595	6413	6415	6416	6418	6424	6447

Notes:
1 $n = 0$ always corresponds to the critical buckling mode.
2 Strzelczyk and Wojciech [7] have also reported quite extensive data.

compilation of pertinent literature together with numerical results for various types of isotropic and orthotropic plates.

Acknowledgments

The author is grateful to the Alexander von Humboldt Foundation for the award of an AvH Fellowship during the course of this work. The help provided by Prof. Dr. W. Schnell in arranging this fellowship is gratefully acknowledged. The author is also thankful to the reviewer for his comments and suggestions.

References

1 Mansfield, E. H., "On the Buckling of an Annular Plate," *Quarterly Journal of Mechanics and Applied Mathematics*, Vol. XIII, Part 1, 1960, pp. 16–23.

2 Mansfield, E. H., "Three-Dimensional Stress Analysis of Cylindrically Wound Fiber Reinforced Annular Discs Surrounding a Circular Hole in a Flat Plate," *International Journal of Mechanical Sciences*, Vol. 18, 1976, pp. 469–479.

3 Lekhnitskii, S. G., *Theory of Elasticity of an Anisotropic Elastic Body*, Holden-Day Series in Mathematical Physics, Holden-Day, Inc., San Francisco, Calif., 1963.

4 Ramaiah, G. K., and Vijayakumar, K., "Buckling of Polar Orthotropic Annular Plates Under Uniform Internal Pressure," *AIAA Journal*, Vol. 12, No. 8, 1974, pp. 1045–1050.

5 Ramaiah, G. K., and Vijayakumar, K., "Elastic Stability of Annular Plates Under Uniform Compressive Forces Along the Outer Edge," *AIAA Journal*, Vol. 13, No. 6, 1975, pp. 832–834.

6 Elishakoff, I., and Charmats, M., "Godunov-Conte Method for Solution of Eigenvalue Problems and Its Application, ASME JOURNAL OF APPLIED MECHANICS, Vol. 44, 1977, pp. 776–779.

7 Strzelczyk, A., and Wojciech, St., "Numerical Solution of the Problem of Stability of an Orthotropic Annular Plate," *Mechanika Teoretyczna Stosowana*, Vol. 15, 1977, pp. 37–55 (in Polish).

8 Johnson, G., and Pilkey, W., "Lumped Parameter Circular Plate Stability Analysis," *Journal of the Structural Division, Proceedings of the ASCE*, Vol. 102, 1976, pp. 1135–1140.

9 Loh, H. C., and Carney, J. F., III, "Vibration and Stability of Spinning Annular Plates Reinforced With Edge Beams," ASME JOURNAL OF APPLIED MECHANICS, Vol. 44, 1977, pp. 499–501.

Table 6 Estimates of critical buckling load parameter ($= p_1a^2h/D_r$) of polar orthotropic annular plates; loading condition $p_0b^2 = p_1a^2$ (radial tension): $\nu_\theta = 0.3$, $D_{r\theta}/D_r = 0.35$

a/b	Values of D_θ/D_r						Values of D_θ/D_r					
	0.5	0.8	1.0	1.25	2.0	5.0	0.5	0.8	1.0	1.25	2.0	5.0
	(1) SC case:						(2) CS case:					
0.1	11.95	16.57	19.97	24.50	39.18	137.5	11.94	15.78	18.47	21.94	32.81	79.22
	(3)	(3)	(3)	(3)	(3)	(4)	(3)	(3)	(3)	(3)	(3)	(3)
0.2	24.95	32.76	38.29	45.47	67.60	146.8	25.15	31.86	36.42	42.17	59.25	112.5
	(4)	(4)	(4)	(4)	(4)	(4)	(4)	(4)	(4)	(4)	(4)	(3)
0.3	44.23	58.22	66.75	77.68	111.0	222.4	44.93	56.96	64.11	73.02	99.09	173.6
	(6)	(5)	(5)	(5)	(5)	(5)	(6)	(5)	(5)	(5)	(5)	(3)
0.4	77.22	98.76	113.5	132.4	183.3	352.2	77.98	97.69	110.8	125.8	165.0	290.3
	(7)	(7)	(7)	(7)	(6)	(6)	(7)	(7)	(7)	(6)	(6)	(5)
0.5	134.8	171.8	195.9	226.5	310.6	602.4	136.2	170.3	192.2	217.9	286.6	495.6
	(10)	(9)	(9)	(9)	(8)	(8)	(10)	(9)	(9)	(8)	(8)	(7)
0.6	246.9	313.4	357.9	411.1	560.5	1091	250.6	313.4	352.7	399.2	528.3	933.8
	(13)	(12)	(12)	(11)	(11)	(10)	(13)	(12)	(12)	(11)	(11)	(10)
0.7	511.9	646.7	730.9	834.6	1136	2236	514.4	643.0	722.7	817.5	1084	1970
	(19)	(17)	(17)	(16)	(15)	(14)	(19)	(17)	(17)	(16)	(15)	(14)
0.8	1310	1646	1860	2117	2862	5647	1314	1643	1847	2091	2781	5199
	(30)	(28)	(27)	(26)	(25)	(23)	(30)	(28)	(27)	(26)	(24)	(22)
	(3) SS case:						(4) CC case:					
0.1	10.12	14.08	16.92	20.62	32.17	79.76	13.89	18.74	21.91	26.06	39.36	98.85
	(3)	(3)	(3)	(3)	(3)	(3)	(4)	(3)	(3)	(3)	(3)	(3)
0.2	21.09	28.02	32.82	38.95	56.69	111.2	28.37	37.85	43.06	49.70	69.92	144.2
	(4)	(4)	(4)	(4)	(3)	(3)	(5)	(4)	(4)	(4)	(4)	(4)
0.3	36.13	49.11	56.61	66.08	92.84	170.7	51.33	65.95	75.94	87.15	117.6	221.5
	(5)	(5)	(5)	(5)	(4)	(4)	(6)	(6)	(6)	(5)	(5)	(5)
0.4	66.13	84.46	95.82	110.1	152.4	261.4	89.04	114.1	128.4	146.3	199.9	354.9
	(7)	(6)	(6)	(6)	(6)	(5)	(8)	(7)	(7)	(7)	(7)	(6)
0.5	115.6	146.6	166.1	190.5	261.5	480.7	156.6	197.4	223.9	253.5	341.4	611.3
	(9)	(8)	(8)	(8)	(7)	(7)	(11)	(10)	(9)	(9)	(9)	(8)
0.6	213.1	286.8	304.7	349.3	472.0	896.6	289.2	363.4	409.5	465.1	621.5	1135
	(12)	(11)	(11)	(10)	(10)	(9)	(14)	(13)	(13)	(12)	(12)	(10)
0.7	437.6	550.8	623.0	709.8	962.6	1864	593.9	744.0	837.4	949.6	1264	2335
	(17)	(16)	(15)	(15)	(14)	(13)	(21)	(19)	(18)	(18)	(16)	(15)
0.8	1119	1406	1589	1809	2450	4827	1517	1900	2136	2418	3213	6023
	(37)	(33)	(34)	(24)	(23)	(21)	(33)	(30)	(29)	(28)	(26)	(24)

Notes:
1 Value in ( ) denotes the number of circumferential waves ($= n$) in the critical buckling mode.
2 The corresponding data in the isotropic case have been reported by Mansfield [1] in the SS and CC cases.

Table 7 Influence of ν_θ on the critical buckling load parameter ($= p_i a^2 h/D_r$) of polar orthotropic annular plates under uniform inplane compressive forces along the inner edge ($p_0 = 0$); $D_{r\theta}/D_r = 0.35$

Case	a/b	$D_\theta/D_r = 0.5$			$D_\theta/D_r = 1.0$			$D_\theta/D_r = 2.0$		
		$\nu_\theta \rightarrow$ 0.2	0.3	0.4	0.2	0.3	0.4	0.2	0.3	0.4
SF FS	0.1	0.450	0.397	0.328	1.107	1.028	0.934	2.766	2.622	2.465
	0.3	0.598	0.522	0.425	1.312	1.218	1.102	2.908	2.771	2.673
	0.5	0.708	0.621	0.507	1.501	1.399	1.272	3.154	3.024	2.867
CF	0.1	0.707	0.608	0.499	1.338	1.219	1.090	2.899	2.732	2.555
	0.3	2.021	1.812	1.593	2.683	2.461	2.229	4.130	3.882	3.624
	0.5	6.082	5.694	5.298	6.786	6.390	5.986	8.240	7.829	7.408
FC	0.1	1.243	1.301	1.352	2.324	2.385	2.439	5.516	5.568	5.615
	0.3	4.332	4.527	4.708	5.615	5.813	5.997	8.597	8.795	8.798
	0.5	13.60	14.06	14.50	15.09	15.55	15.99	18.23	18.69	19.13
SC	0.1	4.511	4.548	4.584	6.044	6.086	6.126	9.637	9.684	9.729
	0.3	22.60	22.76	22.91	24.74	24.90	25.06	29.17	29.34	29.51
	0.5	81.92	82.31	82.70	84.45	84.90	85.29	89.73	90.14	90.54
CS	0.1	2.193	2.024	1.844	2.938	2.745	2.542	4.571	4.333	4.086
	0.3	11.63	11.26	10.86	12.56	12.19	11.80	14.50	14.08	13.66
	0.5	44.21	43.52	42.82	45.33	44.63	43.48	47.57	46.85	46.12
SS	0.1	1.580	1.446	1.302	2.293	2.137	1.970	3.908	3.706	3.492
	0.3	7.519	7.277	7.020	8.397	8.140	7.868	10.22	9.932	9.631
	0.5	27.76	27.37	26.96	28.79	28.39	27.97	30.88	30.46	30.02

Notes:
1 $n = 0$; axisymmetric eigenloads are identical in SF and FS cases.
2 ν_θ has no effect on the value of $(p_i a^2 h/D_r)$ in the CC case.

10 Yamaki, N., "Buckling of a Thin Annular Plate Under Uniform Compression," ASME JOURNAL OF APPLIED MECHANICS, Vol. 25, 1958, pp. 267–273.

11 Vijayakumar, K., and Joga Rao, C. V., "Buckling of Polar Orthotropic Annular Plates," *Journal of the Engineering Mechanics Division, Proceedings of the ASCE*, Vol. 97, No. EM3, 1971, pp. 701–710.

12 Uthgenannt, E. B., and Brand, R. S., "Buckling of Polar Orthotropic Annular Plates," *AIAA Journal*, Vol. 8, No. 11, 1970, pp. 2102–2104.

13 Japan, G. R. C., *Handbook of Structural Stability*, Column Research Committee of Japan, 1971, Corona Publishing Company, Limited, Tokyo.

Journal of Applied Mechanics

Brief Notes

A Brief Note is a short paper which presents a specific solution of technical interest in mechanics but which does not necessarily contain new general methods or results. A Brief Note should not exceed 1500 words *or equivalent* (a typical one-column figure or table is equivalent to 250 words; a one line equation to 30 words). Brief Notes will be subject to the usual review procedures prior to publication. After approval such Notes will be published as soon as possible. The Notes should be submitted to the Technical Editor of the JOURNAL OF APPLIED MECHANICS. Discussions on the Brief Notes should be addressed to the Editorial Department, ASME, United Engineering Center, 345 East 47th Street, New York, N. Y. 10017, or to the Technical Editor of the JOURNAL OF APPLIED MECHANICS. Discussions on Brief Notes appearing in this issue will be accepted until two months after publication. Readers who need more time to prepare a Discussion should request an extension of the deadline from the Editorial Department.

On the Error That Can Be Induced by an Ergodicity Assumption

A. J. Scheurkogel,[1] I. Elishakoff,[2] and J. J. Kalker[3]

Introduction

Buckling of stochastically imperfect structures is governed by random nonlinear differential equations. The exact solution of these equations does not appear to be feasible and approximate methods are resorted to. In a number of papers, the assumption of ergodicity was used to obtain probabilistic characteristics of the solution. For the ergodic theorem one may consult, e.g., Lin [1] or Billingsley [2]; Amazigo [3] reviewed inter alia the probabilistic buckling problems, the solution of which is based on the ergodicity assumption. The question arises whether this assumption is correct.

To our knowledge the only work which considers the validity of the ergodicity assumption in a context of structural mechanics is that of Bolotin [4, pp. 101–105]. He gave an example where the first three terms of the perturbation solution agreed with the solution resulting from the ergodicity assumption.

Here we present an example akin to Bolotin's in which the *exact* solution is given and compared with results obtained by the ergodic approximation. It is found that

1 The ergodicity assumption is correct at only one value of the governing parameter.

2 The ergodicity assumption leads to a good approximation in a large part of the domain of definition of the governing parameter.

3 In the remaining part the error may be very large.

A structural mechanics example is now underway and will be published elsewhere.

Formulation

Consider the random differential equation:

$$\frac{d^2x}{dt^2} + \frac{x}{\xi^2} = (4 - pa^2 - pb^2)^{1/2}; \quad t > 0, 0 \le p \le 4 \tag{1}$$

with initial conditions

$$x(0) = \xi a + \xi^2(4 - pa^2 - pb^2)^{1/2} \tag{2}$$

$$x'(0) = b \tag{3}$$

where

$$\xi^2 = \lim_{T\to\infty} \frac{1}{T} \int_0^T x^2(t)dt, \quad \xi > 0 \tag{4}$$

and p is a governing parameter.

The random variables a and b are jointly uniformly distributed on the unit circle $a^2 + b^2 \le 1$.

We are interested in $E[x(t)]$ and $E[x^2(t)]$ where $E[\ldots]$ denotes mathematical expectation.

Approximate Solution Based on the Ergodicity Assumption

If the solution $x(t)$ is assumed to be mean-square ergodic, the mean-square value follows directly from (2) and (4):

$$\xi^2 = E[x^2(t)] = E[x^2(0)] = E[\xi a + \xi^2(4 - pa^2 - pb^2)^{1/2}]^2$$
$$= \tfrac{1}{4}\xi^2 + (4 - \tfrac{1}{2}p)\xi^4 \tag{5}$$

hence

$$\xi^2 = E[x^2(t)] = \frac{3}{2(8-p)} \tag{6}$$

Taking the expectation of equations (1)–(3) with this value of ξ, we find after solving for $E[x(t)]$:

$$E[x(t)] = \frac{3}{2(8-p)} E[4 - pa^2 - pb^2]^{1/2} \tag{7}$$

Introducing the random variable

$$z = a^2 + b^2, \tag{8}$$

uniformly distributed on the interval (0,1), we finally obtain

$$E[x(t)] = \frac{3}{2(8-p)} E[4 - pz]^{1/2}$$
$$= \frac{3}{2(8-p)} \int_0^1 (4 - pz)^{1/2} dz = \frac{8 - (4-p)^{3/2}}{p(8-p)} \tag{9}$$

[1] Research Associate, Department of Mathematics, Delft University of Technology, Delft, The Netherlands.

[2] Associate Professor, Technion-I.I.T., Department of Aeronautical Engineering, Haifa, Israel.

[3] Professor, Department of Mathematics, Delft University of Technology, Delft, The Netherlands.

Manuscript received by ASME Applied Mechanics Division, July, 1980; final revision, December, 1980.

Exact Solution

For each realization of the solution $x(t)$, ξ is independent of t. Consequently, the solution of equations (1)–(3) is

$$x(t) = a\xi \cos\frac{t}{\xi} + b\xi \sin\frac{t}{\xi} + \xi^2(4 - pa^2 - pb^2)^{1/2}, \qquad (10)$$

where the value of ξ is obtained from substitution of (10) into (4)

$$\xi^2 = \frac{1 - (a^2 + b^2)/2}{4 - p(a^2 + b^2)} \qquad (11)$$

We immediately observe from equation (11) that ξ depends in general on the particular realization of the random variables a and b, which implies that $x(t)$ is not mean-square ergodic for arbitrary p. However, $x(t)$ is wide-sense stationary (i.e., $E[x(t)]$ is constant and the autocorrelation function $E[x(t)x(t+\tau)]$ depends on the time lag τ only but not on t itself [1]). To show this, we first note that a and b are interchangeable in the expression (11) for ξ and, moreover, that ξ is an even function of both a and b. Next, we substitute equation (11) into equation (10) and take the expectation. The first and second terms do not contribute as they are odd functions of a and b, respectively. The mathematical expectation is, therefore,

$$E[x(t)] = E\left[\frac{1 - (a^2 + b^2)/2}{(4 - pa^2 - pb^2)^{1/2}}\right] = \int_0^1 \frac{1 - z/2}{(4 - pz)^{1/2}}\,dz$$

$$= \frac{1}{3p^2}[12p - 16 - (5p - 8)(4 - p)^{1/2}], \qquad (12)$$

independent of t, which establishes the first property of wide-sense stationarity. In order to establish the second property, we form the product:

$$x(t)x(t+\tau) = \tfrac{1}{2}(a^2 + b^2)\xi^2 \cos\frac{\tau}{\xi} + \tfrac{1}{2}(a^2 - b^2)\xi^2 \cos\frac{2t + \tau}{\xi}$$
$$+ ab\xi^2 \sin\frac{2t + \tau}{\xi} + a\xi^3(4 - pa^2 - pb^2)^{1/2}\left(\cos\frac{t}{\xi} + \cos\frac{t + \tau}{\xi}\right)$$
$$+ b\xi^3(4 - pa^2 - pb^2)^{1/2}\left(\sin\frac{t}{\xi} + \sin\frac{t + \tau}{\xi}\right)$$
$$+ \xi^4(4 - pa^2 - pb^2) \qquad (13)$$

with ξ as per equation (11). Taking the expectation, we find by employing symmetry arguments that only the first and last terms contribute to the autocorrelation function. Taking into account equation (8), we are left with

$$E[x(t)x(t+\tau)]$$
$$= E\left[\frac{\frac{z}{2}\left(1 - \frac{z}{2}\right)}{4 - pz}\cos\left(\frac{4 - pz}{1 - \frac{z}{2}}\right)^{1/2}\tau + \frac{\left(1 - \frac{z}{2}\right)^2}{4 - pz}\right], \qquad (14)$$

which is a function of τ only.

The second moment of $x(t)$ is calculated from (14) as

$$E[x^2(t)] = E\left[\frac{1 - z/2}{4 - pz}\right] = \int_0^1 \frac{1 - z/2}{4 - pz}\,dz$$
$$= \frac{1}{2p}\left[1 - \frac{2(p - 2)}{p}\log\left(1 - \frac{p}{4}\right)\right] \qquad (15)$$

In accordance with equation (11), the necessary condition for mean-square ergodicity is that $p = 2$, since otherwise ξ would depend on the particular realization of a and b. From equation (15) we have for $p = 2$, that $E[x^2(t)] = \frac{1}{4}$. On the other hand, from equations (4) and (11) we have

$$\xi^2 = \lim_{T\to\infty}\frac{1}{T}\int_0^T x^2(t)dt = \tfrac{1}{4} \qquad (16)$$

so that $\xi^2 = E[x^2(t)]$. All this implies the mean-square ergodicity of $x(t)$ iff $p = 2$.

Interestingly for $p = 0$ the solution based on the ergodicity assumption also coincides with the exact solution, although for this particular value of p the process is not ergodic in the mean-square sense. In this case the wrong assumption leads to the correct result.

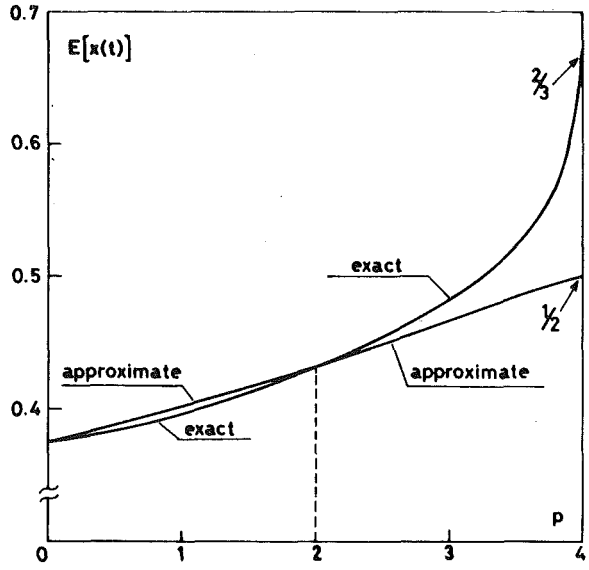

Fig. 1 Mathematical expectation as a function of p

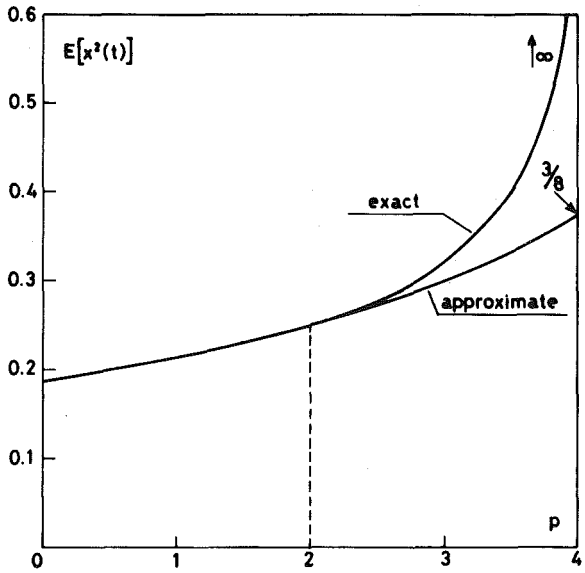

Fig. 2 Mean-square value as a function of p; at $p = 0$ and $p = 2$, the exact and approximate solutions coincide

The mathematical expectation $E[x(t)]$ and the mean-square value $E[x^2(t)]$ are shown in Figs. 1 and 2, respectively. It is remarkable that both the exact and approximate solutions are very close in the range $0 \le p \le 2$, coinciding at the ends of this interval. The percentage error relative to the exact value induced by the ergodicity assumption, is of the order of -0.5 percent in this range.

The foregoing error increases rapidly with p and reaches its maximum value at $p = 4$. For the mathematical expectation, this error is 25 percent, whereas for the mean-square value the error approaches 100 percent: the exact mean-square value $E[x^2(t)]$ tends to infinity, while the approximate one remains finite.

References

1 Lin, Y. K., *Probabilistic Theory of Structural Dynamics*, McGraw-Hill, New York, 1967.
2 Billingsley, P., *Ergodic Theory and Information*, Wiley, 1965.
3 Amazigo, J. C., "Buckling of Stochastically Imperfect Structures,"

Buckling of Structures, Budiansky, B., ed., Springer-Verlag, Berlin, 1976, pp. 172–182.

4 Bolotin, V. V., "Application of the Methods of the Theory of Probability and the Theory of Reliability to Analysis of Structures," Section 1.14, *Methods of Solution of Nonlinear Stochastic Boundary-Value Problems*, State Publishing House for Buildings, Moscow, 1971, in Russian, (English Translation: FTD-MT-24-771-73, Foreign Technology Division, Wright-Patterson AFB, Ohio, 1974).

Note on a Paper by Liu on the Scattering of Water Waves by a Pair of Semi-Infinite Barriers

A. D. Rawlins[1]

Recently, a problem, whose solution was well known in exact form, has been analyzed by Liu (Scattering of Water Waves by a Pair of Semi-Infinite Barriers, ASME JOURNAL OF APPLIED MECHANICS, Vol. 42, 1975, p. 777), by the method of matched asymptotic expansions. From the known exact solution a simple expression is obtained for the transmission coefficient. The exact expression for the transmission coefficient when expanded for low frequency incident waves differs from Liu's result, and therefore casts doubt on Liu's analysis and physical conclusions.

A problem, whose solution was well known in exact form, has recently been tackled by the method of matched asymptotic expansions. The work, to which we are referring, is by Liu [1]. The problem is that of diffraction of a plane water wave by a pair of rigid semi-infinite barriers. This problem has been solved exactly for all values of incident wave frequencies by a number of authors, in particular its solution was available in Noble's book on the Wiener-Hopf technique [2, Section 3.2, Page 100].

Mathematically, the problem that is required to be solved is to determine $\psi(x, y, t) = \phi(x, y)e^{-iwt}$ such that

$$\frac{\partial^2\phi}{\partial x^2} + \frac{\partial^2\phi}{\partial x^2} + k^2\phi = 0,$$

$$\frac{\partial\phi}{\partial y} = 0, \qquad y = \pm a, \qquad x < 0.$$

Also grad ϕ should have no more than an integrable singularity near the two sharp edges $(0, \pm a)$; and the radiation condition is imposed which requires that the only energy which is "incoming" at infinity is that of the incident wave. Referring to Fig. 1, a given wave $\phi_i(x, y) = e^{-ik(x\cos\alpha + y\sin\alpha)}$ is incident on the barriers. Consequently diffraction takes place at the edges and a wave Te^{-ikx} is transmitted into the region between the barriers. The object of Liu's work was to calculate the transmission coefficient T for the low frequency situation $ka \ll 1$. He derived the result to $O[(ka)^2]$ and concluded from his expression that the transmission coefficient at low frequency was independent of the angle of incident α. It is easy to show that this is only true for the terms of order less that $O[(ka)]$, and more specifically Liu's result for T is incorrect.

From Noble [2, p. 105], the exact expression for the transmission coefficient for all incident wave frequencies is given by

$$|T| = \frac{1}{|L_+(k\cos\alpha)L_-(k)|}\left|\frac{\sin(ka\sin\alpha)}{ka\sin\alpha}\right|$$

According to Noble [2, p. 127, ex 3.3], if $0 < ka < \pi$,

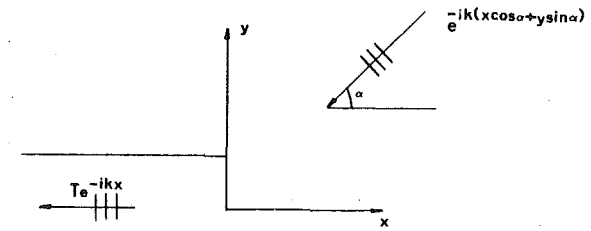

Fig. 1 Coordinate system and breakwater configuration

$$|L_+(k\cos\alpha)| = \left|\frac{\sin(ka\sin\alpha)}{ka\sin\alpha}\right|^{1/2} e^{-(ka/2)\cos\alpha},$$

$$|L_-(k)| = e^{ka/2}.$$

Hence

$$|T| = \left|\frac{\sin(ka\sin\alpha)}{ka\sin\alpha}\right|^{1/2} e^{-(ka/2)(1-\cos\alpha)}; \quad 0 < ka < \pi \qquad (1)$$

This latter expression is valid (and simple enough to calculate) for all $0 < ka < \pi$. In order to compare our result with that of Liu we expand the right-hand side of (1) for small ka giving

$$|T| = \left[1 - ka\sin^2\left(\frac{\alpha}{2}\right) + O[(ka)^2]\right] \qquad (2)$$

A result quite different to Liu's. It will also be seen from (2) that the transmission coefficient *does* depend on α for terms of order (ka) and greater.

References

1 Liu, P.L.-F., "Scattering of Water Waves by a Pair of Semi-Infinite Barriers," ASME JOURNAL OF APPLIED MECHANICS, Vol. 42, 1975, pp. 777–779.

2 Noble, B., *The Wiener-Hopf Technique*, Pergamon, London, 1958.

Magnetohydrodynamic Boundary Layer on a Wedge

B. Nageswara Rao[1] **and M. L. Mittal**[1]

With increasing prospects for using magnetohydrodynamic (MHD) principle in electric power generation, there is a renewed interest in the study of MHD boundary-layer phenomena. In these devices, a partially ionized gas is used as the working medium, which is made to flow in a diverging channel. Thus the study of the phenomena of boundary layers on a wedge-type wall plays an important role in the design and analysis of a MHD power generator. Wilcox [1] has studied the MHD boundary-layer phenomena on a wedge using similarity principle. To localize the electromagnetic effects within the limits of the boundary layer, the variation of conductivity with velocity distribution is considered in his analysis. Since the Hall and the ionslip currents are important, while using the partially ionized gas as the working medium, this analysis is not directly applicable in the study of boundary-layer phenomena in MHD power generator.

In the present analysis, the effects of the Hall and the ionslip cur-

[1] The Mathematics Department, Brunel University, Uxbridge, Middlesex, UB8 3PH, England.

Manuscript received by ASME Applied Mechanics Division, June, 1980.

[1] Department of Mathematics, Indian Institute of Technology, Powai, Bombay 400 076 India.

Manuscript received by ASME Applied Mechanics Division, May, 1980; final revision, December, 1980.

Buckling of Structures, Budiansky, B., ed., Springer-Verlag, Berlin, 1976, pp. 172–182.

4 Bolotin, V. V., "Application of the Methods of the Theory of Probability and the Theory of Reliability to Analysis of Structures," Section 1.14, *Methods of Solution of Nonlinear Stochastic Boundary-Value Problems*, State Publishing House for Buildings, Moscow, 1971, in Russian, (English Translation: FTD-MT-24-771-73, Foreign Technology Division, Wright-Patterson AFB, Ohio, 1974).

Note on a Paper by Liu on the Scattering of Water Waves by a Pair of Semi-Infinite Barriers

A. D. Rawlins[1]

Recently, a problem, whose solution was well known in exact form, has been analyzed by Liu (Scattering of Water Waves by a Pair of Semi-Infinite Barriers, ASME JOURNAL OF APPLIED MECHANICS, Vol. 42, 1975, p. 777), by the method of matched asymptotic expansions. From the known exact solution a simple expression is obtained for the transmission coefficient. The exact expression for the transmission coefficient when expanded for low frequency incident waves differs from Liu's result, and therefore casts doubt on Liu's analysis and physical conclusions.

A problem, whose solution was well known in exact form, has recently been tackled by the method of matched asymptotic expansions. The work, to which we are referring, is by Liu [1]. The problem is that of diffraction of a plane water wave by a pair of rigid semi-infinite barriers. This problem has been solved exactly for all values of incident wave frequencies by a number of authors, in particular its solution was available in Noble's book on the Wiener-Hopf technique [2, Section 3.2, Page 100].

Mathematically, the problem that is required to be solved is to determine $\psi(x, y, t) = \phi(x, y)e^{-iwt}$ such that

$$\frac{\partial^2\phi}{\partial x^2} + \frac{\partial^2\phi}{\partial x^2} + k^2\phi = 0,$$

$$\frac{\partial\phi}{\partial y} = 0, \qquad y = \pm a, \qquad x < 0.$$

Also grad ϕ should have no more than an integrable singularity near the two sharp edges $(0, \pm a)$; and the radiation condition is imposed which requires that the only energy which is "incoming" at infinity is that of the incident wave. Referring to Fig. 1, a given wave $\phi_i(x, y) = e^{-ik(x\cos\alpha + y\sin\alpha)}$ is incident on the barriers. Consequently diffraction takes place at the edges and a wave Te^{-ikx} is transmitted into the region between the barriers. The object of Liu's work was to calculate the transmission coefficient T for the low frequency situation $ka \ll 1$. He derived the result to $O[(ka)^2]$ and concluded from his expression that the transmission coefficient at low frequency was independent of the angle of incident α. It is easy to show that this is only true for the terms of order less that $O[(ka)]$, and more specifically Liu's result for T is incorrect.

From Noble [2, p. 105], the exact expression for the transmission coefficient for all incident wave frequencies is given by

$$|T| = \frac{1}{|L_+(k\cos\alpha)L_-(k)|}\left|\frac{\sin(ka\sin\alpha)}{ka\sin\alpha}\right|$$

According to Noble [2, p. 127, ex 3.3], if $0 < ka < \pi$,

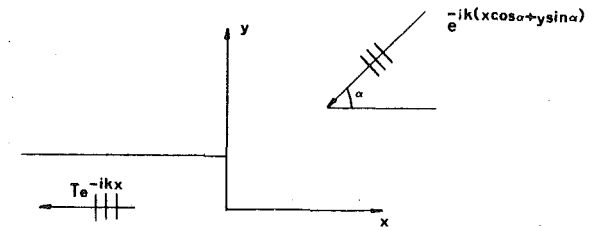

Fig. 1 Coordinate system and breakwater configuration

$$|L_+(k\cos\alpha)| = \left|\frac{\sin(ka\sin\alpha)}{ka\sin\alpha}\right|^{1/2} e^{-(ka/2)\cos\alpha},$$

$$|L_-(k)| = e^{ka/2}.$$

Hence

$$|T| = \left|\frac{\sin(ka\sin\alpha)}{ka\sin\alpha}\right|^{1/2} e^{-(ka/2)(1-\cos\alpha)}; \quad 0 < ka < \pi \qquad (1)$$

This latter expression is valid (and simple enough to calculate) for all $0 < ka < \pi$. In order to compare our result with that of Liu we expand the right-hand side of (1) for small ka giving

$$|T| = \left[1 - ka\sin^2\left(\frac{\alpha}{2}\right) + O[(ka)^2]\right] \qquad (2)$$

A result quite different to Liu's. It will also be seen from (2) that the transmission coefficient *does* depend on α for terms of order (ka) and greater.

References

1 Liu, P.L.-F., "Scattering of Water Waves by a Pair of Semi-Infinite Barriers," ASME JOURNAL OF APPLIED MECHANICS, Vol. 42, 1975, pp. 777–779.

2 Noble, B., *The Wiener-Hopf Technique*, Pergamon, London, 1958.

[1] The Mathematics Department, Brunel University, Uxbridge, Middlesex, UB8 3PH, England.

Manuscript received by ASME Applied Mechanics Division, June, 1980.

Magnetohydrodynamic Boundary Layer on a Wedge

B. Nageswara Rao[1] **and M. L. Mittal**[1]

With increasing prospects for using magnetohydrodynamic (MHD) principle in electric power generation, there is a renewed interest in the study of MHD boundary-layer phenomena. In these devices, a partially ionized gas is used as the working medium, which is made to flow in a diverging channel. Thus the study of the phenomena of boundary layers on a wedge-type wall plays an important role in the design and analysis of a MHD power generator. Wilcox [1] has studied the MHD boundary-layer phenomena on a wedge using similarity principle. To localize the electromagnetic effects within the limits of the boundary layer, the variation of conductivity with velocity distribution is considered in his analysis. Since the Hall and the ionslip currents are important, while using the partially ionized gas as the working medium, this analysis is not directly applicable in the study of boundary-layer phenomena in MHD power generator.

In the present analysis, the effects of the Hall and the ionslip cur-

[1] Department of Mathematics, Indian Institute of Technology, Powai, Bombay 400 076 India.

Manuscript received by ASME Applied Mechanics Division, May, 1980; final revision, December, 1980.

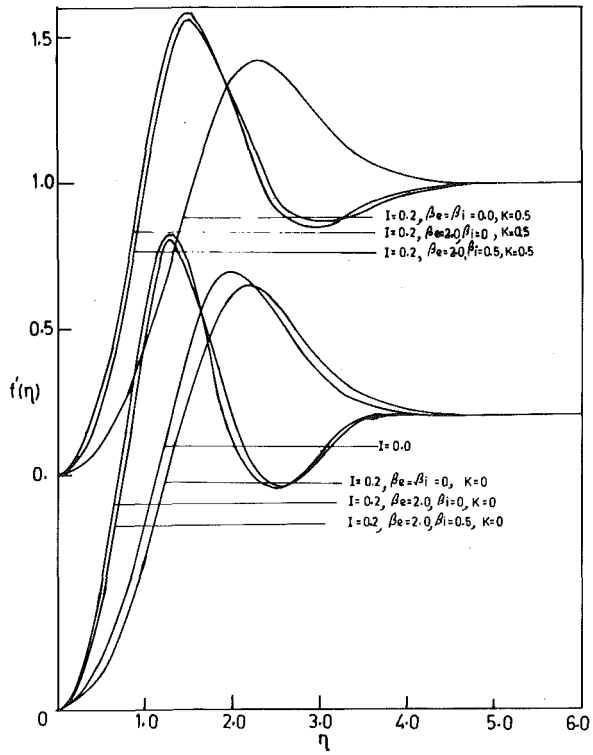

Fig. 3 Separation profiles for different values of load parameter, K

results show that the skin-friction parameter $f''(0)$ increases, and the displacement integral I_1 and the momentum integral I_2 decrease with the pressure gradient parameter β. In the absence of K, the parameter $f''(0)$ decreases and the values of I_1 and I_2 increase with the interaction parameter I. But the values of $f''(0)$, I_1, and I_2 increase with I in the presence of K. For separation of flow, the magnitudes of the pressure gradient parameter $|\beta|$ decreases and values of I_1 increase with I for different values of K.

For the case $K = 0$ and $\beta_e \neq 0$, it is observed that the values of $f''(0)$ decrease and the values of I_1 and I_2 increase with I. With the inclusion of ionslip currents, the values of $f''(0)$ further decrease while the values of I_1 and I_2 increase with I. For the separation of flow, $|\beta|$ decreases with the Hall and the ionslip currents also.

For the case $K = 0.5$, it is found that the values of $f''(0)$, I_1, and I_2 increase with I and further increase with the inclusion of ionslip currents. For the separation of flow, the behavior of the parameter $|\beta|$ is similar as in the absence of K.

It is important to note from Table 3 about the negative values of the momentum integral I_2 for the separation of flow. It is observed that the mometum transport is larger in the boundary layer than in the equivalent inviscid flow. This is accounted for by the large observed velocity overshoots in the boundary layer (see Fig. 3).

Acknowledgment

The authors are grateful to referee for making useful comments for the improvement of the paper.

References

1 Wilcox, M., "Boundary at a Wedge," in *Elements of Magnetogasdynamics*, by Kalikhman, L. E., Moscow Physical-Technical Institute, translated from Russian by Scripta Technica, Inc., ed., Cameron, A. G. W., W.B. Saunders Company, Philadelphia and London, 1967, pp. 193–199; also in *Proceedings of 4th Symposium on MHD*, Northwest University Press, 1962, pp. 277–282.

2 Sherman, A., and Sutton, G. W., *Engineering Magnetohydrodynamics*, McGraw-Hill, New York, 1964.

3 Nachtsheim, P. R., and Swigert, P., "Satisfaction of Asymptotic Boundary Conditions in Numerical Solution of System of Nonlinear Equations of Boundary-Layer Type," NASA TN-3004, 1965.

4 Forbes Dewey, C., Jr., and Gross, J. F., "Exact Similar Solutions of the Laminar Boundary-Layer Equations," *Advances in Heat Transfer*, Vol. 4, 1967, pp. 317–446.

5 Steinheuer, J., "Similar Solutions for the Laminar Wall Jet in a Decelerating Outer Flow," *AIAA Journal*, Vol. 6, No. 11, 1968, pp. 2198–2200.

6 Schlichting, H., *Boundary-Layer Theory*, McGraw-Hill, New York, 1955.

7 Mittal, M. L., Masapati, G. H., and Rao, B. N., "Entrance Flow in a MHD Channel With Hall and Ionslip Currents," *AIAA Journal*, Vol. 14, No. 12, 1976, pp. 1768–1770.

8 Luther, H. A., "An Explicit Sixth-Order Runge-Kutta Formula," *Maths. Computation*, Vol. 22, 1968, pp. 434–436.

Solution of Navier's Equation in Rotational Curvilinear Coordinates

B. S. Berger[1] and D. M. Curtis[2]

Numerical study of the exterior problem for elastic bodies has received considerable attention [1–5]. The satisfaction of boundary conditions at infinity is an important problem for the static, transient, and steady-state cases which has been approximately satisfied by a variety of means. These include the introduction of a viscous boundary [2], a semianalytic energy transmitting boundary [1, 3], and a technique based on the properties of the transmission of D'Alembert forces [4]. The boundary element technique has been shown to be effective in the solution of exterior problems for the static and steady-state cases.

However, as pointed out by Brebbia in [9], equations involving the time variable are usually hyperbolic (or parabolic) in type and as such are unsuitable for solution by the boundary element technique, the Laplace or Fourier transformed equations, however, are in many cases elliptic. The numerical inversion of the Fourier and Laplace transforms involved in this approach, while possible, present serious computational problems [10]. As has been previously shown for the exterior problem for cylindrical bodies [6, 7], the following demonstrates that methods of solution based on coordinate transformation can readily satisfy boundary conditions at infinity for the steady-state, static, and transient cases and accommodate differing surface geometries for exterior bodies of revolution.

In the following, the Navier equations are expressed in orthogonal rotational curvilinear coordinates. The angular variable, $\mathbf{x}_3$, is suppressed through a Fourier or finite-difference expansion. Finite-difference equations are derived for the case of symmetric loading and solved numerically for static problems for which exact solutions may be derived. Comparisons between exact and approximate solutions show excellent agreement. While the formulation given here is sufficient for the static and transient cases, satisfaction of the radiation conditions, at infinity, associated with the steady-state case requires the use of the Lamé potentials. This case is omitted here, but is given for cylindrical geometry in [7].

The vector form of the equations of motion of a linearly elastic, homogeneous, isotropic solid is given by

$$(\lambda + 2\mu)\overline{\nabla}e - \mu\overline{\nabla}x(\overline{\nabla}x\overline{u}) + \rho\overline{b} = \rho\ddot{\overline{u}} \tag{1}$$

where λ and μ are the Lamé constants, $\overline{u}$ the displacement vector, ρ the mass density, and $\overline{b}$ the body force vector [8]. Denote the coordinates of a point in a circular cylindrical coordinate system by $\mathbf{x}_i$, $i = 1, 3$; Fig. 1. Define the rotational coordinate system x_i by $x_1 = x_1(\mathbf{x}_1, \mathbf{x}_2)$, $x_2 = x_2(\mathbf{x}_1, \mathbf{x}_2)$, and $x_3 = \mathbf{x}_3$ where x_1 and x_2 are defined over a rectangular domain $\alpha_1 \leq x_1 \leq \alpha_2$, $\beta_1 \leq x_2 \leq \beta_2$. The components of

[1] Professor, Department of Mechanical Engineering, University of Maryland, College Park, Md. 20742. Assoc. Mem. ASME.

[2] Senior Mechanical Engineer, NKF Engineering Associates, Inc., Vienna, Va. 22180. Assoc. Mem. ASME.

Manuscript received by ASME Applied Mechanics Division, January, 1981; final revision, March, 1981.

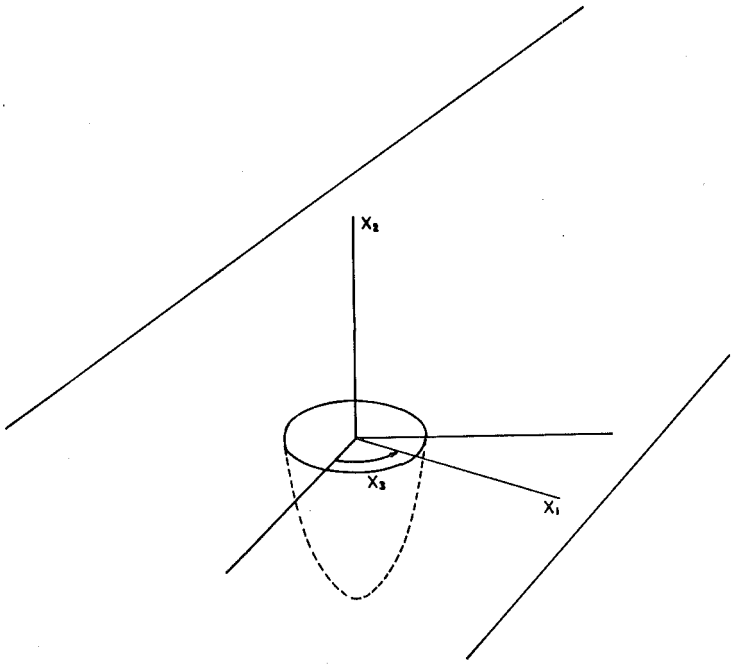

Fig. 1

the metric tensor, g_{ij}, associated with the x_i coordinate system are given by $g_{ij} = \mathbf{X}_{n,i}\mathbf{X}_{n,j}$, $g_{11} = g_{11}(x_1, x_2)$, $g_{22} = g_{22}(x_1, x_2)$, $g_{33} = \mathbf{X}_1{}^2$, $g_{13} = g_{31} = 0, g_{23} = g_{32} = 0$ where $(\ )_{,i} \equiv \partial(\ )/\partial x_i$ and repeated indices are summed. If the x_i coordinate system is assumed to be orthogonal, then in addition to the foregoing, $g_{12} = g_{21} = 0$ or generally $g_{ij} = 0$, $i \neq j$. Expressing (1) in the x_i coordinate system, assuming orthogonality, gives

$$(\lambda + 2\mu)A_{,1} - \mu(\sqrt{g_{11}/g_{22}g_{33}})((\sqrt{g_{33}}\,D)_{,2} - \sqrt{g_{22}}\,C_{,3}) + \rho b_1 = \rho\sqrt{g_{11}}\,\ddot{u} \quad (2)$$

$$(\lambda + 2\mu)A_{,2} - \mu(\sqrt{g_{22}/g_{33}g_{11}})(\sqrt{g_{11}}\,B_{,3} - (\sqrt{g_{33}}\,D)_{,1}) + \rho b_2 = \rho\sqrt{g_{22}}\,\ddot{v} \quad (3)$$

$$(\lambda + 2\mu)A_{,3} - \mu(\sqrt{g_{33}/g_{11}g_{22}})((\sqrt{g_{22}}\,C)_{,1} - (\sqrt{g_{11}}\,B)_{,2}) + \rho b_3 = \rho\sqrt{g_{33}}\,\ddot{w} \quad (4)$$

where

$$A = (1/\sqrt{g})((\sqrt{g_{22}g_{33}}\,u)_{,1} + (\sqrt{g_{11}g_{33}}\,v)_{,2} + \sqrt{g_{11}g_{22}}\,w_{,3}),$$

$$B = (1/\sqrt{g_{22}g_{33}})((\sqrt{g_{33}}\,w)_{,2} - \sqrt{g_{22}}\,v_{,3}),$$

$$C = (1/\sqrt{g_{33}g_{11}})(\sqrt{g_{11}}\,u_{,3} - (\sqrt{g_{33}}\,w)_{,1}),$$

$$D = (1/\sqrt{g_{11}g_{22}})((\sqrt{g_{22}}\,v)_{,1} - (\sqrt{g_{11}}\,u)_{,2}),$$

the physical components of displacements $u^{(i)}$, are denoted by $u^{(1)} = u$, $u^{(2)} = v$, and $u^{(3)} = w$.

For the unsymmetric case the independent variable x_3, in (2)–(4) may be suppressed through a Fourier expansion of u, v, and w in x_3. Equations (2)–(4) then determine the coefficients in the expansion. Equations (2)–(4) simplify for the symmetric case since $u = u(x_1, x_2)$, $v = v(x_1, x_2)$, $w = 0$ and may be expressed in finite-difference form, over the rectangular x_1, x_2 domain, by replacing spatial derivatives with central differences and the temporal derivatives with backward differences. The spatial difference form, assuming symmetrical displacements, is then given by

$$\begin{aligned} &A(5)u_{i+1,j} + A(3)u_{i,j} + A(1)u_{i-1,j} + A(4)u_{i,j+1} + A(2)u_{i,j-1} \\ &+ A(14)v_{i+1,j} + A(13)v_{i,j} + A(9)v_{i,j+1} + A(8)v_{i,j-1} + A(12)v_{i-1,j} \\ &+ A(11)v_{i+1,j+1} + A(10)v_{i+1,j-1} + A(6)v_{i-1,j-1} \\ &+ A(7)v_{i-1,j+1} + \rho b_1 = \rho\sqrt{g_{11}}\,\ddot{u}_{i,j} \end{aligned} \quad (5)$$

$$\begin{aligned} &B(14)u_{i+1,j} + B(13)u_{i,j} + B(12)u_{i-1,j} + B(6)u_{i+1,j+1} \\ &+ B(5)\,u_{i+1,j-1} + B(1)u_{i-1,j-1} + B(2)u_{i-1,j+1} + B(4)u_{i,j+1} \\ &+ B(3)u_{i,j-1} + B(10)v_{i,j+1} + B(9)v_{i,j} + B(8)v_{i,j-1} + B(11)v_{i+1,j} \\ &+ B(7)v_{i-1,j} + \rho b_2 = \rho\sqrt{g_{22}}\,\ddot{v}_{i,j} \end{aligned} \quad (6)$$

where the variable coefficients, $A(I)$ and $B(I)$, are functions of the metric tensor, g_{ij}, and material properties. Expressions for $A(I)$ and $B(I)$ are given in [11].

Displacement and stress boundary conditions will be given over disjoint sets of points on the surface of the body. Since the Navier equations were solved in the x_i coordinate system, it is necessary to express the physical components of displacement, $U^{(i)}$, in the circular cylindrical coordinate system, $\mathbf{X}_i$, in terms of base vectors associated with the x_i coordinate system. This may be accomplished through tensor transformation rules [6, 11].

The efficient numerical construction of coordinate transformations for a variety of shapes is of particular importance. A comprehensive study is given in [11].

Numerical studies were carried out to check the performance of these transformation methods for unbounded problems. The numerical solutions are compared with exact solutions. The values of material constants are as follows: $\nu = 0.3$, $E = 2.07{\cdot}10^{11}$, $\mu = 7.9615{\cdot}10^{10}$, and $\lambda = 1.1942{\cdot}10^{11}$ in mks units. A conformal transformation

$$\mathbf{X}_1 = \sum_{n=1}^{N} a_n x_1{}^{(2n-3)} \cos(3 - 2n)x_2 \quad (7)$$

$$\mathbf{X}_2 = \sum_{n=1}^{N} a_n x_1{}^{(2n-3)} \sin(3 - 2n)x_2 \quad (8)$$

was used in all computations [6, 7, 11]. In cylindrical coordinates a solution to Navier's equation is given by $U_1 = -((\lambda + \mu)/\mu)J_1(\mathbf{X}_1) \exp(-\mathbf{X}_2)$ and $U_2 = -((\lambda + \mu)/\mu)\,J_0(\mathbf{X}_1) \exp(-\mathbf{X}_2)$. Tensor transformation laws imply that $u^{(1)} = ((\partial\mathbf{X}_1/\partial x_1){\cdot}U_1 + (\partial\mathbf{X}_2/\partial x_1){\cdot}U_2)/\sqrt{g_{11}}$ and $u^{(2)} = ((\partial\mathbf{X}_1/\partial x_2){\cdot}U_1 + (\partial\mathbf{X}_2/\partial x_2){\cdot}U_2)/\sqrt{g_{22}}$. The displacements given by $u^{(1)}$ and $u^{(2)}$ were applied over the surface of a hemispherical cavity, with $x_1 = 1$ utilizing the corresponding values of $\mathbf{X}_1$ and $\mathbf{X}_2$, and over the surface of the surrounding plane, $\mathbf{X}_2 = 0$. For this geometry the coefficients in transformations (7) and (8) are $a_1 = 1$ and $a_n = 0$ for $n > 1$. Fig. 2 shows a plot of the exact solution for u and the difference

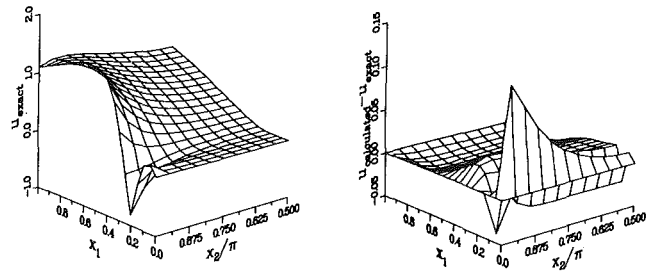

Fig. 2

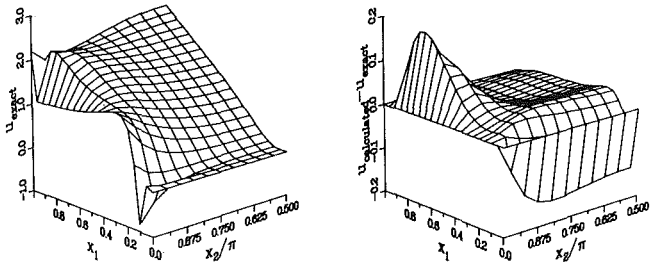

Fig. 3

between the calculated and exact values of u. It is seen that the region of maximum error corresponds to small values of x_1 and therefore large values of $\mathbf{X}_1$. As $x_1 \to 0$, assuming a uniform step size in x_1, the corresponding step size in $\mathbf{X}_1$ becomes infinite. Fig. 3 shows a plot of the exact solution for u and the difference between the calculated and exact values of u for the case of the unindented plane, $\mathbf{X}_2 = 0$, subjected to displacements given by $u^{(1)}$ and $u^{(2)}$. The mapping is given by (7) and (8) with $a_1 = 1/2$, $a_2 = 1/2$, $a_n = 0$ for $n > 2$. Two regions of local maximum error exist, one corresponding to $x_1 = 0$ as before and another near $x_1 = 1$, $x_2 = \pi$. Coordinate lines in the physical plane are very closely spaced and convoluted in the neighborhood of $x_1 = 1$, $x_2 = \pi$ resulting in a loss of accuracy.

References

1 Lysmer, T., and Wass, G., "Shear Waves in Plane Infinite Structures," *Journal of Engineering Mechanics Division*, ASCE, Vol. 98, Feb. 1972, pp. 85–105.

2 Lysmer, J., and Kuhlemeyer, R. G., "Finite Dynamic Model for Infinite Media," *Journal of Engineering Mechanics Division*, ASCE, Vol. 95, Aug. 1969, pp. 859–877.

3 Kansel, E., Roesset, J. M., and Waas, G., "Dynamic Analysis of Footings on Layered Media," *Journal of Engineering Mechanics Division*, ASCE, Vol. 101, Oct. 1975, pp. 679–693.

4 Ang, A. H. S., and Newmark, N. M., "Development of a Transmitting Boundary for Numerical Wave Motion Calculations," Report to the Defense Atomic Support Agency, Washington, D. C., Apr. 1971.

5 Kalaba, R. E., Yakush, A., and Zagustin, C., "On a Conical Punch Pressing Into an Elastic Layer," *Journal of Elasticity*, Vol. 6, No. 4, 1976, pp. 441–449.

6 Berger, B. S., and Alabi, B., "Solution of Navier's Equation in Cylindrical Curvilinear Coordinates," ASME JOURNAL OF APPLIED MECHANICS, Vol. 45, Dec. 1978, pp. 812–816.

7 Berger, B. S., and Alabi, B., "Steady-State Solution of Navier's Equation in Cylindrical Curvilinear Coordinates," ASME JOURNAL OF APPLIED MECHANICS, Vol. 47, Sept. 1980, pp. 682–683.

8 Eringen, A. C., *Nonlinear Theory of Continuous Media*, McGraw-Hill, New York, 1962.

9 Brebbia, C. A., and Walker, S., *Boundary Element Techniques in Engineering*, Newnes-Butterworths, London, 1980.

10 Davis, P. J., and Rabinowitz, P., *Methods of Numerical Integration*, Academic Press, New York, 1975.

11 Curtis, D. M., "Finite-Difference Boundary Deformation Techniques in the Analysis of Elastic Bodies of Revolution," PhD Thesis, Department of Mechanical Engineering, University of Maryland, College Park, Md., Mar. 1980.

The Influence of Random Longitudinal Vibration on Channel and Pipe Flows of a Slightly Non-Newtonian Liquid

N. Phan-Thien[1]

1 Introduction

It has been observed by Mena, et al. [1], that when a non-Newtonian liquid flows through a circular pipe under a constant pressure gradient, the volumetric output is increased with respect to its Newtonian value if the pipe is subjected to a longitudinal sinusoidal vibration. Their experimental investigation pointed to the following conclusions:

1 The fluid has to be shear-thinning in order to exhibit a positive flow-rate enhancement.

2 This is an inertia phenomenon, i.e., as the vibrational Reynolds number tends to zero, the flow enhancement also tends to zero, the fluid elasticity plays only secondary role here.

3 The flow enhancement increases with increasing frequency of fluctuations. At low frequency ω, this dependence is quadratic in ω.

All of the abovementioned features were predicted by Kazakia and Rivlin [2] who assumed a slightly non-Newtonian fluid which obeys the following constitutive law:

$$\tau_E = 2\eta\mathbf{D} + \epsilon\tau, \quad \epsilon \ll 1, \tag{1}$$

where $2\eta\mathbf{D}$ and $\epsilon\tau$ are the fluid Newtonian and non-Newtonian extra stress tensors, respectively.

It is apparent from (1), that, in a flow field where the velocity is a perturbation about the Newtonian velocity, a knowledge of the Newtonian solution suffices to determine the non-Newtonian effects up to terms of order $O(\epsilon)$. Proceeding in this vein, Kazakia and Rivlin [2] were able to show that the mean flow rate in a channel of width $2h$ is given by

$$\langle Q \rangle = \frac{2Ph^3}{3\eta} - \epsilon \frac{p^3 h^5 \bar{\eta}}{\eta^4}\left\{\frac{2}{5} + 3\left(\frac{\eta V}{Ph^2}\right)^2 \Delta\right\},$$

$$\Delta = \frac{(2h^2\mu^2 + 1)\sinh(2h\mu) - (2h^2\mu^2 - 1)\sin(2h\mu)}{2h\mu[\cosh(2h\mu) + \cos(2h\mu)]} - 1$$

$$\mu^2 = \rho\omega/2\eta \tag{2}$$

whereas in the case of pipe flow (a is the pipe radius) we have

$$\langle Q \rangle = \frac{\pi P a^4}{8\eta} - \epsilon \frac{\pi P^3 a^6 \bar{\eta}}{48\eta^4}\left\{1 + 36\left(\frac{\eta V}{Pa^2}\right)^2 \Delta\right\},$$

$$a\mu[\mathrm{ber}^2(a\mu) + \mathrm{bei}^2(a\mu)](\Delta + 1) = a^2\mu^2[\mathrm{ber}(a\mu)\,\mathrm{ber}'(a\mu) + \mathrm{bei}(a\mu)\,\mathrm{bei}'(a\mu)] + 2[\mathrm{ber}(a\mu)\,\mathrm{bei}'(a\mu) - \mathrm{bei}(a\mu)\,\mathrm{ber}'(a\mu)],$$

$$\mu = \rho\omega/\eta \tag{3}$$

In both cases ρ is the density of the liquid, P, the constant pressure drop, ber (x) and bei (x) are the Kelvin functions of zeroth order and the fluid velocity at the boundaries ($y = \pm h$ or $r = a$) is given by $V \sin \omega t$.

[1] Department of Mechanical Engineering, University of Sydney, N.S.W., 2006, Australia.

Manuscript received by ASME Applied Mechanics Division, August, 1980.

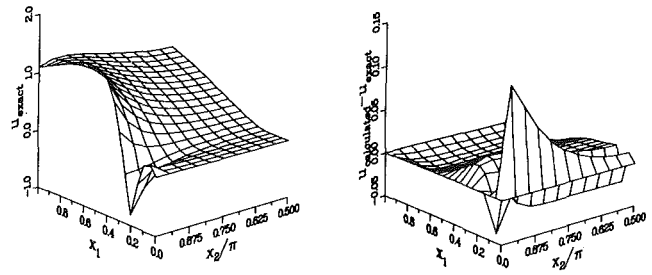

Fig. 2

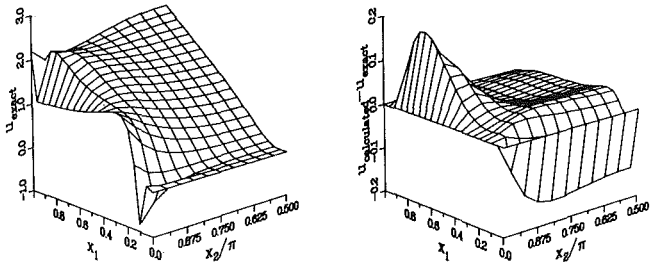

Fig. 3

between the calculated and exact values of u. It is seen that the region of maximum error corresponds to small values of x_1 and therefore large values of $\mathbf{X}_1$. As $x_1 \to 0$, assuming a uniform step size in x_1, the corresponding step size in $\mathbf{X}_1$ becomes infinite. Fig. 3 shows a plot of the exact solution for u and the difference between the calculated and exact values of u for the case of the unindented plane, $\mathbf{X}_2 = 0$, subjected to displacements given by $u^{(1)}$ and $u^{(2)}$. The mapping is given by (7) and (8) with $a_1 = 1/2$, $a_2 = 1/2$, $a_n = 0$ for $n > 2$. Two regions of local maximum error exist, one corresponding to $x_1 = 0$ as before and another near $x_1 = 1$, $x_2 = \pi$. Coordinate lines in the physical plane are very closely spaced and convoluted in the neighborhood of $x_1 = 1$, $x_2 = \pi$ resulting in a loss of accuracy.

References

1 Lysmer, T., and Wass, G., "Shear Waves in Plane Infinite Structures," *Journal of Engineering Mechanics Division*, ASCE, Vol. 98, Feb. 1972, pp. 85–105.

2 Lysmer, J., and Kuhlemeyer, R. G., "Finite Dynamic Model for Infinite Media," *Journal of Engineering Mechanics Division*, ASCE, Vol. 95, Aug. 1969, pp. 859–877.

3 Kansel, E., Roesset, J. M., and Waas, G., "Dynamic Analysis of Footings on Layered Media," *Journal of Engineering Mechanics Division*, ASCE, Vol. 101, Oct. 1975, pp. 679–693.

4 Ang, A. H. S., and Newmark, N. M., "Development of a Transmitting Boundary for Numerical Wave Motion Calculations," Report to the Defense Atomic Support Agency, Washington, D. C., Apr. 1971.

5 Kalaba, R. E., Yakush, A., and Zagustin, C., "On a Conical Punch Pressing Into an Elastic Layer," *Journal of Elasticity*, Vol. 6, No. 4, 1976, pp. 441–449.

6 Berger, B. S., and Alabi, B., "Solution of Navier's Equation in Cylindrical Curvilinear Coordinates," ASME JOURNAL OF APPLIED MECHANICS, Vol. 45, Dec. 1978, pp. 812–816.

7 Berger, B. S., and Alabi, B., "Steady-State Solution of Navier's Equation in Cylindrical Curvilinear Coordinates," ASME JOURNAL OF APPLIED MECHANICS, Vol. 47, Sept. 1980, pp. 682–683.

8 Eringen, A. C., *Nonlinear Theory of Continuous Media*, McGraw-Hill, New York, 1962.

9 Brebbia, C. A., and Walker, S., *Boundary Element Techniques in Engineering*, Newnes-Butterworths, London, 1980.

10 Davis, P. J., and Rabinowitz, P., *Methods of Numerical Integration*, Academic Press, New York, 1975.

11 Curtis, D. M., "Finite-Difference Boundary Deformation Techniques in the Analysis of Elastic Bodies of Revolution," PhD Thesis, Department of Mechanical Engineering, University of Maryland, College Park, Md., Mar. 1980.

The Influence of Random Longitudinal Vibration on Channel and Pipe Flows of a Slightly Non-Newtonian Liquid

N. Phan-Thien[1]

1 Introduction

It has been observed by Mena, et al. [1], that when a non-Newtonian liquid flows through a circular pipe under a constant pressure gradient, the volumetric output is increased with respect to its Newtonian value if the pipe is subjected to a longitudinal sinusoidal vibration. Their experimental investigation pointed to the following conclusions:

1 The fluid has to be shear-thinning in order to exhibit a positive flow-rate enhancement.

2 This is an inertia phenomenon, i.e., as the vibrational Reynolds number tends to zero, the flow enhancement also tends to zero, the fluid elasticity plays only secondary role here.

3 The flow enhancement increases with increasing frequency of fluctuations. At low frequency ω, this dependence is quadratic in ω.

All of the abovementioned features were predicted by Kazakia and Rivlin [2] who assumed a slightly non-Newtonian fluid which obeys the following constitutive law:

$$\tau_E = 2\eta \mathbf{D} + \epsilon \boldsymbol{\tau}, \quad \epsilon \ll 1, \tag{1}$$

where $2\eta\mathbf{D}$ and $\epsilon\boldsymbol{\tau}$ are the fluid Newtonian and non-Newtonian extra stress tensors, respectively.

It is apparent from (1), that, in a flow field where the velocity is a perturbation about the Newtonian velocity, a knowledge of the Newtonian solution suffices to determine the non-Newtonian effects up to terms of order $O(\epsilon)$. Proceeding in this vein, Kazakia and Rivlin [2] were able to show that the mean flow rate in a channel of width $2h$ is given by

$$\langle Q \rangle = \frac{2Ph^3}{3\eta} - \epsilon \frac{p^3 h^5 \bar{\eta}}{\eta^4}\left\{\frac{2}{5} + 3\left(\frac{\eta V}{Ph^2}\right)^2 \Delta\right\},$$

$$\Delta = \frac{(2h^2\mu^2 + 1)\sinh(2h\mu) - (2h^2\mu^2 - 1)\sin(2h\mu)}{2h\mu[\cosh(2h\mu) + \cos(2h\mu)]} - 1$$

$$\mu^2 = \rho\omega/2\eta \tag{2}$$

whereas in the case of pipe flow (a is the pipe radius) we have

$$\langle Q \rangle = \frac{\pi P a^4}{8\eta} - \epsilon \frac{\pi P^3 a^6 \bar{\eta}}{48\eta^4}\left\{1 + 36\left(\frac{\eta V}{Pa^2}\right)^2 \Delta\right\},$$

$$a\mu[\mathrm{ber}^2(a\mu) + \mathrm{bei}^2(a\mu)](\Delta + 1) = a^2\mu^2[\mathrm{ber}(a\mu)\,\mathrm{ber}'(a\mu) + \mathrm{bei}(a\mu)\,\mathrm{bei}'(a\mu)] + 2[\mathrm{ber}(a\mu)\,\mathrm{bei}'(a\mu) - \mathrm{bei}(a\mu)\,\mathrm{ber}'(a\mu)],$$

$$\mu = \rho\omega/\eta \tag{3}$$

In both cases ρ is the density of the liquid, P, the constant pressure drop, ber (x) and bei (x) are the Kelvin functions of zeroth order and the fluid velocity at the boundaries ($y = \pm h$ or $r = a$) is given by $V \sin \omega t$.

[1] Department of Mechanical Engineering, University of Sydney, N.S.W., 2006, Australia.

Manuscript received by ASME Applied Mechanics Division, August, 1980.

In deriving (2) and (3) the non-Newtonian shear stress is assumed to be

$$S = \tilde{\eta}\dot{\kappa} + \hat{\eta}\ddot{\kappa} + \bar{\eta}\kappa^3 \tag{4}$$

where $\tilde{\eta}, \hat{\eta}, \bar{\eta}$ are constants and κ is the shear rate.

In view of the potential applications of this phenomenon and that deterministic vibrations seldom occur in practice, it is attempted here to generalize Kazakia and Rivlin's [2] results to cover the random vibration case.

2 Two-Dimensional Flow

We consider here the channel flow of an incompressible, slightly non-Newtonian fluid which obeys (1) under the action of a constant pressure drop P. The channel walls are located at $y = \pm h$ and are subjected to random vibration. With the no-slip boundary condition, we have

$$u = Vn(t) \quad \text{on} \quad y = \pm h, \tag{5}$$

where u is the x-component velocity, V is a reference velocity, and $n(t)$ is a random function of time which has zero mean. The governing equation for u is

$$\rho \frac{\partial u}{\partial t} = P + \eta \frac{\partial^2 u}{\partial y^2} + \epsilon \frac{\partial S}{\partial y}, \tag{6}$$

where $S = \tau_{12}$ is the non-Newtonian shear stress.

We seek a perturbation solution of the form

$$u = u_0 + \epsilon u_1 + \ldots \tag{7}$$

After solving (5)–(7) for u, the mean volumetric throughput is given by

$$\langle Q \rangle = Q_0 + Q_1 = -\int_{-h}^{h} y \langle \kappa_0 \rangle dy - \epsilon \int_{-h}^{h} y \langle \kappa_1 \rangle dy, \tag{8}$$

where $\kappa_j = \partial u_j / \partial y$ are the shear rates and we have used the fact that $\langle n(t) \rangle = 0$. Here and elsewhere in the paper $\langle \cdot \rangle$ denotes an ensemble average.

The zeroth-order solution is the Newtonian one which obeys

$$\rho \frac{\partial u_0}{\partial t} = P + \eta \frac{\partial^2 u_0}{\partial y^2}, \qquad u_0(\pm h, t) = Vn(t) \tag{9}$$

By taking the Laplace transform of (9) and noting that [3]

$$L^{-1}\left(\frac{\cosh(y\sqrt{P})}{\cosh(h\sqrt{P})}\right) = -\frac{1}{h}\frac{\partial}{\partial y}\theta_1\left(\frac{y}{2h}\middle|\frac{i\pi t}{h^2}\right) = \frac{\pi}{h^2}\sum_{n=0}^{\infty}(-1)^{n+1}(2n+1)e^{-(2n+1)^2\pi^2 t/4h^2} \times \cos\left(\frac{2n+1}{2}\pi y\right),$$

where $L^{-1}[F(p)]$ is the inverse Laplace transform of $F(p)$ and $\theta_1(\cdot|\cdot)$ is the theta function, we have

$$u_0 = \frac{P}{2\eta}(h^2 - y^2) + \frac{\nu\pi V}{h^2}\sum_{n=0}^{\infty}(-1)^n(2n+1)\cos\left(\frac{2n+1}{2}\pi\frac{y}{h}\right) \times \int_{-\infty}^{t} e^{-\alpha_n(t-t')}n(t')dt', \tag{10}$$

$$\kappa_0 = -\frac{Py}{\eta} - \frac{\nu\pi^2 V}{2h^3}\sum_{n=0}^{\infty}(-1)^n(2n+1)^2\sin\left(\frac{2n+1}{2}\pi\frac{y}{h}\right) \times \int_{-\infty}^{t} e^{-\alpha_n(t-t')}n(t')dt', \tag{11}$$

where $\nu = \eta/\rho$ is the kinematic viscosity and

$$\alpha_n = (2n+1)^2\pi^2\nu/4h^2 \tag{12}$$

Note that the lower limit of the integrals appearing in (10)–(11) has been replaced by $-\infty$ since we are interested in the long time behavior of the solution here.

The first-order solution is governed by

$$\rho \frac{\partial u_1}{\partial t} = \eta \frac{\partial^2 u_1}{\partial y^2} + \frac{\partial S_0}{\partial y}, \qquad u_1(\pm h) = 0, \tag{13}$$

where

$$S_0 = S(\kappa_0).$$

If one only looks for long-time behavior of the solution then (13) can be averaged to yield

$$\langle \kappa_1 \rangle = -\langle S_0 \rangle / \eta$$

from which the mean increase in the volumetric output is given by

$$Q_1 = \epsilon \int_{-h}^{h} \frac{\langle S_0 \rangle}{\eta} y\, dy \tag{14}$$

which is identical to the expression given by Kazakia and Rivlin [2].

Following Kazakia and Rivlin [2], we adopt the constitutive law (4) which gives

$$Q_1 = -\epsilon \frac{P^3 h^4 \bar{\eta}}{\eta^4}\left(\frac{2}{5} + 3\left(\frac{\eta V}{Ph^2}\right)^2 \frac{\nu^2\pi^4}{h^4}\sum_{m,n=0}^{\infty}\phi_{mn}\right), \tag{15}$$

where

$$\phi_{mn} = (2n+1)^2(2m+1)^2 \times \left(\frac{1}{3}\delta_{mn} + \frac{2}{\pi^2(m-n)^2}(1-\delta_{mn}) + \frac{2}{\pi^2(m+n+1)^2}\right) \times \int_{-\infty}^{t}\int_{-\infty}^{t} e^{-\alpha_n(t-t') - \alpha_m(t-t'')}\langle n(t')\, n(t'')\rangle\, dt'\, dt'' \tag{16}$$

Note that, since $\bar{\eta} < 0$ and $\phi_{mn} > 0$, (15) shows that there should be an increase in the flow rate.

Also, as Kazakia and Rivlin [2] have pointed out, there are two contributions to the flow enhancement. The first is due to the shear thinning and the second is due to inertia; see (15).

A simplification of (15) and (16) is possible if we assume that $n(t)$ is a stationary random function of time. In this case $n(t)$ can be represented by the following Fourier-Stieltjes integral (spectral representation of $n(t)$ [4])

$$n(t) = \int_{-\infty}^{\infty} e^{i\lambda t}\, dZ(\lambda), \quad i^2 = -1 \tag{17}$$

where $dZ(\lambda)$ is a random function of λ which satisfies

$$\langle dZ(\lambda) \rangle = 0 \tag{18}$$

$$\langle dZ(\lambda_j)\overline{dZ}(\lambda_k)\rangle = \delta_{jk}\,\Omega(\lambda_j)\, d\lambda_j, \quad \text{(no sum)} \tag{19}$$

where the overbar denotes a complex conjugate and $\Omega(\lambda)$ is the spectral power of $n(t)$, viz

$$\Omega(\lambda) = \frac{1}{2\pi}\int_{-\infty}^{\infty} e^{-i\lambda s}\langle n(t+s)\, n(t)\rangle\, ds = \frac{1}{2\pi}\int_{-\infty}^{\infty} e^{-i\lambda s} R(s)\, ds \tag{20}$$

A direct substitution of (17) into (10) yields, after some manipulations,

$$u_0 = \frac{P}{2\eta}(h^2 - y^2) + V\int_{-\infty}^{\infty}\frac{\cosh\left(\sqrt{\frac{i\lambda}{\nu}}y\right)}{\cosh\left(\sqrt{\frac{i\lambda}{\nu}}h\right)}e^{i\lambda t}\, dZ(\lambda) \tag{21}$$

Proceeding as before, we obtain the mean increase in the flow rate as

$$Q_1 = -\epsilon\frac{\overline{\eta}}{\eta}\left(\frac{2P^3h^5}{5\eta^4} + 6\frac{P}{\eta}V^2\int_0^\infty\left(-2h + \sqrt{\frac{2\lambda}{\nu}}\,\frac{\left(h^2+\frac{\nu}{\lambda}\right)\sinh\left(\sqrt{\frac{2\lambda}{\nu}}h\right) - \left(h^2-\frac{\nu}{\lambda}\right)\sin\left(\sqrt{\frac{2\lambda}{\nu}}h\right)}{\cosh\left(\sqrt{\frac{2\lambda}{\nu}}h\right) + \cos\left(\sqrt{\frac{2\lambda}{\nu}}h\right)}\right)\Omega(\lambda)\,d\lambda\right) \quad (22)$$

Denoting

$$\mu^2 = \lambda/2\nu, \quad (23)$$

and

$$\Delta = \frac{(2\mu^2h^2+1)\sinh(2\mu h) - (2h^2\mu^2-1)\sin(2\mu h)}{2\mu h[\cosh(2\mu h)+\cos(2\mu h)]} - 1, \quad (24)$$

we have

$$Q_1 = -\epsilon\frac{P^3h^4\overline{\eta}}{\eta^4}\left(\frac{2}{5} + 12\left(\frac{nV}{Ph^2}\right)^2\int_0^\infty\Delta(\lambda)\,\Omega(\lambda)\,d\lambda\right). \quad (25)$$

For sinusoidal vibration where $n(t) = \cos\omega t$ (or $\sin\omega t$), the spectral power is

$$\Omega(\lambda) = \tfrac{1}{4}[\delta(\lambda+\omega) + \delta(\lambda-\omega)]$$

and Kazakia and Rivlin's results, equation (2), are recovered.

For low-frequency vibrations, $\Omega(\lambda)$ is mainly concentrated at $\lambda \sim 0$ from which we can approximate the integral in (25) by

$$\int_0^\infty\Delta(\lambda)\,\Omega(\lambda)\,d\lambda \sim \frac{h^4}{5\nu^2}\int_0^\infty\lambda^2\Omega(\lambda)\,d\lambda = \frac{h^4}{10\nu^2}\langle\dot{n}^2(t)\rangle + E \quad (26)$$

where $\dot{n}(t) = dn/dt$ and E is an error term of order

$$O\left(\int_{-\infty}^\infty\lambda^4\,\Omega(\lambda)\,d\lambda\right).$$

In this case, the mean increase in the flow rate is directly proportional to the mean square of the pipe acceleration:

$$Q_1 \sim -\epsilon\frac{2P^3h^5\overline{\eta}}{5\eta^4}\left(1 + 3\left(\frac{\rho V}{P}\right)^2\langle\dot{n}^2\rangle\right). \quad (27)$$

Another simplification to (25) is possible if $\Omega(\lambda)$ is mainly contributed by a spike at $\lambda = \omega$ [the "natural" frequency of $n(t)$]. In this case

$$Q_1 \sim -\epsilon\frac{p^3h^5\overline{\eta}}{\eta^4}\left(\frac{2}{5} + 6\left(\frac{\eta V}{Ph^2}\right)^2 \times\left[\left(\Delta_0 + \frac{\omega^2}{2}\Delta''_0\right)\langle n^2\rangle + \frac{1}{2}\Delta''_0\langle\dot{n}^2\rangle + E\right]\right) \quad (28)$$

here we have used the shorthand notation

$$\Delta_0 = \Delta(\omega), \quad \Delta_0'' = \left.\frac{d^2\Delta(\lambda)}{d\lambda^2}\right|_{\lambda=\omega}$$

and E is an error term of order $O\left(\int_{-\infty}^\infty(\lambda-\omega)^4\,\Omega(\lambda)\,d\lambda\right)$.

3 Pipe Flow

Next, we consider the pipe flow problem where the governing equations for the axial velocity u are

$$\rho\frac{\partial u}{\partial t} = \frac{\eta}{r}\frac{\partial}{\partial r}r\frac{\partial u}{\partial r} + \epsilon\frac{1}{r}\frac{\partial}{\partial r}(rS), \quad (29)$$

$$u(a,t) = Vn(t). \quad (30)$$

Again, $S = \tau_{rz}$ is the non-Newtonian shear stress and we seek for a perturbation solution of the form (7). Knowing the axial velocity, the mean volumetric flow rate is given by

$$\langle Q\rangle = Q_0 + Q_1 = -\pi\int_0^a r^2\langle\kappa_0\rangle\,dr - \epsilon\pi\int_0^a r^2\langle\kappa_1\rangle\,dr, \quad (31)$$

where $\kappa_j = \partial u_j/\partial r$ are the shear rates.

The zeroth-order solution is governed by

$$\rho\frac{\partial u_0}{\partial t} = P + \frac{\eta}{r}\frac{\partial}{\partial r}r\frac{\partial u_0}{\partial r}$$

$$u_0(a,t) = V\,n(t) \quad (32)$$

By taking the finite Handel transform of order zero [5]

$$\mathcal{H}[f(r)] = \int_0^a r\,J_0(p_ir)\,f(r)\,dr,$$

where p_ia is a root of the zeroth-order Bessel function $J_0(x)$, we obtain

$$u_0 = \frac{P}{4\eta}(a^2-r^2) + 2\sum_i\frac{V\nu P_i}{a}\frac{J_0(P_ir)}{J_1(P_ia)}\int_{-\infty}^t e^{-\nu P_i^2(t-t')}\,n(t')\,dt', \quad (33)$$

where $J_1(x) = -J'_0(x)$ is the first-order Bessel function. Again the lower limit of the integral appearing in (33) has been replaced by $-\infty$ since we are interested in the long-time behavior here.

Thus the Newtonian shear rate is given by

$$\kappa_0 = \frac{Pr}{2\eta} - 2V\sum_i\frac{\nu P_i^2}{a}\frac{J_1(P_ir)}{J_1(P_ia)}\int_{-\infty}^t e^{-\nu P_i^2(t-t')}\,n(t')dt' \quad (34)$$

Now the first-order solution is governed by

$$\rho\frac{\partial u_1}{\partial t} = \frac{\eta}{r}\frac{\partial}{\partial r}r\frac{\partial u_1}{\partial r} + \frac{1}{r}\frac{\partial}{\partial r}(rS_0).$$

$$u_1(a,t) = 0, \quad (35)$$

where

$$S_0 = S(\kappa_0).$$

Again, if long-time behavior of the solution is sought after then we can average (35) which yields

$$\langle\kappa_1\rangle = -\langle S_0\rangle/\eta \quad (36)$$

Thus the mean increase in the flow rate is given by

$$Q_1 = \pi\int_0^a\frac{\langle S_0\rangle}{\eta}r^2\,dr \quad (37)$$

which is identical to Kazakia and Rivlin's [2] result.

Adopting the constitutive low (4) and expressing $J_1(P_ir)\,J_1(P_jr)$ as a convergent series in terms of the hypergeometric function $F(\alpha, \beta; \gamma; \delta)$, we finally obtain

$$Q_1 = \frac{\pi P^3a^6\overline{\eta}}{48\eta^4}\left(1 + 36\left(\frac{\eta V}{Pa^2}\right)^2\sum_{i,j}\phi_{ij}\right), \quad (38)$$

where

$$\phi_{ij} = \frac{\nu^2a^2P_i^3P_j^3}{J_1(P_ia)\,J_1(P_ja)}\sum_{k=0}^\infty\frac{(-1)^k}{k!(k+1)!\,(k+3)} \times\left(\frac{P_ia}{2}\right)^{2k}F\left(-k,-k-1;2;\frac{P_j^2}{P_i^2}\right) \times\int_{-\infty}^t\int_{-\infty}^t e^{-\nu P_i^2(t-t')-\nu P_j^2(t-t'')}\langle n(t')\,n(t'')\rangle\,dt'\,dt'' \quad (39)$$

A simplification of these unwieldy expressions is possible if we assume that $n(t)$ is a stationary random function of time which obeys (17)–(20). In this case a direct substitution of (17) into (33) yields

$$u_0 = \frac{P}{4\eta}(a^2-r^2) + V \times\int_{-\infty}^\infty\frac{\mathrm{ber}\,(\mu r) + i\,\mathrm{bei}\,(\mu r)}{\mathrm{ber}\,(\mu a) + i\,\mathrm{bei}\,(\mu a)}e^{i\lambda t}\,dZ(\lambda), \quad i^2 = -1, \quad (40)$$

where ber (x), bei (x) are the Kelvin functions of zeroth order and

$$\mu^2 = \lambda/\nu \tag{41}$$

Alternatively we can assume that $n(t)$ is a stationary random function from the outset and look for solution of the form

$$u_0 = \frac{P}{4\eta}(a^2 - r^2) + \int_{-\infty}^{\infty} \phi(r,\lambda)\, e^{i\lambda t}\, dZ(\lambda). \tag{42}$$

A direct substitution of (42) into (32) will reveal that $\phi(r,\lambda)$ takes the form indicated in (40).

Proceeding as before, it is easy to show that the mean increase in the flow rate is given by

$$\begin{aligned} Q_1 &= -\epsilon \frac{\pi\overline{\eta}}{\eta}\left(\frac{p^3a^6}{48\eta^4} + \frac{PV^2}{\eta}\right. \\ &\quad \left. \times \int_0^a dr \int_0^{\infty} d\lambda \frac{\mathrm{ber}'^2(\mu r) + \mathrm{bei}'^2(\mu r)}{\mathrm{ber}^2(\mu a) + \mathrm{bei}^2(\mu a)} r^3\, \Omega(\lambda)\right) \\ &= -\epsilon \frac{\pi P^3 a^6 \overline{\eta}}{48\eta^4}\left(1 + 144\left(\frac{\eta V}{Pa^2}\right)^2 \int_0^{\infty} \Delta(\lambda)\, \Omega(\lambda)\, d\lambda\right), \end{aligned} \tag{43}$$

where $\Delta(\lambda)$ is given by

$$\begin{aligned} &a\mu[\mathrm{ber}^2(a\mu) + \mathrm{bei}^2(a\mu)]\,(\Delta + 1) \\ &\quad = a^2\mu^2[\mathrm{ber}(a\mu)\,\mathrm{ber}'(a\mu) + \mathrm{bei}(a\mu)\,\mathrm{bei}'(a\mu)] \\ &\qquad + 2[\mathrm{ber}(a\mu)\,\mathrm{bei}'(a\mu) - \mathrm{bei}(a\mu)\,\mathrm{ber}'(a\mu)] \end{aligned} \tag{44}$$

If $n(t)$ is sinusoidal with frequency ω, then Kazakia and Rivlin's [2] results, equation (3), are recovered.

Again, the two approximations mentioned in Section 2 are recorded here.

First, for low-frequency vibrations, $\Omega(\lambda)$ is mainly concentrated at $\lambda \sim 0$ from which we have

$$Q_1 \sim -\epsilon \frac{\pi P^3 a^6 \overline{\eta}}{48\eta^4}\left(1 + 3\left(\frac{\rho V}{P}\right)^2 (\langle \dot{n}^2 \rangle + E)\right), \tag{45}$$

where E is an error term of order $O\left(\int_{-\infty}^{\infty} \lambda^4\, \Omega(\lambda)\, d\lambda\right)$.

Finally, if $n(t)$ has a dominant "natural" frequency ω in the sense discussed in Section 2, then

$$\begin{aligned} Q_1 \sim -\epsilon \frac{\pi P^3 a^6 \overline{\eta}}{48\eta^4}\left(1 + 72\left(\frac{\eta V}{Pa^2}\right)^2 \left[\left(\Delta_0 + \frac{\omega^2}{2}\Delta''_0\right)\right.\right. \\ \left.\left. \times \langle n^2 \rangle + \frac{1}{2}\Delta''_0 \langle \dot{n}^2 \rangle + E\right]\right) \end{aligned} \tag{46}$$

where we have used the shorthand notation

$$\Delta_0 = \Delta(\omega), \quad \Delta''_0 = \left.\frac{d^2\Delta(\lambda)}{d\lambda^2}\right|_{\lambda=\omega},$$

and E is an error term of order $O\left(\int_{-\infty}^{\infty} (\lambda - \omega)^4\, \Omega(\lambda)\, d\lambda\right)$.

In summarizing, we have solved the Mena flow problem [1] for a slightly non-Newtonian liquid where the longitudinal vibration is an arbitrary random function of time. Any deterministic vibration which satisfies Dirichlet's conditions so that it can be represented by a Fourier series is a special case of this. If the fluid is markedly non-Newtonian, then an alternative approach to this problem is to consider a perturbation about the "vibrational" Reynolds number, $R_V = aV/\nu \sim 0$. The data of Mena, et al. [1], seem to satisfy this requirement: $R \sim 0.1 - 0.5$. This was considered elsewhere [6].

Acknowledgment

The support of the Australian Research Grants Committee is gratefully acknowledged.

References

1 Mena, B., Menaro, O., and Binding, D. M., *Journal of Non-Newtonian Fluid Mechanics*, Vol. 5, 1979, pp. 427–448.

2 Kazakia, J. Y., and Rivlin, R. S., *Rheology Acta*, Vol. 17, 1978, pp. 210–226.

3 *Bateman Manuscript Project*, ed., Erdélyi, A., Vol. 1, McGraw-Hill, New York, 1954.

4 Yaglom, A. M., *An Introduction to the Theory of Stationary Random Functions*, translated and edited by Silverman, R. A., Prentice-Hall, Englewood Cliffs, N.J., 1962.

5 Tranter, C. J., *Integral Transforms in Mathematical Physics*, Methuen's Monographs on Physical subjects, Methuen & Co., London, 1951.

6 Phan-Thien, N., *Rheology Acta*, Vol. 19, 1980, pp. 539–547.

On the Space of Stress Invariants

V. K. Stokes[1]

The representation of stress through its three invariants I_1, I_2, and I_3 has been examined. It has been shown that all possible states of stress are mapped into a connected region of the space of stress invariants that is bounded by two surfaces which meet in a cusp on a curve which corresponds to states of isotropic stress. All other states of stress for which two principal stresses are equal, lie on this surface. The I_1 axis corresponds to one-dimensional states of stress. Two-dimensional stresses are represented by a connected region of the I_1-I_2 plane. The negative half of the I_2 axis corresponds to pure shear. The positive half of the I_2 axis, and the I_3 axis, do not correspond to any states of stress. The representation of yield surfaces in this space has also been considered.

Introduction

In one representation the state of symmetric stress at a point in a continuum is indicated by a point in the space of principal stresses, in which the three principal stresses σ_1, σ_2, and σ_3 are the rectangular Cartesian coordinates of a point $\boldsymbol{\sigma} = (\sigma_1, \sigma_2, \sigma_3)$. There is a certain lack of uniqueness in this representation. For, corresponding to a state of stress in which the principal stresses are σ_1, σ_2, and σ_3, the associated principal directions forming a right-handed system, there are, in general, six distinct points in principal stress space, namely, $\boldsymbol{\sigma}_1 = (\sigma_1, \sigma_2, \sigma_3)$, $\boldsymbol{\sigma}_2 = (\sigma_2, \sigma_3, \sigma_1)$, $\boldsymbol{\sigma}_3 = (\sigma_3, \sigma_1, \sigma_2)$, $\boldsymbol{\sigma}_4 = (\sigma_1, \sigma_3, \sigma_2)$, $\boldsymbol{\sigma}_5 = (\sigma_3, \sigma_2, \sigma_1)$ and $\boldsymbol{\sigma}_6 = (\sigma_2, \sigma_1, \sigma_3)$.

In some applications the ordering of the principal stresses is not important and each principal stress has the same weightage for the same magnitude. In such situations it is appropriate to use symmetric functions of the principal stresses, whose values would be the same for $\boldsymbol{\sigma}_1$, $\boldsymbol{\sigma}_2$, $\boldsymbol{\sigma}_3$, $\boldsymbol{\sigma}_4$, $\boldsymbol{\sigma}_5$, and $\boldsymbol{\sigma}_6$. The simplest and most important symmetric functions are the principal invariants of the stress tensor.

Preliminary Definitions

For a given symmetric stress tensor $\mathbf{T}$ the principal stresses σ are the roots of the characteristic equation

$$\sigma^3 - I_1\sigma^2 + I_2\sigma - I_3 = 0, \tag{1}$$

Where I_1, I_2, and I_3, the three principal invariants of stress, are given by

$$\begin{aligned} I_1 &= \mathrm{tr}\,\mathbf{T} = \sigma_1 + \sigma_2 + \sigma_3 \\ I_2 &= \tfrac{1}{2}(\mathrm{tr}^2\,\mathbf{T} - \mathrm{tr}\,\mathbf{T}^2) = \sigma_1\sigma_2 + \sigma_2\sigma_3 + \sigma_3\sigma_1 \\ I_3 &= \det \mathbf{T} = \sigma_1\sigma_2\sigma_3 \end{aligned} \tag{2}$$

where σ_1, σ_2, and σ_3 are the three principal stresses. Furthermore, for symmetric $\mathbf{T}$,

[1] General Electric Company, Corporate Research and Development, Schenectady, N. Y. 12301 Mem. ASME.

Manuscript received by ASME Applied Mechanics Division, May, 1980; final revision, February, 1981.

where ber (x), bei (x) are the Kelvin functions of zeroth order and

$$\mu^2 = \lambda/\nu \tag{41}$$

Alternatively we can assume that $n(t)$ is a stationary random function from the outset and look for solution of the form

$$u_0 = \frac{P}{4\eta}(a^2 - r^2) + \int_{-\infty}^{\infty} \phi(r,\lambda)\, e^{i\lambda t}\, dZ(\lambda). \tag{42}$$

A direct substitution of (42) into (32) will reveal that $\phi(r,\lambda)$ takes the form indicated in (40).

Proceeding as before, it is easy to show that the mean increase in the flow rate is given by

$$Q_1 = -\epsilon \frac{\pi\overline{\eta}}{\eta}\left(\frac{p^3a^6}{48\eta^4} + \frac{PV^2}{\eta} \times \int_0^a dr \int_0^{\infty} d\lambda \frac{\mathrm{ber}'^2(\mu r) + \mathrm{bei}'^2(\mu r)}{\mathrm{ber}^2(\mu a) + \mathrm{bei}^2(\mu a)} r^3\, \Omega(\lambda)\right)$$
$$= -\epsilon \frac{\pi P^3 a^6 \overline{\eta}}{48\eta^4}\left(1 + 144\left(\frac{\eta V}{Pa^2}\right)^2 \int_0^{\infty} \Delta(\lambda)\, \Omega(\lambda)\, d\lambda\right), \tag{43}$$

where $\Delta(\lambda)$ is given by

$$a\mu[\mathrm{ber}^2(a\mu) + \mathrm{bei}^2(a\mu)]\,(\Delta + 1) = a^2\mu^2[\mathrm{ber}(a\mu)\,\mathrm{ber}'(a\mu) + \mathrm{bei}(a\mu)\,\mathrm{bei}'(a\mu)] + 2[\mathrm{ber}(a\mu)\,\mathrm{bei}'(a\mu) - \mathrm{bei}(a\mu)\,\mathrm{ber}'(a\mu)] \tag{44}$$

If $n(t)$ is sinusoidal with frequency ω, then Kazakia and Rivlin's [2] results, equation (3), are recovered.

Again, the two approximations mentioned in Section 2 are recorded here.

First, for low-frequency vibrations, $\Omega(\lambda)$ is mainly concentrated at $\lambda \sim 0$ from which we have

$$Q_1 \sim -\epsilon \frac{\pi P^3 a^6 \overline{\eta}}{48\eta^4}\left(1 + 3\left(\frac{\rho V}{P}\right)^2 (\langle \dot{n}^2 \rangle + E)\right), \tag{45}$$

where E is an error term of order $O\left(\int_{-\infty}^{\infty} \lambda^4\, \Omega(\lambda)\, d\lambda\right)$.

Finally, if $n(t)$ has a dominant "natural" frequency ω in the sense discussed in Section 2, then

$$Q_1 \sim -\epsilon \frac{\pi P^3 a^6 \overline{\eta}}{48\eta^4}\left(1 + 72\left(\frac{\eta V}{Pa^2}\right)^2 \left[\left(\Delta_0 + \frac{\omega^2}{2}\Delta''_0\right) \times \langle n^2 \rangle + \frac{1}{2}\Delta''_0\, \langle \dot{n}^2 \rangle + E\right]\right) \tag{46}$$

where we have used the shorthand notation

$$\Delta_0 = \Delta(\omega), \quad \Delta''_0 = \left.\frac{d^2\Delta(\lambda)}{d\lambda^2}\right|_{\lambda=\omega},$$

and E is an error term of order $O\left(\int_{-\infty}^{\infty} (\lambda - \omega)^4\, \Omega(\lambda)\, d\lambda\right)$.

In summarizing, we have solved the Mena flow problem [1] for a slightly non-Newtonian liquid where the longitudinal vibration is an arbitrary random function of time. Any deterministic vibration which satisfies Dirichlet's conditions so that it can be represented by a Fourier series is a special case of this. If the fluid is markedly non-Newtonian, then an alternative approach to this problem is to consider a perturbation about the "vibrational" Reynolds number, $R_V = aV/\nu \sim 0$. The data of Mena, et al. [1], seem to satisfy this requirement: $R \sim 0.1 - 0.5$. This was considered elsewhere [6].

Acknowledgment

The support of the Australian Research Grants Committee is gratefully acknowledged.

References

1 Mena, B., Menaro, O., and Binding, D. M., *Journal of Non-Newtonian Fluid Mechanics*, Vol. 5, 1979, pp. 427–448.

2 Kazakia, J. Y., and Rivlin, R. S., *Rheology Acta*, Vol. 17, 1978, pp. 210–226.

3 *Bateman Manuscript Project*, ed., Erdélyi, A., Vol. 1, McGraw-Hill, New York, 1954.

4 Yaglom, A. M., *An Introduction to the Theory of Stationary Random Functions*, translated and edited by Silverman, R. A., Prentice-Hall, Englewood Cliffs, N.J., 1962.

5 Tranter, C. J., *Integral Transforms in Mathematical Physics*, Methuen's Monographs on Physical subjects, Methuen & Co., London, 1951.

6 Phan-Thien, N., *Rheology Acta*, Vol. 19, 1980, pp. 539–547.

On the Space of Stress Invariants

V. K. Stokes[1]

The representation of stress through its three invariants I_1, I_2, and I_3 has been examined. It has been shown that all possible states of stress are mapped into a connected region of the space of stress invariants that is bounded by two surfaces which meet in a cusp on a curve which corresponds to states of isotropic stress. All other states of stress for which two principal stresses are equal, lie on this surface. The I_1 axis corresponds to one-dimensional states of stress. Two-dimensional stresses are represented by a connected region of the I_1-I_2 plane. The negative half of the I_2 axis corresponds to pure shear. The positive half of the I_2 axis, and the I_3 axis, do not correspond to any states of stress. The representation of yield surfaces in this space has also been considered.

Introduction

In one representation the state of symmetric stress at a point in a continuum is indicated by a point in the space of principal stresses, in which the three principal stresses σ_1, σ_2, and σ_3 are the rectangular Cartesian coordinates of a point $\boldsymbol{\sigma} = (\sigma_1, \sigma_2, \sigma_3)$. There is a certain lack of uniqueness in this representation. For, corresponding to a state of stress in which the principal stresses are σ_1, σ_2, and σ_3, the associated principal directions forming a right-handed system, there are, in general, six distinct points in principal stress space, namely, $\boldsymbol{\sigma}_1 = (\sigma_1, \sigma_2, \sigma_3)$, $\boldsymbol{\sigma}_2 = (\sigma_2, \sigma_3, \sigma_1)$, $\boldsymbol{\sigma}_3 = (\sigma_3, \sigma_1, \sigma_2)$, $\boldsymbol{\sigma}_4 = (\sigma_1, \sigma_3, \sigma_2)$, $\boldsymbol{\sigma}_5 = (\sigma_3, \sigma_2, \sigma_1)$ and $\boldsymbol{\sigma}_6 = (\sigma_2, \sigma_1, \sigma_3)$.

In some applications the ordering of the principal stresses is not important and each principal stress has the same weightage for the same magnitude. In such situations it is appropriate to use symmetric functions of the principal stresses, whose values would be the same for $\boldsymbol{\sigma}_1$, $\boldsymbol{\sigma}_2$, $\boldsymbol{\sigma}_3$, $\boldsymbol{\sigma}_4$, $\boldsymbol{\sigma}_5$, and $\boldsymbol{\sigma}_6$. The simplest and most important symmetric functions are the principal invariants of the stress tensor.

Preliminary Definitions

For a given symmetric stress tensor $\mathbf{T}$ the principal stresses σ are the roots of the characteristic equation

$$\sigma^3 - I_1\sigma^2 + I_2\sigma - I_3 = 0, \tag{1}$$

Where I_1, I_2, and I_3, the three principal invariants of stress, are given by

$$I_1 = \mathrm{tr}\,\mathbf{T} = \sigma_1 + \sigma_2 + \sigma_3$$
$$I_2 = \tfrac{1}{2}(\mathrm{tr}^2\,\mathbf{T} - \mathrm{tr}\,\mathbf{T}^2) = \sigma_1\sigma_2 + \sigma_2\sigma_3 + \sigma_3\sigma_1 \tag{2}$$
$$I_3 = \det \mathbf{T} = \sigma_1\sigma_2\sigma_3$$

where σ_1, σ_2, and σ_3 are the three principal stresses. Furthermore, for symmetric $\mathbf{T}$,

[1] General Electric Company, Corporate Research and Development, Schenectady, N. Y. 12301 Mem. ASME.

Manuscript received by ASME Applied Mechanics Division, May, 1980; final revision, February, 1981.

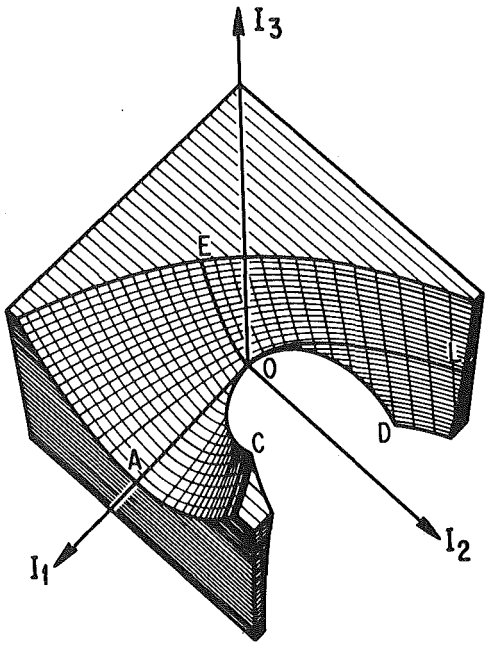

Fig. 1 Perspective view of the region $F \geq 0$ for the range: $|I_1| \leq 50$, $|I_2| \leq 500$, and $|I_3| \leq 1000$

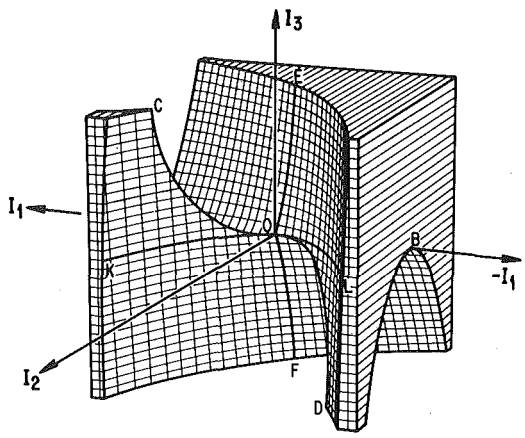

Fig. 2 Perspective view of the region $F \geq 0$ for the range: $|I_1| \leq 50$, $|I_2| \leq 500$, and $|I_3| \leq 1000$

$$F(I_1, I_2, I_3) = I_2^2(I_1^2 - 4I_2) - 27I_3^2 + 2I_1I_3(9I_2 - 2I_1^2) \quad (3)$$

satisfies $F(I_1, I_2, I_3) \geq 0$. When $F = 0$ either two or all three roots of the characteristic equation are equal. The three real roots are distinct when $F > 0$, and in this case there is only one set of mutually orthogonal principal directions.

A stress distribution is one, two, or three-dimensional if only one, only two or all three of the principal stresses are, respectively, nonzero. This gives rise to the following geometrical interpretation for the invariants of stress. A necessary and sufficient condition for a stress distribution to be three-dimensional is that the third invariant of stress be nonzero. A stress distribution is two-dimensional if and only if the third invariant is zero and the second invariant is nonzero. A stress distribution is one-dimensional if and only if the second and third invariants are zero, and the first invariant is nonzero. Finally, a stress distribution is identically zero if and only if all the three invariants are zero.

Space of Stress Invariants

The main purpose of this paper is to investigate the representation of symmetric stress through its three invariants I_1, I_2, and I_3. By definition, the space of stress invariants is a rectangular Cartesian space in which the coordinates of a point are the invariants I_1, I_2, and I_3; so that a typical point has the coordinates $\mathbf{I} = (I_1, I_2, I_3)$. Whereas each state of stress, represented in principal stress space $\boldsymbol{\sigma} = (\sigma_1, \sigma_2, \sigma_3)$, gives rise to a corresponding point $\mathbf{I} = (I_1, I_2, I_3)$ in the space of stress invariants, the converse is not necessarily true. First of all, there are points $\mathbf{I} = (I_1, I_2, I_3)$ to which do not correspond any points in stress space. In fact the regions of $\mathbf{I}$-space which correspond to points in $\boldsymbol{\sigma}$-space are precisely those in which $F(I_1, I_2, I_3) \geq 0$. Second, it must be remembered that the mapping $\boldsymbol{\sigma} \rightarrow \mathbf{I}$ is not one-to-one. For example, as mentioned earlier, the six points $\boldsymbol{\sigma}_1$, $\boldsymbol{\sigma}_2$, $\boldsymbol{\sigma}_3$, $\boldsymbol{\sigma}_4$, $\boldsymbol{\sigma}_5$, and $\boldsymbol{\sigma}_6$ in $\boldsymbol{\sigma}$-space correspond to one point in $\mathbf{I}$-space.

First consider the coordinate axes I_1, I_2, and I_3. It follows from the characteristic equation, in equation (1), that (*i*) $I_2 = 0, I_3 = 0$ implies $\boldsymbol{\sigma} = (I_1, 0, 0)$; (*ii*) $I_3 = 0, I_1 = 0$ implies $\boldsymbol{\sigma} = ((-I_2)^{1/2}, (-I_2)^{1/2}, 0)$; and (*iii*) $I_1 = 0, I_2 = 0$ implies $\boldsymbol{\sigma} = (I_3^{1/3}, I_3^{1/3} \exp(2\pi i/3), I_3^{1/3} \exp(-2\pi i/3))$. Thus the I_1 axis represents one-dimensional states of stress, such that its positive and negative portions correspond, respectively, to uniaxial tension and uniaxial compression. Since a point on the I_2 axis corresponds to the principal stresses $(\sigma, -\sigma, 0)$ where $\sigma = (-I_2)^{1/2}$, only the negative half of the I_2 axis corresponds to real states of stress, and represents states of pure shear. Finally, it is evident that points on the I_3 axis, except for $I_3 = 0$—which corresponds to a zero state of stress, do not represent any real states of stress.

Next consider the coordinate planes. The region of the I_1-I_2 plane which corresponds to real stresses is determined, from equation (3), by $F(I_1, I_2, 0) = I_2^2(I_2^2 - 4I_2) \geq 0$. The boundaries of this region, which must correspond to repeated roots of the characteristic equation, are given: (*i*) by $I_2 = 0, 0$—which is the I_1 axis, and (*ii*) by the parabola $I_1^2 = 4I_2$. In fact the I_1 axis represents the one-dimensional stress distribution $\boldsymbol{\sigma} = (I_1, 0, 0)$, the repeated roots being 0 and 0. With $I_3 = 0$ and $I_1^2 = 4I_2$, the roots of the characteristic equation are $(\sigma, \sigma, 0)$ where $\sigma = \pm(I_2)^{1/2}$. Thus the right half of the parabola $I_1^2 = 4I_2$, for which $\sigma \geq 0$, corresponds to states of two-dimensional isotropic compression. Thus, except for the interior of the parabola $I_1^2 = 4I_2$, the I_1-I_2 plane represents two-dimensional states of stress. The regions of this plane which correspond to real stresses are then determined, from equation (3), by $4I_2^3 + 27I_3^2 \leq 0$, the boundaries of which are given by the curves $4I_2^3 + 27I_3^2 = 0$. Finally, the regions of the I_3-I_1 plane which correspond to real stresses, are determined by the condition $I_3(27I_3^2 + 4I_1^3) \leq 0$, and therefore lie between the curve $27I_3^2 + 4I_1^3 = 0$ and the line $I_3 = 0$.

The region $F \geq 0$ in $\mathbf{I}$-space determines points that correspond to real states of stress. It follows from equation (3) that $F(-I_1, I_2, I_3) = F(I_1, I_2, -I_3)$. Because of this, the surface $F = 0$ need only be determined in the region: $I_1 \geq 0$, $-\infty \leq I_2 \leq \infty$ and $-\infty \leq I_3 \leq \infty$.

A feel for the surface $F = 0$ and the region, $F \geq 0$, which corresponds to real states of stress, can be had from perspective views shown in Figs. 1 and 2 in which the values of $\mathbf{I}$ lie in the ranges: $-50 \leq I_1 \leq 50$, $-500 \leq I_2 \leq 500$ and $-1000 \leq I_3 \leq 1000$. These perspective views are made up of contours of I_1 and I_3. The surface $F = 0$ corresponds to states of stress of the form $\boldsymbol{\sigma} = (\sigma, \sigma, p)$ in which at least two of the principal stresses are equal. It consists of an upper and a lower sheet that meet in a cusp along the curve COD, which represents the isotropic state of stress $\boldsymbol{\sigma} = (\sigma, \sigma, \sigma)$. For all points on this surface, other than those on COD, $\sigma \neq p$. Only the upper sheet of the surface $F = 0$ is visible in Fig. 1. Points on OE correspond to stresses of the form $(\sigma, \sigma, -2\sigma)$ with $\sigma < 0$. Points on the parabola OL correspond to $\boldsymbol{\sigma} = (\sigma, \sigma, 0)$ with $\sigma < 0$. Also, points on the I_1 axis, OA, correspond to $\boldsymbol{\sigma} = (\sigma, 0, 0)$. A view of both sheets of $F = 0$ meeting in a cusp along COD is shown in Fig. 2. In this view both branches KO and OL, of the parabola $I_1^2 = 4I_2$, which correspond to states of stress $\boldsymbol{\sigma} = (\sigma, \sigma, 0)$ with $\sigma > 0$ and $\sigma < 0$, respectively, are visible. Also, both branches OE and OF of the curve $4I_2^3 + 27I_3^2 = 0$, which correspond to stresses of the form $\boldsymbol{\sigma} = (\sigma, \sigma, -2\sigma)$ with $\sigma < 0$ and $\sigma > 0$, respectively, can be seen to meet in a cusp at 0.

Next consider the surface $I_3 = I_1I_2$. It turns out that equation (1) then has the roots $\sigma = I_1$, $(-I_2)^{1/2}$ and $-(-I_2)^{1/2}$. Thus all points on

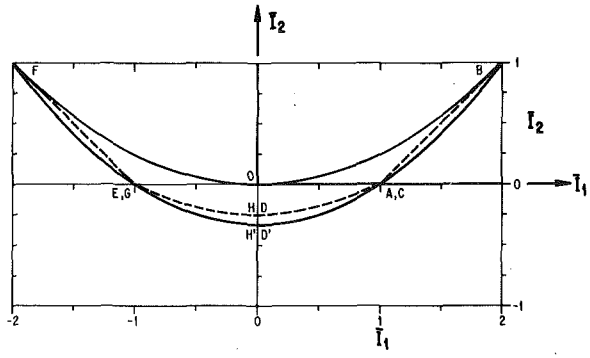

Fig. 3 von Mises' and Tresca's yield loci in the $\bar{I}_1$-$\bar{I}_2$ plane for two-dimensional stress distributions

the surface $I_3 = I_1 I_2$, $I_2 \leq 0$, correspond to the state of stress $\sigma = (\sigma, -\sigma, p)$ where $p = I_1$ and $\sigma = (-I_2)^{1/2}$. The negative half of the I_2 axis, which must lie on this surface, corresponds to pure shear $\sigma = (\sigma, -\sigma, 0)$.

Yield Surfaces

Two important yield criteria are those due to von Mises and Tresca. For von Mises' yield criterion, the yield surface in σ-space is defined by $(\sigma_1 - \sigma_2)^2 + (\sigma_2 - \sigma_3)^2 + (\sigma_3 - \sigma_1)^2 = 2\sigma_0^2 = 6k^2$ where σ_0 is the yield stress in tension and k that in pure shear. In terms of invariants, this yield surface is $f_M(I_1, I_2, I_3) = 0$, where $f_M = I_1^2 - 3I_2 - \sigma_0^2$. Yield occurs if $f_M > 0$.

In terms of principal stresses, the yield surface for Tresca's criterion is given by $|\sigma_1 - \sigma_2| = \sigma_0$, $|\sigma_2 - \sigma_3| = \sigma_0$, and $|\sigma_3 - \sigma_1| = \sigma_0$, which, upon using a representation given in reference [1], reduces to $f_T(I_1, I_2, I_3) = 0$, where $f_T(I_1, I_2, I_3) = F(I_1, I_2, I_3) - \sigma_0^2(I_1^2 - 3I_2 - \sigma_0^2)^2$. Thus f_M and f_T are related through

$$f_T = F - \sigma_0^2 f_M^2. \tag{4}$$

In I-space, the yield surface for von Mises' criterion is then the parabolic right cylinder whose cross section in the I_1-I_2 plane is the parabola $I_1^2 = 3I_2 + \sigma_0^2 = 3(I_2 + k^2)$, and whose generators are parallel to the I_3 axis. Thus all those points in I-space, that correspond to real stresses, which lie inside and on this parabolic cylinder, correspond to unyielded states of stress.

The yield surface for Tresca's criterion is not so simple. In order to remove the dependence of the yield surface $f(I_1, I_2, I_3) = 0$ on the yield stress σ_0, introduce the nondimensional quantities $\bar{\sigma}_i = \sigma_i/\sigma_0$, $i = 1,2,3$. Also, let a bar over a function denote that it is the same function of $\bar{\sigma}_i$ that the unbarred function is of σ_i, i.e., $\bar{I}_r(\bar{\sigma}_1, \bar{\sigma}_2, \bar{\sigma}_3) = I_r(\bar{\sigma}_1, \bar{\sigma}_2, \bar{\sigma}_3)$, etc. Then $\bar{f}_M = \bar{I}_1^2 - 3\bar{I}_2 - 1$ and $\bar{f}_T = \bar{F} - \bar{f}_M^2$.

von Mises' yield surface is then the parabolic right cylinder $\bar{f}_M = 0$ the vertex of whose base in the $\bar{I}_1$-$\bar{I}_2$ plane is located at the point $(0, -1/3)$. Unyielded states of stress are represented by those points in I-space which lie in the region determined by $\bar{F} \geq 0$ and $\bar{f}_M \leq 0$. The surface $\bar{F} = 0$ is the same as $F = 0$ but with a drastic change of scale.

For two-dimensional stress distributions, for which I_3 must equal zero, von Mises' criterion determines the yield locus in the $\bar{I}_1$-$\bar{I}_2$ plane as the parabola $\bar{I}_1^2 = 3\bar{I}_2 + 1$, which is marked BAD'EF in Fig. 3.

For the two-dimensional case, the yield locus in the $\bar{I}_1$-$\bar{I}_2$ plane for Tresca's criterion is given by $\bar{f}_T(\bar{I}_1, \bar{I}_2, 0) = 0$. Now

$$\bar{f}_T(\bar{I}_1, \bar{I}_2, 0) = \bar{I}_2^2(\bar{I}_1^2 - 4\bar{I}_2) - (\bar{I}_1^2 - 3\bar{I}_2 - 1)^2$$
$$= (\bar{I}_1^2 - 4\bar{I}_2 - 1)(\bar{I}_2 + 1 + \bar{I}_1)(\bar{I}_2 + 1 - \bar{I}_1).$$

Unyielded two-dimensional states of stress are then represented by points in the $\bar{I}_1$-$\bar{I}_2$ plane which are inside and on the region bounded by the straight lines $\bar{I}_2 + 1 + \bar{I}_1 = 0$ and $\bar{I}_2 + 1 - \bar{I}_1 = 0$, and the parabola $\bar{I}_1^2 = 4\bar{I}_2 + 1$. For purposes of comparison with the yield locus for von Mises' criterion, the boundary of this region has been shown in Fig. 3 by the dotted curve BADEF.

Concluding Remarks

In the space of stress invariants, one-dimensional states of stress are represented by points on the I_1 axis, and two-dimensional stress distributions are represented by points in the I_1-I_2 plane which lie on and outside the parabola $I_1^2 = 4I_2$. Thus, in the I_1-I_2 plane, the value of I_2 relative to I_1 is a measure of the two-dimensionality of the stress distribution; so that points that are further away from the I_1 axis correspond to increasingly two-dimensional states of stress. Similarly the value of I_3 relative to I_1 is a measure of how three-dimensional a particular stress distribution is.

Regions of I-space which correspond to real stresses in σ-space are determined by $F(I_1, I_2, I_3) \geq 0$. The yield surfaces corresponding to von Mises' and Tresca's yield criteria are given, respectively, by $f_M(I_1, I_2, I_3) = 0$ and $f_M(I_1, I_2, I_3) = 0$. It is rather surprising that F, f_M, and f_T are related, as indicated in equation (4).

Further details regarding the space of stress invariants, including contours of the surface $F = 0$ and additional perspective views, are given in reference [2].

Acknowledgment

The author would like to acknowledge the help of W. E. Lorensen in generating the perspective views shown in Figs. 1 and 2.

References

1 Prager, W., and Hodge, P. G., *Theory of Perfectly Plastic Solids*, Wiley, New York, 1951.

2 Stokes, V. K., "On the Space of Stress Invariants," General Electric Corporate Research & Development Report No. 80CRD053, Mar. 1980.

Finite Elastic-Plastic Deformation of a Rotating Hollow Cylinder

K. K. Lo[1] and R. Abeyaratne[2]

Introduction

In this Note we determine an exact solution for the finite elastic-plastic field in a pressurized hollow cylinder rotating about its axis at a constant angular speed. The material is assumed to be incompressible and elastic-plastic. The plane-strain problem for a pressurized hollow cylinder has been studied by Durban [1], while that for a rotating cylinder composed of a nonlinearly elastic material can be found in Green and Zerna [2].

Formulation

Suppose that the region occupied by a body in its undeformed configuration is a hollow right circular cylinder of internal and external radii a and b, respectively. The body is presumed to be composed of an incompressible, isotropic material.

The cylinder is subjected to an *internal pressure* p while being rotated about its axis with *constant speed* ω relative to some (inertial) frame of reference. Since we are considering the quasi-static change of the applied pressure and the angular speed, we allow the pressure p and the speed ω to depend smoothly, and monotonically, on a parameter $\lambda(\geq 0)$:

[1] Assistant Professor, Division of Engineering, Brown University, Providence, R. I., 02912.

[2] Research Associate, Materials Research Laboratory, Brown University, Providence, R. I., 02912. Assoc. Mem. ASME.

Manuscript received by ASME Applied Mechanics Division, May, 1980; final revision, October, 1980.

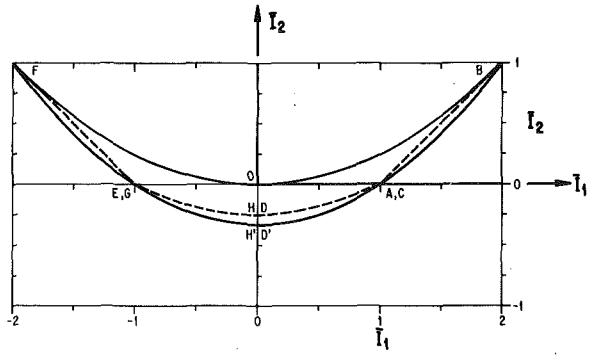

Fig. 3 von Mises' and Tresca's yield loci in the $\bar{I}_1$-$\bar{I}_2$ plane for two-dimensional stress distributions

the surface $I_3 = I_1 I_2$, $I_2 \leq 0$, correspond to the state of stress $\sigma = (\sigma, -\sigma, p)$ where $p = I_1$ and $\sigma = (-I_2)^{1/2}$. The negative half of the I_2 axis, which must lie on this surface, corresponds to pure shear $\sigma = (\sigma, -\sigma, 0)$.

Yield Surfaces

Two important yield criteria are those due to von Mises and Tresca. For von Mises' yield criterion, the yield surface in σ-space is defined by $(\sigma_1 - \sigma_2)^2 + (\sigma_2 - \sigma_3)^2 + (\sigma_3 - \sigma_1)^2 = 2\sigma_0^2 = 6k^2$ where σ_0 is the yield stress in tension and k that in pure shear. In terms of invariants, this yield surface is $f_M(I_1, I_2, I_3) = 0$, where $f_M = I_1^2 - 3I_2 - \sigma_0^2$. Yield occurs if $f_M > 0$.

In terms of principal stresses, the yield surface for Tresca's criterion is given by $|\sigma_1 - \sigma_2| = \sigma_0$, $|\sigma_2 - \sigma_3| = \sigma_0$, and $|\sigma_3 - \sigma_1| = \sigma_0$, which, upon using a representation given in reference [1], reduces to $f_T(I_1, I_2, I_3) = 0$, where $f_T(I_1, I_2, I_3) = F(I_1, I_2, I_3) - \sigma_0^2(I_1^2 - 3I_2 - \sigma_0^2)^2$. Thus f_M and f_T are related through

$$f_T = F - \sigma_0^2 f_M^2. \tag{4}$$

In I-space, the yield surface for von Mises' criterion is then the parabolic right cylinder whose cross section in the I_1-I_2 plane is the parabola $I_1^2 = 3I_2 + \sigma_0^2 = 3(I_2 + k^2)$, and whose generators are parallel to the I_3 axis. Thus all those points in I-space, that correspond to real stresses, which lie inside and on this parabolic cylinder, correspond to unyielded states of stress.

The yield surface for Tresca's criterion is not so simple. In order to remove the dependence of the yield surface $f(I_1, I_2, I_3) = 0$ on the yield stress σ_0, introduce the nondimensional quantities $\bar{\sigma}_i = \sigma_i/\sigma_0$, $i = 1,2,3$. Also, let a bar over a function denote that it is the same function of $\bar{\sigma}_i$ that the unbarred function is of σ_i, i.e., $\bar{I}_r(\bar{\sigma}_1, \bar{\sigma}_2, \bar{\sigma}_3) = I_r(\bar{\sigma}_1, \bar{\sigma}_2, \bar{\sigma}_3)$, etc. Then $\bar{f}_M = \bar{I}_1^2 - 3\bar{I}_2 - 1$ and $\bar{f}_T = \bar{F} - \bar{f}_M^2$.

von Mises' yield surface is then the parabolic right cylinder $\bar{f}_M = 0$ the vertex of whose base in the $\bar{I}_1$-$\bar{I}_2$ plane is located at the point $(0, -1/3)$. Unyielded states of stress are represented by those points in I-space which lie in the region determined by $\bar{F} \geq 0$ and $\bar{f}_M \leq 0$. The surface $\bar{F} = 0$ is the same as $F = 0$ but with a drastic change of scale.

For two-dimensional stress distributions, for which I_3 must equal zero, von Mises' criterion determines the yield locus in the $\bar{I}_1$-$\bar{I}_2$ plane as the parabola $\bar{I}_1^2 = 3\bar{I}_2 + 1$, which is marked BAD'EF in Fig. 3.

For the two-dimensional case, the yield locus in the $\bar{I}_1$-$\bar{I}_2$ plane for Tresca's criterion is given by $\bar{f}_T(\bar{I}_1, \bar{I}_2, 0) = 0$. Now

$$\bar{f}_T(\bar{I}_1, \bar{I}_2, 0) = \bar{I}_2^2(\bar{I}_1^2 - 4\bar{I}_2) - (\bar{I}_1^2 - 3\bar{I}_2 - 1)^2$$
$$= (\bar{I}_1^2 - 4\bar{I}_2 - 1)(\bar{I}_2 + 1 + \bar{I}_1)(\bar{I}_2 + 1 - \bar{I}_1).$$

Unyielded two-dimensional states of stress are then represented by points in the $\bar{I}_1$-$\bar{I}_2$ plane which are inside and on the region bounded by the straight lines $\bar{I}_2 + 1 + \bar{I}_1 = 0$ and $\bar{I}_2 + 1 - \bar{I}_1 = 0$, and the parabola $\bar{I}_1^2 = 4\bar{I}_2 + 1$. For purposes of comparison with the yield locus for von Mises' criterion, the boundary of this region has been shown in Fig. 3 by the dotted curve BADEF.

Concluding Remarks

In the space of stress invariants, one-dimensional states of stress are represented by points on the I_1 axis, and two-dimensional stress distributions are represented by points in the I_1-I_2 plane which lie on and outside the parabola $I_1^2 = 4I_2$. Thus, in the I_1-I_2 plane, the value of I_2 relative to I_1 is a measure of the two-dimensionality of the stress distribution; so that points that are further away from the I_1 axis correspond to increasingly two-dimensional states of stress. Similarly the value of I_3 relative to I_1 is a measure of how three-dimensional a particular stress distribution is.

Regions of I-space which correspond to real stresses in σ-space are determined by $F(I_1, I_2, I_3) \geq 0$. The yield surfaces corresponding to von Mises' and Tresca's yield criteria are given, respectively, by $f_M(I_1, I_2, I_3) = 0$ and $f_M(I_1, I_2, I_3) = 0$. It is rather surprising that F, f_M, and f_T are related, as indicated in equation (4).

Further details regarding the space of stress invariants, including contours of the surface $F = 0$ and additional perspective views, are given in reference [2].

Acknowledgment

The author would like to acknowledge the help of W. E. Lorensen in generating the perspective views shown in Figs. 1 and 2.

References

1 Prager, W., and Hodge, P. G., *Theory of Perfectly Plastic Solids*, Wiley, New York, 1951.

2 Stokes, V. K., "On the Space of Stress Invariants," General Electric Corporate Research & Development Report No. 80CRD053, Mar. 1980.

Finite Elastic-Plastic Deformation of a Rotating Hollow Cylinder

K. K. Lo[1] and R. Abeyaratne[2]

Introduction

In this Note we determine an exact solution for the finite elastic-plastic field in a pressurized hollow cylinder rotating about its axis at a constant angular speed. The material is assumed to be incompressible and elastic-plastic. The plane-strain problem for a pressurized hollow cylinder has been studied by Durban [1], while that for a rotating cylinder composed of a nonlinearly elastic material can be found in Green and Zerna [2].

Formulation

Suppose that the region occupied by a body in its undeformed configuration is a hollow right circular cylinder of internal and external radii a and b, respectively. The body is presumed to be composed of an incompressible, isotropic material.

The cylinder is subjected to an *internal pressure* p while being rotated about its axis with *constant speed* ω relative to some (inertial) frame of reference. Since we are considering the quasi-static change of the applied pressure and the angular speed, we allow the pressure p and the speed ω to depend smoothly, and monotonically, on a parameter $\lambda(\geq 0)$:

[1] Assistant Professor, Division of Engineering, Brown University, Providence, R. I., 02912.

[2] Research Associate, Materials Research Laboratory, Brown University, Providence, R. I., 02912. Assoc. Mem. ASME.

Manuscript received by ASME Applied Mechanics Division, May, 1980; final revision, October, 1980.

$$\omega = \omega(\lambda),\ \omega(0) = 0,\ \omega'(\lambda) > 0,$$

$$p = p(\lambda),\ p(0) = 0,\ p'(\lambda) > 0. \tag{1}$$

Throughout this paper we will use a frame of reference relative to which the tube is stationary. We may, therefore, with no ambiguity, use λ as a "time" parameter.

In view of incompressibility, the plane, axially symmetric deformation of the cylinder corresponding to varying λ, (a quasi-static motion), is described by

$$r = (R^2 + A(\lambda))^{1/2}, \quad \theta = \psi, \quad z = \xi; \quad A(0) = 0. \tag{2}$$

Here (r, θ, z) are the "current" cylindrical coordinates of the point which in the undeformed configuration, ($\lambda = 0$), was located at (R, ψ, ξ). The nature of the loading suggests that we assume $A(\lambda)$, which is as yet undetermined, to be non-negative. We find from (2) that the only nonvanishing components of the Eulerian strain rate $\mathbf{D}$—the symmetric part of the velocity gradient tensor—are

$$D_{rr} = -\dot{A}/2r^2, \quad D_{\theta\theta} = \dot{A}/2r^2, \quad (\dot{A} = dA(\lambda)/d\lambda) \tag{3}$$

The spin-tensor $\mathbf{\Omega}$—the antisymmetric part of the velocity gradient tensor—vanishes identically: $\mathbf{\Omega} = \mathbf{0}$.

In view of the isotropy of the material considered and the purely radial nature of the deformation, we may assume that the only nonvanishing components of the Cauchy (true) stress $\boldsymbol{\sigma}$ are σ_r, σ_θ, and σ_z. If we further suppose that the stress $\boldsymbol{\sigma}$ is axially symmetric, $\boldsymbol{\sigma} = \boldsymbol{\sigma}(r, \lambda)$, the equations of equilibrium reduce to

$$\partial\sigma_r/\partial r + (\sigma_r - \sigma_\theta)/r + \rho\omega^2 r = 0 \tag{4}$$

The last term in (4) is the inertial force and ρ is the (constant) mass density. We will assume that the undeformed configuration corresponding to $\lambda = 0$ is free of stress.

Integrating (4) with respect to the deformed coordinates and using incompressibility and the boundary conditions, we get

$$p + \rho\omega^2(b^2 - a^2)/2 = \int_{r(a)}^{r(b)} (\sigma_\theta - \sigma_r)\, dr/r \tag{5}$$

where p is the pressure at the (undeformed) inner boundary a. Hence the inertial effects involved in a steadily rotating cylinder are equivalent to an "internal pressure" $\rho\omega^2(b^2 - a^2)/2$ for *any* incompressible material.

Solution

Turning to the constitutive relations of the material, we will suppose that these are the classical elastic-plastic relations (in a form appropriate for finite deformations), viz.

$$\mathbf{D} = 3\overset{\nabla}{\mathbf{S}}/2E + [3\Lambda\dot{\epsilon}_p(\sigma_e)/2\sigma_e]\mathbf{S}. \tag{6}$$

Here, $\mathbf{S} \equiv \boldsymbol{\sigma} - \frac{1}{3}(\text{tr } \boldsymbol{\sigma})\,\mathbf{1}$ is the deviator of the Cauchy stress and σ_e is the equivalent stress: $\sigma_e = \frac{3}{2}(\text{tr } \mathbf{S}^2)^{1/2}$. The Jaumann (corotational) rate of the Cauchy stress deviator is denoted by $\overset{\nabla}{\mathbf{S}}$, so that $\overset{\nabla}{\mathbf{S}} = \dot{\mathbf{S}} - \mathbf{\Omega}\cdot\mathbf{S} + \mathbf{S}\cdot\mathbf{\Omega}$. Λ is a loading coefficient with $\Lambda = 1$ during loading and $\Lambda = 0$ during unloading. The Young's modulus is E. A superposed dot denotes differentiation with respect to λ with the (undeformed) reference position held fixed. Finally, $\epsilon_p(\sigma_e)$, the so-called equivalent plastic strain, is a given function of the equivalent stress σ_e; $\epsilon_p = \epsilon_p(\sigma_e)$, $\epsilon_p(0) = 0$, $\epsilon_p'(\sigma_e) > 0$ for $\sigma_e \geq 0$. In particular, according to the Ramberg-Osgood description, $\epsilon_p(\sigma_e) = K(\sigma_e/E)^n$ where K and n are material properties (constants).

In the present context, since the spin-tensor $\mathbf{\Omega}$ vanishes, we have that $\overset{\nabla}{\mathbf{S}} = \dot{\mathbf{S}}$. Expressing (6) in terms of its cylindrical components leads to three nontrivial scalar equations. The third of these (the one associated with the z-direction), and the fact that the undeformed configuration ($\lambda = 0$) is stress-free (so that $S_z(r, 0) = 0$) suggests that we take $S_z(r, \lambda) \equiv 0$. This in turn implies that $\sigma_z = (\sigma_r + \sigma_\theta)/2$. Therefore, we may write the equivalent stress σ_e as

$$\sigma_e = m\frac{\sqrt{3}}{2}(\sigma_\theta - \sigma_r), \quad m = \text{sgn}\,(\sigma_\theta - \sigma_r). \tag{7}$$

As λ increases monotonically, the pressure $p(\lambda)$ and speed $\omega(\lambda)$ also increase continuously. This suggests that we tentatively assume, subject to subsequent verification, that when λ increases the tube is being loaded at each point. Accordingly, we set $\Lambda = 1$ in (6) and integrate the only nonvanishing equation in (6) with respect to λ. Keeping in mind that $A(\lambda) = 0$ in the unstressed configuration ($\lambda = 0$), this leads to

$$\sigma_e/E + \epsilon_p(\sigma_e) = m/\sqrt{3}\,\ln((R^2 + A(\lambda))/R^2). \tag{8}$$

Since σ_e, ϵ_p, and A are non-negative, it follows that $m = +1$. This in turn, because of (7), shows that $\sigma_\theta \geq \sigma_r$. Observe from (8) and the properties of $\epsilon_p(\sigma_e)$ noted previously that we may, with no loss of generality, *assume from hereon* that $\sigma_e > 0$ at each point in the tube.

It is convenient to define a function $h(\sigma_e)$ for $\sigma_e \geq 0$ by

$$h(\sigma_e) = \exp\{\sqrt{3}\,(\sigma_e/E + \epsilon_p\,(\sigma_e))\}. \tag{9}$$

We note that $h(\sigma_e) > 1$, $h'(\sigma_e) > 0$ for $\sigma_e > 0$ and that $h(\sigma_e) \to \infty$ as $\sigma_e \to \infty$. Equations (8), (9), and (2) with $m = +1$ lead to

$$r^2 = A\,h(\sigma_e)/[h(\sigma_e) - 1], \quad R^2 = A/[h(\sigma_e) - 1] \tag{10}$$

when $\sigma_e > 0$. Let σ_a and σ_b be the values of the equivalent stress at the inner and outer boundary, respectively,

$$\sigma_e = \sigma_a \quad \text{at} \quad R = a, \sigma_e = \sigma_b \quad \text{at} \quad R = b; \quad (r^2 = R^2 + A). \tag{11}$$

It then follows from the second of (10) that

$$\frac{a^2}{b^2} = \frac{h(\sigma_b) - 1}{h(\sigma_a) - 1}. \tag{12}$$

In view of (9), it is readily shown that the first of (10) can be uniquely solved for $\sigma_e = \hat{\sigma}_e(r, A)$. This gives us the equivalent stress σ_e once A has been determined.

It is convenient to change the independent variable to σ_e by writing $\sigma_r = \hat{\sigma}_r(\sigma_e, A)$, where $r^2 = Ah(\sigma_e)/[h(\sigma_e) - 1]$. Rewriting the equilibrium equation (4) in terms of $\hat{\sigma}_r$ enables us to integrate it, which, because of (10), (11) and the boundary condition on the inner surface leads to

$$\sigma_r = -p - \int_{\sigma_a}^{\sigma_e} f(\eta)d\eta - \frac{\rho\omega^2}{2}(R^2 - a^2). \tag{13}$$

Here we have set

$$f(\sigma_e) = \sigma_e h'(\sigma_e)/\sqrt{3}\,h(\sigma_e)[h(\sigma_e) - 1], \quad \sigma_e > 0. \tag{14}$$

Therefore, once A is determined, $\sigma_e = \hat{\sigma}_e(r, A)$ and equations (11) and (13) give the stress σ_r. This in turn, because of (7), determines the hoop stress σ_θ.

In order to determine A, we insure that σ_r as given by (13) conforms to the stress-free condition on the outer boundary. This gives

$$p + \frac{\rho\omega^2}{2}(b^2 - a^2) = \int_{\sigma_b}^{\sigma_a} f(\eta)d\eta \tag{15}$$

in view of (11). Given the pressure p and the speed ω, (12) and (15) constitute two equations for the two unknown quantities σ_a, σ_b. Presuming that σ_a and σ_b can be determined from them, we can then use (10) and (11) to find A ($= a^2[h(\sigma_a) - 1]$). This completely determines the stresses and deformation.

What remains therefore is the solution of equations (12) and (15) for σ_a and σ_b. If we confine our attention to the Ramberg-Osgood description of an elastic-plastic material, it can be demonstrated that (12) and (15) *can* be solved for σ_a, σ_b *provided* the left-hand side of (15), $p + \rho\omega^2(b^2 - a^2)/2$, does not exceed some critical value $P_{\max}$. Equation (15) for the special case $\omega = 0$ is the result obtained by Durban [1]. For any incompressible material, the left-hand side of (15) always holds since only the incompressibility condition was used to integrate (4) to give (15).

Results

The graph of the total effective pressure, $p + \rho\omega^2(b^2 - a^2)/2$, versus

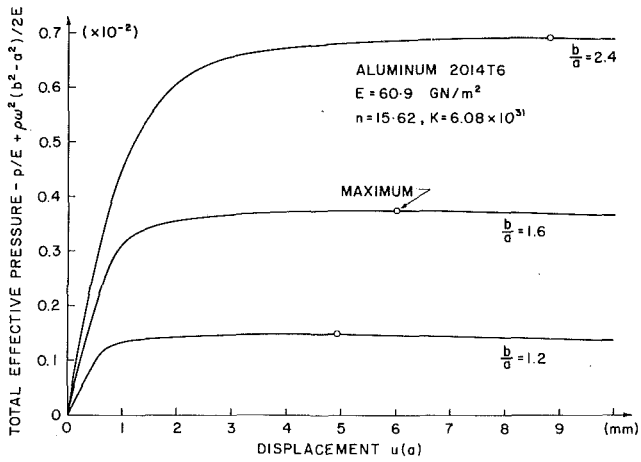

Fig. 1. Load-displacement curves for different thickness ratios

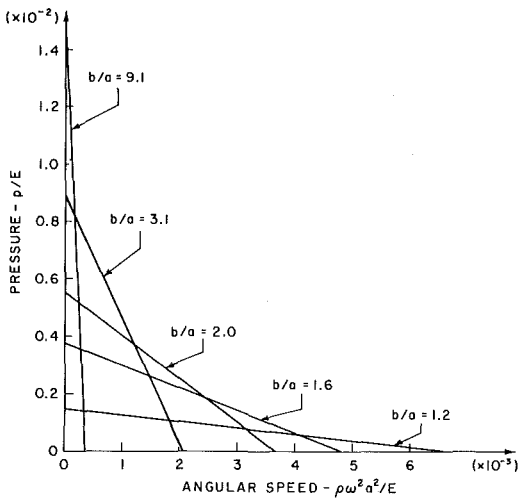

Fig. 2 Critical curves; maximum pressure versus critical speed

the displacement at the inner radius, $u(a)$, is shown in Fig. 1 for different values of b/a. The numerical results were calculated for Aluminum 2014T6 based on the Ramberg-Osgood model. Consistent with the observation made in the previous section, this figure shows that the effective pressure cannot be increased beyond a certain value. Note that when this value is approached the displacement increases substantially with relatively little change in the effective pressure.

The critical curve is the straight line in the (ω^2, p)—plane which bounds the admissible values of the pressure and the angular speed. This line is shown in Fig. 2 for different values of the ratio b/a.

An explicit description of this "critical curve" can be obtained in the special case of a *thin-walled tube*. If the thickness $t = b - a$ is small compared to a, we can expand σ_a, σ_b about their mean value σ_0 by assuming that $\sigma_a - \sigma_b \ll \sigma_0$. The various equations may then be appropriately approximated. For a thickness ratio of $b/a = 1.2$, the thin-wall approximation gives for $P_{\max}$ a value which agrees with the numerical result based on the exact solution to within four significant figures. Finally, it can be shown that the solution derived in this Note corresponds to loading everywhere in the body (provided the total effective pressure is less than $P_{\max}$).

Acknowledgment

The results communicated in this Note were obtained in the course of an investigation supported by the NSF Materials Research Laboratory at Brown University.

References

1 Durban, D., "Large Strain Solution for Pressured Elasto-Plastic Tubes," ASME JOURNAL OF APPLIED MECHANICS, Vol. 46, Mar. 1979, pp. 228–230.

2 Green, A. E., and Zerna, W., *Theoretical Elasticity*, 2nd ed., Oxford University Press, 1968, pp. 100–102.

Stability of a Heavy Column With an End Load

C.-Y. Wang[1] and B. Drachman[2]

Introduction

The stability of a vertical column, one end embedded in a rigid foundation, is very important in structural engineering. Euler [1] first found the critical buckling end loads for a massless column. The heavy column without an end load was investigated by Greenhill [2] who succeeded in obtaining the critical density for the primary (least stable) mode. The combined effect of column density and end load was studied by Grishcoff [3], who obtained part of the stability boundary for the primary mode. In this Note we shall also study the stability due to the combined effect. We shall (a) complete the stability boundary for the primary mode by extending to the case when the column is hanging from the foundation and (b) investigate the higher modes of buckling.

Formulation

We assume the column is slender enough such that the local curvature is proportional to the local moment. Fig. 1 shows the coordinate system. A local moment balance gives

$$EI\frac{d^2\theta}{ds'^2} = -[F + \rho(L - s')]\sin\theta \tag{1}$$

where F is the downward end load, ρ is the density, L is the length, and EI is the flexural rigidity of the column, s' is the arc length, and θ is the local angle of inclination. Let s denote s' normalized by L. Equation (1) can be expressed as

$$\frac{d^2\theta}{ds^2} = -[\alpha + \beta(1 - s)]\sin\theta \tag{2}$$

where $\alpha \equiv FL^2/EI$ and $\beta \equiv \rho L^3/EI$ are nondimensional parameters representing the relative importance of end load and density to the flexural rigidity respectively. α and β are both positive in Fig. 1(a). Negative α means the direction of the force is away from the fixed end. Negative β can be realized in the case of a hanging column (Fig. 1(b)), or when the upright column is immersed in a higher-density medium.

The boundary conditions are

$$\theta(0) = 0, \frac{d\theta}{ds}(1) = 0 \tag{3}$$

Stability

Equation (2) can be linearized to give the stability equation

[1] Professor, Department of Mathematics, Michigan State University, East Lansing, Mich. 48824

[2] Associate Professor, Department of Mathematics, Michigan State University, East Lansing, Mich. 48824

Manuscript received by ASME Applied Mechanics Division, February, 1981.

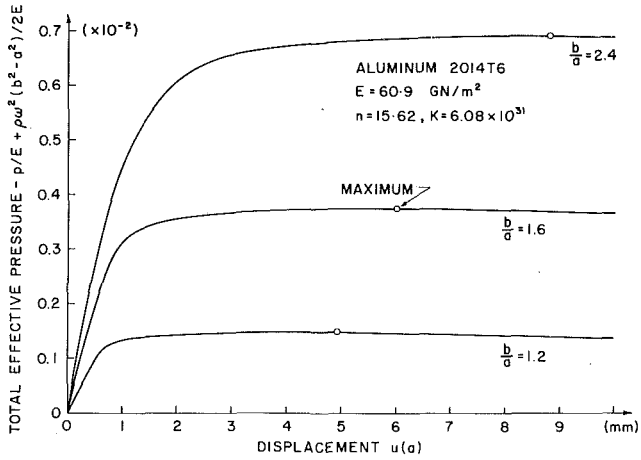

Fig. 1. Load-displacement curves for different thickness ratios

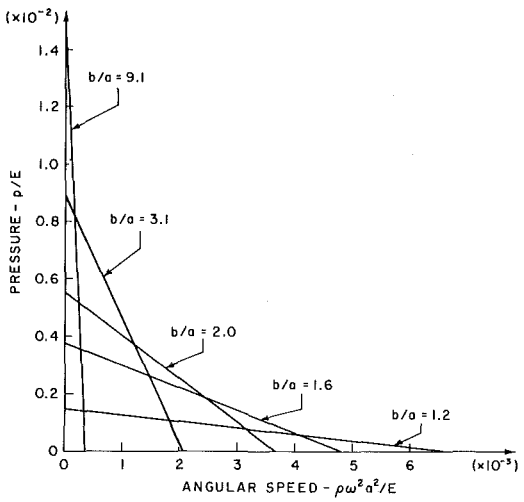

Fig. 2 Critical curves; maximum pressure versus critical speed

the displacement at the inner radius, $u(a)$, is shown in Fig. 1 for different values of b/a. The numerical results were calculated for Aluminum 2014T6 based on the Ramberg-Osgood model. Consistent with the observation made in the previous section, this figure shows that the effective pressure cannot be increased beyond a certain value. Note that when this value is approached the displacement increases substantially with relatively little change in the effective pressure.

The critical curve is the straight line in the (ω^2, p)—plane which bounds the admissible values of the pressure and the angular speed. This line is shown in Fig. 2 for different values of the ratio b/a.

An explicit description of this "critical curve" can be obtained in the special case of a *thin-walled tube*. If the thickness $t = b - a$ is small compared to a, we can expand σ_a, σ_b about their mean value σ_0 by assuming that $\sigma_a - \sigma_b \ll \sigma_0$. The various equations may then be appropriately approximated. For a thickness ratio of $b/a = 1.2$, the thin-wall approximation gives for $P_{\max}$ a value which agrees with the numerical result based on the exact solution to within four significant figures. Finally, it can be shown that the solution derived in this Note corresponds to loading everywhere in the body (provided the total effective pressure is less than $P_{\max}$).

Acknowledgment

The results communicated in this Note were obtained in the course of an investigation supported by the NSF Materials Research Laboratory at Brown University.

References

1 Durban, D., "Large Strain Solution for Pressured Elasto-Plastic Tubes," ASME JOURNAL OF APPLIED MECHANICS, Vol. 46, Mar. 1979, pp. 228–230.

2 Green, A. E., and Zerna, W., *Theoretical Elasticity*, 2nd ed., Oxford University Press, 1968, pp. 100–102.

Stability of a Heavy Column With an End Load

C.-Y. Wang[1] and B. Drachman[2]

Introduction

The stability of a vertical column, one end embedded in a rigid foundation, is very important in structural engineering. Euler [1] first found the critical buckling end loads for a massless column. The heavy column without an end load was investigated by Greenhill [2] who succeeded in obtaining the critical density for the primary (least stable) mode. The combined effect of column density and end load was studied by Grishcoff [3], who obtained part of the stability boundary for the primary mode. In this Note we shall also study the stability due to the combined effect. We shall (a) complete the stability boundary for the primary mode by extending to the case when the column is hanging from the foundation and (b) investigate the higher modes of buckling.

Formulation

We assume the column is slender enough such that the local curvature is proportional to the local moment. Fig. 1 shows the coordinate system. A local moment balance gives

$$EI\frac{d^2\theta}{ds'^2} = -[F + \rho(L - s')]\sin\theta \tag{1}$$

where F is the downward end load, ρ is the density, L is the length, and EI is the flexural rigidity of the column, s' is the arc length, and θ is the local angle of inclination. Let s denote s' normalized by L. Equation (1) can be expressed as

$$\frac{d^2\theta}{ds^2} = -[\alpha + \beta(1 - s)]\sin\theta \tag{2}$$

where $\alpha \equiv FL^2/EI$ and $\beta \equiv \rho L^3/EI$ are nondimensional parameters representing the relative importance of end load and density to the flexural rigidity respectively. α and β are both positive in Fig. 1(a). Negative α means the direction of the force is away from the fixed end. Negative β can be realized in the case of a hanging column (Fig. 1(b)), or when the upright column is immersed in a higher-density medium.

The boundary conditions are

$$\theta(0) = 0, \frac{d\theta}{ds}(1) = 0 \tag{3}$$

Stability

Equation (2) can be linearized to give the stability equation

[1] Professor, Department of Mathematics, Michigan State University, East Lansing, Mich. 48824

[2] Associate Professor, Department of Mathematics, Michigan State University, East Lansing, Mich. 48824

Manuscript received by ASME Applied Mechanics Division, February, 1981.

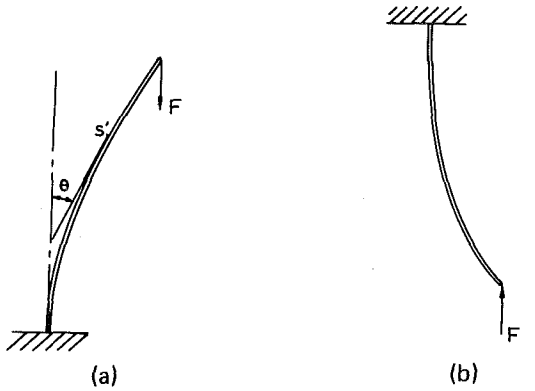

Fig. 1 Buckling of a heavy column; (a) $\alpha > 0$, $\beta > 0$ and (b) $\alpha > 0$, $\beta < 0$

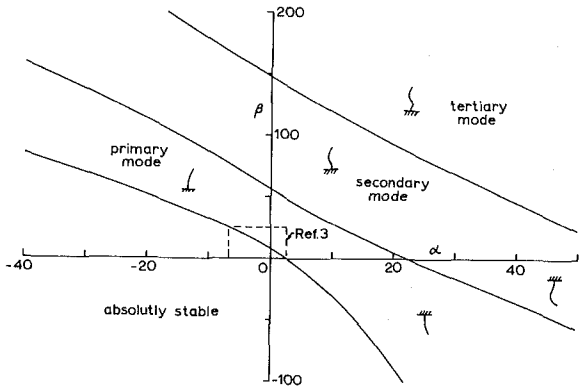

Fig. 2 The stability boundaries for the first three modes

$$\frac{d^2\theta}{ds^2} = -[\alpha + \beta(1-s)]\theta \tag{4}$$

We introduce a new variable

$$r \equiv \left(1 - s + \frac{\alpha}{\beta}\right)|\beta|^{1/3} \tag{5}$$

Equation (4) becomes

$$\frac{d^2\theta}{dr^2} = -(\text{sign }\beta)r\theta \tag{6}$$

The boundary conditions are

$$\text{At } r = \left(1 + \frac{\alpha}{\beta}\right)|\beta|^{1/3} \equiv r_1, \quad \theta = 0 \tag{7}$$

$$\text{At } r = \frac{\alpha}{\beta}|\beta|^{1/3} \equiv r_2, \quad \frac{d\theta}{dr} = 0 \tag{8}$$

The solution to equation (6) can be expressed in terms of Airy functions

$$\theta = c_1 A_i(-(\text{sign }\beta)r) + c_2 B_i(-(\text{sign }\beta)r) \tag{9}$$

The condition for nontrivial solutions may be obtained from equations (7)–(9). By choosing the proper branches in the related Bessel functions, we obtain the following cases:

For $\alpha > -\beta > 0$ or $\alpha > 0$, $\beta > 0$, or $-\alpha > \beta > 0$,

$$J_{-1/3}(\zeta_1)J_{-2/3}(\zeta_2) + J_{1/3}(\zeta_1)J_{2/3}(\zeta_2) = 0 \tag{10}$$

where $\zeta_1 \equiv \frac{2}{3}|r_1|^{3/2}$, $\zeta_2 \equiv \frac{2}{3}|r_2|^{3/2}$. For $-\beta > \alpha > 0$,

$$I_{-1/3}(\zeta_1)J_{-2/3}(\zeta_2) - I_{1/3}(\zeta_1)J_{2/3}(\zeta_2) = 0. \tag{11}$$

For $\beta > -\alpha > 0$,

$$J_{-1/3}(\zeta_1)I_{2/3}(\zeta_2) + J_{1/3}(\zeta_1)I_{-2/3}(\zeta_2) = 0 \tag{12}$$

For given α, equations (10)–(12) are solved numerically for β. Fig. 2 shows the complete stability boundaries. Our results agree well with Grishcoff in the range he investigated: $25 > \beta \geq 0$, $-7 < \alpha \leq \pi^2/4$.

Discussion

As far as we know negative β has never been studied before. Our analysis show that the stability for $\alpha > 0$, $\beta < 0$ is not a mere reflection of $\alpha < 0$, $\beta > 0$. This is also illustrated in Fig. 2. In general, the stability curves are so nonlinear that any global straight-line approximation is meaningless. Below each curve, the column is stable with respect to the particular mode. The column is absolutely stable under the primary stability curve.

The α intercepts of the curves in Fig. 3 agree with the normalized Euler buckling loads $\pi^2/4$, $9\pi^2/4$, $25\pi^2/4$. The β intercepts are at 7.83735, 55.9872, 148.512. Our values are more accurate than those of Greenhill and Grishcoff who use infinite series to obtain the values of 7.95 and 7.85, respectively, for the primary mode.

References

1 Euler, L., De Curvis Elasticis, 1744.

2 Greenhill, A. G., "Determination of the Greatest Height Consistent With Stability That a Vertical Pole or Mast Can Be Made, and of the Greatest Height to Which a Tree of Given Proportions Can Grow," *Cambridge Philosophical Society Proceedings*, Vol. 4, 1881, pp. 65–73.

3 Grishcoff, N., in *Theory of Elastic Stability*, Timoshenko, S. P., and Gere, J. M., McGraw-Hill, New York, 1961, p. 104.

The Vibrating Beam With Nonhomogeneous Boundary Conditions

C. R. Edstrom[1]

In Mindlin and Goodman [1] a procedure is described for extending the method of separation of variables to obtain solutions of linear partial differential equations with nonhomogeneous boundary conditions. This procedure utilizes a change of dependent variable to produce homogeneous boundary conditions. Moreover, if the partial differential equation is originally homogeneous, the equation in the new dependent variable becomes nonhomogeneous and the existence of a set of orthogonal functions must be assumed. However, if a property chosen change of dependent variable is made, a homogeneous linear partial differential equation will remain homogeneous as well as have homogeneous boundary conditions, but the initial conditions will be nonhomogeneous. Thus the assumption of the existence of a set of orthogonal functions is not necessary [2]. Also, if a linear partial differential equation is nonhomogeneous, a properly chosen change of dependent variable will reduce the equation to a homogeneous equation as well as produce homogeneous boundary conditions and nonhomogeneous initial conditions. In order to find a proper change of dependent variable, a system of ordinary differential equations with two point boundary conditions must have a solution. However, when the change of dependent variable can be established, the resulting problem can be easily solved.

[1] Associate Professor, Department of Mathematics, Air Force Institute of Technology, Wright-Patterson Air Force Base, Ohio 45433.

Manuscript received by ASME Applied Mechanics Division, April, 1980; final revision, March, 1981.

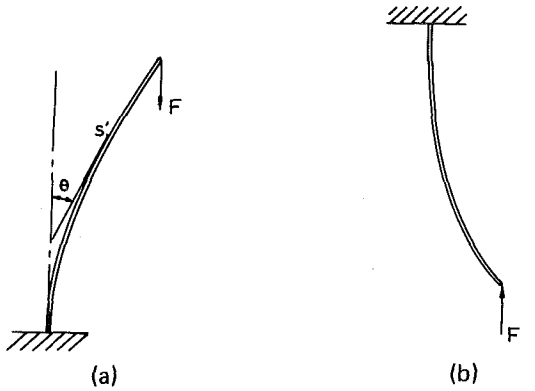

Fig. 1 Buckling of a heavy column; (a) $\alpha > 0$, $\beta > 0$ and (b) $\alpha > 0$, $\beta < 0$

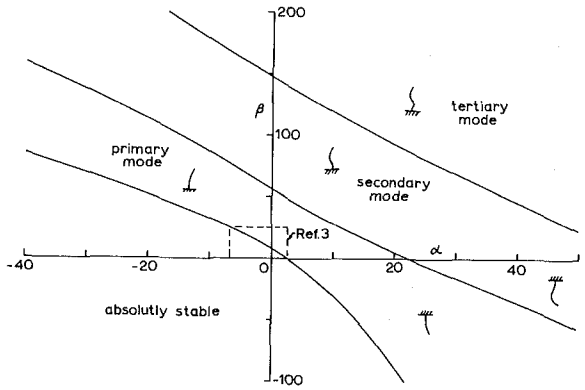

Fig. 2 The stability boundaries for the first three modes

$$\frac{d^2\theta}{ds^2} = -[\alpha + \beta(1-s)]\theta \tag{4}$$

We introduce a new variable

$$r \equiv \left(1 - s + \frac{\alpha}{\beta}\right)|\beta|^{1/3} \tag{5}$$

Equation (4) becomes

$$\frac{d^2\theta}{dr^2} = -(\text{sign }\beta)r\theta \tag{6}$$

The boundary conditions are

$$\text{At } r = \left(1 + \frac{\alpha}{\beta}\right)|\beta|^{1/3} \equiv r_1, \quad \theta = 0 \tag{7}$$

$$\text{At } r = \frac{\alpha}{\beta}|\beta|^{1/3} \equiv r_2, \quad \frac{d\theta}{dr} = 0 \tag{8}$$

The solution to equation (6) can be expressed in terms of Airy functions

$$\theta = c_1 A_i(-(\text{sign }\beta)r) + c_2 B_i(-(\text{sign }\beta)r) \tag{9}$$

The condition for nontrivial solutions may be obtained from equations (7)–(9). By choosing the proper branches in the related Bessel functions, we obtain the following cases:

For $\alpha > -\beta > 0$ or $\alpha > 0$, $\beta > 0$, or $-\alpha > \beta > 0$,

$$J_{-1/3}(\zeta_1)J_{-2/3}(\zeta_2) + J_{1/3}(\zeta_1)J_{2/3}(\zeta_2) = 0 \tag{10}$$

where $\zeta_1 \equiv \frac{2}{3}|r_1|^{3/2}$, $\zeta_2 \equiv \frac{2}{3}|r_2|^{3/2}$. For $-\beta > \alpha > 0$,

$$I_{-1/3}(\zeta_1)J_{-2/3}(\zeta_2) - I_{1/3}(\zeta_1)J_{2/3}(\zeta_2) = 0. \tag{11}$$

For $\beta > -\alpha > 0$,

$$J_{-1/3}(\zeta_1)I_{2/3}(\zeta_2) + J_{1/3}(\zeta_1)I_{-2/3}(\zeta_2) = 0 \tag{12}$$

For given α, equations (10)–(12) are solved numerically for β. Fig. 2 shows the complete stability boundaries. Our results agree well with Grishcoff in the range he investigated: $25 > \beta \geq 0$, $-7 < \alpha \leq \pi^2/4$.

Discussion

As far as we know negative β has never been studied before. Our analysis show that the stability for $\alpha > 0$, $\beta < 0$ is not a mere reflection of $\alpha < 0$, $\beta > 0$. This is also illustrated in Fig. 2. In general, the stability curves are so nonlinear that any global straight-line approximation is meaningless. Below each curve, the column is stable with respect to the particular mode. The column is absolutely stable under the primary stability curve.

The α intercepts of the curves in Fig. 3 agree with the normalized Euler buckling loads $\pi^2/4$, $9\pi^2/4$, $25\pi^2/4$. The β intercepts are at 7.83735, 55.9872, 148.512. Our values are more accurate than those of Greenhill and Grishcoff who use infinite series to obtain the values of 7.95 and 7.85, respectively, for the primary mode.

References

1 Euler, L., De Curvis Elasticis, 1744.

2 Greenhill, A. G., "Determination of the Greatest Height Consistent With Stability That a Vertical Pole or Mast Can Be Made, and of the Greatest Height to Which a Tree of Given Proportions Can Grow," *Cambridge Philosophical Society Proceedings*, Vol. 4, 1881, pp. 65–73.

3 Grishcoff, N., in *Theory of Elastic Stability*, Timoshenko, S. P., and Gere, J. M., McGraw-Hill, New York, 1961, p. 104.

The Vibrating Beam With Nonhomogeneous Boundary Conditions

C. R. Edstrom[1]

In Mindlin and Goodman [1] a procedure is described for extending the method of separation of variables to obtain solutions of linear partial differential equations with nonhomogeneous boundary conditions. This procedure utilizes a change of dependent variable to produce homogeneous boundary conditions. Moreover, if the partial differential equation is originally homogeneous, the equation in the new dependent variable becomes nonhomogeneous and the existence of a set of orthogonal functions must be assumed. However, if a property chosen change of dependent variable is made, a homogeneous linear partial differential equation will remain homogeneous as well as have homogeneous boundary conditions, but the initial conditions will be nonhomogeneous. Thus the assumption of the existence of a set of orthogonal functions is not necessary [2]. Also, if a linear partial differential equation is nonhomogeneous, a properly chosen change of dependent variable will reduce the equation to a homogeneous equation as well as produce homogeneous boundary conditions and nonhomogeneous initial conditions. In order to find a proper change of dependent variable, a system of ordinary differential equations with two point boundary conditions must have a solution. However, when the change of dependent variable can be established, the resulting problem can be easily solved.

[1] Associate Professor, Department of Mathematics, Air Force Institute of Technology, Wright-Patterson Air Force Base, Ohio 45433.

Manuscript received by ASME Applied Mechanics Division, April, 1980; final revision, March, 1981.

As an illustration of this method, consider the following example. The boundary-value problem

$$\alpha^2 y_{xxxx} + y_{tt} = 0, \quad \alpha \text{ is a constant,} \tag{1}$$

with $y(0,t) = y(\pi,t) = y_{xx}(0,t) = y(x,0) = y_t(x,0) = 0$ and $y_{xx}(\pi,t) = 4A\pi \sin \alpha t$, A is a constant, would describe a beam of length π, initially at rest with no initial velocity, with one simply supported end and with a time-dependent bending moment at the other end. Make the change of dependent variable

$$y(x,t) = Y(x,t) + F(x) \sin \alpha t + \alpha G(x) t \cos \alpha t. \tag{2}$$

This form for the change of dependent variable was selected because of the form of the nonhomogeneous boundary condition associated with equation (1). Substituting $y(x,t)$ from equation (2) into equation (1), we have

$$\alpha^2 Y_{xxxx} + Y_{tt} = 0 \tag{3}$$

with

$$Y(0,t) = Y(\pi,t) = Y_{xx}(0,t) = Y_{xx}(\pi,t) = 0 \tag{4}$$

if $F(x)$ and $G(x)$ satisfy the system

$$F''''(x) - F(x) = 2G(x)$$

$$G''''(x) - G(x) = 0$$

subject to the two-point boundary conditions

$$F(0) = F(\pi) = F''(0) = G(0) = G(\pi) = G''(0) = G''(\pi) = 0$$
$$\text{and } F''(\pi) = 4A\pi.$$

A solution of this system of ordinary differential equations is

$$F(x) = 2Ax \cos x - 5A \sin x + \frac{2A\pi \sinh x}{\sinh \pi}$$

$$G(x) = 4A \sin x \tag{5}$$

Thus substituting $F(x)$ and $G(x)$ from equation (5) into equation (2), we have

$$y(x,t) = Y(x,t) + 2Ax \cos x \sin \alpha t + A(4\alpha t \cos \alpha t - 5 \sin \alpha t) \sin x + \frac{2A\pi \sinh x \sin \alpha t}{\sinh \pi} \tag{6}$$

The initial conditions for the function $Y(x,t)$ become

$$Y(x,0) = 0 \text{ and } Y_t(x,0) = \alpha A \left(\sin x - 2x \cos x - \frac{2\pi \sinh x}{\sinh \pi} \right). \tag{7}$$

Applying the method of separation of variables to equation (3) with homogeneous boundary conditions (4) and nonhomogeneous initial conditions (7), the solution of this new problem is

$$Y(x,t) = 8A \sum_{n=2}^{\infty} \frac{(-1)^{n+1}}{n(n^4 - 1)} \sin \alpha n^2 t \sin nx. \tag{8}$$

Substituting $Y(x,t)$ from equation (8) into equation (6), we have the solution of the original problem. Also from equation (6) we observe that $y(x,t)$ is unbounded as $t \to \infty$. Thus the time-dependent bending moment produces resonance. Actually, there are infinitely many time-dependent bending moments which will produce resonance.

References

1 Mindlin, R. D., and Goodman, L. E., "Beam Vibrations With Time-Dependent Boundary Conditions," ASME JOURNAL OF APPLIED MECHANICS, Vol 17, 1950, pp. 377–380.

2 Wylie, C. R., *Advanced Engineering Mathematics*, 4th ed., McGraw-Hill, New York, 1975, p. 363.

Similarity Solutions to the Non-isothermal, Two-Dimensional Squeezing Flow of a Viscous Fluid

N. Phan-Thien[1]

1 Introduction

Recently, Cantwell [1] has shown that the two-dimensional unsteady flow of a viscous fluid admits the following 10-parameter Lie group of transformations, written in an infinitesimal manner [2],

$$\begin{aligned} \tilde{x} &= x + \epsilon \xi(x, y, t, \psi) + O(\epsilon^2), \\ \tilde{y} &= y + \epsilon \rho(x, y, t, \psi) + O(\epsilon^2), \\ \tilde{t} &= t + \epsilon \zeta(x, y, t, \psi) + O(\epsilon^2), \\ \tilde{\psi} &= \psi + \epsilon \eta(x, y, t, \psi) + O(\epsilon^2), \end{aligned} \tag{1}$$

where x, y, t are space-time coordinates, ψ is the stream function and ξ, ρ, ζ, η are given by [1]

$$\begin{aligned} \xi &= ax + by + cty + f_1(t) + d, \\ \rho &= -bx + ay - ctx + f_2(t) + e, \\ \zeta &= 2at + h, \\ \eta &= \tfrac{1}{2}c(x^2 + y^2) - \dot{f}_2(t)x + \dot{f}_1(t)\, y + s(t) + p, \end{aligned} \tag{2}$$

where the dot denotes a time derivative. This group has seven explicit parameters, a, b, c, d, e, h, and p and three implicit parameters contained in $f_1(t)$, $f_2(t)$, and $s(t)$.

In this Note, we extend (1) to cover the nonisothermal case and illustrate the technique with the squeezing flow problem where either the temperature or the heat flux boundary condition is specified on the plate.

2 Invariant Group

The nonisothermal flow of an incompressible Newtonian fluid can be adequately described by

$$\nabla^2 \psi_t + \psi_y \nabla^2 \psi_x - \psi_x \nabla^2 \psi_y = \nu \nabla^4 \psi \tag{3}$$

$$T_t + \psi_y T_x - \psi_x T_y = D \nabla^2 T, \tag{4}$$

where ψ is the stream function, T the absolute temperature, and D is the thermal diffusivity of the liquid, with a kinematic viscosity ν. Throughout the Note, the subscript denotes a partial derivative with respect to the subscript.

Consider a one-parameter (ϵ) Lie group of space-time transformations [2], written in an infinitesimal manner,

$$\begin{aligned} \tilde{x} &= x + \epsilon \xi(x, y, t) + O(\epsilon^2), \\ \tilde{y} &= y + \epsilon \rho(x, y, t) + O(\epsilon^2), \\ \tilde{t} &= t + \epsilon \zeta(x, y, t) + O(\epsilon^2), \\ \tilde{\psi} &= \psi + \epsilon \eta(x, y, t, \psi, T) + O(\epsilon^2), \\ \tilde{T} &= T + \epsilon \pi(x, y, t, \psi, T) + O(\epsilon^2), \end{aligned} \tag{5}$$

where $\tilde{x}, \tilde{y}, \tilde{t}, \tilde{\psi}, \tilde{T}$ are the new variables.

Equations (3)–(4) are said to be invariant under (6) if they remain unchanged in the new coordinates $(\tilde{x}, \tilde{y}, \tilde{t}, \tilde{\psi}, \tilde{T})$, viz.,

$$\tilde{\nabla}^2 \tilde{\psi}_{\tilde{t}} + \tilde{\psi}_{\tilde{y}} \tilde{\nabla}^2 \tilde{\psi}_{\tilde{x}} - \tilde{\psi}_{\tilde{x}} \tilde{\nabla}^2 \tilde{\psi}_{\tilde{y}} = \nu \tilde{\nabla}^4 \tilde{\psi}, \tag{6}$$

[1] Department of Mechanical Engineering, University of Sydney, Sydney. N.S.W. 2006 Australia.

Manuscript received by ASME Applied Mechanics Division, December, 1980.

As an illustration of this method, consider the following example. The boundary-value problem

$$\alpha^2 y_{xxxx} + y_{tt} = 0, \quad \alpha \text{ is a constant,} \tag{1}$$

with $y(0,t) = y(\pi,t) = y_{xx}(0,t) = y(x,0) = y_t(x,0) = 0$ and $y_{xx}(\pi,t) = 4A\pi \sin \alpha t$, A is a constant, would describe a beam of length π, initially at rest with no initial velocity, with one simply supported end and with a time-dependent bending moment at the other end. Make the change of dependent variable

$$y(x,t) = Y(x,t) + F(x) \sin \alpha t + \alpha G(x) t \cos \alpha t. \tag{2}$$

This form for the change of dependent variable was selected because of the form of the nonhomogeneous boundary condition associated with equation (1). Substituting $y(x,t)$ from equation (2) into equation (1), we have

$$\alpha^2 Y_{xxxx} + Y_{tt} = 0 \tag{3}$$

with

$$Y(0,t) = Y(\pi,t) = Y_{xx}(0,t) = Y_{xx}(\pi,t) = 0 \tag{4}$$

if $F(x)$ and $G(x)$ satisfy the system

$$F''''(x) - F(x) = 2G(x)$$

$$G''''(x) - G(x) = 0$$

subject to the two-point boundary conditions

$$F(0) = F(\pi) = F''(0) = G(0) = G(\pi) = G''(0) = G''(\pi) = 0$$
$$\text{and } F''(\pi) = 4A\pi.$$

A solution of this system of ordinary differential equations is

$$F(x) = 2Ax \cos x - 5A \sin x + \frac{2A\pi \sinh x}{\sinh \pi}$$

$$G(x) = 4A \sin x \tag{5}$$

Thus substituting $F(x)$ and $G(x)$ from equation (5) into equation (2), we have

$$y(x,t) = Y(x,t) + 2Ax \cos x \sin \alpha t + A(4\alpha t \cos \alpha t$$
$$- 5 \sin \alpha t) \sin x + \frac{2A\pi \sinh x \sin \alpha t}{\sinh \pi} \tag{6}$$

The initial conditions for the function $Y(x,t)$ become

$$Y(x,0) = 0 \text{ and } Y_t(x,0) = \alpha A \left(\sin x - 2x \cos x - \frac{2\pi \sinh x}{\sinh \pi}\right). \tag{7}$$

Applying the method of separation of variables to equation (3) with homogeneous boundary conditions (4) and nonhomogeneous initial conditions (7), the solution of this new problem is

$$Y(x,t) = 8A \sum_{n=2}^{\infty} \frac{(-1)^{n+1}}{n(n^4 - 1)} \sin \alpha n^2 t \sin nx. \tag{8}$$

Substituting $Y(x,t)$ from equation (8) into equation (6), we have the solution of the original problem. Also from equation (6) we observe that $y(x,t)$ is unbounded as $t \to \infty$. Thus the time-dependent bending moment produces resonance. Actually, there are infinitely many time-dependent bending moments which will produce resonance.

References

1 Mindlin, R. D., and Goodman, L. E., "Beam Vibrations With Time-Dependent Boundary Conditions," ASME JOURNAL OF APPLIED MECHANICS, Vol 17, 1950, pp. 377–380.

2 Wylie, C. R., *Advanced Engineering Mathematics*, 4th ed., McGraw-Hill, New York, 1975, p. 363.

Similarity Solutions to the Non-isothermal, Two-Dimensional Squeezing Flow of a Viscous Fluid

N. Phan-Thien[1]

1 Introduction

Recently, Cantwell [1] has shown that the two-dimensional unsteady flow of a viscous fluid admits the following 10-parameter Lie group of transformations, written in an infinitesimal manner [2],

$$\begin{aligned}
\tilde{x} &= x + \epsilon \xi(x, y, t, \psi) + O(\epsilon^2), \\
\tilde{y} &= y + \epsilon \rho(x, y, t, \psi) + O(\epsilon^2), \\
\tilde{t} &= t + \epsilon \zeta(x, y, t, \psi) + O(\epsilon^2), \\
\tilde{\psi} &= \psi + \epsilon \eta(x, y, t, \psi) + O(\epsilon^2),
\end{aligned} \tag{1}$$

where x, y, t are space-time coordinates, ψ is the stream function and ξ, ρ, ζ, η are given by [1]

$$\begin{aligned}
\xi &= ax + by + cty + f_1(t) + d, \\
\rho &= -bx + ay - ctx + f_2(t) + e, \\
\zeta &= 2at + h, \\
\eta &= \tfrac{1}{2}c(x^2 + y^2) - \dot{f}_2(t)x + \dot{f}_1(t)\, y + s(t) + p,
\end{aligned} \tag{2}$$

where the dot denotes a time derivative. This group has seven explicit parameters, a, b, c, d, e, h, and p and three implicit parameters contained in $f_1(t)$, $f_2(t)$, and $s(t)$.

In this Note, we extend (1) to cover the nonisothermal case and illustrate the technique with the squeezing flow problem where either the temperature or the heat flux boundary condition is specified on the plate.

2 Invariant Group

The nonisothermal flow of an incompressible Newtonian fluid can be adequately described by

$$\nabla^2 \psi_t + \psi_y \nabla^2 \psi_x - \psi_x \nabla^2 \psi_y = \nu \nabla^4 \psi \tag{3}$$

$$T_t + \psi_y T_x - \psi_x T_y = D \nabla^2 T, \tag{4}$$

where ψ is the stream function, T the absolute temperature, and D is the thermal diffusivity of the liquid, with a kinematic viscosity ν. Throughout the Note, the subscript denotes a partial derivative with respect to the subscript.

Consider a one-parameter (ϵ) Lie group of space-time transformations [2], written in an infinitesimal manner,

$$\begin{aligned}
\tilde{x} &= x + \epsilon \xi(x, y, t) + O(\epsilon^2), \\
\tilde{y} &= y + \epsilon \rho(x, y, t) + O(\epsilon^2), \\
\tilde{t} &= t + \epsilon \zeta(x, y, t) + O(\epsilon^2), \\
\psi &= \psi + \epsilon \eta(x, y, t, \psi, T) + O(\epsilon^2), \\
\tilde{T} &= T + \epsilon \pi(x, y, t, \psi, T) + O(\epsilon^2),
\end{aligned} \tag{5}$$

where $\tilde{x}, \tilde{y}, \tilde{t}, \tilde{\psi}, \tilde{T}$ are the new variables.

Equations (3)–(4) are said to be invariant under (6) if they remain unchanged in the new coordinates $(\tilde{x}, \tilde{y}, \tilde{t}, \tilde{\psi}, \tilde{T})$, viz.,

$$\tilde{\nabla}^2 \tilde{\psi}_{\tilde{t}} + \tilde{\psi}_{\tilde{y}} \tilde{\nabla}^2 \tilde{\psi}_{\tilde{x}} - \tilde{\psi}_{\tilde{x}} \tilde{\nabla}^2 \tilde{\psi}_{\tilde{y}} = \nu \tilde{\nabla}^4 \tilde{\psi}, \tag{6}$$

[1] Department of Mechanical Engineering, University of Sydney, Sydney. N.S.W. 2006 Australia.

Manuscript received by ASME Applied Mechanics Division, December, 1980.

$$\tilde{T}_{\tilde{t}} + \tilde{\psi}_{\tilde{y}}\tilde{T}_{\tilde{x}} - \tilde{\psi}_{\tilde{x}}\tilde{T}_{\tilde{y}} = D\tilde{\nabla}^2\tilde{T}, \quad \tilde{\nabla} = \partial^2/\partial\tilde{x}^2 + \partial^2/\partial\tilde{y}^2 \tag{7}$$

The mathematics of invariance are well presented in the monograph of Bluman and Cole [2], and it can be shown that up to an error terms of $O(\epsilon^2)$, (6) and (7) lead to (the so-called invariant surface conditions [2]).

$$\begin{aligned} \xi &= ax + by + cty + f_1(t) + d \\ \rho &= bx + ay - ctx + f_2(t) + e \\ \zeta &= 2at + h \\ \eta &= \tfrac{1}{2}c(x^2 + y^2) - \dot{f}_2(t)x + \dot{f}_1(t)y + s(t) + p \\ \pi &= 2aT + q \end{aligned} \tag{8}$$

This represents an 11-parameters group of transformations; eight are explicit (a, b, c, d, e, h, p, q) and three implicitly contained in $f_1(t)$, $f_2(t)$, and $s(t)$.

For any function F that remains invariant under (8), it must satisfy the invariant surface condition [2]

$$\xi F_x + \rho F_y + \zeta F_t + \eta F_\psi + \pi F_T = 0$$

which can be solved by the characteristics method

$$\frac{dx}{\xi} = \frac{dy}{\rho} = \frac{dt}{\zeta} = \frac{d\psi}{\eta} = \frac{dT}{\pi} = \frac{dF}{0} \tag{9}$$

Similarity variables can be generated by (9). To illustrate its application, we take up the squeezing flow next.

3 Squeezing Flow

The problem of squeezing a viscous fluid between two parallel plates occurs in the unsteady loading of bearings; however, its solution using the full Navier-Stokes equations is still unknown and existing analyses invariably assume the quasi-static and lubrication approximation. Thus similarity solutions to this problem are welcome from a numerical analysis point of view. To this end Wang [3] noted that if the approach velocity of the plates is proportional to $(1 - \alpha t)^{-1/2}$, where α is a constant, then a similarity solution is possible. This was confirmed in Phan-Thien [4] using Cantwell's [1] similarity group. We consider here the nonisothermal squeezing flow where the boundary conditions are

On the upper plate where $y = \mathrm{H}(t)$, the velocities must satisfy

$$u(y = \mathrm{H}(t)) = 0; \quad v(y = \mathrm{H}(t)) = \dot{\mathrm{H}}(t) \tag{10}$$

For the temperature field, we may choose either to prescribe the temperature (Case a),

$$T(y = \mathrm{H}(t)) = T_1(t) \tag{11}$$

or to prescribe the heat flux (Case b),

$$T_y(y = \mathrm{H}(t)) = -Q(t), \tag{12}$$

where $T_1(t)$, $Q(t)$ are some known functions of time.

Only symmetrical flow fields are considered; thus

$$v(y = 0) = 0 = T_y(y = 0) \tag{13}$$

Now we select a subgroup of (8) that also preserves the boundary conditions (10)–(13).

Invariance of the boundary curve $y = \mathrm{H}(t)$ requires that $\tilde{y} = \mathrm{H}(\tilde{t})$ which implies

$$\rho = \dot{\mathrm{H}}(t)\zeta, \quad \text{at} \quad y = \mathrm{H}(t),$$

that is,

$$-bx + a\mathrm{H}(t) - ctx + f_2(t) + e = (2at + h)\,\dot{\mathrm{H}}(t)$$

This is satisfied identically if $b = c = 0$ and

$$f_2(t) = \dot{\mathrm{H}}(t)\,(2at + h) - a\mathrm{H}(t) - e \tag{14}$$

Next, the invariance of (10) implies

$$\tilde{u}(y = \mathrm{H}(t)) = 0, \quad \tilde{v}(y = \mathrm{H}(t)) = \dot{\mathrm{H}}(\tilde{t}) \tag{15}$$

which leads to $\dot{f}_1 = 0$ or that $f_1(t) =$ constant. Similarly, the invariance of $y = 0$ requires that $f_2 = e$. Thus, from (14),

$$(2at + h)\,\dot{\mathrm{H}}(t) - a\mathrm{H}(t) = 0$$

or that

$$\mathrm{H}(t) = r(2at + h)^{1/2}, \quad \dot{\mathrm{H}}(t) = s(2at + h)^{-1/2}. \tag{16}$$

where r, s are some constants.

Next, the invariance of $T_y(y = 0) = 0$ is satisifed automatically. For Case (a), the invariance of (11) requires

$$\tilde{T}(y = \mathrm{H}(t)) = T_1(\tilde{t})$$

which leads to

$$2aT_1(t) + q = \dot{T}_1(t)\,(2at + h)$$

or

$$T_1(t) = m(2at + h) + n, \tag{17}$$

where m, n are some constants.

Finally, for Case (b) we require that (12) in invariant, viz.,

$$\tilde{T}_{\tilde{y}}(y = \mathrm{H}(t)) = -Q(\tilde{t})$$

which implies

$$(2at + R)\,\dot{Q} + aQ = 0,$$

or

$$Q(t) = k(2at + h)^{1/2}, \tag{18}$$

where k is a constant.

Therefore if the approach velocity is given by (16) and the prescribed temperature (or temperature gradient) is given by (17) (or (18)) then the plane nonisothermal squeezing flow admits similarity solutions described by the following characteristics (cf. (9)):

$$\frac{dx}{ax} = \frac{dy}{ay} = \frac{dt}{2at + h} = \frac{d\psi}{s(t) + p} = \frac{dT}{2aT + q} \tag{19}$$

The first two equalities yield the similarity variable

$$\xi_1 = x(2at + h)^{-1/2}, \quad \xi_2 = y(2at + h)^{-1/2} \tag{20}$$

from which the stream function and the temperature is given by

$$\psi = \int_0^t \frac{s(t') + p}{2at' + h}\,dt' + \phi(\xi_1, \xi_2), \tag{21}$$

$$T = (2at + h)\,\theta\,(\xi_1, \xi_2), \tag{22}$$

where ϕ and θ can be found by substituting (21)–(22) back in (3)–(4).

4 A Similarity Solution at Small "Reynolds" and "Peclet" Number

To construct a similarity solution, we assume the gap thickness to be

$$2\mathrm{H}(t) = 2a(1 - \alpha t)^{1/2} \tag{23}$$

Note that (23) is equivalent to (16) and $2a$ is the initial gap thickness. We only discuss Case (a) where

$$T_1(t) = T_0(1 - \alpha t) \tag{24}$$

which is equivalent to (17); T_0 is the initial plate temperature.

Similarity variables are (cf. (20))

$$\xi_1 = \frac{x}{a}(1 - \alpha t)^{-1/2}, \quad \xi_2 = \frac{y}{a}(1 - \alpha t)^{-1/2} \tag{25}$$

A similarity solution can be constructed when $s(t) + p = 0$ and

$$\phi(\xi_1, \xi_2) = -\tfrac{1}{2}a^2\alpha\xi_1 f(\xi_2), \quad \theta(\xi_1, \xi_2) = \theta(\xi_2) \tag{26}$$

which yields for the velocity field

$$u = \frac{\alpha x}{2(1-\alpha t)} f'(\xi_2), \tag{27}$$

$$v = \frac{a}{2(1-\alpha t)^{1/2}} f(\xi_2). \tag{28}$$

This is the similarity solution presented by Wang [3].

The structure of this solution is obvious: it does not permit material planes to experience any "buckling" during subsequent deformations.

Assuming (27)–(28), the temperature field is given by

$$T = T_0(1-\alpha t)\theta(\xi_2), \tag{29}$$

where $f(\xi_2)$ and $\theta(\xi_2)$ are given through (cf. (3)–(4)).

$$\xi_2 f''' + 3f'' + f'f'' - ff''' = \frac{1}{R} f'''', \tag{30}$$

$$\xi\theta' - f\theta' - 2\theta = \frac{1}{P}\theta'' \tag{31}$$

In (30)–(31) R and P are the Reynolds and Peclet numbers defined by

$$R = \frac{\alpha a^2}{2\nu}, \quad P = \frac{\alpha a^2}{2D}, \tag{32}$$

and the boundary conditions on f and θ are

$$f(0) = f''(0) = 0 = f'(1) = \theta'(0)$$

$$f(1) = \theta(1) = 1 \tag{33}$$

When $R \sim P \ll 1$ the solutions take the form

$$f = f_0 + Rf_1 + R^2 f_2 + O(R^3), \tag{34}$$

$$\theta = \theta_0 + P\theta + P^2\theta_2 + O(P^3, R^3, R^2P, RP^2) \tag{35}$$

where

$$f_0 = -\tfrac{1}{2}\xi_2^3 + \frac{3}{2}\xi_2, \quad \theta_0 = 1, \tag{36}$$

$$f_1 = \frac{1}{280}(\xi_2^7 - 28\xi_2^5 + 53\xi_2^3 - 26\xi_2),$$

$$\theta_1 = 1 - \xi_2^2, \tag{37}$$

and

$$f_2 = \frac{1}{280}\left(\frac{1}{330}\xi_2^{11} + \frac{1}{72}\xi_2^9 - \frac{193}{70}\xi_2^7 + \frac{53}{5}\xi_2^5 - \frac{18017}{1386}\xi_2^3 + \frac{47489}{9240}\xi_2\right),$$

$$\theta_2 = \frac{1}{60}\left(-2\xi_2^6 + 15\xi_2^4 - 60\xi_2^2 + 47\right). \tag{38}$$

The zeroth-order solution is the Stokes flow in which the temperature is uniform throughout. Up to terms of $O(P)$, the temperature is not influenced by the velocity field and is quadratic in ξ_2. The influence of the velocity field on the temperature can be felt at the $O(P^2)$ level via the term $f_0\theta_1'$. At moderate Reynolds and Peclet numbers ($R, P \sim O(1)$), there will be boundary layers near the plates and a matching method must be used to find a solution to (30)–(31).

References

1 Cantwell, B. J., "Similarity Transformations for the Two-Dimensional Unsteady Stream Function Equation," *Journal of Fluid Mechanics*, Vol. 85, 1978, pp. 257–271.

2 Bluman, G. W., and Cole, J. D., *Similarity Methods for Differential Equations*, Springer-Verlag, 1974.

3 Wang, C.-Y., "The Squeezing of a Fluid Between Two Plates," ASME JOURNAL OF APPLIED MECHANICS, Vol. 43, 1976, pp. 579–587.

4 Phan-Thien, N., "On the Invariance Group of the Plane Squeezing Flow of a Viscous Fluid," ASME JOURNAL OF APPLIED MECHICS, Vol. 47, 1980, pp. 213–214.

Application of the Reissner Method to a Timoshenko Beam

J. S. Rao,[1] S. V. Kulkarni,[2] and K. B. Subrahmanyam[3]

The Reissner and the potential energy methods have been applied to a Timoshenko beam vibrating in flexure. Frequency equations are developed using shape functions for bending moment, shearing force, deflection, and slope in series form through the Ritz process. Natural frequencies and mode shapes are obtained and comparison is made between the results of the two approaches from which it is observed that the Reissner method indicates a quicker convergence and gives better mode shapes.

Nomenclature

A = area of cross section of beam at any section
E, G = Young's modulus, modulus of rigidity
I_{xx} = second moment of area about principal axis
L = length of beam
M, V = bending moment, shearing force
p = circular frequency
t = time
xx, yy = coordinate axes through the centroid
y, ϕ = dynamic deflection and slope of the beam in yz-plane
z = coordinate distance measured from the fixed end
$Z = z/L$
ρ = mass density of the material of the beam
$'$ = dash represents differentiation with respect to z

Introduction

The objectives of the present Note are to apply the Reissner principle [1–3] to the simplest idealization of a turbomachine blade—a Timoshenko beam vibrating in flexure and to compare the results with those obtained from the classical potential energy method.

To this end, the shape functions for bending moment, shearing force, deflection, and slope are developed in the series form. Making use of these in the Reissner and the potential energy functionals, the respective frequency equations are obtained through the Ritz process and the convergence rates of the two approaches are studied for a Timoshenko beam of given parameters.

Analysis

The Reissner and the total potential energy functionals for a uniform symmetric Timoshenko beam, without body forces and surface tractions, are, respectively [1]:

$$I_R = -\int_0^L \left[\frac{M^2}{2EI_{xx}} + \frac{V^2}{2KGA} + M\phi' - V(y' - \phi)\right] dz \tag{1}$$

$$\Pi = \tfrac{1}{2}\int_0^L [EI_{xx}(\phi')^2 + KGA(y' - \phi)^2] dz \tag{2}$$

The kinetic energy of the beam vibrating in the yz-plane is

$$T = \tfrac{1}{2}\int_0^L [\rho I_{xx}\dot{\phi}'^2 + \rho A\dot{y}^2] dz \tag{3}$$

The dynamic Reissner functional L_R and the Lagrangian L_Π can be formulated in the usual way by letting

[1] Professor of Mechanical Engineering, Indian Institute of Technology, New Delhi-110029 India.

[2] Professor and Head, Mechanical Engineering Department, Regional Engineering College, Kurukshetra-132119 India.

[3] Lecturer, Mechanical Engineering Department, Regional Engineering College, Kurukshetra-132119 India.

Manuscript received by ASME Applied Mechanics Division, May, 1980; final revision, November, 1980.

which yields for the velocity field

$$u = \frac{\alpha x}{2(1-\alpha t)} f'(\xi_2), \tag{27}$$

$$v = \frac{a}{2(1-\alpha t)^{1/2}} f(\xi_2). \tag{28}$$

This is the similarity solution presented by Wang [3].

The structure of this solution is obvious: it does not permit material planes to experience any "buckling" during subsequent deformations.

Assuming (27)–(28), the temperature field is given by

$$T = T_0(1-\alpha t)\theta(\xi_2), \tag{29}$$

where $f(\xi_2)$ and $\theta(\xi_2)$ are given through (cf. (3)–(4)).

$$\xi_2 f''' + 3f'' + f'f'' - ff''' = \frac{1}{R} f'''', \tag{30}$$

$$\xi\theta' - f\theta' - 2\theta = \frac{1}{P}\theta'' \tag{31}$$

In (30)–(31) R and P are the Reynolds and Peclet numbers defined by

$$R = \frac{\alpha a^2}{2\nu}, \quad P = \frac{\alpha a^2}{2D}, \tag{32}$$

and the boundary conditions on f and θ are

$$f(0) = f''(0) = 0 = f'(1) = \theta'(0)$$

$$f(1) = \theta(1) = 1 \tag{33}$$

When $R \sim P \ll 1$ the solutions take the form

$$f = f_0 + Rf_1 + R^2 f_2 + O(R^3), \tag{34}$$

$$\theta = \theta_0 + P\theta + P^2\theta_2 + O(P^3, R^3, R^2P, RP^2) \tag{35}$$

where

$$f_0 = -\tfrac{1}{2}\xi_2^3 + \frac{3}{2}\xi_2, \quad \theta_0 = 1, \tag{36}$$

$$f_1 = \frac{1}{280}(\xi_2^7 - 28\xi_2^5 + 53\xi_2^3 - 26\xi_2),$$

$$\theta_1 = 1 - \xi_2^2, \tag{37}$$

and

$$f_2 = \frac{1}{280}\left(\frac{1}{330}\xi_2^{11} + \frac{1}{72}\xi_2^9 - \frac{193}{70}\xi_2^7 + \frac{53}{5}\xi_2^5 - \frac{18017}{1386}\xi_2^3 + \frac{47489}{9240}\xi_2\right),$$

$$\theta_2 = \frac{1}{60}\left(-2\xi_2^6 + 15\xi_2^4 - 60\xi_2^2 + 47\right). \tag{38}$$

The zeroth-order solution is the Stokes flow in which the temperature is uniform throughout. Up to terms of $O(P)$, the temperature is not influenced by the velocity field and is quadratic in ξ_2. The influence of the velocity field on the temperature can be felt at the $O(P^2)$ level via the term $f_0\theta_1'$. At moderate Reynolds and Peclet numbers ($R, P \sim O(1)$), there will be boundary layers near the plates and a matching method must be used to find a solution to (30)–(31).

References

1 Cantwell, B. J., "Similarity Transformations for the Two-Dimensional Unsteady Stream Function Equation," *Journal of Fluid Mechanics*, Vol. 85, 1978, pp. 257–271.

2 Bluman, G. W., and Cole, J. D., *Similarity Methods for Differential Equations*, Springer-Verlag, 1974.

3 Wang, C.-Y., "The Squeezing of a Fluid Between Two Plates," ASME JOURNAL OF APPLIED MECHANICS, Vol. 43, 1976, pp. 579–587.

4 Phan-Thien, N., "On the Invariance Group of the Plane Squeezing Flow of a Viscous Fluid," ASME JOURNAL OF APPLIED MECHICS, Vol. 47, 1980, pp. 213–214.

Application of the Reissner Method to a Timoshenko Beam

J. S. Rao,[1] S. V. Kulkarni,[2] and K. B. Subrahmanyam[3]

The Reissner and the potential energy methods have been applied to a Timoshenko beam vibrating in flexure. Frequency equations are developed using shape functions for bending moment, shearing force, deflection, and slope in series form through the Ritz process. Natural frequencies and mode shapes are obtained and comparison is made between the results of the two approaches from which it is observed that the Reissner method indicates a quicker convergence and gives better mode shapes.

Nomenclature

A = area of cross section of beam at any section
E, G = Young's modulus, modulus of rigidity
I_{xx} = second moment of area about principal axis
L = length of beam
M, V = bending moment, shearing force
p = circular frequency
t = time
xx, yy = coordinate axes through the centroid
y, ϕ = dynamic deflection and slope of the beam in yz-plane
z = coordinate distance measured from the fixed end
$Z = z/L$
ρ = mass density of the material of the beam
$'$ = dash represents differentiation with respect to z

Introduction

The objectives of the present Note are to apply the Reissner principle [1–3] to the simplest idealization of a turbomachine blade—a Timoshenko beam vibrating in flexure and to compare the results with those obtained from the classical potential energy method.

To this end, the shape functions for bending moment, shearing force, deflection, and slope are developed in the series form. Making use of these in the Reissner and the potential energy functionals, the respective frequency equations are obtained through the Ritz process and the convergence rates of the two approaches are studied for a Timoshenko beam of given parameters.

Analysis

The Reissner and the total potential energy functionals for a uniform symmetric Timoshenko beam, without body forces and surface tractions, are, respectively [1]:

$$I_R = -\int_0^L \left[\frac{M^2}{2EI_{xx}} + \frac{V^2}{2KGA} + M\phi' - V(y' - \phi)\right] dz \tag{1}$$

$$\Pi = \tfrac{1}{2}\int_0^L [EI_{xx}(\phi')^2 + KGA(y' - \phi)^2] dz \tag{2}$$

The kinetic energy of the beam vibrating in the yz-plane is

$$T = \tfrac{1}{2}\int_0^L [\rho I_{xx}\dot{\phi}'^2 + \rho A\dot{y}^2] dz \tag{3}$$

The dynamic Reissner functional L_R and the Lagrangian L_Π can be formulated in the usual way by letting

[1] Professor of Mechanical Engineering, Indian Institute of Technology, New Delhi-110029 India.

[2] Professor and Head, Mechanical Engineering Department, Regional Engineering College, Kurukshetra-132119 India.

[3] Lecturer, Mechanical Engineering Department, Regional Engineering College, Kurukshetra-132119 India.

Manuscript received by ASME Applied Mechanics Division, May, 1980; final revision, November, 1980.

$$L_R = T - I_R \tag{4}$$

$$L_\Pi = T - \Pi \tag{5}$$

It can be seen that L_R is a functional of the form

$$L_R = f(M,V,y,y',\dot{y},\phi,\phi',\dot{\phi},z,t) \tag{6}$$

where z and t are independent variables. Application to equation (6) of the standard procedure of calculus or variations [4] leads to the stress-strain relations, equations of motion and boundary conditions which agree with those derived by Carnegie [5].

The time averaged Reissner and potential energy functionals for flexural vibration of a Timoshenko beam are given by

$$\mathsf{L}_R = \int_0^L \left[\frac{\rho p^2 I_{xx}}{2}\phi^2 + \frac{\rho p^2 A}{2}y^2 + \frac{M^2}{2EI_{xx}} + \frac{V^2}{2KGA} + M\phi' - V(y' - \phi)\right] dz \tag{7}$$

$$\mathsf{L}_\Pi = \tfrac{1}{2}\int_0^L [\rho p^2 I_{xx}\phi^2 + \rho p^2 A y^2 - EI_{xx}(\phi')^2 - KGA(y' - \phi)^2]dz \tag{8}$$

The shape functions are assumed in series form as

$$y = \sum_i \{A_i Z^i + A_{i+1} Z^{i+1}\} \tag{9}$$

$$\phi = \sum_i \{B_i Z^i + B_{i+1} Z^{i+1}\} \tag{10}$$

$$M = \sum_i \{C_i(1 - Z)^i + C_{i+1}(1 - Z)^{i+1}\} \tag{11}$$

$$V = \sum_i \{D_i(1 - Z)^i + D_{i+1}(1 - Z)^{i+1}\} \tag{12}$$

which satisfy the boundary conditions

$$\begin{aligned} y = \phi = 0 \quad &\text{at} \quad Z = 0 \\ M = V = 0 \quad &\text{at} \quad Z = 1 \end{aligned} \tag{13}$$

The arbitrary constants A_{i+1} and B_{i+1} are eliminated from the conditions

$$(y' - \phi) = \phi' = 0 \quad \text{at} \quad Z = 1 \tag{14}$$

and C_{i+1} and D_{i+1} from the conditions

$$M' = V; \quad V' = 0 \quad \text{for all values of } Z. \tag{15}$$

Substituting the resulting shape functions in equations (7) and (8), performing the necessary calculus and applying the Ritz process for minimization of L_R and L_π with respect to $A_i, \ldots D_i$, we get the familiar eigenvalue problems of the form

$$\mathbf{A} + p^2\mathbf{B}' = 0 \tag{16}$$

where $\mathbf{A}$ and $\mathbf{B}$ are symmetric square matrices

The eigenvalues and mode shapes of the two problems as defined by equation (10) are obtained from a computer program developed in Fortran language and run on a TDC-316 computer for a beam with the following data:

$L = 3.62$ in. (9.1948 cm) $\quad A = 0.128$ sq. in. (0.8258 cm^2)

$E = 30 \times 10^6$ lb/in.^{2} (206.85) GPa) $G = 12 \times 10^6$ lb/in.^{2} (82.74G Pa)

$I_{xx} = 0.001388$ in.^{4} (0.05777 cm^4), $\rho = 0.283$ lb/in.^{3} (0.00783 kg/cm^3)

$$K = 10(1 + \nu)/(12 + 11\nu)$$

where ν is Poisson's ratio.

Results and Discussion

Table 1 gives a comparison of the results obtained here with those of Sutherland and Goodman [6].

Table 1 Frequency ratio $= \left[\dfrac{\text{frequency corrected for shear and rotary inertia}}{\text{classical uncorrected frequency}}\right]$

Number of terms in solution	Reissner method			Potential energy method		
	I Mode	II Mode	III Mode	I Mode	II Mode	III Mode
1	1.028	—	—	2.261	—	—
2	0.992	1.082	—	1.002	1.827	—
3	0.992	0.951	1.126	0.992	0.967	1.557
4	0.992	0.951	0.902	0.992	0.995	0.924
5	0.992	0.950	0.897	0.992	0.951	0.909
6	—	—	—	0.992	0.951	0.899
Frequency ratio from reference [6]	0.99	0.95	0.89			

Table 2 Nodal locations: fraction of length from fixed end

Mode number	Nodal location		
	Reissner method	Potential energy method	Exact solution [7]
II	0.783	0.783	0.783
III	0.500	0.493	0.504
	0.868	0.875	0.868

It can be seen that the frequency ratio decreases as the number of terms in the assumed solutions increase. The frequency ratios for the first two modes obtained from the Reissner method with a three-term solution show convergence to three significant figures while the potential energy method indicates a five-term solution for a similar accuracy. While it has been observed that the mode shapes obtained by both of these methods are close to the exact ones, the nodal locations given by the Reissner method, Table 2, are seen to be closer to the exact ones [7].

From the results presented, the Reissner method appears to indicate a quicker convergence and gives better mode shapes than the classical potential energy method.

Acknowledgment

The authors gratefully acknowledge the financial assistance rendered by the University Grants Commission, Government of India, for this investigation.

References

1 Subrahmanyam, K. B., Kulkarni, S. V., and Rao, J. S., "Analysis of a Cantilever Beam Under Steady Lateral Force," *Proceedings of the ISTAM*, 1978.

2 Idem, "Static Bending of Pretwisted Cantilever Blading," Paper No. MS-33, 24th Congress of ISTAM held at Rourkela, India, 1979–1980.

3 Idem, "Static Deflection of Asymmetric Aerofoil Blading," submitted to *Journal of the Aero. Soc. India.*

4 Forsyth, A. R., *Calculus of Variations*, Cambridge University Press, 1950.

5 Carnegie, W., "A Note on the Use of Variational Method to Derive the Equations of Motion of Vibrating Beam of Uniform Cross Section Taking Into Account of Shear Deflection and Rotary Inertia," *BMEE*, Vol. 2, 1961, p. 35.

6 Sutherland, J. G., and Goodman, L. E., "Vibration of Prismatic Bars Including Rotary Inertia and Shear Corrections," Department of Civil Engineering, University of Illinois, Urbana, Ill., April 15, 1951.

7 Harris, C. M., and Crede, C. E., *Shock and Vibration Handbook*, Vol. 1, McGraw-Hill, New York, 1961, pp. 7–14.

Instability of a Damped Rotor Partially Filled With an Inviscid Liquid

S. L. Hendricks[1]

This Brief Note proves that a simple pin–pin rotor that is partially filled with an inviscid liquid is inherently unstable when an external damper is added to the rotor.

Background

During experiments performed on a rotor partially filled with liquid, Kollman [1] discovered a wide range of rotor spin speeds for which the system was unstable. Kuipers [2], Wolfe [3], and Hendricks and Morton [4] have analyzed the Kollmann experiment. All three investigators were able to calculate stability limits for an undamped rotor partially filled with an inviscid liquid.

Kuipers [2] and Hendricks [4] added an external damper to the rotor and noted that the system became unstable for all spin frequencies and all nonzero damping factors that were calculated. Neither author offered a proof of this fact.

Theory

The stability characteristics of a damped rotor partially filled with an inviscid fluid are controlled by the characteristic equation [4].

$$(\gamma+\mu)S_0^4 + 2(iC\gamma + A[\gamma-1])S_0^3 + (A^2[\gamma-5-4\mu] + 2iCA[\gamma-2] - \gamma)S_0^2 + 2A(1-3iCA - 2[1+\mu]A^2)S_0 + A^2(1-2iCA - A^2[1+\mu]) = 0 \quad (1)$$

where

$\gamma = [1 + (b/a)^2]/[1 - (b/a)^2]$ = nondimensional fill parameter
$\mu = \pi\rho a^2 L/m$ = nondimensional fluid density
$C = \hat{C}/2m\omega_0$ = nondimensional damping factor
$A = \Omega/\omega_0$ = nondimensional spin frequency
S_0 = eigenvalue which determines both frequency and stability

and

a = radius of the rotor
b = radius of the fluid free surface
ρ = fluid density
L = rotor height
$\hat{C}$ = damper coefficient
m = mass of the rotor
Ω = rotor spin frequency
ω_0 = dry rotor critical frequency

To investigate the stability of equation (1), the following constants are formed:

$$\begin{aligned} A_0 &= 0 & B_0 &= \gamma+\mu \\ A_1 &= -2C\gamma & B_1 &= -2A(\gamma-1) \\ A_2 &= 2AC(\gamma-2) & B_2 &= A^2(\gamma-4\mu-5)-\gamma \\ A_3 &= 6A^2C & B_3 &= -2A(1-2A^2[1+\mu]) \\ A_4 &= -2A^3C & B_4 &= A^2(1-A^2[1+\mu]) \end{aligned}$$

The necessary and sufficient conditions for stability are that the 4 determinants

$$\nabla_{2r} = \begin{vmatrix} A_0 & A_1 & \cdots & A_{2r-1} \\ B_0 & B_1 & \cdots & B_{2r-1} \\ 0 & A_0 & \cdots & A_{2r-2} \\ 0 & B_0 & \cdots & B_{2r-2} \\ \cdot & \cdot & \cdots & \cdot \\ \cdot & \cdot & \cdots & \cdot \end{vmatrix} \quad (r = 1, 2, 3, 4)$$

(where A_k and B_k are zero if $k > 4$ and Δ_{2r} is of the $2r$th order) be positive. (See Porter [5]). These conditions are known as the generalized Hurwitz inequalities.

After much algebra,

$$\nabla_2 = 2C\gamma(\gamma+\mu)$$
$$\nabla_4 = 4C^2(\gamma+\mu)(\gamma^3 + 3A^2\mu\gamma^2 + A^2\mu\gamma - 4A^2\mu)$$
$$\nabla_6 = 8A^4C^3\mu(\gamma-1)(\gamma+1)(\gamma+\mu)(5\gamma^2 + [20 - A^2\mu]\gamma + A^2\mu + 16)$$
$$\nabla_8 = -16A^{10}C^4\mu^2(\gamma+\mu)(\gamma-1)^2(\gamma+1)^3$$

Since $\nabla_8 < 0$ for all damping factors (C), all spin speeds (A), all fill parameters (γ), and all fluid densities (μ), it follows that the original system is completely unstable. When $C = 0$ all of the determinants are identically zero, a condition that is characteristic of undamped systems.

Conclusion

When an external damper is added to a rotor containing an inviscid fluid, the resulting system has been shown to be unstable over all spin speeds and all nonzero damping factors.

This result although true is unrealistic because rotors have been shown to run stably while containing liquid [1, 3]. The discrepancy lies not in the mathematics but in the physics. If the theory includes dissipation due to an external damper, then it must also include dissipation due to the viscosity of the entrapped fluid [4].

References

1 Kollmann, F. G., "Experimentelle und theoretische Untersuchungen Uber die Kritischen Drezahlen flussigkeitsgefulter Hohlkorper," *Fordschund auf dem Gebiete des Ingenieurwessens*, Ausgabe B, Vol. 28, 1962, pp. 115–123.

2 Kuipers, M., "On the Stability of a Flexible Mounted Rotating Cylinder Partially Filled With Liquid," *Applied Scientific Research*, Section A, Vol. 13, 1964, pp. 121–137.

3 Wolfe, J. A., Jr., "Whirl Dynamics of a Rotor Partially Filled With Liquid," ASME JOURNAL OF APPLIED MECHANICS, Vol. 35, 1968, pp. 676–682.

4 Hendricks, S. L., and Morton, J. B., "Stability of a Rotor Partially Filled With a Viscous Incompressible Fluid," ASME JOURNAL OF APPLIED MECHANICS, Vol. 46, 1969, pp. 913–918.

5 Porter, B., *Stability Criteria for Linear Dynamical Systems*, Academic Press, New York, 1967.

[1] Assistant Professor, Department of Engineering Science and Mechanics, Virginia Polytechnic Institute and State University, Blacksburg, Va. 24061.

Manuscript received by ASME Applied Mechanics Division, April, 1981; final revision, June, 1981.

Effects of a Circular Hole on States of Uniform Twisting and Shearing in Shallow Spherical Shells

J. E. Reissner[1]

Introduction

It is the purpose of what follows to complement recent results by E. Reissner on the subject of this Note [1, 2] in such a way as to have values of stress-concentration factors in the entire range of parameter values, in place of the results in [1, 2] which are valid for small and for large values only.

Given the discussion of the physical aspects of the two problems and of the relevant general analytical developments in [1, 2] we begin by restating the results which are the starting point of the work of this Note in the following manner.

Transverse Twisting [1]

The values of membrane and bending stress-concentration factors

[1] Department of Physical Science, Pembroke State University, Pembroke, N.C. 28372.

Manuscript received by ASME Applied Mechanics, February, 1981.

Table 2 Stress-concentration factors for membrane shear

	k_b						k_m			
	$\nu = 0$		$\nu = 1/3$		$\nu = 1/2$		$\nu = 0$	$\nu = 1/3$	$\nu = 1/2$	
μ	N	A_1	N	A_1	N	A_1	N	N	N	A_1
0	0		0		0		4	4	4	
0.1	0.0396		0.0385		0.0380		4.0158	4.0157	4.0156	
0.3	0.247		0.254		0.261		4.140	4.137	4.136	
0.5	0.558		0.598		0.631		4.376	4.367	4.363	
0.8	1.166		1.312		1.425		4.908	4.880	4.867	
1.0	1.655		1.909		2.104		5.362	5.316	5.296	
2.0	5.068		6.317		7.263		8.545	8.391	8.321	
3.0	10.127		13.113		15.374	13.500	12.964	12.690	12.562	
4.0	16.87		22.32		26.46	24.00	18.47	18.08	17.89	
5.0	25.33		33.97		40.52	37.50	25.02	24.50	24.26	
6.0	35.50		48.05	44.09	57.58	54.00	32.60	31.95	31.65	
7.0	47.40		64.57	60.01	77.63	73.50	41.18	40.42	40.05	
8.0	61.03	55.43	83.54	78.38	100.68	96.00	50.78	49.89	49.47	
9.0	76.38	70.15	104.95	99.20	126.72	121.50	61.38	60.37	59.89	
10.0	93.46	86.61	128.81	122.47	155.76	150.00	72.98	71.86	71.31	
15.0	204.8	194.9	284.8	275.6	345.9	337.5	146.0	144.3	143.5	112.5
20.0	359.5	346.4	502.1	489.9	611.1	600.0	244.1	241.8	240.7	200.0
25.0	557.4	541.3	780.5	765.5	951.3	937.5	367.2	364.3	362.9	312.5
50.0	2,197	2,165	3,091	3,062	3,777	3,750	1,358	1,352	1,349	1,250
100.0	8,722	8,660	12,305	12,247	15,054	15,000	5,214	5,202	5,196	5,000
200.0	34,764	34,641	49,106	48,990	60,106	60,000	20,426	20,402	20,391	20,000
400.0	138,810	138,564	196,191	195,959	240,213	240,000	80,850	80,803	80,779	80,000

check, as they must, the correctness of the limiting results for $\mu = 0$ and, as it was hoped that they would, the correctness of the asymptotic results *for sufficiently large values of* μ. As expected, the meaning of "sufficiently large" is different for the problem of twisting where two-term asymptotic formulas had been obtained, and for the problem of membrane shear where one-term asymptotic formulas only had been derived. Evidently, in the latter case the asymptotic results come close to the results obtained by solving the 4 by 4 system numerically only when $50 < \mu$. In the former case the two-term asymptotic formulas are quite close to the numerical results in the larger range $10 < \mu$. In summary, it is possible to say that the present evaluation, insofar as the problem of transverse twisting is concerned, adds little to the information of technical interest which had previously been obtained in [1]. On the other hand, insofar as the problem of membrane shear is concerned the present calculations add considerably to qualitative and quantitative insights of technical interest to the preliminary quantitative results which were obtained in [2].

Description of Numerical Procedure

Tabulated values of *zero*-order Kelvin functions for $\mu < 100$ are available in Nosova [3] and Abramowitz and Stegun [4], together with recursion relations for the computation of the second-order functions and their derivatives. Computer subroutines for the zero-order functions are also available [5]. For larger values of μ, a simple closed-form asymptotic expression provides these functions accurate to the fifth significant figure or better. At these values of the arguments, the magnitude of the functions is of the order of $\exp(-\mu/\sqrt{2})$, leading to values of the determinant of the 4 by 4 system which are close enough to zero to cause underflow difficulties. In these cases, the Kelvin functions and derivatives appearing in the system may be rescaled by any common factor, leading to a determinant modified by multiplication by the square of the scaling factor and to solutions c_3 and c_4 modified by division by this factor. The use of these solutions, together with the rescaled Kelvin functions, in equations (1) and (3) then provides values for the stress-concentration factors that are independent of the scale factor.

References

1 Reissner, E., On the Transverse Twisting of Shallow Spherical Ring Caps," ASME JOURNAL OF APPLIED MECHANICS, Vol. 47, 1980, pp. 101–105.

2 Reissner, E., "On the Effect of a Small Circular Hole on States of Uniform Membrane Shear in Spherical Shells," ASME JOURNAL OF APPLIED MECHANICS, Vol. 47, 1980, pp. 430–431.

3 Nosova, L. N., *Tables of Thomson Functions and Their First Derivatives*, Pergamon Press, New York, 1961.

4 Abramowitz, M., and Stegun, J. A., *Handbook of Mathematical Tables*, Dover Publications, Inc., New York, 1965.

5 *IMSL*, The International Mathematical and Statistical Libraries, Inc., Houston, Texas, 1979.

Optimal Isolation of a Single-Degree-of-Freedom System With Quadratic-Velocity Damping[1]

T. L. Alley[2]

The response of a mass isolated by a linear spring and a quadratic-velocity damper subjected to a step-and-decay velocity input at the base is found in closed form. This solution leads immediately to the optimal isolation system for this input. The parameters of the optimal isolation system are given by a simple formula.

Brief Note

Consider a single-degree-of-freedom oscillator initially at rest and subjected to a specific input motion at the base. Define x as the inertial motion of the mass, y as the intertial motion of the base, and z as the relative displacement

$$z = x - y. \tag{1}$$

A common optimization criterion for the design of the isolation system is to require that the peak inertial acceleration of the mass be limited and that the peak relative displacement between the mass and the base be minimized.

[1] Supported by U.S. Air Force Space Division.

[2] Design Analysis Department, The Aerospace Corporation, El Segundo, Calif. 90245. Mem. ASME.

Manuscript received by ASME Applied Mechanics Division, December, 1980; final revision, April, 1981.

Now consider a specific form of the input motion as

$$\dot{y} = 0; \quad t < 0 \tag{2a}$$

$$\dot{y}(t) = V - at; \quad t \geq 0 \tag{2b}$$

$$y(t = 0) = 0 \tag{2c}$$

where V and a are positive and the time of interest is less than V/a. If a is zero then this is the common velocity-step problem. For zero initial conditions of the mass and a general isolation force $h(z, \dot{z})$ the system to be solved is

$$m\ddot{z} = h(z, \dot{z}) + ma = h'(z, \dot{z}) \tag{3a}$$

$$z(0) = 0 \tag{3b}$$

$$\dot{z}(0) = -V \tag{3c}$$

Note that h' differs from h by only a constant. The time of interest will be further restricted to the interval $[0, T]$ where T satisfies

$$\dot{z}(T) = 0 \tag{4}$$

for the first time. Also consider the functional

$$J = |z(T)| \tag{5}$$

which depends on h' and is the extremal of z. If J is minimized subject to the condition that

$$|h'(z, \dot{z})| \leq H_0 \tag{6}$$

where H_0 is a constant then it has been shown by Troitskii [1], Karnopp and Trikha [2] and elsewhere that this optimal isolation is given by

$$h'(z, \dot{z}) = -H_0 \operatorname{sign}(\dot{z}(0)) \tag{7}$$

over the interval $[0, T]$. After T the relative displacement can be brought to zero in any manner as long as $z(T)$ and H_0 are not exceeded. Note that the optimal isolator generates a constant force such that the mass acceleration equals the limiting acceleration up to the time of peak relative displacement but that the form or mechanization of this optimal isolator is unknown.

Let us now construct an isolation system composed of a linear spring and a quadratic velocity damper. Hydraulic dampers exhibit such behavior and are in widespread use. Equation (3a) now becomes

$$m\ddot{z} + c\dot{z}|\dot{z}| + kz = ma \tag{8}$$

where c and k are positive constants. Because we are interested only in the motion up to peak relative displacement there may be written

$$|\dot{z}| = |\dot{x} - \dot{y}| = -\dot{z}$$

because $\dot{z}$ is negative. The system to be considered is now

$$m\ddot{z} - c\dot{z}^2 + kz = ma \tag{9a}$$

$$z(0) = -V \tag{9b}$$

$$z(0) = 0. \tag{9c}$$

The order of equation (9a) may be reduced from two to one, time eliminated, and the equation made linear by the transformation

$$s(z) = \left(-\frac{dz}{dt}\right)^2 \tag{10a}$$

$$\frac{ds}{dz} = 2\frac{dz}{dt}\cdot\frac{dt}{dz}\frac{d}{dt}\left(\frac{dz}{dt}\right) = 2\ddot{z} \tag{10b}$$

The system to be solved is now

$$\frac{1}{2}\frac{ds}{dz} - \frac{c}{m}s + \frac{k}{m}z = a \tag{11a}$$

$$s(0) = V^2. \tag{11b}$$

The solution of system (11) is

$$s = \left(V^2 - \frac{mk}{2c^2} + \frac{ma}{c}\right)e^{2cz/m} + \frac{k}{c}z + \frac{mk}{2c^2} - \frac{ma}{c}. \tag{12}$$

But from equations (1), (10b), and (12) there may be written

$$\ddot{x} = \frac{c}{m}\left(V^2 - \frac{mk}{2c^2} + \frac{ma}{c}\right)e^{2cz/m} + \frac{1}{2}\frac{k}{c} - a \tag{13}$$

and the inertial acceleration is expressed as function of z, rather than t, for our problem.

Suppose now that we select k and c such that

$$V^2 - \frac{mk}{2c^2} + \frac{ma}{c} = 0 \tag{14}$$

in equation (13). This would yield a case of constant acceleration which characterizes the optimal isolation system. The optimal acceleration will now be denoted as $\ddot{x}_0$ and is

$$\ddot{x}_0 = \frac{1}{2}\frac{k}{c} - a. \tag{15}$$

From equations (1), (2b), and (15) there follows:

$$\dot{z} = \dot{x} - \dot{y} = \frac{1}{2}\frac{k}{c}t - V. \tag{16}$$

Note that at $z = -R$, or peak relative deflection, there must be $\dot{z} = 0$ and from equation (16) this occurs at

$$T = 2V\frac{c}{k}. \tag{17}$$

Integrating equation (16) once more and evaluating the result at T yields

$$R = V^2\frac{c}{k}. \tag{18}$$

For this solution to be valid requires

$$T < \frac{V}{a}$$

$$a < \frac{1}{2}\frac{k}{c} \tag{19}$$

which implies that $\ddot{x}_0$ is positive from equation (15).

Equation (19) may be recast in the form

$$a < \frac{1}{2}\frac{V^2}{R} \tag{20}$$

using equation (18). This is more convenient for optimization.

Because the optimal isolation system for the general problem described by equations (3)–(6) resulted in a constant mass acceleration equal to the limit over $[0, T]$ it is asserted that this optimal result may be achieved by the isolation system selected in equation (8). That is, for the optimization conditions of

$$\min J = \min |z(T)|$$

$$\text{subject to} \qquad |h'(z, \dot{z})| \leq H_0$$

no better minimum can be achieved than that resulting from the linear spring and quadratic velocity damper system.

After first verifying that condition (20) holds, the optimal acceleration and isolation parameters may be found by performing the following calculations derived from those just given.

$$\ddot{x}_0 = \frac{1}{2}\frac{V^2}{R} - a \tag{21}$$

$$k_0 = \frac{m}{R}\ddot{x}_0 \tag{22}$$

and

$$c_0 = k_0 \frac{R}{V^2} \tag{23}$$

where the subscripts denote optimal values.

In comparison with equation (21), for the special case of a constant-velocity input, a linear undamped system yields

$$\ddot{x}_0 \text{ (undamped)} = V^2/R$$

and a linear, viscously damped system yields

$$\ddot{x}_0\text{(viscous)} = 0.5204(V^2/R)$$

Thus the performance of the quadratic-velocity isolation system is much better than an undamped system and slightly better than the viscous system.

References

1 Troitskii, V. A., "On the Synthesis of Optimal Dampers," *PMM*, Vol., 31, No. 4, 1967, pp. 624–630.

2 Karnopp, D. C., and Trikha, A. K., "Comparative Study of Optimization Techniques for Shock and Vibration Isolation," ASME *Journal of Engineering for Industry*, Vol. 91, No. 4, 1969, pp. 1128–1132.

Journal of Applied Mechanics

Discussion

Torsion of Pretwisted Beams Due to Axial Loading[1]

Aviv Rosen.[2] The coupling between extension and torsion of pretwisted beams was examined in a supplement to a report [1] published several years ago entitled "Re-Examination of the Commonly Used Equations of Motion of Pretwisted Rotor Blades." This coupling appears in the commonly used equations of motion of pretwisted rotor blades which were derived in the classical work of Houbolt and Brooks [2]. The following two results were pointed out in this supplement:

1 If it is assumed that the previous derivation is correct, then this phenomenon is negligible within the accuracy of the theory.

2 It was shown by a rigorous derivation that the terms associated with the tension-torsion coupling effect due to pretwist are not only negligible but are, in fact, incorrect. The reason for the appearance of these incorrect terms was the fact that, while the derivation leading to their appearance is done by using a nonorthogonal system of coordinates, the appropriate theory for such a system was not applied.

These results raised strong objections from those who used this theory [2] in the past, including Dr. Hodges. I was, therefore, pleased to see in the subject paper that he now agrees with the aforementioned results. He also claims that nowadays some rotor blades are built out of composite materials so that equivalent G/E-values may be much less than unity. Therefore, in these cases, the untwisting of the blade, due to tension, may be more significant than for regular blades. As a result the author presents a derivation similar to the one which was presented in reference [1], including warping. He concludes that there is an untwisting of the beam due to axial loading which is caused by the influence of pretwist on the warping contributions.

In the derivation of the supplement [1] warping was not included. As pointed out, this was done because the basic derivation of Houbolt and Brooks did not include warping and the intention was to do the derivation [1] along the same lines. Even so, the mutual relation between warping and pretwist was pointed out, but as indicated [1] in the case of usual rotor blades, the neglect of that influence of warping and pretwist was fully justified. Furthermore, it was clearly indicated that the inclusion of warping and determination of its influence on the derivation can be observed following a similar procedure. *In fact, the subject paper is a result of following the path which was marked in reference [1].* This path was also followed by the author of [1] showing the influence of warping and pretwist on the torsional rigidity of beams [3]. The foregoing description is given here to provide a background on [1] and the subject paper. In concluding this part of my discussion, I would like to state that I believe that the subject paper has an important contribution in establishing the understanding of the behavior of pretwisted beams for which the author should be given credit.

Up to this point the discussion was general, but the following three specific points associated with the subject paper, will be pointed out:

1 As stated by the author, his derivation becomes important in the case of blades which are built out of composite materials. The cases of interest are those where, because of the presence of longitudinal fibers, the longitudinal stiffness of the blade is much higher than its torsional rigidity. This causes a classical example of an anisotropic beam, where strong fibers are immersed in a weak matrix. These fibers are twisted with respect to the beam axis and therefore one is faced with a complicated problem of anisotropic nonorthogonal system. Equation (20), of the supplement [1] is appropriate for these cases. Instead the author restricts his derivation to pure isotropic cases (equations (15) and (16)), and in order to take into account the nature of the composite blades he introduces the concept of equivalent G/E. An indication that this concept may not be correct at all is given by the following example: Consider a circular beam which is composed of an extremely weak matrix together with strong fibers which are uniformly twisted inside the matrix. Since the "equivalent isotropic beam" is circular there is no warping. Therefore, according to the subject paper's results there will not be any untwisting due to axial forces, no matter what the ratio G/E is. On the other hand, from simple physical reasoning, it is clear that this beam will exhibit untwisting due to axial tension. In this special case one also expects an addition to the torsional rigidity due to the fibers. This contribution, which may be significant above certain values of pretwist, is not predicted by the equivalent G/E theory. Therefore, unless the author will present concrete proof, the usefulness of the concept of equivalent G/E to describe the behavior of rotor blades made of composit materials, may be very limited.

2 The author neglected the influence that pretwist may have on the torsional rigidity of beams. He states that this contribution is *negligible for slender beams.* Unfortunately, this statement is inaccurate. A careful examination of the results of previous research [3,4], which also confirms physical reasoning, reveals that this contribution depends on the initial twist and the geometry of the cross section only, and is not influenced by the slenderness of the beam. An indication that there is a mistake in the author's derivation is obtained from the fact that the numerator of the left side of equation (33) has the dimension of (1/length^2) while all the other terms in the equation are dimensionless.

In a recent paper [5] a theory describing the nonlinear torsion and extension of initially twisted beams under the action of axial load and twisting moment, was derived. Comparison [5] of theoretical and experimental results showed very good agreement. It is beyond the scope of this discussion to be descriptive of that work and so only its results (equation (12) and reference [5]) when applied to the same example which appears in the subject paper, are presented in Fig. 1.

The cross section of the beam is elliptical with principal axes $2a$ and $2b$, while $(T/EA) = 0.005$ and $G/E = 0.025$. If the contributions of pretwist, together with other nonlinear contributions to the torsional

[1] By D. H. Hodges, and published in the June, 1980, issue of the ASME JOURNAL OF APPLIED MECHANICS, Vol. 47, pp. 393–397.

[2] Senior Lecturer, Department of Aeronautical Engineering, Technion—Israel Institute of Technology, Haifa, Israel.

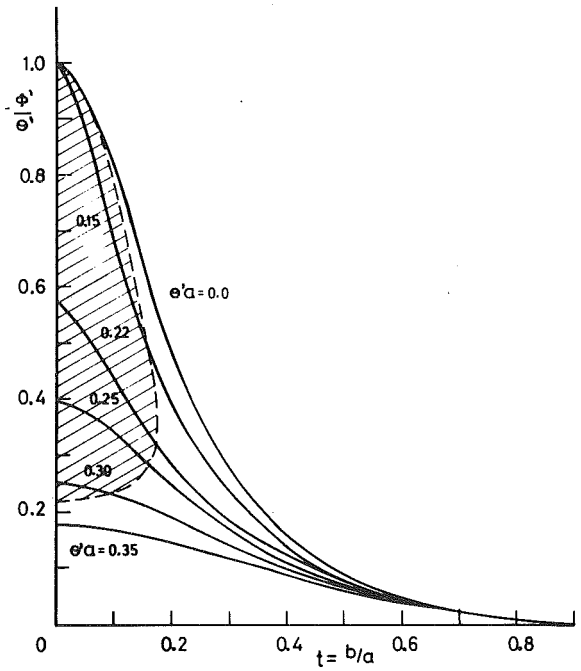

Fig. 1 Torsion per unit pretwist of a slender beam with elliptical cross section

rigidity of the beam are retained, it is found that in contrast to equation (34) of the subject paper, ϕ'/θ' is a function of $(\theta' a)$. In Fig. 1 the value of ϕ'/θ' for different values of pretwist $(\theta' a)$ are presented. The shadowed area indicates a region where the accuracy of the theory is in doubt [5]. The curve for $(\theta' a) = 0$ is identical to the curve presented in Fig. 2 of the subject paper. Comparison between the two figures indicates that the results of the subject paper are misleading. The torsion per unit pretwist of a slender beam with elliptical cross section is not a function of (b/a) only, as stated, but in addition depends on the magnitude of the pretwist. Using equation (34) of the subject paper may also cause large errors in many other cases.

3 It was shown in previous derivations [1] that using an orthogonal system of coordinates instead of the nonorthogonal twisted system of coordinates, yields the same results but reduces the work considerably. These conclusions were also confirmed in later works [3,5]. Due to the tedious derivation of the subject paper which uses the nonorthogonal system, it is worthwhile mentioning again the advantages of using an orthogonal system of coordinates whenever possible.

References

1 Rosen, A., and Friedmann, P., "Nonlinear Equations of Equilibrium for Elastic Helicopter or Wind Turbine Blades Undergoing Moderate Deformation," UCLA-ENG-7718, Revised Edition, June 1977.

2 Houbolt, J. C., and Brooks, G. W., "Differential Equations of Motion for Combined Flapwise Bending, Chordwise Bending, and Torsion of Twisted Nonuniform Rotor Blades," NACA Report 1346, 1958.

3 Rosen, A., "The Effect of Initial Twist on the Torsional Rigidity of Beams—Another Point of View," ASME JOURNAL OF APPLIED MECHANICS, Vol. 47, June 1980, pp. 389–392, condensed version of TAE Report No. 360, Apr. 1978.

4 Chen, C., "The Effect of Initial Twist on the Torsional Rigidity of Thin Prismatical Bars and Tubular Members," *Proceedings of the First U.S. National Congress of Applied Mechanics*, June 11–16, 1951, pp. 265–269.

5 Rosen, A., "Theoretical and Experimental Investigation of the Nonlinear Torsion and Extension of Initially Twisted Beams," ASME JOURNAL OF APPLIED MECHANICS. Vol. 47, 1980, pp. 389–392.

Author's Closure

While I appreciate Dr. Rosen's interest in the subject paper, I do not agree with some of his statements. To begin, I would like to address the two points from the supplement of [1] with which Dr. Rosen says I now agree. Both points concern the terms that couple tension and torsion in beam theory. These two terms account for the well-known increase in torsion stiffness due to tension and a twisting moment due to tension proportional to pretwist. His first point is that the phenomenon is negligible within the accuracy of the theory of [2]. He argues this point in [1] on the basis of G/E values for a beam made of a single, homogeneous, isotropic material. Actually, I do not agree with this point now nor have I ever. A careful reading of the Introduction to the subject paper will substantiate this for the reader's benefit. My "strong objections" in the beginning, mentioned by Dr. Rosen, still stand and they focus on the simplistic nature of his argument. Houbolt and Brooks [2] developed their theory using an isotropic representation for Hooke's law, but it is reasonable to assume that their theory was intended to be applied to composite blades. After all, how many rotor blades are built from a single homogeneous, isotropic material? It is customarily assumed in such applications that equivalent beam properties can be obtained for use in the theory by evaluating certain integrals over the cross section, hence averaging the effects of different materials present in the cross section. Averaging leads to effective values of G/E which may differ from those encountered in isotropic structures by one or more orders of magnitude. It is recognized that this process of averaging has its shortcomings, yet for some typical composite rotor blades it produces rather accurate results and will likely continue to be used until more rigorous theories are developed. It is not at all surprising, however, that it fails in Dr. Rosen's example of a circular cylindrical beam with pretwisted fibers. A more general constitutive law is obviously needed in that case. This example is not too important, however, since this example beam is not typical of rotor blade structures. The point is that the terms in question are not negligible for certain composite rotor blades, especially the flexbeam portion of bearingless rotor blades [3]. Moreover, the notion of an effective G/E value is not introduced in the subject paper as if it were a new and comprehensive concept. Instead, it is employed as an aid in gaining some physical insight from a simplified theory. The only conclusion that is drawn from it in the subject paper is simply that the terms in question may be more important than indicated in [1] in modeling certain composite blades. Thus it should be clear that I do not agree with the first result that Dr. Rosen cites from the supplement of [1].

The second result from the supplement of [1] with which Dr. Rosen says I now agree is that the tension-torsion coupling term due to pretwist derived in [2] is incorrect. Here, however, Dr. Rosen's discussion is inconsistent with the conclusions of [1]. It is not alleged in [1] that the coupling term in [2] is simply incorrect but, instead, it is clearly stated that the term proportional to pretwist that couples tension and torsion is *nonexistent* (Conclusion A, p. 39 [1]). I rejected that conclusion when [1] was published; I still reject it. The subject paper clearly establishes that the tension-torsion coupling due to pretwist does exist and that the term from [2], while not strictly correct, nevertheless produces results that are reasonably accurate, certainly more accurate than those of [1]. It is difficult for me to see how Dr. Rosen can say I now agree with the two results that he cites from [1].

Next, Dr. Rosen proceeds to extol the virtues of the analysis in [1]. There are other problems with [1], as discussed in [4], but I will confine my remarks here to the issue of tension-torsion coupling. A point stressed in [1] was that the authors had finally achieved their objective: derivation of a "consistent" set of equations without qualification. No indication was given that further work was needed to clarify the terms in question. In the subject paper, I endeavored to clarify the issue of the tension-torsion terms because of what I perceived as a fundamental error in [1]. It is true as Rosen states that a "path" can be found in [1] if it is desired to incorporate the effects of warp. However, other paths can be found in the older references cited in the subject paper. Why should I acknowledge following a path that I did not follow—a path clearly inferior to those in the older references that I did follow? The idea of including warp in a pretwisted beam analysis did not originate with Dr. Rosen. Rosen, in fact, belabors the point

in [1] that neglecting warp is "completely justified" in rotor blades. Is this really the case? It is true, as shown in the subject paper, that the torsion moment term proportional to pretwist and tension vanishes for warp-free beams. The notion that rotor blades are warp-free is totally ill-conceived, however. Houbolt and Brooks [2] neglected warping *rigidity* but they maintained what they considered to be an appropriate slender-beam approximation of warp effects in that: (1) they utilized the Saint Venant torsion rigidity, which depends on warp; and (2) they invoked the Wagner hypothesis, where longitudinal stress is assumed to act normal to a warped surface, in calculating the twisting moments. What resulted was an approximation that is virtually indistinguishable from the more accurate model developed in the subject paper, which includes warp. The differences are only significant for beams with warp-free or quasi warp-free cross sections. The subject paper shows that warping influences terms other than the torsion rigidity. In [1] the twisting moment was calculated by blindly following the Euler-Bernoulli hypothesis, where longitudinal stress is assumed to act normal to the plane of the cross section. The torsion rigidity had to be artificially modified in the "consistent" equations of [1] in order to match the known result of Saint Venant, which includes warping. The authors of [1] did not mention that other errors may have been created by their restrictive kinematics. As shown in the subject paper, even in a slender-beam approximation, warp does affect the tension-torsion coupling. The fundamental error in [1] was the assumption that since rotor blades are closed cross sections and thus have small warping *rigidity*, all warping could be removed from the kinematics. That this is false is well established in the literature and confirmed by the results of the subject paper.

It should be noted that the subject paper is not really definitive nor was it intended to be. In the subject paper, the undeformed beam cross section is assumed to be plane. It seems more reasonable to assume that the undeformed surface of the cross section of a pretwisted beam should also be warped so that the surface is, at each point in the cross section, normal to the helical "fiber" that goes through that point. Then, stresses referred to this surface would be normal to the helix. The geometry of this warped surface may or may not closely resemble that described by the Saint Venant warp function. The question is what should this surface look like? Is there an exact solution from elasticity theory that is analogous to the Saint Venant result? Can a tractable small-strain constitutive law be found for geometric nonlinear analysis of pretwisted laminated composite beams with possible anisotropy? Is a laminated helicoidal shell theory that is somehow simplified to one-dimensional form possibly the answer? These questions and others form the basis for future research projects and it is hoped that this discussion will stimulate further interest.

I now turn to the three specific items listed by Dr. Rosen in the latter part of the discussion. I have already addressed the first item, concerning equivalent G/E, and now I would like to address the second and third of these items. Dr. Rosen claims in his second point that $a\, d\theta/dx$ is a key parameter in this problem and that slenderness ratio a/L has no effect at all. Unfortunately, I failed to specify in the subject paper that from equation (33) on, all variables are dimensionless and thus $(\ )' = d(\ )/d\bar{x}$ where $\bar{x} = x/L$. Hence, $a\, d\theta/dx$ becomes $a/L\, d\theta/d\bar{x}$ just as in the subject paper. It should be noted that a/L and $d\theta/d\bar{x}$ are independent quantities. That the magnitudes of both a/L and $d\theta/d\bar{x}$ are important is evident in equation (33) by virtue of which the validity of equation (34) is bounded. Equation (33) implies, for any fixed value of $d\theta/d\bar{x}$, that the torsion per unit pretwist is independent of $a/L\ d\theta/d\bar{x}$ if a/L is sufficiently small. For example, consider rotor blades where, normally, $d\theta/d\bar{x}$ is no more than 0.8 rad even for highly twisted blades. The maximum cross-section dimension $2a$ is normally less than about $0.1L$ for a slender blade. Thus, for typical rotor blades, $a\, d\theta/dx = a/L\ d\theta/d\bar{x} \lesssim 0.04$ and the result is barely distinguishable from the $a\, d\theta/dx = 0$ curve in Fig. 1 of the discussion (equivalent to Fig. 2 of the subject paper). Therefore, contrary to Dr. Rosen's comments, the slenderness ratio a/L is a key parameter and obviously equation (34) in the subject paper is neither in error nor at all misleading.

Dr. Rosen's third item is that the use of orthogonal coordinates is preferable because there is considerably less work. Actually, this choice is largely a matter of personal preference and is highly problem-dependent.

Finally, I would like to correct several typographical errors in the subject paper. The first term in the middle row of equation (9) should be $\partial\psi^1/\partial y^2$. The third and fourth terms in the first row of equations (13) are $\lambda\alpha' + u'^2/2$ and the left-hand side of equation (34) should read $\partial\phi'/\partial\theta'$.

References

1 Rosen, A., and Friedmann, P., "Nonlinear Equations of Equilibrium for Elastic Helicopter or Wind Turbine Blades Undergoing Moderate Deformation," University of California, Los Angeles, School of Engineering and Applied Science Report UCLA-ENG-7718 (revised edition), June 1977.

2 Houbolt, J. C., and Brooks, G. W., "Differential Equations of Motion of Combined Flapwise Bending, Chordwise Bending, and Torsion of Twisted, Nonuniform Rotor Blades," NACA Report 1346, 1958.

3 Dixon, P. G. C., "Derivation of Control Loads for Bearingless Rotor Systems," *Proceedings of the AHS/NASA-Ames Conference on Helicopter Structures Technology*, Paper No. 3, Nov. 1977.

4 Hodges, D. H., Ormiston, R. A., and Peters, D. A., "On the Nonlinear Deformation Geometry of Euler-Bernoulli Beams," NASA TP-1566, 1980.

Transient Response of a Finite Crack in a Strip With Stress-Free Edges[1]

E. P. Chen.[2]

Professor Itou solved the same problem which was treated by the discusser. His justification for doing so was twofold:

1 He used an alternate method to formulate the problem in the Laplace transform domain.

2 He used a more refined Laplace inversion scheme and claimed a better numerical result than reported in [1].

The discusser would like to clarify these two points in this discussion.

The formulation and solution method used in [1] has been well established for solving mixed boundary-value problems e.g., [2, 3]. Alternative methods such as the singular integral equation method [4] and the method used by Sneddon and Srivastav [5] exist. However, the choice of these methods for a given problem mostly depends on the author's familiarity with them and there is no definite advantage by using one method over the other. Thus point one hardly justifies the republication of the same paper. As for the second point, Professor Itou used the same numerical Laplace inversion scheme as the discusser. Using the notation in Itou's paper, two parameters β and δ' and the number of terms to retain in an infinite sum, N must be chosen. As Professor Itou stated in his paper ". . . However, there is no best way of selecting these values . . ." The values $\beta = 0.0$, $\delta' = 0.2$, and $N = 5$ were arrived in [1] by comparing the solution for a finite crack in an infinite medium and subjected to the action of impact loads with the exact solution by Thau and Lu [6] at earlier times. Itou used another scheme to determine these parameters which presumably gave better results than those in [1]. However, the comparison between these results showed less than 10 percent difference at the worst. Owing to the approximate nature of the numerical scheme, the discusser considers his results in [1] being satisfactory.

Another point involves the small disturbance at earlier times observed in [1]. The discusser suggested that this may be caused by the wave interaction between the free surface and the crack. The discusser did not "insist" on this point as stated in Itou's paper. Observing from Itou's Fig. 2, the slope of the curves at earlier times also exhibit some

[1] By S. Itou, and published in the December, 1980, issue of the ASME JOURNAL OF APPLIED MECHANICS, Vol. 47, pp. 801–805.

[2] Member of Technical Staff, In-Situ Technologies Division, Sandia National Laboratories, Albuquerque, New Mex. 87185.

in [1] that neglecting warp is "completely justified" in rotor blades. Is this really the case? It is true, as shown in the subject paper, that the torsion moment term proportional to pretwist and tension vanishes for warp-free beams. The notion that rotor blades are warp-free is totally ill-conceived, however. Houbolt and Brooks [2] neglected warping *rigidity* but they maintained what they considered to be an appropriate slender-beam approximation of warp effects in that: (1) they utilized the Saint Venant torsion rigidity, which depends on warp; and (2) they invoked the Wagner hypothesis, where longitudinal stress is assumed to act normal to a warped surface, in calculating the twisting moments. What resulted was an approximation that is virtually indistinguishable from the more accurate model developed in the subject paper, which includes warp. The differences are only significant for beams with warp-free or quasi warp-free cross sections. The subject paper shows that warping influences terms other than the torsion rigidity. In [1] the twisting moment was calculated by blindly following the Euler-Bernoulli hypothesis, where longitudinal stress is assumed to act normal to the plane of the cross section. The torsion rigidity had to be artificially modified in the "consistent" equations of [1] in order to match the known result of Saint Venant, which includes warping. The authors of [1] did not mention that other errors may have been created by their restrictive kinematics. As shown in the subject paper, even in a slender-beam approximation, warp does affect the tension-torsion coupling. The fundamental error in [1] was the assumption that since rotor blades are closed cross sections and thus have small warping *rigidity*, all warping could be removed from the kinematics. That this is false is well established in the literature and confirmed by the results of the subject paper.

It should be noted that the subject paper is not really definitive nor was it intended to be. In the subject paper, the undeformed beam cross section is assumed to be plane. It seems more reasonable to assume that the undeformed surface of the cross section of a pretwisted beam should also be warped so that the surface is, at each point in the cross section, normal to the helical "fiber" that goes through that point. Then, stresses referred to this surface would be normal to the helix. The geometry of this warped surface may or may not closely resemble that described by the Saint Venant warp function. The question is what should this surface look like? Is there an exact solution from elasticity theory that is analogous to the Saint Venant result? Can a tractable small-strain constitutive law be found for geometric nonlinear analysis of pretwisted laminated composite beams with possible anisotropy? Is a laminated helicoidal shell theory that is somehow simplified to one-dimensional form possibly the answer? These questions and others form the basis for future research projects and it is hoped that this discussion will stimulate further interest.

I now turn to the three specific items listed by Dr. Rosen in the latter part of the discussion. I have already addressed the first item, concerning equivalent G/E, and now I would like to address the second and third of these items. Dr. Rosen claims in his second point that $a\ d\theta/dx$ is a key parameter in this problem and that slenderness ratio a/L has no effect at all. Unfortunately, I failed to specify in the subject paper that from equation (33) on, all variables are dimensionless and thus $(\ )' = d(\ )/d\bar{x}$ where $\bar{x} = x/L$. Hence, $a\ d\theta/dx$ becomes $a/L\ d\theta/d\bar{x}$ just as in the subject paper. It should be noted that a/L and $d\theta/d\bar{x}$ are independent quantities. That the magnitudes of both a/L and $d\theta/d\bar{x}$ are important is evident in equation (33) by virtue of which the validity of equation (34) is bounded. Equation (33) implies, for any fixed value of $d\theta/d\bar{x}$, that the torsion per unit pretwist is independent of $a/L\ d\theta/d\bar{x}$ if a/L is sufficiently small. For example, consider rotor blades where, normally, $d\theta/d\bar{x}$ is no more than 0.8 rad even for highly twisted blades. The maximum cross-section dimension $2a$ is normally less than about $0.1L$ for a slender blade. Thus, for typical rotor blades, $a\ d\theta/dx = a/L\ d\theta/d\bar{x} \lesssim 0.04$ and the result is barely distinguishable from the $a\ d\theta/dx = 0$ curve in Fig. 1 of the discussion (equivalent to Fig. 2 of the subject paper). Therefore, contrary to Dr. Rosen's comments, the slenderness ratio a/L is a key parameter and obviously equation (34) in the subject paper is neither in error nor at all misleading.

Dr. Rosen's third item is that the use of orthogonal coordinates is preferable because there is considerably less work. Actually, this choice is largely a matter of personal preference and is highly problem-dependent.

Finally, I would like to correct several typographical errors in the subject paper. The first term in the middle row of equation (9) should be $\partial\psi^1/\partial y^2$. The third and fourth terms in the first row of equations (13) are $\lambda\alpha' + u'^2/2$ and the left-hand side of equation (34) should read $\partial\phi'/\partial\theta'$.

References

1 Rosen, A., and Friedmann, P., "Nonlinear Equations of Equilibrium for Elastic Helicopter or Wind Turbine Blades Undergoing Moderate Deformation," University of California, Los Angeles, School of Engineering and Applied Science Report UCLA-ENG-7718 (revised edition), June 1977.

2 Houbolt, J. C., and Brooks, G. W., "Differential Equations of Motion of Combined Flapwise Bending, Chordwise Bending, and Torsion of Twisted, Nonuniform Rotor Blades," NACA Report 1346, 1958.

3 Dixon, P. G. C., "Derivation of Control Loads for Bearingless Rotor Systems," *Proceedings of the AHS/NASA-Ames Conference on Helicopter Structures Technology*, Paper No. 3, Nov. 1977.

4 Hodges, D. H., Ormiston, R. A., and Peters, D. A., "On the Nonlinear Deformation Geometry of Euler-Bernoulli Beams," NASA TP-1566, 1980.

Transient Response of a Finite Crack in a Strip With Stress-Free Edges[1]

E. P. Chen.[2]

Professor Itou solved the same problem which was treated by the discusser. His justification for doing so was twofold:

1 He used an alternate method to formulate the problem in the Laplace transform domain.

2 He used a more refined Laplace inversion scheme and claimed a better numerical result than reported in [1].

The discusser would like to clarify these two points in this discussion.

The formulation and solution method used in [1] has been well established for solving mixed boundary-value problems e.g., [2, 3]. Alternative methods such as the singular integral equation method [4] and the method used by Sneddon and Srivastav [5] exist. However, the choice of these methods for a given problem mostly depends on the author's familiarity with them and there is no definite advantage by using one method over the other. Thus point one hardly justifies the republication of the same paper. As for the second point, Professor Itou used the same numerical Laplace inversion scheme as the discusser. Using the notation in Itou's paper, two parameters β and δ' and the number of terms to retain in an infinite sum, N must be chosen. As Professor Itou stated in his paper ". . . However, there is no best way of selecting these values . . ." The values $\beta = 0.0$, $\delta' = 0.2$, and $N = 5$ were arrived in [1] by comparing the solution for a finite crack in an infinite medium and subjected to the action of impact loads with the exact solution by Thau and Lu [6] at earlier times. Itou used another scheme to determine these parameters which presumably gave better results than those in [1]. However, the comparison between these results showed less than 10 percent difference at the worst. Owing to the approximate nature of the numerical scheme, the discusser considers his results in [1] being satisfactory.

Another point involves the small disturbance at earlier times observed in [1]. The discusser suggested that this may be caused by the wave interaction between the free surface and the crack. The discusser did not "insist" on this point as stated in Itou's paper. Observing from Itou's Fig. 2, the slope of the curves at earlier times also exhibit some

[1] By S. Itou, and published in the December, 1980, issue of the ASME JOURNAL OF APPLIED MECHANICS, Vol. 47, pp. 801–805.

[2] Member of Technical Staff, In-Situ Technologies Division, Sandia National Laboratories, Albuquerque, New Mex. 87185.

fast transition. Because of the numerical nature of the solutions, the discusser does not think this point can be settled at this time.

References

1 Chen, E. P., "Sudden Appearance of a Crack in a Stretched Finite Strip," ASME JOURNAL OF APPLIED MECHANICS, Vol. 45, 1978, pp. 277–280.

2 Sih, G. C., and Loeber, J. F., "Wave Propagation in an Elastic Solid With a Line of Discontinuity or Finite Crack," *Quarterly of Applied Mathematics*, Vol. 27, 1969, pp. 193–213.

3 Kassir, M. K., and Sih, G. C., *Three-Dimensional Crack Problems*, Noordhoff International Publishing, Leyden, The Netherlands, 1975.

4 Erdogan, F., Gupta, G. D., and Cook, T. S., "Numerical Solution of Singular Integral Equations," *Mechanics of Fracture*, Vol. 1, ed., Sih, G. C., Noordhoff International Publishing, Leyden, The Netherlands, 1973, pp. 368–425.

5 Sneddon, I. N., and Srivastav, R. P., "The Stress Field in the Vicinity of a Griffith Crack in a Strip of Finite Width," *International Journal of Engineering Science*, Vol. 9, 1971, pp. 479–488.

6 Thau, S. A., and Lu, T. H., "Transient Stress-Intensity Factors for a Finite Crack in an Elastic Solid Caused by a Dilatational Wave," *International Journal of Solids and Structures*, Vol. 7, 1971, pp. 731–750.

Author's Closure

1 The author's method for solving the dual integral equations is a very simplified one. The crack surface displacement is directly expanded in a series which is automatically zero outside the crack. Therefore, the integral equations can be immediately solved by the Schmidt method. The quality of the solution is equivalent to those obtained in [1, 2, 4, 5]. This method is easily applicable for solving more difficult problems which concern rectangular-shaped crack(s) in an infinite elastic body or in a semispace [7–11]. It may be meaningless to publish the paper if it is only to say that the same problem has been reworked. However, it can be considered that the publication of this paper is justified on the grounds that the application of such a simple method is successful in solving such a dynamic crack problem.

2 The author agrees in principle with Dr. Chen's second point. The word "insist" which was used was improper and the author is sorry for this. The difference between the result in [6] and that in [1] for $a/h = 0.0$ is not of importance from an engineering viewpoint, and at the same time, it is still desired to lessen such a difference, if it can be done, in spite of the numerical approach to the problem.

References

7 Itou, S., "Dynamic Stress Concentration Around a Rectangular Crack in an Infinite Elastic Medium," *Zeitschrift für Angewandte Mathematik und Mechanik*, Band 60, 1980, pp. 317–322.

8 Itou, S., "Dynamic Stress Concentration Around Two Rectangular Cracks in an Infinite Elastic Medium (in Japanese)," *Transactions of the Japan Society of Mechanical Engineers*, Vol. 46, 1980, pp. 575–583.

9 Itou, S., "Transient Analysis of Stress Waves Around a Rectangular Crack Under Impact Load," ASME JOURNAL OF APPLIED MECHANICS, Vol. 47, 1980, pp. 958–959.

10 Itou, S., "Dynamic Stress Concentration Around Four Rectangular Cracks in an Infinite Elastic Medium (in Japanese)," *Transactions of the Japan Society of Mechanical Engineers*, Vol. 47, 1981, pp. 492–500.

11 Itou, S., "Dynamic Stress-Intensity Factors Around a Rectangular Crack in a Half Space Under Impact Load," in contribution.

On the Nonbuckling of a Circular Ring Under "Wrapping" Loading[1]

A. Kornecki.[2] The interesting result that circular rings under wrapping-type loads will not buckle was noted among others by Feodosyev [1]. Independently, and exhaustive analysis of this problem in the framework of the nonlinear theory of elastic stability was made by Oery [2].

References

1 Feodosyev, V. I., *Selected Problems in Strength of Materials* (translated from Russian), published by "Mir," Moscow, 1966.

2 Oery, H., "The Load Capacity of a Thin-Walled Circular Ring Under Wrapping Loading." (in German), PhD dissertation, published by Munich Technical University, 1976, 83 pages.

A Nonlinear Theory of Viscoelasticity for Application to Elastomers[1]

K. N. Morman.[2] Dr. Christensen refers to his constitutive equation, equation (22C)[3] as "... the form sought as the simplest, physically, meaningful generalization of the kinetic theory of rubber elasticity to model viscoelastic effects." The present author wishes to take issue with this statement and present arguments that the constitutive relation best suited to Dr. Christensen's statement is

$$\sigma_{ij} = -p\delta_{ij} + x_{i,K}x_{j,L}\left[g_0\delta_{KL} + \int_0^t \bar{g}_1(t-\tau)(\delta_{KM}X_{L,k}X_{N,k} + \delta_{LM}X_{K,k}X_{N,k})\frac{\partial E_{MN}(\tau)}{\partial\tau}d\tau\right] \quad (1)$$

where the relaxation modulus, $\bar{g}_1(t)$ is to be distinguished from $g_1(t)$ appearing in equation (22C). Equation (1) may be obtained from the finite linear viscoelasticity theory[4] by neglecting all relaxation functions except $\phi_1(t)$ which involves the integral expression

$$\int_{-\infty}^t \phi_1(t-\tau)[B_{ik}\dot{C}^t_{kj}(\tau) + \dot{C}^t_{ik}(\tau)B_{kj}]d\tau \quad (2)$$

where $B_{ij} = x_{i,K}x_{j,K}$ and $C^t_{ij}(\tau) = x_{k,i}(\tau)x_{k,j}$, and by setting $\phi_1(t) = \bar{g}_1(t)$.

Dr. Christensen's requirement that "Under a sufficiently slow process, the viscoelasticity theory must reduce to the kinetic theory of rubber elasticity ..." is easily satisfied by requiring

$$\bar{g}_1(\infty) \equiv 0. \quad (3)$$

However, the present author does not believe that this requirement is sufficiently strong to justify truncation of the Rivlin/Green expansion represented by equation (3C) to obtain equation (22C) i.e.,

$$\sigma_{ij} = -p\delta_{ij} + x_{i,K}X_{j,L}\left[g_0\delta_{KL} + \int_0^t g_1(t-\tau)\frac{\partial E_{KL}(\tau)}{\partial\tau}d\tau\right] \quad (22C)$$

A more rigorous requirement should have the viscoelasticity theory reduce to the kinetic theory of rubber elasticity in both the extremes of very rapid processes and sufficiently slow processes. That the latter requirement is readily satisfied by equation (1) is seen by considering the single-step stress relaxation process which yields:

For Multiaxial Configurations

$$\sigma_{ij} = -p\delta_{ij} + x^0_{i,K}x^0_{j,L}\delta_{KL}\mu(t) \quad (4)$$

[1] By T. J. Lardner, and published in the December, 1980, issue of the ASME JOURNAL OF APPLIED MECHANICS, Vol. 47, p. 973.

[2] Visiting Professor, Department of Civil Engineering, University of Delaware, Newark, Del. 19711; on leave from Technion, Israel Institute of Technology, Haifa, Israel.

[1] By R. M. Christensen, and published in the December, 1980, issue of the ASME JOURNAL OF APPLIED MECHANICS, Vol. 47, No. 4, pp. 762–768.

[2] Supervisor, Ford Motor Co., Engineering Computer Center, 20000 Rotunda Drive, Dearborn, Mich. 48121.

[3] Equation or figure numbers followed by C refer to those in footnote one.

[4] Coleman B. D., and Noll, W., *Rev. Mod. Phys.*, Vol. 33, 1961, p. 239; erratum, ibid, Vol. 36, 1964, p. 1103.

fast transition. Because of the numerical nature of the solutions, the discusser does not think this point can be settled at this time.

References

1 Chen, E. P., "Sudden Appearance of a Crack in a Stretched Finite Strip," ASME JOURNAL OF APPLIED MECHANICS, Vol. 45, 1978, pp. 277–280.

2 Sih, G. C., and Loeber, J. F., "Wave Propagation in an Elastic Solid With a Line of Discontinuity or Finite Crack," *Quarterly of Applied Mathematics*, Vol. 27, 1969, pp. 193–213.

3 Kassir, M. K., and Sih, G. C., *Three-Dimensional Crack Problems*, Noordhoff International Publishing, Leyden, The Netherlands, 1975.

4 Erdogan, F., Gupta, G. D., and Cook, T. S., "Numerical Solution of Singular Integral Equations," *Mechanics of Fracture*, Vol. 1, ed., Sih, G. C., Noordhoff International Publishing, Leyden, The Netherlands, 1973, pp. 368–425.

5 Sneddon, I. N., and Srivastav, R. P., "The Stress Field in the Vicinity of a Griffith Crack in a Strip of Finite Width," *International Journal of Engineering Science*, Vol. 9, 1971, pp. 479–488.

6 Thau, S. A., and Lu, T. H., "Transient Stress-Intensity Factors for a Finite Crack in an Elastic Solid Caused by a Dilatational Wave," *International Journal of Solids and Structures*, Vol. 7, 1971, pp. 731–750.

Author's Closure

1 The author's method for solving the dual integral equations is a very simplified one. The crack surface displacement is directly expanded in a series which is automatically zero outside the crack. Therefore, the integral equations can be immediately solved by the Schmidt method. The quality of the solution is equivalent to those obtained in [1, 2, 4, 5]. This method is easily applicable for solving more difficult problems which concern rectangular-shaped crack(s) in an infinite elastic body or in a semispace [7–11]. It may be meaningless to publish the paper if it is only to say that the same problem has been reworked. However, it can be considered that the publication of this paper is justified on the grounds that the application of such a simple method is successful in solving such a dynamic crack problem.

2 The author agrees in principle with Dr. Chen's second point. The word "insist" which was used was improper and the author is sorry for this. The difference between the result in [6] and that in [1] for $a/h = 0.0$ is not of importance from an engineering viewpoint, and at the same time, it is still desired to lessen such a difference, if it can be done, in spite of the numerical approach to the problem.

References

7 Itou, S., "Dynamic Stress Concentration Around a Rectangular Crack in an Infinite Elastic Medium," *Zeitschrift für Angewandte Mathematik und Mechanik*, Band 60, 1980, pp. 317–322.

8 Itou, S., "Dynamic Stress Concentration Around Two Rectangular Cracks in an Infinite Elastic Medium (in Japanese)," *Transactions of the Japan Society of Mechanical Engineers*, Vol. 46, 1980, pp. 575–583.

9 Itou, S., "Transient Analysis of Stress Waves Around a Rectangular Crack Under Impact Load," ASME JOURNAL OF APPLIED MECHANICS, Vol. 47, 1980, pp. 958–959.

10 Itou, S., "Dynamic Stress Concentration Around Four Rectangular Cracks in an Infinite Elastic Medium (in Japanese)," *Transactions of the Japan Society of Mechanical Engineers*, Vol. 47, 1981, pp. 492–500.

11 Itou, S., "Dynamic Stress-Intensity Factors Around a Rectangular Crack in a Half Space Under Impact Load," in contribution.

On the Nonbuckling of a Circular Ring Under "Wrapping" Loading[1]

A. Kornecki.[2] The interesting result that circular rings under wrapping-type loads will not buckle was noted among others by Feodosyev [1]. Independently, and exhaustive analysis of this problem in the framework of the nonlinear theory of elastic stability was made by Oery [2].

References

1 Feodosyev, V. I., *Selected Problems in Strength of Materials* (translated from Russian), published by "Mir," Moscow, 1966.

2 Oery, H., "The Load Capacity of a Thin-Walled Circular Ring Under Wrapping Loading." (in German), PhD dissertation, published by Munich Technical University, 1976, 83 pages.

A Nonlinear Theory of Viscoelasticity for Application to Elastomers[1]

K. N. Morman.[2] Dr. Christensen refers to his constitutive equation, equation (22C)[3] as "... the form sought as the simplest, physically, meaningful generalization of the kinetic theory of rubber elasticity to model viscoelastic effects." The present author wishes to take issue with this statement and present arguments that the constitutive relation best suited to Dr. Christensen's statement is

$$\sigma_{ij} = -p\delta_{ij} + x_{i,K}x_{j,L}\left[g_0\delta_{KL} + \int_0^t \bar{g}_1(t-\tau)(\delta_{KM}X_{L,k}X_{N,k} + \delta_{LM}X_{K,k}X_{N,k})\frac{\partial E_{MN}(\tau)}{\partial\tau}d\tau\right] \quad (1)$$

where the relaxation modulus, $\bar{g}_1(t)$ is to be distinguished from $g_1(t)$ appearing in equation (22C). Equation (1) may be obtained from the finite linear viscoelasticity theory[4] by neglecting all relaxation functions except $\phi_1(t)$ which involves the integral expression

$$\int_{-\infty}^t \phi_1(t-\tau)[B_{ik}\dot{C}^t_{kj}(\tau) + \dot{C}^t_{ik}(\tau)B_{kj}]d\tau \quad (2)$$

where $B_{ij} = x_{i,K}x_{j,K}$ and $C^t_{ij}(\tau) = x_{k,i}(\tau)x_{k,j}$, and by setting $\phi_1(t) = \bar{g}_1(t)$.

Dr. Christensen's requirement that "Under a sufficiently slow process, the viscoelasticity theory must reduce to the kinetic theory of rubber elasticity ..." is easily satisfied by requiring

$$\bar{g}_1(\infty) \equiv 0. \quad (3)$$

However, the present author does not believe that this requirement is sufficiently strong to justify truncation of the Rivlin/Green expansion represented by equation (3C) to obtain equation (22C) i.e.,

$$\sigma_{ij} = -p\delta_{ij} + x_{i,K}X_{j,L}\left[g_0\delta_{KL} + \int_0^t g_1(t-\tau)\frac{\partial E_{KL}(\tau)}{\partial\tau}d\tau\right] \quad (22C)$$

A more rigorous requirement should have the viscoelasticity theory reduce to the kinetic theory of rubber elasticity in both the extremes of very rapid processes and sufficiently slow processes. That the latter requirement is readily satisfied by equation (1) is seen by considering the single-step stress relaxation process which yields:

For Multiaxial Configurations

$$\sigma_{ij} = -p\delta_{ij} + x^0_{i,K}x^0_{j,L}\delta_{KL}\mu(t) \quad (4)$$

---

[1] By T. J. Lardner, and published in the December, 1980, issue of the ASME JOURNAL OF APPLIED MECHANICS, Vol. 47, p. 973.

[2] Visiting Professor, Department of Civil Engineering, University of Delaware, Newark, Del. 19711; on leave from Technion, Israel Institute of Technology, Haifa, Israel.

[1] By R. M. Christensen, and published in the December, 1980, issue of the ASME JOURNAL OF APPLIED MECHANICS, Vol. 47, No. 4, pp. 762–768.

[2] Supervisor, Ford Motor Co., Engineering Computer Center, 20000 Rotunda Drive, Dearborn, Mich. 48121.

[3] Equation or figure numbers followed by C refer to those in footnote one.

[4] Coleman B. D., and Noll, W., *Rev. Mod. Phys.*, Vol. 33, 1961, p. 239; erratum, ibid, Vol. 36, 1964, p. 1103.

Journal of Applied Mechanics

Book Reviews

B.M. Fraeijs de Veubeke Memorial Volume of Selected Papers. Edited by M. Geradin. Published by Sijthoff & Noordhoff, The Netherlands. 1980. Pages xvii-752. Price $57.50.

REVIEWED BY R. D. COOK[1]

This volume of papers by Prof. Fraeijs de Veubeke was prepared by several of his colleagues. Of his some 80 varied publications, the following 17 are included: *Influence of Internal Damping on Aircraft Resonance*, *Upper and Lower Bounds in Matrix Structural Analysis*, *Displacement and Equilibrium Models in the Finite Element Method*, *Variational Principles in Fluid Mechanics*, *Strain-Energy Bounds in Finite-Element Analysis by Slab Analogy*, *A Conforming Finite Element for Plate Bending*, *An Equilibrium Model for Plate Bending*, *The Theoretical Design Laws of Warping-Free Multicellular Box Beams*, *The Dual Principles of Elastodynamics: Finite-Element Applications*, *Nonlinear Shell Theory*, *Dual Analysis for Heat Conduction Problems by Finite Elements*, *A New Variational Principle for Finite-Elastic Displacements*, *Matrix Structural Analysis*, *Diffusive Equilibrium Models*, *Variational Principles and the Patch Test*, *Stress Function Approach*, and *The Dynamics of Flexible Bodies*.

The collection centers around the development of variational methods in continuum mechanics and their adaptation to finite-element methods. The papers are all in English. They have been retyped from journals in camera-ready format.

The appeal of the book is to those who study fundamentals and the theory of computational methods. The papers are clearly written and are original and significant contributions.

Geophysical Fluid Dynamics. By J. Pedlosky. Springer-Verlag, New York, Heidelberg, Berlin. 1979. Pages xii-624, Price $39.80.

REVIEWED BY S. LEIBOVICH[2]

Geophysical fluid mechanics, the study of fluid motions occurring naturally in the earth's interior, oceans, and atmosphere, emerged as a distinct and vital subject in the 1960's. The span of the scales of interest to the field is vast, ranging from centimeters such as capillary waves, to those on a planetary scale.

Professor Pedlosky's book rose from a five quarter series of courses at the University of Chicago, and covers the theory of those large-scale phenomena of importance to the oceans and atmosphere. These are motions characterized by, usually dominated by, the effects of coriolis acceleration, and ultimately driven by buoyancy created by differential heating. The physics is complex, and the book builds the theory by first describing the effects of rotation on a fluid of constant density. This part of the theory, to which half the book is devoted, is itself rich in content; one encounters an impressive array of wave phenomena (Poincare, Kelvin, and Rossby waves), nearly frictionless flows (in the geostrophic approximation) controlled by boundary (Ekman) layers, and a wide variety of boundary layer/shear layer effects (including western intensification of currents such as the Gulf Stream). Baroclinic effects—those due to density variations—are added in the second half of the book which includes a substantial chapter on stability. The author derives the governing equations, discusses the relevant scaling assumptions, and educes models for each class of effects with care and skill.

I particularly like the author's insistence on physical interpretations and explanations of equations and their solutions, and useful insights abound. Almost all of the theory is linear—although resonant wave interaction is considered and there are occasional glimpses of other nonlinear effects. Perhaps this is appropriate for a beginning series of courses, but believe it is necessary to discuss the limitations of linear theory more explicitly.

The book is apparently intended to serve as a textbook for a series of graduate courses. It is unfortunate that the author elected not to include exercises. This is a significant detriment to its use as a textbook. Nevertheless, the book is the first available introduction to a subject which, until now, has been scattered in the meteorological and oceanographical literature. Its systematic exposition by Professor Pedlosky, who has made important contributions to the development of geophysical fluid dynamics, will make the subject much more accessible to those trained in mechanics, and is heartily welcomed.

Methoden der analytischen Störungsrechnung und ihre Anwendunge. By U. Kirchgraber and E. Stiefel. Vol. 44 of the series *Leitfäden der angewandten Mathematik und Mechanik*. B. G. Teubner. Stuttgart. 1978. pp. viii–294.

REVIEWED BY W. S. LOUD[3]

The method of averaging with systems of ordinary differential equations has many areas of application in mechanics. Because of this, the present book is a welcome addition to the literature on the subject. The book is written as a "handbook" on the method of averaging, and as such it succeeds very well. It is very definitely aimed at an applications-oriented audience, as is shown by two important features. Numerous, often complicated, examples are discussed in considerable detail. The necessary mathematical aspects are presented in a simple, clear, and insightful manner. Unless the German language is an insurmountable obstacle, this book should prove to be a very useful reference for perturbation techniques based on the method of averaging. The reviewer is very pleased to have this book in his library.

The book consists of an introduction and four chapters. The introduction gives an overview of the contents along with several examples and a description of the method of averaging.

---

[1] University of Wisconsin, College of Engineering, Madison, Wisc. 53706.

[2] Professor, Sibley School of Mech. & Aero. Engineering, Cornell University, Ithaca, N. Y. 14853.

[3] Professor, School of Mathematics, University of Minnesota, Minneapolis, Minn. 55455.

Chapter I is a necessary prerequisite to the rest of the book. It is a development of the method of averaging based on Lie series, and introduces concepts and notations used throughout the remaining chapters. The presentation is extremely clear, and every step is illustrated by examples.

Chapter II is a discussion of several important applications, including problems of gyroscopes, satellites, and the bifurcation of periodic solutions (Hopf bifurcation). The mechanical examples are carried out in great detail with very helpful explanations. A two-cell Turing model is studied to illustrate bifurcation.

Chapter III is a further development of the general formal aspects of perturbation theory and the method of averaging.

Chapter IV gives the mathematical foundation of the method of averaging. Error estimates are obtained for both a finite time interval and an infinite time interval. As applications domains of attraction of stable solutions, bifurcations, and an error estimate with Lajapunov functions are discussed. The concept of invariant manifolds is introduced. The final section deals with invariant manifolds for Hamiltonian systems and the twist theorem. The authors have attempted to present this theory in a simple manner to permit the reader to perceive the ideas without unnecessary mathematical sophistication.

At the end if each chapter there is a discussion with references to relevant literature both for further mathematical developments and for other applications. There is a bibliography of about 140 items.

In conclusion, this is a well-conceived, clearly written book with a strong emphasis on applications. It should prove a useful addition to the reference library of anyone working in theoretical mechanics.

Mechanical Properties at High Rates of Strain. 1979. Proceedings of the Second Conference on the Mechanical Properties of Materials at High Rates of Strain. Held in Oxford, March 28–30, 1979. Edited by J. Harding. Conference Series Number 47, The Institute of Physics, Bristol and London. 1980. Pages ix-409. Price $90.

REVIEWED BY L. E. MALVERN[4]

This volume contains the four invited and 33 contributed papers presented at the conference. The book is divided into four chapters, each introduced by an invited lecture which gives some idea of the state of the art in the area without purporting to be a general survey. The volume as a whole gives a good account of developments since the first Oxford Conference in 1974. Space limitations preclude even listing all the authors or titles. Selections which follow reflect the reviewer's interest.

Chapter 1 has two parts captioned "Testing techniques" and "Material Behaviour." The opening paper was to have been given by Dr. J. D. Campbell, late Reader in Engineering Science at Oxford and one of the principal organizers of the conferences, whose untimely death in the autumn of 1978 came as a great shock to his many friends and colleagues. J. Duffy gave the opening paper as the "J. D. Campbell Memorial Lecture: Testing Techniques and Material Behavior at High Rates of Strain." A tribute to Campbell's diverse contributions was followed by an excellent discussion of recent developments in the use of the Kolsky apparatus or split Hopkinson's bar, both in the compressional form introduced by Kolsky in 1949 and in the torsional bar form developed by Campbell and his associates. Special attention was given to jump tests in which a sudden change in strain rate is introduced with the aim of separating instantaneous rate effects from rate-history effects.

D. A. Gorham described a miniaturized modified Hopkinson bar capable of testing strong materials at rates up to $10^5\ s^{-1}$. Other papers discussed biaxial testing and superimposed hydrostatic pressure. Material behavior papers included one on localization of plastic flow in tubes under dynamic torsion and one on an ultrasonic method of detecting dislocation behavior. Analytical and computational representations were included in some papers, as well as experimental characterization in others.

Chapter 2: "Wave Propagation Effects and Fracture" was introduced by R. J. Clifton with a lucid account of disagreement between theory and experiment in two types of plate impacts. Most of the papers in this chapter were concerned with dynamic fracture, including crack initiation, interference optical measurements of large deformations at the tip of a running crack in a glassy thermoplastic, and metallurgical aspects.

Chapter 3: "Applications" was introduced by W. Johnson, who gave a dynamic survey of topics including demolition, machining, extrusion, superplastic forming and metal powder compaction. Other applications papers discussed machining, extrusion, explosive forming, and explosive welding.

The editor concluded that, since the previous conference, progress has been made on several fronts, including measurement techniques and experimental characterization of a wider class of materials, "while, in studies of more fundamental aspects of material behavior, experiments involving sudden changes in strain rate are being increasingly used to develop constitutive equations involving internal state variables and to obtain a correlation between microscopic mechanisms and the macroscopic response."

This book will be a valuable reference for researchers on dynamic mechanical properties.

Structural Control. By H. H. E. Leipholz (editor). North-Holland SM Publications, Amsterdam and New York. 1980. Pages xv–810. Price $87.75.

REVIEWED BY T. T. SOONG[5]

Structural Control is a collection of papers presented at the International IUTAM Symposium on Structural Control held at the University of Waterloo in June, 1979. According to Leipholz, Chairman of the organization committee and Editor of this volume, the aim of the Symposium was to provide an opportunity for exchange of ideas, data, and information among workers in the following three groups.

1 Researchers concerned with the fundamentals of control and optimization theory.

2 Researchers and engineers involved in the application of control and optimization theory to industrial processes and aerospace structures.

3 Researchers and engineers interested and active in the application of control theory to large civil engineering structures.

While the Symposium participants did represent a good mix of these three groups, the dominant theme was clearly civil engineering structural control. Indeed, out of 43 papers included in this book, the authors had civil engineering structures in mind in over 30 of them. And, in this respect, the organization committee and the editor are to be congratulated on providing a comprehensive overview of civil engineering structural control, an emerging and exciting area of research, and an authoritative account of current work and, more important, current thinking on this research topic.

By and large, research activities in civil engineering structural control are concerned with the possible use of control mechanisms for the purpose of reducing vibration levels in tall buildings, bridges,

[4] Professor of Engineering Sciences, University of Florida, Gainesville, Fla. 32611; also Associate Editor, ASME JOURNAL OF APPLIED MECHANICS, Mem. ASME.

[5] Professor of Civil Engineering, State University of New York at Buffalo, Buffalo, N.Y. 14214.

ERRATA

Erratum on "Some Considerations on Thermal Shock Problem in a Plate," by Y. Takeuti and T. Furukawa, and published in the March, 1981, issue of the ASME JOURNAL OF APPLIED MECHANICS, Vol. 48, pp. 113–118.

Table 1 should read 3.74×10^{-16} under the column heading "Mild steel," 2.16×10^{-14} under the column heading "Aluminum," and 5.95×10^{-14} under the last column heading "Copper."